Studying Turbulence Using Numerical Simulation Databases - VII

Proceedings of the 1998 Summer Program

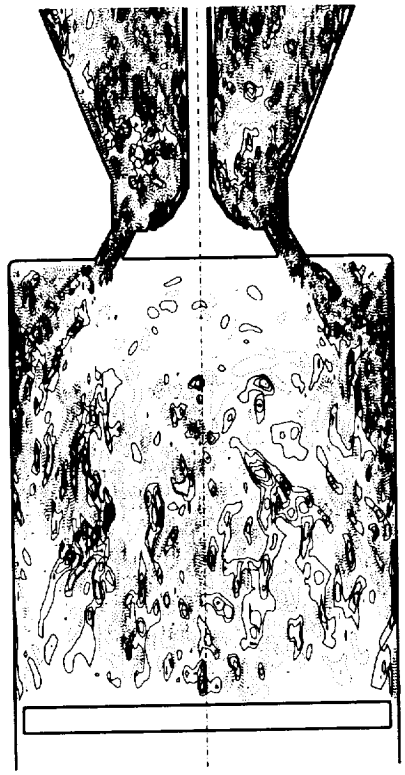

Center for Turbulence Research

November 1998

Ames Research Center

Stanford University

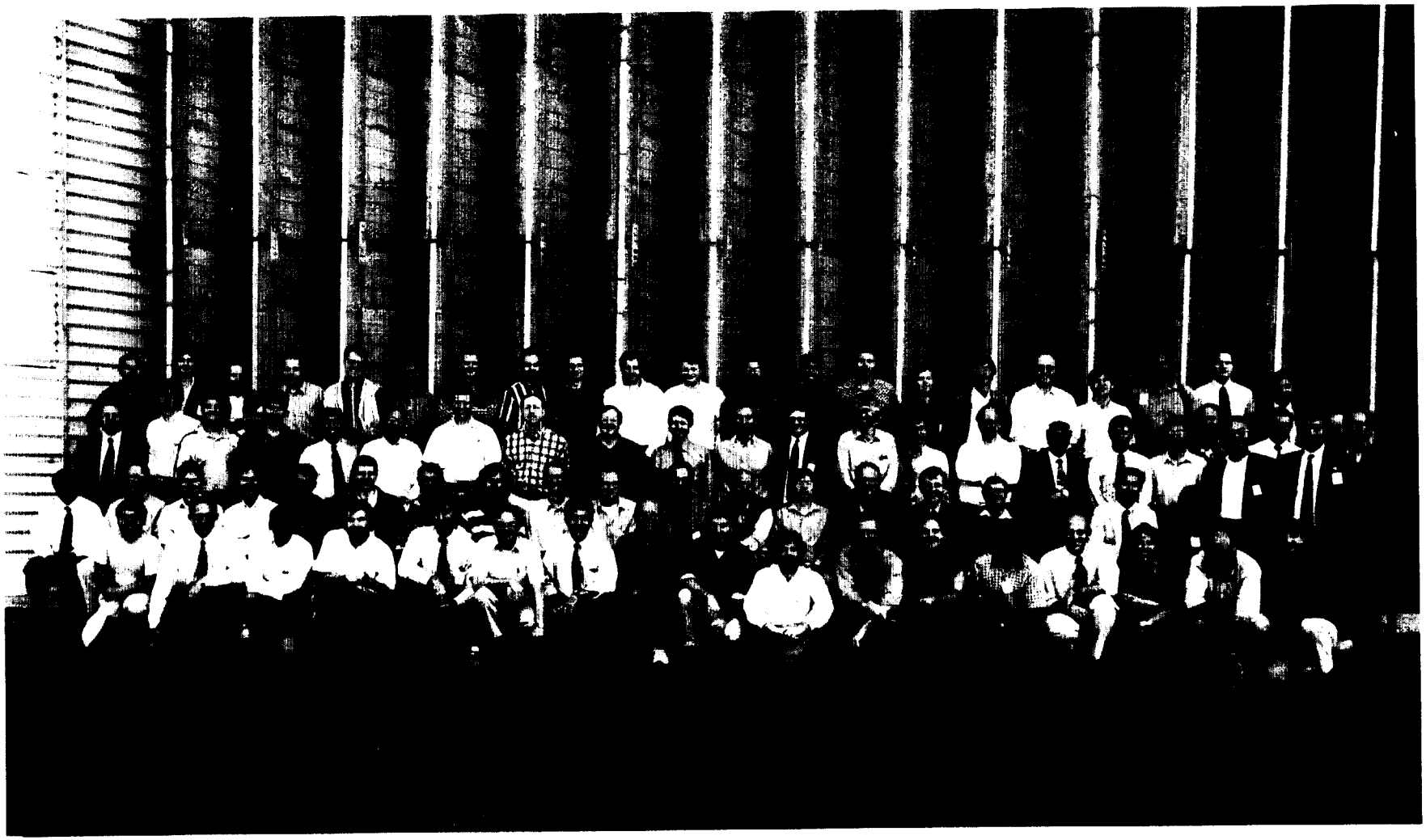

CONTENTS

Preface

The Seventh Summer Program of the Center for Turbulence Research took place in the four-week period, July 5 to July 31, 1998. This was the largest CTR Summer Program to date, involving thirty-six participants from the U. S. and nine other countries. Thirty-one Stanford and NASA-Ames staff members facilitated and contributed to most of the Summer projects. A new feature, and perhaps a preview of the future programs, was that many of the projects were executed on non-NASA computers. These included supercomputers located in Europe as well as those operated by the Departments of Defense and Energy in the United States. In addition, several simulation programs developed by the visiting participants at their home institutions were used. Another new feature was the prevalence of laptop personal computers which were used by several participants to carry out some of the work that in the past were performed on desk-top workstations. We expect these trends to continue as computing power is enhanced and as more researchers (many of whom CTR alumni) use numerical simulations to study turbulent flows. CTR's main role continues to be in providing a forum for the study of turbulence for engineering analysis and in facilitating intellectual exchange among the leading researchers in the field.

Once again the combustion group was the largest. Turbulent combustion has enjoyed remarkable progress in using simulations to address increasingly complex and practically more relevant questions. The combustion group's studies included such challenging topics as fuel evaporation, soot chemistry, and thermonuclear reactions. The latter study was one of three projects related to the Department of Energy's ASCI Program (www.llnl.gov/asci); the other two (rocket propulsion and fire safety) were carried out in the turbulence modeling group. The flow control and acoustics group demonstrated a successful application of the so-called evolution algorithms which actually led to a previously unknown forcing strategy for jets yielding increased spreading rate. A very efficient algorithm for flow in complex geometries with moving boundaries based on the immersed boundary forcing technique was tested with very encouraging results. Also a new strategy for the destruction of aircraft trailing vortices was introduced and tested. The Reynolds Averaged Modeling (RANS) group demonstrated that the elliptic relaxation concept for RANS calculations is also applicable to transonic flows with shocks; however, prediction of laminar/turbulent transition remains an important pacing item. A large fraction of the LES effort was devoted to the development and testing of a new algorithmic procedure (as opposed to phenomenological model) for subgrid scale modeling based on regularized de-filtering of the flow variables. This appears to be a very promising approach, and a significant effort is currently underway to assess its robustness in high Reynolds number flows and in conjunction with numerical methods for complex flows.

As part of the Summer Program two review tutorials were given on *Turbulent structures in hydrocarbon pool fires* (Sheldon Tieszen), and *Turbulent combustion*

modeling: from RANS to LES via DNS (Luc Vervisch); and two seminars entitled *Assessment of turbulence models for engineering applications* (Paul Durbin) and *Subgrid-scale modeling for non-premixed, turbulent reacting flows* (James Riley) were presented. A number of colleagues from universities, government agencies, and industry attended the final presentations of the participants on July 31 and participated in the discussions.

There are twenty-six papers in this volume grouped in five areas. Each group is preceded with an overview by its coordinator. Early reporting of twelve of the projects occurred at the Forty-Ninth Meeting of the Division of Fluid Dynamics of the American Physical Society in Philadelphia, November 22-24, 1998.

Thanks are due to Debra Spinks for her diligent efforts in the organization of the Program and compilation of this report. Her efforts in the administrative planning and operation of the Summer Program is very much appreciated.

Parviz Moin
William C. Reynolds

The combustion group

The 1998 Combustion group of the CTR summer program gathered more than twenty scientists to work on seven projects. Summer combustion programs are evolving rapidly from one year to another, exploring new fields of research in many cases. In 1998, new tools were developed and tested while new applications fields for existing tools were opened.

The main new tool studied by three groups in 1998 was Large Eddy Simulation (LES) for reacting flows. Even though it is obvious that LES will be an important tool to both study combustion on a fundamental level and address practical applications in the near future, the status of LES for combustion is still far from mature. Multiple questions linked to the fundamentals of LES in reacting flows and to the practical feasibility of LES for such flows (in comparison with existing Reynolds-averaged formulations) remain open. During this program, the fundamental aspects of LES for combustion were studied for premixed, partially premixed, and diffusion flames. Cook and Bushe investigated one of the building blocks of all LES models for diffusion flames: the modeling of the scalar dissipation which measures the rate at which fuel and oxidizer are mixed by turbulence. Using existing CTR DNS data, they analyzed the validity of existing models. Trouvé and Vervisch also addressed a central problem for LES of diffusion flames: most LES of such flows are performed using infinitely fast chemistry assumptions which lead to nonphysical results in many cases. Relaxing this assumption is a necessary but complex task. Using DNS data, Trouvé and Vervisch developed a description of the ignition zones of turbulent diffusion flames and proposed modeling approaches for such simulations. In the field of premixed and partially premixed flames, Angelberger, Poinsot, Veynante, and Egolfopoulos focused on the development of simplified realistic chemistry and its coupling with LES. A thickened flame model based on DNS of flame vortex interactions was used to describe flame/turbulence interaction, and the final LES tool was shown to be efficient in computing flame transfer functions in combustion instabilities. The effect of pulsating equivalence ratio in lean flames was also investigated.

New topics were also studied using DNS codes coupled to particle solvers: Réveillon and Vervisch studied the importance of fuel vaporization on the variance of fuel mass fraction, which is a crucial quantity for turbulent combustion models. They showed that, in addition to fuel vapor, vaporizing droplets were also creating high levels of fuel vapor variance, which must be included in LES or RANS models. Along the same lines of research (coupling DNS solvers for gas with particle tracking codes), Smith, Oefelein, Ruetsch, and Ferziger studied the formation of reactive particles in a turbulent flow with a specific emphasis on soot formation, which is a key problem in multiple diffusion burners.

New practical questions were also addressed using existing tools: for example, the NTMIX CHEMKIN code, which can perform DNS with complex chemistry and transport, was used by Haworth, Cuenot, Poinsot, and Blint to study flame

propagation in direct injection engines. In these engines, gasoline is injected directly inside the combustion chamber so that the flame propagates into a highly stratified mixture, leading to multiple new fundamental challenges for combustion research. Haworth *et al.* performed the first DNS of such propagation phenomena using a 29 species chemical scheme for propane air flames.

Finally, totally new fields for CTR were studied this year: DNS tools developed for hydrocarbon flames at CTR were adapted by Niemeyer, Bushe, and Ruetsch to investigate flame propagation in thermonuclear flames. These flames have many common features with flames studied in the combustion community even though the parameter range and the chemical mechanisms differ by orders of magnitude. Using CTR DNS tools for such flames led to new insights into their physics and to an efficient interaction between two communities which do not meet often.

Being able to introduce more realistic chemistry into DNS and LES is one necessary ingredient of CFD for combustion. Interestingly, the collaboration between chemists and CFD experts was very intensive and fruitful in 1998: Bowman, Blint, and Egolfopoulos proposed and modified chemical schemes in direct interaction with DNS or LES scientists to find the best compromises. This iterative procedure demonstrated that the stiffness of these schemes may be decreased significantly while preserving accuracy simply by promoting an efficient interaction between chemistry experts and DNS/LES users.

Thierry Poinsot

Numerical simulation of turbulent propane-air combustion with non-homogeneous reactants: initial results

By D. Haworth,[1] B. Cuenot,[2] T. Poinsot,[3] AND R. Blint[1]

High-resolution two-dimensional numerical simulations have been initiated for premixed turbulent propane-air flames propagating into regions of non-homogeneous reactant stoichiometry. Simulations include complex chemical kinetics, realistic molecular transport, and fully resolved hydrodynamics (no turbulence model). Aerothermochemical conditions (pressure, temperature, stoichiometry, and turbulence velocity scale) approach those in an automotive gasoline direct-injection (GDI) engine at a low-speed, light-load operating condition. Initial results suggest that: 1) There is no leakage of the primary fuel (propane) behind an initial thin premixed heat-release zone. This 'primary premixed flame' can be described using a monotonic progress variable and laminar premixed flamelet concepts. 2) Following an initial transient, global heat release with non-homogeneous reactants is lower than with homogeneous reactants for the same overall reactant stoichiometry. Flame area (length) is greater with non-homogeneous reactants. 3) Beyond three-to-four flame thicknesses behind the primary flame, practically all hydrocarbon fuel has broken down into CO and H_2. 4) The rate of heat release in the 'secondary reaction zone' behind the primary premixed flame is governed by turbulent mixing and the kinetics of CO_2 production. Mixture-fraction-conditioned secondary heat release, CO, and CO_2 production rates are qualitatively similar to results from a first-order conditional-moment-closure (CMC) model; CMC gives poor results for H_2, H_2O, and radical species. Description of the secondary heat release using simple laminar diffusion flamelet concepts is problematic. 5) Computational considerations demand modifications to chemical mechanisms involving C_3H_7 and CH_3CO. Specific changes are proposed to strike a satisfactory balance between accuracy and computational efficiency over a broad range of reactant stoichiometry.

1. Introduction

Stratification of the in-cylinder fuel-air mixture has the potential to reduce significantly the fuel consumption of automotive reciprocating internal-combustion (IC) engines. As a result, both spark-ignition gasoline (Lai *et al.* 1997) and compression-ignition Diesel (Krieger *et al.* 1997) direct-injection engines currently are subjects

1 GM R&D Center, Warren, MI

2 Centre Européen de Recherche et de Formation Avancée en Calcul Scientifique, Toulouse

3 Institut de Mécanique des Fluides de Toulouse, Toulouse

of intense research. In a direct-injection engine, liquid fuel is injected directly into the combustion chamber to generate a highly non-homogeneous fuel/air/residual mixture at the time of ignition and flame propagation.

The motivation for the present research is to determine the effects of reactant stratification on turbulent flame propagation, and to incorporate this new understanding into turbulent combustion models. The application of interest is the gasoline direct-injection (GDI) engine. Specifically, we seek: 1) to validate or invalidate a conceptual framework initially adopted for modeling this combustion regime (Fig. 1); 2) to quantify differences in the primary heat release process between homogeneous and non-homogeneous reactants; and 3) to determine the chemical composition and heat-release rates for the fuel fragments and oxidizer that penetrate behind the primary heat-release zone.

The tool selected is high-fidelity numerical simulation including turbulence, complex chemical kinetics, and full multi-component molecular transport. Propane-air ($C_3H_8/O_2/N_2$ reactants) is the simplest hydrocarbon system that exhibits chemical behavior, laminar flame speeds and thicknesses, and extinction limits that are comparable to those of heavier paraffin fuels (Turns 1996). It is probably the smallest system from which quantitative information directly relevant to the oxidation of heavier liquid gasoline and Diesel fuels can be extracted, and is therefore an appropriate choice for this study.

In addition to addressing specific physics and modeling issues, this work also advances the state-of-the-art in 'direct' numerical simulation of turbulent combustion (*i.e.*, computations in which all spatial and temporal scales are resolved without filtering or turbulence modeling). Simulation is extended to detailed propane-air chemistry and transport and to high pressure and temperature reactants with extreme fuel-lean and fuel-rich stoichiometry. Propane-air chemical kinetics is based on a 29-species, 73-reaction mechanism originally published by Warnatz (1981) and subsequently modified and extended to IC-engine conditions by Blint (1988, 1991). Modifications to reaction steps involving C_3H_7 and CH_3CO are introduced for computational practicality. The chemical mechanism is implemented in the numerical code NTMIX-CHEMKIN (Baum 1994), which has been used in a number of earlier numerical turbulent combustion studies including hydrogen-oxygen flames (Baum *et al.* 1994) and methane-air systems (Hilka *et al.* 1995). The formulation is similar to that used by other researchers for turbulent hydrogen-air (Im *et al.* 1998) and methane-air (Gran *et al.* 1996; Chen & Im 1998) combustion. Earlier numerical studies of turbulent premixed flames with non-homogeneous reactants have used one-step irreversible chemistry (Poinsot *et al.* 1996; Hélie and Trouvé 1998) and have focused on the primary premixed burn. Here secondary reaction (heat release occurring behind the primary flame) is emphasized.

2. Stratified Turbulent Combustion in a GDI Engine

2.1 Combustion regime

Many of the combustion issues to be resolved in GDI automotive engines arise during low-speed light-load operation. At 2,000 r/min and 330 kPa NMEP (net

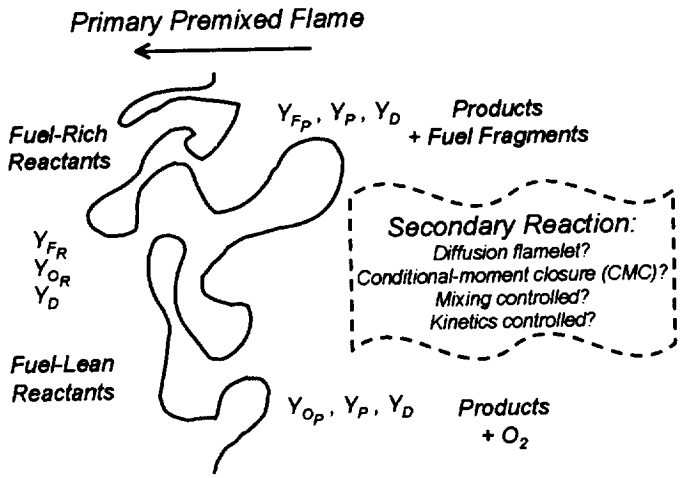

FIGURE 1. A schematic of turbulent flame propagation into a region of non-homogeneous reactants. The six mass fractions Y_α correspond to the six streams defined in the skeletal combustion model of Eqs. (1) and (2).

mean effective pressure), the in-cylinder fuel/air mixture is globally fuel-lean. A typical overall fuel-based equivalence ratio is $\Phi \approx 0.3$, where Φ is reactant fuel-to-air mass ratio, divided by the stoichiometric fuel-to-air mass ratio (Section 3.4). Moreover, the mixture remains highly non-homogeneous at the time of ignition. The local equivalence ratio ranges from below the lean flammability limit ($\Phi \approx 0.5$) to above the rich flammability limit ($\Phi \approx 3$) over a distance of less than one centimeter. The in-cylinder pressure and temperature at time of ignition are approximately four atmospheres and 700 K, respectively. Global turbulence rms velocity u'_T and integral length scale l_T are estimated based on a number of experimental measurements and computational studies (Haworth & Poinsot 1992): $u'_T \approx 6$ m/s and $l_T \approx$ 2-4 mm.

The mixture is ignited via spark discharge at a location where the local equivalence ratio is close to unity. At four atmospheres and 700 K, a stoichiometric premixed laminar flame propagates at about 1.6 m/s (the steady unstrained laminar flame speed, s_l^0) and has a thickness of about 0.1 mm (the laminar flame thickness based on maximum temperature gradient, δ_l^0). The initially healthy propagating turbulent premixed flame soon encounters fuel-rich and fuel-lean extremes in reactant stoichiometry.

The turbulent combustion regime is characterized by comparing turbulence (hydrodynamic) scales with laminar-flame (chemical) scales. Either velocity- and length-scale ratios or equivalently, Reynolds and Damköhler numbers, can be used. Values corresponding to this engine example are $u'_T/s_l^0 \approx 4$ and $l_T/\delta_l^0 \approx 20 - 40$ ($Re_T \equiv u'_T l_T/\nu \approx 600 - 1,200$ and $Da \equiv (l_T/u'_T)\cdot(s_l^0/\delta_l^0) \approx 5 - 10$). The parameter range corresponding to the rotational speeds, loads, and dilution levels of interest in IC engines is $u'_T/s_l^0 \approx 0.5 - 20$ and $l_T/\delta_l^0 \approx 3 - 50$ (Haworth & Poinsot 1992). It

is flame propagation into spatially varying reactant stoichiometry in this parameter range that we seek to understand and to model. Of primary interest is the rate at which chemical energy is converted to sensible energy (heat).

2.2 A conceptual framework for modeling heat release

We hypothesize a two-stage combustion process (Fig. 1). Fuel and oxidizer are well mixed at the molecular level in the unburned reactants, but the mixture composition is spatially non-uniform. Fuel and oxidizer initially react to release heat and form product in a primary premixed flame. Behind the premixed flame are hot combustion products. In locally fuel-rich regions, excess fuel or fuel fragments pass through the primary flame; in locally fuel-lean regions, there is excess oxidizer behind the primary flame. Secondary heat release occurs as the post-flame fuel (or fuel fragments) and oxidizer mix at the molecular level and react. A skeletal model is constructed to provide a conceptual basis for analysis (El Tahry 1997). We consider six 'streams:' (1) 'reactant' fuel Y_{F_R} - that is, fuel in front of the primary premixed flame; (2) reactant oxidizer Y_{O_R}; (3) 'product' fuel Y_{F_P}; (4) product oxidizer Y_{O_P}; (5) combustion product Y_P; and (6) inert diluent Y_D. We denote by b the stoichiometric mass of oxidizer per unit mass of fuel and by d the mass of diluent per unit mass of oxidizer. The overall reaction then can be represented on a per-unit-mass-of-fuel basis as,

$$F_R + b(O_R + dD) \rightarrow (1+b)P + bdD \; ; \; F_P + b(O_P + dD) \rightarrow (1+b)P + bdD \; . \quad (1)$$

The turbulent combustion model comprises partial differential equations (pde's) for the mean mass fractions $\langle Y_\alpha \rangle, \alpha = 1, \ldots, 6$. An equation for the mean enthalpy $\langle h \rangle$ and auxiliary relations (*e.g.*, fluid properties; Kee *et al.* 1983) also are needed. Here and in the following, angled brackets $\langle\ \rangle$ denote ensemble mean quantities. Pde's for the mean mass fractions have the form:

$$\begin{aligned}
&\frac{D\rho\langle Y_{F_R}\rangle}{Dt} = D_{F_R} - R_{F_R\rightarrow P} - S_{F_R\rightarrow F_P} \; ; \; \frac{D\rho\langle Y_{O_R}\rangle}{Dt} = D_{O_R} - bR_{F_R\rightarrow P} - S_{O_R\rightarrow O_P} \; ; \\
&\frac{D\rho\langle Y_{F_P}\rangle}{Dt} = D_{F_P} - R_{F_P\rightarrow P} + S_{F_R\rightarrow F_P} \; ; \; \frac{D\rho\langle Y_{O_P}\rangle}{Dt} = D_{O_P} - bR_{F_P\rightarrow P} + S_{O_R\rightarrow O_P} \; ; \\
&\frac{D\rho\langle Y_P\rangle}{Dt} = D_P + (1+b)R_{F_R\rightarrow P} + (1+b)R_{F_P\rightarrow P} \; ; \; \frac{D\rho\langle Y_D\rangle}{Dt} = D_D \; .
\end{aligned} \quad (2)$$

Here D/Dt denotes a material derivative following the mean fluid velocity and D_α is an effective (laminar-plus-turbulent) diffusion term. Reaction source terms $R_{F_R\rightarrow P}$ and $R_{F_P\rightarrow P}$ are the rates at which reactant and product fuel, respectively, are converted to combustion product. Terms $S_{F_R\rightarrow F_P}$ and $S_{O_R\rightarrow O_P}$ are the rates at which reactant fuel and oxidizer, respectively, are converted to product fuel and oxidizer without participating in the primary heat release. These account for locally fuel-rich or fuel-lean reactants, and phenomena including local quenching of the primary flame or vaporization of liquid fuel that occurs behind the primary flame.

2.3 Modeling issues

In this preliminary report, we limit our attention to the reaction source terms.

2.3.1 Primary heat release

We consider first the primary flame ($R_{F_R \to P}$). Here the goal is to determine to what extent existing models for homogeneous turbulent premixed combustion must be modified to account for reactant stratification (assuming, for the moment, that they remain appropriate at all). Laminar premixed flamelet models have proven successful in modeling the overall heat-release rate in homogeneous-charge IC engines. For example, a model developed by El Tahry (1990) has been applied to practical engine configurations (Khalighi *et al.* 1995). In this model, the reaction source term is written as $R_{F_R \to P} = \rho_u \langle Y_{F_R} \rangle \gamma \langle s_l / \delta_l \rangle$, where ρ_u is the unburned gas density, s_l is a laminar flame speed, δ_l is a laminar flame thickness, and γ is the probability of encountering an active reaction zone. Equivalently, one can write $R_{F_R \to P} = \rho_u \langle Y_{F_R} \rangle \langle s_l \rangle \Sigma$, where Σ is the flame surface-to-volume ratio (*e.g.*, Boudier *et al.* 1992).

Important issues include the time evolution of flame area (γ or Σ), the global heat release rate for non-homogeneous reactants compared to those for homogeneous reactants having the same overall stoichiometry, and determination of the extent to which the local structure of the primary premixed flame differs from that of a steady one-dimensional laminar flame under the same thermochemical conditions.

2.3.2 Secondary reaction

It is less clear how to proceed in modeling the secondary heat release ($R_{F_P \to P}$). One-step irreversible chemistry (fuel+oxidizer $\to$ product) implies that either fuel or oxidizer must be depleted on passing through the primary flame (Poinsot *et al.* 1996; Hélie & Trouvé 1998). However, in a hydrocarbon-air system, the fuel might be partially or completely broken down into smaller fragments, all species are present in non-zero concentrations behind the primary flame, and each species diffuses at a different rate—resulting, for example, in segregation of hydrogen-containing and carbon-containing species that originated in the fuel.

Important questions related to the secondary combustion include: Is there any leakage of fuel (propane) behind the primary flame? What is the composition of fuel fragments behind the primary flame? What is the rate-controlling process governing secondary heat release and what type of turbulent combustion model is most appropriate (*e.g.*, chemical-kinetics-controlled versus turbulent-mixing-controlled versus laminar-diffusion-flamelet versus conditional-moment-closure (CMC) models)?

3. The model problem

3.1 Governing equations and configuration

The system considered is a compressible multi-component reacting ideal-gas mixture. Principal equations express conservation of mass (mixture density ρ), linear momentum (mixture velocity $\underline{u}$), N_S chemical species (mass fractions Y_α, $\alpha = 1, \ldots, N_S$), and energy (total energy density e_t). Chemical production terms are

expressed in Arrhenius form, and species molecular transport is modeled using a multicomponent form of Fick's law. Soret and Dufour effects are not included. All fluid properties, molecular transport coefficients, and chemical production terms are computed using the CHEMKIN and TRANSPORT packages (Kee *et al.* 1980, 1983). The full system of governing equations and assumptions can be found in Baum (1994) and Baum *et al.* (1994).

Here the focus is on chemical reaction source terms. The pde governing the evolution of species mass fraction Y_α is,

$$\frac{\partial \rho Y_\alpha}{\partial t} + \frac{\partial \rho Y_\alpha u_j}{\partial x_j} = -\frac{\partial \rho Y_\alpha V_{\alpha j}}{\partial x_j} + W_\alpha \dot{\omega}_\alpha \ , \tag{3}$$

where $\dot{\omega}_\alpha$ is the molar chemical production rate of species α and W_α is its molecular weight. The quantity $V_{\alpha j}$ is the diffusion velocity (j^{th} Cartesian component) for species α. In terms of species production rates and formation enthalpies $\Delta h^0_{f\alpha}$, the heat-release rate $\dot{\omega}_Q$ (the rate of conversion from chemical to sensible enthalpy) is,

$$\dot{\omega}_Q = -\sum_{\alpha=1}^{N_S} \dot{\omega}_\alpha \Delta h^0_{f\alpha} \ . \tag{4}$$

All chemical source terms are specified functions of the local mixture composition and temperature (Section 3.2): $\dot{\omega}_\alpha = \dot{\omega}_\alpha(\underline{Y}, T)$; $\dot{\omega}_Q = \dot{\omega}_Q(\underline{Y}, T)$. The pressure is approximately uniform.

The governing equations are solved in a Cartesian frame of reference using sixth-order compact finite-differences (Lele 1992) for spatial derivatives and third-order Runge-Kutta time integration. Computational considerations preclude carrying out spatially three-dimensional simulations with realistic chemistry and transport in the parameter range of interest. The available options are: spatially two-dimensional computations with detailed chemistry and transport for hydrodynamic scales approaching relevant values; or spatially three-dimensional computations with simple chemistry and transport at lower Re and Da. To address the issues of interest here, we have chosen the former.

Calculations are initialized with reactants on one side of the computational domain and products on the other; these are separated by a stoichiometric planar laminar premixed flame. The initial flame is a steady one-dimensional solution to the full set of governing equations. Initially isotropic two-dimensional turbulence is prescribed using a two-parameter turbulence energy spectrum $E(k)$ (Haworth & Poinsot 1992). The parameters correspond to the initial rms turbulence velocity $u'_{T\,0}$ and to the wavenumber of the spectrum peak k_{max}. Here the product $\rho u'_{T\,0}$ is uniform through the flame, so that the rms turbulence level $u'_{T\,0}$ is higher in the hot burned products than in the cooler reactants. The initial turbulence integral length scale $l_{T\,0}$ corresponds to $l_{T\,0} \approx 0.3 \cdot \frac{2\pi}{k_{max}}$. On lateral boundaries, periodic conditions are enforced while non-reflecting boundary conditions are used on inflow/outflow boundaries.

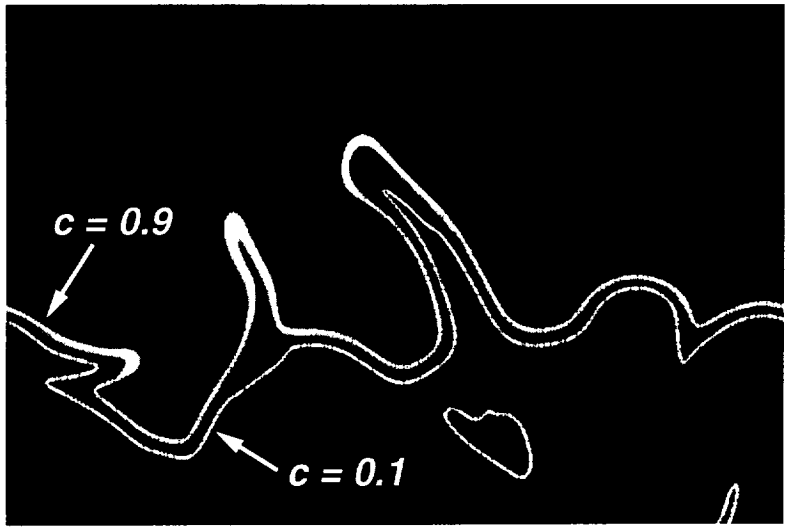

FIGURE 2. Computed two-dimensional heat-release field for homogeneous stoichiometric reactants (Table I) at time $t/\tau_f = 3.5$. Black corresponds to minimum heat release (0.0) and white to maximum (0.36). Iso-contours of reaction progress variable (white lines: $c = 0.1$ and $c = 0.9$, Eq. 8) are superposed. The $c = 0.9$ iso-contour is close to the peak heat release.

Reactant non-homogeneity is introduced by varying the mass fractions of C_3H_8, O_2, and N_2 in the reactants. This is done in a manner that maintains the same total quantity of fuel and oxidizer as for a baseline homogeneous stoichiometric case, and maintains a uniform ratio of N_2 to O_2 (uniform air composition). Here we consider a large-scale sinusoidal non-homogeneity where the variation in composition parallel to the initially planar flame (the periodic y direction) is of the form $\sin(2\pi y/L_y)$, L_y being the y-direction length of the computational domain. The equivalence ratio ranges from a minimum at $y = 0$ and $y = L_y$ to a maximum at $y = L_y/2$. The time required for the change in reactant stoichiometry to penetrate the primary premixed flame is estimated as,

$$\tau_f = 2\delta_l^0 \; / \; \left(s_l^0(1 + \rho_u/\rho_b)\right) \; . \tag{5}$$

Here ρ_u and ρ_b refer to the unburned- and burned-gas mass density, respectively. This chemical flame time accounts for the acceleration of gases as they pass from the cooler reactants to the hotter products. To explore secondary reaction, it is anticipated that one must integrate to times on the order of several τ_f's.

Key aerothermochemical parameters for the two cases considered in this report are summarized in Table I. Reactant composition, temperature, and pressure are selected to match the engine condition of Section 2.1. The initial rms turbulence level is within the range of interest in IC-engine combustion. However, the turbulence integral length scale is low by a factor of ten. This is, in part, a consequence of the small box size chosen for these initial runs. The computed heat-release field of Fig. 2 serves to illustrate the configuration.

3.2 Base propane-air mechanism

The base 29-species 73-reaction chemical mechanism (Warnatz 1981; Blint 1988, 1991) will be referred to as mechanism $M1$. Mechanism $M1$ has been validated against available experimental measurements of laminar flame speed for ambient-pressure-and-temperature reactants (Blint & Tsai 1998). It has been used to explore in-cylinder engine combustion issues including dilution (Blint 1988) and stretch (Blint 1991) effects, and has been used to generate a laminar flame library (Blint & Tsai 1998) that has been coupled with a turbulent combustion model similar to that of Section 2.2 and applied both to homogeneous and non-homogeneous spark-ignited combustion in practical engine configurations. For present purposes, nitrogen is treated as an inert diluent. In all computations, reactant air is defined on a volume basis as 21% O_2, 79% N_2 ($(Y_{N_2}/Y_{O_2})_{\text{reactants}} = 3.25$).

Table I. Parameters for initial $M2$ homogeneous-reactant and non-homogeneous-reactant cases. Pressure is four atmospheres, reactant temperature is 700 K, and the global reactant equivalence ratio is unity.

Case	L_x/n_x	L_y/n_y	Φ_{min}/Φ_{max}	$\frac{\tau_l}{\tau_{T0}}$	$\frac{u'_{T0}}{s^0_{l\,\Phi=1}}$	$\frac{l_{T0}}{\delta^0_{l\,\Phi=1}}$	Re_{T0}
Homogeneous	2 mm/301	3 mm/451	1.0/1.0	0.92	3.8	1.8	71
Non-homogeneous	2 mm/301	3 mm/451	0.0/4.0	0.92	3.8	1.8	71

3.3 Modified chemical mechanisms

The maximum allowable computational time step and mesh spacing are determined, respectively, by the shortest time and length scales encountered in solving the coupled set of governing pde's. In the absence of chemical reaction, the smallest hydrodynamic length scale to be resolved is the Kolmogorov turbulence microscale. In that case, the time step for the fully compressible numerical methodology is limited by a CFL condition based on the local sound speed: $\Delta t < \Delta x/a$, where $a = (kRT)^{1/2}$ ($k \equiv c_p/c_v$, the ratio of specific heats; R is the specific gas constant). Chemical reaction introduces additional time and length scales. For a stoichiometric four-atmosphere propane-air flame, mechanism $M1$ requires a computational time step that is nearly 1,000 times smaller than the CFL limit.

Clearly, a judicious reduction of the chemical mechanism is needed. A modified mechanism $M2$ incorporates two changes to $M1$ that together return the time-step limitation to a CFL condition: two of the rate-limiting species C_3H_7(N) and C_3H_7(I) are removed; and an equilibrium assumption is introduced for the remaining rate-limiting species CH_3CO. Rate coefficients in several reaction steps are adjusted accordingly.

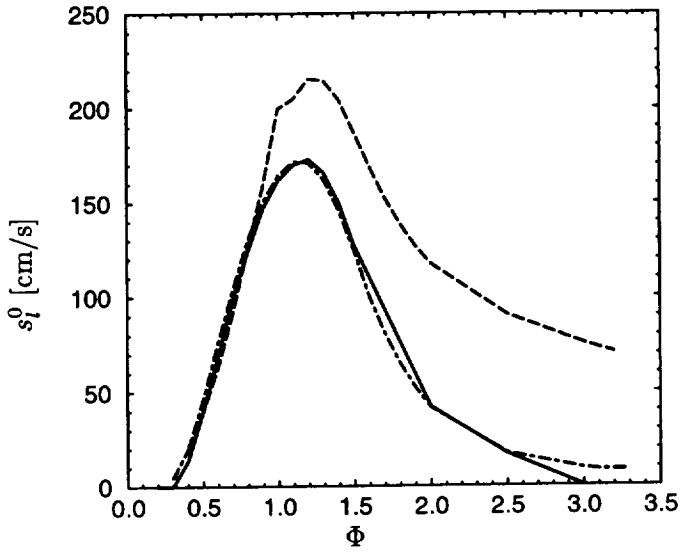

FIGURE 3. Computed variation of steady unstrained laminar flame speed s_l^0 with equivalence ratio Φ at four atmospheres for 700 K reactants. Results are shown for three versions of the propane-air chemical mechanism: —— $M1$; ---- $M2$; —-— $M3$.

The changes from $M1$ to $M2$ degrade the mechanism's performance on the fuel-rich side of stoichiometric. Fig. 3 shows computed steady unstrained one-dimensional laminar flame speed as a function of equivalence ratio for four-atmosphere, 700 K reactants. The two mechanisms behave similarly on the fuel-lean side of stoichiometric; $M2$'s peak laminar flame speed is 23% higher than $M1$'s; and on the fuel-rich side, $M2$'s decrease in flame speed with increasing equivalence ratio is too slow: burning remains robust even at $\Phi = 3$.

A third mechanism that attempts to address the shortcomings of $M2$ on the fuel-rich side is designated as $M3$. Mechanism $M3$ retains one isomer of C_3H_7 (C_3H_7(I)), and includes modified rate coefficients for several related reactions. The resulting flame-speed-versus-equivalence ratio behavior is practically identical to that of $M1$ (Fig. 3). Also, CH_3CO no longer introduces a time-step-limiting time scale. Unfortunately, while C_3H_7(I) is crucial to satisfactory fuel-rich behavior, it requires a time step that is about a factor of ten smaller than CFL.

At the time of this writing, work continues towards a well-balanced (accuracy versus computational efficiency) chemical mechanism, following along the lines of $M3$. In the meantime, preliminary turbulent simulations using $M2$ were initiated with the purpose of generating a 'first look' database for non-homogeneous turbulent propane-air flames. For these initial simulations, a 2 mm × 3 mm computational domain is discretized on a 301 × 451 node mesh (Table I). The computational time step is limited by a sound-speed CFL condition. In spite of the known shortcomings of $M2$, extreme fuel-lean and fuel-rich stoichiometry are included. This has been done in the spirit of generating large effects that can be readily discerned, and to facilitate diagnostics development.

3.4 Diagnostics

Global quantities and primary-premixed-flame-front quantities of interest have been introduced in the course of earlier numerical studies of propagating premixed turbulent flames (Haworth & Poinsot 1992; Baum 1994; Baum *et al.* 1994; Poinsot *et al.* 1996; Hélie & Trouvé 1998). Quantities related to specific secondary-combustion models will be defined in Section 5. Here we discuss two quantities that are particularly germane to mixed-mode (premixed/non-premixed) combustion: mixture fraction and progress variable.

3.4.1 Mixture fraction

A mixture fraction field $z = z(\underline{x}, t)$ in a reacting flow quantifies the local mass fraction of material that originated from the reactant fuel (versus oxidizer or diluent); it is particularly useful in the analysis and modeling of laminar and turbulent non-premixed systems (Turns 1996). Mixture fractions are defined in such a way that they do not depend directly on chemical reaction. That is, the transport equation for $z(\underline{x}, t)$ contains no chemical source term. Element mass fractions serve for this purpose. With subscript β referring to a chemical element (one of C or H here, as there is no O or N in the propane fuel), a mixture fraction z_β is defined as,

$$z_\beta \equiv \sum_{\alpha=1}^{N_S} n_{\beta\alpha} W_\beta Y_\alpha / W_\alpha \ . \tag{6}$$

Here $n_{\beta\alpha}$ is the number of atoms of element β in species α, and W_β is the molecular weight of element β.

Equations (3) and (6) guarantee that the pde governing $z_\beta(\underline{x}, t)$ is free of a chemical source term. At the same time, the particular linear combination of species mass fractions that yields $\dot{\omega}_\beta \equiv 0$ cannot simultaneously cancel the diffusion term. Except in unusual cases (*e.g.*, equal and constant diffusivities for all species), z_β will vary through the reaction zone in a laminar premixed flame, even while it takes on the same value in pure reactants as in equilibrium products. Moreover, while the ratio z_C/z_H is constant in homogeneous reactants, differential diffusion causes this ratio to vary in a reacting flow.

To account for all local mass that originated in the fuel stream, a carbon-plus-hydrogen mixture fraction $z_{C+H} = z_C + z_H$ is used: in pure reactants, $z_{C+H} = Y_{\mathrm{C_3H_8}}$. This mixture fraction reduces to that introduced for one-step irreversible chemistry by Poinsot *et al.* (1996) in their studies of non-homogeneous turbulent premixed combustion.

For a hydrocarbon-air system, reactants are said to be in *stoichiometric* proportion when there is exactly enough oxygen to oxidize all carbon in the fuel to CO_2 and all hydrogen to H_2O. For propane-air, this corresponds to five moles of oxygen per mole of fuel. Corresponding stoichiometric mixture fraction values are: $z_{C\,st} = 0.04980$; $z_{H\,st} = 0.01115$; and $z_{C+H\,st} = 0.06095$.

Closely related to mixture fraction are quantities including equivalence ratio and air-fuel ratio that are widely used in the engineering combustion community. A fuel-based equivalence ratio Φ, for example, is defined as the reactant fuel-to-air mass

ratio divided by the fuel-to-air mass ratio for stoichiometric reactants. Equivalence ratio and mixture fraction are related by,

$$\Phi = \frac{z_{C+H}}{1 - z_{C+H}} \frac{1 - z_{C+H\,st}}{z_{C+H\,st}} , \tag{7}$$

where it is understood that Φ is defined only in pure reactants (well ahead of the primary flame).

3.4.2 Progress variable

In the analysis and modeling of laminar or turbulent premixed flames, it is convenient to work with a quantity that increases monotonically from zero in fresh reactants to unity in fully-burned products. For quantitative work, it is necessary to associate this 'reaction progress variable' $c = c(\underline{x}, t)$ with specific physical quantities such as species mass fractions or temperature.

In their report on turbulent premixed flames with non-homogeneous reactants, Poinsot *et al.* (1996) introduced a reaction progress variable defined in terms of local mixture fraction. Their definition was appropriate for single-step irreversible chemistry where either fuel (in fuel-lean regions) or oxidizer (in fuel-rich regions) is completely depleted in passing through the primary premixed flame. With complex chemistry, it is not clear *a priori* whether there exists any simple combination of physical variables that unambiguously marks a primary flame zone. In the present work, it is found that the primary fuel (propane) does not survive the initial heat-release zone even in locally fuel-rich regions. Following Poinsot *et al.* (1996), we therefore propose the following reaction progress variable:

$$c \equiv 1 - Y_{C_3H_8}/z_{C+H} \cdot \tag{8}$$

In unburned reactants, $z_{C+H} = Y_{C_3H_8}$ so that $c = 0$; and at any point where there is no propane, $c = 1$. The appropriateness of this choice will become clear in Section 5.

4. One-dimensional unsteady laminar premixed flames

As a prelude to two-dimensional turbulent cases, computations were performed for one-dimensional laminar premixed flames propagating into a step change in reactant stoichiometry. Two cases are considered: an initially steady stoichiometric flame propagating into fuel-lean ($\Phi = 0.5$) reactants; and an initially steady stoichiometric flame propagating into fuel-rich ($\Phi = 2.0$) reactants.

Figure 4 shows the time evolution of computed heat-release profiles (mechanism $M2$, four atmospheres, 700 K reactants). For the stoichiometric-to-lean case, peak heat release drops monotonically as the heat-release profile shifts towards the product side. The peak heat release for the steady-state $\Phi = 0.5$ laminar flame is 12% that of the stoichiometric flame.

In the stoichiometric-to-rich case (Fig. 4b), the peak heat release initially increases as the flame encounters excess fuel; it then decreases to a steady-state value that is 53% of the initial $\Phi = 1.0$ peak. The heat-release profile develops a double-peaked structure that persists to the $\Phi = 2.0$ steady state. For a stoichiometric-to-rich transient to $\Phi = 4.0$, the heat-release 'valley' actually becomes negative (not shown).

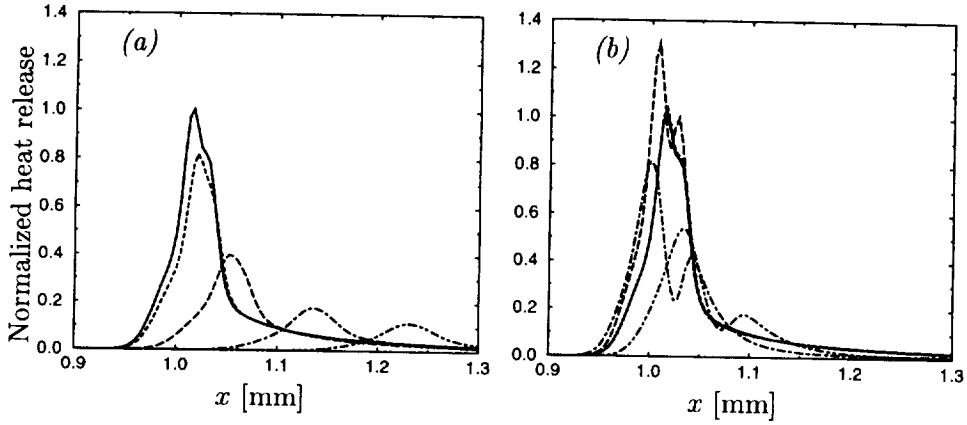

FIGURE 4. Computed heat-release profiles at several instants of time for unsteady unstrained laminar premixed propane-air flames propagating through a step change in reactant stoichiometry: four-atmosphere 700 K reactants, mechanism $M2$. Heat release is normalized by the peak value for the initial stoichiometric flame: —— $t/\tau_f = 0$; ····· $t/\tau_f = 1.4$; ---- $t/\tau_f = 4.1$; —·— $t/\tau_f = 8.2$; —··— $t/\tau_f = 12.2$. a) Stoichiometric to $\Phi = 0.5$. b) Stoichiometric to $\Phi = 2.0$.

5. Two-dimensional turbulent flames

5.1 Global observations

Results at the latest available time ($t/\tau_f = 3.5$; $t/\tau_{T0} = 3.2$) are analyzed. A single computed field (heat release) is shown for homogeneous stoichiometric reactants (Fig. 2). Isocontours of progress variable are superposed. Figure 2 illustrates visually the extent to which turbulence has perturbed the initially planar flame to increase its surface area (length) by this time.

Figure 2 can be compared to the corresponding non-homogeneous-reactant case at the same instant (Fig. 5a). The same initial 'realization' of a turbulent flow field has been used in both cases, and the resulting overall shapes of the primary reaction zone (progress variable iso-contours) are similar. This suggests that at early times, turbulence determines the shape of the propagating primary premixed flame sheet. At later times, it is anticipated that differences between the homogeneous and non-homogeneous flames will be greater.

Examples of several other computed fields are shown in Fig. 5 for the non-homogeneous-reactants case. Three important initial observations are made.

First, there is no leakage of propane fuel past the primary heat-release zone, even in locally fuel-rich regions. As long as the flame does not completely quench, similar behavior is expected even with improved fuel-rich mechanisms. To the extent that this conclusion is general, it largely validates the two-stage conceptual framework of Fig. 1.

Second, the disappearance of primary fuel (propane) coincides with the zone of maximum heat release. This validates the specific choice of progress variable adopted in Eq. (8) and suggests that classic premixed flamelet concepts might remain appropriate for modeling the primary heat release.

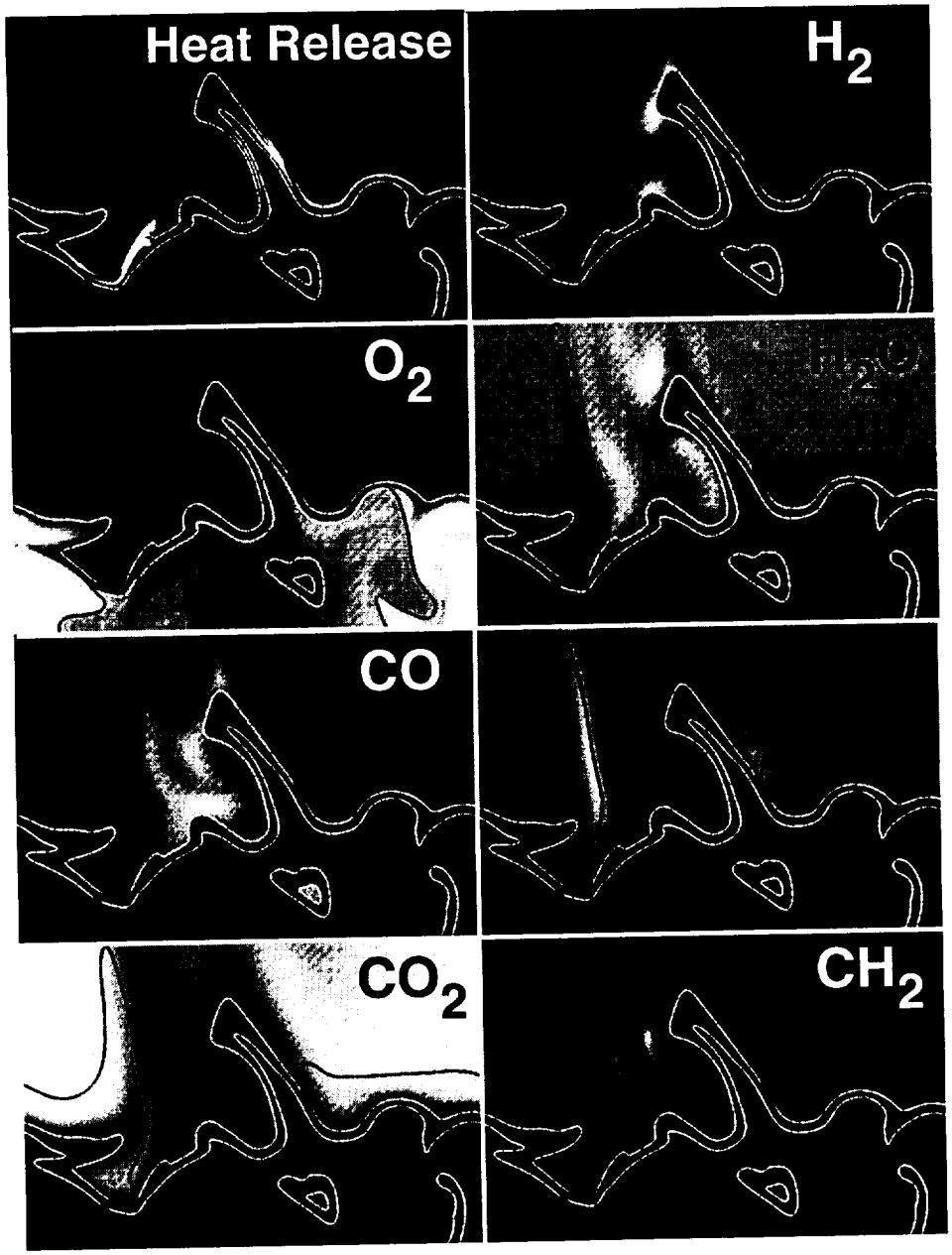

FIGURE 5. Computed two-dimensional fields at time $t/\tau_f = 3.5$ for non-homogeneous reactants (Table I). Black corresponds to (0.0) within each frame and white to the maximum value. Iso-contours of reaction progress variable (white lines: $c = 0.1$ and $c = 0.9$, Eq. 8) and stoichiometric mixture fraction (dark line: $z_{C+H} = z_{C+H\,st} = 0.06095$, Eq. 6) are superposed. Heat release: $\dot{\omega}_Q$ (Eq. 4) (0.24 max). Y_{O_2}: (0.233 max). Y_{CO}: (0.140 max). Y_{CO_2}: (0.142 max). Y_{H_2}: (0.00751 max). Y_{H_2O}: (0.111 max). Y_{OH}: (0.00689 max). Y_{CH_2}: (0.000238 max).

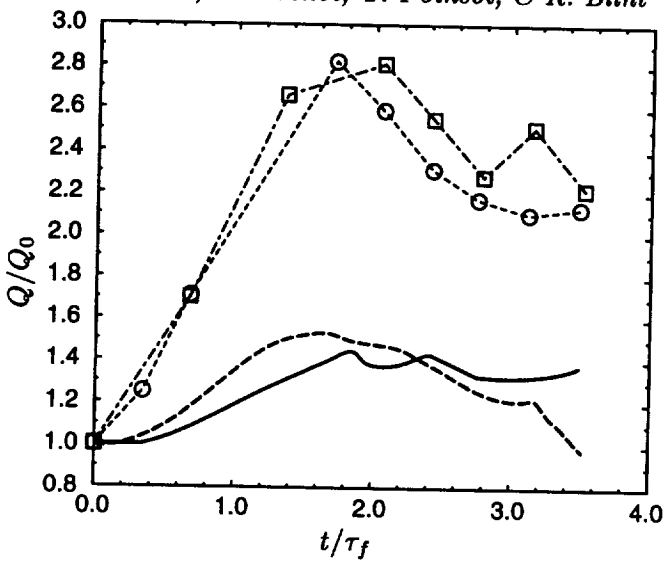

FIGURE 6. Time evolution of global heat release and flame length ($c = 0.5$ iso-contour, Eq. 8) for homogeneous stoichiometric reactants and for non-homogeneous reactants (Table I). Time is normalized by flame time τ_f (Eq. 5). Heat release and flame length are normalized by their initial values: —— heat release, homogeneous; ---- heat release, non-homogeneous; o ---- o flame length, homogeneous; □ —-— □ flame length, non-homogeneous.

And third, relatively short integration times suffice to observe effects of reactant non-homogeneity behind the primary premixed flame. For example, already at $t/\tau_f = 3.5$ the product zone behind the fuel-rich reactants is largely depleted of O_2, O, and OH. This is a fortuitous result for numerical simulation: meaningful results concerning the secondary combustion regime can be extracted earlier in the simulations than initially thought.

The accelerating mechanism is turbulence. Counter-rotating vortex pairs pull tongues of reactants into the hot burned product region, where they quickly are consumed along their sides and highly curved tips to deposit products of rich or lean combustion behind the primary flame. Several such tongues have already appeared and burned out by the instant shown in Fig. 5, and one in the process of burning out can be seen there. This effect is exacerbated by the spatial two-dimensionality of the simulations.

5.2 The primary premixed flame

Time evolution of global heat release and flame length are plotted in Fig. 6. Flame length is computed as the length of a progress variable iso-contour ($c = 0.5$, Eq. 8); global heat release is the area integral over the entire computational box of $\dot{\omega}_Q$ (Eq. 4). Time is reported in flame-time units (Eq. 5) and heat release and flame length are normalized by their respective values for the initial one-dimensional stoichiometric flame.

Flame length increases approximately linearly in time initially, and by the latest

time shown is settling to a value corresponding to about twice the length of the initial planar stoichiometric flame. If there is any systematic difference in flame length between the homogeneous and non-homogeneous case, it is less than 10%, with the non-homogeneous case being longer. This result seems reasonable for the large-scale non-homogeneity studied here. Laminar flame speed is highest for reactants just rich of stoichiometric. Those parts of the flame penetrate deepest into the unburned reactants, while richer and leaner parts do not advance as rapidly as in the stoichiometric case, yielding a longer active flame front.

Global heat release increases much less rapidly than flame length. This is attributed to a combination of chemical kinetic and hydrodynamic strain effects. For the homogeneous case, presumably the latter dominates. It is well established that a propagating premixed flame tends to align itself with extensive strain in the tangent plane (Poinsot & Haworth 1992): the net influence of turbulent staining is to reduce the heat release per unit area of flame. This effect apparently is quite strong for the conditions simulated. For the homogeneous case, the turbulent flame length is twice that of the initial planar flame, while global heat release is only about 1.4 times the laminar value. This suggests a reduction of about 30% in the mean heat release per unit flame length relative to the initial planar flame.

For non-homogeneous reactants, the global heat-release behavior combines turbulent straining and chemical kinetic effects. Global heat release increases initially at a rate that is systematically higher than that of the homogeneous stoichiometric flame; this is consistent with the transient one-dimensional results of Section 4.3. As the flame adjusts to the reactant non-homogeneity, global heat release drops dramatically so that by the end of the simulation, it is below that of the initial planar stoichiometric flame.

Heat-release profiles in the fuel-rich region are double-peaked along a direction normal to a progress variable iso-contour (Fig. 5a); between the peaks, the local heat-release rate is negative. The progress variable iso-contour $c = 0.9$ neatly tracks the heat-release valley through the fuel-rich region, and follows close to the heat-release peak for locally lean-to-stoichiometric mixtures. The $c = 0.9$ iso-contour coincides roughly with the temperature iso-contour $T \approx 1,700$ K. Normalized temperature is less satisfactory than propane mass fraction as a progress variable for non-homogeneous reactants, as temperature does not increase monotonically.

5.3 Secondary reaction

To isolate information related to post-primary combustion, it suffices to condition on a near-unity value of the reaction progress variable. Here $c > c^* = 0.999$ defines the zone of secondary reaction. Turbulent combustion closures are assessed to determine which have the most potential for modeling the secondary heat-release process (R_{F_P} in the skeletal model of Eq. 2). The approach is to analyze the mean chemical source terms $\langle \dot{\omega}_\alpha(\underline{Y}, T) \rangle_{c>c^*}$ and $\langle \dot{\omega}_Q(\underline{Y}, T) \rangle_{c>c^*}$ of Eqs. (3) and (4).

5.3.1 Chemical composition

Qualitative insight can be gained by examining the computed two-dimensional fields of Fig. 5. As for the steady stoichiometric one-dimensional laminar flame,

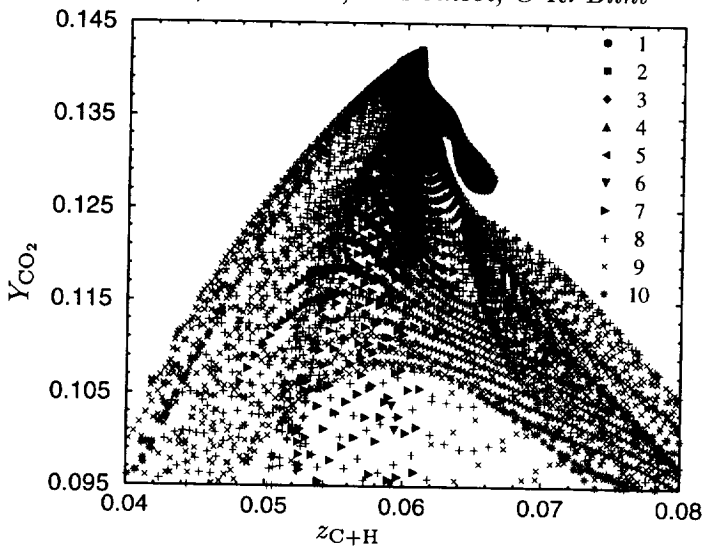

FIGURE 7. Scatter plot of Y_{CO_2} versus mixture fraction z_{C+H} and dissipation rate $\log(\chi_{C+H}/(2D))$ in the post-primary-flame gases ($c > c^* = 0.999$, Eq. 8). Dissipation is 'binned' into ten uniformly-spaced intervals from $\min\{\log(\chi_{C+H}/(2D))\}$ to $\max\{\log(\chi_{C+H}/(2D))\}$, 1 being the lowest values of $\chi_{C+H}/(2D)$ and 10 being the highest.

species H_2O_2 and HO_2 appear along the leading edge of the turbulent flame. Progressively smaller hydrocarbon fragments mark the conversion from reactants towards products in the fuel-rich region, with only the smallest (CH and CH_2) penetrating noticeably behind the $c = 0.9$ iso-contour. Beyond three-to-four flame thicknesses behind the primary premixed flame, the only remaining fuel fragments are CO and H_2.

5.3.2 Laminar diffusion flamelet model

Laminar flamelet theory (Peters 1984) provides an approach for decoupling detailed chemical kinetics from hydrodynamics in modeling non-premixed turbulent reacting flows. It is hypothesized that chemical reaction occurs primarily in a thin sheet that is anchored at the stoichiometric surface $z = z_{st}$. Through a formal transformation, the spatial and temporal variations of the chemical composition fields in the turbulent flow are made implicit through their dependence on mixture fraction $z(\underline{x}, t)$ and its dissipation rate $\chi(\underline{x}, t) = 2D\nabla z \cdot \nabla z$ (D being molecular diffusivity of z). A necessary, but not sufficient, condition for flamelet combustion can be expressed as,

$$Y_\alpha(\underline{x}, t) = Y_\alpha\big(z(\underline{x}, t), \chi(\underline{x}, t)\big) \ . \tag{9}$$

That is, the local chemical composition should be a unique function of the local mixture fraction and its dissipation rate. A second and more restrictive condition is that the functional dependence expressed in Eq. (9) be the same in the turbulent flame as in an archetypical laminar diffusion flame - usually taken to be a steady laminar counterflow diffusion flame. Only the first condition is examined here.

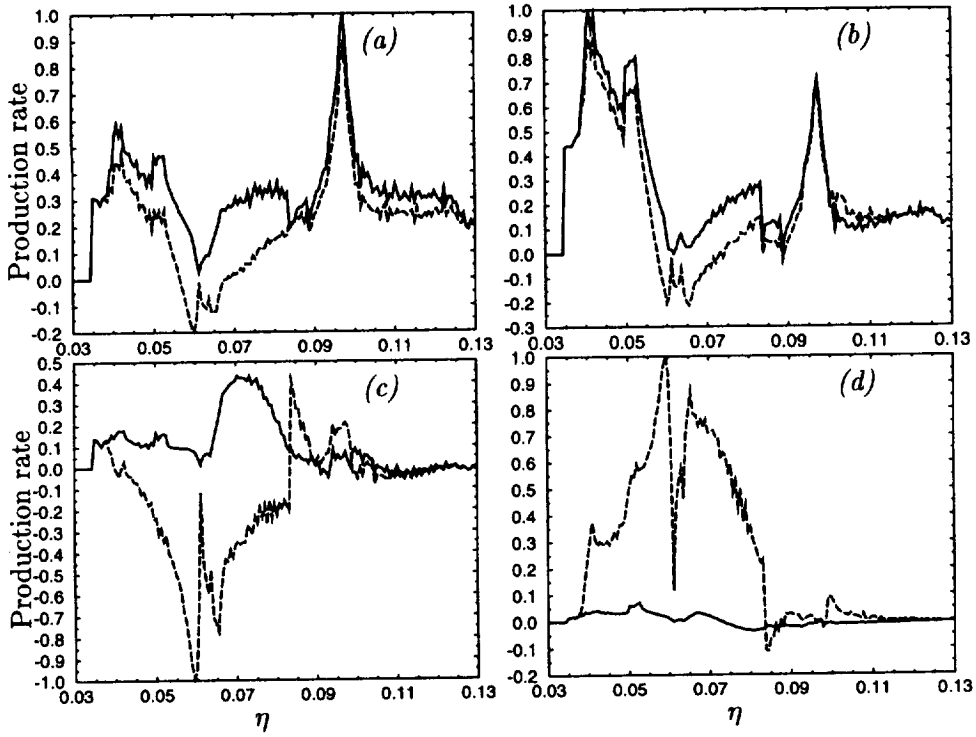

FIGURE 8. Quantities relevant to a first-order CMC model: —— $\langle \dot{\omega}_\alpha(\underline{Y}, T)|z = \eta\rangle$; ---- $\dot{\omega}_\alpha(\langle \underline{Y}|z = \eta\rangle, \langle T|z = \eta\rangle)$. Mean quantities are conditioned on $c > c^* = 0.999$. The ordinate is normalized by the maximum value for each frame. a) Heat release rate. b) Chemical production rate of CO_2. c) Chemical production rate of H_2O. d) Chemical production rate of OH.

In Fig. 7, we plot the local mass fraction of a major product species (CO_2) as a function of the local mixture fraction z_{C+H} with $\chi_{C+H}/(2D)$ as a parameter. If the combustion corresponded to a simple laminar diffusion flamelet regime, then for a given value of z_{C+H}, Y_{CO_2} would increase monotonically with decreasing χ_{C+H}. Figure 7 would display a 'rainbow' structure with $\chi_{C+H} = 0$ defining the upper boundary; and moving downward, successive parallel bands would correspond to increasing values of χ_{C+H}. No such pattern is evident. Nevertheless, there does appear to be some structure to this scatter plot (*e.g.*, the roughly horizontal stripes with monotonic variation in χ_{C+H}). This suggests that more sophisticated flamelet models that include conditioning variables, time-dependency (Haworth *et al.* 1988), or partial premixing of fuel and oxidizer might be appropriate.

5.3.3 Conditional moment closure (CMC) model

In conditional moment closure (CMC) (Bilger 1993), one considers conditionally averaged transport equations where the conditioning variable(s) is (are) chosen to be one(s) on which the chemical production terms are expected to have a strong dependence. Mixture fraction is, presumably, the single most appropriate conditioning

variable for non-premixed combustion.

A 'first-order' CMC hypothesis is that the conditional average of a chemical production term $\langle \dot{\omega}_\alpha(\underline{Y}, T)|z = \eta\rangle$ is equal to the chemical production rate evaluated using the conditionally averaged composition $\langle \underline{Y}|z = \eta\rangle$ and temperature $\langle T|z = \eta\rangle$:

$$\langle \dot{\omega}_\alpha(\underline{Y}, T)|z = \eta\rangle = \dot{\omega}_\alpha(\langle \underline{Y}|z = \eta\rangle, \langle T|z = \eta\rangle) \ , \tag{10}$$

and similarly for heat release. Here the notation $\langle Q|z = \eta\rangle$ denotes the mean value of Q conditioned on the mixture fraction z having the value η. The unconditional mean is recovered by integrating over the probability density function (pdf) of z, $f_z(\eta)$,

$$\begin{aligned} \langle \dot{\omega}_\alpha\rangle &= \int \langle \dot{\omega}_\alpha(\underline{Y}, T)|z = \eta\rangle f_z(\eta) d\eta \ , \\ \langle \dot{\omega}_\alpha\rangle_{CMC} &\equiv \int \dot{\omega}_\alpha(\langle \underline{Y}|z = \eta\rangle, \langle T|z = \eta\rangle) f_z(\eta) d\eta \ . \end{aligned} \tag{11}$$

The first-order CMC model is evaluated by comparing the actual and CMC mixture-fraction-conditioned means (left- and right-hand sides of Eq. 10, respectively; Fig. 8). Here the mixture fraction z_{C+H} has been used. First-order CMC captures the general shapes of the mixture-fraction-conditioned mean production rates for CO, CO_2, and heat release but not for H_2, H_2O, and most radical species. This is consistent with the expectation that the kinetics of CO_2 production dominates the secondary heat release. In classic turbulent diffusion flames, heat release and species production rates peak close to the stoichiometric value of mixture fraction. That is not the case here: most of the post-primary stoichiometric mixture in the present configuration corresponds to products of stoichiometric premixed combustion.

6. Next steps

While all results reported herein must be regarded as preliminary, significant progress has been made towards simulating non-homogeneous turbulent combustion in a specific parameter range of interest and towards understanding and modeling this combustion regime. Three principal issues remain to be addressed before definitive conclusions can be drawn: further work is needed on the chemical mechanism to strike a satisfactory balance between accuracy and computational efficiency on the fuel-rich side of stoichiometric; computations must be extended to larger computational domains (a minimum of one-centimeter square) to allow the simulation of turbulence length scales up to 2 mm; and, computations should be integrated longer in time (a minimum of five-to-ten τ_f's) to ensure that results are free from the influence of initial conditions.

Acknowledgments

The first author thanks Mr. Nick Gallopoulos of the GM R&D Center for his continuing support of fundamental research and the opportunity to participate in this program. Several other GM personnel contributed to the success of this project: Mr. Mark Huebler assisted with customized post-processing software; and technical

discussions with Drs. Tom Sloane, Mike Drake, and Sherif El Tahry helped to guide this study. Dr. Markus Baum of NEC provided technical assistance in the use of NTMIX-CHEMKIN. Computational resources were generously provided by CERFACS. Finally, we thank the CTR organizers, hosts, and fellow visiting researchers for a stimulating and productive four weeks: in particular, Professor Parviz Moin and our CTR host Dr. W. Kendal Bushe.

REFERENCES

BAUM, M. 1994 Etude de l'allumage et de la structure des flames turbulentes. *Ph.D. Thesis,* Ecole Centrale.

BAUM, M., POINSOT, T. J., HAWORTH, D. C., & DARABIHA, N. 1994 Direct numerical simulation of $H_2/O_2/N_2$ flames with complex chemistry in two-dimensional turbulent flows. *J. Fluid Mech.* **281,** 1-32.

BILGER, R. W. 1993 Conditional moment closure for turbulent reacting flow. *Phys. Fluids A.* **5,** 436-444.

BLINT, R. J. 1988 Flammability limits for exhaust gas diluted flames. *Twenty-Second Symposium (International) on Combustion.* (The Combustion Institute, Pittsburgh PA), 1547-1554.

BLINT, R. J. 1991 Stretch in premixed laminar flames under IC engine conditions. *Combust. Sci. Tech.* **75,** 115-127.

BLINT, R. J. & TSAI, P.-H. 1998 C_3H_8-air-N_2 laminar flames calculated for stratified IC engine conditions. *Twenty-Seventh Symposium (International) on Combustion.* (The Combustion Institute, Pittsburgh PA), Poster W1E18.

BOUDIER, P., HENRIOT, S., POINSOT, T., & BARITAUD, T. 1992 A model for turbulent flame ignition and propagation in spark ignition engines. *Twenty-Fourth Symposium (International) on Combustion.* (The Combustion Institute, Pittsburgh PA), 503-510.

CHEN, J. H. & IM, H. G. 1998 Correlation of flame speed with stretch in turbulent premixed methane/air flames. *Twenty-Seventh Symposium (International) on Combustion.* (The Combustion Institute, Pittsburgh PA), to appear.

EL TAHRY, S. H. 1990 A turbulent combustion model for homogeneous charge engines. *Combust. Flame.* **79,** 122-140.

EL TAHRY, S. H. 1997 Personal communication.

GRAN, I. R., ECHEKKI, T., & CHEN, J. H. 1996 Negative flame speed in an unsteady 2-D premixed flame: a computational study. *Twenty-Sixth Symposium (International) on Combustion.* (The Combustion Institute, Pittsburgh PA), 323-329.

HAWORTH, D. C., DRAKE, M. C., POPE, S. B., & BLINT, R. J. 1988 The importance of time-dependent flame structures in stretched laminar flamelet models for turbulent jet diffusion flames. *Twenty-Second Symposium (International) on Combustion.* (The Combustion Institute, Pittsburgh PA), 589-597.

HAWORTH, D. C. & POINSOT, T. J. 1992 Numerical simulations of Lewis number effects in turbulent premixed flames. *J. Fluid Mech.* **244,** 405-436.

HÉLIE, J. & TROUVÉ, A. 1998 Turbulent flame propagation in partially premixed combustion. *Twenty-Seventh Symposium (International) on Combustion.* (The Combustion Institute, Pittsburgh PA), to appear.

HILKA, M., VEYNANTE, D., BAUM, M., & POINSOT, T. 1995 Simulation of flame-vortex interactions using detailed and reduced chemical kinetics. *Tenth Symposium on Turbulent Shear Flows.* Pennsylvania State University.

IM, H. G., CHEN, J. H., & LAW, C. K. 1998 Ignition of hydrogen/air mixing layer in turbulent flows. *Twenty-Seventh Symposium (International) on Combustion.* (The Combustion Institute, Pittsburgh PA), to appear.

KEE, R. J., MILLER, J. A., & JEFFERSON, T. H. 1980 Chemkin: a general-purpose, problem-independent, transportable fortran chemical-kinetics package. *Sandia Tech. Rep. SAND80-8003.*

KEE, R. J., WARNATZ, J., & MILLER, J. A. 1983 A fortran computer code package for the evaluation of gas-phase viscosities, conductivities, and diffusion coefficients. *Sandia Tech. Rep. SAND83-8209.*

KHALIGHI, B., EL TAHRY, S. H., HAWORTH, D. C., & HUEBLER, M. S. 1995 Computation and measurement of flow and combustion in a four-valve engine with intake variations. *SAE Paper No. 950287.*

KRIEGER, R. B., SIEWERT, R. M., PINSON, J. A., GALLOPOULOS, N. E., HILDEN, D. L., MONROE, D. R., RASK, R. B., SOLOMON, A. S. P., & ZIMA, P. 1997 Diesel engines: one option to power future personal transportation vehicles. *SAE Paper No. 972683.*

LAI, M. C., ZHAO, F. Q., & HARRINGTON, D. L. 1997 A review of mixture preparation and combustion control strategies for spark-ignited direct-injection gasoline engines. *SAE Paper No. 970627.*

LELE, S. 1992 Compact finite difference schemes with spectral-like resolution. *J. Comput. Phys.* **103,** 16-42.

PETERS, N. 1984 Laminar diffusion flamelet models in non-premixed turbulent combustion. *Prog. Energy Combust. Sci.* **10,** 319-339.

POINSOT, T., VEYNANTE, D., TROUVÉ, D, & REUTSCH, G.R. 1996 Turbulent flame propagation in partially premixed flames. *Proceedings of the Summer Program,* Center for Turbulence Research, NASA Ames/Stanford University, 111-136.

TURNS, S. R. 1996 *An Introduction to Combustion.* McGraw-Hill, Inc., New York.

WARNATZ, J. 1981 The structure of laminar alkane-, alkene-, and acetylene flames. *Eighteenth Symposium (International) on Combustion.* (The Combustion Institute, Pittsburgh PA), 369-384.

Accounting for spray vaporization in turbulent combustion modeling

By J. Réveillon[1] AND L. Vervisch[1]

Three dimensional Direct Numerical Simulations (DNS) of droplet vaporization in the presence of turbulent micromixing have been performed. The transport equations for basic components of non-premixed turbulent combustion modeling, namely the mean of the mixture fraction and its fluctuations, are presented for the case of a dilute spray. The unclosed terms describing vaporization in the equation for the fluctuations of mixture fraction are analyzed via the DNS data, and a One Droplet Model (ODM) is proposed for those terms.

1. Introduction

Liquid fuel injection is one of the most common procedures in devices where non-premixed turbulent flames are utilized (e.g. diesel engines, aeronautical combustion chambers, and furnaces). Although much work has been devoted to gas-phase turbulent combustion modeling (Borghi 1988, Poinsot *et al.* 1995, Bray 1996), relatively few studies have focused on the development of combustion models accounting for spray vaporization. Thus, when either Reynolds Averaged Navier Stokes Simulation (RANS) or Large Eddy Simulation (LES) are considered for the calculation of practical combustion chambers, turbulent combustion models accounting for spray vaporization are strongly needed.

Nonpremixed combustion is usually approached using conserved scalars where the mixture fraction, Z, and the magnitude of its gradient, $|\nabla Z|$, are used to parameterize the flame in analytical studies (Liñàn 1974). In RANS or LES of non-premixed turbulent flames (Peters 1986, Pierce & Moin 1998), $\widetilde{Z}$, the mean of the mixture fraction, together with $\widetilde{Z''^2}$, its level of fluctuation, are used in most combustion models. These quantities measure the extent of mixing between fuel and air, and along with the mixture fraction dissipation rate $\overline{\rho\chi} = \overline{\rho D|\nabla Z''|^2}$ are used to estimate a micro-mixing time scale. When vaporization of fuel occurs, Z is not a conserved scalar due to local sources of fuel, resulting in additional unclosed terms appearing in the transport equations for $\widetilde{Z}$ and $\widetilde{Z''^2}$.

We have used DNS to simulate a dilute spray for the study of the vaporization terms found in the transport equation for $\widetilde{Z''^2}$. From the results, we discuss modeling of terms using the conditional mean value of the vaporization source of fuel, the conditioning quantity being the mixture fraction. Analytical results characterizing a dilute spray are utilized to derive an expression for this conditional mean value.

1 LMFN,UMR CNRS 6614-CORIA, University and INSA of Rouen.

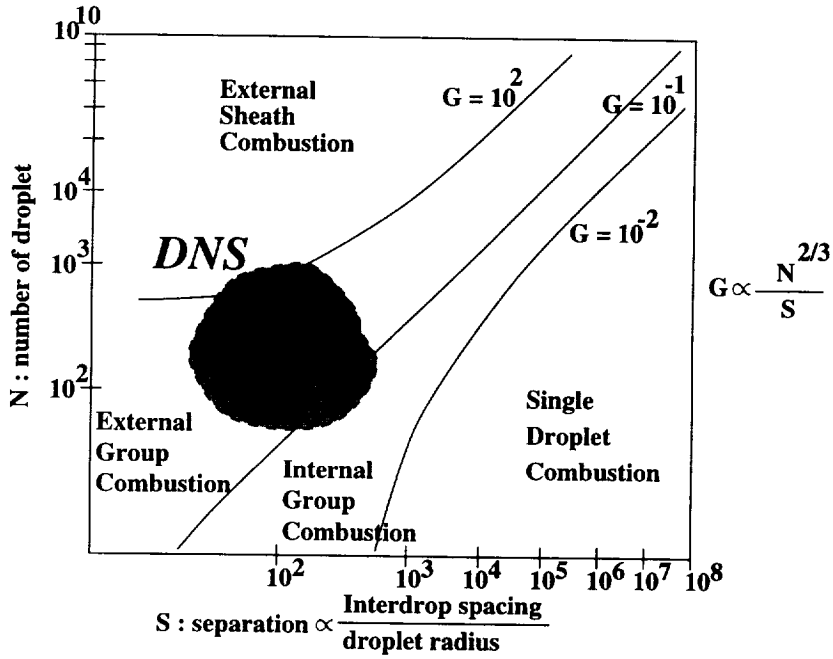

FIGURE 1. Classification of spray combustion regime. Group combustion diagram of Chiu *et al.* (1982).

The results are based on exact solutions obtained for a single droplet vaporizing in a given volume. Then, the accuracy of this One Droplet Model (ODM) is compared against the DNS data. These problems involving a dilute spray mimic situations that may be observed in aeronautical or rocket engines at a particular stage of the combustion process (Borghi 1996).

At the end of this report, the case of a flame attached to a droplet laden jet is also discussed as a challenging problem for DNS.

2. DNS of a turbulent spray

2.1 Introduction

Direct numerical simulation, in theory, allows for a model-free simulation; however, the resources required to perform the simulation of both the turbulent gas phase and the detailed motion of the liquid phase are too great. In our simulations, the flows around an individual drop and inside the drop are not fully resolved; instead available closures are introduced for the liquid phase along with its vaporization rate (Faeth 1983, Law 1982, Sirignano 1983). A Lagrangian description of the spray with two-way coupling (Faeth 1983) is employed. These simulations are restricted to droplets that are smaller than the Kolmogorov length scale. Therefore, in the group combustion diagram of Chiu *et al.* (1982) classifying different combustion regimes (Fig. 1), the present simulations are limited to problems observed in external combustion around clusters of droplets.

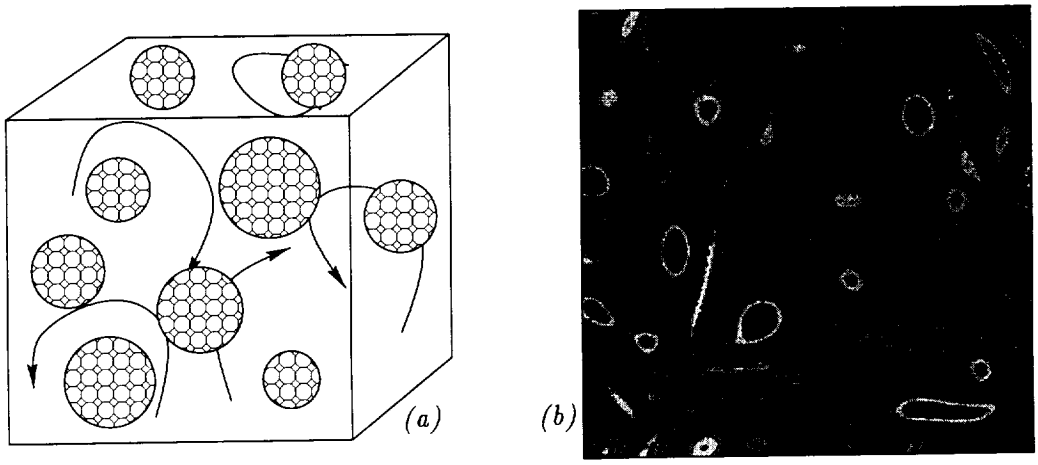

FIGURE 2. (a) Sketch of the initial repartition of the droplets. (b) 2D-snapshot of clusters dispersion after one eddy turn over time. Isolines: vorticity; dot: droplets.

2.2 Governing equations and numerics

A Lagrangian description is adopted for modeling the spray of fuel. The properties of the droplets are estimated by solving a system of three equations for each droplet: its position X^k, its diameter Θ^k, and its velocity V^k. This system (Faeth 1983, Kuo 1986) may be written for each droplet as:

$$\frac{dX_i^k}{dt} = V_i^k \quad ,$$
$$\frac{d\left(\Theta^k\right)^3}{dt} = -Aw_v^k \quad ,$$
$$\frac{d\left(\Theta^k\right)^3 V_i^k}{dt} = A\left(D_i^k - w_v^k V_i^k\right) \quad ,$$

with the mass evaporation rate and drag force given by:

$$w_v^k = \pi \frac{\mu S_{hc}^k}{R_e S_c} \ln\left(1 + B_Y{}^k\right) \Theta^k \quad , \tag{1}$$
$$D_i^k = \frac{\pi}{8} \rho \left(\Theta^k\right)^2 C_D^k \left|U_i^k - V_i^k\right| \left(U_i^k - V_i^k\right) \quad ,$$

In the above equations, C_D is the drag force coefficient, S_{hc} is the convective Sherwood number taking the value 2 in a quiescent flow, and $A = 6/(\pi\rho_l)$ is a constant parameter in which ρ_l is the liquid constant density. The properties of the gas (μ viscosity, ρ density, and U_i velocity) are obtained at the droplet position from the grid nodes using a third order interpolation algorithm (Guichard *et al.* 1998). These equations have been made dimensionless with R_e as the acoustic Reynolds number of the DNS problem, and S_c and P_r are the Schmidt number of the fuel and the Prandtl number, where $Pr = Sc = 0.7$.

To construct the thermal budget, we assume all the energy reaching the surface contributes to the droplet skin vaporization without any transfer or accumulation in the liquid core (thin skin approximation, Faeth 1983). With this description, only an infinitely thin layer of fuel around the droplet is heated and vaporized while the temperature and the liquid mass fraction of the droplet core remain constant and equal to the conditions of injection.

The properties of vaporization are characterized by the species Spalding parameter, $b = Y_F/(Y_F^s - 1)$, from which the Spalding number is defined: $B_Y = b^\infty - b^s$. The fuel mass fractions Y_F^s and Y_F^∞ are taken at the surface of the droplet and in the pure gas respectively. Defined in this manner, B_Y characterizes the diffusion rate of the fuel and may be estimated with three different levels of complexity. In a first approximation B_Y is assumed constant, then the droplet diameter follows a d-square law, $\Theta^2(t) = \Theta^2(t=0) - \beta t$, where β is the vaporization coefficient. Other possibilities are to consider B_Y as linearly related to the gas temperature around the droplet or to calculate B_Y as a function of the saturation, the local pressure and temperature, and, eventually, the gaseous fuel mass fraction. The simulations of turbulent mixing have been performed with a constant Spalding number corresponding to situations where the temperature of the spray is close to saturation, whereas the second possibility ($B_Y = B_Y(T)$) is retained for the spray flame calculations.

The flow is described by solving the following equations accounting for the two-way coupling:

$$\frac{\partial \rho}{\partial t} + \frac{\partial \rho U_j}{\partial x_j} = \frac{1}{\mathcal{V}} \sum_k w_v^k \quad ,$$

$$\frac{\partial \rho U_i}{\partial t} + \frac{\partial \rho U_i U_j}{\partial x_j} = -\frac{\partial P}{\partial x_i} + \frac{1}{R_e}\frac{\partial \sigma_{ij}}{\partial x_j} - \frac{1}{\mathcal{V}} \sum_k \left(D_i^k - w_v^k V_i^k\right) \quad ,$$

$$\frac{\partial \rho E_t}{\partial t} + \frac{\partial \rho E_t U_j}{\partial x_j} = \frac{\partial}{\partial x_i}\left(\frac{\mu C_p}{R_e Pr}\frac{\partial T}{\partial x_i}\right) + \frac{1}{R_e}\frac{\partial \sigma_{ij} U_j}{\partial x_i} - \frac{1}{\mathcal{V}} \sum_k \left[\frac{1}{2} V_i^k \left(D_i^k - w_v^k V_i^k\right)\right] \quad ,$$

$$\frac{\partial \rho Y_F}{\partial t} + \frac{\partial \rho Y_F U_j}{\partial x_j} = \frac{\partial}{\partial x_i}\left(\frac{\mu}{R_e Sc}\frac{\partial Y_F}{\partial x_i}\right) + \frac{1}{\mathcal{V}} \sum_k w_v^k \quad ,$$

$$\frac{\partial \rho Y_O}{\partial t} + \frac{\partial \rho Y_O U_j}{\partial x_j} = \frac{\partial}{\partial x_i}\left(\frac{\mu}{R_e Sc}\frac{\partial Y_O}{\partial x_i}\right) \quad ,$$

where $\mathcal{V}$ is the volume defined in the vicinity of the grid point. In this volume we accumulate the vaporization source from each droplet in order to achieve the coupling between the Eulerian and Lagrangian descriptions.

A third order Runge-Kutta scheme with a minimal data storage method (Wray 1998) is used for time stepping. Spatial derivatives are estimated using the sixth order Lele's PADE scheme (Lele 1992). Non-reflecting boundary conditions of Poinsot and Lele (1992) have been used for calculations with combustion.

2.3 DNS parameters

The droplets are organized in clusters (or clouds) homogeneously embedded in a 3D freely decaying turbulence with an initial integral length scale that is twice the mean radius of these clusters (see Fig. 2). The density of droplets in the clusters is chosen to reproduce, in the mean, a near-stoichiometric dilute spray of n-heptane with the stoichiometric value $Z_{st} = 0.0625$. Table 1 summarizes the parameters used in the four different simulations with variable Spalding number and, therefore, variable mean vaporization time. To allow comparison of micromixing with and without droplet vaporization, we have also performed a simulation with an infinite value for the Spalding number B_Y (instantaneously vaporizing droplets).

Case	B_Y	Θ_0/l_t	τ_t/τ_V	τ_V/τ_k	Re_{lt}
TV_1	4	0.014	1.37	7.5	104
TV_2	2.7	0.014	1.18	8.66	104
TV_3	1.9	0.014	0.94	10.97	104
TV_G	∞	0.014	∞	0	104

Table 1. Parameters of the simulations ($65 \times 65 \times 65$, 10800 droplets organized in 9 clusters): The turbulence is characterized by its integral length scale l_t, the eddy turnover time τ_t, the Kolmogorov time τ_k, and the Reynolds number $Re_{lt} = (u' l_t/\nu) \approx (\tau_t/\tau_k)^2$. The properties of the spray are: Θ_0 the initial diameter of the droplets, B_Y the Spalding number, and its related vaporization time τ_v.

3. One Droplet Model (ODM)

As mentioned in Section 1, determining both the mean mixture fraction, $\widetilde{Z}$, and its fluctuations, $\widetilde{Z''^2}$, is a major issue of numerical modeling for nonpremixed turbulent flames (Peters 1986). We will limit our discussion to closure for the RANS/Lagrangian approach where the spray is modeled through a mean lagrangian description (Lixing 1993). The RANS/Lagrangian approach brings an approximation of the mean vaporization rate $\widetilde{W}_v$ entering the transport equation for $\widetilde{Z}$, which is then closed (Lixing 1993). Unfortunately, this method does not close many terms found in the transport equation for $\widetilde{Z''^2}$, thus additional modeling is needed.

3.1 Budget equation for $\widetilde{Z''^2}$

The mixture fraction is defined as $Z = (\Phi Y_F/Y_{F,o} - Y_O/Y_{O,o} + 1)/(\Phi + 1)$. The mass fractions in pure fuel and pure oxidizer are denoted by $Y_{F,o}$ and $Y_{O,o}$, respectively, and the stoichiometric point is $Z_{st} = 1/(1+\Phi)$. The equivalence ratio

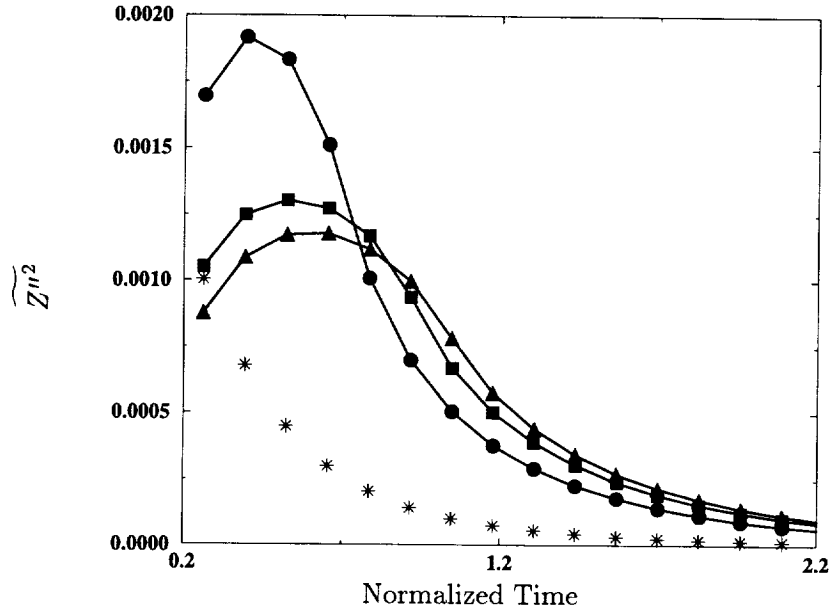

FIGURE 3. Time evolution of the fluctuations $\widetilde{Z''^2}$; the time is normalized by the eddy turn over time. Symbols: *: TV_G; • , TV_1; ■, TV_2; ▲, TV_3.

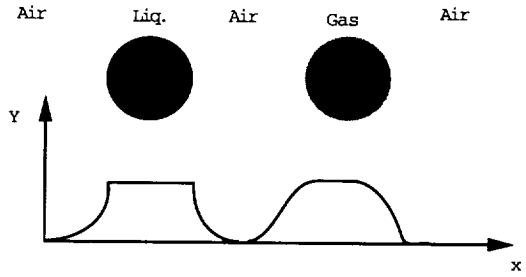

FIGURE 4. Sketch of Y_F through a drop or a pocket of gas.

of the mixture is $\Phi = (\nu_O \mathcal{M}_O Y_{F,o})/(\nu_F \mathcal{M}_F Y_{O,o})$, with the molecular weights $\mathcal{M}_O$, $\mathcal{M}_F$ and the stoichiometric coefficients ν_O, ν_F, ν_P corresponding to the reaction $\nu_F Y_F + \nu_O Y_O \rightarrow \nu_P Y_P$. The transport equation for Z is:

$$\frac{\partial \rho Z}{\partial t} + \frac{\partial \rho Z U_j}{\partial x_j} = \frac{\partial}{\partial x_i}\left(\rho D \frac{\partial Z}{\partial x_i}\right) + \frac{1}{(1+\Phi)}\left(\frac{\Phi + Y_{F,o}}{Y_{F,o}}\right)\rho \dot{W}_v \ ,$$

where $\rho \dot{W}_v = \frac{1}{\mathcal{V}} \sum_k \dot{\omega}_k$ is the vaporization rate defined in Section 2.2. From this

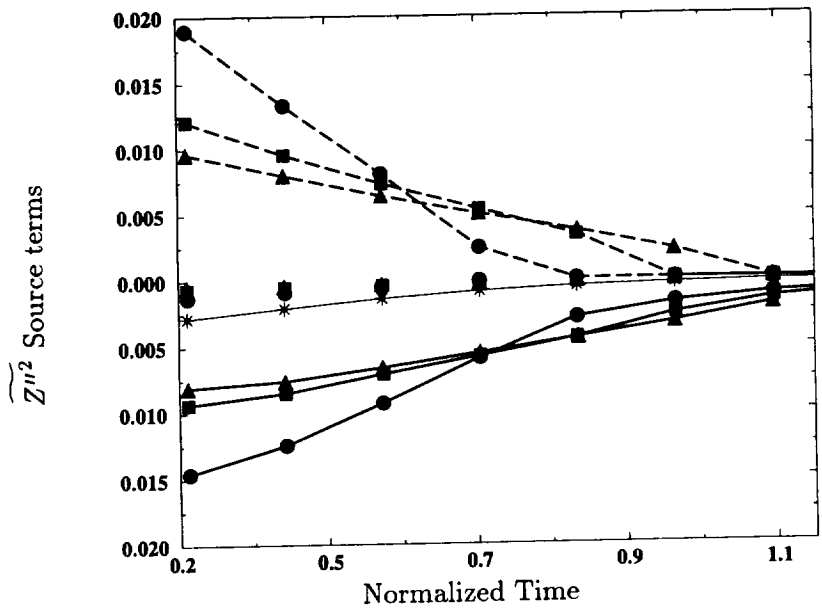

FIGURE 5. Source terms for $\widetilde{Z''^2}$ (see Eq. (2)). Lines with symbols: Dissipation rate $\overline{\rho}\widetilde{\chi}$. ---- with symbols: $\overline{\rho}\widetilde{S^+}$. Symbols: $\overline{\rho}\widetilde{S^-}$. *: pure gas mixing simulation TV_G; ●, ■, and ▲: two-phase simulations TV_1, TV_2, TV_3 (see table 1).

equation, the balance equation for the fluctuations $\widetilde{Z''^2}$ may be written,

$$\frac{\partial \overline{\rho}\widetilde{Z''^2}}{\partial t} + \frac{\partial \overline{\rho}\widetilde{Z''^2}\widetilde{U}_i}{\partial x_i} = \overbrace{-\frac{\partial}{\partial x_i}\left(\overline{\rho}\widetilde{Z''^2U_i''}\right)}^{\textit{Turbulent convection}} \underbrace{-2\overline{\rho}\widetilde{Z''U_i''}\frac{\partial \widetilde{Z}}{\partial x_i}}_{\textit{Production}} \overbrace{-2\rho D\overline{\frac{\partial Z''}{\partial x_i}\frac{\partial Z''}{\partial x_i}}}^{\textit{Dissipation}}$$
$$\underbrace{+2\overline{\rho}\widetilde{Z''\dot{W}_v}\left(\frac{1}{(1+\Phi)}\left(\frac{\Phi+Y_{F,o}}{Y_{F,o}}\right)-\widetilde{Z}\right)-\overline{\rho}\widetilde{Z''^2\dot{W}_v}}_{\textit{Vaporization}} \quad , \tag{2}$$

in which the dissipation rate $\overline{\rho}\widetilde{\chi} = \overline{2\rho D|\nabla Z''|^2}$ appears with two unclosed source terms that are directly related to spray vaporization. The objective is to model those two terms:

$$\overline{\rho}\widetilde{S^+} = 2\overline{\rho}\widetilde{Z''\dot{W}_v}\left(\frac{1}{(1+\Phi)}\left(\frac{\Phi+Y_{F,o}}{Y_{F,o}}\right)-\widetilde{Z}\right) \quad \text{and} \quad \overline{\rho}\widetilde{S^-} = -\overline{\rho}\widetilde{Z''^2\dot{W}_v} \quad .$$

The time evolution of $\widetilde{Z''^2}$ is considered first. Since the distributions of fuel and oxidizer are homogeneous, the equation for $\widetilde{Z''^2}$ reduces to $\partial(\overline{\rho}\widetilde{Z''^2})/\partial t = \overline{\rho S^+} + \overline{\rho S^-} - \overline{\rho\chi}$. Furthermore, in the case of pure gas mixing obtained for an infinitely small vaporization time (TV_∞ in table 1), $\widetilde{Z''^2}$ can be expressed as $\partial(\overline{\rho}\widetilde{Z''^2})/\partial t =$

$-\overline{\rho\chi}$. As expected (Dopazo 1994), one observes in Fig. 3 the well-known exponential decay of $\widetilde{Z''^2}$ for this reference situation.

When the liquid phase is present, $\widetilde{Z''^2}$ behaves differently. Fluctuations of mixture fraction are generated by the local sources of fuel, and $\widetilde{Z''^2}$ increases quickly to reach a maximum point. The value of $\widetilde{Z''^2}$ at this maximum depends on the characteristic time of vaporization (Fig. 3), when the shorter the vaporization time, the larger this value. After reaching this maximum, turbulent micro-mixing becomes the dominant effect and the exponential decay is recovered.

A previous study had discussed how the mean turbulent mixing time and related quantities are dramatically affected by the liquid phase (Réveillon *et al.* 1998). In dilute spray, this is partly due to the impact of vaporization source on the small scales of the fuel field. Because of the non-diffusing reservoir of fuel in the core of the drop, the value taken by $|\nabla Y_F|$ when $Y_F \rightarrow 1$ tends to be larger in the case of droplets than for a pocket of gas (Fig. 4). One consequence of this is the increase in dissipation rate $\overline{\rho\chi}$ following the introduction of the spray (Fig. 3).

It is also observed in Fig. 5 that the production term $\overline{\rho S^+}$ is positive and of the same order as the dissipation rate, $\overline{\rho\chi}$, while $\overline{\rho S^-}$ is small. This is expected since vaporization first generates large positive value of Z'', and $\overline{\rho S^+}$ is linear in Z'', whereas $\overline{\rho S^-}$ is quadratic in Z''.

3. ODM closure for $\overline{\rho S^+}$ and $\overline{\rho S^-}$

The unknowns contained in the terms $\overline{\rho S^+}$ and $\overline{\rho S^-}$ are $\overline{\rho Z'' \dot{W}_v}$ and $\overline{\rho Z''^2 \dot{W}_v}$. Introducing $\widetilde{P}(Z^*)$, the probability density function (pdf) of Z, we will reduce the modeling of $\overline{\rho S^+}$ and $\overline{\rho S^-}$ to the determination of $\left(\overline{\dot{W}_v \mid Z^*}\right)$, the mean of the vaporization rate calculated for a particular value $Z = Z^*$ of the mixture fraction. It turns out that this conditional mean can be approximated from the exact solution of a dilute spray problem in a quiescent flow. In calculations of practical combustion chambers, a beta function (Bray 1996) is usually utilized for presuming $\widetilde{P}(Z^*)$ from $\widetilde{Z}$ and $\widetilde{Z''^2}$. One may write,

$$\overline{\rho Z'' \dot{W}_v} = \overline{\rho} \int_0^1 (Z - \widetilde{Z}) \left(\overline{\dot{W}_v \mid Z^*}\right) \widetilde{P}(Z^*) dZ^*$$

and

$$\overline{\rho Z''^2 \dot{W}_v} = \overline{\rho} \int_0^1 (Z - \widetilde{Z})^2 \left(\overline{\dot{W}_v \mid Z^*}\right) \widetilde{P}(Z^*) dZ^*$$

In the above equations, $\left(\overline{\dot{W}_v \mid Z^*}\right) = \left(\overline{\frac{1}{\mathcal{V}} \sum_n \dot{\omega}_v^k \mid Z = Z^*}\right)$ depends on the statistics of both the diameters Θ of the droplets and the Spalding number B_Y, so we consider the case of a constant B_Y first.

In the class of two phase flow problems described with dilute spray, the droplets are smaller than the Kolmogorov scale and tend to follow the turbulent structures

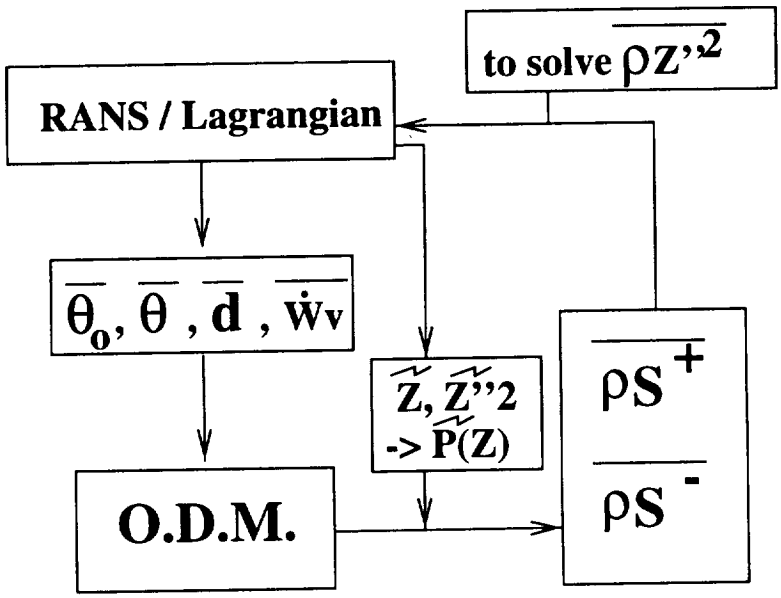

FIGURE 6. Sketch of the ODM procedure.

(weak drag force). As a consequence, during vaporization large values of Z are expected in zones where high vaporization rates exist. Moreover, one should observe the largest values of $\left(\overline{\dot{W}_v \mid Z^*}\right)$ in the vicinity of $Z^* = Z_{max}$, the maximum value taken by the mixture fraction in the flow at a particular time. Hence, we anticipate $\left(\overline{\dot{W}_v \mid Z^*}\right)$ as being a monotonic function of Z^*,

$$\left(\overline{\dot{W}_v \mid Z^*}\right) = \left(\alpha_{B_Y}(\overline{\Theta}, \overline{d})Z^*\right)^n \quad , \tag{3}$$

where $\overline{\Theta}$ and $\overline{d}$ are the mean diameter of the droplets and the mean spray density provided by the RANS/Lagrangian solver, and n is a parameter dynamically determined and accounting for the effect of turbulence on the spray. The physical properties of the liquid phase enter ODM through the function $\alpha_{B_Y}(\overline{\Theta}, \overline{d})$. Considering the spray to be homogeneous, we estimate $\alpha_{B_Y}(\overline{\Theta}, \overline{d})$ by replacing the collection of droplets by a unique drop of initial diameter $\overline{\Theta}_0$, vaporizing in a quiescent flow of volume $1/\overline{d}$ where $\overline{d}$ is the mean spray density. From Eq. (1) giving the vaporization

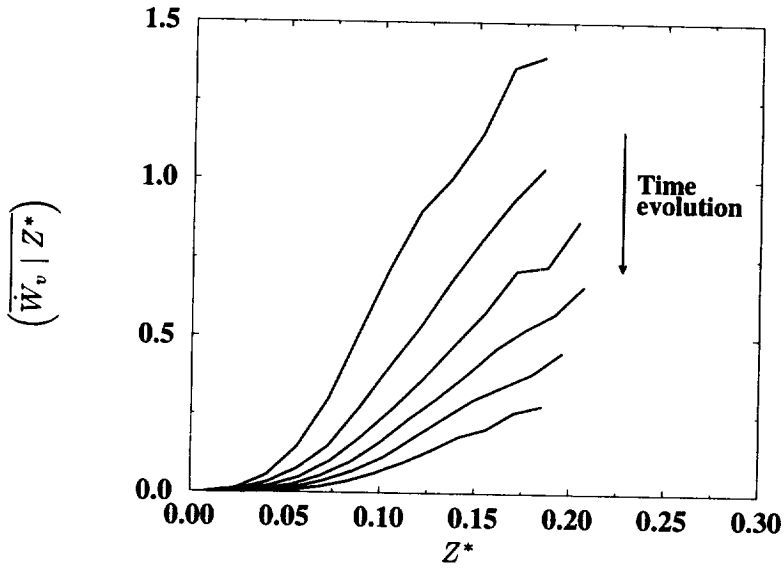

FIGURE 7. Time evolution of $\left(\overline{\dot{W}_v \mid Z^*}\right)$, the conditional mean value of the vaporization rate.

rate, we write for this unique drop:

$$\rho \dot{W}_v(\overline{\Theta}, \overline{d}) = \pi \frac{\mu S_{hc}}{ReSc} ln(1 + B_Y) \overline{\Theta}\ \overline{d} \quad ,$$

$$\rho Z^*(\overline{\Theta}, \overline{d}) = \frac{1}{(1+\Phi)} \left(\frac{\Phi + Y_{F,o}}{Y_{F,o}} \right) \rho_l \left(\overline{\Theta}_o^3 - \overline{\Theta}^3 \right) \overline{d} \quad .$$

One may then calculate $\alpha_{B_Y}(\overline{\Theta}, \overline{d})$ by combining the behavior of the isolated droplet with the proposed closure for the conditional source (Eq. (3)),

$$\dot{W}_v(\overline{\Theta}, \overline{d}) = \left(\alpha_{B_Y}(\overline{\Theta}, \overline{d}) Z^*(\overline{\Theta}) \right)^n \quad .$$

leading to:

$$\alpha_{B_Y}(\overline{\Theta}, \overline{d}) = \frac{\left(\pi \frac{\mu S_{hc}}{\rho ReSc} ln(1 + B_Y) \overline{\Theta}\ \overline{d} \right)^{1/n}}{\left(\frac{1}{(1+\Phi)} \left(\frac{\Phi + Y_{F,o}}{Y_{F,o}} \right) \rho_l \left(\overline{\Theta}_o^3 - \overline{\Theta}^3 \right) \overline{d} \right)} .$$

When using ODM, $\overline{\Theta}_0$ is the initial mean diameter of the droplets, for instance, their mean diameter at the exit of an injection system.

The coupling between ODM and a CFD code is sketched in Fig. 6. Part of this coupling is achieved via the mean vaporization rate $\widetilde{\dot{W}}_v$. This rate is provided by the RANS/Lagrangian solver, and the ODM approximation of $\left(\overline{\dot{W} | Z^*}\right)$ must capture $\widetilde{\dot{W}}_v$, resulting in the constraint:

$$\widetilde{\dot{W}}_v = \int_0^1 \left(\overline{\dot{W}_v \mid Z^*} \right) \widetilde{P}(Z^*)\ dZ^* = \int_0^1 \left(\alpha_{B_Y}(\overline{\Theta}) Z^* \right)^n \widetilde{P}(Z^*)\ dZ^* \quad , \qquad (4)$$

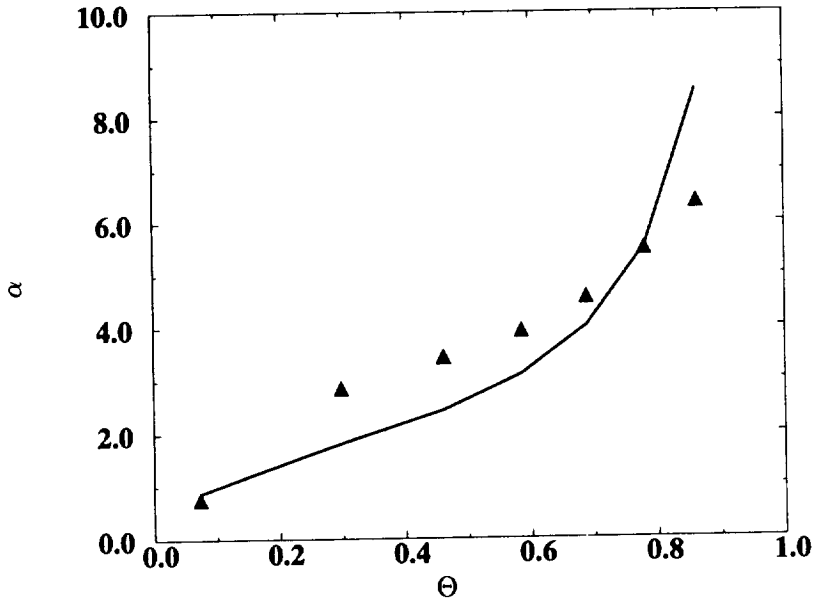

FIGURE 8. Comparison of the value of α given by ODM (———) and by DNS (▲).

Equation 4 is then utilized to determine the parameter n. Here the DNS is used to extract $\widetilde{\dot{W}}_v$, and n takes on values between 1.8 and 2.2. In practical problems, we expect n to depend on the turbulent spray regime. From the DNS, $\left(\overline{\dot{W}_v \mid Z^*}\right)$ features a parabolic shape which depends on time (Fig. 7). In Fig. 8 an interesting agreement is observed when the function $\alpha_{B_Y}(\overline{\Theta}, \overline{d})$ is measured from DNS and compared with the estimation given by ODM (Eq. 4).

We have computed with ODM the two terms $\overline{\rho S^+}$ and $\overline{\rho S^-}$, and the comparison with DNS presented in Fig. 9 is satisfactory. Even though this does not appear as a major shortcoming so far, notice that the fluctuations of $\dot{W}_v$ for a given value of Z are not directly introduced in this closure.

4. A challenging problem for DNS

We now discuss some preliminary results which represent a first step towards a full DNS of turbulent spray combustion. Droplets of fuel have been injected in a two-dimensional double-wake configuration, and a flame is stabilized on the liquid jet while simple step chemistry is retained. The Spalding number B_Y depends on temperature; therefore, the stabilization of the flame results from the diffusion of heat vaporizing the liquid. A diffusion flame develops, and its main body is attached to the spray by a triple flame (Ruetsch *et al.* 1995) composed of a rich premixed flame where the droplets are vaporizing and two lean premixed flames on both sides of the jet (Fig. 10). The vorticity field shows that heat release affects the flow through gas expansion even at the end of the core of the dilute spray. Those simulations suggest that, despite the large number of physical parameters

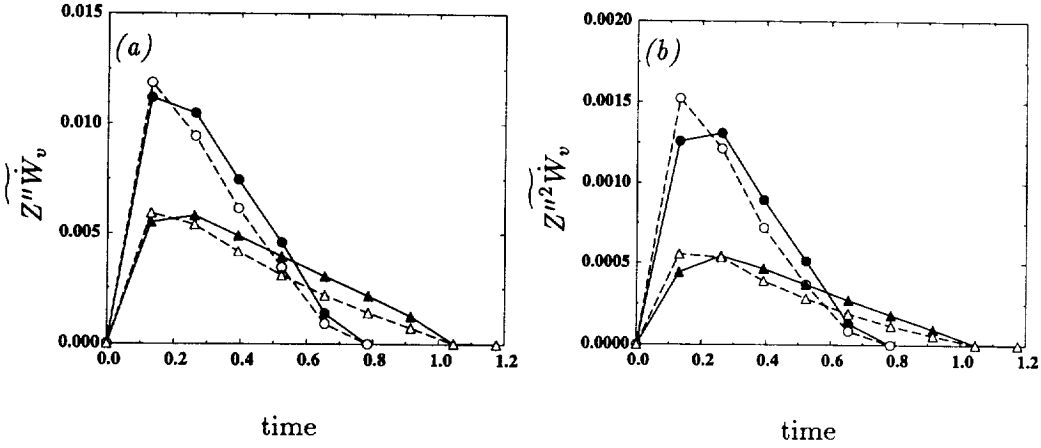

FIGURE 9. Comparisons DNS / ODM. (a) $\widetilde{S^+}$, (b) $\widetilde{S^-}$. Symbols: • : DNS-TV1; ○ : ODM-TV1; ▲: DNS-TV3; △: ODM-TV3.

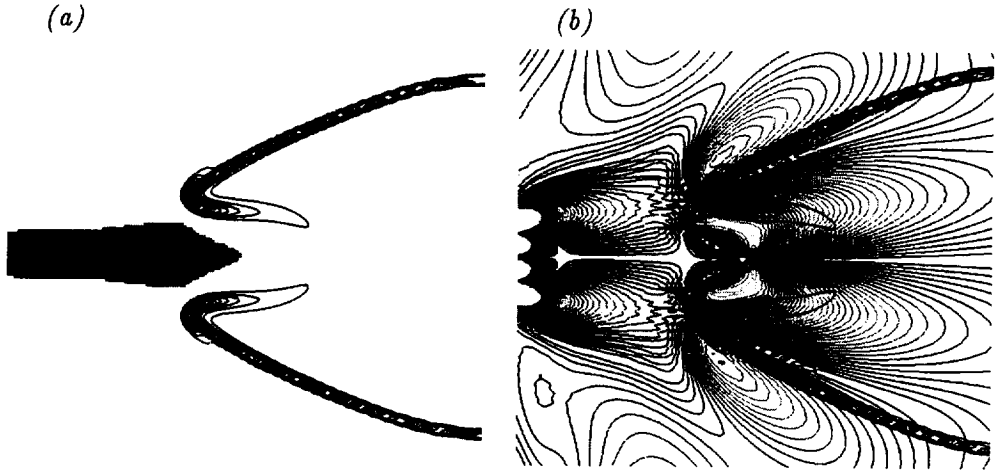

FIGURE 10. Flame attached on a spray. (a) Reaction rate around vaporizing droplets. (b) Reaction rate and vorticity.

embedded in liquid fuel combustion, DNS will soon emerge as an efficient tool to help understand and model turbulent spray combustion.

5. Conclusion

Direct numerical simulations of turbulent mixing of a vaporizing spray have been performed. From the results, closures are proposed for the source terms appearing in the transport equation for the fluctuations of the mixture fraction. They are based on a simple One Droplet Model utilized to express the conditional mean of the turbulent vaporization rate. In the same context, first DNS of a flame attached

to liquid jet have been performed.

Acknowledgment

This work has benefited from many stimulating and exciting discussions with the members of the CTR Summer Program; in particular, the authors gratefully acknowledge their CTR hosts Prof. J. Ferziger, and Drs. G. Ruetsch and J. Oefelein.

REFERENCES

BORGHI R. 1988 Turbulent combustion modeling. *Prog. Energy Combust. Sci.* **14,** 245-292.

BORGHI, R. 1996 Background on droplets and spray. *Combustion and Turbulence in Two-Phase Flows. von Karman Institute for Fluid Dynamics, Lecture Series 1996-02, (Eds M. Manna & D. Vandromme) VKI-Belgium.*

BRAY, K. N. C. 1996 The Challenge of turbulent combustion. *Proceedings of the 26th Symp. (Int.) on Combustion, Naples.* The Combustion Institute, Pittsburgh.

CHIU H. H. & KIM H. Y. & CROKE E. J. 1982 Internal group combustion of liquid droplets. *Proceedings of the nineteenth Symposium (International) on combustion.* **19,** 971-980.

DOPAZO, C. 1994 Recent developments in pdf methods. In *Turbulent Reacting Flows.* Academic Press London (Eds P. A. Libby and F. A. Williams), 375-474.

ELGOBASHI S. & TRUESDELL G. C. 1992 Direct numerical simulation of particle dispersion in a decaying isotropic turbulence. *J. Fluid Mech.* **242,** 655-700.

FAETH G. M. 1983 Evaporation and combustion of sprays. *Prog. Energy Combust. Sci.* **9,** 1-76.

GUICHARD L. & LECORDIER B. & RÉVEILLON J. 1998 Evaluation des algorithmes utilisés en PIV grâce à la simulation numérique directe. *6ieme Congrès francophone de Vélocimétrie Laser.* **F-5,** Saint-Louis, France.

GUICHARD L. & VERVISCH L. & DOMINGO P. 1995 Two-dimensional weak shock-vortex interaction in a mixing zone. *AIAA J.* **33,** 1797-1802.

KUO K. K. 1986 *Principles of combustion.* John Wiley and Sons.

LAW C. K. Recent advances in droplet vaporization and combustion 1982. *Prog. Energy Combust. Sci.* **8,** 171-201.

LELE S. K. 1992 Compact finite difference schemes with spectral like resolution. *J. Comput. Phys.* **103,** 16-42.

LIÑÁN, A. 1974 The asymptotic structure of counterflow diffusion flames for large activation energies. *Acta Astronautica.* **1,** 1007.

LIXING, Z. 1993 *Theory and numerical modeling of turbulent gas-particle flows and combustion. Science Press and CRC Press, Inc. ISBN 0-8493-7721-8.*

PETERS, N. 1986 Laminar flamelet concepts in turbulent combustion. In *Proceedings of the 21st Symposium (international) on Combustion, Irvine.* The Combustion Institute Pittsburgh, 1231-1250.

PIERCE, C. D. & MOIN, P. 1998 Large eddy simulation of a confined coaxial jet with swirl and heat release. *AIAA 98-2892,*29th AIAA Fluid Dynamics Conference, Albuquerque, NM June 15-18.

POINSOT, T., CANDEL, S. & TROUVÉ, A. 1996 Direct numerical simulation of premixed turbulent combustion. *Prog. Energy Combust. Sci.* **12,** 531-576.

POINSOT T. & LELE S. K. 1992 Boundary conditions for direct simulations of compressible viscous flows. *J. Comput. Phys.* **101,** 104-129.

RÉVEILLON J. & BRAY K. N. C. & VERVISCH L. 1998 DNS study of spray vaporization and turbulent micro-mixing. *AIAA 98-1028.*

RUETSCH, G. R., VERVISCH, L. & LIÑÁN, A. 1995 Effects of heat release on triple flame. *Phys. Fluids.* **7,** (6) 1447-1454.

SIRIGNANO W. A. 1983 Fuel droplet vaporization and spray combustion theory. *Prog. Energy Combust. Sci.* **9,** 291-322.

VERVISCH L. & POINSOT T. 1998 Direct numerical simulation of non-premixed turbulent flame. *Ann. Rev. Fluid Mech.* **30,** 655-692.

WRAY A. A. 1998 Minimal storage time-advancement schemes for spectral methods. Personal communication.

Simulation and modeling of reacting particles in turbulent nonpremixed combustion

By N. S. A. Smith[1], G. R. Ruetsch, J. Oefelein, AND J. H. Ferziger

A conditional moment closure model is proposed for reacting particles in turbulent nonpremixed combustion. The new model for particles differs significantly from the traditional uniform diffusivity gas-phase conditional moment closure model. The new features of the model and its effectiveness are examined against direct numerical simulation data for soot-like and droplet-like particles in turbulent nonpremixed combustion. The influence of differing particle sizes and types on the effectiveness of the model closure is examined in detail.

1. Introduction

Condensed-phase particles are frequently present in turbulent combustion systems and can have a profound influence on the thermochemical nature of their surroundings. Fuel droplets and soot particles are two examples of important condensed phase species in combustion. The evaporation of the former largely determines the distribution of the combustible gaseous fuel/air mixture, while the presence of the latter impacts strongly on the degree of radiant heat transfer from the system. It is thus desirable to be able to predict the mean behavior of these particles, in a turbulent combusting environment, in response to their local thermochemical conditions.

A number of difficulties surround the modeling of the mean rate of particle reactions in turbulent combustion. Perhaps the most significant difficulty is associated with determining the mean influence of carrier fluid properties such as temperature and chemical species concentrations upon the particle population. Wherever the local properties of the carrier fluid fluctuate due to turbulence, the variations can couple with the non-linear particle reactions to preclude first order closure of the mean rates with mean properties. This type of closure problem is the same as that encountered in modeling the mean rate of purely gas phase chemical reactions using conventional averaging techniques.

The Conditional Moment Closure (CMC) method (see Klimenko 1990, Bilger 1993) for modeling turbulent gas phase nonpremixed combustion makes use of averages which are conditional upon the local value of a conserved scalar (mixture fraction), which is indicative of the state of mixing between fuel and air masses. Conditional averaging upon mixture fraction captures much of the turbulence-induced fluctuations, and a first order conditionally averaged closure is often possible. The success of the CMC model in predicting gas phase combustion makes it of some interest in modeling particle reactions in turbulent flow.

1 Aeronautical & Maritime Research Laboratory, DSTO, Australia

The purpose of this study was to simulate the dynamics of reactive particle mass and motion in a turbulent combusting environment in an attempt to model the observed mean thermochemical behavior of the reacting particles using a derivative of the CMC method. In this report, the simulation and modeling of pseudo-soot and pseudo-droplet particles are described. The former type of particles were smaller than the latter, and they were subject to relatively strong processes of growth and consumption. These processes were meant to represent soot surface growth and oxidation. The pseudo-droplet particles were subject to an evaporative process only. In both the simulations and modeling, particle-particle interactions were disallowed, thus rendering the results of this study valid only for low particle mass loadings of the gas phase.

2. Simulation conditions

Direct numerical simulations were conducted using a pseudo-spectral solution technique for forced isotropic turbulent flow on a 32-cubed grid. The flow was incompressible in nature, but a passive scalar (mixture fraction) field was used in conjunction with an equilibrium temperature profile in passive scalar space to determine a false temperature map throughout the domain. This false temperature was computed for the purpose of determining instantaneous particle reaction rates at every step. The passive scalar field was forced at large scales through the interaction of turbulent motions with an imposed mean scalar gradient in the x direction in the same manner as the simulations of Overholt and Pope (1996). Cubic spline tensor-products as described by Yeung and Pope (1988, 1989) were employed to determine local fluid velocities and temperatures at all particle locations. Particle properties were advanced in time using a fourth-order Adams-Bashforth timestepping routine.

The following Lagrangian equation for particle motion was solved,

$$\frac{dv_i}{dt} = \frac{\alpha^*}{\tau_k}(m^*)^{-2/3}(u_i(\underline{x}) - v_i) \quad , \tag{1}$$

where v_i denotes the particle velocity, $u_i(\underline{x})$ denotes the local fluid velocity at the particle location, m^* is the nondimensional particle mass, τ_k is the Kolmogorov timescale, and α^* is the nondimensional characteristic particle rate given by,

$$\alpha^* = 18\left(\frac{\rho_f}{\rho_p}\right)\left(\frac{\mathrm{L}_k}{d}\right)^2 \quad . \tag{2}$$

In the above, L_k is the Kolmogorov length scale, d is the reference particle diameter, ρ_p is the particle material density, and ρ_f is the fluid density.

The Stokes drag expression above (Eq. 1) strictly applies only in the limit of a purely laminar flow around the particle. This assumption is valid for the smaller soot particles but is not as well justified for the droplets. Empirical corrections for changes in particle drag with higher slip Reynolds numbers are available but have not been applied in the simulations reported here.

For droplets, the rate of change of the mass of any particle was given by

$$\frac{dm^*}{dt} = -\frac{2}{3}\frac{\beta}{\tau_k}(m^*)^{1/3}\ln(1+T^*) \ , \tag{3}$$

where β is a generic rate coefficient, nominally equal to α^* for inertial particles, and T^* is a nondimensional temperature equivalent to the local *Spalding transfer number*. The value of the temperature varied from zero in non-reactive regions of passive scalar space to a peak value of 3.4 at stoichiometric conditions. The peak value corresponds to the transfer number for kerosene droplets evaporating within enveloping flames (see Kuo 1986).

The rate of change of mass for any given soot particle was given by

$$\frac{dm^*}{dt} = \frac{\beta}{\tau_k}(m^*)^{1/3}\left(f_{gr} - f_{co}(m^*)^{1/3}\right) \ , \tag{4}$$

where β is a rate coefficient not directly related to α^*, and f_{gr} and f_{co} are normalized functions of local mixture fraction (and thus an inferred reactive gas phase composition) which mimic surface growth and consumption respectively. The growth and consumption reactions were designed to embody the basic features of the soot processes they represent, but with one notable difference. Namely, the reaction rate profiles were defined so as to be symmetric in mixture fraction space about the mean mixture fraction. Particle surface growth was strongest at the mean mixture fraction, and particle consumption was strongest somewhat to the lean and rich sides of the mean mixture fraction. This symmetry of thermochemical properties about the mean mixture fraction allowed conditional statistics on either side of the mean to be combined to increase statistical significance in each half-plane of mixture fraction space.

The reference particle rates (α^*, β) differed between simulations to reflect different sizes and reactivity of the particles, while flow and mixing conditions were the same for all cases. The details of the simulation cases studied are given in Table I. Some inertial particle simulations were repeated with inertia-less particles (denoted by i-suffixed case designations in Table I) to ascertain the influence of particle slip velocity on the reactive particle statistics.

Table I. Parameters and durations for the reactive particle simulations.

Case	Type	α^*	β	τ_{sim}/τ_{eddy}	τ_{sim}/τ_{pop}
d1	droplet	0.014	0.014	193	34.7
d1i	droplet	∞	0.014	96.1	15.0
s1	soot	0.7	2.8	3.5	0.46
s2	soot	0.7	0.7	104	23.1
s2i	soot	∞	0.7	104	23.1

In the table, the ratios of the duration (τ_{sim}) of each case to both the large eddy turnover time (τ_{eddy}) and the mean time for total particle population change through injection (τ_{pop}) are given. Owing to explicit method time step limitations, the cases with longer characteristic timescales such as the droplet and less-reactive soot cases were less expensive to compute. These cases, therefore, could be continued for a larger number of eddy-turnover times for a given amount of real time.

In each case, 8192 particles were maintained in the domain at a constant mean number density by continuous injection. Particle simulations commenced only after the forcing had produced a statistically stationary flow field over a period of many hundreds of eddy turnover times. The simulations were conducted at a Taylor Reynolds number of ~ 24 with a value of approximately 0.22 for the ratio of integral length scale to domain width and 2.4 for the product of Kolmogorov lengthscale and maximum wavenumber in the simulation.

The actual size of the soot particles used in the *inertial* simulations of this study were at the upper limit of realistic soot particles. In a sense, these simulation cases embody a *worst case scenario* for modeling soot. In practical applications, the bulk of soot particles are much smaller and follow the flow field much more closely. These smaller reacting particles were better simulated using an inertia-less particle tracking method in conjunction with the direct numerical simulations of turbulence.

2.1 Particle injection

The imposed mean scalar gradient in the x direction of the simulation domain required that special consideration be given to particles which crossed the domain boundaries in this direction. In the other directions, all properties were periodic and particles were simply returned to the domain by a periodic mapping. The same mapping was not applied in the x direction as that would allow particles to transfer between very lean and very rich mixture conditions in crossing the domain boundary.

Instead, any particle which crossed an x boundary was deemed to have left the domain permanently, and was replaced via a periodic mapping by a fresh particle with a velocity equal to the departing particle and mass equal to the injection mass. This type of fresh particle injection allowed a statistically stationary particle state to be reached as a balance between the processes of particle reaction, and transport to and from the injection boundaries occurs.

Injection across the two x-bounding planes was characterized by a relatively weak influence on conditional mean particle statistics at very rich and lean mixture fractions. The source terms for the conditional mean and variance equations for particle mass fraction which result from these injection schemes are described in Section 3.2.

2.2 Mixing and reaction statistics

Statistical data based on particle mass fractions were measured from the simulations for comparison with model predictions. These data were recorded only after the statistical stationarity of the particle ensemble had been established by monitoring initial transients in the data.

As each particle, on average, occupied four grid cells to the exclusion of other particles, it was not possible to determine meaningful spatial gradients in particle properties within the carrier fluid. It was possible, however, to derive conditional statistical information from the data by binning particles in mixture fraction space according to their local value of mixture fraction. The particle density in each bin allowed gradients of conditional quantities in mixture fraction space to be determined for comparison with modeled terms.

Mixing statistics such as conditional mean scalar dissipation rate, conditional mean scalar diffusion rate, and the mixture fraction probability density function (PDF) were determined from the statistically stationary simulation data.

The mean scalar dissipation rate ($N_\eta \equiv \langle \mathcal{D}(\nabla\xi)^2 \mid \xi(\underline{x},t) = \eta \rangle$), conditional upon the value (η) of the local instantaneous value of mixture fraction (ξ), was found to be independent of mixture fraction as reported by Overholt and Pope (1996) and Pope and Ching (1993). Thus the significant simplification,

$$N_\eta = \langle N \mid \eta \rangle = \langle N \rangle \quad , \tag{5}$$

was employed in the modeling described below.

The mixture fraction PDF (P_η) for the whole domain was found to agree closely with a superposition of Gaussian PDFs with equal variance, but with mean values varying with position in the x direction according to the imposed mean mixture fraction gradient. Given values of mean mixture fraction on the x boundaries of ξ_0 and ξ_1 and a spatially uniform mixture fraction variance σ^2, the mixture fraction PDF can be written as,

$$P_\eta = \frac{\sigma}{\xi_0 - \xi_1}\left(\phi\left(\frac{\eta - \xi_1}{\sigma}\right) - \phi\left(\frac{\eta - \xi_0}{\sigma}\right)\right) \quad , \tag{6}$$

where $\phi(\ldots)$ is the integral of the Gaussian distribution between the given argument and infinity.

The conditional mean scalar diffusion rate ($M_\eta \equiv \langle \mathcal{D}\nabla^2\xi \mid \xi(\underline{x},t) = \eta \rangle$) is yielded by,

$$\frac{\partial}{\partial\eta}\left(P_\eta M_\eta\right) = \frac{\partial^2}{\partial\eta^2}\left(P_\eta N_\eta\right) \quad , \tag{7}$$

which holds for homogeneous mixing conditions. The simplification afforded by Eq. 5, thus gives M_η as,

$$M_\eta = \frac{\langle N \rangle}{P_\eta}\frac{\partial P_\eta}{\partial\eta} \quad . \tag{8}$$

The conditional diffusion profile given by the equation above was found to closely agree with the simulation data.

The forms of the mixture fraction PDF and conditional diffusion rate profiles given by the above equations are plotted in Fig. 1. The mixture fraction PDF is somewhat broadened around the peak compared to any single Gaussian profile with the same mean and variance. As a result, the conditional diffusion rate profile has

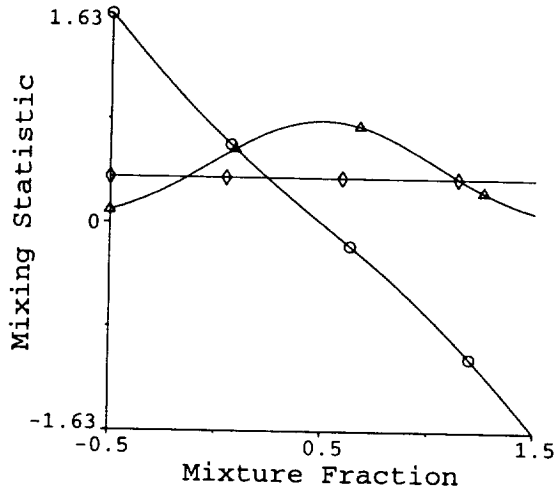

FIGURE 1. Profiles for mixture fraction PDF ($\triangle$), conditional mean scalar dissipation rate ($\diamond$), and conditional mean diffusion rate ($\circ$) expected and observed in simulation data.

a mean slope which is about 35% shallower than that of the purely linear profile which results from a single Gaussian PDF with an equivalent mean and variance, and equivalent conditional mean dissipation rate.

All of the simulations exhibited profiles of the nature depicted in the figure since they all shared exactly the same mixing characteristics. The spatially uniform value of variance of mixture fraction was equal to ~ 0.34 in each case, with mean mixture fractions on the x boundaries of zero and unity and an overall domain-averaged mean mixture fraction of one half.

Notice from Fig. 1 that the quantity ξ, referred to here as *mixture fraction*, is normalized to have a unit value on the rich boundary of the domain and zero value on the lean boundary, but this *does not* denote pure fuel and oxidizer states. It is possible, and indeed required in the current simulation configuration, to have values of ξ which are greater than unity and less than zero. Pure fuel and oxidizer states can be considered to exist only in the limits of $\xi \rightarrow \pm\infty$.

3. Modeling method

Application of the CMC model for gas phase turbulent combustion to the modeling of condensed-phase fields requires some consideration of the differences in behavior between the two phases. Firstly, it was assumed that the particles were, in the mean, small enough to follow the smallest scales of motion. This was true in the inertia-less particle simulations, but was somewhat less justified for the inertial (particularly droplet) simulations.

Secondly, it is clear that the particle phase does not diffuse appreciably on a molecular level, and thus the particle phase and the gas phase-based mixture fraction are transported in a completely different manner at this level. The effect of this differential diffusion must, therefore, be incorporated into the CMC model.

Further, at the smallest scales a distinct difference between the distribution of gaseous species and condensed phase species is expected (see Klimenko 1990). Significant local structure can exist in the particle field at scales where gas phase fields have been completely smeared by molecular diffusion. The existence of such local structure implies that instantaneous local deviations of particle mass fractions from means, conditional upon mixture fraction, can be large.

In the present study, particle effects upon the gas phase were neglected, leaving the effect of gas phase fluctuations on particle evolution to be examined in isolation. In reality, however, reciprocal interactions between gaseous and condensed-phase species is likely to be very important. In the case of droplet evaporation, it is the addition of vaporized fuel to the continuous phase which largely determines the way in which combustion proceeds. In the case of soot particles, the removal of sensible enthalpy from the continuous phase occurs as a result of proximity to soot, which can strongly effect localized combustion dynamics. In both of these instances, large conditional variance in particle properties could lead to similarly elevated levels of conditional variance in *sympathetic* gas phase species and thereby increase the difficulty of the chemical closure problem in the gas phase. This increase in conditional variance for gas phase species can be viewed as arising from the different gas phase behavior, at the same mixture fraction, which will result depending on whether a parcel of gas is adjacent to a particle or not.

It is for this reason that it is important to be able to predict the level of conditional variance of particle mass fraction. The CMC model proposed in this study made use of a particle-specific differential diffusion variant of the second-order conditional moment closure proposed by Li and Bilger (1996).

3.1 Model derivation

In the following, a CMC model for particle reactions in turbulent nonpremixed combustion is derived for general flow and mixing conditions. The spatial and temporal simplifications afforded by the simulation conditions of the present study are introduced in Section 3.2.

The local instantaneous equations for mixture fraction and a particle mass fraction continuum form the basis for the derivation of the model. The equation for mixture fraction ξ can be written as,

$$\frac{\partial \xi}{\partial t} + u_i \frac{\partial \xi}{\partial x_i} - \mathcal{D} \frac{\partial^2 \xi}{\partial x_j^2} = 0 \ , \tag{9}$$

where the flow field is assumed to be incompressible, u_i is the component of carrier fluid velocity in the i-th direction, and $\mathcal{D}$ is the diffusivity of mixture fraction under a Fickian transport assumption.

The equation for local instantaneous mass fraction of the particle continuum is given by,

$$\frac{\partial Y}{\partial t} + v_i \frac{\partial Y}{\partial x_i} - \mathcal{D}_y \frac{\partial^2 Y}{\partial x_j^2} = \dot{\omega} \ , \tag{10}$$

where $\dot{\omega}$ is the local reaction rate of the particle continuum, $\mathcal{D}_y$ is the effective diffusivity of this continuum, and v_i is the velocity component in the i-th direction of the field of particles. The particle diffusivity $\mathcal{D}_y$ is expected to be very much smaller than the mixture fraction diffusivity; however, the term is retained in the derivation for completeness. Multiplying Eq. 10 by the particle mass fraction yields,

$$\frac{\partial Y^2}{\partial t} + v_i \frac{\partial Y^2}{\partial x_i} - 2\mathcal{D}_y Y \frac{\partial^2 Y}{\partial x_j^2} = 2Y\dot{\omega} \ , \tag{11}$$

which is used in the derivation of the equation for conditional variance of particle mass fraction.

The *fine-grain* probability density function (see Pope 1985) for mixture fraction is defined as,

$$\psi(\underline{x}, t, \eta) \equiv \delta(\xi(\underline{x}, t) - \eta) \ , \tag{12}$$

and has an expectation over the statistical ensemble equal to the mixture fraction PDF (P_η) as given by,

$$P_\eta(\underline{x}, t, \eta) = \langle \psi \rangle \ . \tag{13}$$

The local instantaneous equation for the *fine-grained* PDF can be derived from the differential properties of ψ and Eq. 9 so that,

$$\frac{\partial \psi}{\partial t} + \frac{\partial}{\partial x_i}(u_i \psi) + \frac{\partial}{\partial \eta}\left(\mathcal{D}\psi \nabla^2 \xi\right) = 0 \ . \tag{14}$$

Klimenko and Bilger (1998) derived a conditional mean equation for the differential diffusion of gaseous species in turbulent combustion through the combination of Eqs. 11 and 14 given above. Their methodology is largely followed here except that a conditional variance equation is also derived and some significant differences in closure assumptions are made in the final stages. In the section immediately following, derivation of the equation for the product of the square of particle mass fraction and the fine grain PDF is described as a prerequisite to the derivation of the conditional variance equation for particle mass fraction. The derivation of the corresponding equation for conditional mean mass fraction is analogous except where noted otherwise.

3.1.1. Derivation of ψY^2 equation

The derivation proceeds by adding Eq. 11, multiplied by ψ, to Eq. 14, multiplied by Y^2. The resultant equation is given by,

$$\frac{\partial}{\partial t}\left(\psi Y^2\right) + \frac{\partial}{\partial x_i}\left(u_i \psi Y^2\right) = (u_i - v_i)\,\psi \frac{\partial Y^2}{\partial x_i} + 2\psi Y \dot{\omega} + A_y - A_\xi \ , \tag{15}$$

where

$$A_y = 2\mathcal{D}_y \psi Y \frac{\partial^2 Y}{\partial x_j^2} \ , \quad A_\xi = Y^2 \frac{\partial}{\partial \eta}\left(\psi \mathcal{D} \nabla^2 \xi\right),$$

are convenient groupings of the $\mathcal{D}$ and $\mathcal{D}_y$ diffusive terms. The mixture fraction diffusivity term, first expanded by using the inhomogeneous-flow form of Eq. 7, is

$$A_\xi = Y^2 \left(\frac{\partial^2}{\partial \eta^2} \left(\psi \mathcal{D} (\nabla \xi)^2 \right) - \mathcal{D} \frac{\partial^2}{\partial x_j^2} (\psi) \right) \quad . \tag{16}$$

The latter right-hand side term appearing in Eq. 16 also appears in the full expansion of $\mathcal{D} \frac{\partial^2}{\partial x_j^2} (Y^2 \psi)$. Substitution of the expansion into Eq. 16 yields a final expression for A_ξ,

$$A_\xi = \frac{\partial^2}{\partial \eta^2} \left(Y^2 \psi \mathcal{D} (\nabla \xi)^2 \right) - \frac{\partial}{\partial \eta} \left(\mathcal{D} \psi \frac{\partial \xi}{\partial x_j} \frac{\partial Y^2}{\partial x_j} \right) - \mathcal{D} \frac{\partial^2}{\partial x_j^2} (Y^2 \psi) + \mathcal{D} \frac{\partial}{\partial x_j} \left(\psi \frac{\partial Y^2}{\partial x_j} \right) \quad . \tag{17}$$

The particle diffusivity term A_y, as given above in connection with Eq. 15, appears in the full expansion of $\mathcal{D}_y Y \frac{\partial}{\partial x_j} \left(\psi \frac{\partial Y}{\partial x_j} \right)$. Expressing A_y as the subject of this expansion yields

$$A_y = \frac{\partial}{\partial \eta} \left(\mathcal{D}_y \psi \frac{\partial \xi}{\partial x_j} \frac{\partial Y^2}{\partial x_j} \right) + 2 \mathcal{D}_y Y \frac{\partial}{\partial x_j} \left(\psi \frac{\partial Y}{\partial x_j} \right) \quad . \tag{18}$$

Rearrangement of the latter right-hand side term of the above equation via the chain rule gives A_y in final form,

$$A_y = \frac{\partial}{\partial \eta} \left(\mathcal{D}_y \psi \frac{\partial \xi}{\partial x_j} \frac{\partial Y^2}{\partial x_j} \right) + \mathcal{D}_y \frac{\partial}{\partial x_j} \left(\psi \frac{\partial Y^2}{\partial x_j} \right) - 2 \mathcal{D}_y \psi \left(\frac{\partial Y}{\partial x_j} \right)^2 \quad , \tag{19}$$

The substitution of Eqs. 7 and 19 into Eq. 15 yields,

$$\frac{\partial}{\partial t} (\psi Y^2) + \frac{\partial}{\partial x_i} (u_i \psi Y^2) = 2 \psi Y \dot{\omega} - 2 \mathcal{D}_y \psi \left(\frac{\partial Y}{\partial x_j} \right)^2 + \frac{\partial F_{Y2}}{\partial \eta} + R_{Y2} \quad , \tag{20}$$

where the flux of squared particle mass in mixture fraction space is given by,

$$F_{Y2} = (\mathcal{D}_y + \mathcal{D}) \psi \frac{\partial \xi}{\partial x_j} \frac{\partial Y^2}{\partial x_j} - \frac{\partial}{\partial \eta} \left(Y^2 \psi \mathcal{D} (\nabla \xi)^2 \right) \quad , \tag{21}$$

and the collected residual terms can be written as,

$$R_{Y2} = (u_i - v_i) \psi \frac{\partial Y^2}{\partial x_i} + (\mathcal{D}_y - \mathcal{D}) \frac{\partial}{\partial x_j} \left(\psi \frac{\partial Y^2}{\partial x_j} \right) + \mathcal{D} \frac{\partial^2}{\partial x_j^2} (Y^2 \psi) \quad . \tag{22}$$

3.1.2. Averaging and closure of ψY equation

It is illustrative to average and close the simpler equation for conditional mean particle mass fraction before employing the same approach on the conditional variance equation. The conditional mean equation is required before further derivation

of the conditional variance equation can proceed. In this section, some of the key closure assumptions of Klimenko and Bilger (1998) have been relaxed out of necessity for the modeling of particles.

A set of equations similar to Eqs. 20-22 applies for the product of the fine-grain PDF and particle mass fraction and can be written as,

$$\frac{\partial}{\partial t}(\psi Y) + \frac{\partial}{\partial x_i}(u_i \psi Y) = \psi\dot{\omega} + \frac{\partial F_Y}{\partial \eta} + R_Y \quad , \tag{23}$$

where

$$F_Y = (\mathcal{D}_y + \mathcal{D})\,\psi \frac{\partial \xi}{\partial x_j}\frac{\partial Y}{\partial x_j} - \frac{\partial}{\partial \eta}\left(Y\psi\mathcal{D}(\nabla\xi)^2\right) \quad , \tag{24}$$

and

$$R_Y = (u_i - v_i)\,\psi\frac{\partial Y}{\partial x_i} + (\mathcal{D}_y - \mathcal{D})\frac{\partial}{\partial x_j}\left(\psi\frac{\partial Y}{\partial x_j}\right) + \mathcal{D}\frac{\partial^2}{\partial x_j^2}(Y\psi) \quad . \tag{25}$$

Averaging Eq. 23 over mixture fraction space yields the PDF-product form of the conditional moment closure (CMC) equation for conditional mean particle mass fraction,

$$\frac{\partial}{\partial t}(P_\eta Q_\eta) + \frac{\partial}{\partial x_i}\left(\langle u_i Y \mid \eta\rangle P_\eta\right) = \langle\dot{\omega} \mid \eta\rangle P_\eta + \frac{\partial F_Q}{\partial \eta} + R_Q \quad , \tag{26}$$

where $Q_\eta \equiv \langle Y \mid \eta\rangle = \langle Y\psi\rangle / P_\eta$, and F_Q and R_Q are the conditionally averaged flux and residual terms. The averaged residual term can be written as follows,

$$R_Q = \left\langle (u_i - v_i)\frac{\partial Y}{\partial x_i} \mid \eta \right\rangle P_\eta + (\mathcal{D}_y - \mathcal{D})\frac{\partial}{\partial x_j}\left(P_\eta\left\langle\frac{\partial Y}{\partial x_j} \mid \eta\right\rangle\right) + \mathcal{D}\frac{\partial^2}{\partial x_j^2}(QP_\eta) \quad , \tag{27}$$

and contains terms which are assumed to be small for high Reynolds number flow with only small particle slip velocities. The conditional mean flux term, equal to

$$F_Q = (\mathcal{D}_y + \mathcal{D})\,P_\eta\left\langle\frac{\partial \xi}{\partial x_j}\frac{\partial Y}{\partial x_j} \mid \eta\right\rangle - \frac{\partial}{\partial \eta}\left(\mathcal{D}P_\eta\left\langle Y(\nabla\xi)^2 \mid \eta\right\rangle\right) \quad , \tag{28}$$

is approximated by Klimenko and Bilger (1998) after assuming that the gradient of Y is well correlated with the gradient of mixture fraction and that there is only a weak correlation between Y and $(\nabla\xi)^2$. In the following, the latter assumption is relaxed, so that

$$F_Q \approx c\,P_\eta N_\eta \frac{\partial Q_\eta}{\partial \eta} - Q_\eta\frac{\partial}{\partial \eta}(P_\eta N_\eta) - \frac{\partial}{\partial \eta}(P_\eta C_\eta) \quad , \tag{29}$$

where $N_\eta \equiv \left\langle \mathcal{D}(\nabla\xi)^2 \mid \eta\right\rangle$ is the scalar dissipation rate and C_η is the covariance between scalar dissipation rate and particle mass fraction. The symbol c denotes a *mixing mode* variable which is equal to unity in the case of mixing in the absence of

differential diffusion but is not known for the case of differentially diffusing scalars (Klimenko & Bilger 1998). This variable is discussed in greater detail in Section 3.2.

The final form of the equation for conditional mean particle mass fraction is obtained by substituting Eq. 29 into Eq. 26, followed by subtraction of the mixture fraction PDF equation (averaged form of Eq. 14) and normalization by the PDF to give,

$$\frac{\partial Q_\eta}{\partial t}+\langle u_i \mid \eta\rangle \frac{\partial Q_\eta}{\partial x_i} = \langle \dot{\omega} \mid \eta\rangle + cN_\eta \frac{\partial^2 Q_\eta}{\partial \eta^2} + (c-1)M_\eta \frac{\partial Q_\eta}{\partial \eta} - \frac{1}{P_\eta}\frac{\partial^2}{\partial \eta^2}\left(P_\eta C_\eta\right) \quad . \tag{30}$$

In the above expression, R_Q has been neglected as has the conditional correlation between velocity fluctuations and particle mass fraction. As in Eq. 7, the symbol M_η denotes the conditional mean diffusion rate.

3.1.3. Averaging and closure of ψY^2 equation

The equation for the conditional variance of particle mass fraction, defined as $q_\eta^2 \equiv \langle y^2 \mid \eta\rangle = \langle Y^2\psi\rangle / P_\eta - Q_\eta^2$, can be derived from Eq. 20 through several stages. Averaging of Eq. 20 yields a mean-square-PDF product equation,

$$\frac{\partial}{\partial t}\left(P_\eta \langle Y^2 \mid \eta\rangle\right) + \frac{\partial}{\partial x_i}\left(\langle u_i Y^2 \mid \eta\rangle P_\eta\right) = 2\langle Y\dot{\omega} \mid \eta\rangle P_\eta + \frac{\partial F_q}{\partial \eta} - P_\eta \epsilon_Y + R_q \quad , \tag{31}$$

where F_q denotes the flux of mean square mass in mixture fraction space, R_q is the average of the Y^2 residual term of Eq. 22,

$$R_q = P_\eta \left\langle (u_i - v_i)\frac{\partial Y^2}{\partial x_i} \mid \eta \right\rangle + (\mathcal{D}_y - \mathcal{D})\frac{\partial}{\partial x_j}\left(P_\eta \left\langle \frac{\partial Y^2}{\partial x_j} \mid \eta \right\rangle\right) + \mathcal{D}\frac{\partial^2}{\partial x_j^2}\left(P_\eta \langle Y^2 \mid \eta\rangle\right) \quad , \tag{32}$$

and ϵ_Y is the conditional mean square mass dissipation rate, given by

$$\epsilon_Y \equiv 2\mathcal{D}_y \left\langle (\nabla Y)^2 \mid \eta \right\rangle \quad . \tag{33}$$

Following the closure argument for flux of conditional mean mass in mixture fraction space (Eq. 29), the flux of the conditional mean square particle mass fraction,

$$F_q = (\mathcal{D}_y + \mathcal{D})\, P_\eta \left\langle \frac{\partial \xi}{\partial x_j}\frac{\partial Y^2}{\partial x_j} \mid \eta \right\rangle - \frac{\partial}{\partial \eta}\left(P_\eta \left\langle Y^2 \mathcal{D} (\nabla \xi)^2 \mid \eta \right\rangle\right) \quad , \tag{34}$$

is approximated by the following, where the mixing mode variable c has a value equal to that employed in Eq. 29,

$$F_q \approx c\, P_\eta N_\eta \frac{\partial q_\eta^2}{\partial \eta} - q_\eta^2 \frac{\partial}{\partial \eta}\left(P_\eta N_\eta\right) + 2c\, P_\eta C_\eta \frac{\partial Q_\eta}{\partial \eta} - 2Q_\eta \frac{\partial}{\partial \eta}\left(P_\eta C_\eta\right)$$

$$+ cP_\eta N_\eta \frac{\partial Q_\eta^2}{\partial \eta} - Q_\eta^2 \frac{\partial}{\partial \eta}\left(P_\eta N_\eta\right) \quad . \tag{35}$$

Following the substitution of Eq. 35 into Eq. 31, the decomposition of Y into $Q_\eta + y$, and the subtraction of the equation for the conditional mean mass fraction, the equation for the product of conditional variance and mixture fraction PDF is derived. The decomposition of this equation via the chain rule and subtraction of the PDF equation multiplied by q_η^2 yields the final form of the conditional variance equation,

$$\frac{\partial q_\eta^2}{\partial t} + \langle u_i \mid \eta \rangle \frac{\partial q_\eta^2}{\partial x_i} = 2 \langle y\dot{\omega}' \mid \eta \rangle + cN_\eta \frac{\partial^2 q_\eta^2}{\partial \eta^2} + (c-1) M_\eta \frac{\partial q_\eta^2}{\partial \eta} + S_q - \epsilon_q \ , \quad (36)$$

where S_q denotes the collected conditional source terms for particle mass fraction variance,

$$S_q \equiv 2cC_\eta \frac{\partial^2 Q_\eta}{\partial \eta^2} + \frac{2}{P_\eta}(c-1) \frac{\partial}{\partial \eta}(P_\eta C_\eta) \frac{\partial Q_\eta}{\partial \eta} + 2\left(c - \frac{\mathcal{D}_y}{\mathcal{D}}\right) N_\eta \left(\frac{\partial Q_\eta}{\partial \eta}\right)^2 \ , \quad (37)$$

and ϵ_q is the dissipation rate of conditional variance,

$$\epsilon_q \equiv 2\mathcal{D}_y \left\langle (\nabla y)^2 \mid \eta \right\rangle \ . \quad (38)$$

Note that the conditional variance equation in the form given above neglects conditional covariance between velocity and mass fraction and all of the terms associated with the difference between R_q and $2Q_\eta R_Q$ which appear in the derivation.

The final forms of the equations for the conditional mean and variance of particle mass fraction (Eqs. 30 and 36) contain two unclosed quantities, namely the mixing mode variable c, which parameterizes the level of differential diffusion, and the covariance between scalar dissipation rate and particle mass fraction C_η. A discussion of these two quantities is provided in the following sections.

3.2 Solution of model equations

Equations 30 and 36 of the preceding section were solved to match the simulated conditions of spatially homogeneous, steady conditional statistics. The statistically stationary, spatially degenerate form of the conditional mean particle mass fraction profile is given by,

$$0 = \langle \dot{\omega} \mid \eta \rangle + cN_\eta \frac{\partial^2 Q_\eta}{\partial \eta^2} + (c-1) M_\eta \frac{\partial Q_\eta}{\partial \eta} - \frac{1}{P_\eta} \frac{\partial^2}{\partial \eta^2}(P_\eta C_\eta) + I_Q \ , \quad (39)$$

where I_Q is the conditional mean particle mass injection rate which results from the injection process described in Section 2.1. The conditional variance of particle mass fraction profile was found from,

$$0 = 2 \langle y\dot{\omega}' \mid \eta \rangle + cN_\eta \frac{\partial^2 q_\eta^2}{\partial \eta^2} + (c-1) M_\eta \frac{\partial q_\eta^2}{\partial \eta} + S_q + I_q \ , \quad (40)$$

where I_q is the conditional variance source due to particle injection. Note that the effective diffusivity of the particle field ($\mathcal{D}_y$) was assumed to be identically zero, thus the absence of the ϵ_q term given in Eq. 36 from the above equation. The conditional particle injection source terms included in the above (I_Q & I_q) are given by,

$$I_Q = \frac{P_I}{\tau_{pop}} (1 - Q_\eta) \tag{41}$$

$$I_q = \frac{P_I}{\tau_{pop}} \left((1 - Q_\eta)^2 - q_\eta^2 \right) \tag{42}$$

where P_I is the PDF of particle injection mixture fraction and τ_{pop} is the time required for the number of injections to equal the size of the particle population. In the above it was assumed that particles were injected to replace those which leave the system, and all freshly injected particles had unit mass as described in Section 2.1. The form of the injection PDF consisted of the normalized sum of two Gaussian distributions with variances equal to the domain variance and mean mixture fraction values of zero and unity.

Chemical source terms in Eqs. 39 and 40 were determined using instantaneous local temperature (taken from an invariant chemical equilibrium profile) and the conditional mean and variance of particle mass fraction in truncated Taylor series expansions of the instantaneous reaction rate expressions.

The *mixing mode* variable c, included in the CMC equations above, provides a means of accounting for differential diffusion effects. In the limit where mixing is overwhelmingly due to turbulent stirring, the mixing mode variable tends to unity. In cases where a larger proportion of the mixing is due to molecular mass transfer, the mixing mode variable will vary substantially from unity. The greatest allowable deviation of c from unity is given by the ratio of the molecular diffusivity of the species in question to that of the mixture fraction.

From a modeler's perspective, it is highly desirable that c be independent of Q_η, q_η^2, and mixture fraction. In that eventuality, one could hypothesize that the degree of departure from mixing that is dominated by strong turbulent stirring might be expressed as,

$$c = 1 + \left(\frac{\mathcal{D}_y}{\mathcal{D}} - 1 \right) f_{mix} \ , \tag{43}$$

where f_{mix} is a function which varies between zero and unity according to some dependence on global properties of the flow field. One possibility for f_{mix} is some power of the Kolmogorov scalar scale ξ_k appropriately normalized by the maximum globally realizable range in mixture fraction. The Kolmogorov scalar scale is a measure of the characteristic size of scalar fluctuations at dissipative scales. For mixture fraction this scale varies between zero and unity for high and low intensity turbulent mixing respectively. As this study consists of data from a single set of mixing conditions, it is not possible to validate any model for variation in c with mixing conditions. It is, however, possible to examine whether a single value of c

is appropriate independently of local values of Q_η, q_η^2, and mixture fraction. This issue is examined in the next section.

It should be noted that Kronenburg and Bilger (1997) successfully account for differential diffusion in the CMC model through the use of an alternate treatment to that proposed above. Their methodology has much to recommend it, but when applied to multi-component reacting systems, it requires an additional conditional moment equation to be solved for each species. The method presented here seeks to avoid that added cost.

It was found that the profile shape and magnitude of the conditional covariance between particle mass fraction and scalar dissipation rate (C_η) was critical to the transport of particles in mixture fraction space. While the form of this profile is, in general, not known, its behavior at mixture fraction bounds is prescribed by the integration of Eq. 26, with respect to mixture fraction, between these bounds. This integration should yield the unconditional mean mixture fraction equation, which implies that the bounding values of the mixture fraction flux term (Eq. 29) are zero. It follows that the slope of the product $P_\eta C_\eta$ must be zero at the bounding mixture fractions.

Modeling of the C_η term was achieved using a simple heuristic approach to best match the observed simulation profiles for C_η. This model took the form,

$$C_\eta = \left(a_q \sqrt{(q_\eta^2)} - a_Q Q_\eta + a_{cor}\right) N_\eta \ , \tag{44}$$

where a_q, a_Q, and a_{cor} were constants determined from the goodness of fit with the C_η profile observed from the corresponding simulation. The above fitting technique is similar to that employed by Li and Bilger (1996) except for the inclusion of the conditional mean value (Q_η) and the zero-boundary correction term a_{cor}. It was found that it was necessary to include these terms to match the observed simulation data. Due to the case-specific nature of the covariance profiles, they are discussed in turn in the following section.

4. Results

In the following, the results from the modeling of soot particles and droplets are discussed separately.

4.1 Soot

Examining the conditional covariance between scalar dissipation rate and particle mass fraction (C_η), the simulation data revealed the characteristic form of the covariance profile for soot as possessing a large negative spike near the mean mixture fraction. The location of this spike in mixture fraction space corresponded with the location of the peak conditional mean mass fraction. Through careful selection of the coefficients in the C_η model equation (Eq. 44), it was possible to produce the similar profile as was observed in the simulation data while producing good predictions for Q_η and q_η^2.

The profile match derived for conditional covariance in soot case *s1* can be seen in Fig. 2. Note that the observed simulation profile has been slightly smoothed

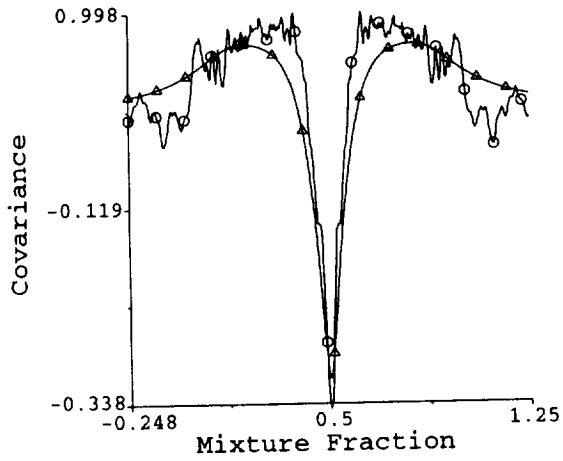

FIGURE 2. Modeled and observed conditional covariance between mass fraction and scalar dissipation rate for case *s1*. Symbols denote the following profiles: △ - prediction of covariance, and o - simulated covariance.

and averaged about the symmetry point at the mean mixture fraction to facilitate comparison with the smooth symmetric model profile. It is evident that the model profile agrees reasonably well with the observed profile, particularly in the vicinity of the mean mixture fraction. The model profile does not match the observed maximum value of the covariance at mixture fractions slightly leaner and richer than the mean value. Unfortunately, it is the first and second derivatives of the conditional covariance which appear in the model equations. The value of the slope and curvature of the model C_η profile are believed to reflect the general behavior of the simulation data; however, it is difficult to make any stronger statement due to the limited data available for statistical analysis. Future simulations with larger particle populations will be used to better understand this behavior.

The characteristic effect on the conditional mean particle mass fraction of varying the mixing mode variable, c, can be seen in Fig. 3 for case *s1* along with the conditional mean profile which results from chemical reactions and particle injection alone. It can be seen that the arbitrary increase of c causes the predicted mean mass fraction profile to simultaneously increase in peak value and decrease in minimum value. Further, increases in c tend to decrease the value of conditional mean mass fraction at very rich and very lean mixture fractions.

The governing conditional mean particle mass fraction equation (Eq. 39) has the property that increased values of c tend to favor a mode of mass transfer *in mixture fraction space* which is essentially diffusive in nature. Lower values of c favor the mode associated with the drift of particle mass *in mixture fraction space* which results from gas phase species diffusing at a more rapid rate in physical space than the particles they surround. Thus c can be thought of as a measure of to what degree particle mass diffuses against a mixture fraction coordinate instead of undergoing an apparent convection-like process in mixture fraction space due to the differential

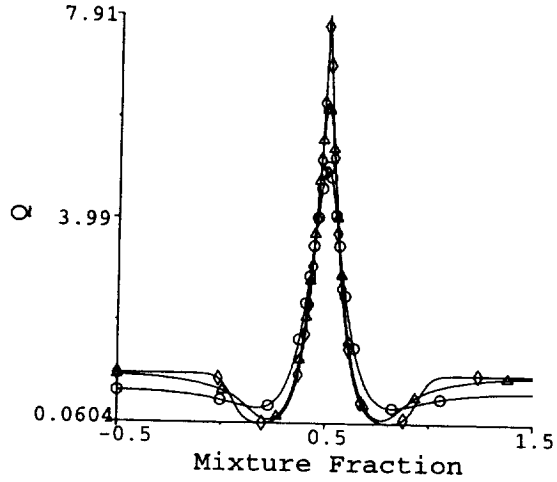

FIGURE 3. Predicted conditional mean mass fraction profiles for case *s1* with arbitrarily varied levels of differential diffusion. Symbols denote the following profiles: △ - prediction with $c = 0.05$, ○ - prediction with $c = 1.00$, and ◇ - chemical equilibrium with particle injection.

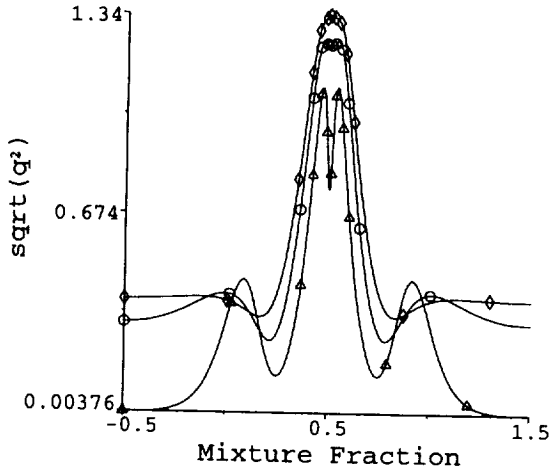

FIGURE 4. Predicted conditional root mean square deviation ($\sqrt{(q_\eta^2)}$) mass fraction profiles for case *s1* with arbitrarily varied levels of differential diffusion. Symbols denote the following profiles: △ - prediction with $c = 0.05$, ○ - prediction with $c = 0.50$, and ◇ - prediction with $c = 1.00$.

diffusion of the coordinate and mass fraction fields in physical space. The tendency towards smoother conditional mean profiles, in Fig. 3, with increased c values is indicative of this trend.

Variation in the predicted conditional mass fraction variance profiles with arbitrary variation in the mixing mode variable can be seen in Fig. 4 for case *s1*. It is apparent that increasing the value of c leads to an increased peak value in the

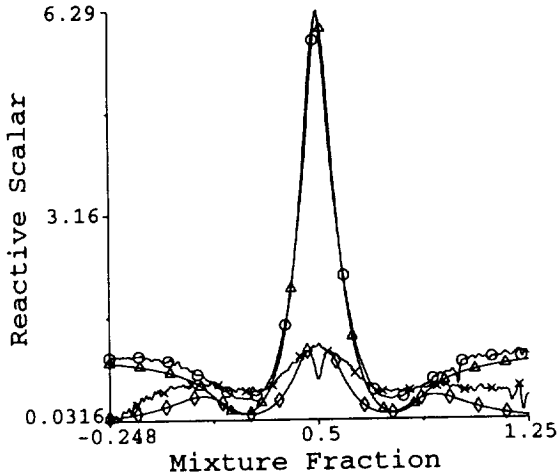

FIGURE 5. Modeled and observed conditional mean and variance of particle mass fraction for case *s1*. Symbols denote the following profiles: $\triangle$ - Q_η prediction, $\circ$ - simulated Q_η, $\diamond$ - q_η prediction, and $\times$ - simulated q_η.

conditional mean variance profiles and an increased value of variance at very rich and lean mixture fractions. The elevated level of conditional variance in the high c case is due to the source contribution from the last term of S_q (see Eq. 37).

A low value of c results in a dip in variance near the mean mixture fraction where the model equations do not predict any variance production. This dip is not present in higher c cases where diffusive transport in mixture fraction space is strong enough to smooth out sharp changes in gradient.

The result of matching the conditional covariance profile and minimizing the mixing mode variable to $c = 0.05$ (minimum numerically stable value) provided the predicted conditional mean and variance profiles plotted in Fig. 5.

Employing the same value of c and the same constants in the model for the mass-dissipation covariance C_η from Eq. 44 provided accurate predictions for the conditional mean and variance of particle mass in soot case *s2i*. These predictions are plotted against simulation data in Fig. 6.

It is evident that there is reasonable qualitative agreement between the predicted and observed profiles in Figs. 5 and 6. The CMC model captures the essential changes in profile shape in the more reactive case (Fig. 5) but appears to incorrectly predict rich and lean side behavior to greater extent in the less reactive case. Good quantitative agreement is found near the mean mixture fraction in both cases; however, the predicted profiles deviate substantially from the observed data at mixture fractions away from the mean. This discrepancy may have been due to the poor modeling of the conditional covariance term (C_η) at those same mixture fractions. It is difficult to be sure that the model fit to C_η provided by Eq. 44 provides accurate C_η gradients and curvatures as is required in the CMC equations. It is clear that the modeling of the mass-dissipation covariance requires further attention.

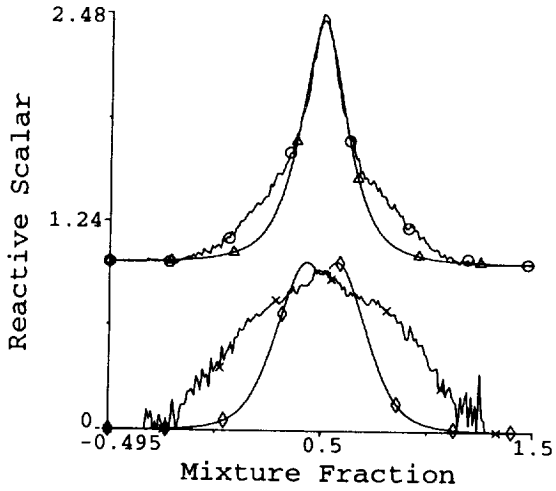

FIGURE 6. Modeled and observed conditional mean and variance of particle mass fraction for case *s2*. Symbols denote the following profiles: $\triangle$ - Q_η prediction, $\circ$ - simulated Q_η, $\diamond$ - q_η prediction, and $\times$ - simulated q_η.

4.1.1 Effect of particle slip velocity

Soot cases *s2* and *s2i* were simulated to examine the effect of slip velocities between particles and their carrier fluid. The former simulated case took account of particle inertia and the difference in local velocities which can arise from the kinetic lag between fluid flow variations and particle response to those variations. The latter simulation case (*s2i*) did not account for particle inertia and thus no slip velocities were present.

The differences in the conditional mean and variance particle mass fraction profiles between these two simulation cases can be seen in Fig. 7. It is evident that the introduction of particle inertia, all else being equal, causes the conditional mean particle field to behave in a more diffusive manner in mixture fraction space. Simultaneously, a rise in conditional variance results, particularly at mixture fractions away from the mean mixture fraction. Although not plotted, there appeared to be little change in the C_η profiles between the simulation pair, indicating that the vee-shaped form of the covariance profile is not a result of inertial particle transport.

Conditional source terms related to particle slip velocity appear in the neglected residual groupings of Eqs. 39 and 40. The conditional mean equation contains the slip transport term $\langle (u_i - v_i) \mid \eta \rangle \frac{\partial}{\partial \eta} (Q_\eta)$, whereas the variance equation contains a transport term $\langle (u_i' - v_i') \mid \eta \rangle \frac{\partial}{\partial \eta} (q_\eta^2)$, and the source term $\langle (u_i' - v_i') y \mid \eta \rangle \frac{\partial}{\partial \eta} (Q_\eta)$. The difference in behavior observed in the above simulation cases corresponds with the expected effect of the neglected slip velocity terms in the CMC equations. It is clear that the introduction of larger inertial particles to the model problem gives rise to a significant increase in the difficulty of modeling particle behavior.

4.2 Droplets

Unlike the soot particles, the droplet particle simulations exhibited very weak

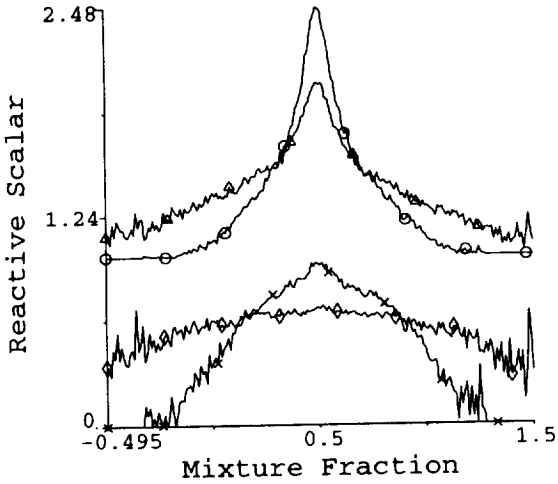

FIGURE 7. Observed conditional mean and variance of particle mass fraction for inertial (*s2*) and inertia-less (*s2i*) soot cases. Symbols denote the following profiles: $\triangle$ - Q_η inertial, $\circ$ - Q_η inertia-less, $\diamond$ - q_η inertial, and $\times$ - q_η inertia-less.

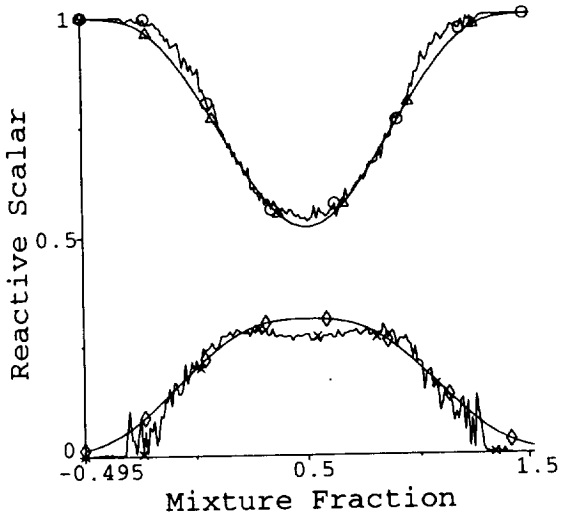

FIGURE 8. Modeled and observed conditional mean and variance of particle mass fraction for case *d1i*. Symbols denote the following profiles: $\triangle$ - Q_η prediction, $\circ$ - simulated Q_η, $\diamond$ - q_η prediction, and $\times$ - simulated q_η.

conditional covariance between scalar dissipation rate and particle mass fraction. This distinction between the particle types suggests that the form of the covariance (C_η) profile is linked to the types of reactions which act upon the particles. It would seem that strong reactions, as in the soot cases, give rise to sharp changes in particle properties in mixture fraction space which in turn impact strongly upon the transport statistics between adjacent mixture fractions. The weak reactions of

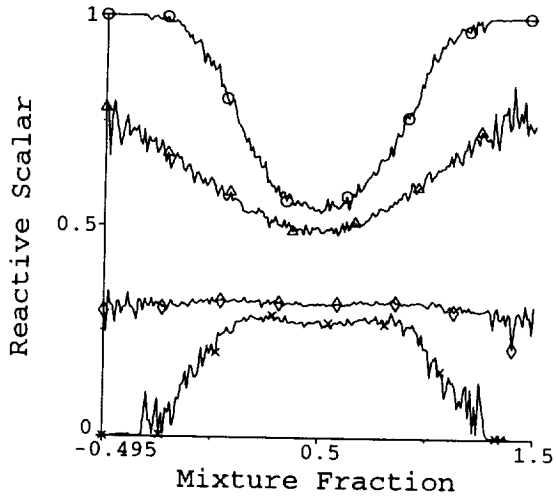

FIGURE 9. Observed conditional mean and variance of particle mass fraction for inertial (*d1*) and inertia-less (*d1i*) droplet cases. Symbols denote the following profiles: $\triangle$ - Q_η inertial, o - Q_η inertia-less, $\diamond$ - q_η inertial, and $\times$ - q_η inertia-less.

the droplet cases do not impart sharp changes in value to the conditional statistical profiles and thus do not seem to cause strong covariance between mass fraction and scalar dissipation rate. Further investigation of this behavior is clearly warranted.

Due to the observed behavior in the droplet cases, the covariance profile was modeled as being zero for all mixture fractions. As with the soot cases, the value of the mixing mode parameter, which gave best predicted agreement with the observed mass fraction profiles, was very low ($c = 0.1$). The degree of agreement between the observed and predicted profiles for the inertia-less droplet case (*d1i*) can be inferred from Fig. 8. It is clear that the CMC model predicts the conditional mean and variance of droplet mass fraction with a good degree of accuracy.

4.2.1 Effect of particle slip velocity

While it is clear that the CMC model can capture the behavior of very small fuel droplets in the terminal stage of evaporation, the modeling of particles with significant inertia is more problematic.

In Fig. 9, the conditional statistics from the simulation pair of *d1* and *d1i* are compared. It is evident that, as with the soot comparison of Fig. 7, the larger inertial particles tend to exhibit a tendency towards conditional mean profiles which have a lower level of curvature as though smoothed by enhanced diffusive transport. The conditional variance profile exhibits virtually no change in slope in the case of the inertial particles. The existence of slip velocities, larger than in the inertial soot case, causes a great deal of conditional variance generation to occur at mixture fractions away from the mean.

The noted inertial-particle behavior is even stronger in nature than that described in Section 4.1.1 for smaller soot particles. This suggests that the larger the particles

under consideration, the less effective a continuum model will be in describing their behavior.

5. Remarks

The results of this preliminary study indicate that a tailored variant of the Conditional Moment Closure (CMC) method can be applied successfully to modeling the evolution of soot-like and droplet-like reacting particles in a turbulent combusting environment. For the soot particle cases, a single set of constants were sufficient to correctly predict particle evolution under for a variety of reaction intensities. This finding suggests that it is appropriate to simultaneously model condensed and gas phase reactions in turbulence using the CMC model within an Eulerian frame.

However, significant caveats apply to this modeling approach. Firstly, it is clear that the conditional covariance between scalar dissipation rate and reactive scalar mass fraction cannot, in general, be neglected. It is apparent that some species can exhibit strong non-zero covariance profiles which play the foremost role, of all transport terms, in transporting scalar properties in mixture fraction space. An examination of simulation cases with different particle reactivities suggest that those species subject to more intense reactions exhibit stronger covariance profiles. This may be due to the establishment of large changes in scalar values and gradients between adjacent mixture fractions, which can result from strong reactions taking place. It was found that changes in particle inertia, while keeping all else constant, had virtually no effect on the form of the conditional covariance profile. Further work is obviously required to study the dependence of mixing covariance on particle reactivity and to devise an improved model for predicting its profile shape in mixture fraction space.

Secondly, it was found that the CMC model is not well suited to predicting the behavior of particles with substantial levels of inertia. Relatively large particles such as fuel droplets can develop significant slip velocities relative to their surrounding fluid. These slip velocities appear as unclosed transport and variance production terms in the CMC equations. They appear to enhance transport of particle properties in mixture fraction space over that exhibited by smaller particles with smaller slip velocities but similar reactivity. Further, as one would expect, because the larger particles are not transferred in space in the same way as gaseous mixture fraction, the conditional variance of particle properties at any given mixture fraction is higher than that for gaseous species. While it was found that the modeling of inertial particle transport in mixture fraction space could largely be accounted for by increasing the level of diffusive transport (through increasing c to unrealistically high levels), the model could not account for the increased conditional variance which was observed.

The mixing mode variable (c) approach to treating differential diffusion in the CMC model deserves further attention. In varying the value of c between the extreme value given by the ratio of molecular diffusivities and unity, according to changes in global mixing conditions, the CMC equations change in a natural way to embody differential diffusion effects to a greater or lesser degree as required.

A single value of c was found to suffice for the prediction of particle behavior in the cases studied here under uniform mixing conditions, but with widely different reactive behavior. This suggests c may well be independent of local variations in mixture fraction and particle mass fraction and a function only of global mixing parameters. Further work is required to properly test this hypothesis and the model for c proposed in Eq. 43.

Future work involving the CMC-particle model derived here will focus on validation of the model against larger simulations which incorporate more realistic chemistry, higher turbulence levels, and a more diverse set of mixing and reaction conditions.

REFERENCES

BILGER, R. W. 1993 Conditional Moment Methods for Turbulent Reacting Flow. *Phys. Fluids.* **5,** 436-444.

KLIMENKO, A. YU. 1990 Multicomponent Diffusion of Various Admixtures in Turbulent Flow. *Fluid Dyn.* **25,** 327-334.

KLIMENKO, A. YU., BILGER, R. W. 1998 Conditional Moment Closure for Turbulent Combustion. Submitted to *Progress in Energy and Combustion Science.*

KRONENBURG, A., & BILGER, R. W. 1997 Modeling of Differential Diffusion Effects in Nonpremixed Nonreacting Turbulent Flow. *Phys. Fluids.* **9,** 1435-1447.

KUO, K. K., *Principles of Combustion*, John Wiley and Sons, New York. 1986.

LI, J. D., & BILGER, R. W. 1996 The diffusion of conserved and reactive scalars behind line sources in homogeneous turbulence. *J. Fluid Mech.* **8,** 339-372.

OVERHOLT, M. R., & POPE, S. B. 1996 Direct numerical simulation of a passive scalar with an imposed mean gradient in isotropic turbulence. *Phys. Fluids.* **8,** 3128-3148.

POPE, S. B. 1985 PDF Methods for Turbulent Flows. *Progress in Energy and Comb. Sci.* **11,** 119-192.

POPE, S. B., & CHING, E. S. C. 1993 Stationary probability density functions: An exact result. *Phys. Fluids.* **5,** 1529.

YEUNG, P. K., & POPE, S. B. 1988 An Algorithm for Tracking Fluid Particles in Numerical Simulations of Homogeneous Turbulence. *J. Comp. Phys.* **79,** 373-416.

YEUNG, P. K., & POPE, S. B. 1989 Measurements of particle dispersion obtained from direct numerical simulation of isotropic turbulence. *J. Fluid Mech.* **207,** 531-586.

Large eddy simulations of combustion instabilities in premixed flames

By C. Angelberger[1], D. Veynante[2], F. Egolfopoulos[3] AND T. Poinsot[4]

Our objective is to build a complete tool, based on large eddy simulations, to determine the forced response of a turbulent premixed burner, which is the missing information in models describing combustion instabilities. The developed code includes: (1) a chemistry model based on a new reduction technique (ICC) for propane and methane; (2) a flame thickening approach to handle flame turbulence interactions; and (3) specific boundary conditions to control and measure acoustic wave reflections on inlets and outlets. The chemistry reduction is derived and validated by comparison with full schemes/full transport results obtained from stagnation point flame codes. The flame thickening approach requires subgrid scale parameterization derived from flame/vortex interactions DNS. The code itself is a compressible parallel finite volume solver able to handle hybrid grids. The combustor forced response to acoustic wave excitations and to equivalence ratio modulations is compared in the geometry where experimental data are available (Poinsot *et al.*, 1987).

1. Motivations and objectives

Large eddy simulation (LES) is a promising tool to predict combustion instabilities in practical systems and to numerically test passive or active control techniques (McManus *et al.*, 1993). Flows submitted to such instabilities are controlled by very large eddies (Poinsot *et al.*, 1987; Candel *et al.*, 1996), and LES may be easier in these situations than in usual turbulent reacting flows where an extended range of eddies has to be incorporated to describe turbulence and chemistry interactions.

To satisfy emission regulations, modern gas turbines operate in very lean combustion regimes. These flames are extremely sensitive to combustion oscillations, but the exact phenomena leading to instabilities are still discussed. A central question is to determine the phenomena inducing unsteady reaction rates, required to sustain oscillations when an acoustic wave enters the combustion chamber. This effect may be due (at least) to two main effects. First, vortices formed in the combustion chamber may capture a large pocket of fresh gases burning only at later times in a violent process leading to high reaction rates. An acoustic wave propagating into feeding lines may also induce a local change of the equivalence ratio and, therefore, a modification of the burning rate. When the burner operates in a very lean

1 CERFACS, France
2 Laboratoire EM2C, CNRS and Ecole Centrale Paris, France
3 University of Southern California
4 Institut de Mecanique des Fluides de Toulouse and CERFACS, France

mode, non-flammable mixture pockets may enter the combustion zone, leading to extinction.

An important issue in combustion instabilities modeling is to choose between these two mechanisms: the first one requires a detailed computation of the flow field inside the chamber while the second one may be addressed with more global tools. Both may be studied together or separately using large eddy simulations. LES is used to examine which mechanism is predominant in the case of a backward facing step premixed burner developed at Ecole Centrale Paris (ECP) for which an extensive set of experimental results for the homogeneous case is available (Poinsot *et al.*, 1987). This configuration is also similar to many classical combustion instabilities experiments (for example Keller *et al.*, 1981) and multiple industrial devices. To achieve this objective, several tools were integrated:

- (1) An LES solver able to handle complex geometries. Various techniques have been previously proposed for LES in turbulent premixed combustion (see a review in Veynante and Poinsot, 1997a), but few of them have been used in a realistic configuration (see, for example, Kailasanath *et al.*, 1991). Real combustion chambers require meshes able to deal with highly complex geometries.
- (2) The choice of a proper chemical description remains a critical issue in reacting flows. Reduced chemical schemes able to predict changes in equivalence ratio for methane and propane are developed here using a new technique called ICC (Integrated Complex Chemistry), described in section 3.
- (3) Thermal boundary conditions at the walls of the combustion chamber control flame stabilization and quenching (Veynante and Poinsot 1997b). In the ECP burner, ceramic walls are assumed to be adiabatic (Poinsot *et al.*, 1987).
- (4) Combustion is handled using the thickened flame (TF) approach (section 4) initially proposed by O'Rourke and Bracco (1979) and tested by Veynante and Poinsot (1997b). As the thickened flame is more sensitive to strain than the real flame, TF approach and ICC methodology are coupled, requiring that the thickened flame behaves dynamically like the real thin flame.

2. Configuration and scope of present study

The generic configuration is displayed in Fig. 1. An acoustic wave traveling along the feeding line of a backward facing step combustor induces an air flow rate perturbation $\dot{m}'_a$ of the mean air flow rate $\dot{m}_a$ and a fluctuation $\dot{m}'_f$ of the mean fuel flow rate $\dot{m}_f$. The perturbation ϕ' of the mean equivalence ratio ϕ is given by:

$$\frac{\phi'}{\phi} = \frac{\dot{m}'_f}{\dot{m}_f} - \frac{\dot{m}'_a}{\dot{m}_a} \tag{1}$$

This perturbation influences burning rate, but the hydrodynamic perturbation, $\dot{m}'_a$, also induces the formation of a vortex near the chamber dump. These two effects may be isolated by performing the following simulations:

- Case A: Aerodynamical (or acoustic) forcing of the chamber. In this case the inlet flow rate fluctuates, keeping the equivalence ratio constant.

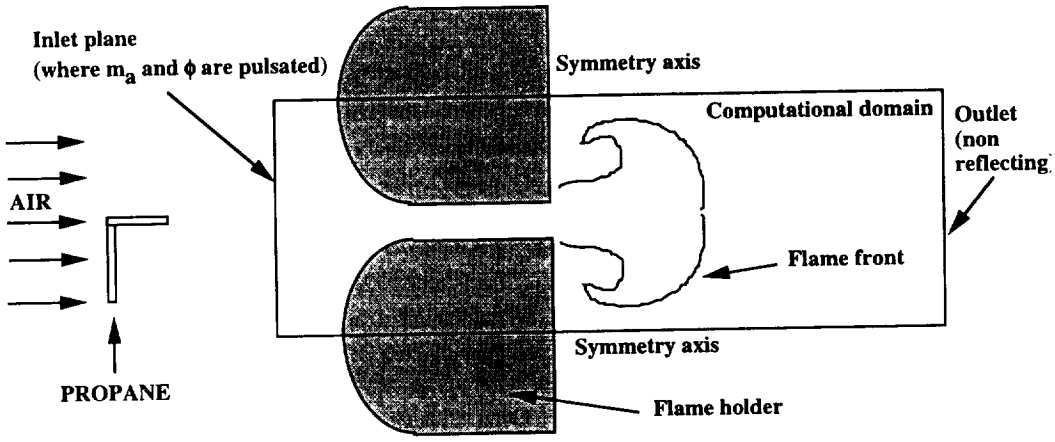

FIGURE 1. Configuration for simulations of combustion instabilities: the propane - air burner used by Poinsot *et al.* (1987). Only one of the injection slots is computed (the real system had five slots). The computational domain is 22.4 cm long and 2 cm high.

- Case C: Chemical forcing of the chamber (modulation of inlet equivalence ratio) without hydrodynamic forcing.
- Case F: Full forcing of the chamber. Obviously the real situation corresponds to a case where chemical and acoustic forcing are combined, but this case is not investigated here where only cases A and C are compared.

3. Reducing chemistry for LES: the ICC technique

Simplified kinetic schemes closely matching several flame properties for variable equivalence ratio are developed for lean methane/air and propane/air mixtures in the operating conditions of the ECP experiment (pressure $P = 1$ atm, fresh gases temperature $T_0 = 300$ K), using the ICC technique (Mantel *et al.*, 1996; Bedat *et al.*, 1997). Usually, one-step chemistry simplified schemes have been derived by only matching laminar flame speeds (Westbrook and Dryer, 1981). The ICC technique adds the constraint to match strain rates effects and to achieve numerical goals such as limitations of activation energies.

First, laminar flame speeds, flame structure, and the response to strain rate are determined in one-dimensional configurations using Chemkin-based codes and a detailed description of chemical kinetics and molecular transport to predict a reference case. The laminar flame speeds and flame structure (e.g. thickness) are determined through the one-dimensional PREMIX code (Kee *et al.*, 1985). For premixed flames, the response to strain rate includes the determination of extinction strain rates in the symmetric, twin-flame, opposed-jet configuration (fresh mixture counterflowing against an identical fresh mixture) and the variation of the spatially-integrated heat release with strain rate in the opposed-jet, fresh mixture against equilibrium

products configuration. This latter configuration is probably of dominant importance in turbulent premixed combustion, while the interaction of two streams of fresh mixtures may be of reduced but still non-negligible importance. On the other hand, experimental data are available for the twin-flame configuration (Law *et al.*, 1986) used as a data-base to test the ability of the detailed chemistry to predict extinction. Extinction strain rates are accurately determined by the opposed-jet code through the inclusion of one-point continuation (Egolfopoulos and Dimotakis, 1998), allowing for the description of turning-point behavior in the strain rate domain.

In a second part, similar simulations are conducting using simplified chemistry. The main goal is to "tune" the kinetic parameters to closely mimic several flame properties. Mantel *et al.* (1996) and Bedat *et al.* (1997) have shown that one-step global chemistry can predict flame propagation as well as flame extinction for a given fuel-to-air equivalence ratio, ϕ, tuning independently the pre-exponential factor A and the activation energy E_a. An important element of the ICC technique, compared to other reduction methods, is that the simplified chemistry is tested by modified versions of Chemkin-based codes, allowing for the use of simplified transport coefficients that are compatible with the ones used in the actual DNS or LES simulations. It has been found that results obtained by using simplified chemistry and detailed transport may be noticeably different compared to the ones obtained with simplified chemistry and simplified transport. Furthermore, thermal radiation from CO_2 and H_2O at the optically-thin limit (Egolfopoulos, 1994) are included. Thermal losses may be of particular importance on flame propagation and extinction (Law and Egolfopoulos, 1992; Egolfopoulos, 1994) in lean premixed combustion applications, such as gas turbines. Finally, the ICC technique produces kinetic schemes with relatively low level of stiffness, reducing thus the cost of DNS or LES simulations.

In the previous ICC studies, simplified chemical mechanisms were derived for a fixed equivalence ratio. The technique is extended here to account for variable equivalence ratio as well as for flame thickening. A one-step global chemistry model was derived, satisfactorily describing several flame properties of lean propane/air mixtures at $P = 1$ atm and $T_0 = 300$ K. The scheme is $C_3H_8+5O_2 \rightarrow 3CO_2+4H_2O$ with the specific reaction rate given by:

$$\dot{\omega} = A\,[C_3H_8]^a[O_2]^b exp(-E_a/RT)$$

where $[C_3H_8]$ and $[O_2]$ are the reactants molar concentrations, a and b the corresponding concentration exponents, A the pre-exponential factor, E_a the activation energy, R the gas constant, and T the absolute local gas temperature. The reference detailed chemistry for C_3H_8 was compiled by combining a C3 submechanism (Pitz and Westbrook, 1986) with the well-established C1-C2 GRI 2.1 mechanism (Bowman *et al.*, 1996). Two sets of parameters were finally kept for propane:

Set 1: $a = 1.0$, $b = 0.5$, $A = 1.60E09$ (cgs units), $E_a = 14,000$ (cal/mole).

Set 2: $a = 1.0$, $b = 0.5$, $A = 1.50E10$ (cgs units), $E_a = 20,000$ (cal/mole).

The use of concentration exponents as fitting parameters was essential to better describe variable equivalence ratio effects for a given set of Arrhenius parameters,

as suggested by Westbrook and Dryer (1981). E_a was kept at the lowest possible values to assure low stiffness and a thicker reaction zone. Accordingly, the flame thickening factor, F, required for LES is reduced compared to higher E_a schemes. For example, for Set 1 with $E_a = 14,000$ cal/mole a flame thickening factor $F = 4$ may be used in the LES while for Set 2 with $E_a = 20,000$ cal/mole, $F = 6 - 8$ is required for the same level of flame resolution. Although the flame thickening results in flames which are easily resolved by LES and with practically the same laminar flame speed, the thicker flames will be more susceptible to strain rate effects compared to the "real" thinner flames. Thus, by minimizing the flame thickening factor F, the strain rate effect discrepancy is minimized.

Figure 2 depicts the experimental (Vagelopoulos and Egolfopoulos, 1998) laminar flame speeds, s_l^0, for atmospheric, lean C_3H_8/air mixtures as well as the predictions obtained by using detailed chemical kinetics and transport and the proposed simplified scheme. The agreement is quite satisfactory. Extinction strain rates, κ_{ext}, were also determined for the twin-flame, opposed-jet configuration (Fig. 3). As expected, the predictions of κ_{ext} with $F = 4$ were found to be quite low compared to the $F = 1$ simulations, but still high compared to the $E_a = 14,000$ cal/mole scheme with $F = 8$. Representative comparison of the extinction response for $F = 1$ and $F = 4$ for a ϕ=0.9 flame is shown in Fig. 4 for the $E_a = 14,000$ cal/mole scheme. However, the flame response to strain rate for the fresh reactants against equilibrium products configuration, which is the prevailing one in the LES simulations, is in quite favorable agreement between the detailed and simplified chemistry simulations. The variation of the spatially integrated heat release rate with strain rate is shown in Fig. 5 for the detailed chemistry simulations as well as the simplified chemistry simulations with $F = 1$ and $F = 4$. Extinction is not possible for such a configuration, and the overall response of the $F = 4$ flames appears to be in close agreement with the detailed simulations.

4. Incorporating subgrid-scale effects into the thickened flame model

A complete description of the thickened flame (TF) model may be found for RANS models in Butler and O'Rourke (1977) and for LES models in Veynante and Poinsot (1997b). The key idea is to thicken the flame while maintaining its propagation speed. Following classical premixed laminar flame theories, this may be achieved simply by multiplying the thermal and molecular diffusivities a by a thickening factor F and dividing the preexponential constant A by the same factor F. With this transformation, the flame is thickened by a factor F and may be explicitly resolved on the LES mesh for sufficiently large values of F.

Unfortunately, when the flame is thickened from δ_l^0 to $F\delta_l^0$, the chemical time, estimated as $\tau_c = \delta_l^0/s_l^0$, becomes $F\tau_c$. Accordingly, the interaction between turbulence and chemistry may be modified because the Damköhler number, $Da = \tau_t/\tau_c$, comparing turbulent and chemical time scales is also decreased by a factor F. The interaction between flame and turbulence is altered in two main ways. First, eddies smaller than $F\delta_L^0$ do not interact with the flame any more, and their effects have to be incorporated in the modeling as a subgrid scale effect. Eddies larger than $F\delta_L^0$ interact with the flame front, but their efficiency may be affected.

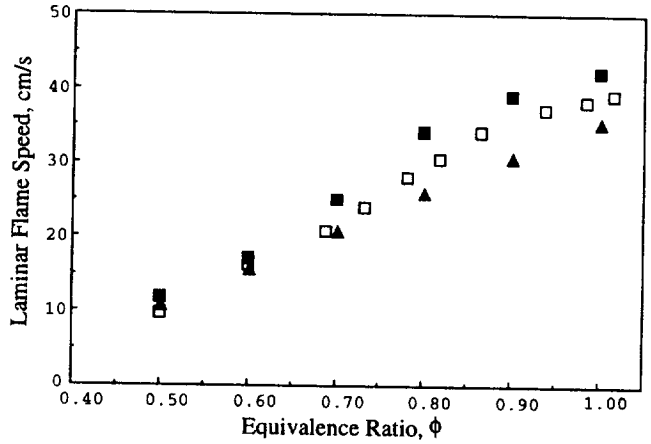

FIGURE 2. Variation of laminar flame speed with equivalence ratio for atmospheric C_3H_8/air mixtures (fresh gases initial temperature $T_0 = 300$ K). □ : experiments; ■ : predictions by detailed chemistry; ▲ : predictions by proposed simplified chemistry.

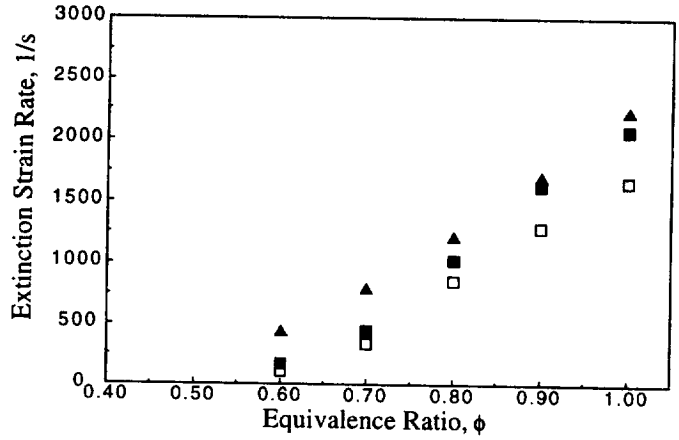

FIGURE 3. Variation of extinction strain rates κ_{ext} with equivalence ratio ϕ for atmospheric C_3H_8/air mixtures with reactants at initial temperature $T_0 = 300$ K, in the twin-flame, opposed-jet configuration. □ : experiments; ■ : predictions by detailed chemistry; ▲ : predictions by proposed simplified chemistry and $F = 1$.

4.1 DNS of flame/vortex interaction

Direct numerical simulation (DNS) of flame/vortex interactions is used to investigate how flame/turbulence interaction is affected by the thickening of the flame front and to propose a subgrid scale model to compensate these effects. A pair of counter-rotating vortices interacts with an initially planar laminar flame (Poinsot *et al.*, 1991). The ratio of the vortex size r to the initial flame thickness δ_l^0 is kept constant whereas three values of the vortex to laminar flame speeds ratio, v'^0/s_l^0,

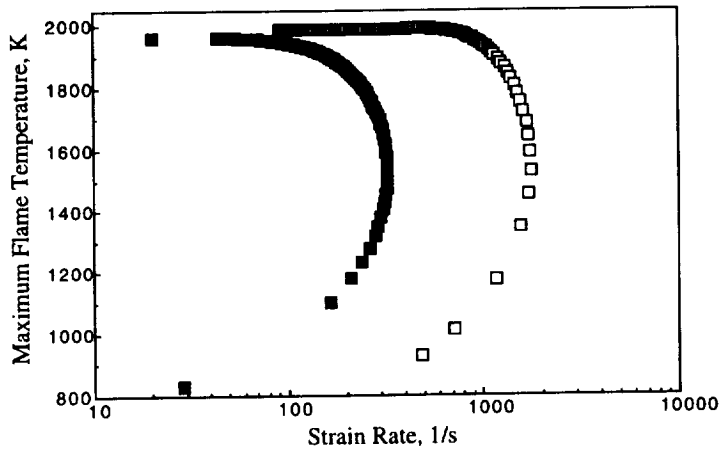

FIGURE 4. Variation of maximum flame temperature with strain rate for an atmospheric, $\phi = 0.9$ C_3H_8/air mixture (fresh gases initial temperature $T_0 = 300$ K), in the twin-flame, opposed-jet configuration. Predictions using the proposed simplified chemistry for $F = 1$ (□) and $F = 4$ (■).

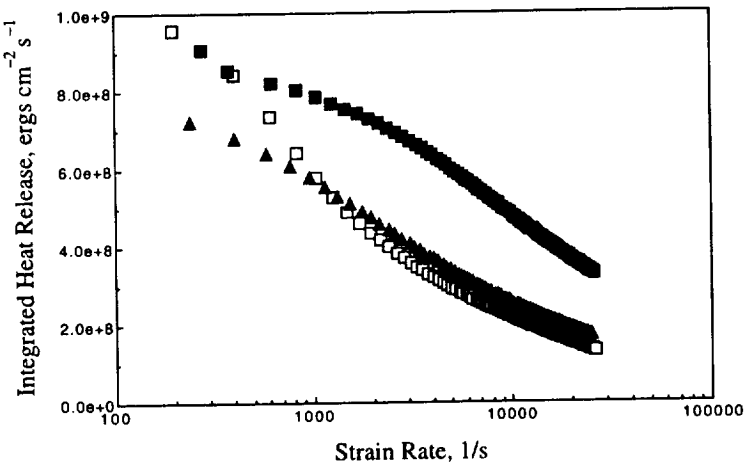

FIGURE 5. Variation of integrated heat release rate with strain rate for an atmospheric, $\phi = 0.9$ C_3H_8/air mixture with reactants at initial temperature $T_0 = 300$ K, in the fresh reactants against equilibrium products, opposed-jet configuration. □ : predictions by detailed chemistry; ■ : predictions by the proposed simplified chemistry and $F = 1$; ▲ : predictions by the proposed simplified chemistry and $F = 4$.

are considered (cases A, B, and C). Five values of the thickening factor F are investigated ($F = 1.0$, 2.5, 5., 10., and 25.). Two additive cases (D1 and D2) are used to check the influence of the length scale ratio r/δ_l^0. Numerical parameters are summarized in Table I.

TABLE I: Flow conditions for DNS of flame/vortex interactions. For all flows: the acoustic Reynolds number Re_a is $= c_0 L/\nu_0 = 15000$; the temperature change through the flame front is $T_2/T_1 = 4$ ($\alpha = (T_2 - T_1)/T_2 = 0.75$); the sound speed in the fresh gas is c_0; the activation temperature T_a is such that $\beta = \alpha T_a/T_2 = 8$; the flame Mach number s_l^0/c_0 is 0.0159; δ_l^1 is the flame thickness after thickening ($\delta_l^1 = F\,\delta_l^0$). The initial flame thickness, δ_l^0, estimated from $\delta_l^0 s_l^0/\nu = 4$, is $\delta_l^0/L = 0.0168$. The vortex size, r, is estimated from the distance between the two vortex cores. v' measures the vortices velocity. The computational domain is $L_x \times L_y$, discretized on $N_x \times N_y$ grid points.

RUN	r/δ_l^0	v'^0/s_l^0	F	r/δ_l^1	L_x/L	L_y/L	N_x	N_y
A1	30.	8.	1.0	30.	3.	3.	1025	1025
A2	30.	8.	2.5	12.	6.	3.	801	401
A3	30.	8.	5.0	6.	3.	3.	201	201
A4	30.	8.	10.	3.	3.	3.	129	129
A5	30.	8.	25.	1.2	10.	3.	257	129
B1	30.	4.	1.0	30.	3.	3.	1025	1025
B2	30.	4.	2.5	12.	6.	3.	801	401
B3	30.	4.	5.0	6.	3.	3.	201	201
B4	30.	4.	10.	3.	3.	3.	129	129
B5	30.	4.	25.	1.2	10.	3.	257	129
C1	30.	0.8	1.0	30.	3.	3.	1025	1025
C2	30.	0.8	2.5	12.	6.	3.	801	401
C3	30.	0.8	5.0	6.	3.	3.	201	201
C4	30.	0.8	10.	3.	3.	3.	129	129
C5	30.	0.8	25.	1.2	10.	3.	257	129
D1	60.	8.	10.	6.	6.	6.	257	257
D2	60.	1.6	10.	6.	6.	6.	257	257

The temporal evolution of the total reaction rate and the corresponding values of the flame surface (estimated from the iso-surface $c^* = 0.8$ of the reaction progress variable) are plotted in Fig. 6 for Cases C1 to C5. As expected, as F is increased the total reaction rate decreases. Reduced values of the total reaction rate and total flame surface are in close agreement, showing that the local reaction rate is not affected by the thickening process whereas the vortices become unable to create flame surface by wrinkling.

Flame surface evolutions depend on the vortices-induced flame stretch $\langle\kappa\rangle_s$. Values of $\langle\kappa\rangle_s$, extracted from DNS as done by Meneveau and Poinsot (1991), are displayed in Fig. 7. As expected, $\langle\kappa\rangle_s$ increases with the vortex-induced strain rate v'/r and decreases with decreasing values of the length scale ratio r/δ_l^1 because vortices become inefficient (Poinsot *et al.*, 1991). For cases D1 and D2, the length scale ratio r/δ_l^0 corresponding to the actual flame is increased by a factor of 2 compared

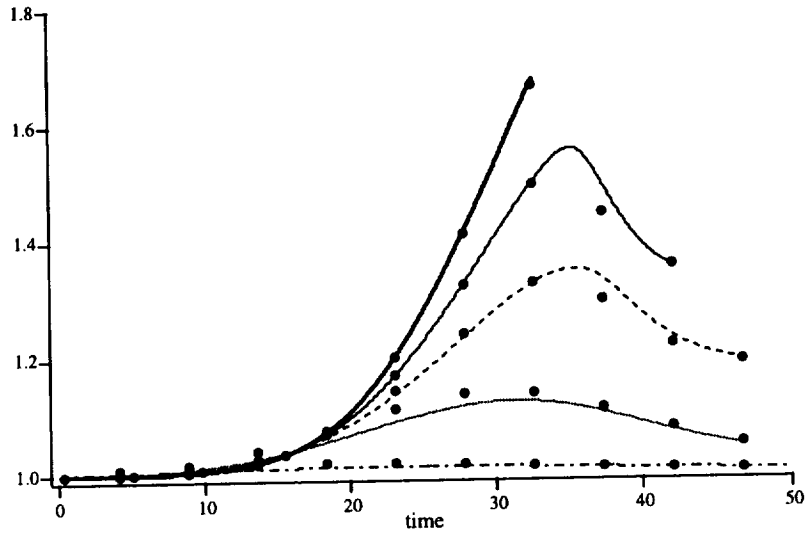

FIGURE 6. Total reaction rate versus time during flame vortex interaction for different values of the thickening factor F: cases C1 (——— , $F = 1.$), C2 (——— , $F = 2.5$), C3 (---- , $F = 5.$), C4 (····· , $F = 10.$) and C5 (—·— , $F = 25.$). Reaction rate values are made non-dimensional using the corresponding planar laminar flame quantities. Reduced flame surfaces are also plotted (•). Times are reduced using the flame time δ_l^0/s_l^0.

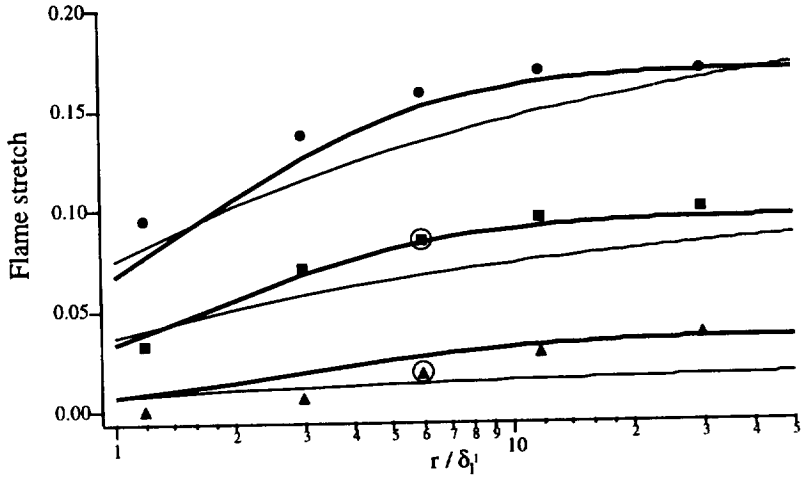

FIGURE 7. Flame stretch $\langle K \rangle$ induced by the pair of vortices plotted as a function of the length scale ratio r/δ_l^1 for cases An (•), Bn (■), Cn (▲), Dn (○). The bold solid line (———) corresponds to the proposed efficiency function C_n (Eq. 7). The efficiency function C_{MP} (Eq. 6) proposed by Meneveau and Poinsot (1991) is also plotted (———). Stretches are reduced using the flame characteristic time δ_l^0/s_l^0.

to previous cases. For case D1, the vortex-induced strain rate v'/r corresponds to cases B (whereas the maximum vortex velocity is the same as in cases A). The length scale ratio r/δ_l^1 is 6, and the stretch extracted from DNS corresponds to case B3 despite an increased value of the thickening factor F by a factor of 2. A similar result is found for case D2 having similar values of vortex induced strain rate, length scale ratio r/δ_l^1, and flame stretch as case C3.

To summarize our results, an increase of the flame thickening leads to a decrease of the flame front wrinkling because of a decreasing efficiency of vortices as length scale ratio r/δ_l^1 is decreased, as pointed out by Poinsot *et al.* (1991). The reduced efficiency of a vortex to wrinkle a flame front depends mainly on the value of r/δ_l^1 and not on the actual value of F (compare cases D1/B3 and D2/C3).

4.2 Estimation of the wrinkling of the flame front

A model incorporating the effects previously described should be based on the comparison between real and thickened flame wrinklings. Filtering the instantaneous flame surface density balance equation (Candel and Poinsot, 1990) leads to (Piana *et al.*, 1997; Boger *et al.*, 1998):

$$\frac{\partial\overline{\Sigma}}{\partial t} + \nabla.\left[\langle\mathbf{u}\rangle_s\overline{\Sigma}\right] + \nabla.\left[\langle w\mathbf{n}\rangle_s\overline{\Sigma}\right] = \langle\nabla.\mathbf{u} - \mathbf{nn} : \nabla\mathbf{u}\rangle_s\overline{\Sigma} + \langle w\nabla.\mathbf{n}\rangle_s\overline{\Sigma} = \langle\kappa\rangle_s\overline{\Sigma} \quad (2)$$

where $\overline{\Sigma}$ is the filtered flame surface density and corresponds to the subgrid scale flame surface. w is the flame front displacement speed, assumed here to be equal to the unstrained laminar flame speed s_l^0. $\mathbf{n}$ is the unit vector normal to the flame front pointing toward fresh gases, $\nabla.\mathbf{n}$ denotes the flame surface curvature, $a_T = \nabla.\mathbf{u} - \mathbf{nn} : \nabla\mathbf{u}$ corresponds to the strain rate induced by the flow field and acting on the flame front, and κ is the flame stretch. $\langle Q\rangle_s$ denotes averaging along the flame surface at the subgrid scale level. A complete analysis would require modeling and resolution of Eq. (2), but a simplified approach is proposed here. The subgrid scale surface averaged curvature $\langle\nabla.\mathbf{n}\rangle_s$ may be estimated as:

$$|\langle\nabla.\mathbf{n}\rangle_s| \approx \frac{1}{L_f} \approx \frac{1}{\alpha}\frac{\Xi - 1}{\Delta} \quad (3)$$

where L_f is the subgrid scale wrinkling length scale. Ξ is the wrinkling factor (i.e. the subgrid scale flame surface divided by its projection in the propagating direction) and Δ the filter size. α is a model constant of the order of unity. Assuming a subgrid scale equilibrium between flame surface and turbulence ($\langle\kappa\rangle_s \approx 0$), the wrinkling factor of the flame surface, Ξ, may be estimated as:

$$\Xi \approx 1 + \alpha\frac{\Delta}{s_l^0}\langle a_T\rangle_s \quad (4)$$

Estimating the subgrid scale strain rate as $\langle a_T\rangle_s \approx u'_\Delta/\Delta$, where u'_Δ is the subgrid scale turbulent velocity, leads to:

$$\Xi \approx 1 + \alpha\frac{\Delta}{s_l^0}\frac{u'_\Delta}{\Delta} = 1 + \alpha\frac{u'_\Delta}{s_l^0}, \quad (5)$$

recovering the wrinkling function (corresponding to the ratio of the subgrid scale turbulent flame speed $\overline{S}_T$ and the laminar flame speed s_l^0 used, for example, in the G-equation approach (Im *et al.*, 1997). The limited ability of small vortices to wrinkle the flame front must be parametrized and incorporated in a model for the strain rate $\langle a_T \rangle_s$ through an efficiency function as already done in RANS by Meneveau and Poinsot (1991) to derive the ITNFS (Intermittent Turbulent Net Flame Stretch) model.

4.3 Spectral analysis

Meneveau and Poinsot (1991) have modeled the effective strain rate induced by a pair of vortices (size r, velocity v') acting on a flame front as:

$$S_r = C_{MP}\left(\frac{r}{\delta_l^1}\right)\left[\frac{v'}{r}\right] = 10^{-c(s)}\left[\frac{v'}{r}\right] \quad with \quad c(s) = \frac{0.545}{log_{10}\left(\frac{4r}{\delta_l^1}\right) + 0.364} \tag{6}$$

where the efficiency function C_{MP} is only a function of the length scale ratio r/δ_l^1 whereas a clear dependence on the velocity ratio v'/s_l^0 is observed in our DNS. For example, cases A1 to A4 exhibit almost the same temporal evolution of the total reaction rate (not displayed here) whereas with a lower velocity ratio cases C1 to C4 lead to large differences (Fig. 6). A new efficiency function, compared to DNS data in Fig. 7, is then proposed:

$$C_n\left(\frac{r}{\delta_l^1}, \frac{v'}{s_l^0}\right) = \frac{1}{2}\left[1 + erf\left(0.6\, ln\left(\frac{r}{\delta_l^1}\right) - \frac{0.6}{\sqrt{\frac{v'}{s_l^0}}}\right)\right] \tag{7}$$

C_{MP}, also plotted on the figure, slightly underestimates the efficiency of small vortices and tends slowly toward its asymptotic value.

The effective strain rate due to a pair of vortices now has to be integrated over all length scales to estimate $\langle a_t \rangle_s$. Two cases are considered. First, a Heaviside efficiency function $C_H\left(r/\delta_l^c\right) = H\left(r - \delta_l^c\right)$, assuming that vortices lower than the cut-off length scale δ_l^c are unable to affect the flame, leads to a simple analytic solution. Then, the efficiency function C_n is considered. Meneveau and Poinsot have incorporated turbulence intermittency effects (various possible values of the velocity v' for a given vortex size r), but as these effects lead only to a weak modification of the final results, compared to modeling uncertainties they are not considered in the following to simplify numerical integrations. Assuming a homogeneous and isotropic turbulence, velocity v' and length r' scales are related:

$$v' = \left(\frac{r}{l_t}\right)^{\frac{1}{3}} u' = \left(\frac{r}{\Delta}\right)^{\frac{1}{3}} u'_\Delta \tag{8}$$

where l_t is the turbulence integral length scale, corresponding to the velocity u'. Then, following Meneveau and Poinsot (1991):

$$\langle a_T \rangle_s = \frac{0.28}{ln(2)} \int_{scales} C\left(\frac{r}{\delta_l^1}, \frac{v'}{s_l^0}\right) \frac{v'}{r}\, d\left[ln\left(\frac{l_t}{r}\right)\right] \tag{9}$$

leading to:

$$\langle a_T \rangle_s = \frac{0.28}{ln(2)} \frac{u'_\Delta}{\Delta} \left(\frac{\Delta}{l_t}\right)^{\frac{2}{3}} \int_{max\left[ln\left(\frac{l_t}{\Delta}\right),0\right]}^{ln\left(\frac{l_t}{\eta_k}\right)=\frac{3}{4}ln(Re)} C\left(\frac{l_t}{\delta_l^1}e^{-p}, \left(\frac{l_t}{\Delta}\right)^{\frac{1}{3}} \frac{u'_\Delta}{s_l^0} e^{-\frac{p}{3}}\right) e^{\frac{2}{3}p}\, dp \tag{10}$$

where η_k is the Kolmogorov length scale, and $Re = l_t u'/\nu \approx 4(l_t/\delta_l^0)(u'/s_l^0)$ the turbulence Reynolds number. The integration is performed on all length scales lower than the filter size Δ.

For a Heaviside efficiency function C_H, $\langle a_T \rangle_s$ has an analytical expression:

- a) For $\delta_l^c \leq \eta_k$:
$$\langle a_T \rangle_s = \frac{0.42}{ln(2)} \frac{u'_\Delta}{\Delta} \left[\left(\frac{\Delta}{l_t}\right)^{\frac{2}{3}} Re^{1/2} - 1\right] \tag{11}$$

- b) For $\eta_k \leq \delta_l^c \leq \Delta \leq l_t$:
$$\langle a_T \rangle_s = \frac{0.42}{ln(2)} \frac{u'_\Delta}{\Delta} \left[\left(\frac{\Delta}{\delta_l^c}\right)^{\frac{2}{3}} - 1\right] \tag{12}$$

Of course, if $\Delta \leq \delta_l^c$, $\langle a_T \rangle_s = 0$. If $\Delta \geq l_t$, Δ should be replaced by l_t in the previous expressions. In case b, corresponding to the general case, the strain rate depends only on local quantities for a given cut-off scale δ_l^c.

For the efficiency function C_n (Eq. 7), the integration is performed numerically, and the reduced strain rate $\Gamma_n = \langle a_T \rangle_s \Delta / u'_\Delta$ is plotted in Fig. 8. Γ_n increases with Δ/δ_l^1, contrary to the result expected from expressions (11) and (12) (Heaviside efficiency function), because Δ/δ_l^1, Δ/l_t and u'_Δ/s_l^0 are related. An increase of Δ/δ_l^1 corresponds to an increase of the turbulence Reynolds number Re. As the dependence of Γ_n with l_t/Δ is weak compared to the model uncertainties, Γ_n may be fitted by:

$$\Gamma_n\left(\frac{\Delta}{\delta_l^1}, \frac{u'_\Delta}{s_l^0}\right) = 0.75\, exp\left[-\frac{1.2}{(u'_\Delta/s_l^0)^{0.3}}\right] \left(\frac{\Delta}{\delta_l^1}\right)^{\frac{2}{3}} \tag{13}$$

which is in close agreement with the numerical integration of Γ_n as shown in Fig. 8. For comparison, Γ_{MP} estimated from the efficiency function C_{MP} (Eq. 6) is also displayed. Γ_{MP} is almost independent of the velocity ratio u'_Δ/s_l^0 (the only dependence comes through the turbulence Reynolds number and remains weak, as already pointed out by Meneveau and Poinsot, 1991) and depends weakly on the length scale ratio l_t/δ_l^1, as Γ_n.

4.4 Comments and practical implementation

Following the previous analysis, the wrinkling of the subgrid scale flame front may be estimated as:

$$\Xi = 1 + \alpha\Gamma\left(\frac{\Delta}{\delta_l^1}, \frac{u'_\Delta}{s_l^0}\right) \frac{u'_\Delta}{s_l^0} \tag{14}$$

This expression may also be used in a G-equation formalism (Im *et al.*, 1997) to estimate the subgrid scale turbulent flame speed or in a flame surface density approach (Boger *et al.*, 1998). A dynamic formulation could also be derived.

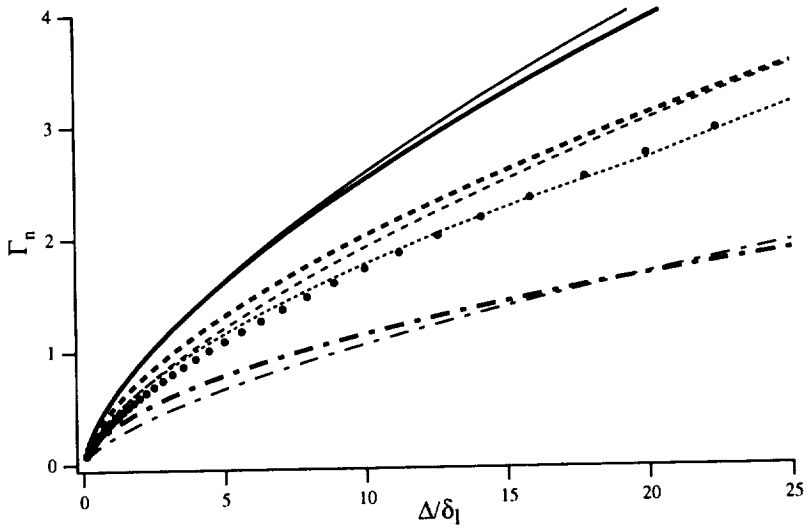

FIGURE 8. Reduced strain rate $\Gamma_n = \langle a_T \rangle_s \Delta / u'_\Delta$ versus the length scale ratio Δ/δ_l^1 estimated from the efficiency function C_n (Eq. 7). Γ_n is plotted for $l_t/\delta_l^1 = 100$ with $u'_\Delta/s_l^0 = 100$ (———), $u'_\Delta/s_l^0 = 10$ (----) and $u'_\Delta/s_l^0 = 1$ (—·—). Bold lines are obtained from numerical integrations of Eq. (10) whereas thin lines correspond to the proposed fit (Eq. 13). Γ_n is also plotted for case $l_t/\delta_l^1 = 20$ and $u'_\Delta/s_l^0 = 10$ (·····). Γ_{MP} (———), estimated from the efficiency function C_{MP} (Eq. 6) proposed by Meneveau and Poinsot, is displayed for comparison (• , $l_t/\delta_l^1 = 100$; $u'_\Delta/s_l^0 = 10$).

For a given turbulence and using Eq. (12), Ξ may be recast as:

$$\Xi = 1 + 0.42 \frac{\alpha}{ln(2)} \frac{u'}{s_l^0} \left(\frac{\Delta}{l_t}\right)^{\frac{1}{3}} \left[\left(\frac{\Delta}{\delta_l^c}\right)^{\frac{2}{3}} - 1\right] \tag{15}$$

For a thin flame front (i.e. $\Delta >> \delta_l^c$), Ξ increases linearly with Δ in a log-linear diagram and reaches a constant value when $\Delta \geq l_t$. This finding is in agreement with the experimental data obtained by Piana *et al.* (1997).

With a thickened flame, the actual wrinkling of the flame front is underestimated by an efficiency factor $E = \Xi\left(\delta_l^0\right) / \Xi\left(\delta_l^1\right)$. In practical applications, Δ is lower than the thickness δ_l^1. Accordingly, the thickened flame will not be wrinkled by subgrid scale turbulence and $\Xi\left(\delta_l^1\right) \approx 1$. The underestimation of the flame front wrinkling by the thickened flame approach should be corrected by increasing the flame speed by the efficiency factor E. This could be achieved by increasing the pre-exponential factor by a factor E^2 as done here, but the flame thickness may be kept constant by multiplying both the pre-exponential factor and the molecular and thermal diffusivities by a factor E. In this case, a subgrid scale diffusivity,

depending on the flame characteristics, is introduced. E is estimated here from:

$$E \approx \Xi\left(\delta_l^0\right) \approx 1 + \alpha\Gamma\left(\frac{\Delta}{\delta_l^0}, \frac{u'_\Delta}{s_l^0}\right)\frac{u'_\Delta}{s_l^0} \approx 1 + \alpha\Gamma\left(\frac{\Delta}{\delta_l^0}, \frac{u'_\Delta}{s_l^0}\right) C_s \frac{\Delta}{s_l^0}\sqrt{2S_{ij}S_{ij}}$$

where C_s is a model constant used in the estimate of u'_Δ from S_{ij}:

$$S_{ij} = \frac{1}{2}\left(\frac{\partial \widetilde{u}_i}{\partial x_j} + \frac{\partial \widetilde{u}_j}{\partial x_i}\right)$$

In the present preliminary tests, we use $\alpha\,\Gamma\,C_s = 0.1$.

To summarize, the thickening of the flame has two main effects:

- eddies smaller than $F\delta_L^0$ do not interact with the flame any more, and their effects have to be incorporated at the subgrid scale level using an efficiency factor E. Our preliminary results show that neglecting the efficiency function (i.e. $E = 1$, assuming a plane laminar subgrid scale flame) leads to an unexpected blow-off. In fact, the global reaction rate is underestimated, and the predicted flame becomes unable to sustain the incoming fresh gases flow.
- eddies larger than $F\delta_L^0$ interact with the flame front, but their efficiency may also be affected as described in Section 4.1. This effect was not incorporated here, but could be corrected by estimating an efficiency function at a test level $\widehat{\Delta} \approx 10F\delta_L^0$, corresponding to the size of the larger vortices affected by the flame front (see Fig 7).

5. Full simulations of the Ecole Centrale burner with no acoustic forcing

Simulations of the unforced flow in the ECP burner are performed using the AVBP code, a CFD package built on COUPL (CERFACS and Oxford University Parallel Library). AVBP has been used for a variety of unsteady flows in DNS and LES (Nicoud *et al.*, 1996; Nicoud, 1997; Ducros *et al.*, 1997). AVBP can handle hybrid meshes and is fully parallel. The previous models for chemistry and flame turbulence interaction were incorporated into this code and tested separately. Then, computations for the ECP burner were started for the operating conditions summarized in Table II. Propane combustion is modeled using chemistry parameters described in Section 3 (Set 2 with a thickening factor $F = 8$).

Table II. Physical parameters for the Ecole Centrale Paris burner simulation

Inlet temperature	Equivalence ratio	Inlet velocity	Flame speed	Adiabatic flame temperature
300 K	1	6.4 m/s	0.36 m/s	2190 K

All computations were performed in two dimensions since flow visualizations have indicated that large scale structures produced in this chamber were indeed two-dimensional. Common numerical parameters for all computations are described in

Table III. For all cases, the combustion chamber is computed as an amplifier system (and not as a resonator): inlet and outlet boundary conditions are non reflecting, and all acoustic waves produced in the combustor are allowed to leave the chamber so that no self-induced low-frequency mode can occur. The combustor may be forced to study its response. Forcing is introduced at the inlet of the combustor by modulating the incoming acoustic wave or the incoming gas equivalence ratio following the NSCBC technique (Poinsot and Lele, 1992).

Table III. Numerical parameters for the Ecole Centrale Paris burner simulation

Total number of points	LES model	Time Advancement	Range of Mesh size	CFL limit	F
41000	Filtered Smagorinski	RK3	0.07-0.3 mm	0.5	8

Typical simulations run during 500000 iterations, corresponding to 100 acoustic travel times in the chamber and more than 4 convective times. Initialization of computations in such cases is not simple since the LES code has very low levels of dissipation. The overall procedure used here is the following:

- Starting phase: the computation starts from an initial state where a strip of fresh gas is located in the combustion chamber and surrounded by two strips of burnt gas on each side. To allow stabilization during this first phase, fourth-order artificial viscosity is used.
- Transition phase: when the flow is established, artificial viscosity levels are reduced to negligible values, and the LES viscosity μ_t picks up while the flow becomes unsteady. Maximum values of the ratio μ_t/μ_{lam} (where μ_{lam} is the laminar viscosity in the fresh gases) are of the order of 20. The mean value of μ_t/μ_{lam} over the whole domain, however, is of the order of 0.3, showing that μ_t is distributed very intermittently.
- Measurement phase: after a few transit times in the burner, the mean flow is established, and measurements can be performed (with or without forcing).

In the absence of forcing, the flow stabilizes around a mean regime where two types of oscillations are observed. Small scale vortices are shed on the jet and propagate downstream. These vortices were also observed in the experiment (Zikikout, 1986). The frequency observed in the LES is of the order of 5 kHz while the measurements gave values closer to 3.8 kHz. Large scale movements of the reacting jet are also visible, both on the sinuous and varicose modes. These movements diminish as time goes by because the acoustic activity in the cavity decreases.

A typical snapshot of the flow for this regime is given in Fig. 9. The flame is only slightly corrugated and corresponds to the state observed in the experimental set-up in the absence of instabilities (Fig. 6 in Poinsot *et al.*, 1987).

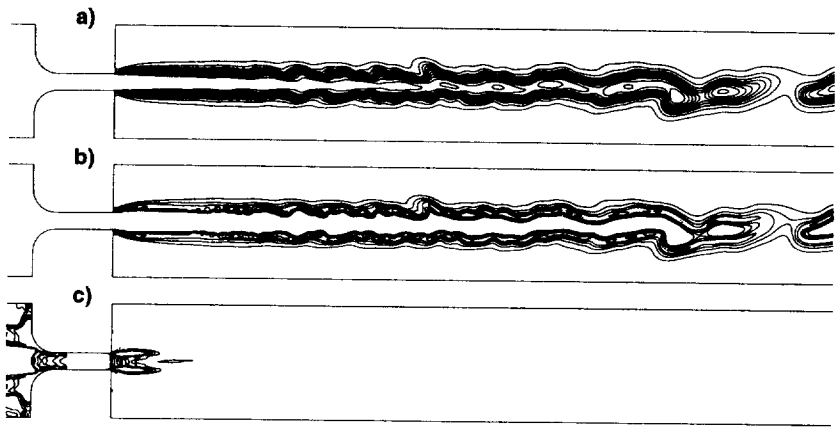

FIGURE 9. Instantaneous fields of temperature (a), reaction rate (b), and subgrid scale turbulent velocity (c) for an unforced regime.

6. Forced response of the Ecole Centrale burner

6.1 Response to an acoustic perturbation (Case A)

The objective is to reproduce the combustor response to a 530 Hz excitation of the inlet flow rate corresponding to one of the strongest instability modes observed in the ECP burner. More precisely, LES is used to measure the time delay between inlet flow rate perturbations and reaction rate oscillations. This delay was experimentally found to be close to 0.9 ms (Fig. 12 in Poinsot *et al.*, 1987). The wave amplitude is chosen to induce a flow rate change equal to 50 percent of the mean flow rate. Snapshots of temperature and reaction rate during one cycle of forcing are displayed respectively in Figs. 10 and 11.

The general features observed in the LES match those observed in the experiment: a large mushroom-shaped structure is produced (similar to vortices observed in impulsively-started jets) and leads to a high increase of flame surface and reaction rate. Fig. 12 displays time variations of inlet flow rate and heat release. The reaction rate lags the inlet flow rate by approximately 0.9 ms as observed in the experiment. The experimental heat release is also displayed, and a very good agreement on phases is obtained. Note that amplitudes cannot be compared because the experimental data contained only normalized values.

6.2 Response to a change in equivalence ratio (Case C)

In a second step, the combustor was forced by modulating the inlet equivalence ratio ϕ between 0.3 and 1.7 using a sinusoidal function (frequency 530 Hz). A large modulation amplitude is chosen to maximize the effects. To achieve such levels, both fuel and air flow rates would have to be affected by the acoustic wave in opposite directions. Since this is unlikely to happen in practice, the present simulations provide a maximization of potential effects of unmixedness on combustor response.

As the overall mass flow rate was kept constant, no vortices were formed at the inlet, and only the chemistry effects are observed. Fig. 13 (fuel mass fraction) and

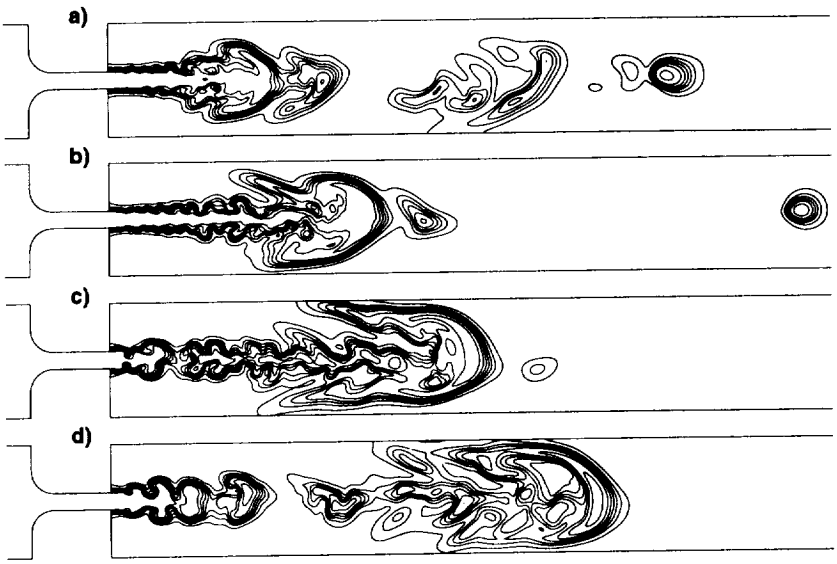

FIGURE 10. Temperature fields during one forcing cycle at 530 Hz. The time separation between each picture corresponds to a quarter period (0.47 ms)

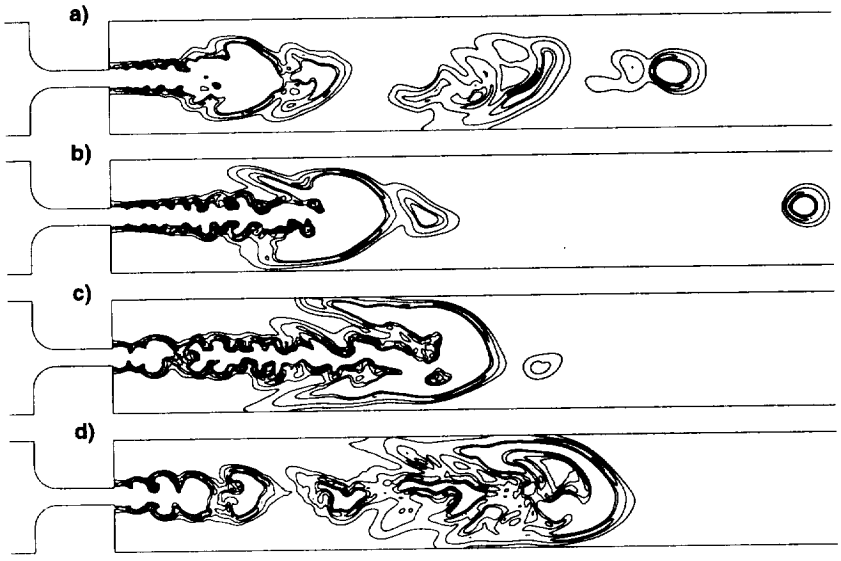

FIGURE 11. Reaction rate fields during one forcing cycle at 530 Hz.The time separation between each picture corresponds to a quarter period (0.47 ms)

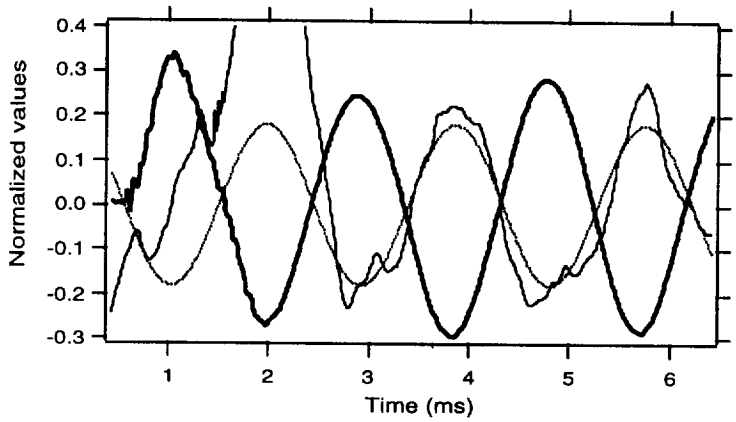

FIGURE 12. Time evolutions of inlet flow rate (——), window-integrated reaction rate in the LES (——) and in the Poinsot *et al.* experiment (----).

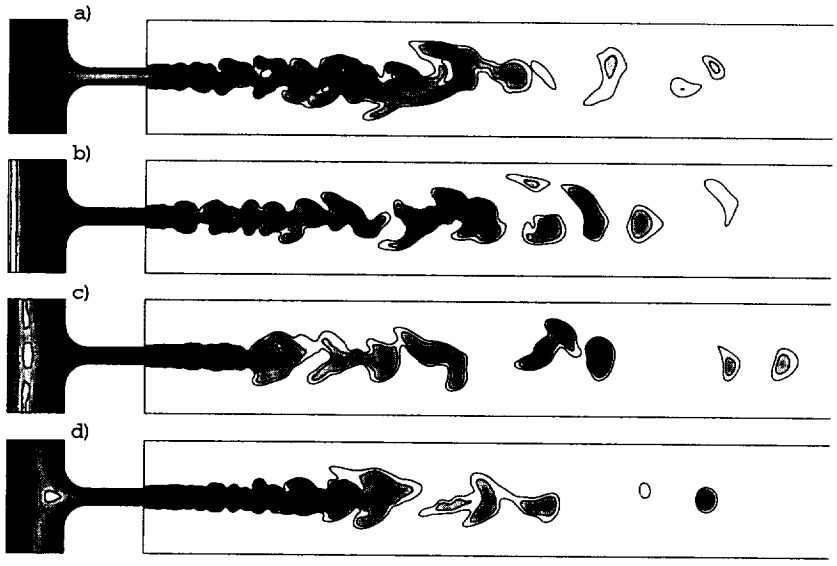

FIGURE 13. Fuel mass fraction fields during one forcing cycle of the equivalence ratio ϕ at 530 Hz. Dark and white regions correspond respectively to rich ($\phi = 1.7$) and lean ($\phi = 0.3$) gases.

Fig. 14 (reaction rate) show how the lean and rich regions created at the inlet enter the combustor and affect the flame front.

The total reaction rate is modified by the pulsation of the inlet fuel mass fraction as shown in Fig. 15: the inlet fluctuations of fuel mass fraction are slightly damped before entering the combustor (because they pass through the convergent), but combustion is modulated by these perturbations.

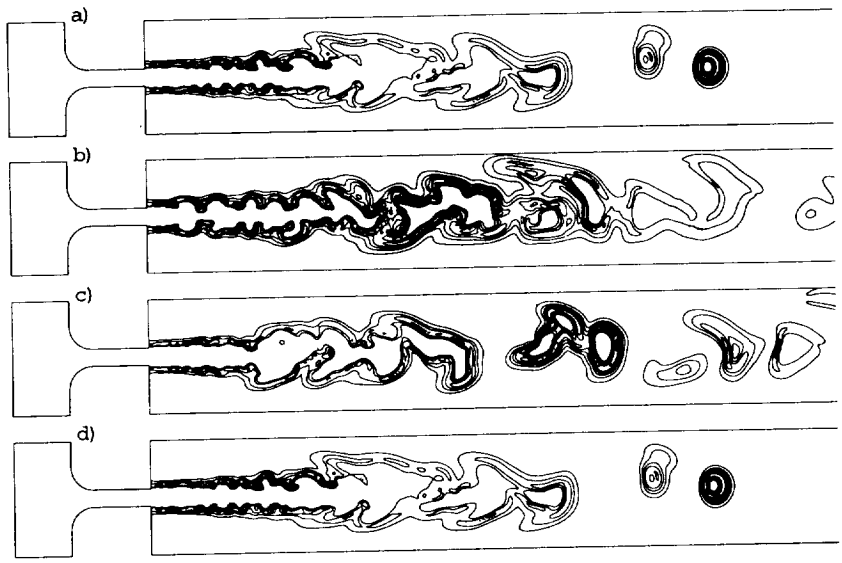

FIGURE 14. Reaction rate fields during one forcing cycle at 530 Hz (modulation of equivalence ratio ϕ).

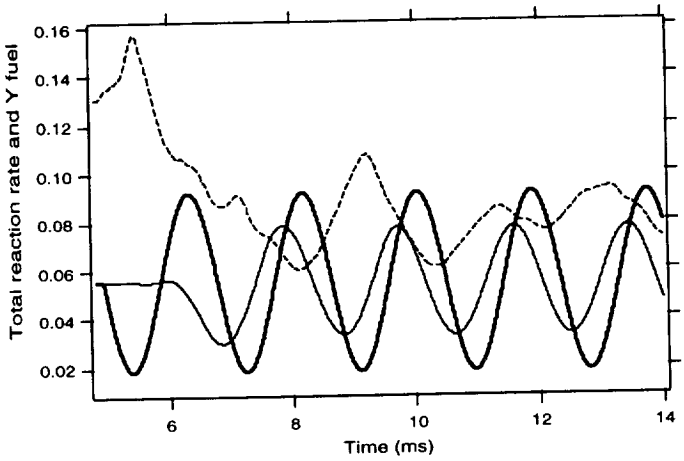

FIGURE 15. Fuel mass fraction at the inlet of the domain (premixing chamber) (———), in the jet at the dump section (———), and total reaction rate (----).

Finally, Fig. 16 compares the effects of acoustic forcing (case A) with those of chemical forcing (Case C). The case without forcing is added for reference. Obviously, runs should be continued to confirm this analysis, but it appears that acoustic forcing has a stronger effect on the total reaction rate than chemical forcing. Since we chose a very large range of variations for the chemical forcing, it seems that acoustic forcing is the main phenomenon to consider for combustion instabilities in the present system.

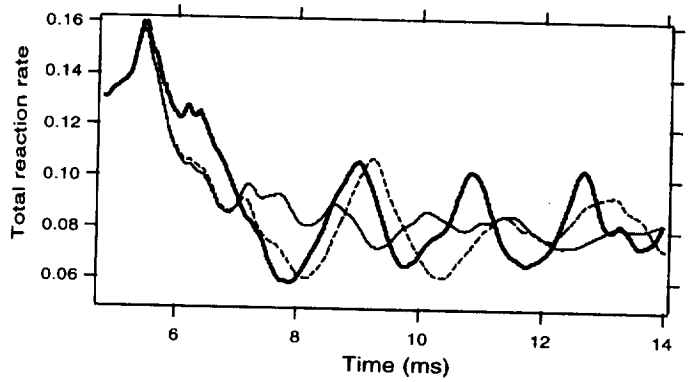

FIGURE 16. Total reaction rate vs time for unforced flow (———), acoustic forcing at 530 Hz with an amplitude of 50 percent (———) and for a modulation of equivalence ratio between 0.3 and 1.7 (----).

7. Conclusion

Large eddy simulations of the effects of acoustic waves and equivalence ratio variations on flame response have been performed for a premixed turbulent flame stabilized in a backward-facing step combustor. The developed code includes: (1) a chemistry model based on a new reduction technique, ICC, for propane and methane; (2) a flame thickening methodology, incorporating subgrid scale modeling, to handle flame turbulence interactions; and (3) specific boundary conditions to control and measure acoustic wave reflections on inlets and outlets. The code itself is a compressible parallel finite volume solver able to handle hybrid grids (AVBP).

Results indicate that the final tool was able to predict forced combustor response over many excitation cycles and to reproduce the phenomena observed in the experiment of Ecole Centrale Paris. The phase between flow rate oscillations and unsteady heat release, for example, was recovered in the case of acoustic forcing. Modulating the inlet equivalence ratio also led to unsteady heat release but with lower amplitudes than with acoustic forcing.

Numerical simulations were carried out at IDRIS (Institut du Développement et des Ressources en Informatique Scientifique, Orsay, France).

REFERENCES

BEDAT B., EGOLFOPOULOS F. ET POINSOT T. 1997 Integrated Combustion Chemistry (ICC) for Direct Numerical Simulations: Application to premixed and non-premixed combustion. *Western States Section Meeting of the Combustion Institute*, Los Angeles, Paper WSS/CI 97F-122.

BOGER, M., VEYNANTE, D., BOUGHANEM, H. & TROUVÉ T. 1998 Direct numerical simulation analysis of flame surface density concept for large eddy simulation of turbulent premixed combustion. *27th Symp. (Int.) on Combustion.*

The Combustion Institute, Pittsburgh.

BOWMAN, C.T., FRENCKLACK, M, GARDINER, W. & SMITH, G. 1996 The GRI 2.1 Mechanism. *Personal Communication.*

BUTLER T.D. & O' ROURKE P.J. 1977 *16th Symp. (Int.) on Combustion*, The Combustion Institute, Pittsburgh, 1503-1515.

CANDEL, S. & POINSOT, T. 1990 Flame stretch and the balance equation for the flame area. *Comb. Sci. Tech.* **70,** 1.

CANDEL, S., HUYNH, C. & POINSOT, T. 1996 Unsteady combustion. *Nato ASI Series*, Kluwer Academic Publishers, Dordrecht. 83-112.

DUCROS, F., NICOUD, F. AND SCHÖNFELD, T. 1997 Large Eddy Simulations of compressible Flows on Hybrid Meshes. *11th Symp. on Turbulent Shear Flows*, Grenoble, France.

EGOLFOPOULOS F.N. 1994 Geometric and Radiation Effects on Steady and Unsteady Strained Laminar Flames. *25th Symp. (Int.) on Combustion*, The Combustion Institute, Pittsburgh, 1375-1381.

EGOLFOPOULOS F.N. & DIMOTAKIS P.E. 1998 Non-Premixed Hydrocarbon Ignition at High Strain Rates. *27th Symp. (Int.) on Combustion*, The Combustion Institute, Pittsburgh.

LAW C.K. & EGOLFOPOULOS F.N. 1992 A Unified Chain-Thermal Theory of Fundamental Flammability Limits. *24th Symp. (International) on Combustion*, The Combustion Institute, Pittsburgh, 137-144.

IM, H.G., LUND, T. & FERZIGER, J. 1997 Large eddy simulation of turbulent front propagation with dynamic models. *Phys. Fluids A.* **9,** 3826-3833.

KAILASANATH, K., GARDNER, J. H., ORAN, E. S. & BORIS, J. P. 1991 Numerical simulations of unsteady reactive flows in a combustion chamber. *Comb. Flame.* **86,** 115-134.

KEE, R. J., GRCAR, J. F., SMOOKE, M. D. & MILLER J. A. 1985 A Fortran Program for Modeling Steady Laminar One-Dimensional Premixed Flames. *Sandia Report SAND85-8240.*

KELLER, J. O., VANEVELD, L., KORSCHELT, D., HUBBARD, G. L., GHONIEM, A. F., DAILY, J. W. & OPPENHEIM, A. K. 1981 Mechanism of instabilities in turbulent combustion leading to flashback. *AIAA J.* **20,** 254-262.

LAW, C.K., ZHU, D.L. & YU, G. 1986 Propagation and extinction of stretched premixed flames. *21st Symp. (Int.) on Combustion*, The Combustion Institute, Pittsburgh, 1419-1426.

MANTEL, T., EGOLFOPOULOS F. AND BOWMAN, C.T. 1996 A new methodology to determine kinetic parameters for one- and two- step chemical models. *Stanford CTR Summer Program 1996*, Center for Turbulence Research, NASA Ames/Stanford Univ., 137-149.

MCMANUS, K., POINSOT, T. &CANDEL, S. 1993 A review of active control of combustion instabilities. *Prog. Energy Comb. Sci.* **19,** 1-29.

MENEVEAU, C. & POINSOT, T. 1991 Stretching and quenching of flamelets in premixed turbulent combustion. *Comb. Flame.* **86,** 311-332.

NICOUD, F., DUCROS, F., SCHÖNFELD, T. 1996 Towards Direct and Large Eddy Simulations of compressible Flows in complex geometries. *5th French-German Workshop*, Munich.

NICOUD, F. 1997 Effects of strong wall injection on the structure of a low-Reynolds turbulent flow. *Submitted to Int. J. Num. Meth. Fluids.*

PIANA, J., DUCROS, F. & VEYNANTE, D. 1997 Large eddy simulations of turbulent premixed flames based on the G equation and a flame front wrinkling description. *11^{th} Symp. on Turbulent Shear Flows*, Grenoble, France.

PITZ, W. J. & WESTBROOK, C. K. 1986 Chemical Kinetics of the High Pressure Oxidation of n-Butane and its Relation to Engine Knock. *Combust. Flame.* **63,** 113-133.

POINSOT, T., TROUVÉ, A., VEYNANTE, D., CANDEL, S. & ESPOSITO, E. 1987 Vortex driven acoustically coupled combustion instabilities. *J. Fluid Mech.* **177,** 265-292.

POINSOT, T. & LELE, S. 1992 Boundary conditions for direct simulations of compressible viscous flows. *J. Comp. Physics.* **101,** 104-129.

POINSOT, T., VEYNANTE, D., CANDEL, S. 1991 Quenching processes and premixed turbulent combustion diagrams. *J. Fluid Mech.* **228,** 561-606.

O'ROURKE, P.J. & BRACCO, F.V. 1979 Two scaling transformations for the numerical computation of multidimensional unsteady laminar flames. *J. Comp. Physics.* **33,** 2, 185-203.

TROUVÉ, A. & POINSOT, T. 1994 The evolution equation for the flame surface density. *J. Fluid Mech.* **278,** 1-31.

VAGELOPOULOS C.M. & EGOLFOPOULOS F.N. 1998 Direct Experimental Determination of Laminar Flame Speeds. *27^{th} Symp. (International) on Combustion.* The Combustion Institute, Pittsburgh.

VEYNANTE, D. & POINSOT, T. 1997a Reynolds-averaged and Large Eddy Simulation modeling for turbulent combustion. In *New tools in turbulence modeling,* O. Metais and J. Ferziger Eds, Les Editions de Physique.

VEYNANTE, D. & POINSOT, T. 1997b Large Eddy Simulation of combustion instabilities in turbulent premixed burners. *Annual Research Briefs*, Center for Turbulence Research, NASA Ames/Stanford Univ., 253-274.

WESTBROOK, C. AND DRYER, F. 1981 Simplified Reaction Mechanism for the Oxidation of Hydrocarbon Fuels in Flames. *Comb. Sci. Tech.* **27,** 31-43.

ZIKIKOUT, S., CANDEL, S., POINSOT, T., TROUVÉ, A.& ESPOSITO, E. 1986 High frequency oscillations produced by mode selective acoustic excitation. *21^{st} Symp. (Int.) on Combustion*, The Combustion Institute, Pittsburgh.

LES modeling for lifted turbulent jet flames

By Luc Vervisch[1] AND Arnaud Trouvé[2]

The LES method is an attractive approach for the simulation of turbulent jet flames. In this method, the effects of large scale structures controlling the mixing process are resolved while small-scale effects such as the leading-edge flames involved in the flame base dynamics are accounted for by the subgrid-scale models. The LES approach is examined in this study with a particular emphasis on a simple formulation for combustion based on the assumption of infinitely fast chemistry. When applied to the problem of turbulent jet flames, this formulation is limited to the description of a regime where the flame remains attached to the fuel injector. Using DNS and LES databases, a modification of the infinitely fast chemistry formulation is proposed in the present study with the objective of numerically capturing transitions to the lifted flame regime and the flame blowout regime. The DNS database corresponds to leading-edge flames evolving in isotropic turbulent flow and is used to describe the structure of the flame base. The LES database corresponds to the near-field region of plane turbulent jets and is used to describe the turbulent mixing process. Preliminary results from *a priori* tests of the new subgrid-scale combustion model are found to be encouraging.

1. Introduction

The model problem of a gaseous fuel jet flowing into a reservoir of air is a generic configuration in combustion theory that has many of the ingredients found in practical non-premixed combustion systems. The numerical simulation of this configuration remains a difficult task, however, for standard Reynolds-Averaged Navier-Stokes (RANS) methods. Indeed, RANS models have difficulties in describing the complex coupling between mixing and chemical reaction that occurs in turbulent jet flames. This coupling leads to 3 possible regimes for flame stabilization: (1) the attached flame regime where the flame is anchored to the fuel injector; (2) the lifted flame regime where the flame is stabilized further downstream at a finite distance from the fuel injector; and (3) the flame blowout regime where the flame cannot be stabilized. Liftoff heights and blowout velocities are quantities of practical engineering interest, and their prediction remains a great challenge for current CFD tools.

The difficulties of RANS models in describing the stabilization region of turbulent jet flames is in part due to the conflicting underlying theories for this problem. The theories differ in the following important aspects (Pitts 1988): (1) the

1 INSA and UMR-CNRS-6614-CORIA, Rouen, France, vervisch@coria.fr

2 Institut Francais du Pétrole, Rueil-Malmaison, France, arnaud.trouve@ifp.fr

degree of premixing upstream of the flame base (for instance Vanquickenborne & van Tiggelen (1966) assume full premixing between fuel and air, whereas Peters & Williams (1983) consider that fuel/air premixing remains negligible); (2) the controlling mechanism for flame stabilization (turbulent premixed flame propagation according to Vanquickenborne & van Tiggelen (1966); laminar diffusion flamelet quenching according to Peters & Williams (1983); large scale turbulent mixing of cold reactants with hot burnt products according to Broadwell *et al.* (1984); turbulent propagation of triple flamelets in partially premixed reactants according to Müller *et al.* (1994)).

Consistent with some aspects of current theories, experimental evidence emphasizes the role of large-scale vortex structures that control the mixing process in the turbulent jet. They also emphasize the role of small-scale, laminar-like, leading-edge (triple) flames that control the flame base motion process (Muñiz & Mungal 1997). Both RANS and large-eddy simulation (LES) approaches have difficulty in capturing leading edge phenomena. In RANS formulations, however, these large- and small-scale effects are not decoupled and remain in the models. It can be argued that this coupling accounts in part for the deficiencies of RANS models. In contrast, the LES approach resolves the large scale structures and only small-scale effects need to be modeled.

Therefore, the ability of LES methods to numerically capture the properties of the unsteady large scales is an attractive feature that allows a new look on the problem of simulating turbulent jet flames (Cook & Riley 1994, Réveillon & Vervisch 1996, Pierce & Moin 1998, Réveillon & Vervisch 1998, Jaberi & James 1998). As far as subgrid-scale modeling is concerned, the standard first step is to assume that the chemical processes are infinitely fast. In this situation, the knowledge of the extent of mixing between fuel and oxidizer is sufficient to fully describe the diffusion flame (Burke & Schumann 1928). The mixing field is characterized using the classical concept of a mixture fraction Z ($Z = 1$ in the fuel feeding stream, $Z = 0$ in the oxidizer reservoir). The temperature and species mass fractions are known functions of Z, and the Z-field is simply obtained in the LES computations from a presumed statistical distribution (via for instance a beta-function probability density function (pdf) $\widetilde{P}(Z)$, where $\widetilde{P}(Z)$ is parametrized in terms of the first and second moments of the Z-distribution, see Libby and Williams 1994).

While the assumption of infinitely fast chemistry remains a valuable first step in applying the LES approach to non-premixed flames, it has also some well-known deficiencies. For instance, Fig. 1 shows that this assumption leads to a flame that is always attached to the fuel injector. For problems where it is important to account for phenomena such as ignition or flame stabilization, the infinitely fast chemistry assumption cannot be invoked, and some alternative description of the turbulent flame must be used.

In the following, we use DNS of leading-edge flames evolving in isotropic turbulent flow and LES of the near-field region of plane turbulent jets. The DNS data are used to describe the structure of the flame base (§2) and to propose a new subgrid-scale combustion model for flame stabilization (§3). The LES data are used to describe

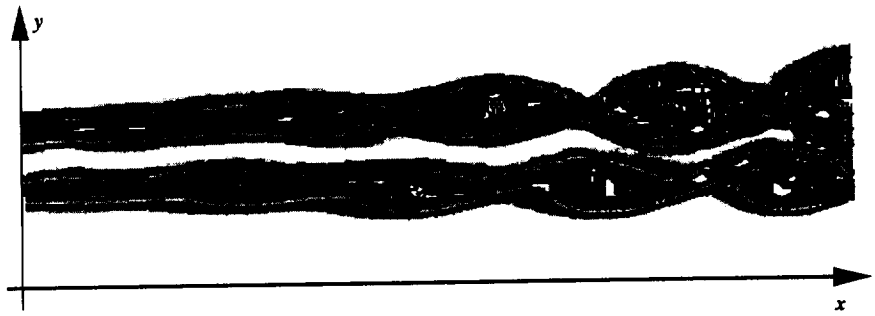

FIGURE 1. LES results of the near-field region of a plane turbulent jet flame. Instantaneous snapshot showing isocontours of the LES-filtered temperature in a constant z-plane. The LES formulation uses the assumption of infinitely fast chemistry, and the simulations are, therefore, limited to a description of the attached flame regime. This simulation was performed using the LES code presented in §4.

the turbulent mixing process and to examine the behavior of the turbulent mixing time scale that is used by the combustion sub-model (§4).

2. DNS of a turbulent edge-flame

2.1 Introduction

Focusing on the stabilization region of turbulent flames implies studying the point where the transition from non-burning to burning occurs (Muñiz & Mungal 1997). In a non-premixed situation, this transition is related to the appearance of edge-flames (Vervisch & Poinsot 1998). Experimental studies of the structure of the edge of diffusion flames have suggested that partially premixed combustion controls the properties of those edges (Phillips 1965, Kioni *et al.* 1993, Plessing *et al.* 1998). A possible model problem for partially premixed combustion is the triple flame configuration composed of a curved partially premixed flame front followed by a trailing diffusion flame. The triple flame analogy has been an effective tool to gain some understanding on the properties of propagation of diffusion flames (Hartley & Dold 1991, Veynante *et al.* 1994, Ruetsch *et al.* 1995, Ghosal & Vervisch 1998), the role of partially premixed combustion in auto-ignition problems (Domingo & Vervisch 1996), the chemical structure of the edge of diffusion flames (Echekki & Chen 1998), and diffusion flame holding (Buckmaster & R. Weber 1996) together with the effects of edge flames in liftoff situations (Favier & Vervisch 1998).

To increase our basic understanding and help the modeling of liftoff in non-premixed jet flames, we use direct numerical simulations of the edge of a diffusion flame interacting with freely decaying turbulence. The calculation starts with the establishment of a fully compressible laminar triple flame, using one-step chemistry and following the procedure proposed by Ruetsch *et al.* (1995) for unity Lewis

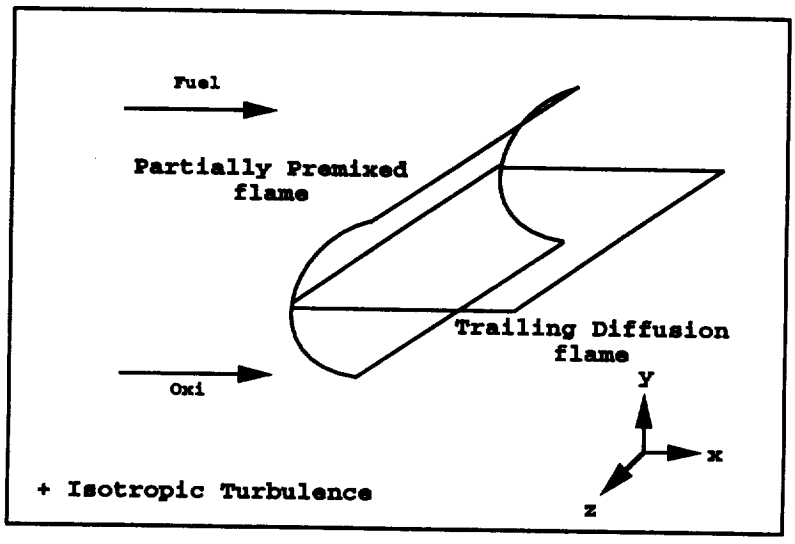

FIGURE 2. Sketch of the DNS configuration corresponding to the edge of a diffusion flame interacting with isotropic turbulence.

number. A three-dimensional initial condition for the mixture and the velocity field is obtained by repeating the two-dimensional triple flame in the spanwise direction z (Fig. 2). The flame is then allowed to interact with the turbulence. The DNS solver follows the methodology of Poinsot *et al.* (1996). We refer the reader to Domingo & Vervisch (1996) for more details on the solver. The DNS database include two synthetic problems corresponding to different characteristic length and time scales of the flame-flow interaction (see Table 1). Case I corresponds to the edge of a diffusion flame interacting with vortices that are large compared to the characteristic length of the flame, while case II is representative of an interaction with a more energetic turbulence, in which more scales are present.

Case	δ_m/l_t	δ_R/l_t	u'/S_l^o	u'/S_{TF}^o	Re_{lt}
I	0.10	0.25	5.64	3.64	157
II	0.20	0.40	11.3	7.30	125

Table 1. Parameters of the simulations ($129 \times 129 \times 65$). The initial laminar triple flame propagates with a velocity S_{TF}^o in a mixing zone of thickness δ_m, while the thickness of the reaction zone in the trailing diffusion flame is δ_R. The propagation speed of the stoichiometric mixture is S_l^o. The temperature ratio between fully burnt stoichiometric mixture and fresh gases is set to 4, and the stoichiometric composition corresponds to $Z_{st} = 0.5$. The turbulence is characterized by its integral length scale l_t, the amplitude u' of the velocity fluctuation, and the turbulent Reynolds number $Re_{l_t} = (u' l_t/\nu)$.

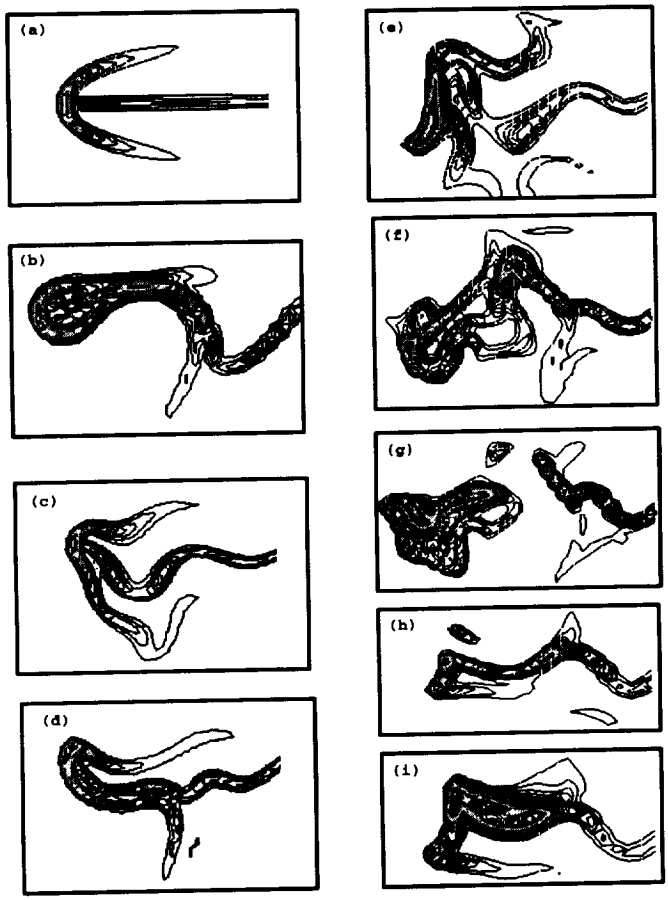

FIGURE 3. Instantaneous snapshots showing isocontours of the reaction rate in different constant z-planes. Initial laminar triple flame: (a); Case I: (b) - (c) - (d); Case II: (e) - (f) - (g) - (h) - (i).

2.2 Topology of the turbulent edge flame

After two eddy turn-over times, the turbulent mixing of the reactants is fully developed, and the initially laminar triple flame has evolved into the edge of a non-premixed turbulent flame. Instantaneous snapshots of the reaction zone reveal a complex structure (Fig. 3), showing that the partially premixed front and the trailing diffusion flame have been strongly modified by the turbulence. This is particularly true in case II (Figs. 3e-i) where the flame is exposed to intense turbulence.

One basic effect of the turbulent flow is to produce a number of zones with high values of the reaction rate at the extremity of the main body of the diffusion flame. The multiplication of these chemically super-active regions appears as the result of two mechanisms: (1) the development of a turbulent partially premixed front with a flame surface that is wrinkled by the vorticity field; (2) the stretching of the diffusion

flame due to local high levels of the scalar dissipation rate. Diffusion flame stretching tends to locally increase the burning rate. It may also lead to local quenching of the diffusion flame, generating new edges that are in turn associated with high burning rates. The first mechanism above is illustrated in Fig. 3f, displaying a plane where the edge of the reaction zone is composed of two stoichiometric points, each being supported by a turbulent partially premixed front and followed by a trailing diffusion flame. The possible increase of the burning rate in the trailing diffusion flame (the second mechanism above) is visible in Fig. 3b where the diffusion flame is pinched by a pair of vortices, also pushing the wings of the partially premixed front towards the diffusion flame. The second mechanism with local quenching of the diffusion flame may be observed in Fig. 3g, where the quenching is responsible for the development of a partially premixed kernel isolated from the downstream diffusion flame.

Despite the complexity of the fine scale structure of these flames, it is important to note that the turbulent edge of the reaction zone is always composed, in the mean, of a turbulent partially premixed front followed by a turbulent trailing diffusion flame. This fact becomes obvious when studying the flame structure in mixture fraction space.

2.9 The structure of laminar and turbulent edge flames in mixture fraction space

We now analyze the flame structure at a given time by averaging all quantities in the homogeneous spanwise direction z and considering that these averaged quantities are functions of the streamwise and cross-stream coordinates x and y. Profiles of fuel mass fraction $Y_F(x,y)$, temperature $T(x,y)$, and reaction rate $\dot{\omega}(x,y)$ are plotted versus the mixture fraction $Z(x,y)$ in Figs. 4 and 5, for various streamwise locations. Figure 4 corresponds to the analysis of the initial laminar triple flame; Fig. 5 to the analysis of the turbulent flame.

In mixture fraction space, the fuel mass fraction profile $Y_F(Z)$ lies between the limit of mixing without reaction, corresponding to $Y_F = Z$, and the infinitely fast chemistry limit, corresponding to $Y_F = 0$ for $Z \leq Z_{st}$ and $Y_F = (Z - Z_{st})/(1 - Z_{st})$ for $Z > Z_{st}$. Note that the reference problem for non-premixed combustion is the strained counter-flowing fuel/oxidizer diffusion flame (Peters 1986). In this model problem, the mixing of the reactants occurs together with their consumption, and the pure mixing line $Y_F = Z$ cannot be observed (except under quenching conditions). This is not the case when the edge of the diffusion flame is composed of a partially premixed front where some cold premixing of the reactants must take place prior to combustion. As a consequence, the structure in mixture fraction space of the edge flame is expected to be different from that observed in a counter-flowing fuel/oxidizer diffusion flame.

This is confirmed by the present DNS in both the laminar and the turbulent flame configurations. First, we observe a preheating region (curves marked by circles in Figs. 4 and 5) developing in the vicinity of the stoichiometric triple point. Then, as we move downstream from the partially premixed front into the trailing diffusion flame, we observe that for conditions close to stoichiometry, $Z = Z_{st}$, the fuel mass fraction decays from $Y_F = Z_{st}$ to $Y_F = 0$. In this transition region, the fluid particles coming from the oxidizer stream ($Z = 0$) always undergo some premixing with fuel

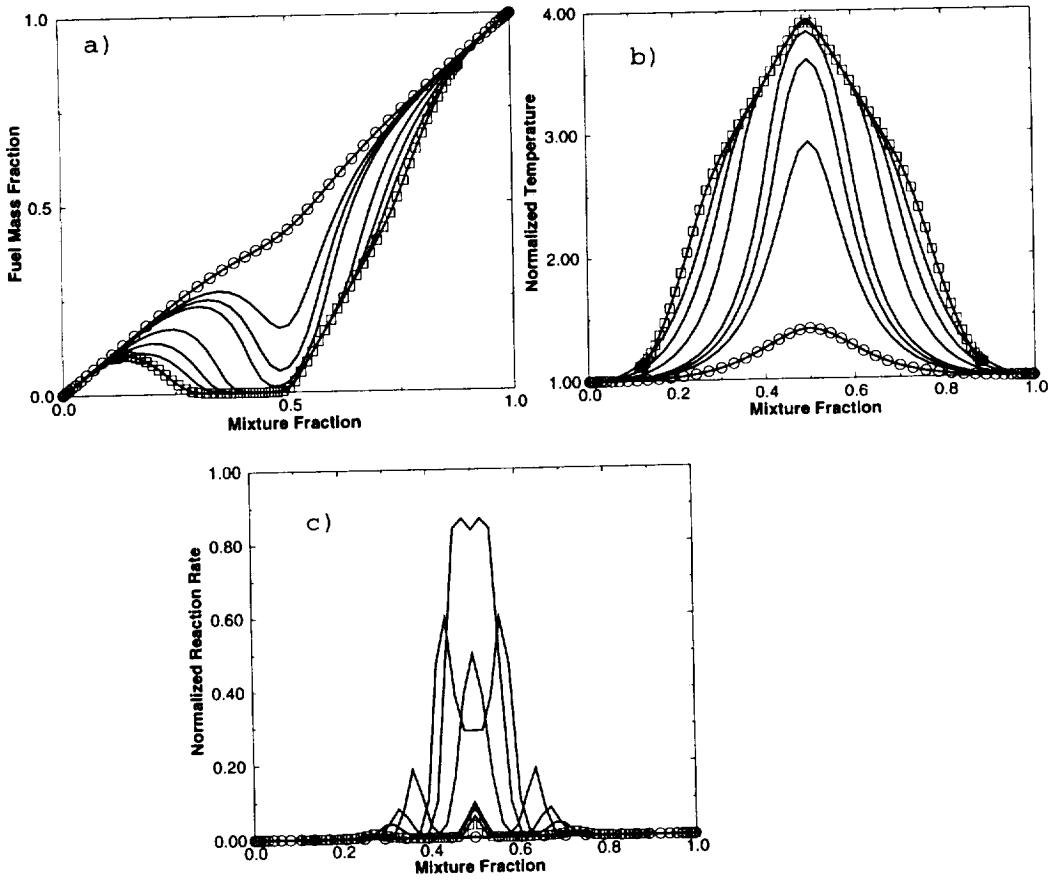

FIGURE 4. Fuel mass fraction (a), temperature (b), and reaction rate (c) plotted versus mixture fraction at various streamwise positions x of a laminar edge-flame configuration (Fig. 3a). o : x is slightly upstream of the flame and serves to describe the preheat zone; □ : x is downstream of the triple point and serves to describe the trailing diffusion flame. Temperature and reaction rate are respectively normalized with the temperature of the fresh gases and with the maximum reaction rate in a stoichiometric plane laminar flame.

before reaching the diffusion flame at $Z = Z_{st}$. Similarly, the fluid particles coming from the fuel stream ($Z = 1$) always undergo some premixing with oxidizer before reaching the diffusion flame at $Z = Z_{st}$.

When the triple flame interacts with the turbulent flow, large differences are observed between the laminar and turbulent cases for the profiles of reaction rate (compare Fig. 4 right with Fig. 5 bottom right). In contrast, the results show that the profiles of fuel mass fraction are similar in the laminar and turbulent cases if considered in $Z-$space. These profiles can be considered as more generic, and we now use this result to propose a skeletal description of the turbulent edge-flame in mixture fraction space.

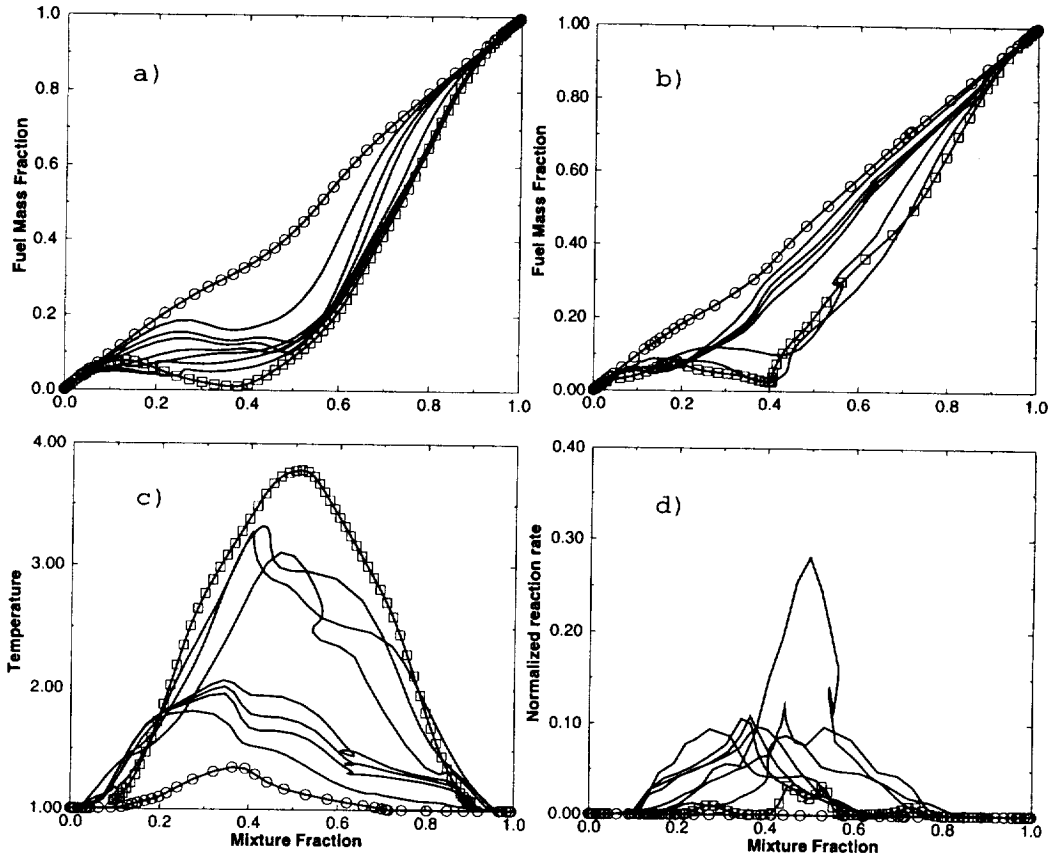

FIGURE 5. Fuel mass fraction in case I (a) and case II (b), temperature (c) and reaction rate (d) plotted versus mixture fraction at various streamwise positions x of a turbulent edge-flame configuration (Fig. 3). o : x is slightly upstream of the flame and serves to describe the preheat zone; □ : x is downstream of the triple point and serves to describe the trailing diffusion flame. Temperature and reaction rate are respectively normalized with the temperature of the fresh gases and with the maximum reaction rate in a stoichiometric plane laminar flame.

3. Simple EDge Flame Model (SEDFM)

3.1 Introduction

Flame stabilization results from complex interactions between the edge flames previously discussed and the large scale coherent structures present in the turbulent flow. The state of the art in LES of combustion chambers is based on the use of the Infinitely Fast Chemistry Model (IFCM) (Pierce & Moin 1998). With infinitely fast chemistry, the fuel mass fraction is calculated by presuming the probability density function of the mixture fraction $\widetilde{P}(Z;\underline{x},t)$ from its first and second moments, $\widetilde{Z}$ and $\widetilde{Z''^2}$, as obtained from the resolution of the large eddy field. The LES-resolved fuel mass fraction is then computed as $\widetilde{Y}_F(\underline{x},t) = \int_0^1 Y_F^{IFCM}(Z)\widetilde{P}(Z;\underline{x},t)dZ$, where

$Y_F^{IFCM}(Z)$ is the equilibrium structure of the flame in mixture fraction space (Fig. 6 top). To include finite rate chemistry effects in LES, we propose to conserve this simple and attractive formalism by simply replacing $Y_F^{IFCM}(Z)$ by a modified function accounting for the presence of edge flames. This new flame structure in mixture fraction space is parametrized using a partially stirred reactor subgrid model.

3.2 Skeletal description of turbulent edge flames

The infinitely fast chemistry assumption makes Y_F a piecewise linear function of Z. In Fig. 6 (top figure), this function is constructed from three points A, C, and E, defined by their (Z, Y_F) coordinates: $A(0,0)$; $C(Z_{st},0)$; $E(1,Y_{F,o})$ (the subscript o denotes a concentration taken in the feeding stream of fuel or oxidizer).

We propose to improve this skeletal description of the flame by introducing two additional points B and D located on the pure mixing line $Y_F = Z$. We thereby allow for variable, non-zero concentration of fuel at point C corresponding to stoichiometric conditions (Fig. 6 bottom). In this new skeletal structure, the limit of pure mixing is obtained when B, C, and D are such that $Y_{F_B} = Y_{F_C} = Y_{F_D} = Z_{st}$ (Fig. 6 bottom left); the limit of equilibrium chemistry is obtained when $B = A$, $D = E$, and C is such that $Y_{F_C} = 0$. Finite rate chemistry effects with edge flames are mimicked by letting the skeletal structure evolve from the pure mixing case to the equilibrium chemistry case. In the SEDFM model, we choose to meet this requirement by using the relations presented in Table 2. These relations give the flame structure in mixture fraction space as a function of a single parameter Y_{F_C}.

$\mathbf{Z}$	$\mathbf{Y_F^{SEDFM}(Z)} =$
$Z \leq Y_{F_B}$	Z
$Y_{F_B} < Z \leq Z_{st}$	$(Z - Y_{F_B})(Y_{F_C} - Y_{F_B})/(Z_{st} - Y_{F_B}) + Y_{F_B}$
$Z_{st} < Z \leq Y_{F_D}$	$(Z - Z_{st})(Y_{F_D} - Y_{F_C})/(Y_{F_D} - Z_{st}) + Y_{F_C}$
$Y_{F_D} < Z$	Z
$Y_{F_B} = (Z_{st}^2 - (Y_{F_C} - Z_{st})^2)^{1/2}$ and $Y_{F_D} = (1 - Z_{st})(Z_{st} - Y_{F_B})/Z_{st} + Z_{st}$	

Table 2: Flame structure in mixture fraction space in the SEDFM model.

The fuel concentration at point C may be viewed as a measure of the conditional mean value of fuel mass fraction at $Z = Z_{st}$, $Y_{F_C} = \left(\overline{Y_F \mid Z = Z_{st}}\right)$ (Smith 1996). Figure 7 shows a test of the model where Y_{F_C} has been extracted from the DNS. The results indicate that this skeletal description is an acceptable compromise to describe the flame in mixture fraction space including finite rate chemistry effects. We now turn to the yet unspecified parameter of the model: the conditional fuel mass fraction Y_{F_C}.

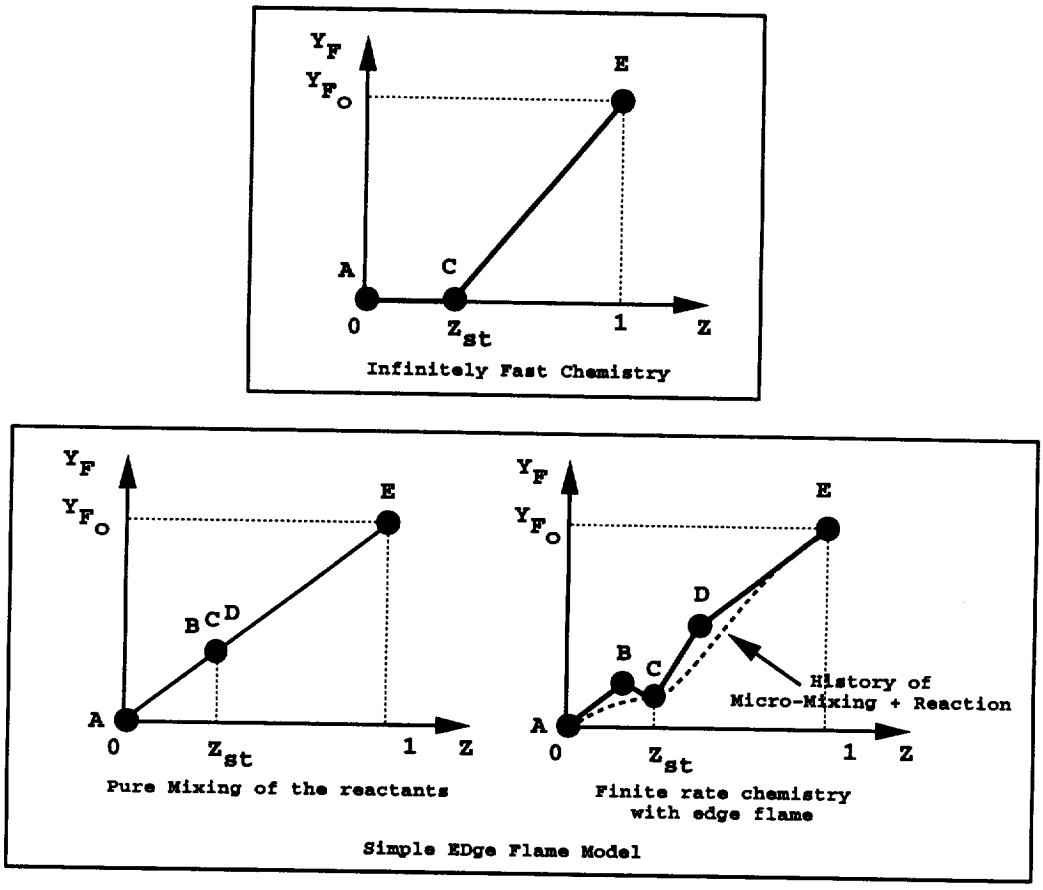

FIGURE 6. Skeletal description of the turbulent edge-flame in the SEDFM model.

3.3 Subgrid-scale reactor modeling to determine Y_{F_C}

Broadwell & Lutz (1998) have recently proposed a model for the production of NO_x in turbulent jet flames based on a description of chemical reaction at every axial location by a partially stirred reactor. Along the same lines, Borghi (1988) has proposed various turbulent combustion models using trajectories in composition space, and Ravet & Vervisch (1998) have developed a multi-level pdf-generator for RANS simulations of aeronautical engines. We follow the same approach for determining Y_{F_C}, the key parameter of SEDFM.

At each LES mesh point and at every time step t, the conservation equation of fuel mass evolving in a partially stirred reactor (PaSR) may be cast in the form:

$$\frac{dY_F}{dZ} = \frac{(\widetilde{Y}_F^t - Y_F) + \widetilde{\tau}^t \dot{\omega}(Y_F, Z)}{(\widetilde{Z}^t - Z)} \quad , \tag{1}$$

where $\widetilde{Y}_F^t$ and $\widetilde{Z}^t$ are respectively the known LES-filtered fuel mass fraction and mixture fraction. The subgrid mixing time $\widetilde{\tau}^t$ is estimated from the resolved flow

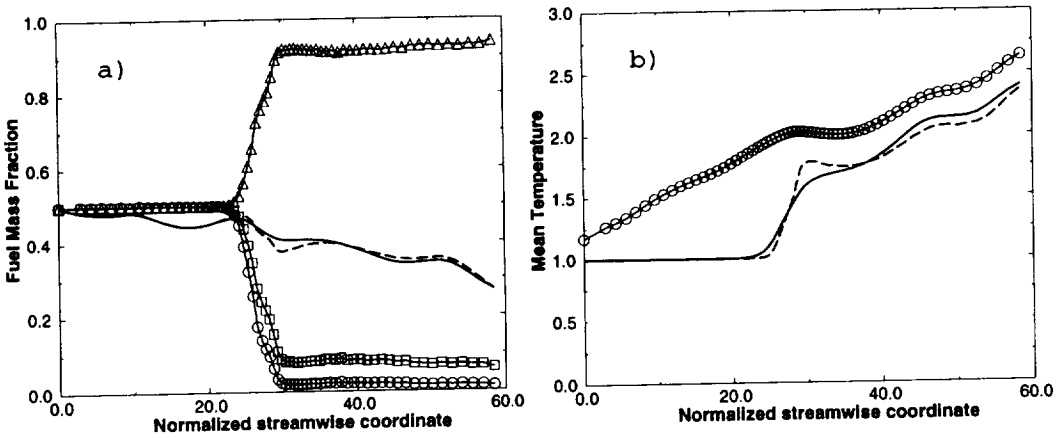

FIGURE 7. *A priori* test of the SEDFM model. a): streamwise variations of the fuel mass fraction at points B, C and D in the SEDFM model. Comparison between the SEDFM model and the DNS data for the mean (spanwise and cross-stream averaged) fuel mass fraction. o : Y_{F_C}; □ : Y_{F_B}; △ : Y_{F_D}; ---- : SEDFM; ——— : DNS. b): Comparison between the SEDFM model, the IFCM model, and the DNS data for the mean (spanwise and cross-stream averaged) temperature. The x-coordinate is normalized with the thickness of the premixed stoichiometric plane laminar flame. ——— : DNS; o : IFCM; ---- : SEDFM.

field (see §4), and finite rate chemistry effects enter the model via $\dot{\omega}(Y_F, Z)$ given for instance by a one-step finite rate chemical scheme.

The solution of the PaSR equation (1) gives $Y_F^{PaSR}(Z)$, a fuel trajectory in Z-space accounting for the interaction between subgrid-scale micro-mixing and chemical reaction. Indeed when $(\widetilde{\tau}^t\dot{\omega})/(\widetilde{Y}_F^t - Y_F) \gg 1$, the solution of (1) approaches the infinitely fast chemistry solution $Y_F^{IFCM}(Z)$. In addition, when $\widetilde{\tau}^t \to 0$, the solution of (1) approaches the mixing line solution, $Y_F = Z$. Since our objective is to determine Y_{F_C}, only half of the trajectory needs to be computed: for fuel rich conditions ($\widetilde{Z} > Z_{st}$) the PaSR equation is solved with the initial condition on the fuel lean side ($Z = 0, Y_F = 0$), whereas for fuel lean conditions ($\widetilde{Z} < Z_{st}$) the initial condition is taken on the fuel rich side ($Z = 1, Y_F = Y_{F,o}$). In both cases the point $Y_F^{PaSR}(Z_{st})$ determines Y_{F_C}, and thereby the new fuel concentration $\widetilde{Y}_F^{t+\delta t}$ using the flame structure $Y_F^{SEDFM}(Z)$ discussed above.

Note that Eq. (1) is similar to the equation solved for the trajectory of a Monte-Carlo particle in Z-space as obtained from a pdf method using the LMSE mixing closure (Pope 1985, Dopazo 1994). This equation can also be understood as a local dynamic subgrid flamelet where the contribution of diffusion, $D\nabla^2 Y_F$, is modeled as a linear relaxation term: $(\widetilde{Y}_F - Y_F)/\overline{\tau}$.

4. LES of the near-field region of plane turbulent jets

The LES simulations are performed using a three-dimensional, compressible Navier-Stokes solver. The solver features a high-order finite difference scheme that is sixth-order accurate in space (Lele 1992) and third-order in time. It is similar to the DNS solver used for the direct simulations of turbulent leading-edge flames (§2). Boundary conditions are specified with the NSCBC method proposed by Poinsot & Lele (1992). The LES formulation corresponds to the subgrid-scale (SGS) models proposed by Moin *et al.* (1991). The SGS models are variants of the Smagorinsky model based on an eddy-diffusivity assumption for the momentum, heat and mass SGS turbulent fluxes, and a variant of the Yoshizawa model for the SGS turbulent kinetic energy. While the LES solver may be run using the dynamic procedure proposed by Moin *et al.* (1991), the present simulations are performed using constant model coefficients: $C_S = 0.033$; $C_I = 0.1$; $Pr_t = 0.6$; $Sc_t = 0.8$, where C_S is the standard Smagorinsky coefficient, C_I the Yoshizawa coefficient, Pr_t the SGS turbulent Prandtl number, and Sc_t the SGS turbulent Schmidt number.

The computational configuration corresponds to the near-field region of a three-dimensional plane jet, $0 \leq x/H \leq 20$, where H is the initial jet height. The jet Reynolds number $Re_j \equiv (U_j H/\nu)$ is 6000, with U_j the mean jet inlet velocity and ν the fluid kinematic viscosity. The left x-boundary corresponds to inflow conditions with prescribed velocity and scalar values; the right x-boundary corresponds to outflow conditions, the y-boundaries to non-reflecting conditions ($-5 \leq y/H \leq 5$), and the z-boundaries to periodic conditions ($0 \leq z/H \leq 5$). The mean inlet x-velocity and scalar profiles are given by the following expressions:

$$\widetilde{u}(0,y,z) = \frac{U_j + U_{co}}{2} + \frac{U_j - U_{co}}{2}\, tanh(\frac{H/2 - |y|}{2\theta}) \tag{2}$$

$$\widetilde{Z}(0,y,z) = \frac{1}{2} + \frac{1}{2}\, tanh(\frac{H/2 - |y|}{2\theta}) \tag{3}$$

where θ is the LES-filtered initial thickness of the jet shear layers, U_{co} is a co-flow velocity that is added to maintain convective outflow conditions at the right x-boundary, and $\widetilde{Z}$ is the LES-filtered mixture fraction. In the present study, we use $\theta/H = 0.1$ and $U_{co}/U_j = 1/6$. The jet is also weakly forced at the inlet (left) x-boundary using a NSCBC variant of the random fluctuation method of Lee *et al.* (1992). The jet inlet velocity fluctuations are specified using an auxiliary field corresponding to homogeneous isotropic turbulence and a prescribed model energy spectrum (Passot-Pouquet). The perturbations are characterized by moderate levels of the forcing intensity, $u'/U_j \approx 2\%$, and an integral length scale of $l_t/H \approx 0.5$. Note that the particular implementation of the forcing method used in the present study also induces some weak scalar fluctuations at inlet (see Fig. 8 at $x = 0$). Furthermore, in the present study, the grid spacing is uniform and the resolution is $101 \times 200 \times 50$.

The LES simulations describe the mixing dynamics occurring in the near-field region of the turbulent jet. As shown in Fig. 8, the scalar field in the vicinity of the injector features a dramatic transition from an early stage ($0 \leq x/H \leq$

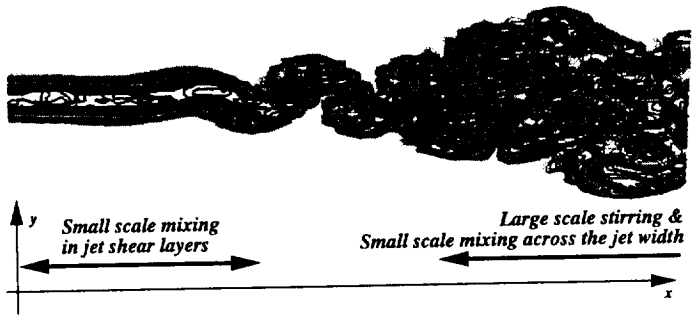

FIGURE 8. Mixing dynamics in the near-field region of a plane turbulent jet. Instantaneous snapshot showing isocontours of the LES-filtered mixture fraction in a constant z-plane.

7), where mixing remains confined within the jet shear layers, to a second stage ($x/H > 7$) characterized by large scale stirring motions. These stirring motions are associated with the jet coherent structures, resulting in faster spreading rates and more distributed small scale mixing across the jet width.

This transition is also observed in Fig. 9 where the mean total and SGS scalar dissipation rates, $< \widetilde{\chi} >$ and $< \widetilde{\chi}_{SGS} >$, are plotted as a function of streamwise location. Following Pierce & Moin (1998), we write:

$$\widetilde{\chi} = \frac{2}{\overline{\rho}} \left(\frac{\overline{\mu}}{Sc} + \frac{\mu_t}{Sc_t}\right) |\nabla \widetilde{Z}|^2 \tag{4}$$

$$\widetilde{\chi}_{SGS} = \frac{2}{\overline{\rho}} \frac{\mu_t}{Sc_t} |\nabla \widetilde{Z}|^2 \tag{5}$$

where $\overline{\rho}$ is the LES-filtered mass density, $\overline{\mu}$ the LES-filtered molecular viscosity, Sc the molecular Schmidt number, and μ_t the Smagorinsky turbulent eddy viscosity. In Fig. 9, these quantities are both spatially averaged in $(y-z)$ planes and time averaged over a period of time: $< \widetilde{\chi} >= (\int \widetilde{\chi}\, dydzdt)/(L_y L_z T)$, where L_y (L_z) is the y-size (z-size) of the computational domain, and T the averaging time period. T corresponds approximately to twice the mean time of flight of a jet fluid particle across the computational domain.

Figure 9 allows some refinement of the two-zone description of mixing presented in Fig. 8. Figure 9 suggests that mixing in the near-field region of the turbulent jet can in fact be described by a sequence of 3 stages: (1) an early stage ($0 \leq x/H \leq 7$) where $< \widetilde{\chi} >$ is approximately constant; (2) an intermediate stage ($7 \leq x/H \leq 15$) where $< \widetilde{\chi} >$ increases; and (3) a fully-developed stage ($x/H > 15$) where $< \widetilde{\chi} >$ decreases. Note that $< \widetilde{\chi} >$ carries information on both the spatial extent of mixing (on the jet thickness) and the local values of the rates of mixing (on the values of $\widetilde{\chi}$). The transition from the first to the second stage is related to the onset of large scale turbulent mixing and a corresponding rapid increase in the turbulent

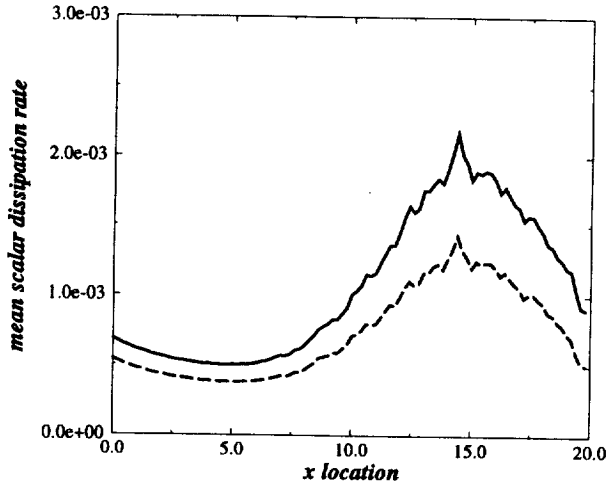

FIGURE 9. Streamwise evolution of the mean total and SGS scalar dissipation rates, $< \widetilde{\chi} >$ (———) and $< \widetilde{\chi}_{SGS} >$ (----) *vs* x. The mean scalar dissipation rates are made non-dimensional with the initial jet time scale, (H/U_j). x is made non-dimensional with the initial jet height H.

jet thickness. The transition from the second to the third fully-developed stage is related to the lower local instantaneous values of the scalar dissipation rate that are found downstream, as the jet fluid is further decelerated and the turbulence levels are progressively reduced.

The downstream evolution from fast to slow SGS mixing rates, as observed in Fig. 9 for $x/H > 15$, is the key mechanism that controls flame stabilization in the LES combustion sub-model proposed in §3. The corresponding key quantity in the SEDFM model is the turbulent mixing time scale $\widetilde{\tau}^t$, and a basic requirement of the model is that $\widetilde{\tau}^t$ increases (at least in a mean sense) with downstream distance. Figure 10 shows that this requirement is correctly met using the local SGS turbulent time scale as an estimate for $\widetilde{\tau}^t$:

$$\widetilde{\tau}^t = \frac{\Delta}{\sqrt{\widetilde{k}_{SGS}}} = \frac{1}{\sqrt{C_I}|\widetilde{S}|} \tag{6}$$

where Δ is the LES filter size, $\Delta \equiv (\Delta_x \Delta_y \Delta_z)^{1/3}$, $\widetilde{k}_{SGS}$ the SGS turbulent kinetic energy, and $|\widetilde{S}| \equiv (2\widetilde{S}_{ij}\widetilde{S}_{ij})^{1/2}$, with $\widetilde{S}_{ij} \equiv (\partial\widetilde{u}_i/\partial x_j + \partial\widetilde{u}_j/\partial x_i)/2$. Note that in Fig. 10, the analysis is conditioned on being in the mixing zone: $\widetilde{\tau}^t$ is conditioned on $|\nabla\widetilde{Z}|$ being larger than a threshold value that corresponds to approximately 20% of the maximum value of the mixture fraction gradient at $x = 0$.

Figure 10 shows a classical evolution from fast to slow time scales for mixing, with $< \widetilde{\tau}^t >$ approximately twice as long at $x/H = 20$ compared to its initial value at $x/H = 0$. This evolution is also observed in Fig. 11 where the pdf of $\widetilde{\tau}^t$ is presented

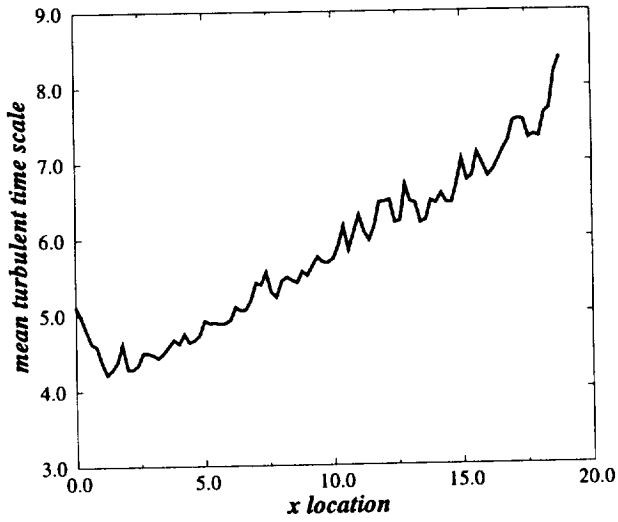

FIGURE 10. Streamwise evolution of the mean SGS turbulence time scale, $< \widetilde{\tau}^t >$ *vs* x. The mean SGS turbulence time scale is made non-dimensional with the initial jet time scale (H/U_j). x is made non-dimensional with the initial jet height H.

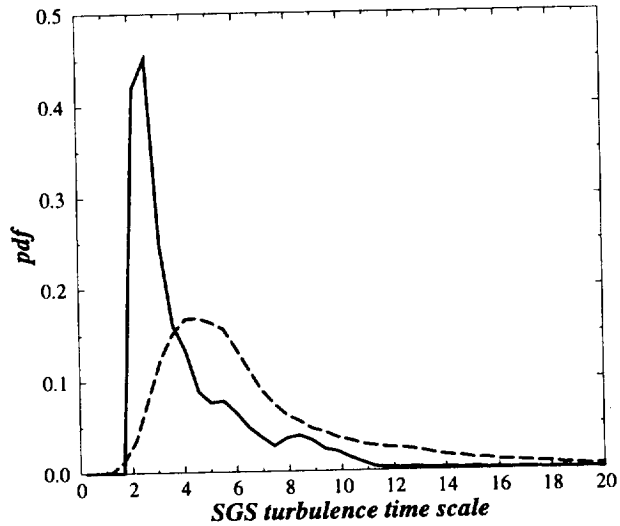

FIGURE 11. Probability distribution of the SGS turbulence time scale, $\widetilde{\tau}^t$, at $x/H = 1.8$ (———) and $x/H = 17.8$ (----). $\widetilde{\tau}^t$ is made non-dimensional with the initial jet time scale, (H/U_j).

at 2 streamwise locations. Figure 11 reveals a weak downstream trend towards wider statistical distributions of mixing time scales. The $\widetilde{\tau}^t$-distribution at $x/H = 17.8$ covers a range of time scales that can vary by an order of magnitude. It is expected that the SEDFM model will be sensitive to the largest values in this distribution

and will allow flame stabilization at grid locations where $\widetilde{\tau}^t$ is sufficiently large.

5. Conclusion

Direct numerical simulations of leading-edge flames evolving in isotropic turbulent flow are used in the present study to propose a new subgrid-scale combustion model (the SEDFM model) for large eddy simulations of the stabilization region of turbulent jet flames. The SEDFM model is based on a skeletal description of the flame structure in mixture fraction space and a transition in that description from the pure mixing line solution to the equilibrium solution. The transition occurs at a rate given by a simple analogy with a partially stirred reactor (PaSR) configuration. The PaSR model measures the relative speeds of subgrid-scale mixing and chemical reaction. The key parameter in the SEDFM model is the turbulent mixing time scale $\widetilde{\tau}^t$.

Large eddy simulations of the near-field region of plane turbulent jets are also used to describe the turbulent mixing process and to propose an estimate of the turbulent mixing time scale $\widetilde{\tau}^t$. It is found that a simple estimate of $\widetilde{\tau}^t$ based on the local subgrid-scale turbulent time scale, $(\Delta/(\widetilde{k}_{SGS})^{1/2})$, is sufficient to describe the downstream evolution from fast to slow mixing rates.

Preliminary results from *a priori* tests of the SEDFM model are found to be encouraging. *A posteriori* tests and a full evaluation of the performance of the model in LES simulations are currently in progress.

Acknowledgment

This work has benefited from many stimulating and exciting discussions with the members of the CTR Summer Program, in particular the authors gratefully acknowledge their CTR hosts Prof. J. Ferziger, Dr. G. Ruetsch, and C. D. Pierce.

REFERENCES

BORGHI, R. 1988 Turbulent combustion modeling. *Prog. Energy Combust. Sci.* **14,** 245-292.

BRAY, K. N. C. 1996 The Challenge of turbulent combustion. *Twenty-sixth Symp. (Intl.) on Combust.* The Combustion Institute, Pittsburgh.

BROADWELL, J. E. & LUTZ A. 1998 A turbulent jet chemical reaction model: NO_x production in jet flames. *Combust. Flame.* **114,** 319-335.

BROADWELL, J. E., DAHM, W. J. A. & MUNGAL, M. G. 1984 Blowout of turbulent diffusion flames. *Twentieth Symp. (Intl) on Combust.* The Combustion Institute, 303-310.

BUCKMASTER, J. & WEBER, R. 1996 Edge-Flame Holding. *Twenty-sixth Symp. (Intl) on Combust.* The Combustion Institute, Pittsburgh.

BURKE, S. P. & SCHUMANN, T. E. W. 1928 Diffusion flames. *Industr. Eng. Chem.* **20,** 998-1004.

COOK, A. W. & RILEY, J. J. 1994 A subgrid model for equilibrium chemistry in turbulent flows. *Phys. Fluids.* **8**(6), 2868-2870.

DOMINGO, P. & VERVISCH, L. 1996 Triple flames and partially premixed combustion in autoignition of nonpremixed mixtures. *Twenty-sixth Symp. (Intl) on Combust.* The Combustion Institute, Pittsburgh.

DOPAZO, C. 1994 Recent developments in pdf methods. *In Turbulent Reacting Flows.* (ed. P. A. Libby & F. A. Williams). Academic Press London, 375-474.

ECHEKKI, T. & CHEN, J. H. 1998 Structure and propagation of methanol-air triple flames. *Combust. Flame.* **114,** 231-245.

FAVIER, V. & VERVISCH, L. 1998 Investigating the effects of edge-flames in liftoff in non-premixed turbulent combustion. *Twenty-seventh Symp. (Intl) on Combust.* The Combustion Institute, Pittsburgh.

GHOSAL, S. & VERVISCH, L. 1998 Asymptotic theory of triple flame including effects of heat release. Submitted to *J. Fluid Mech.*

HARTLEY, L. J. & DOLD, J. W. 1991 Flame propagation in a nonuniform mixture: analysis of a propagating triple-flame. *Combust. Sci. Tech.* **80,** 23-46.

JABERI, F. A. & JAMES, S. 1998 A dynamic similarity model for large eddy simulation of turbulent combustion. *Phys. Fluids.* **10**(7), 1775-1777.

KIONI, P. N., ROGG, B., BRAY K.N.C. & LIÑÁN, A. 1993 Flame spread in laminar mixing layers: the triple flame. *Combust. Flame.* **95,** 276.

LEE, S., LELE, S. K. & MOIN, P. 1992 Simulation of spatially evolving turbulence and the applicability of Taylor's hypothesis in compressible flow. *Phys. Fluids A.* **4,** 1521.

LELE, S. K. 1992 Compact finite difference schemes with spectral-like resolution. *J. Comp. Phys.* **103,** 16-42.

LIBBY, P. A., WILLIAMS, F. A. 1994 Fundamental aspects: a review. In *Turbulent Reacting Flows.* (ed. P. A. Libby & F. A. Williams). Academic Press London, 1-57.

MOIN, P., SQUIRES, K., CABOT, W. & LEE, S. 1991 A dynamic subgrid-scale model for compressible turbulence and scalar transport. *Phys. Fluids A.* **3,** 2746-2757.

MÜLLER, C. M., BREITBACH, H. & PETERS, N. 1994 Partially premixed turbulent flame propagation in jet flames. *Twenty-Fifth Symp. (Intl) on Combust.* The Combustion Institute, 1099-1106.

MUÑIZ, L. & MUNGAL, M. G. 1997 Instantaneous flame-stabilization velocities in lifted-Jet diffusion flames. *Combust. Flame.* **111,** 16-31.

PETERS, N. 1986 Laminar flamelet concepts in turbulent combustion. *Twenty-first Symp. (Intl) on Combust.* The Combustion Institute, 1231-1250.

PETERS, N. & WILLIAMS, F. A. 1983 Liftoff characteristics of turbulent jet diffusion flames. *AIAA J.* **21,** 423-429.

PHILLIPS, H. 1965 Flame in a buoyant methane layer. *Tenth Symp. (Intl) on Combust.* The Combustion Institute, 1277.

PIERCE, C. D. & MOIN, P. 1998 Large eddy simulation of a confined coaxial jet with swirl and heat release. *AIAA Paper 2892* 29th AIAA Fluid Dynamics Conference, Albuquerque NM.

PITTS, W. M. 1988 Assessment of theories for the behavior and blowout of lifted turbulent jet diffusion flames. *Twenty-Second Symp. (Intl) on Combust.* The Combustion Institute, 809-816.

PLESSING, T., TERHOEVEN, P., PETERS, N., MANSOUR, M. S. 1998 An experimental and numerical study of a laminar triple flame. *Combust. Flame.* **115(3),** 335-353.

POINSOT, T. & LELE, S. K. 1992 Boundary conditions for direct simulations of compressible viscous flows. *J. Comp. Phys.* **101,** 104-129.

POINSOT, T., CANDEL, S. & TROUVÉ, A. 1996 Direct numerical simulation of premixed turbulent combustion. *Prog. Energy Combust. Sci.* **12,** 531-576.

POPE, S. B. 1985 Pdf method for turbulent reacting flows. *Prog. Energy Combust. Sci.* **11,** 119-195.

RAVET, F. & VERVISCH, L. 1998 Modeling non-premixed turbulent combustion in aeronautical engines using PDF-Generator. *AIAA Paper 1027,* 36th Aerospace Sciences Meeting and Exhibit, Reno Nv.

RÉVEILLON, J. & VERVISCH, L. 1996 Response of the dynamic LES model to heat release induced effects. *Phys. Fluids.* **8**(8).

RÉVEILLON, J. & VERVISCH, L. 1998 Subgrid mixing modeling: a dynamic approach. *AIAA J.* **36**(3), 336-341.

RUETSCH, G. R., VERVISCH, L. & LIÑÁN, A. 1995 Effects of heat release on triple flame. *Phys. Fluids.* **7**(6), 1447-1454.

SMITH, N. S. 1996 Conditional moment closure of mixing and reaction in turbulent nonpremixed combustion. *Annual Research Briefs.* Center for Turbulence Research, NASA Ames/Stanford Univ., 85-99.

VANQUICKENBORNE, L. & VAN TIGGELEN, A. 1966 The stabilization mechanism of lifted diffusion flames. *Combust. Flame.* **10,** 59-69.

VERVISCH, L. & POINSOT, T. 1998 Direct numerical simulation of non-premixed turbulent flame. *Ann. Rev. Fluid Mech.* **30,** 655-692.

VEYNANTE, D., VERVISCH, L., POINSOT, T., LIÑÁN, A., RUETSCH, G. 1994 Triple flame structure and diffusion flame stabilization. *CTR 1994 Summer Proceedings.* Center for Turbulence Research, NASA Ames/Stanford Univ., 55-73.

56-25

Center for Turbulence Research
Proceedings of the Summer Program 1998

A subgrid-scale model for the scalar dissipation rate in nonpremixed combustion

By A. W. Cook[1] AND W. K. Bushe

A subgrid-scale model is presented for the scalar dissipation rate in nonpremixed turbulent reacting flows. Inputs to the model are the filtered density, the Favre-filtered temperature, and the Favre-filtered mixture-fraction. The model contains a coefficient which is determined by assuming a form for the scalar energy spectrum. Inputs to the presumed spectrum are the integral and dissipation length scales of the scalar field. These quantities are estimated locally from the Favre-filtered velocity field, resulting in a model coefficient which is spatially and temporally dependent. The model is tested *a priori* using data from a Direct Numerical Simulation (DNS) of a temporal reacting mixing layer. Estimated values of the dissipation rate are found in good agreement with dissipation rates computed directly from the DNS data. Furthermore, the presumed spectrum methodology is found to accurately predict the mean value of the model coefficient as well as its spatial and temporal variations.

1. Introduction

The Large Eddy Simulation (LES) of chemically reacting turbulent flows has become a topic of much interest in recent years. The application of LES to nonpremixed combustion is motivated by a large amount of evidence demonstrating that mixing rates are controlled by large-scale eddies. Additional motivation is provided by the need to simulate unsteady flows such as the combustion cycle in a diesel engine; LES is well-suited to unsteady combustion problems since it yields time-accurate information.

A common practice in the modeling of nonpremixed combustion is to relate the various chemical mass fractions to a conserved scalar mixture-fraction (Bilger 1980). Chemical reaction rates are known to be strong functions of the mixture fraction, and several models of nonpremixed combustion such as the Laminar Flamelet Model (LFM) (Peters 1985) and the Conditional Moment Closure (CMC) (Bilger 1993) take advantage of this to achieve closure of the highly non-linear chemical source terms. Application of such theories in LES involves characterizing the state of mixing within each grid cell. A useful measure of subgrid-scale mixing is the scalar variance, which can either be modeled or else computed by integrating its transport equation.

An important term in the scalar variance equation is the scalar dissipation rate. This term represents the rate at which reactants are brought together at the molecular level. High rates of dissipation can, in the presence of cold reactants, cause

1 Lawrence Livermore National Laboratory

flames to extinguish or else fail to ignite. Mixture-fraction-based models of turbulent combustion usually express reaction rates as functions of the scalar dissipation rate. The scalar dissipation rate is a highly intermittent phenomenon, exhibiting large fluctuations associated with the smallest turbulent length scales; however, the net dissipation is determined by the rate at which energy is fed to the turbulence at large (resolvable) scales. Therefore, there is more information available for modeling the scalar dissipation rate in an LES than there is in a Reynolds averaged calculation.

De Bruyn Kops *et al.* (1998) proposed a model for the subgrid-scale scalar dissipation rate which has the same form as the leading term in a model proposed by Girimaji and Zhou (1996). The model contains a coefficient which can be spatially and temporally dependent. The primary motivation for this work is to determine whether an assumed spectrum methodology can be employed in determining the model coefficient. Another goal is to investigate the accuracy of the model for a flow with large density variations, due to heat release, and a temperature dependent scalar diffusivity.

2. Definitions

Consider a turbulent reacting flow in which streams of fuel and oxidizer meet in a combustion chamber where mixing and reaction take place. During the combustion process, many chemical species may be produced and/or destroyed; however, elemental mass fractions are conserved. Let $Z = Z(\mathbf{x},t)$ be a conserved scalar mixture-fraction, defined as

$$Z \equiv \frac{(Z_i - Z_{i,o})}{(Z_{i,f} - Z_{i,o})} \ , \ i = 1,2,...,N \tag{1}$$

where Z_i is the mass fraction of element i, N is the total number of elements, and the indices f and o refer to values in the fuel and oxidizer streams, respectively. It can be seen that $Z = 1$ in the fuel stream and $Z = 0$ in the oxidant stream. Now let the dissipation rate of scalar fluctuations be denoted by 2χ, where

$$\chi(\mathbf{x},t) \equiv D \bigtriangledown Z \cdot \bigtriangledown Z \ . \tag{2}$$

Here D represents the scalar diffusivity, which may be a function of temperature, i.e., $D = D(T)$. In order to characterize the mean scalar dissipation rate within an LES grid cell, it is necessary to specify the spatial filter associated with the LES mesh. The filter is defined by

$$\overline{Z}(\mathbf{x}) \equiv \int G(|\mathbf{x} - \mathbf{x}'|;\Delta) Z(\mathbf{x}')\, d\mathbf{x}' \ , \tag{3}$$

where the integral is taken over all 3-dimensional space (for brevity, the t dependence has been dropped). The filter kernel $G(|\mathbf{x} - \mathbf{x}'|;\Delta)$ is normalized,

$$\int_{-\infty}^{\infty} G(r;\Delta)\, dr = 1 \ , \tag{4}$$

and has a characteristic width Δ which is directly related to the grid spacing of the LES mesh. The goal is to derive a model for the filtered value of the density-weighted scalar dissipation rate, i.e., $\overline{\rho\chi}$. Results of de Bruyn Kops *et al.* (1998) suggest this term be modeled in the following way,

$$\overline{\rho\chi} \equiv \overline{\rho D \bigtriangledown Z \cdot \bigtriangledown Z} \approx C\overline{\rho} D(\widetilde{T}) \bigtriangledown \widetilde{Z} \cdot \bigtriangledown \widetilde{Z} \ , \tag{5}$$

where a tilde $\widetilde{()}$ is used to denote a Favre-filtered variable, e.g., $\widetilde{Z} \equiv \overline{\rho Z}/\overline{\rho}$. The model contains a coefficient C which can be spatially and temporally dependent, i.e., $C = C(\mathbf{x}, t)$. In the next section, a new method will be described for computing $C(\mathbf{x}, t)$; such that (5) is correct on average. The method utilizes an assumed form for the Z energy spectrum.

3. Determination of model coefficient

In order to relate C to an energy spectrum, Z must be transformable to wavenumber space. Fourier's integral theory assumes that $\int |Z(\mathbf{x})|\, d\mathbf{x}$ is bounded. For this to be the case, $Z(\mathbf{x})$ will be considered to be zero outside a very large box. The box can be made arbitrarily large so that an assumption of homogeneity may also be made. Forward and inverse Fourier transforms of Z are defined as

$$\widehat{Z}(\mathbf{k}) \equiv \frac{1}{2\pi} \int \exp(-i\mathbf{k} \cdot \mathbf{x}) Z(\mathbf{x})\, d\mathbf{x} \ , \tag{6}$$

$$Z(\mathbf{x}) \equiv \int \exp(i\mathbf{k} \cdot \mathbf{x}) \widehat{Z}(\mathbf{k})\, d\mathbf{k} \ , \tag{7}$$

where $\mathbf{k}$ is a wavevector given in *radians per unit length.* The Fourier transform of $\partial\overline{Z}/\partial x_j$ is

$$\widehat{\frac{\partial \overline{Z}}{\partial x_j}} = -ik_j \widehat{G}(k;\Delta) \widehat{Z}(\mathbf{k}) \ , \tag{8}$$

where $\widehat{G}$ is a function only of the magnitude of $\mathbf{k}$, i.e., $k^2 \equiv \mathbf{k} \cdot \mathbf{k} = k_j k_j$. Writing $\partial\overline{Z}/\partial x_j$ as the inverse transform of (8) and squaring both sides (and summing on j) leads to

$$\left| \frac{\partial \overline{Z}}{\partial x_j} \right|^2 = \iint \exp(i(\mathbf{k} + \mathbf{k}') \cdot \mathbf{x})(-k_j k_j') \widehat{G}(k;\Delta) \widehat{G}(k';\Delta) \widehat{Z}(\mathbf{k}) \widehat{Z}(\mathbf{k}')\, d\mathbf{k}\, d\mathbf{k}' \ . \tag{9}$$

Since $Z(\mathbf{x})$ is real, $\widehat{Z}(\mathbf{k}') = \widehat{Z}^*(-\mathbf{k}')$ where the asterisk denotes the complex conjugate. For homogeneous turbulence, the Fourier amplitudes $\widehat{Z}(\mathbf{k})$ and $\widehat{Z}^*(-\mathbf{k}')$ are statistically orthogonal; hence, the ensemble average $\left\langle \widehat{Z}(\mathbf{k}) \widehat{Z}^*(-\mathbf{k}') \right\rangle$ is zero unless $-\mathbf{k}' = \mathbf{k}$ (Batchelor 1953). The ensemble average of (9) thus becomes

$$\left\langle \frac{\partial \overline{Z}}{\partial x_j} \frac{\partial \overline{Z}}{\partial x_j} \right\rangle = \int k^2 \widehat{G}^2(k;\Delta) \left\langle \widehat{Z}^*(\mathbf{k}) \widehat{Z}(\mathbf{k}) \right\rangle d\mathbf{k} \ . \tag{10}$$

The integral in (10) may be cast as an integral over a spherical shell of radius k, followed by integration over all shells. For example, if $d\sigma$ denotes a differential surface element of a shell, then (10) can be written

$$\int k^2\widehat{G}^2(k;\Delta)\left\langle\widehat{Z}^*(\mathbf{k})\widehat{Z}(\mathbf{k})\right\rangle\,d\mathbf{k} = \int_0^\infty k^2\widehat{G}^2(k;\Delta)\oint\left\langle\widehat{Z}^*(\mathbf{k})\widehat{Z}(\mathbf{k})\right\rangle\,d\sigma\,dk\ . \quad (11)$$

The shell integral in Eq. (11) is equal to twice the three-dimensional, scalar energy spectrum, i.e., $2E_Z(k)$; hence,

$$\left\langle\frac{\partial\overline{Z}}{\partial x_j}\frac{\partial\overline{Z}}{\partial x_j}\right\rangle = 2\int_0^\infty k^2\widehat{G}^2(k;\Delta)E_Z(k)\,dk\ . \quad (12)$$

Repeating the analysis for $\partial Z/\partial x_j$ leads to the result

$$\left\langle\overline{\frac{\partial Z}{\partial x_j}\frac{\partial Z}{\partial x_j}}\right\rangle = \left\langle\frac{\partial Z}{\partial x_j}\frac{\partial Z}{\partial x_j}\right\rangle = 2\int_0^\infty k^2E_Z(k)\,dk\ . \quad (13)$$

The coefficient C can be determined by taking the average of (5), i.e.,

$$C = \frac{\left\langle\overline{\rho D\bigtriangledown Z\cdot\bigtriangledown Z}\right\rangle}{\left\langle\overline{\rho}D(\widetilde{T})\bigtriangledown\widetilde{Z}\cdot\bigtriangledown\widetilde{Z}\right\rangle} \approx \frac{\left\langle\overline{\bigtriangledown Z\cdot\bigtriangledown Z}\right\rangle}{\left\langle\bigtriangledown\overline{Z}\cdot\bigtriangledown\overline{Z}\right\rangle} = \frac{\int_0^\infty k^2E_Z(k)\,dk}{\int_0^\infty k^2\widehat{G}^2(k;\Delta)E_Z(k)\,dk}\ . \quad (14)$$

Here it has been assumed that ρD approximately cancels in the numerator and denominator and that $\left\langle\bigtriangledown\widetilde{Z}\cdot\bigtriangledown\widetilde{Z}\right\rangle \approx \left\langle\bigtriangledown\overline{Z}\cdot\bigtriangledown\overline{Z}\right\rangle$.

4. Assumed energy spectrum

In order to compute C using (14), it is necessary to specify the functions $\widehat{G}(k;\Delta)$ and $E_Z(k)$. For the present analysis, the LES grid filter is assumed to be a 'top-hat' function, which, in Fourier space, is defined as

$$\widehat{G} = \frac{2\sin(k\Delta/2)}{k\Delta}\ . \quad (15)$$

The scalar energy spectrum is assumed to be that of isotropic turbulence at high Reynolds number (Tennekes and Lumley 1972), i.e.,

$$E_Z(k) = A\,\exp[-1.73(kl_Z)^{-4/3}]k^{-5/3}\exp[-2.25(k\eta_Z)^{4/3}]\ , \quad (16)$$

which is applicable for fluids with Schmidt numbers near unity. For fluids with a very low or very high Schmidt number, an inertial-diffusive or viscous-convective subrange should be included in the assumed spectrum. Equation (16) contains three unknown parameters: a constant A, a scalar integral scale l_Z, and a dissipation scale η_Z (Corrsin 1951). The constant A divides out of Eq. (14) and, hence, is irrelevant to the modeling. The length scales l_Z and η_Z determine roughly where

the spectrum peaks and where it goes to zero. If l_Z and η_Z are estimated locally and/or instantaneously, then C will be obtained as a function of space and/or time. In the present analysis, l_Z and η_Z are assumed to be related to the integral scale l and Kolmogorov microscale η of the velocity field u_i. This implies that the flow is sufficiently developed such that the statistics of the velocity field are reflected in the scalar field. The length scale estimates are as follows:

$$l_Z \approx l \approx \frac{V}{\langle S_{ij}S_{ij}/9\rangle^{1/2}} , \tag{17}$$

$$V \equiv \langle \widetilde{u}_i \widetilde{u}_i \rangle^{1/2} , \tag{18}$$

$$S_{ij} \equiv \frac{1}{2}\left(\frac{\partial \widetilde{u}_i}{\partial x_j} + \frac{\partial \widetilde{u}_j}{\partial x_i}\right) , \tag{19}$$

$$\eta_Z \approx \eta Sc^{-1/2} , \tag{20}$$

$$\eta \approx \alpha l Re_l^{-3/4} , \tag{21}$$

$$Re_l \equiv lV/\langle \nu \rangle , \tag{22}$$

$$\langle \nu \rangle \equiv Sc\left\langle D(\widetilde{T})\right\rangle . \tag{23}$$

where Sc is the global Schmidt number and α is a constant.

In the present analysis, α was set to 2 in order to bring the model into agreement with the DNS data (to be described in the next section). The estimates for η_Z and η are strictly valid only at high Reynolds number. Due to the low Reynolds number of DNS, the dissipation range makes up most of the energy spectrum; thus, in *a priori* tests, C can be sensitive to the estimate for η_Z. In a high Reynolds number flow, however, the energy in the dissipation range contributes only slightly to the integral of the spectrum. Hence, there is good reason to expect that, at higher Reynolds numbers, $C(x,t)$ will be less sensitive to the estimate for η_Z so that α can probably be set to 1 if the Reynolds number is high enough.

5. DNS data

The model was tested using data from DNS of a reacting temporal mixing layer (Bushe *et al.* 1998). The DNS utilized a computational mesh consisting of 240 $\times$ 120 $\times$ 120 points in the x, y, and z directions, respectively. It was initialized with a planar laminar flame centered in the domain. Isotropic turbulent velocity fluctuations taken from a previous simulation of forced incompressible turbulence were superimposed on the flow induced by the heat release of the flame. Periodic boundaries were imposed in the y and z directions. Outflow boundary conditions, as described in Poinsot and Lele (1992), were employed in the x direction to allow for expansion due to heat release. In order to avoid unphysical generation of vorticity by the imposed outflow conditions, the velocity fluctuations were filtered to zero at the x boundaries. A two-step reduced chemical kinetic mechanism for methane

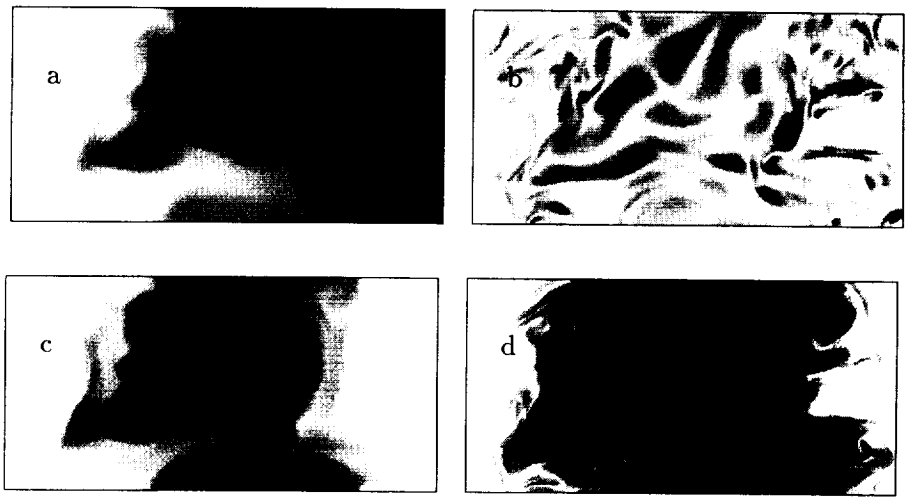

FIGURE 1. Grayscale plots of (a) Mixture-fraction, (b) Enstrophy, (c) Temperature and (d) Logarithm of scalar dissipation rate on an $x-y$ plane in the DNS flow field at $t = 15$.

was used with a further step added to approximate NO_x chemistry. The maximum possible density ratio, based on the adiabatic flame temperature, was 7.4; the maximum density ratio achieved in the simulation was 6.3. The global acoustic Reynolds number was $Re_a = 2000$, and, for the case used here, the Schmidt number of all species was set to $Sc = 0.75$. The ratio of specific heats was set to $\gamma = 1.3$, and the scalar diffusivity was prescribed as the following function of temperature

$$D = \frac{[(\gamma - 1)T]^{0.76}}{ReSc} \,. \tag{24}$$

Figure 1a shows the mixture-fraction field on a slice in the three-dimensional domain after the flow had evolved for 15.0 acoustic time units. The gas on the right is fuel and the gas on the left is oxidant. The enstrophy field on the same slice is shown in Fig. 1b. Figure 1c shows the temperature field resulting from the exothermicity of the reactions. The scalar dissipation rate is shown in Fig. 1d; it is clear that this field has structures associated with fine length scales.

6. Results

In the *a priori* tests, the DNS data were averaged onto a $24 \times 12 \times 12$ point LES grid such that each LES grid cell was comprised of 10^3 DNS data points. Ensemble averages were approximated by averaging in the homogeneous directions, i.e., over $(y - z)$ planes. The model coefficient C was thus computed as a function of the inhomogeneous direction x and time t.

Figure 2 shows the true and modeled values of C as a function of x at four different times in the simulation. At $t = 7.5$, C is overpredicted. This is due to the fact that insufficient time has elapsed for a turbulent spectrum to have developed for the Z

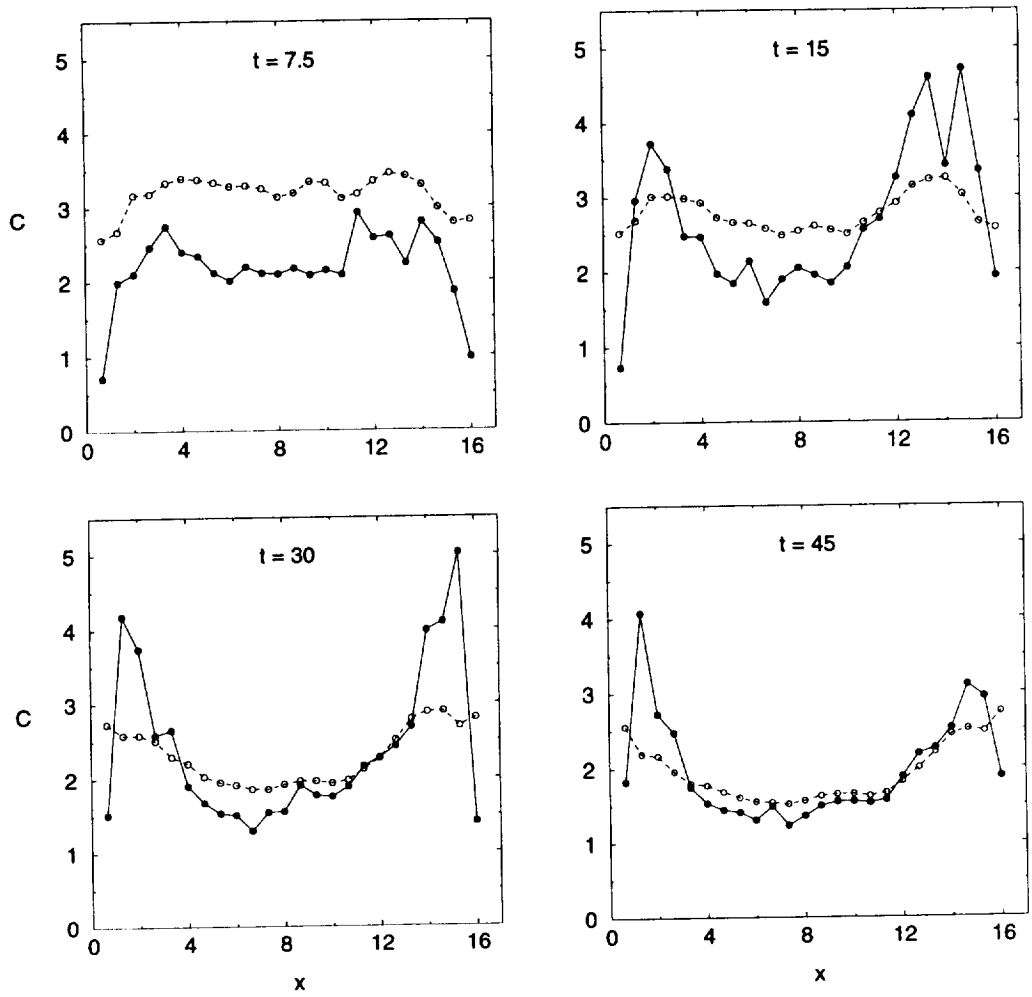

FIGURE 2. Coefficient in model for $\overline{\rho\chi}$ as a function of x and t from DNS of temporal reacting mixing layer: • - DNS; o - assumed spectrum method.

field. However, as time elapses, the model for $C(x,t)$ becomes increasingly more accurate. Furthermore, it is encouraging that the model appears most accurate near the middle of the domain where the bulk of the reactions are occurring. The large oscillations in the DNS values of $C(x,t)$ near the ends of the domain are due to the fact that $Z(\mathbf{x},t)$ is nearly constant close to the boundaries such that the scalar dissipation rates are very small. Computation of the DNS values for C near the boundaries involves taking the ratio of two very small numbers; hence, the results are subject to numerical noise.

In Fig. 3, true versus estimated values of $\overline{\rho\chi}$ are plotted for every point on the LES grid. The model values were computed from (5) using C as shown in Fig. 1, i.e., $\overline{\rho\chi}_{\text{est}} = C(x,t)\overline{\rho}D(\widetilde{T}) \bigtriangledown \widetilde{Z} \cdot \bigtriangledown \widetilde{Z}$. The results show good agreement between the

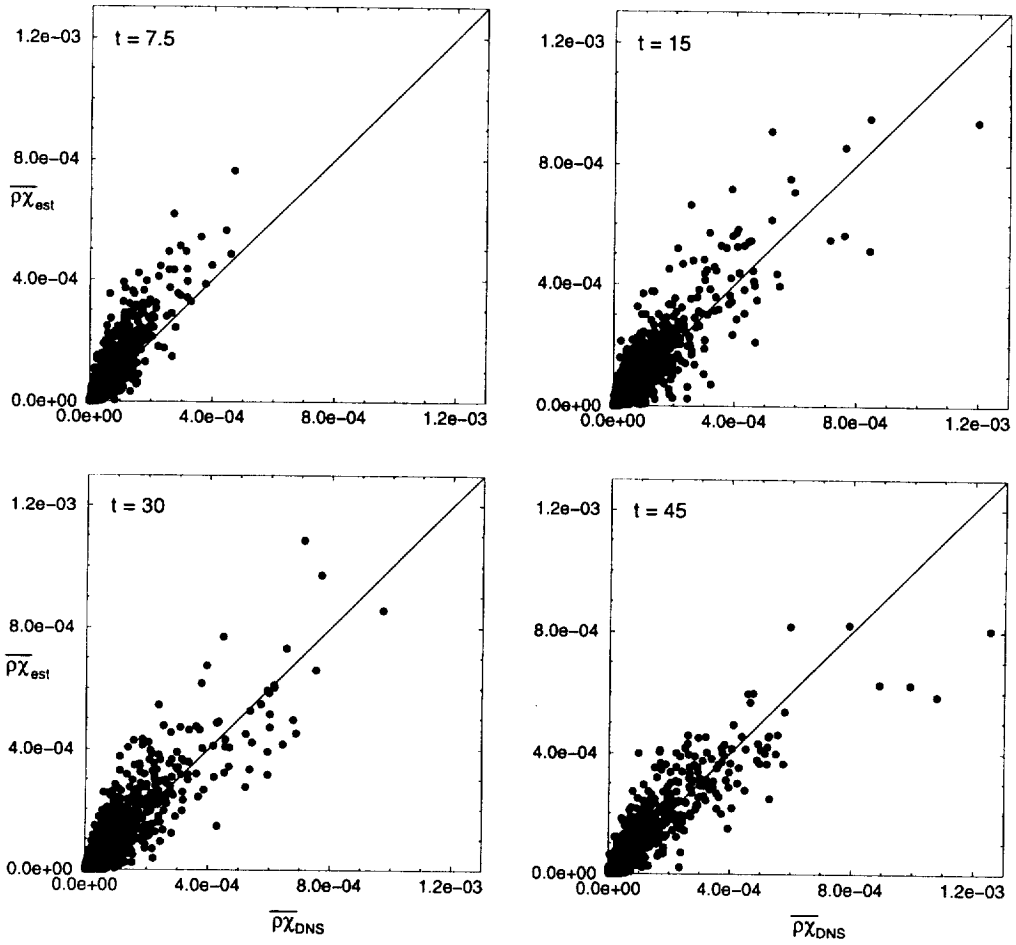

FIGURE 3. Estimated (est) versus true (DNS) values of $\overline{\rho\chi}$, computed by filtering $240 \times 120 \times 120$ point DNS data onto $24 \times 12 \times 12$ point LES grid.

true and estimated values of $\overline{\rho\chi}$. Linear correlation coefficients for $\overline{\rho\chi}_{\text{est}}$ and $\overline{\rho\chi}_{\text{DNS}}$ are: 0.911, 0.897, 0.898 and 0.913 for $t = 7.5$, 15, 30 and 45, respectively.

7. Conclusions

A model has been presented for the scalar dissipation rate in nonpremixed turbulent combustion. The model contains a coefficient which can be computed by assuming a form for the scalar energy spectrum. The scalar integral scale l_Z and dissipation length scale η_Z appear as parameters in the assumed spectrum. The model was evaluated *a priori* using DNS results for a turbulent reacting mixing layer. It was found that the assumed spectrum, when combined with local estimates for l_Z and η_Z, gave accurate predictions of the model coefficient, including its spatial and temporal variations. Furthermore, the tests revealed a high correlation between true and modeled values of the scalar dissipation rate, which appears

to validate the model for turbulent reacting flows in the presence of heat release.

Acknowledgments

Partial support for this work was provided by the U.S. Department of Energy through Lawrence Livermore National Laboratory under Contract No. W-7405-Eng-48.

REFERENCES

BATCHELOR, G. K. 1953 *The Theory of Homogeneous Turbulence.* Cambridge University Press.

BILGER, R. W. 1980 Turbulent Flows with Nonpremixed Reactants. In *Topics in Applied Physics* vol. 44, chap. 3, pp 2-36. Berlin: Springer-Verlag.

BILGER, R. W. 1993a Conditional moment closure for turbulent reacting flow. *Phys. Fluids A.* **5**(2), 436.

BUSHE, W. K., BILGER, R. W. & RUETSCH, G. R. 1998 Direct Numerical Simulation of nonpremixed combustion with realistic chemistry. To be submitted to *J. Fluid Mech.*

CORRSIN, S. 1951 On the spectrum of isotropic temperature fluctuations in isotropic turbulence. *J. App. Phys.* **22,** 469.

DE BRUYN KOPS, S. M., RILEY, J. J., KOSALY, G. & COOK, A. W. 1998 Investigation of modeling for non-premixed turbulent combustion. Submitted to *Flow, Turbulence and Combustion.*

GIRIMAJI, S. S. & ZHOU, Y. 1996 Analysis and modeling of subgrid scalar mixing using numerical data. *Phys. Fluids.* **8,** 1224–1236.

PETERS, N. 1984 Laminar diffusion flamelet models. *Prog. Energy Combust. Sci.* **10,** 319.

POINSOT, T., & LELE, S. 1992 Boundary conditions for direct simulations of compressible viscous flows. *J. Comp. Phys.* **101,** 104.

TENNEKES, H. & LUMLEY, J. L. 1972 *A First Course in Turbulence.* Cambridge: MIT Press.

Approaches to modeling thermonuclear flames

By J. C. Niemeyer[1], W. K. Bushe, AND G. R. Ruetsch

Turbulence-flame interactions of thermonuclear fusion flames occurring in Type Ia Supernovae were studied by means of incompressible DNS with a highly simplified flame description. The flame is treated as a single diffusive scalar field with a non-linear source term. It is characterized by its Prandtl number, $Pr \ll 1$, and laminar flame speed, S_L. We find that if $S_L \geq u'$, where u' is the *rms* amplitude of turbulent velocity fluctuations, the local flame propagation speed does not significantly deviate from S_L even in the presence of velocity fluctuations on scales below the laminar flame thickness. This result is interpreted in the context of subgrid-scale modeling of supernova explosions.

1. Introduction

A class of astrophysical explosions, so-called Type Ia Supernovae (SN Ia's), is believed to involve the formation and propagation of thin thermonuclear fusion fronts. These fronts are similar in many ways to premixed chemical flames and are often referred to as "thermonuclear flames". The issues addressed in this work are motivated in the framework of supernova research, but the results obtained apply equally well to premixed chemical flames with low Prandtl numbers and small thermal expansion rates.

Type Ia Supernovae occur at a rate of approximately two per century per galaxy; their observables include optical spectra indicating the compositional structure of the explosion ejecta, the evolution of the total emitted light with time, and, indirectly, their contribution to the isotopic abundances in the solar neighborhood. Owing to their high optical luminosity, reaching the equivalent of approximately ten billion suns at maximum light, SN Ia's can be observed out to very large extragalactical distances. Theoretically, they are associated with thermonuclear explosions of white dwarf stars composed of carbon and oxygen and stabilized against gravitational collapse by the degeneracy pressure of a relativistic electron gas (Arnett 1969). In one scenario which has been proposed to explain these explosions, a white dwarf at the Chandrasekhar mass limit—the maximum equilibrium mass of a star supported by electron degeneracy, $M_{ch} \approx 1.4$ solar masses—accretes matter from a binary companion and eventually becomes gravitationally unstable. Compressional heating of the core region leads to the ignition of thermonuclear fusion reactions that "burn" carbon and oxygen to heavier nuclei. Slowly at first but with increasing

1 University of Chicago, Department of Astronomy and Astrophysics, 5640 S. Ellis Avenue, Chicago, IL 60637

intensity as cooling by neutrino emission fails to keep up with the nuclear energy release, a thermonuclear runaway begins at the center of the white dwarf. As the core reaches the critical temperature of $T \approx 1.5 \times 10^9$ K (at a density of $\rho \approx 2 - 3 \times 10^9$ g cm^{-3}), the time scale for nuclear energy release drops to $\sim 10^{-12}$ s, giving rise to the formation of a highly localized burning front that propagates outward as either a detonation or a deflagration (Woosley 1990). This marks the beginning of the actual explosion, terminating in the complete disruption of the white dwarf.

Based on the observational evidence of intermediate elements in SN Ia spectra, detonations can be ruled out as the initial mode of propagation, as they would predict the complete incineration of the white dwarf to iron group nuclei. Deflagrations, on the other hand, are hydrodynamically unstable to both flame intrinsic (Landau-Darrieus) and buoyancy-driven (Rayleigh-Taylor, RT) instabilities. While the former is stabilized in the nonlinear regime, the latter produces a growing, fully turbulent RT-mixing region of hot burning products and cold "fuel" separated by the thin thermonuclear flame (for a more detailed discussion of flame instabilities in this context, see, e.g., Niemeyer & Woosley 1997). Driven predominantly by the shear flow surrounding buoyant large-scale bubbles, turbulent velocity fluctuations cascade down to the Kolmogorov scale l_k, which may, under certain conditions, be smaller than the laminar flame thickness (Section 2).

As the explosion proceeds, the turbulence intensity grows while the flame slows down and thickens as a consequence of the decreasing material density of the expanding star. After some time, small scale turbulence must be expected to significantly alter the flame structure and its local propagation velocity with respect to the laminar solution. On the other hand, most subgrid-scale models for the turbulent thermonuclear flame brush in numerical simulations of supernovae depend crucially on the assumption of a (nearly) laminar flame structure on small scales (Niemeyer & Hillebrandt 1995, Khokhlov 1995). The intent of this work is to present a first approach to study the regions of validity and the possible breakdown of this "thermonuclear flamelet" assumption.

This paper is organized as follows: we shall summarize the most important parameters and dimensional relations of thermonuclear flames and buoyancy-driven turbulence in Section 2, followed by a brief description of the numerical methods employed for this work (Section 3). In Section 4, the results of a series of direct simulations of a highly simplified flame propagating through a turbulent medium are discussed and interpreted in the framework of SN Ia modeling.

2. Flame properties and model formulation

The laminar properties of thermonuclear flames in white dwarfs were investigated in detail by Timmes & Woosley (1992), including all relevant nuclear reactions and microscopic transport mechanisms. The authors found that the laminar flame speed, S_L, varies between 10^7 and 10^4 cm s^{-1} as the density declines from 3×10^9 to $\sim 10^7$ g cm^{-3}. The thermal flame thickness, δ, grows from 10^{-5} to 1 cm for the same density variation. Microscopic transport is dominated entirely by electrons close to the Fermi energy by virtue of their near-luminal velocity distribution and

large mean-free-paths. As a consequence, ionic diffusion of nuclei is negligibly small compared with heat transport and viscosity. Comparing the latter two, one finds typical values for the Prandtl number of $Pr \approx 10^{-5} \ldots 10^{-4}$ (Nandkumar & Pethick 1984). Further, partial electron degeneracy in the burning products limits the density contrast, $\mu = \Delta\rho/\rho$, between burned and unburned material to very small values, $\mu \approx 0.1 \ldots 0.5$.

To within reasonable accuracy, one may estimate the magnitude of large-scale turbulent velocity fluctuations, $u(L)$, from the rise velocity of buoyant bubbles with diameter L, $u_{\rm rise} \sim (0.5\mu g L)^{1/2}$, where g is the gravitational acceleration. Inserting typical values, $L \approx 10^7$ cm, $g \approx 10^8$ cm s^{-2}, and $\mu \approx 0.3$, one finds $u(L) \approx 10^7$ cm s^{-1}. For a viscosity of $\nu \approx 1$ cm^2 s^{-1} (Nandkumar & Pethick 1984), this yields the integral-scale Reynolds number $Re \approx 10^{14}$ and a characteristic Kolmogorov scale $l_{\rm k} \approx LRe^{-3/4} \approx 10^{-4}$ cm. Hence, it is clear that soon after the onset of the explosion, turbulent eddies are present on scales smaller than the laminar flame thickness. According to this length scale analysis alone, the flamelet assumption cannot be justified.

However, the low Prandtl number of degenerate matter allows a situation in which the eddy turn-over time on the Kolmogorov time scale, $\tau_{\rm k} \sim l_{\rm k}/u(l_{\rm k}) \sim l_{\rm k}^2/\nu$, is larger than the reaction time scale $\tau_{\rm r} \sim \dot{w}^{-1}$, where $\dot{w}$ is the fuel consumption rate (Niemeyer & Kerstein 1997). This is readily seen by setting $\tau_{\rm r}$ equal to the diffusion time scale $\tau_{\rm d} \sim \delta^2/\kappa$ for stationary flames (where κ is the microscopic thermal diffusivity), yielding

$$\frac{\tau_{\rm k}}{\tau_{\rm r}} = Pr^{-1} \left(\frac{l_{\rm k}}{\delta} \right)^2 .$$

Even if the length scale ratio on the *rhs* is less than unity, the *lhs* can be large for a sufficiently small Pr. In this case, small eddies are burned before their motion can appreciably affect the flame structure.

An alternative, Pr-independent criterion for flamelet breakdown has been proposed (Niemeyer & Kerstein 1997), based on the relative importance of eddy diffusivity, $\kappa_{\rm e} \sim u(l)l$, and microscopic heat conductivity on scales $l \leq \delta$. As $\kappa_{\rm e}$ is, in general, a growing function of scale, the condition $\kappa_{\rm e}(\delta) \leq \kappa$ is sufficient and can be invoked to define the flamelet burning regime. Using the relation $S_{\rm L} \sim \delta/\tau_{\rm d}$, one finds the more intuitive formulation $u(\delta) \leq S_{\rm L}$. In other words, the flame structure on scales δ and below is dominated by heat diffusion as long as the characteristic velocity associated with eddies of a length scale the same order as the laminar flame thickness is smaller than the laminar flame speed. If heat diffusion is the only relevant microscopic transport process, the local flame speed is expected to remain comparable to $S_{\rm L}$ despite the presence of eddies within the flame.

In order to be able to efficiently address this question, we make three assumptions that greatly simplify the problem without violating the underlying physics. Firstly, we note that nuclear energy generation is dominated by a single reaction, ^{12}C(^{12}C,^{24}Si), which is a strong function of temperature only ($\dot{w} \sim T^{21}$). Therefore, the flame dynamics can be well approximated by a single, diffusive progress variable

c that is advected by the fluid and coupled to a strongly nonlinear source term that mimics nuclear burning. Second, the small value of μ suggests that dilatation effects do not play a significant role and may be neglected for the purpose of this study. This, together with the small Mach number of turbulent fluctuations on very small scales, justifies the use of the incompressible Navier-Stokes equations. Finally, we assume that the effect of the turbulent cascade from large scales can be adequately modeled by forcing the flow field on the lowest wavenumbers of the simulation.

3. Numerical technique

The code used to simulate the thermonuclear flame used the pseudo-spectral approach where derivatives are taken in Fourier space but non-linear terms are evaluated in real space (see Ruetsch and Maxey, 1991). The diffusive term is evaluated implicitly such that the code provided stable, accurate solutions even for very small Prandtl numbers. All boundary conditions were periodic, and energy was added at every time step to the lowest wavenumbers by solving a Langevin equation as described in Eswaran and Pope (1988a, 1988b). All of the simulations were carried out in a 64^3 domain and were run for several eddy-turnover times so as to obtain statistical stationarity.

As was mentioned in the previous section, the temperature dependence of the main reaction participating in thermonuclear flame is roughly T^{21}. It was found that a source term $\dot{w} = kc^{21}(1-c)$ (where the $(1-c)$ arises from the dependence of the reaction on reactant concentration) produced too narrow a reaction zone to be easily resolved in space in a three-dimensional simulation. Instead, it was decided to use a source term of $\dot{w} = kc^4(1-c)$, which is still strongly non-linear but produces a reaction zone that can be resolved in a practical three-dimensional simulation. One difficulty that arises in using a pseudo-spectral code to simulate premixed combustion is that the scalar field—in this case, the progress variable—must be periodic. This was achieved by separating the scalar field into two components: a uniform gradient in the direction of propagation of the flame was subtracted such that the remaining field was zero at each end of the periodic box in that direction. Thus, where

$$\frac{\partial c}{\partial t} + u_i \frac{\partial c}{\partial x_i} = \mathcal{D} \frac{\partial^2 c}{\partial x_i \partial x_i} + \dot{w}$$

is the transport equation for the progress variable with constant properties, if a uniform gradient β in the x_3 direction (the direction of propagation of the flame) is subtracted,

$$c = \beta x_3 + \theta$$

then the transport equation for the periodic fluctuating component θ is:

$$\frac{\partial \theta}{\partial t} + u_i \frac{\partial \theta}{\partial x_i} + \beta u_3 = \mathcal{D} \frac{\partial^2 \theta}{\partial x_i \partial x_i} + \dot{w}.$$

So long as the reaction zone remained relatively thin and did not approach the boundaries, c remained bounded between 0 and 1. In order to keep the reaction

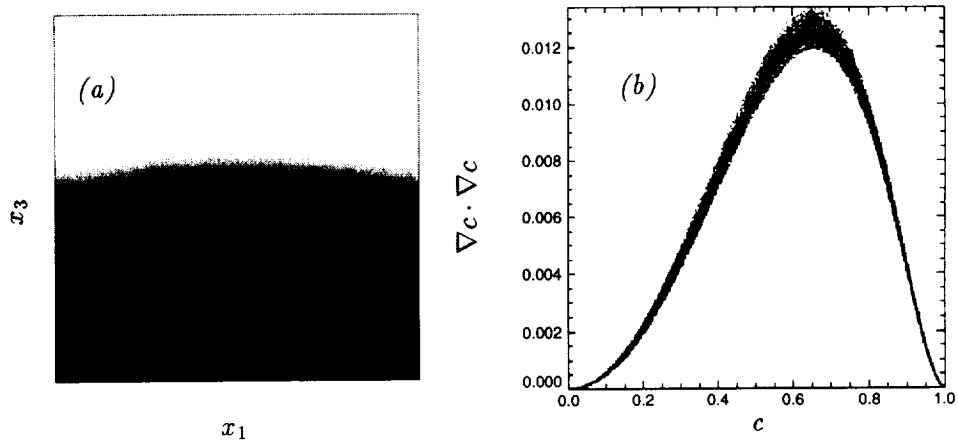

FIGURE 1. a) Snapshot of the scalar field c for $S_L/u' = 11.5$ and $Pr = 0.005$ (color scale is linear with $c = 1$ being white and $c = 0$ being black). b) Scalar dissipation rate as a function of reaction progress variable at a fixed time. Superimposed is the line corresponding to the laminar solution.

away from the boundaries, the mean velocity in the direction of propagation was set to the propagation speed of the flame. This propagation speed was determined at each time step from a volume integral of the source term. The need to keep reaction away from the boundaries was found to restrict the simulation to a limited ratio of Prandtl number to k—the flame speed could not be significantly lower than u' or wrinkles in the flame would become too large to be contained in the domain.

3. Discussion of the results

The results of three simulations with varying laminar flame speeds and Prandtl numbers are illustrated in Figs. (1), (2), and (3) (see figure captions for the model parameters). Note that S_L/u', with the root-mean-square velocity fluctuation u' dominated in the simulation by eddies on the scale of the laminar flame thickness, corresponds roughly to the parameter $S_L/u(\delta)$ employed in Section (2) to describe the validity of the flamelet assumption based on dimensional analysis. Therefore, one may expect noticeable deviations from locally laminar flame propagation for $S_L/u' < 1$. Conversely, the dimensional argument predicts that changes of the total burning rate are exclusively due to the growth of the flame surface area by turbulent wrinkling as long as $S_L/u' \geq 1$.

We define the turbulent flame speed in terms of the volume integral of the source term, $S_T \equiv \Lambda^{-2} \int_V \dot{w} \mathrm{d}^3\lambda$, where Λ is the grid length. The wrinkled flame surface area, A_T, is measured by triangular discretization of the $c = 0.5$ isosurface. For the three cases with $S_L/u' = 11.5$, 1.15, and 0.95 we find S_T/S_L (A_T/Λ^2) of 1.008 (1.008), 1.31 (1.27), and 1.51 (1.56), respectively. Hence, to within 5% accuracy the ratio of turbulent and laminar flame speeds is identical to the increase of the flame surface area with respect to the laminar surface, implying that the local flame speed is, on average, equal to S_L in all cases.

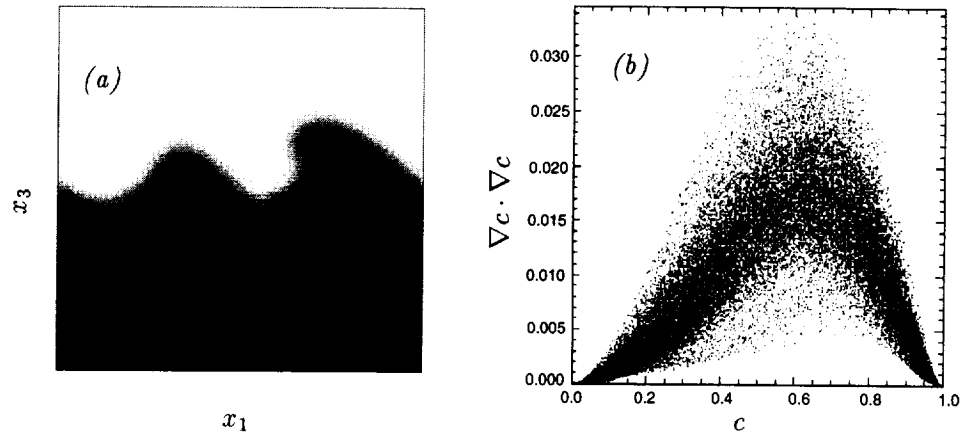

FIGURE 2. a) Snapshot of the scalar field c for $S_L/u' = 1.15$ and $Pr = 0.05$ (same color scale as in figure 1a). b) Scalar dissipation rate as a function of reaction progress variable at a fixed time. Superimposed is the line corresponding to the laminar solution.

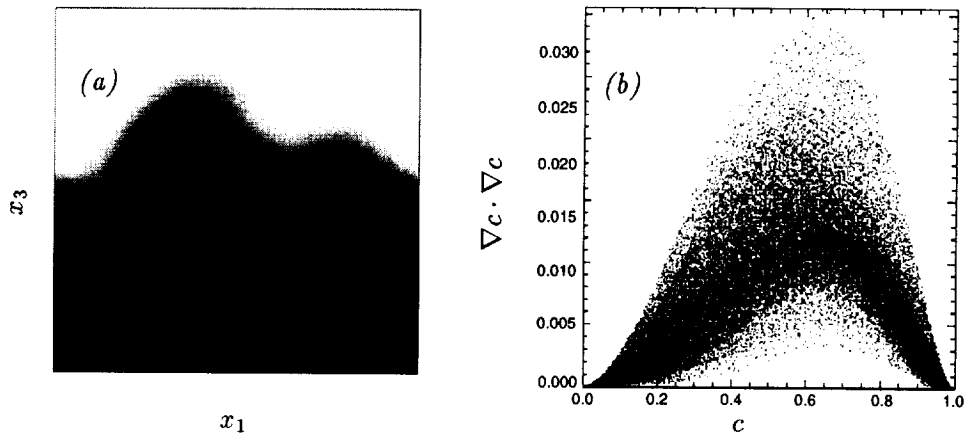

FIGURE 3. a) Snapshot of the scalar field c for $S_L/u' = 0.95$ and $Pr = 0.05$ (same color scale as in figure 1a). b) Scalar dissipation rate as a function of reaction progress variable at a fixed time. Superimposed is the line corresponding to the laminar solution.

In conclusion, we have confirmed, within the limitations of the simplified flame description used, that the local propagation speed of turbulent low-Pr premixed flames remains equal to S_L if $S_L \geq v(\delta)$ even if eddies exist on scales smaller than the flame thickness. For smaller values of S_L/u', large scale flame wrinkling forces regions with nonvanishing $\dot{w}$ over the streamwise grid boundaries, violating the requirement of periodicity of the non-linear component of the progress variable. Further investigations using a different numerical technique are needed to observe the breakdown of locally laminar propagation.

In the framework of supernova modeling, this result helps to formulate a subgrid-scale model for the turbulent thermonuclear flame brush in large-scale hydrodynamical simulations. Specifically, it is possible to estimate $S_L/v(\delta)$ from the filtered density and velocity strain, using an assumed spectrum for the turbulent velocity cascade. If $S_L/v(\delta) \geq 1$, a subgrid-scale model based purely on the surface increase by turbulent wrinkling can be employed (Niemeyer & Hillebrandt 1995). In practice, this is possible for densities above $\sim 10^7$ g cm^{-3} where most of the explosion energy is released. For lower densities (in the late stages of the explosion) relevant for the nucleosynthesis of intermediate mass elements and a possible deflagration-detonation-transition (Niemeyer & Woosley 1997), a more detailed model accounting for small-scale turbulence flame interactions needs to be developed.

Acknowledgments

We wish to thank J. H. Ferziger, N. S. A. Smith, and D. Haworth for interesting discussions. This research was supported in part by DOE contract no. B341495.

REFERENCES

ARNETT, W. D. 1969 A possible model of supernovae: Detonation of $^{1}2C$. *Astrophys. Space Sci.* **5,** 180.

ESWARAN, V. & POPE, S. B. 1988 An examination of forcing in direct numerical simulations of turbulence. *Comput. Fluids.* **16,** 257.

ESWARAN, V. & POPE, S. B. 1988 Direct numerical simulations of the turbulent mixing of a passive scalar. *Phys. Fluids.* **31,** 506.

KHOKHLOV, A. M. 1995 Propagation of turbulent flames in supernovae. *Astrophys. J.* **449,** 695.

NANDKUMAR, R. & PETHICK, C. J. 1984 Transport coefficients of denise matter in the liquid metal regime. *MNRAS.* **209,** 511.

NIEMEYER, J. C. & HILLEBRANDT, W. 1995 Turbulent nuclear flames in Type Ia supernovae. *Astrophys. J.* **452,** 769.

NIEMEYER, J. C. & KERSTEIN, A. R. 1997 Burning regimes of nuclear flames in SN Ia explosions. *New Astronomy.* **2,** 239.

NIEMEYER, J. C. & WOOSLEY, S. E. 1997 The thermonuclear explosion of Chandrasekhar mass white dwarfs. *Astrophys. J.* **475,** 740.

TIMMES, F. X. & WOOSLEY, S. E. 1992 The conductive propagation of nuclear flames. *Astrophys. J.* **396,** 649.

RUETSCH, G. R. & MAXEY, M. R. 1991 Small-scale features of the vorticity and passive scalar fields in homogeneous isotropic turbulence. *Phys. Fluids A.* **3,** 1587.

WOOSLEY, S. E. 1990 *Supernovae* ed. A Petschek (D. Reidel: Dordrecht). 182.

The jet control group

Current jet control goals are mixing enhancement, flow tailoring for high-performance aerodynamic applications, and noise reduction. The four projects in this group were motivated by these broad objectives.

The first project took steps toward developing real-time closed-loop controls for both mixing enhancement and flow tailoring applications. A necessary element of this approach is a model for the jet which is accurate yet simple enough to be able to predict the jet's response to actuation in real time. Alan Cain of the Boeing Company was assisted by Bewley, Freund, and Colonius in developing such a model. Locally unstable linear modes were used to compute shear stresses which were then used in a streamwise evolution equation for the shear layer thickness. The novel aspect of this work was the use of analytically tractable approximate mean flow profiles which provided closed-form analytical expressions for the stability problem. Because of this, the entire model can, once optimized, be evaluated rapidly enough for a real-time application.

Koumoutsakos, Freund, and Parekh tested evolution algorithms, which are motivated by the well-known "mutate and compete" principles that govern the evolution of biological systems, as a tool for optimizing nozzle actuation for jet mixing enhancement. An important advantage of this type of algorithm over many other approaches is its portability. In this project, the same program subroutines were used to optimize actuation in both a low Reynolds number DNS and a vortex method simulation. Starting from a random initial guess for the actuation parameters in the DNS, the evolution strategy "found" parameters that had previously been shown to be highly effective in both laboratory experiments and in simulations. In the vortex method simulation, having also started from a random initial guess, the evolution algorithm found parameters that produced the well-known bifurcating jet flow. Surprisingly, the algorithm also found a previously unknown set of parameters that added a kink to the bifurcating flow pattern which further increased the spreading rate of the jet.

It is well known that the downstream evolution of a jet is closely tied to large turbulent structures in the flow. In an effort to understand these better with an eventual goal of using them to improve controls, a study of the large scale dynamics of jets was conducted by Danaila and Beorsma using a spherical coordinates DNS code. Combinations of axisymmetric and $n = \pm 1$ modes were excited in the jet causing pulsing, flapping, and bifurcating jet flows. These results were analyzed in detail, and a new mechanism leading to jet bifurcation was proposed. This is of particular interest because bifurcation can greatly enhance the spreading of the jet and thereby increase its mixing.

Using an existing DNS database of a Mach 1.92 jet, Colonius, Mohseni, Freund, Lele, and Moin undertook an effort to study the mechanisms of jet noise. The eventual goal of this effort is to develop new models and test existing models that could be incorporated into a control scheme. An important result of this study was

the successful computation of the Lighthill acoustic source and verification of its ability to produce the correct acoustic radiation. In addition, an analysis based upon the linear adjoint equations was completed, which will provide a means for utilizing the available DNS databases to evaluate linear models for noise.

Jonathan Freund

Center for Turbulence Research
Proceedings of the Summer Program 1998

Evolution strategies for parameter optimization in jet flow control

By P. Koumoutsakos, J. Freund[1] AND D. Parekh[2]

We present results from the application of evolution strategies for parameter optimization in direct numerical simulations and vortex models of controlled jet flows. It is shown that evolution strategies are a portable, highly parallel method that can complement our physical intuition in the parameter optimization of such flows.

1. Introduction

For centuries engineers have taken inspiration from nature in designing efficient aerodynamic configurations. It is no coincidence that the shape of an aircraft's wing resembles a bird's. We wish to approach the problem of flow control, not from the perspective of imitating existing natural forms, but from the perspective of developing efficient control algorithms, by employing techniques inspired by biological processes. These techniques, which we will refer to as "machine learning algorithms", are gaining significance in the areas of modeling and optimization for fluid dynamics problems as a technology that could help reduce cost and time to market of new designs.

1.1 Evolution strategies

Some of the seminal work in this field (Rechenberg 1971, Schwefel 1974, Hoffmeister 1991) actually was aimed at improving aerodynamic shapes. As stated in (Schwefel, 1974):

"In 1963 two students at the Technical University of Berlin met and were soon collaborating on experiments which used the wind tunnel of the Institute of Flow Engineering. During the search for the optimal shape of bodies in a flow, which was then a matter of laborious intuitive experimentation, the idea was conceived of proceeding strategically. However, attempts with the coordinate and simple gradient strategies were unsuccessful. Then one of the students, Ingo Rechenberg, now professor of Bionics and Evolutionary Engineering, hit upon the idea of trying random changes in the parameters defining the shape, following the example of natural mutations. The evolution strategy was born." (The second student was Hans Paul Schwefel).

Since this pioneering work, stochastic optimization techniques have gained recognition and popularity in several fields of engineering, but this has not been the case

1 University of California, Los Angeles

2 Georgia Institute of Technology

in the field of fluid dynamics in the last three decades. Recent work by Rechenberg (1994) focuses on the shape optimization approach with the construction and experimental testing of shapes that have been produced via evolutionary strategies using computer simulations. Evolution strategies have also been implemented in order to optimize the motions of an artificial tuna (M. Triantafyllou, private communication).

Here, we report preliminary results from the application of evolution strategies in the optimization of actuator parameters in active jet flow control and in the optimization of bifurcating and blooming jets.

1.2 Jet flow control

It is desirable in many circumstances to enhance mixing in the exhaust from aircraft engines. Applications include lift enhancement, signature reduction, and temperature reduction on blown flaps. This work focuses on the latter case. The blown flap on a C-17 (Fig. 1) is currently made out of titanium to avoid melting. If mixing can be significantly enhanced so that the plume temperature is reduced, the flap could be constructed from aluminum, a much less heavier and expensive alternative.

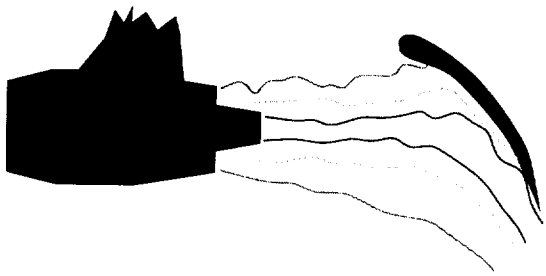

FIGURE 1. Blown flap as on a C-17.

Recently, actuators have been developed and tested on a full-scale engine which have the control authority to accomplish this objective. The goal of this work is to optimize their parameters to maximize their effectiveness. This is being undertaken as a joint experimental, numerical, and control theory effort. The discussion here is limited to the simulations and the application of evolution strategies to the problem.

1.3 Optimization of bifurcating and blooming jets

The proper combination of axial and helical excitation at different frequencies generates the unique class of flows known as bifurcating and blooming jets (Lee and Reynolds 1985, Parekh *et al.* 1987). The axial forcing causes the shear layer to roll up into distinct vortex rings at the forcing frequency. The helical excitation perturbs the rings radially, producing a small eccentricity in the ring alignment. This initial eccentricity is amplified by the mutual ring interactions leading to dramatic changes in jet evolution. When the axial frequency is exactly twice that of the helical excitation, the jet bifurcates into two distinct jets, with successive rings moving alternately on one of two separate trajectories. This Y-shaped jet spreads at angles

over 80 degrees, depending on forcing frequency and amplitude. The relative phase, ϕ, between the axial and helical forcing signals determines the plane in which the jet bifurcates. When the ratio, β, of axial to helical excitation frequency is non-integer, the vortex rings scatter along a conical trajectory. When viewed from downstream, the vortex ring pattern often resembles a bouquet of flowers, hence the name "blooming jet."

In applying the evolution strategies to this class of flows, we are exploring whether the phenomena discovered experimentally could also be obtained in our simulations via an "evolutionary process" and whether new phenomena could be found. Here a vortex model describes the jet dynamics. The optimization algorithm is tuned to maximize jet spreading by varying the excitation parameters.

2. Evolution strategies for optimization

We discuss first the formulation of evolution strategies for the optimization of N-dimensional functions:

$$F(\mathbf{x}) = F(x_1, x_2, ..., x_M)$$

We define a vector in the parameter space as an *individual.* The whole discrete parameter space can then be considered as a *population* of individuals. Evolution strategies try to identify the *best* individual from this population based on the *fitness value*, prescribed by the function F. The optimization proceeds by following to a certain extent models of biological evolution.

2.1 Two membered evolution strategies

The simplest (and earliest) form of evolution strategies is based on populations that consist of two competing individuals (*"a two-membered strategy"*). The evolution process consists of the two operations that Darwin (1859) considered as the most important in natural evolution: *mutation* and *selection.* Each individual (i.e. vector in the parameter space) is represented using a pair of floating point valued vectors:

$$\mathbf{u} = \mathbf{u}(\mathbf{x}, \boldsymbol{\sigma})$$

where $\boldsymbol{\sigma}$ is an M-dimensional vector of standard deviations.

Following Rechenberg (1971) and using terminology from biology, the optimization algorithm may be described as follows:

a - *Initialization:* A parent genotype consisting of M-genes is specified initially ($\mathbf{x}^0$). At each generation an individual $\mathbf{u}_p^n = (\mathbf{x}_p^n, \boldsymbol{\sigma}_p^n)$ is identified.

b - *Mutation:* The parent of generation-n produces a descendant, whose genotype differs slightly from that of the parent. The operation of mutation is then realized by modifying $\mathbf{x}$ according to:

$$\mathbf{x}_c^n = \mathbf{x}_p^n + \mathcal{N}(0, \boldsymbol{\sigma}_p^n) \qquad 2.1$$

where $\mathcal{N}(0, \boldsymbol{\sigma})$ denotes an M-dimensional vector of random Gaussian numbers with zero mean and standard deviations $\boldsymbol{\sigma}$.

c - *Selection:* Due to their different genotypes the two individuals of the population can have a different fitness for survival. This fitness is evaluated by the function f. Only the fittest of the two individuals is allowed to produce descendants at the following generation. Hence to *minimize* F we write:

$$\mathbf{x}_p^{n+1} = \begin{cases} \mathbf{x}_p^n, & \text{if } F(\mathbf{x}_p^n) \leq F(\mathbf{x}_c^n); \\ \mathbf{x}_c^n, & \text{otherwise.} \end{cases} \qquad 2.2$$

Note that in this two-membered algorithm the vector σ of standard deviations remains unchanged throughout the evolutionary process.

For *regular optimization problems* (see Michalewicz, 1996 for a definition) it is possible to prove the convergence of the method to a global minimum. However, this theorem does not provide a convergence rate of the method.

In this work we have implemented the *1/5 success rule* proposed by Rechenberg (1971). According to this rule: *During the optimum search the frequency of successful mutations is checked periodically by counting the ratio of the number of successes to the total number of trials. The variance is increased if this ratio is greater than 1/5 and it is decreased if it is less than 1/5.* The period over which this performance is being checked depends on the number of parameters that are being optimized. We refer to Schwefel (1995) for further details on the implementation of the two-membered evolution strategies.

2.2 Multi-membered evolution strategies

One of the drawbacks of the 1/5 rule for the two-membered strategy is that it may lead to premature convergence, as the step lengths can be reduced to zero, thus not improving the progress towards a global optimum. There are several possible remedies to this drawback. Of particular interest are those that can be constructed by further developing the model of evolution to resemble natural processes. In that context, a higher level of imitation of an evolutionary process can be achieved by increasing the number of members in a population. Such multi-membered strategies are usually formulated in terms of μ-parents and λ-descendants. The most common strategies are then described as (μ, λ) and $(\mu + \lambda)$. In the (μ, λ) case at each generation the μ-fittest individuals are selected only among the λ children of the generation, whereas in the $(\mu+\lambda)$ case the parents are also included in the evaluation process. Schwefel (1995) presents an extensive comparison of multi-membered and two-membered evolution strategies for a series of optimization problems.

2.3 Handling of constraints

One of the advantages of evolution strategies is the ease and simplicity by which they can handle problem constraints. Such constraints are usually formulated as inequalities. For example in the case of q constraints of the parameters $\mathbf{x}$ we require that:

$$C_j(\mathbf{x}) \geq 0 \qquad \text{for all } j = 1, ..., q$$

Descendants of a certain parent that do not satisfy the constraints are accounted as results of unsuccessful mutations. Occasionally the boundaries of the constrained

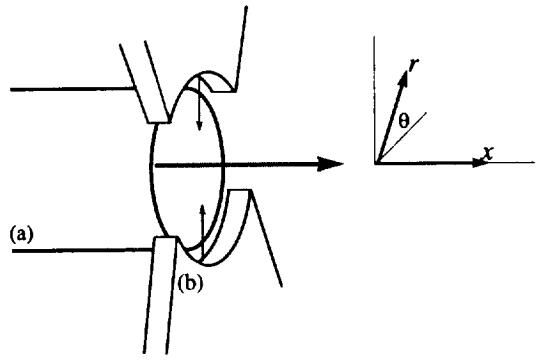

FIGURE 2. Schematic shows the nozzle (a) and actuators (b).

regions are smoothed out in order to facilitate the convergence of the method in highly constrained problems.

3. Jet flow control

The compressible flow equations were solved with direct numerical simulation using a combination of sixth order compact finite differences, spectral methods, and fourth order Runge Kutta time advancement. Further details of the numerical algorithm and techniques for including actuators into the calculations were recently reported by Freund & Moin (1998). Naturally, in a direct numerical simulation we are restricted to highly simplified geometries (Fig. 2); nevertheless, the actuators were able to reproduce the effects observed in experiments by Parekh *et al.* (1996). Figure 3 shows a visualization of a jet forced into a flapping mode and an unforced jet. Clearly, the mixing is enhanced downstream.

For this preliminary study, only three types actuation parameters were varied: the amplitude, frequency, and phase. The actuation was a simple waveform sum of harmonic waveforms:

$$v_r = \sum_{i=1}^{N} A_i \left(1 + \sin\left(\frac{USt_i}{D}t + \phi_i\right) \mathrm{sgn}(\cos(\theta))\right), \qquad 3.1$$

where v_r is the radial velocity at the actuator exit and A_i are the amplitudes, St_i are the Strouhal numbers, and ϕ_i are the phases of the different modes. The $\mathrm{sgn}(\cos(\theta))$ causes each waveform to excite a flapping mode in the jet. Note that the phases, ϕ_i, are the relative phases of the different modes setting the two actuators always at 180° out of phase. The flow rate out of either actuator was constrained to be less than $U/2$ where U is the jet velocity. This was accomplished by simply "clipping" the velocities to be below this level.

The only constraint on A_i was that they be non-negative. Strouhal numbers were restricted to be $0 \leq St \leq 0.8$ and the phases were constrained to be $\phi_i \in [0, 2\pi]$.

A very low Reynolds number ($Re = 500$) jet at Mach 0.9 was simulated in this preliminary effort to minimize the computational expense. The computational mesh

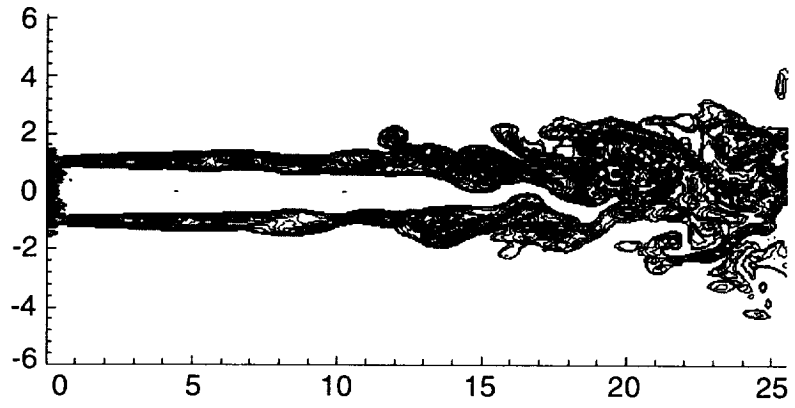

FIGURE 3A. Unforced turbulent jet. Visualization of vorticity magnitude.

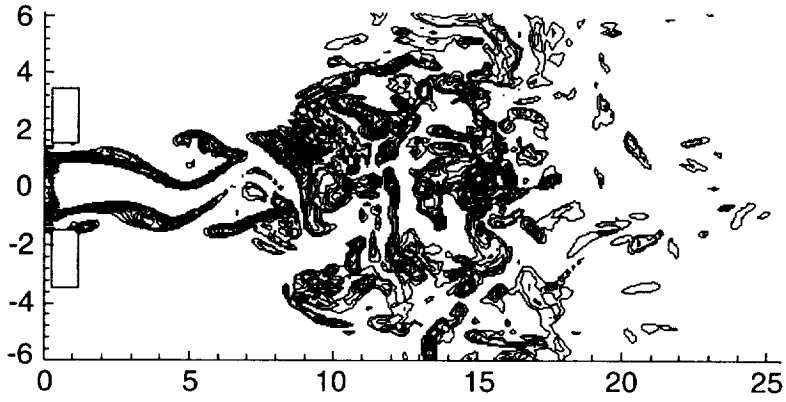

FIGURE 3B. Forced turbulent jet. Visualization of vorticity magnitude.

was $112 \times 42 \times 16$ in the streamwise, radial, and axial direction respectively and the computational domain extended to 16 radii downstream and 5 radii in the radial direction. A stretched-mesh boundary zone was positioned outside of the region to cleanly absorb fluctuations convecting out of the domain. In each iteration of the evolution strategy, the jet was simulated starting from an unforced case for several periods of forcing after the passing of initial transients. Because the flow becomes quasi-periodic, this was sufficient to provide a measure of the long-time actuator effectiveness. Each iteration required approximately 10 minutes and in total 200 iterations were made (the best case was found after approximately 150 iterations).

Three wave forms ($N = 3$) where used and the initial control parameters were

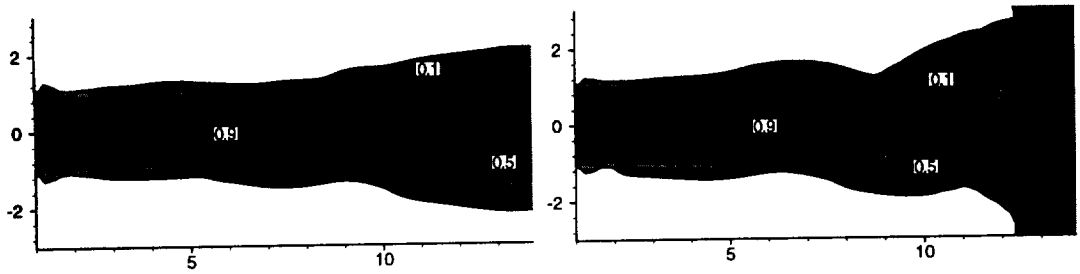

FIGURE 4A.Jet mixture fraction for the first guess parameters.

FIGURE 4B. Jet mixture fraction with the best case parameters after 200 iterations.

A_i/U	St_i	ϕ_i
0.45	0.5	0.0
0.40	0.2	0.7
0.35	0.5	1.0

The goal set for the evolution strategy was to maximize

$$Q = \int_0^{\infty} \int_0^{2\pi} \int_{4r_o}^{8r_o} v_r^2 r dr d\theta dx.$$

This metric Q, was increased by over a factor of 10 from the initial case by the best case parameters:

A_i/U	St_i	ϕ_i
0.04	0.33	0.54
0.42	0.17	0.31
0.07	0.45	1.57

It is interesting to note that the evolution strategy "chose" to reduce the amplitude of two of the wave modes to a very low level. Effectively, it found the same *ad hoc* scheme that was shown to be successful by Parekh *et al.* (1996) and Freund & Moin (1998). A forced and unforced case are visualized in Fig. 4. The best case clearly shows a high amplitude flapping mode which would greatly enhance mixing downstream.

4. Vortex model of bifurcating and blooming jets

In this work we model a circular jet by the combination of discrete vortex filaments and a semi-infinite cylindrical sheet of vorticity. The cylindrical sheet models the nozzle source flow whereas the ring filaments model the vortex rings generated by the axial excitation of the shear layer.

The semi-infinite sheet of vorticity extends from $-\infty$ to the origin. Its axis defines the jet centerline, and the end of the sheet is identified with the jet exit. The helical excitation used in the experiments of Lee and Reynolds (1985) is modeled

by rotating the axis of the vortex cylinder about the nominal jet centerline. The displacement, A_h, of the jet centerline from the nominal centerline corresponds to the amplitude of excitation, and $\bar{A}_h \equiv A_h/R$. The rotation frequency is given by:

$$f_h = \frac{f_a}{\mathcal{R}_f}, \tag{4.1}$$

where the orbital frequency is defined as:

$$f_a = St_a \frac{\gamma}{D}, \tag{4.2}$$

The frequency f_a is the rate at which filaments are generated at the origin.

The interaction of the vortex sheet with the filaments is assumed to be such that the sheet influences the motion of the filaments but the filaments do not influence the sheet. The velocities induced by each filament and by the jet function are superimposed to determine the trajectory of each filament. The Strouhal number sets the time between creation of new ring filaments at the origin.

The circulation of each filament is identical and is determined from circulation conservation constraints. Assuming the thickness of the cylindrical sheet to be much smaller than its radius, the vorticity flux (per unit of circumference) within the sheet through any plane perpendicular to the jet's axis is given by $U^2/2$. By the assumption of a perfect fluid, the vorticity convected from the cylindrical sheet must equal the vorticity convected by the discrete filaments. This conservation relation can be expressed in terms of Γ and γ as

$$\frac{\Gamma}{\Delta t} = \frac{\gamma^2}{2}, \tag{4.3}$$

where Γ is the circulation of each ring filament, γ is the circulation per unit length of the cylindrical vortex sheet, and Δt is the time between generation of ring filaments. By Eqs. 4.8 and 4.9, one obtains

$$\gamma = St_a \frac{\Gamma}{R}. \tag{4.4}$$

Further details concerning the applicability of this model and its numerical implementation are reported in Parekh *et al.* (1988).

4.1 Parameter optimization using evolution strategies

The primary parameters that govern the jet evolution St_a, β (frequency ratio of axial and orbital excitation), A_a, A_h, and ϕ. The effect of the axial excitation, A_a, is approximated by generating distinct vortex rings at the axial forcing frequency. The sensitivity to axial forcing amplitude is not modeled. In these simulations the other four parameters are allowed to vary over the following ranges: $0 \leq A_a \leq 1$, $0.1 \leq St_a \leq 1$, $0.2 \leq \beta \leq 5$, $0 \leq \phi \leq 2\pi$. Different flow patterns can be observed with variations in β for fixed values of the other parameters. The simulation is able

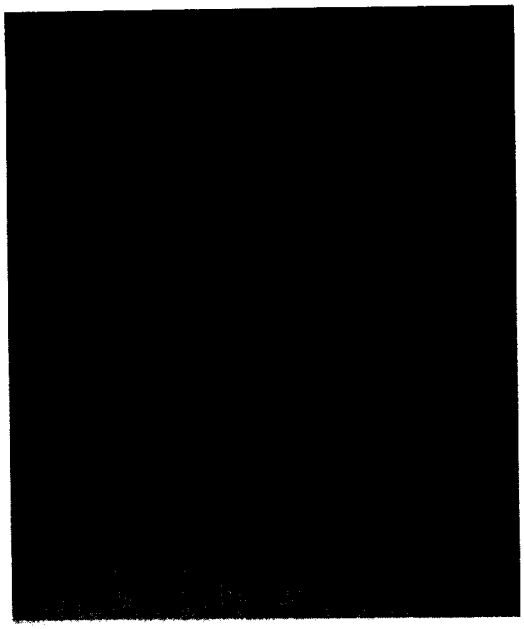

FIGURE 4.1A. Blooming jets: Experimental Results of Lee and Reynolds (1985): $\beta = 1.7, A_h = 0.04, St_a = 0.46$, $Re = 4300$.

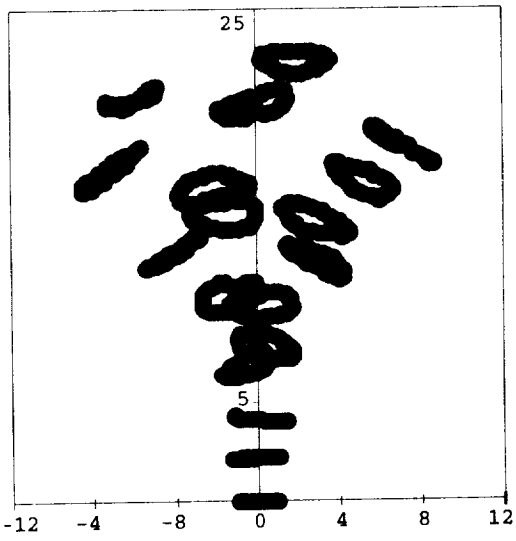

FIGURE 4.1B. Blooming Jets: Simulations $\beta = 1.7, A_h = 0.05, St_a = 0.55$.

to represent qualitatively the full range of jet phenomena observed in experiments, including bifurcating and blooming jets (Fig. 4.1).

For the optimization, several metrics for jet spreading angle were considered, including the average radial displacement of the vortex elements, jet spreading angle, and ring trajectory angles. We also considered amplitude normalized formulations of these metrics to account for the cost of excitation. The metrics were evaluated over a broad range of test cases to check if they would be robust enough to provide the proper relative rating over the parameter space considered. Some metrics are artificially biased by the initial displacement of the rings or by normalization with very small excitation amplitudes. One metric that is both simple and effective for this simulation is the average angle of the nominal ring trajectories. For each case, this metric is evaluated after the same number of periods (typically, eleven) of axial excitation. The nominal ring trajectory angle, θ, is defined as the angle between the jet centerline and the line that connects the center of the jet exit to the centroid of the vortex ring nodes.

Starting with an initial guess for each of these parameters and constraints on the range of values allowable for each parameter, the genetic algorithm searches to optimize jet spreading. The scope of this work did not allow for an exhaustive investigation of the parameter space and convergence characteristics, but even these preliminary simulations yielded promising results. With all four parameters varied simultaneously, the genetic algorithm selects a blooming jet similar to what has

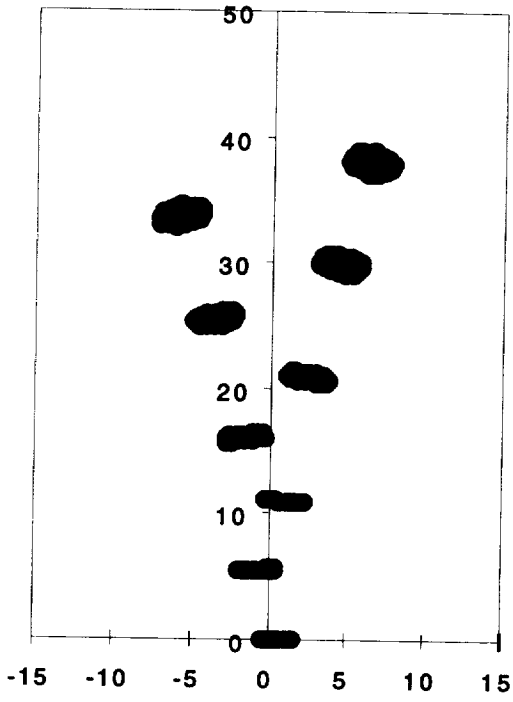

FIGURE 4.2A. Hybrid bifurcating jet with $St_a = 0.28, A_h = 0.63, \beta = 2$, and $\phi = 0$ (side view).

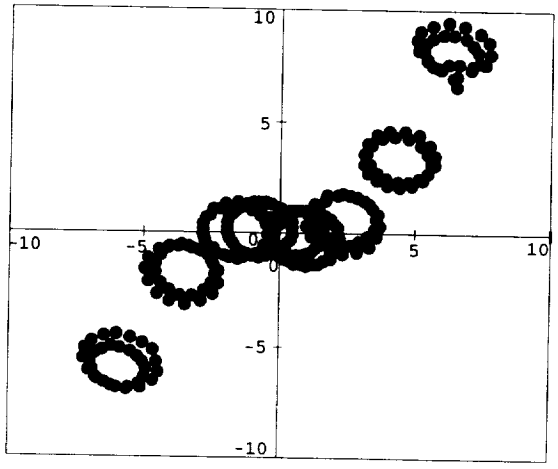

FIGURE 4.2B. End view. Each ring's 32 nodes are plotted as solid circle.

been observed in experiments.

The most striking result was found when we constrained $\beta = 2$ and kept ϕ fixed. Initially we expected the algorithm to select a bifurcating jet similar to Fig. 4.1A with values of $St_a and A_h$ that maximize the spreading angle. Instead, a unique jet flow (Fig. 4.2) was found that had never been observed in previous experiments or calculations. This jet flow initially resembles a bifurcating jet. Several diameters downstream, however, the two branches of the jet exhibit a secondary bifurcation in which the rings change direction along a path with an azimuthal angle about $\pi/4$ different from their original trajectory. This results in a wide spreading angle as seen in Fig. 4.2B.

The simulation often has difficulty providing valid solutions for $St_a > 0.4$ since the initial ring filaments get tangled together and quickly degrade to an unrealistic state. This constraints were implemented in the evolution strategy by simply considering these cases as unsuccessful tries for the optimization algorithm.

5. Summary and conclusions

These preliminary results from the application of evolution strategies to the problem of flow control suggest that stochastic optimization can be a valuable tool that can complement physical understanding and deterministic optimization techniques.

As a closing remark, we quote from Schwefel:

Since according to the "No-Free-Lunch" (NFL) theorem (Wolpert and Macready, 1996) there cannot exist any algorithm for solving all optimization problems that is on average superior to any competitor, the question of whether evolutionary algorithms are inferior/superior to any alternative approach is senseless. The NFL theorem can be corroborated in the case of EA versus many classical optimization methods insofar as the latter are more efficient in solving linear, quadratic, strongly convex, unimodal, separable, and many other problems. On the other hand, EA's do not give up so early when discontinuous, nondifferentiable, multimodal, noisy, and otherwise unconventional response surfaces are involved. Their robustness thus extends to a broader field of applications, of course with a corresponding loss of efficiency when applied to the classes of simple problems classical procedures have been specifically devised for."

Hence, in the realm of flow control, the key issue is the identification of a suitable optimization method for the specific problem in hand. The portability, ease of parallelization, and the results reported herein and in (Müller et al. 1999), suggest that EA's present a powerful technique for parameter optimization in problems of flow control.

REFERENCES

DARWIN, C. 1859 *The origin of species by means of natural selection.*

FREUND, J. B. & MOIN, P. 1998 *Mixing enhancement in jet exhaust using fluidic actuators: direct numerical simulations*, ASME FEDSM98-5235.

HOFFMEISTER F. & BÄCK T. 1991 Genetic algorithms and evolution strategies: Similarities and differences. Proc. of 1st International Conference on Parallel Problem Solving from Nature, Berlin. *Springer.*

LEE, M. & REYNOLDS, W. C. 1985 Bifurcating and blooming jets. *Fifth Symp. on Turbulent Shear Flows,* Ithaca, New York. 1.7–1.12.

MICHALEWICZ, Z. 1996 *Genetic Algorithms + Data Structures = Evolution Programs.* Springer-Verlag Berlin.

MÜLLER, S. MILANO, M. & KOUMOUTSAKOS, P. 1999 Evolution strategies for turbulent channel flow control using rotors. (in preparation).

PAREKH, D. E., REYNOLDS, W. C. & MUNGAL, M. G. 1987 Bifurcation of round air jets by dual-mode acoustic excitation. *AIAA 87-0164.*

PAREKH, D. E. 1988 Bifurcating jets at high Reynolds numbers. *PhD thesis.* Department of Mechanical Engineering, Stanford University.

PAREKH, D. E., KIBENS, V., GLEZER, A., WILTSE, J. M. & SMITH, D. M. 1996 Innovative jet flow control: mixing enhancement experiments. *AIAA Paper 96-0308.* 34th Aerospace Sciences Meeting and Exhibit

RECHENBERG, I. 1971 *Evolutionsstrategie - Optimierung technischer Systeme nach Prinzipien der biologischen Evolution.* Fromman-Holzboog.

RECHENBERG, I. 1994 *Evolution Strategy '94*, Frommann-Holzboog, Stuttgart.

SCHWEFEL, H. P. 1974 *Numerische Optimierung von Computer-Modellen.* Birkhäuser, Basel.

SCHWEFEL, H. P. P. E. 1995 *Evolution and Optimum Seeking.* Wiley Interscience.

WOLPERT, D. H. & MACREADY, W. G. 1996 No Free Lunch Theorem for Search. *Technical Report SFI-TR-95-02-010,*Santa Fe Institute.

An approach to systems modeling for real-time control of jet flows

By A. B. Cain[1], T. Bewley[2], J. B. Freund[3], AND T. Colonius[4]

1. Introduction

The past 25 years have seen many examples of open-loop control of jet flows with significant practical importance. During the same time, there have been tremendous developments in the area of closed-loop feedback control strategies for linear and nonlinear systems. It has been seen in many applications that coordination of control application with state measurements in the closed-loop setting is essential for optimum system performance. Thus, the possibility of feedback control of flow systems such as turbulent jets should be carefully examined. However, such control problems also pose technical difficulties as turbulent flow systems are multi-scale and difficult to compute with a high degree of fidelity. Thus, the present work explores the development of low-order system models for use in the feedback control framework for the jet control problem. The present work is part of a collaboration involving Georgia Tech, Stanford University, UCLA, UCSD, and The Boeing Company under the support of the Air Force Office of Scientific Research.

To design feedback control algorithms, it is very useful to have a simple model that accurately captures the relevant physics of the phenomena under consideration. Such a model, which should have sufficient simplicity to enable real-time state estimation, is developed in the present work using linear stability theory to model the initial development of the instabilities leading to the turbulent breakdown of a jet. Direct numerical simulations of turbulent jets carried out by Freund *et al.* (1998) will be used as validation for these models; when performed properly, such simulations can capture the relevant flow physics "exactly", albeit at a very large computational expense.

System identification techniques may also be used (instead of linear stability theory) to develop input-output system models of jets for use in the feedback control setting, as explored by Ikeda (1998). Such models may be constructed without any reference to the equations which govern or approximate the flow physics. The present work is an intermediate-level approach that uses inviscid linear stability theory to approximate the jet system. A key feature of the present work is a piecewise quadratic approximation of the mean flow that permits rapid solution of the equations. The authors acknowledge the careful work of Pal (1998) in deriving the stability equations used.

1 Boeing Company
2 Current address: University of California, San Diego
3 University of California, Los Angeles
4 California Institute of Technology

2. Large scale structures in inflectionally-dominated flows

It is well established that the inviscid inflectional instability characterized by Kelvin and Helmholtz dominates the large-scale development of inflectionally-dominated flows even into non-linear turbulent regimes. An excellent review discussing many important aspects of this problem is given by Ho and Huerre (1984). Supporting articles covering other aspects of the problem (including the nature of nonlinear interaction and wall effects) are described in Cain and Thompson (1986) and Cain, Roos, and Kegelmen (1990). The dominance of the inviscid inflectional instability in the present flow motivates the use of the incompressible inviscid stability equations as the system model.

A comparison between the prediction of linear theory and the nonlinear evolution of the jet shear layers is given by Morris *et al.* (1990) and Viswanathan & Morris (1992) for planar and round jets respectively. These works derive systems comprised of parabolic equations for the mean flow development that depend upon the local instability eigenproblem for the forcing. Solution of this eigensystem is generally the most computationally-intensive aspect of generating the solution to the evolution model for the jet. The need for very rapid solutions for real-time systems modeling motivates our new approach to approximate solution of the disturbance eigenvalue problem.

3. Linear stability analysis

Motivated by the need for rapid evaluation, piecewise linear and quadratic approximations of the velocity profiles are used to simplify the inviscid linear disturbance equations. In addition, mathematical solutions are somewhat easier to obtain for the temporal evolution problem. All the work described here will use the temporal analysis combined with Gaster's relation to approximate the behavior of the spatially evolving problem. The approach so describing an inflectionally dominated flow is given by Drazen and Reid (1981). A few examples of the piecewise linear analysis for planar flows will be presented before describing a piecewise quadratic approximation that will be used as an approximation in the round jet geometry.

3.1 The piecewise linear approximation for planar geometries

The simplest example of the piecewise linear approach is a three-segment representation of the plane shear layer. This approach has been shown to provide consistent and reasonable characterization of the stability behavior of this flow, and it compares well with a more accurate (but more time consuming) analysis with a hyperbolic tangent representation of the mean velocity profile. The characterization of the disturbances is given by the exponential coefficient for temporal disturbance growth rate and phase speed and is a function of the disturbance wavenumber. As shown in Fig. 1, the phase speed computed using such an approach varies from U to $3U$, where U is the velocity of the slow stream. The complex wave speed comes as complex conjugate pairs, and the actual phase velocity is the mean of the two branches plotted. The imaginary part of the wave speed (which in product with the wavenumber gives the exponential growth rate) vanishes at a wavenumber slightly greater that 0.3.

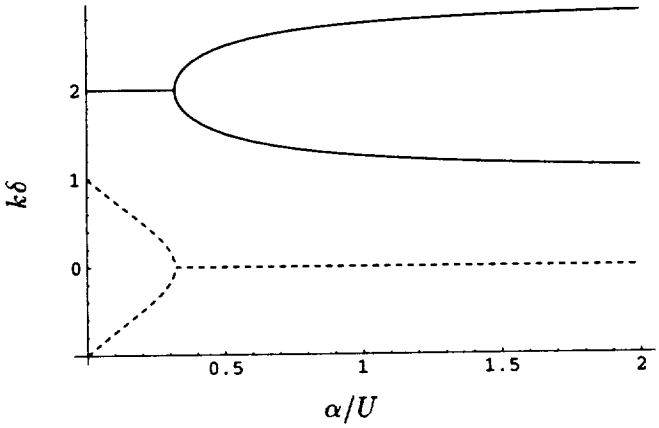

FIGURE 1. Phase speed —— and growth rate ---- for piecewise linear planar shear layer.

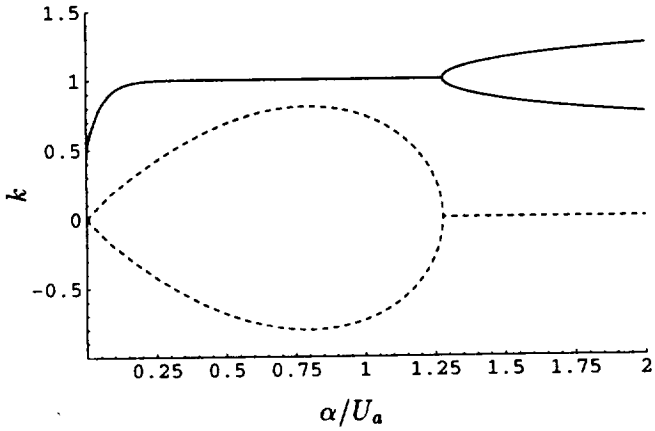

FIGURE 2. Phase speed —— and growth rate ---- of a sinuous mode in a piecewise linear planar jet.

The next piecewise linear flow considered is the planar jet. Figure 2 shows the Gaster transformed and scaled spatial growth rate and phase speed versus wavenumber for the sinuous mode of a planar jet having a potential core of 18 jet radii (r_o) long, a shear layer of 1 unit width, and a free-stream velocity equal to 1/3 of the jet velocity $1.5U_a$, where U_a is the average of the jet and co-flow velocities. Note that in this case the long wavelength (low wavenumber) disturbances have a phase speed of the free-stream speed while shorter disturbances have a phase speed of the mean shear layer speed. Figure 3 shows the behavior of the varicose mode. Note that the varicose mode has a phase speed equal to that of the jet centerline for long wavelength disturbances and the same phase speed as the sinuous mode for shorter wavelength disturbances. When the shear layers are thin and separated by a large region of potential flow, the stability of the planar jet is nearly the same as that of the planar shear layer except at very long wave lengths. At smaller separation,

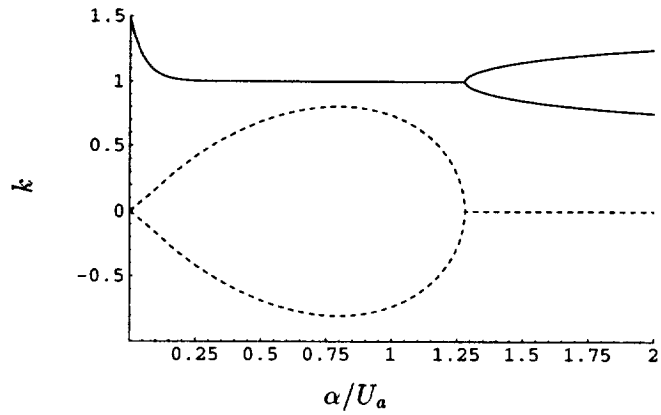

FIGURE 3. Phase speed —— and growth rate ---- of a varicose mode in a piecewise linear planar jet.

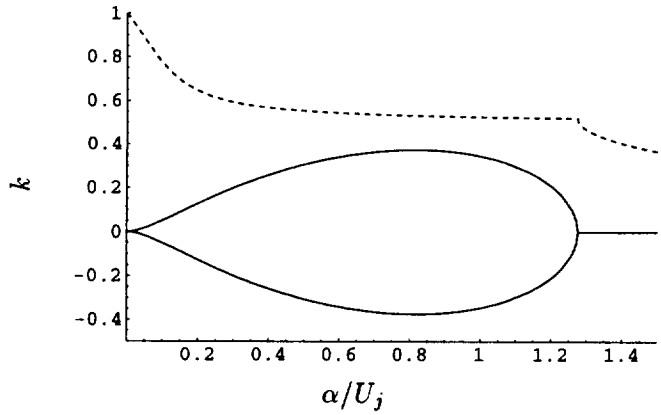

FIGURE 4. Phase speed —— and growth rate ---- of a varicose mode in a piecewise linear planar jet.

disturbances of the two shear layers exhibit a strong coupling. These behaviors for both the varicose and the sinuous modes are characteristic of the actual physical system.

3.2 The piecewise quadratic approximation for cylindrical geometries

A piecewise representation of the mean velocity profile simplifies the round jet stability problem to Bessel's equation. The solutions are constrained by requiring finite levels in the inner potential region and solutions that vanish at infinity in the outer potential region. These inner and outer solutions (in terms of Bessel functions) are coupled by matching conditions. The matching is achieved by a combination of the inner and outer Bessel solutions (a linear combination of Bessel functions is a valid solution within the finite thickness shear layer). This problem was formulated by Pal (1998). This approach results in an involved complex-valued quadratic dispersion relation that was solved using Mathematica.

The behavior of the axisymmetric disturbances for a round jet with a potential

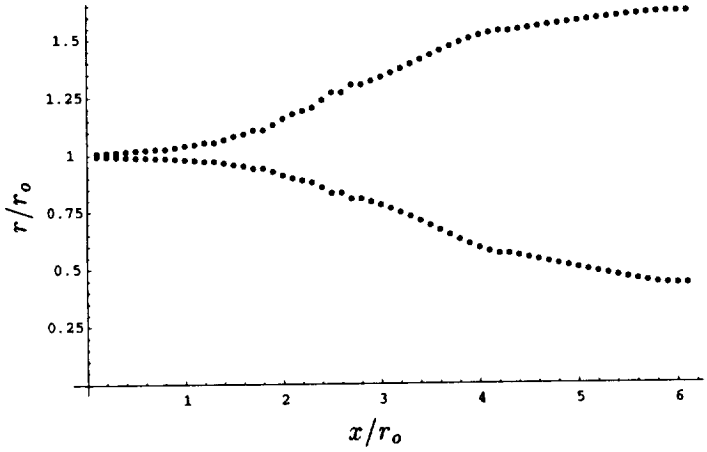

FIGURE 5. Inner and outer shear layer edges.

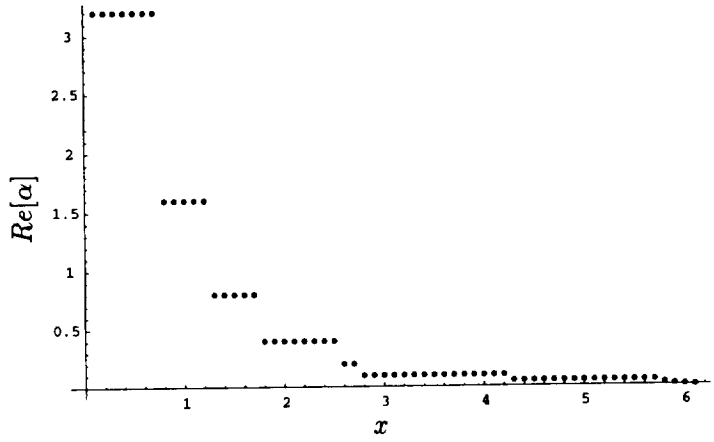

FIGURE 6. Locally dominant instability wave number.

core diameter of $18r_o$ and jet velocity U_j with zero free stream velocity is given in Fig. 4. Note that the appropriately-scaled growth rate and phase speed behave in a manner which is qualitatively similar to the varicose mode of the analogous planar jet.

4. Prediction of jet spreading

The formulation of Viswanathan and Morris (1992) was implemented using the piecewise quadratic stability formulation. An example of the predicted evolution of the shear layer edges using only the $n = 0$ axisymmetric disturbance is shown in Fig. 5. Figure 6 shows the locally dominant wavenumber versus downstream distance in jet radii. It is assumed that, when a disturbances saturates (due to the thickening of the shear layer), the sub-harmonic will become dominant and evolve until saturation, and so on. The results shown in Figs. 5 and 6 are for an initial

shear layer thickness of 1% of the jet radius.

5. Conclusions

An approximate analytic solution to the appropriate linear stability problem, and the role of this solution in the evolution of the round jet, has been investigated. When fully implemented, such a formulation may model the physical behavior of the jet with sufficient accuracy to be used as a state model in a feedback control setting. Once programmed in an efficient manner, the computational expense of this model should be manageable. The use of such a model as a state estimator in a feedback control framework thus appears promising though the "real" problem prediction must include at least the $n = \pm 1$ modes in addition to the $n = 0$ mode given here. In the case of a thin shear layer, the $n = \pm 1$ modes behave similarly to the $n = 0$ mode and may be analyzed with the $n = 0$ analysis. However, the solution for $n = \pm 1$ is required as the shear layer thickness becomes significant relative to the jet radius. For the mixing problem it is likely that the solution near the end of the potential core will need to be calculated. A transformation analogous to the Squire reformulation (of the three-dimensional planar stability problem into an equivalent two-dimensional problem in the transformed variables) will be pursued in the round jet problem.

REFERENCES

CAIN, A. AND THOMPSON, M. 1986 Linear and Weakly Nonlinear Aspects of Free Shear Layer Instability, Roll-Up, Subharmonic Interaction and Wall Influence. *AIAA Paper 86-1047.* AIAA/ASME 4th Fluid Mechanics, Plasma Dynamics and Lasers Conference, Atlanta, May.

CAIN, A., ROOS, F., AND KEGELMAN, J. 1990 Computational and Experimental Observations on Near Field Characteristics of an Excited Free Shear Layer. Presented at the Twelfth Symposium on Turbulent Flows, Rolla, MO, Sept.

DRAZEN, P. G. AND REID, W. H. 1981 *Hydrodynamic Stability*, Cambridge Univ. Press.

FREUND, J. B. AND MOIN, P. 1998 Mixing enhancement in jet exhaust using fluidic actuators: direct numerical simulations. *ASME FEDSM98-5235.*

GASTER, M. 1962 A Note on the Relationship between Temporally Increasing and Spatially Increasing Disturbances in Hydrodynamic Stability.. *J. Fluid Mech.* **14,** 222-224.

HO, C. M. AND HUERRE, P. 1984 Perturbed Free Shear Layers. *Ann. Rev. Fluid Mech.* **365-424.**

IKEDA, Y. 1998 Real-Time Active Flow Control Based on Modern Control Theory. *AIAA Paper 98-2911.* Presented at the AIAA Fluid Dynamics Meeting, Albuquerque, NM.

MORRIS, P. J., GIRIDHARAN, M. G., AND LILLEY, G. M. 1990 On the turbulent mixing of compressible free shear layers. *Proceedings of the Royal Society of London A.* **431**, 219-243.

PAL, A. 1998 Instability Modes of a Cylindrical Jet Based on Incompressible, Inviscid Model; Piecewise Continuous Velocity Profile. *Report to the Boeing Company,*April.

VISWANATHAN, K. AND MORRIS, P. J. 1992 Predictions of Turbulent Mixing in Axisymmetric Compressible Shear Layers. *AIAA J.* **30**(6), 1529-1536.

Mode interaction in a forced homogeneous jet at low Reynolds numbers

By I. Danaila[1] AND B. J. Boersma

The near-field evolution of a forced axisymmetric jet was investigated by means of Direct Numerical Simulation (DNS). The numerical configuration simulated a low Reynolds number jet ($Re_D = 1500$) issuing from a circular orifice in a solid wall. Periodic streamwise velocity disturbances were applied at the nozzle. Four modal distributions of forcing were studied. The first and the second type of perturbation contained only one of the two fundamental instability modes of the round jet: the *axisymmetric* $m = 0$ mode and the *helical* $m = 1$ mode. A 'classical' evolution of the jet flow was obtained for these cases. This provided a reference to the third case, which consisted of forcing simultaneously the counter-rotating helical modes $m = \pm 1$ with the same amplitude and the same frequency (*flapping mode*). The jet split into two branches, taking a distinct 'Y' shape characteristic of the *bifurcating jets* (cf. Lee & Reynolds, 1985). A different evolution of the bifurcating jet is observed when superposing the axisymmetric mode, at the most amplified unstable frequency, with the flapping mode, with the same amplitude but with subharmonic frequency. This combination led to resonant growth of the jet with a spectacular increase of the spreading angle up to 90^o.

1. Introduction

Considering the many practical applications of round jets (aeroacoustic, combustion, propulsion, mixing), numerous attempts have been made to control jet mixing and entrainment. A full listing of the proposed control approaches would easily exceed one hundred references.

All the control techniques use active or passive devices to alter the vortex dynamics close to the nozzle. From a theoretical point of view, the large coherent structures characterizing the near field evolution can be assimilated with instability modes, described by their azimuthal wavenumber m. Several fundamental results derived from linear stability analysis and experimental observations offer a complete picture of the mode selection in the near field of a *natural* (unforced) axisymmetric jet:

(i) The two linearly dominating modes are the axisymmetric (or varicose, $m = 0$) and first helical ($m = 1$) modes. For jets with thin initial shear layer, the linear amplification characteristics of these two fundamental modes are similar (e.g. Batchelor & Gill 1962, Michalke 1982). This has been confirmed in experiments (e.g. Cohen & Wygnanski 1987, Corke *et al.* 1991).

1 I. R. P. H. E., 12 Av. Général Leclerc, 13003 Marseille, France.

(ii) Higher helical modes ($m \geq 2$) are always less amplified than the fundamental modes (Mattingly & Chang 1974, Plasko 1979) and were rarely (if ever) observed in experiments.

(iii) Although the linear characteristics of the fundamental modes are almost identical, only one mode ($m = 0$ or $m = 1$) will dominate at the early stages of the near field evolution. The dominant mode is selected by amplification of coherent initial perturbations such as the pressure field at the lip (Morris 1976). In most laboratory jets, only planar disturbances are emanating from the nozzle and, consequently, the axisymmetric mode plays the dominant role (Cohen & Wygnanski 1987b). If the disturbances at the jet exit lip are stochastic, the switch from one mode to the other can occur, but the two fundamental modes never exist together (Corke *et al.* 1991).

(iv) Since the linear stability characteristics of the counter-rotating helical modes $m = 1$ and $m = -1$ are indistinguishable (Batchelor & Gill 1962, Danaila *et al.* 1998), there is a greater likelihood to observe both $m = \pm 1$ modes in the flow rather than a single helical mode. The nonlinear interaction of these two modes lead to characteristic flow patterns (Dimotakis *et al.*, 1983, Danaila *et al.* 1997). When the $m = \pm 1$ modes have the same frequency and amplitude, the so-called *flapping mode* is obtained (see, for example, Morrison & McLaughlin 1980). In conclusion, the linear superpositions of the $m = \pm 1$ modes (in particular the flapping mode) can also be considered as fundamental modes.

In the light of these results, the jet control techniques can be watched as attempts either to control the dynamics of a single fundamental mode or to force simultaneously several of these modes:

(1) The evolution of the axisymmetric mode characterized by vortex ring roll-up offers many possibilities of control. Many researchers have investigated the effects of axial acoustic forcing on the vortex ring generation (Crow & Champagne 1971, Bouchard & Reynolds 1982), spacing and pairing (Hussain & Zaman 1980, Hussain & Clark 1981, Ho & Huang 1982). The amplitude and frequency of the forcing excitation can determine the number of pairings and their locations and, consequently, the spreading rate of the jet. The azimuthal instability of rings and the formation of streamwise vortex filaments were reported as an important entrainment mechanism in jets (Liepmann & Gharib 1992). When combined with axial acoustic disturbances, passive azimuthal forcing (obtained by using corrugated nozzles) could be very effective in mixing and entrainment enhancement (Lasheras *et al.* 1991).

(2) The helical modes $m = \pm 1$ can be generated by controlled acoustic excitation (Parekh & Reynolds 1988, Corke & Kusek 1993) or triggered by passive devices which break the axial symmetry (e.g. tabs - Bradbury & Khadem 1975, sawtooth nozzles - Longmire & Duong 1995). Although less studied than the axisymmetric mode, the helical modes showed some interesting mixing properties. Mankbadi & Liu (1981) showed that helical modes are more efficient than the axisymmetric one in pumping energy into turbulent small scales due to its shorter streamwise lifespan. The subharmonic resonance of the $m = \pm 1$ modes can lead to a net increase (300%) of the jet momentum thickness compared to the unforced jet (Corke & Kusek 1993).

(3) The most interesting mixing and entrainment properties are obtained when combined axial and helical forcing are used. Lee & Reynolds (1985) used axial acoustic excitation to generate vortex rings and moved the nozzle in a circular path perpendicular to the jet axis (*orbital excitation*). Neighboring generated rings are radially shifted in different azimuthal planes and induce one another to move on distinct branches. The ratio R between the axial and the orbital forcing frequency set the number of branches. *Bifurcating* ($R = 2$), *trifurcating* ($R = 3$), and *blooming* ($1.6 < R < 3.2$ and non-integer) jets are obtained with a spectacular increase of the spreading angle (from 18^o for the unforced jet up to 80^o for the bifurcating jet). Parekh, Leonard & Reynolds (1988) obtained high Reynolds bifurcating jets using axial and flapping acoustic excitation produced by four speakers placed around the perimeter of the nozzle exit. The bifurcation occurred above a critical forcing amplitude, increasing with the Reynolds number. Higher forcing frequencies yielded bifurcating jets with larger spreading angles.

Similar (albeit more distorted) bifurcating jets were reported in jet experiments using axial forcing and passive control devices. Stepped or sawtooth trailing edges attached at the nozzle exit (Longmire & Duong 1995) or inclined nozzles (Webster & Longmire 1997) generated complex helical structures which altered the downstream evolution of vortex rings. The bifurcating effect was found to be strongest when low forcing frequencies were used, a trend opposite to that seen by Lee & Reynolds (1985). Zaman, Reeder & Samimy (1996) used a combination of two diametrically opposed tabs placed at the nozzle exit to obtain bifurcating supersonic jets. Further work (Zaman & Raman 1997) showed that, in low Mach number jets, tabs and axial excitation independently increased jet spreading while a combination of the two had an opposite effect.

This study was especially inspired by the experiments of Parekh *et al.* (1988), who studied the effects on the round jet evolution of four types of acoustic excitation: axisymmetric, helical, flapping, and *bifurcating* (i.e. axial + flapping). The spectacular increase in spreading of the bifurcating jet was compared to the reference cases provided by the axially and helically excited jets. One of the main conclusions of this study was the independence of the bifurcation phenomenon of the Reynolds number. For the explored range of high Reynolds numbers ($10\,000 < Re < 100\,000$), an optimum set of parameters (frequency and amplitude of excitation) can be found in order to obtain bifurcating jets similar to those reported by Lee & Reynolds (1985) for low Reynolds numbers ($2\,800 < Re < 10\,000$).

This observation suggests that bifurcating phenomena can be approached by Direct Numerical Simulation (DNS). Recent DNS of spatially evolving low Reynolds number jets proved very effective in investigating properties of the transitional (Danaila *et al.* 1997) or turbulent (Boersma *et al.* 1998) regimes of free incompressible jets. In this work we make use of DNS to assess the influence of the four abovementioned excitations on the jet evolution. Although the vortex dynamics of some bifurcating jets can be simulated by simpler numerical approaches, as the vortex filaments method (see Parekh *et al.* 1988), DNS is expected to offer a complete description of the underlying mechanisms involved in such flows.

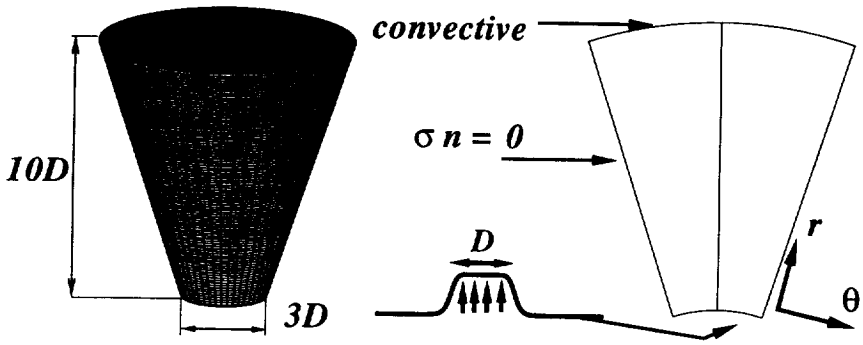

FIGURE 1. Computational domain and boundary conditions.

2. Numerical details

The numerical solver simulates a free round jet issuing from a circular orifice of diameter D in a solid wall. The solver solves the incompressible Navier-Stokes equations in a spherical coordinate system with (r, θ, ϕ) denoting the radial, azimuthal, and tangential directions. Details of the numerical scheme can be found in Boersma *et al.* (1998). The computational domain shown in Fig. 1 results from the intersection between the shell defined by the surfaces $r = 5D$ and $r = 15D$ and the cone starting from the center of the sphere with an opening angle of 36^o. The obtained geometry covers a domain with a streamwise extent of $15D$ and a spanwise diameter of $3D$ for the inflow section and $10D$ for the outflow section. Such a discretization is able to follow the streamwise spreading of the jet and allows a well-balanced resolution of the flow field with a reasonable number of grid points. For convenience, the cylindrical coordinates (r_c, θ_c, z) with r_c the radial, θ_c the azimuthal, and z the axial directions will be used to analyze the results.

The boundary conditions are also illustrated in Fig. 1. At the inflow section, the mean streamwise velocity profile is imposed as initial and boundary condition. We used the 'classical' hyperbolic tangent (*tanh*) profile, which matches very well with profiles measured in experiments (see Michalke 1984). In cylindrical coordinates it reads:

$$V_{z0}(r_c)/V_0 = 0.5\{1 + \tanh[0.25D/\Theta_0(D/(4r_c) - r_c/D)]\}, \qquad (1)$$

where V_0 is the centerline velocity (at $r_c = 0$) and Θ_0 the initial momentum thickness. At the lateral boundary, traction-free boundary conditions are used (see, for example, Gresho 1991): $\sigma_{ij} \cdot n_j = 0$, where σ_{ij} is the stress tensor and n_j the unit normal on the boundary. The main advantage of this traction-free condition over the largely used free-slip or no-slip boundary conditions is that fluid exchange across the boundary is allowed. This appeared to be very useful to properly simulate the entrainment of ambient fluid in the spreading jet flow. A so-called convective boundary condition (Orlanski 1976, Lowery & Reynolds 1986) was used to evacuate the vortex structures through the downstream boundary. This condition is numerically stable but physically not very realistic in elliptic flows. However, the convective nature of the homogeneous jet flow (Huerre & Monkewitz 1990) allows it to eventually evacuate spurious reflections at the outflow boundary.

3. Selection of physical parameters

The guidelines for the selection of physical parameters used in our spatial simulation were found in Parekh *et al.* (1988). In their experiments, the Reynolds number was varied in the range $10^4 < Re_D = V_0 D/\nu < 10^6$. The measured ratio between the jet diameter and the momentum thickness of the inflow mean velocity profile was $D/\Theta_0 = 66$ for $Re_D = 10^4$ and about seven times larger for $Re_D = 10^6$. The acoustic excitation was characterized by the axial Strouhal number $St_a = f_a D/V_0$ when the axisymmetric mode was forced at the frequency f_a. The corresponding helical Strouhal number $St_h = f_h D/V_0$ was defined for the helical or flapping mode excitation. The dual-mode excitation was characterized in terms of the frequency ratio $R_f = f_a/f_h$ and the axial Strouhal number St_a.

The bifurcating jet was obtained only if $R_f = 2$ and for a well defined range of axial Strouhal numbers: $0.4 < St_a < 0.7$. Nevertheless, the maximum jet spreading occurred around $St_a = 0.55$ for all investigated Reynolds numbers. The same optimum value for St_a was reported by Lee & Reynolds (1985) for the bifurcating jet at $Re_D = 3700$. No satisfactory explanation of this phenomenon was provided. We believe that the invariance of St_a with the Reynolds number can be connected to another unexplained phenomenon reported in free jets, which is the locking of the jet *preferred* Strouhal number for large ratios D/Θ_0 (see Ho & Huerre 1984). Indeed, it is well known that the most amplified frequency at the end of the potential core is independent of the Reynolds number and results from nonlinear interactions (Crow & Champagne 1971). The value of the Strouhal number based on this preferred frequency and the jet diameter varies from one experiment to another between 0.2 and 0.5 (Gutmark & Ho 1983). The preferred Strouhal number scales with the shear-layer frequency for small D/Θ_0 and 'locks' at a constant value of 0.44 for $D/\Theta_0 \geq 240$ (Ho & Huerre 1984). A similar phenomenon can occur in high Reynolds bifurcating jets, where collective interactions of vortex rings at the end of the potential core cause the jet to split in two distinct branches. Consequently, the value $St_a = 0.55$ can be considered as the preferred axial Strouhal number of the bifurcating jets characterized by large ratios D/Θ_0.

In view of these experimental observations, we chose the following physical parameters to define the inflow velocity profile given by Eq. (1): $D/\Theta_0 = 60$ and $Re_D = 1500$. For this low Reynolds number, a uniform mesh of $(192 \times 128 \times 96)$ grid-points in the (r, θ, ϕ) directions is sufficient to resolve the smallest scales of the motion in the considered computational domain (see Boersma *et al.* 1998). As a result of this discretization, 12 grid-points are situated in the initial shear region at the nozzle, offering a correct resolution of the instability waves.

The simulated jet is forced by superposing oscillating components on the mean nozzle exit velocity. Only streamwise velocity disturbances are used. The analytical form of the resulting inflow velocity profile is:

$$V_z(r_c, t) = V_{z0}(r_c)\left[1 + \sum_m A_m \sin\left(2\pi \frac{St_m V_0}{D} t - m\theta_c\right)\left(\frac{2r_c}{D}\right)^{|m|}\right], \qquad (2)$$

where V_{z0} is given by Eq. (1) and m is the azimuthal wavenumber of the excitation.

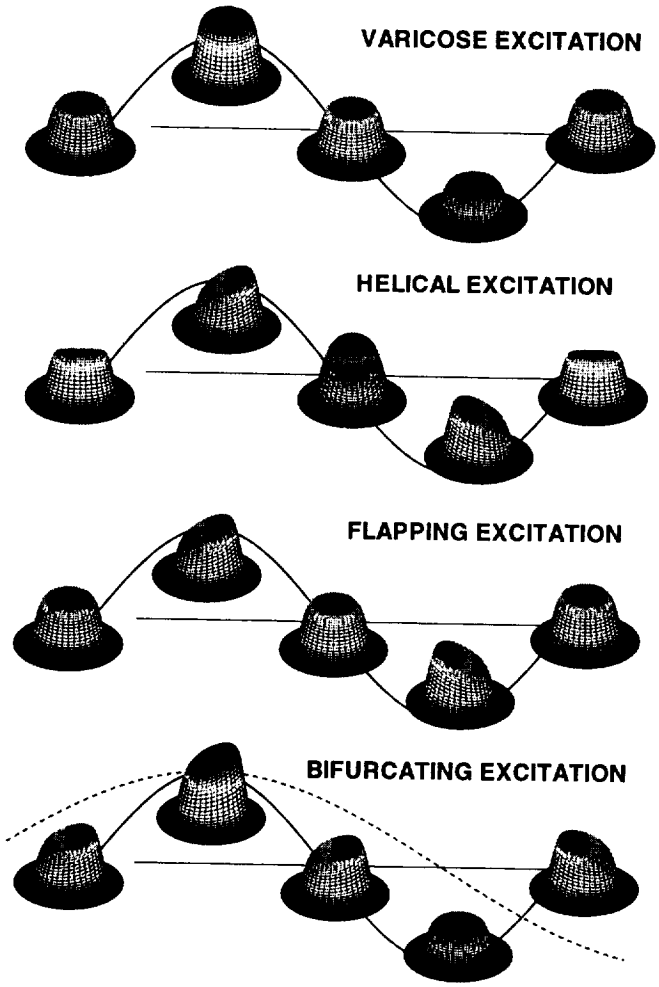

FIGURE 2. Three-dimensional representation of the streamwise velocity profile at the nozzle. Evolution during one cycle of excitation.

Four types of excitation were considered, as in experiments. The time evolution of the inflow velocity profile during one cycle of excitation can be followed in Fig. 2.

[(A)-jet] Axisymmetric excitation ($m = 0$); $St_a = 0.55$; $A_a = 0.15$.

The up and down 'movement' of the velocity profile around the mean value (Fig. 2) mimics the perturbation introduced by a speaker placed in the plenum chamber of a laboratory jet. The excitation parameters (St_a, A_a) were fixed in order to provide a reference case for the bifurcating jet (see below).

[(H)-jet] Helical excitation ($m = 1$); $St_h = 0.55$; $A_h = 0.15$.

This perturbation approaches the disturbances produced by an azimuthal array of acoustic drivers placed close to the jet lip and controlled by a helical input (Parekh *et al.* 1988, Corke & Kusek 1993). The asymmetric velocity profile makes a complete rotation during one period of excitation.

[(F)-jet] Flapping excitation $[(m = 1) + (m = -1)]$; $St_f = 0.55$; $A_f = 0.15$.

The flapping excitation results from the superposition of the counter-rotating helical modes with the same amplitude and frequency. An equivalent form of the inflow velocity profile (Eq. 2) is in this case:

$$\frac{V_z(r_c,t)}{V_{z0}(r_c)} = \left[1 + A_f \sin\left(2\pi \frac{St_f V_0}{D} t\right) \cos(\theta_c) \left(\frac{2r_c}{D}\right)\right] \tag{3}$$

Compared to the helical excitation, the time evolution of the velocity profile (Fig. 2) is phase locked in the plane $\theta_c = 0$.

[(BF)-jet] Bifurcating excitation $[(m = 0) + (m = 1) + (m = -1)]$; $St_a = 0.55$; $St_f = St_a/2$; $A_a = A_f = 0.15$.

The bifurcating perturbation is obtained by imposing a dual-mode (axisymmetric + flapping) and dual-frequency ($R_f = St_a/St_f = 2$) excitation. Since both the experiments of Lee & Reynolds (1985) and Parekh *et al.* (1988) indicated a maximum spreading of the bifurcating jet for an axial Strouhal number of 0.55, the same value is considered here. The large excitation amplitude (15%) is close to that used by Lee & Reynolds (1985). Along with the amplitude, the relative phase (Φ) between the axial and the flapping excitations is very important. Bifurcation occurs only if the peak of the axial signal is approximately aligned with the peak of the flapping signal (Parekh *et al.* 1988). The measured values were $\Phi = 47^o \pm 15^o$ at $Re_D = 10^6$ and $\Phi = 31^o \pm 15^o$ at $Re_D = 50 \cdot 10^3$. In our simulations, we imposed the theoretical value $\Phi = 45^o$ to obtain the peak alignment (see the last frame of Fig. 2, with the dashed line representing the flapping component of the perturbation). The final form of the velocity profile can be written as:

$$\frac{V_z(r_c,t)}{V_{z0}(r_c)} = \left[1 + A_a \sin\left(2\pi \frac{St_a V_0}{D} t\right) + A_f \sin\left(2\pi \frac{St_f V_0}{D} t + \Phi\right) \cos(\theta_c) \left(\frac{2r_c}{D}\right)\right] \tag{4}$$

4. Results

The response of the jet flow to the excitations described above is analyzed both instantaneously and statistically. As in experiments, flow visualization is emphasized. For this purpose, a passive scalar conservation equation with Fickian diffusion assumption is solved with the same numerical scheme. Two different types of scalar injection are considered. The first scalar (S1) has the same mean inflow profile as the injection velocity (Eq. 1). This tracer marks all the jet fluid and provides a qualitative estimation of the entrainment through the interface between ambient and jet fluid. The second tracer (S2) is injected with a mean profile corresponding to the vorticity profile of the initial shear-layer (derivative of Eq. 1). This is useful to mark the vorticity-bearing jet mixing-layer and to track large coherent structures. For our numerical tracers, a very small diffusivity was chosen in order to avoid rapid contamination of all the computational domain. This is good assumption for water flow visualization, where the viscous diffusion of the (fluorescein) dye can be neglected.

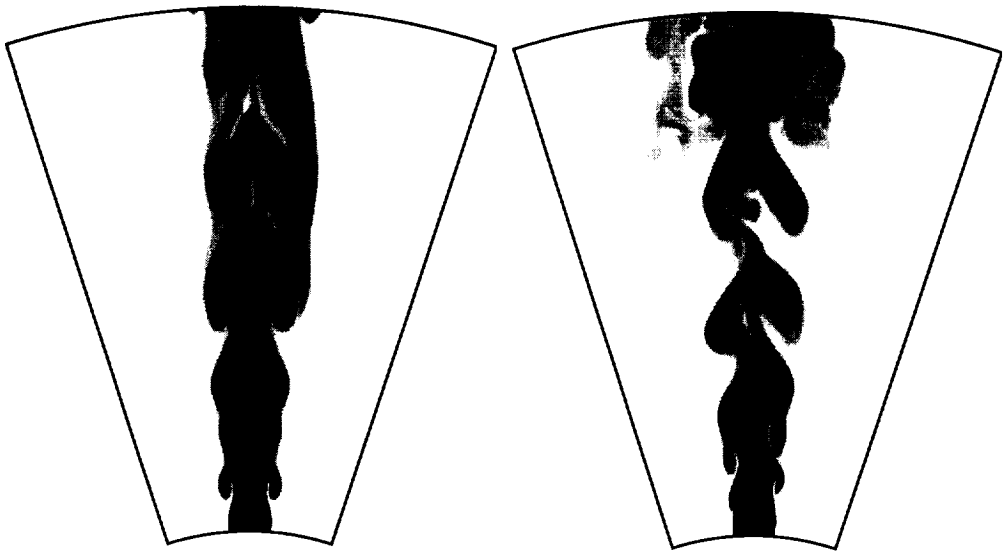

FIGURE 3. (A)-jet (left) and (H)-jet (right). Instantaneous cross-section ($\theta_c = 0$) in the (S1) passive scalar field.

4.1 Axisymmetric and helical excitations

Instantaneous cross-sections in the scalar field (S1) are displayed in Fig. 3 for the axially (left) and helically (right) excited jets. The large forcing amplitude expedites the transition of the the initially laminar jet mixing layers. In both cases the transition consists of formation of coherent structures of Kelvin-Helmholtz type (*cat-eyes*). These structures are spatially organized in toroidal vortex rings in case (A) and helical patterns in case (H).

It should be noted that, for the hyperbolic tangent velocity profile (1) with $D/\Theta_0 = 60$, the linear stability analysis (Michalke 1984) showed that the axisymmetric and the helical modes have almost the same 'most amplified' (or 'natural') frequency (f_n). In terms of Strouhal number based on the momentum thickness, its theoretical value is: $St_{\Theta_0} = f_n \Theta_0 / V_0 = 0.017$. The corresponding Strouhal number based on the jet diameter will be $St_D = 1.02$. As a result, the forcing frequency ($St_a = St_h = 0.55$) is very close to the subharmonic 'natural' frequency and will cause 'collective interactions' of vortex structures (Ho & Huang 1982). Figure 3 also captures the vortex rings pairing process in the axially excited jet. For the helically excited jet, the coalescence of two neighboring vortex loops of the helix can be observed (Fig. 3). This phenomenon was never reported in experiments with a single helical mode input. A similar 'helical pairing' process was reported by Corke & Kusek (1993) in their jet, simultaneously forced with $m = \pm 1$ modes.

In both jets, vortex amalgamations generate larger coherent structures and increase the local momentum thickness of the shear layer. The streamwise wavelength is doubled by pairings as illustrated in Fig. 4 presenting a snapshot of the (S2) tracer evolution near the nozzle. The vortex cores are easily identified by high tracer

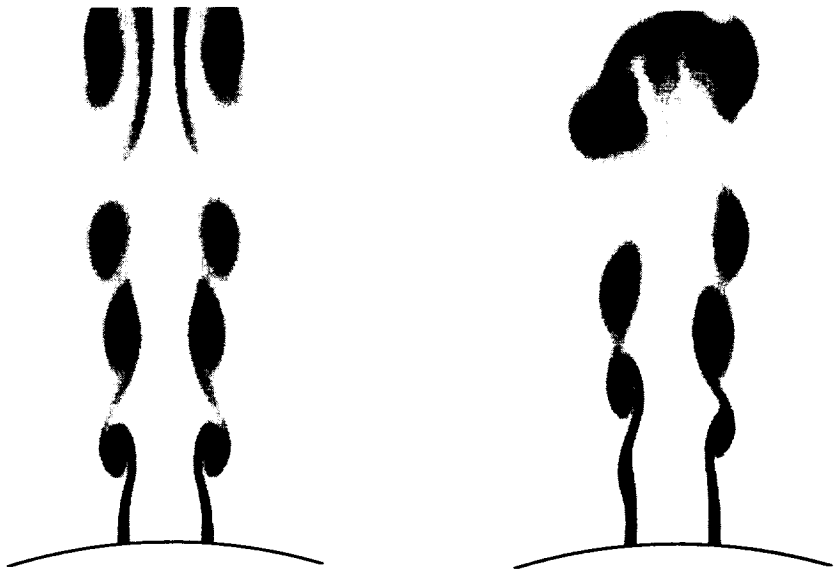

FIGURE 4. (A)-jet (left) and (H)-jet (right). Instantaneous cross-section ($\theta_c = 0$) in the (S2) passive scalar field. Zoom in the region close to the nozzle.

concentrations. From this visualization, the instability wavelength is estimated to $\lambda_a/D \approx 1.03$ for the case (A) and $\lambda_h/D \approx 0.86$ for the case (H). As the forcing frequency is higher than $f_n/2$, the response frequency of the shear will be equal to the forcing frequency (Ho & Huerre 1984). With this assumption, the convection velocity of the unstable modes can be calculated as $V_c/V_0 = \lambda/D\,St_D$. The obtained values $(V_c/V_0)_a = 0.56$ and $(V_c/V_0)_h = 0.47$ are very close to the theoretical value of 0.5.

Different azimuthal sections offer similar images for both cases. Figure 5 presents a three-dimensional picture of the large coherent structures dominating the near-field. The fundamental ($m = 0$) and ($m = 1$) unstable modes are clearly identified by means of iso-surfaces of low pressure (see Jeong & Hussain 1995).

However, the azimuthal symmetry of the axially forced jet is broken downstream of the pairing location. Stretched lateral ejection of the passive scalar (Fig. 3) suggests that secondary azimuthal instability develops and forms side-jets (see Liepmann & Gharib 1992). The azimuthally distorted structure of the last vortex ring displayed in Fig. 5 confirms this observation. Subsequent simulation of the axially forced jet with additional low amplitude (2%) white noise disturbances at the nozzle showed a more rapid breakup of the vortex rings into turbulent puffs beyond $z/D \approx 5$ (pictures not shown here). On the other hand, the helical structure is less stable and breaks up in small eddies without any additional disturbances (Fig. 3). This observation matches the results of Mankbadi & Liu (1981), showing that helical modes have a shorter streamwise lifespan than the axisymmetric mode. This property makes the helical modes more effective in transferring energy into small turbulent scales.

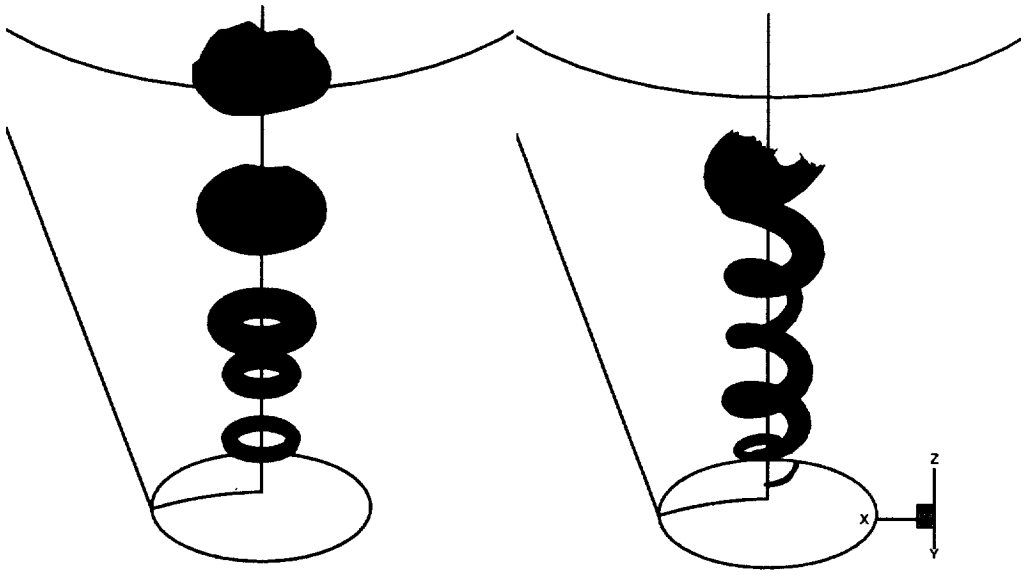

FIGURE 5. (A)-jet (left) and (H)-jet (right). Identification of large coherent structures by instantaneous iso-surfaces of low pressure ($p = 0.2 \cdot p_{min}$).

4.2 Flapping and bifurcating excitations

The structure of the simulated jet changes dramatically when flapping or bifurcating excitation are applied at the nozzle. A spectacular increase of the jet spreading angle is observed in the *bifurcating plane*. This plane of maximum spreading is fixed by the azimuthal position where the flapping perturbation locks ($\theta_c = 0$ in our case). The plane perpendicular to the bifurcation plane is also called *bisecting plane*. Figure 6 depicts instantaneous pictures of the (S1) scalar evolution in the bifurcating plane for the jet with flapping (left) and bifurcating (right) perturbation. The same picture taken in the bisecting plane is presented in Fig. 7. Both jets exhibit different behavior in the two planes.

In the bifurcating plane, the flapping excitation causes the jet to split into two distinct branches (Fig. 6-left). Approximately at the same downstream location ($z/D \approx 5$), the jet with bifurcation excitation spreads in a wide-angle turbulent structure (Fig. 6-right). In the bisecting plane, the scalar evolution is similar for both jets. The tracer, organized in large axisymmetric structures, seems to disappear downstream of $z/D \approx 5$ (Fig. 7). Practically no spreading is observed in this plane.

This different evolution in two perpendicular planes is a characteristic of experimentally observed bifurcating jets. Nevertheless, only the (F)-jet displays the Y-shaped structure, reported as the most striking feature of bifurcating jets at low Reynolds numbers ($Re_D \leq 10\,000$). On the other hand, the (BF)-jet shares features of the higher Reynolds number experimental bifurcating jets (see Lee & Reynolds 1985 and Parekh *et al* 1988). This is a surprising result, suggesting that new mechanisms are involved in our simulated jets.

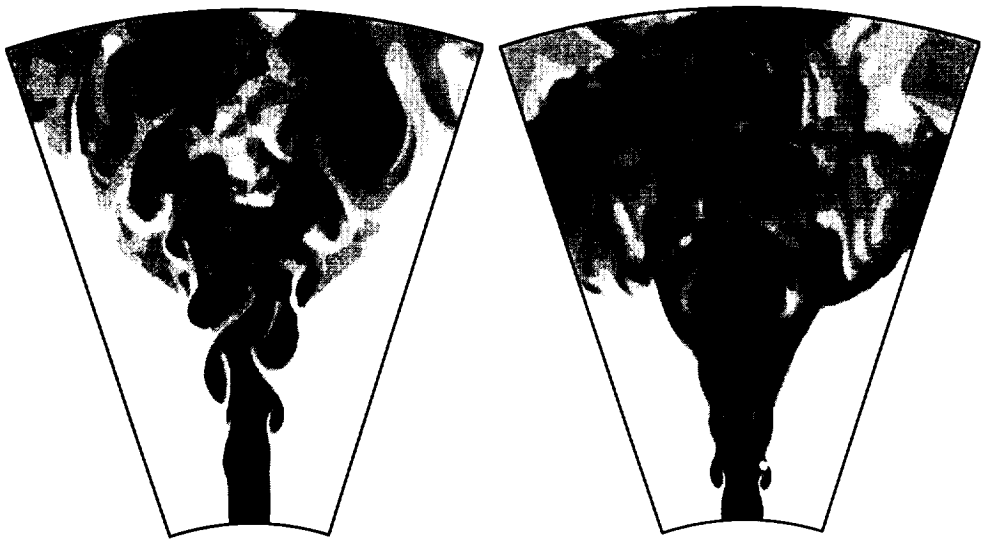

FIGURE 6. (F)-jet (left) and (BF)-jet (right). Instantaneous snapshot of the (S1) passive scalar field in the bifurcating plane ($\theta_c = 0$).

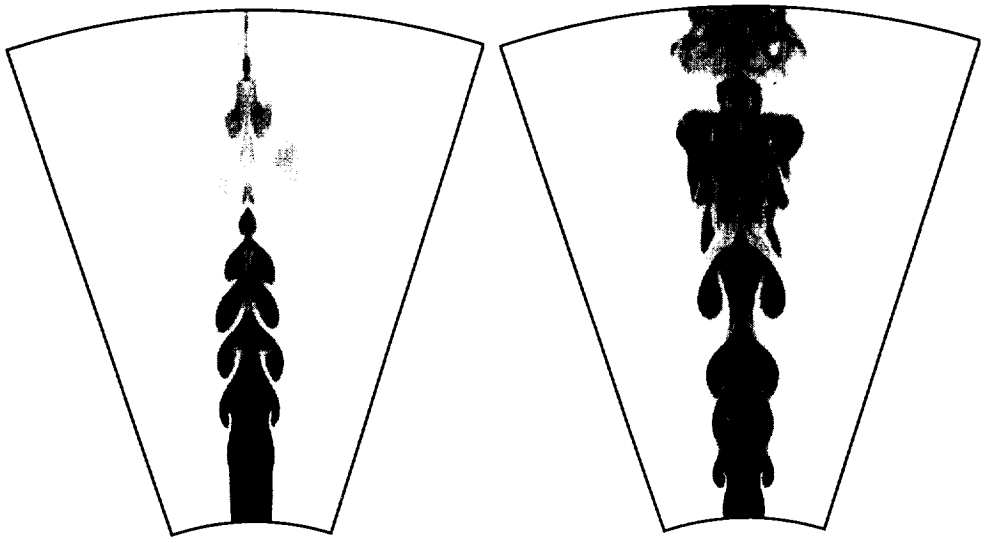

FIGURE 7. Same caption as in Fig. 6. Evolution in the bisecting plane ($\theta_c = 90$).

In experimental bifurcating jets, the combined axial and flapping forcing created a periodic array of vortex rings, which were alternatively shifted in the radial direction. The helical disturbances reached their maximum amplification at the end of the potential core. As a result, the rings tilted and propagated along two different trajectories. In our simulated jets, different 'bifurcating' mechanisms are revealed by the analysis of the space-time evolution of vortex structures.

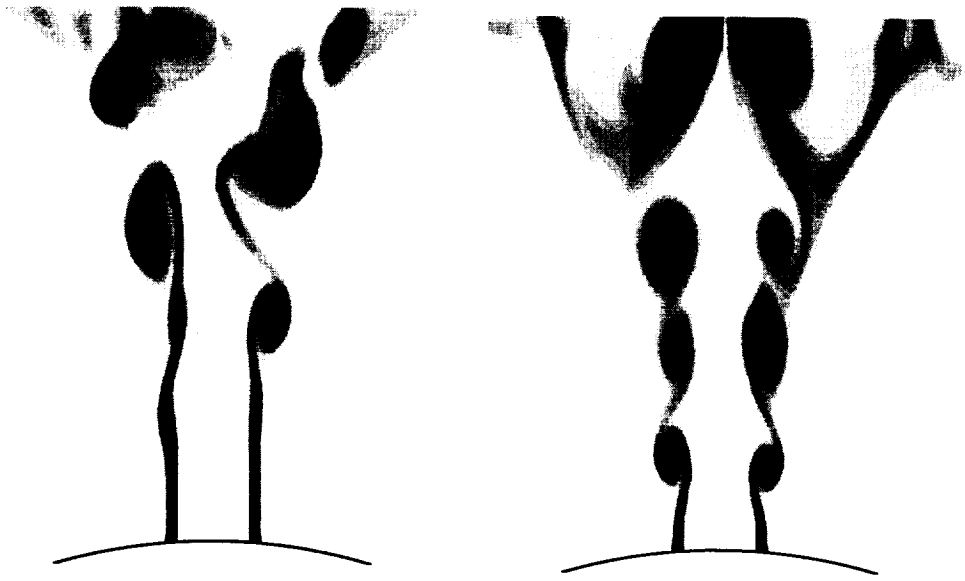

FIGURE 8. (F)-jet (left) and (BF)-jet (right). Instantaneous snapshot of the (S2) passive scalar field in the bifurcating plane ($\theta_c = 0$). Zoom near the nozzle.

Figures 8 and 9 offer a more detailed image of the large structures dominating the simulated jet flows. The near-field evolution of the (S2) tracer shows that flapping excitation delays the roll-up of the jet shear layer (Fig. 8-left). The first *cat-eyes* are formed at $z/D \approx 2.25$, compared to $z/D \approx 1.2$ for the (H)-jet. A greater percentage of the tracer is captured at azimuthal locations corresponding to maxima of the local velocity profile. At the diametrically opposite locations, weaker tracer filaments connect the staggered vortices at the azimuthal maxima. This observation is supported by the three-dimensional image of the coherent structures identified by means of iso-surfaces of low pressure (Fig. 9-left). Ring-like vortical structures roll up up in alternatively tilted planes every half-period of excitation. The core of these structures progressively diminishes towards the region of minimum perturbation amplitude. At this azimuthal location, the vortex ends do not merge in a toroidal loop. They bend downstream and merge with the next vortex, generating a large intertwined structure. This continuous structure breaks-up at $z/D \approx 5$. As a result, vortex structures similar to distorted rings propagate along two distinct branches. This last phase of vortex evolution is similar to that observed in experiments. However, the initial stages of formation of the involved 'ring' structures is different since we never observed the usual (see Fig. 5) toroidal rings in our simulation.

The shear-layer of the (BF)-jet rolls up into coherent vortex rings (Fig. 8-right) similar to those characterizing the axially excited jet (Fig. 4-left) except for the slight tilt of the vortices. The vortex pairing occurs at approximately the same downstream location. Farther downstream, the vortex ring undergoes strong azimuthal instabilities and finally break up into small and irregular vortex structures

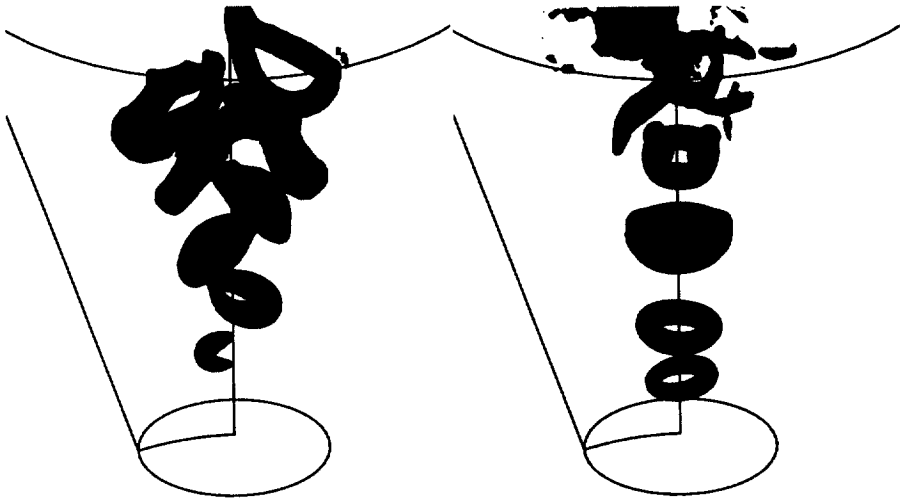

FIGURE 9. (F)-jet (left) and (BF)-jet (right). Identification of large coherent structures by instantaneous iso-surfaces of low pressure ($p = 0.2 \cdot p_{min}$).

(Fig. 9-right). As observed from Figs. 6 and 8, the flow abruptly spreads in the bifurcating plane before the complete destruction of the vortex rings. The tracer is ejected directly from the vortex sheet connecting the rings (braid region). This phenomenon can be explained by the excessive growth of streamwise filaments in the braid region (see Liepmann & Gharib 1992). The streamwise filaments are stretched by the high field strain and pulled outward from the jet by the moving vortex rings. The streamwise component of the vorticity vector is dominant in these regions (pictures not shown) and generates strong expulsion of passive tracer. In conclusion, the 'bifurcating' mechanism for the (BF)-jet concerns mainly the evolution of secondary streamwise vortice, rather than that of primary vortex rings. It should also be noted that the phase difference (Φ) between the axial and the flapping excitation (see Eq. 4) is essential to obtain bifurcation. The simulation with $\Phi = 0$ revealed small spreading in the excitation plan similar to that obtained for the (A)-jet.

4.3 Mean flow evolution

To assess if the behavior observed in the instantaneous pictures is highly repeatable, the mean flow fields were calculated. The statistical analysis is conducted within the same time period $T = 2D/(St_a \cdot V_0)$ for all the simulated cases. This period corresponds to the lowest forcing frequency ($\sim St_a/2$) used in the (BF)-case. The average procedure uses the information at every time step in the considered time interval. A converged mean flow field is obtained by averaging the mean data calculated for $2T$ time periods in the (A) and (H)-case and $4T$ time periods in the (F) and (BF)-case.

Figures 10 and 11 depict the mean fields of the (S1) scalar variable for all the simulated cases. The (A) and (H) jets display a very small spreading rate in all of the azimuthal planes. A dramatic increase of jet spreading in the bifurcating

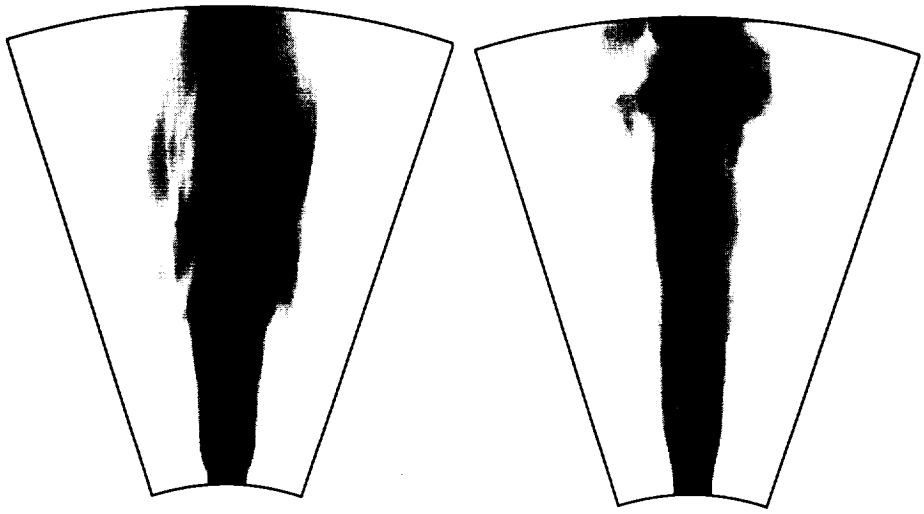

FIGURE 10. (A)-jet (left) and (H)-jet (right). Mean (S1) passive scalar field.

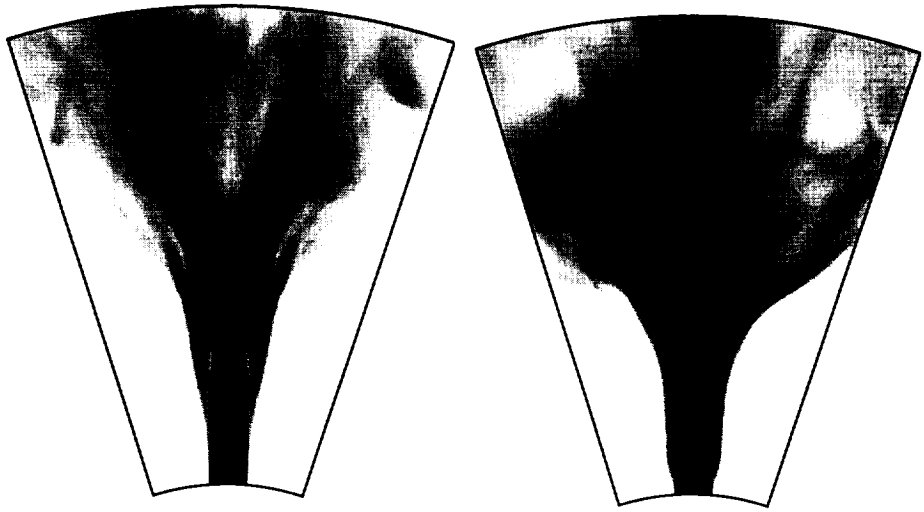

FIGURE 11. (F)-jet (left) and (BF)-jet (right). Mean (S1) passive scalar field in the bifurcating plane.

plane is observed for the (F) and (BF) cases. The Y-shaped structure of the (F)-jet (already observed in Fig. 6) is clearly displayed in this picture. Note the similarity with the pictures provided by the *product* visualizations in the bifurcating jets of Lee & Reynolds (1985). The (BF)-jet shows the greatest spreading rate. Although two distinct branches can be identified, the tracer concentration near the jet axis has a great value. The complicated *tree*-structure of the (BF)-jet can be generically described as Ψ-shaped. Based on these visualizations, we can speculate that the rapid breaking of the large structures in this jet enhances mixing and entrainment.

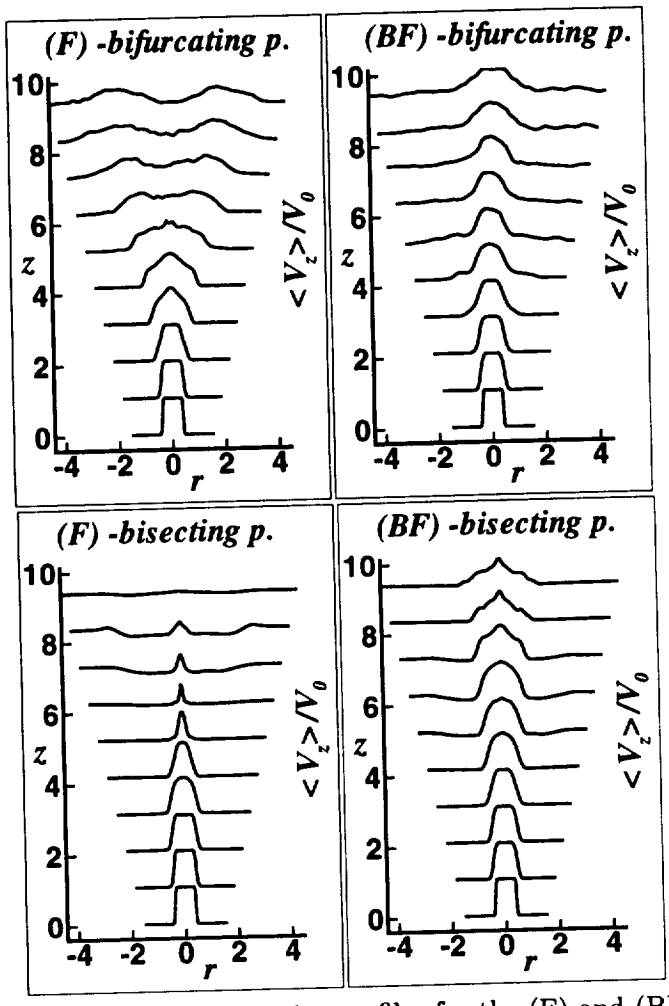

FIGURE 12. Mean streamwise velocity profiles for the (F) and (BF) jets.

Therefore, the (BF)-jet can be very interesting for practical applications.

The trends observed in the evolution of the (F) and (BF) jets can be summarized by plotting the mean streamwise velocity profiles (Fig. 12). In the far-region of the (F)-jet ($z/D \geq 5$), double-peak profiles can be observed in the bifurcating plane and very flat profiles in the bisecting plane. This evolution indicates that the jet flow splits into two distinct jets in the bifurcating plane and gradually vanishes in the perpendicular plane. The splitting of the jet main column in two branches directed in a well-defined azimuthal plane was reported as the most sticking feature of experimental bifurcating jets. The (BF)-jet displays a different evolution of the mean velocity. Bell-shaped profiles are observed in both bifurcating and bisecting planes. Nevertheless, the wider profiles in the bifurcating plane demonstrate the increased total momentum thickness and jet spreading in this plane.

5. Summary and final discussion

The evolution of a low Reynolds number round jet under periodic forcing was examined by means of DNS. The selection of the physical parameters of the spatial simulation was guided by the experimental studies of Lee & Reynolds (1985) and Parekh, Leonard & Reynolds (1988). The periodic forcing was numerically modeled by superposing streamwise velocity perturbations on the mean inflow velocity profile. The four considered types of perturbations represented linear combinations of the fundamental unstable modes in jets: (A) axisymmetric [$m = 0$], (H) helical [$m = 1$], (F) flapping [$(m = 1) + (m = -1)$], and (BF) bifurcating [$(m = 0) + (m = 1) + (m = -1)$].

The evolution of the axially and helically forced jets is in very good qualitative and quantitative agreement with previous theoretical and experimental studies. The flapping and the bifurcating perturbations generate jets with a spectacular increase of the spreading rate in the plane where the excitation locks (from 16^o for the (A)-jet to approximately. 90^o for the (BF)-jet).

In their attempt to semantically define bifurcating jets, Parekh *et al* (1988) emphasized that a jet which spreads more rapidly in one plane than in the perpendicular plane is not necessarily a bifurcating jet since elliptic jets exhibit the same characteristic. Based on flow-visualizations, they proposed two criteria to define a bifurcating jet: the jets split into two separate jets and/or the far-field streamwise velocity profiles consist of two separate peaks. The first criterion is fulfilled when the jet fluid disappears as one moves downstream in the plane perpendicular to the excitation plane.

The surprising result displayed in our simulations was that only the (F)-jet fulfilled the two criteria. The involved bifurcating mechanism was similar to that experimentally reported except for the formation of coherent ring-like structures. The (BF)-jet showed some similaritie, but also some clear differences when compared to experimental bifurcating jets. A new bifurcating mechanism based on the growth of secondary streamwise vortices was proposed to explain the observed behavior. Consequently, we propose a more general definition classifying a jet as bifurcating jet if it spreads rapidly in one plane but not in the perpendicular plane, without axis switching. This definition will exclude jets with non-circular nozzles (elliptic, triangular) and will include indeterminate-origin bifurcating jets.

Acknowledgments

We would like to acknowledge the helpful input of Prof. W. C. Reynolds and Prof. P. Moin in positioning this investigation. We also thank Prof. D. Parekh for stimulating discussions. The computing time on the IBM-SP2 was made available by the Maui High Performance Computing Center (MHPCC).

REFERENCES

BATCHELOR, G. K. & GILL, A. E. 1962 Analysis of the stability of axisymmetric jets. *J. Fluid Mech.* **14**, 529.

BOERSMA, B. J., BRETHOUVER, G., & NIEUWSTADT, F. T. M. 1998 A numerical investigation the effect of the inflow conditions on the self-similar region of a round jet. *Phys. Fluids.* **10,** 899.

BOUCHARD, E. E. JR. & REYNOLDS, W. C. 1982 The role of large scale structures in the initial development of circular jets. *Report No. TF-17,* Department of Mechanical Engineering, Stanford University.

BRADBURY, L. J. S. & KHADEM, A. H. 1975 The distortion of a jet by tabs. *J. Fluid Mech.* **70,** 801.

COHEN, J. & WYGNANSKI, I. 1987 The evolution of instabilities in the axisymmetric jet. Part 1. The linear growth of disturbances near the nozzle. *J. Fluid Mech.* **176,** 191.

COHEN, J. & WYGNANSKI, I. 1987b The evolution of instabilities in the axisymmetric jet. Part 2. The flow resulting from the interaction between waves. *J. Fluid Mech.* **176,** 221.

CORKE, T. C., SHAKIB, F., & NAGIB, H. M. 1991 Mode selection and resonant phase locking in unstable axisymmetric jets. *J. Fluid. Mech.* **223,** 253.

CORKE, T. C. & KUSEK, S. M. 1993 Resonance in axisymmetric jets with controlled helical-mode input. *Fluid. Mech.* **249,** 307.

CROW, S. C. & CHAMPAGNE, F. H. 1971 Orderly structure in jet turbulence. *J. Fluid Mech.* **48,** 547.

DANAILA, I., DUSEK J., ANSELMET, F. 1998 Nonlinear dynamics at a Hopf bifurcation with axisymmetry breaking in a jet. *Phys. Rev. E.* **57,** 3696.

DANAILA, I., DUSEK J., ANSELMET, F. 1997 Coherent structures in a round, spatially evolving, unforced, homogeneous jet at low Reynolds numbers. *Phys. Fluids.* **9,** 3323.

DIMOTAKIS, P. E., MIAKE-LIE, R. C., & PAPANTONIOU, D. A 1983 Structure and dynamics of round turbulent jets. *Phys. Fluids.* **26,** 3185.

GRESHO, P. M. 1991 Incompressible fluid dynamics: Some fundamental formulations issues. *Ann. Rev. Fluid Mech.* **23,** 413.

GUTMARK, G. & HO, C. M. 1983 Preferred modes and the spreading rates of jets. *Phys. Fluids.* **26,** 2932.

HO, C. M. & HUERRE, P. 1984 Perturbed free shear layers. *Ann. Rev. Fluid Mech.* **16,** 365.

HO, C. M. & HUANG, L. S. 1982 Subharmonics and vortex merging in mixing layers. *J. Fluid Mech.* **119,** 443.

HUERRE, P. & MONKEWITZ, P. A. 1990 Local and global instabilities in spatially developing flows. *Ann. Rev. Fluid Mech.* **22,** 473.

HUSSAIN, A. K. M. F. & ZAMAN, Z. B. M. Q. 1980 Vortex pairing in a circular jet under control excitation. Part 2. Coherent structure dynamics. *J. Fluid Mech.* **101,** 493.

HUSSAIN, A. K. M. F. & CLARK, A. R. 1981 On the coherent structure of the axisymmetric mixing layer: a flow-visualization study. *J. Fluid Mech.* **104,** 263.

JEONG, J. & HUSSAIN, F. 1995 On the identification of a vortex. *J. Fluid Mech.* **285,** 69.

LASHERAS, J. C., LECUONA, A., & RODRIGUEZ, P. 1991 Three-dimensional vorticity dynamics in the near field of coflowing forced jets. *Lect. Appl. Math.* **28,** 403.

LEE, M. & REYNOLDS, W. C. 1985 Bifurcating and blooming jets. *Report No. TF-22,* Department of Mechanical Engineering, Stanford University.

LIEPMANN, D. & GHARIB, M. 1992 The role of streamwise vorticity in the near-field entrainment of round jets. *J. Fluid Mech.* **643.**

LONGMIRE, E. K. & DUONG, L. H. 1995 Bifurcating jets generated with stepped and sawtooth nozzles. *Phys. Fluids.* **8,** 978.

LOWERY, P. S. & REYNOLDS, W. C. 1986 Numerical simulation of a spatially-developing, forced, plane mixing layer. *Report No. TF-26,* Department of Mechanical Engineering, Stanford University.

MANKBADI, R. R. & LIU, J. T. C. 1981 A study on the interactions between large scale coherent structures and fine-grained turbulence in a round jet. *Phil. Trans. R. Soc. Lond.* **A28,** 541.

MATTINGLY, G. E. & CHANG C. C. 1974 Unstable waves on a axisymmetric jet column. *J. Fluid Mech.* **65,** 541.

MICHALKE, A. 1984 Survey on jet instability theory. *Prog. Aerospace Sci.* **21,** 159.

MORRIS, P. J. The spatial viscous instability of axisymmetric jets 1976. *J. Fluid Mech.* **77,** 511.

MORRISON, G. L. & MCLAUGHLIN, D. K. 1980 Instability process in low Reynolds number supersonic jets. *AIAA J.* **18,** 793.

ORLANSKI, I. 1976 A simple boundary condition for unbounded hyperbolic flows. *J. Comp. Physics.* **21,** 251.

PAREKH, D., LEONARD, A., & REYNOLDS, W. C. 1988 Bifurcating jets at high Reynolds numbers. *Report No. TF-35,* Department of Mechanical Engineering, Stanford University.

PLASCHKO, P. 1979 Helical instabilities of slowly divergent jets. *J. Fluid Mech.* **92,** 209.

WEBSTER, D. R. & LONGMIRE, E. K. 1997 Vortex dynamics in jets from inclined nozzles . *Phys. Fluids.* **9,** 655.

ZAMAN, K. B. M. Q., REEDER, M. F., & SAMIMY, M. 1994 Control of an axisymmetric jet using vortex generators. *Phys. Fluids.* **6,** 778.

ZAMAN, K. B. M. Q. & RAMAN, G. 1997 Reversal in spreading of a tabbed circular jet under controlled excitation. *Phys. Fluids.* **9,** 3733.

Evaluation of noise radiation mechanisms in a turbulent jet

By T. Colonius[1], K. Mohseni[1], J. B. Freund[2], S. K. Lele, AND P. Moin

Data from the direct numerical simulation (DNS) of a turbulent, compressible (Mach=1.92) jet has been analyzed to investigate the process of sound generation. The overall goals are to understand how the different scales of turbulence contribute to the acoustic field and to understand the role that linear instability waves play in the noise produced by supersonic turbulent jets. Lighthill's acoustic analogy was used to predict the radiated sound from turbulent source terms computed from the DNS data. Preliminary computations (for the axisymmetric mode of the acoustic field) show good agreement between the acoustic field determined from DNS and acoustic analogy. Further work is needed to refine the calculations and investigate the source terms. Work was also begun to test the validity of linear stability wave models of sound generation in supersonic jets. An adjoint-based method was developed to project the DNS data onto the most unstable linear stability mode at different streamwise positions. This will allow the evolution of the wave and its radiated acoustic field, determined by solving the linear equations, to be compared directly with the evolution of the near- and far-field fluctuations in the DNS.

1. Background

Jet noise prediction is a particularly difficult problem because the complexity of turbulent flow permits only approximate experimental and theoretical description of the acoustic sources. Meanwhile, aeroacoustic theory requires such a description as input and attempts to predict jet noise *a posteriori* via solution of a linear wave equation for the radiated sound. Despite many years of investigation of acoustic sources in turbulent flows, fundamental questions persist which cannot be addressed without access to very detailed measurements of the near field turbulence.

Fortunately, computer power has increased to the point where it is now possible to simulate low Reynolds number turbulent jets without modeling approximations. Because this approach provides full knowledge of the jet flow, it permits a detailed examination of the acoustic sources.

Data from a Direct Numerical Simulation (DNS) of a Mach 1.92 (Freund, Lele & Moin 1998) jet is used here to investigate several issues related to the mechanisms of sound generation in turbulent jets:

1 California Institute of Technology
2 University of California, Los Angeles

- What is the relative contribution of large and small scales to the acoustic sources terms in turbulent jets?
- What role do linear instability waves play in the noise produced by supersonic turbulent jets?

In order to investigate the first question, we use the DNS data to compute the source terms for Lighthill's acoustic analogy. The solution to the acoustic analogy with these sources is then found and compared to the directly computed acoustic field. The results of this calculation are presented in Section 2. Once the efficacy of the acoustic analogy is established, the turbulent source terms can be investigated to understand how different scales of motion contribute to the overall acoustic field– we make some preliminary observations regarding the structure of the source in Section 2. The relevance of different scales, and how accurately significant scales may be represented on a hypothetical coarser mesh, has important implications for subgrid scale modeling in LES applications.

In Section 3, we investigate the radiation of acoustic waves by instability waves in supersonic jets. While it has been shown (*e.g.* Tam 1995) that the linear model correctly predicts certain trends in turbulent mixing noise in supersonic jets, it relies on an assumed distribution (and amplitude) of turbulence fluctuations at the nozzle exit, and detailed measurements and comparisons with the theory have not yet been made. In Section 3 we present a framework that we have developed to test some of the underlying assumptions of the linear theory and to attempt to validate its predictions against the directly computed acoustic field.

2. Acoustic analogy

An important issue in using an acoustic analogy to predict jet noise is the degree to which an acoustic analogy can predict the sound field given an "exact" representation of the source terms from numerical simulation as input. This depends, on one hand, to what extent discretization errors may affect the acoustic sources and, on the other hand, how reliable are the approximations made in separating source terms from propagation terms in the acoustic analogy. These issues were addressed in detail for vortex pairing in a two-dimensional mixing layer (Colonius, Lele & Moin 1997), but it is unclear to what extent the conclusions may be extended to a fully turbulent flow. To address these issues in the Mach 1.92 turbulent jet, we first consider the well-known equation of Lighthill (1952):

$$\ddot{\rho} - a_o^2 \rho_{,jj} = T_{ij,ij}, \tag{1}$$

where,

$$T_{ij} = \rho u_i u_j + (p - a_o^2 \rho)\delta_{ij} \tag{2}$$

with viscosity neglected. It is straightforward to compute the right-hand side of the equation and then solve Eq. (1) for the radiated acoustic field.

2.1 The Mach 1.92 turbulent jet and post-processing of DNS database

In this section we briefly discuss some of the issues pertaining to how the DNS database for the Mach 1.92 turbulent jet was analyzed. DNS of the fully compressible, turbulent round jet were performed by Freund (1998) using a method which

relies on 6th-order-accurate compact finite difference schemes in the axial and radial directions, Fourier spectral differentiation in the azimuthal direction, and 4th-order-accurate explicit Runge-Kutta time advancement. The computational domain extends to 31 jet radii downstream and 12 radii in the radial direction, and thus includes the near acoustic field. 640 x 270 x 128 nodes were used in the axial, radial, and azimuthal directions, respectively. The Reynolds number based on diameter was 2000, and the temperature ratio $T_j/overT_\infty$ was 1.12.

In order to simulate the turbulent jet inflow (thereby eliminating the need to simulate the nozzle as well as the jet), data from a turbulent streamwise periodic jet simulation (Freund, Moin & Lele 1997) was fed into the spatial computation. The simulations used to generate the inflow turbulence had a streamwise period of 21 radii. The amplitudes at the inflow were "jittered" by up to 5% to break any periodicity of the data.

The full instantaneous flow field was archived at roughly 7000 times (at increments of 10 computational time steps). For practical reasons, the data was saved on a mesh which consisted of every other computational node. Even at 1/8 of the full resolution, this yields a database nearly a quarter of a terabyte in size. A principal limitation in post-processing is the total amount of data that may be stored on disk and read into memory.

A large number of terms are involved in computing Lighthill's source term in cylindrical coordinates (the transformations are straightforward but tedious, and will not be reproduced here). Such terms involve second spatial derivatives of the computational data, and a problem was encountered in computing source terms smoothly through the coordinate singularity at $r = 0$. In this report we only consider predictions for Lighthill's equation for the axisymmetric ($m = 0$) mode, for which there were no accuracy issues near the centerline. However, we have recently devised a way to compute the sources on an interpolated Cartesian mesh, which appears to alleviate the centerline difficulty–an example of the source computed in this way is given in Section 2.3.

2.2 Numerical solution of the wave equation

In order to determine the acoustic field which results from a particular measured source term, Eq. (1) must be inverted. A variety of methods are available for this task. From a theoretical point of view, the simplest method would be to convolve the source with the Green's function for the three-dimensional wave equation. However, the resulting integrals depend on the source at retarded times. Given the enormous amount of data which would have to be sorted and interpolated for every such combination of source and observer location, this approach was deemed impractical. Instead we employ the less computationally intensive method of solving the wave equation directly in the time domain using finite differences. We discretize the wave equation with the same 6th-order-accurate compact finite difference scheme used in the jet computations, and integrate forward in time with a 4th order Runge-Kutta time algorithm. The source is Fourier transformed in the azimuthal direction since the wave equation is linear and each azimuthal mode may, in turn, be found independently. The computational grid is chosen to be identical to that on which

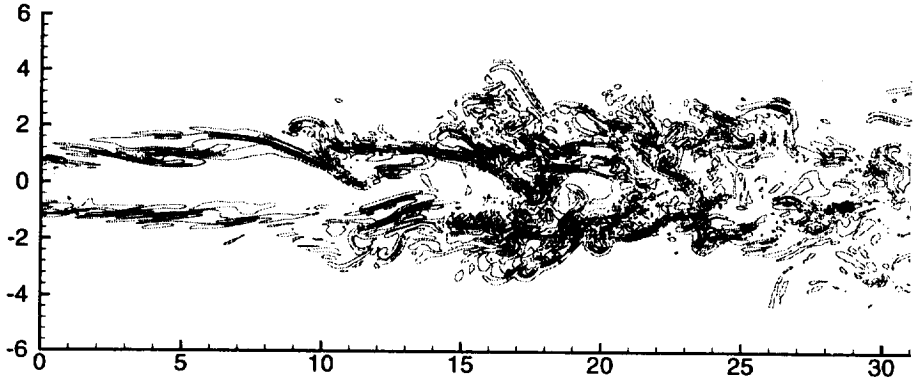

FIGURE 1. Contours of the instantaneous $T_{ij,ij}$ in the plane $\theta = 0, \pi$.

the source data was saved except that in the radial direction we interpolate the source (using a 6th-order-accurate compact interpolation scheme) to a staggered mesh where accurate differencing through the polar coordinate singularity may be achieved (Mohseni & Colonius 1997). One-dimensional characteristic boundary conditions are used together with a buffer region near the computational boundary where the damping terms are added to the wave equation (Freund 1997).

The source terms at a given instant in time are found by performing a cubic spline interpolation of the sources saved at discrete intervals in time. In order to avoid sharp initial transients produced by turning on the source at $t = 0$, we ramp-up the forcing over a time period which is long compared to the dominant frequencies in the acoustic field.

2.3 Results

Figure 1 shows an instantaneous view of the Lighthill source term, $T_{ij,ij}$, at the plane $\theta = 0, \pi$ through the jet. It is clear that, instantaneously, small-scales are dominant contributors to the source. As discussed below, one cannot conclude that these are also dominant contributors to the acoustic field since the source field is comprised of fluctuations whose wavenumber/frequency characteristics prohibit radiation to the far field.

Nevertheless, it is interesting to see how accurately the acoustic field predicted from the full instantaneous source agrees with the directly computed field. The source field was computed (for the $m = 0$ mode only) for 500 of the archived DNS fields and input into the wave equation solver. For the axisymmetric mode in the acoustic field, the instantaneous prediction at the final time is compared in Fig. 2 with the directly computed acoustic field. The quantitative agreement is quite

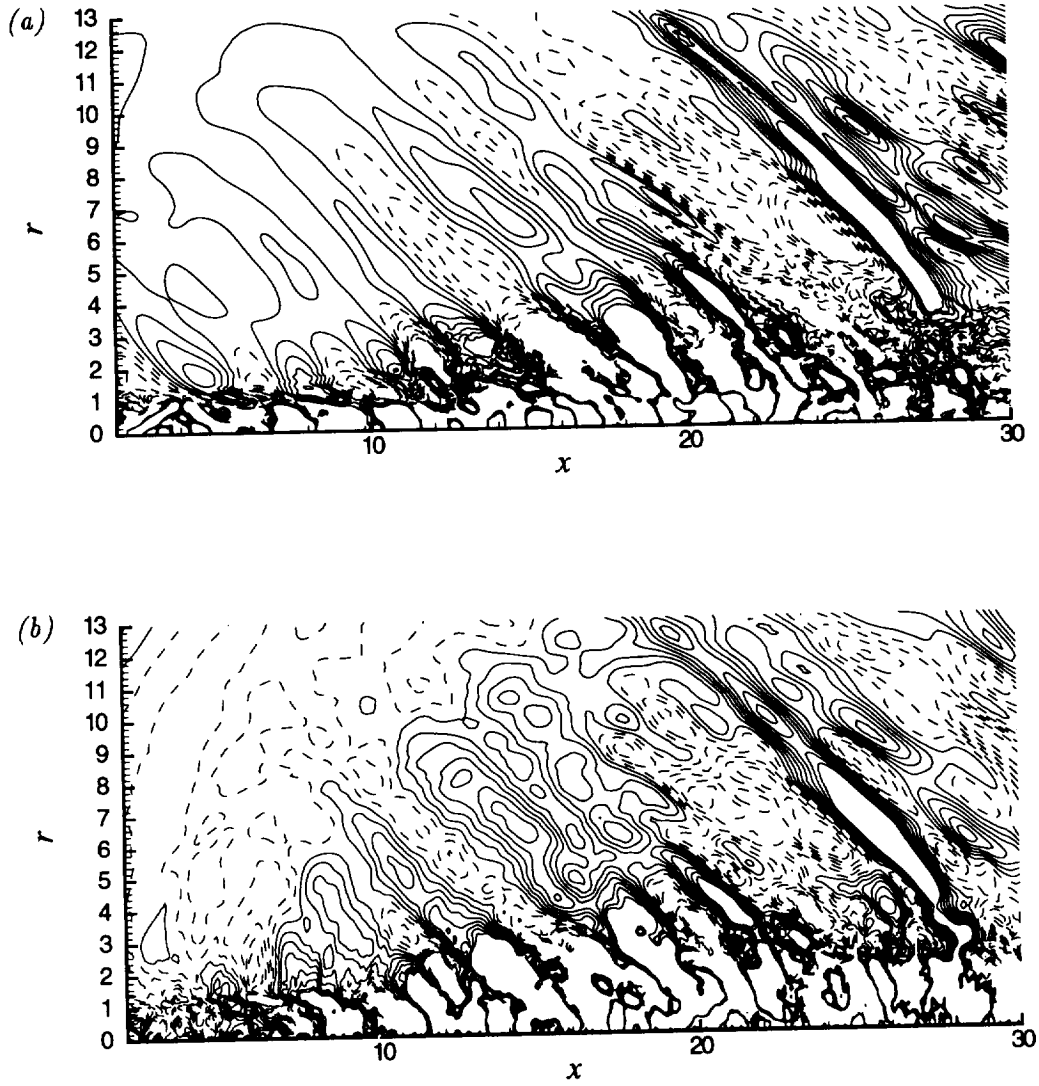

FIGURE 2. Contours of the instantaneous dilatation for the $m = 0$ mode, directly computed via (a) DNS and (b) by the solution of Lighthill's equation. Contour levels (both figures), 15 contours between -0.02 to 0.02, negative contours are dashed.

good, with the Lighthill solution accurately reproducing the major features of the acoustic field such as the strong Mach wave radiation at angles between 45 and 55 degrees from the jet axis. Further work is needed to compute the solution for other azimuthal modes.

Once the acoustic analogy has been validated in this way, we may proceed to

analyze the sources to understand and, ultimately, model in a simple way the physics of sound generation by the flow. An important first step in this process is to (approximately) decompose the source term into its radiating and non-radiation components. As noted above, small scales dominate the instantaneous value of the source; however, physical space and real time are not the most natural space in which to examine the acoustic sources. This is because a large portion of the source is composed of wavenumber/frequency combinations which are not able to radiate to the acoustic field. It can be shown that only those wavenumber/frequency combinations whose phase speed is supersonic with respect to any ambient flow may radiate to the far field (Crighton 1975).

An exact decomposition into wavenumber/frequency space requires strict periodicity (or infinite extent) of the source. For spatially evolving flows on a finite computational domain, this condition is not met, and further information regarding the decay of the acoustic sources downstream of the computational boundary must be supplied in order to accurately transform the source in the axial direction. This can be done in a semi-analytical way if the acoustic source is simple enough (*e.g.* Colonius *et al.* 1997, Mitchell, Lele & Moin 1995, Wang, Lele & Moin 1996). It is likely, however, that such methods will fail for a fully turbulent source, and thus we seek an alternative. We anticipate using approximate band-pass filters which can be constructed in real space (*e.g.* Lele 1992) for non-periodic data.

3. Linear stability theory

For jets with sufficiently high Mach number (essentially with a convective Mach number greater than 1), it is know that linear instability waves directly radiate sound to the far field (*e.g.* Tam & Burton 1984). This observation gives rise to an alternative to the acoustic analogy approach in this case. The near field and far field are constructed simultaneously as a solution to linear equations, and the flow acts, in essence, as an amplifier of some prescribed disturbances, with the amplification and eventual decay giving rise to the production of acoustic waves.

Such linear modeling has been shown to produce trends in the radiated sound pressure level similar to noise measurements at various frequencies and at angles where the acoustic field is thought to be dominated by contributions from the large scale structures (Tam 1995). However, the model cannot, without further ad-hoc assumptions, predict the amplitude of the acoustic radiation (devoid of any measurements of the turbulence incident from the nozzle), and a detailed computational or experimental verification of the linear modeling has not previously been attempted.

In application of the linear model, the mean jet flow (from experiment or RANS modeling) is assumed known, and initial amplitude for the eigenfunctions (at a particular frequency) are specified according to an assumed frequency spectrum. Typically only the most unstable mode is considered. The evolution of the mode in the slightly non-parallel mean flow is then found by marching downstream at a particular frequency. Unstable modes eventually stabilize and decay as the mean flow spreads. The envelope function, which describes the growth, saturation, and decay of the mode, can then be used to compute the radiated acoustic field using

the method of matched asymptotic expansions. For details, the reader is referred to Tam & Burton (1984).

We believe that the DNS data for the Mach 1.92 jet will be useful in testing the validity of the linear theory. We present here a framework that we developed to compare the linear stability predictions with the (nonlinear) DNS solution. Though straightforward, the calculations are laborious and have not yet been completed. We hope to give the results in a future publication.

At streamwise locations throughout the jet, we transform the DNS data into frequency space and wavenumber space in the azimuthal direction. These fluctuations are then the initial condition for the instability wave calculation. To determine the initial amplitude of the most unstable wave, we observe that an arbitrary fluctuation field can be completely decomposed into a discrete set of unstable waves plus a continuous spectrum of stable modes of the linearized equations (*e.g.* Drazin & Reid 1981). Furthermore, if the adjoint eigenfunctions corresponding to the most unstable mode can be computed, the amplitude of the most unstable mode can be found *without* computing the entire continuous spectrum of stable modes.

This approach may be unfamiliar to some readers, so we briefly discuss the derivation of the equations. We have a (locally) parallel base flow with streamwise velocity, $\bar{u}(r)$, density $\bar{\rho}(r)$, and pressure $\bar{p}$ =constant. Let $\phi(x,r,\theta,t) = \{u,v,w,p\}^T$ be the velocity components (streamwise, radial, and azimuthal) and pressure, and let $\tilde{\phi}(x,r,\theta,t)$ be the solution to the adjoint equations. Then, substituting $\phi(x,r,\theta,t) = \phi(r)e^{i(\alpha x+n\theta-\omega t)}$ into the Euler equations linearized about the base flow, we obtain:

$$\begin{aligned} i(\alpha\bar{u}-\omega)\bar{\rho}u + \bar{\rho}\frac{\partial\bar{u}}{\partial r}v + i\alpha p = 0 \\ i(\alpha\bar{u}-\omega)\bar{\rho}v + \frac{\partial p}{\partial r} = 0 \\ i(\alpha\bar{u}-\omega)\bar{\rho}w + \frac{in}{r}p = 0 \\ i(\alpha\bar{u}-\omega)\frac{p}{\gamma\bar{p}} + i\alpha u + \frac{1}{r}\frac{\partial(rv)}{\partial r} + \frac{in}{r}w = 0. \end{aligned} \tag{3}$$

The corresponding adjoint equations may be found in a straightforward way:

$$\begin{aligned} i(\tilde{\alpha}\bar{u}-\tilde{\omega})\bar{\rho}\tilde{u} + i\tilde{\alpha}\tilde{p} = 0 \\ i(\tilde{\alpha}\bar{u}-\tilde{\omega})\bar{\rho}\tilde{v} + \bar{\rho}\frac{\partial\bar{u}}{\partial r}\tilde{u} + \frac{\partial\tilde{p}}{\partial r} = 0 \\ i(\tilde{\alpha}\bar{u}-\tilde{\omega})\bar{\rho}\tilde{w} + \frac{i\tilde{n}}{r}\tilde{p} = 0 \\ i(\tilde{\alpha}\bar{u}-\tilde{\omega})\frac{\tilde{p}}{\gamma\bar{p}} + i\tilde{\alpha}\tilde{u} - \frac{1}{r}\frac{\partial(r\tilde{v})}{\partial r} + \frac{i\tilde{n}}{r}\tilde{w} = 0. \end{aligned} \tag{4}$$

where $\tilde{\phi}(x,r,\theta,t) = \tilde{\phi}(r)e^{-i(\tilde{\alpha}x+\tilde{n}\theta-\tilde{\omega}t)}$.

One can easily check that the following Lagrange identity is satisfied

$$i(\tilde{\omega}-\omega)Z(r) - i(\tilde{\alpha}-\alpha)\{\tilde{u}Z(r)+p\tilde{u}+\tilde{p}u\} - i(\tilde{n}-n)\frac{1}{r}(p\tilde{w}+\tilde{p}w) = -\frac{1}{r}\frac{\partial}{\partial r}(r(\tilde{v}p-v\tilde{p})), \tag{5}$$

where $Z(r) = \bar{\rho}(u\tilde{u} + v\tilde{v} + w\tilde{w}) + \frac{p\tilde{p}}{\gamma\bar{p}}$.

For the spatially evolving instability waves we have $\tilde{\omega} = \omega$ and $n = \tilde{n}$. Therefore if ϕ_i and $\tilde{\phi}_j$ are the eigenfunctions to the flow equations (3) and the adjoint equations (4) corresponding to the eigenvalues α_i and α_j, we have the *biorthogonality* relation

$$[\phi_{\alpha_i}, \tilde{\phi}_{\alpha_j}] = 0 \qquad \text{if} \quad \mathrm{i} \neq \mathrm{j} \tag{6}$$

where

$$[\phi, \tilde{\phi}] = \int_0^\infty (\bar{u}Z(r) + p\tilde{u} + u\tilde{p})rdr. \tag{7}$$

Let us denote the DNS data (transformed into frequency and azimuthal wave space at a particular streamwise location) by ϕ_{DNS}. Then we expand ϕ_{DNS} in terms of the eigenfunctions:

$$\phi_{DNS}(r) = \sum_{j=1}^{N} c_j \phi_j(r) + \text{Integral over continuous spectrum} \tag{8}$$

where N is the number of discrete spatial modes. Now multiply both sides of Eq. (8) by the adjoint eigenfunction $\tilde{\phi}_{\alpha_i}$, and, using the biorthogonality relation (6), we obtain

$$c_i = \frac{[\phi_{DNS}, \tilde{\phi}_{\alpha_i}]}{[\phi_{\alpha_i}, \tilde{\phi}_{\alpha_i}]} \tag{9}$$

Of particular interest will be the evolution of the most unstable wave as a function of streamwise location in the jet, and the acoustic field predicted from the (matched asymptotic expansion of the) linear equations, as compared to the acoustic field from the DNS.

4. Closing remarks

We have analyzed data from the DNS of a turbulent Mach=1.92 jet to address several issues related to noise generation mechanisms. As a first step towards understanding the turbulent sources of sound, we have computed the full Lighthill source terms and found solutions of the wave equation with these sources. We have found a good agreement for the $m = 0$ mode, paving the way for a detailed analysis of the sources to determine how various scales in the near field turbulence contribute to the radiated acoustic field.

For supersonic jets, we have also developed a framework to test the validity of the well-known linear stability wave model (*e.g.* Tam 1995) of sound generation by the large-scale turbulence. By using the adjoint to the linear stability equations, we are able to compute the projection of the DNS data onto the most unstable mode at different streamwise positions. The amplitude of the stability wave thus set, we may proceed to compute the evolution of the wave and its radiated acoustic field by solving the linear equations and compare the resulting acoustic field with the DNS. We hope to present the results of the analysis in a future publication.

REFERENCES

COLONIUS, T., LELE, S. K. & MOIN, P. 1997 Sound generation in a mixing layer. *J. Fluid Mech.* **330,** 375-409.

CRIGHTON, D. G. 1975 Basic principles of aerodynamic noise generation. *Prog. Aerospace Sci.* **16,** 31-96.

DRAZIN, P. & REID, W. 1981 *Hydrodynamic Stability.* Cambridge University Press.

FREUND, J. B. 1997 Proposed inflow/outflow boundary condition for direct computation of aerodynamic sound. *AIAA J.* **35,** 740-742.

FREUND, J. B. 1998 On the role of linear instability modes in a turbulent annular mixing layer. *Submitted to Phys. Fluids.*

FREUND, J., LELE, S. & MOIN, P 1998 Direct simulation of a Mach 1.92 jet and its sound field. *AIAA/CEAS 98-2291.*

FREUND, J., MOIN, P. & LELE, S. 1997 Compressibility effects in a turbulent annular mixing layer. *Technical Report TF-72,* Department of Mechanical Engineering, Stanford University.

LELE, S. K. 1992 Compact finite difference schemes with spectral-like resolution. *J. Comput. Phys.* **103,** 16–42.

LIGHTHILL, M. J. 1952 On sound generated aerodynamically. I: General theory. *Proc. Royal Soc. London A.* **211,** 564-587.

MITCHELL, B. E., LELE, S. K. & MOIN, P. 1995 Direct computation of the sound generated by subsonic and supersonic axisymmetric jets. *Technical Report TF-66,* Department of Mechanical Engineering, Stanford University.

MOHSENI, K. & COLONIUS, T. 1997 Numerical treatment of polar coordinate singularities in finite difference and pseudo-spectral schemes. *Division of Engineering and Applied Science, Caltech.*

TAM, C. K. 1995 Supersonic jet noise. *Ann. Rev. Fluid Mech.* **27,** 17-43.

TAM, C. K. W. & BURTON, D. 1984 Sound generated by instability waves of supersonic flows. Part 1. Two-dimensional mixing layers, Part 2. Axisymmetric jets. *J. Fluid Mech.* **138,** 249-295.

WANG, M., LELE, S. K. & MOIN, P. 1996 Computation of quadrupole noise using acoustic analogy. *AIAA J.* **34,** 2247-4344.

The fundamentals group

Four of the summer projects were put in a category called Fundamentals because they involved fundamental ideas not clearly associated with any of the other project groups. This does not imply that other projects were any less fundamental.

The project on LES in complex boundaries, by Verzicco, Mohd-Yusof, Orlandi, and Haworth, was designed to test the *immersed boundary method* for representing fixed and moving boundaries on a stationary Cartesian mesh as applied to flow in a motored axisymmetric piston-cylinder system. Calculations were made assuming axisymmetric flow (2D mesh) for the purposes of method development, followed by DNS and LES with a full 3D concentric structured mesh initialized by a perturbation on the axisymmetric initial field. The method was shown to be extremely effective and relatively inexpensive compared to calculations on a deforming unstructured mesh.

The DNS study of trailing vortices by Orlandi, Carnevale, Lele, and Shariff was an exploration of some new ideas for accelerating the breakup of aircraft trailing vortices. The group first studied a basic short-wavelength instability associated with interaction of the two vortices and then turned their attention to an exploration of how density variation along the axis of the vortices (perhaps produced by modulated engine exhaust entrainment) might be used to accelerate the breakup. The work showed that these density variations could indeed accelerate the rapid cross-diffusion of vorticity between the primary vortices when they are close to one another and thus opened the door to a possible new way of aircraft trailing vortex control.

A method for predicting the statistics of turbulence using a Rayleigh-Ritz variational formulation was explored by Eyink and Wray. This was an attempt to bring ideas from non-linear dynamics to bear on study of turbulence. The theory provides a procedure for calculating the evolution of the two-time velocity cospectra from the evolution of k and ε as found from a k-ε model, using a modeled Langevin equation for the Fourier coefficients of the velocity fluctuations. The goal of the project was to test this model and, if possible, to improve it. The k-ε-RR model appeared to work well for short time separations. A simple convection correction seemed to improve things for longer time separations, suggesting to the authors that a RANS-RR model could give much better long-time predictability.

Oberlack has been applying Lie Group Analysis to a variety of turbulent flow problems, most recently flow in a channel being rotated about a streamwise axis. This is a model flow for studying the effects of frame rotation in axial flow turbomachinery. The group analysis predicts the scaling that one should find in this flow, and the objective of the paper by Oberlack, Cabot, and Rogers was to test this using DNS. The work confirms the basic linear mean streamwise and spanwise velocity variations predicted by the group analysis. The DNS was limited by the size of the computational domain, but it was sufficient to show that this is a very interesting canonical test case. Common two-equation models do not account

for rotation effects, so this flow is both a challenge to turbulence modeling and a possible source for inspiration and calibration of new turbulence models.

W. C. Reynolds

Center for Turbulence Research
Proceedings of the Summer Program 1998

LES in complex geometries using boundary body forces

By R. Verzicco[1], J. Mohd-Yusof, P. Orlandi[1] AND D. Haworth[2]

A numerical method is presented which can simulate flows in complex geometries with moving boundaries while still retaining all the advantages and the efficiency of solving the Navier-Stokes equations on cylindrical grids. The boundary conditions are applied independently of the grid by assigning body forces over surfaces that need not coincide with coordinate lines.

The method has been validated by a large-eddy simulation of the flow in a motored axisymmetric piston-cylinder assembly for which experimental measurements are available. The comparison of the results has shown a very good agreement for mean and rms velocity profiles, thus confirming the accuracy of the present approach. This numerical method, in addition, runs on a small PC-like workstation ten times faster than corresponding simulations on supercomputers.

In large-eddy simulations the dynamic subgrid-scale model is very efficient in combination with the body force procedure because it automatically accounts for the walls without requiring ad hoc damping functions. This feature is very useful in the present approach since the body surface in general does not coincide with a coordinate line and the computation of the wall distance is time consuming.

1. Introduction

Numerical simulations are extensively used by industries as a fundamental tool in the design and test of prototypes. Computer simulations allow for the rapid investigation of wide parameter ranges or the testing of novel technological solutions without resorting to expensive experimental setups and measurements.

The most detailed numerical simulations up to now have been performed in extremely simple geometries since in these conditions the efficiency of the solution procedures is maximized and the storage requirements of the computer codes are the least. For example, homogeneous isotropic turbulence in a tri-periodic box has been simulated using 512^3 nodes or more, and comparable high resolutions have been achieved in the plane channel flow or in mixing layers.

Unfortunately, in the majority of industrial applications, the flow is strongly dominated by the domain geometry, and even the simplest flow features can not be reproduced if the shape of the boundary is not properly accounted for. In such

1 Università di Roma "La Sapienza" Dipartimento di Meccanica e Aeronautica, via Eudossiana 18 00184 Roma, Italy.

2 Engine Research Department, GM R&D Center, 30500 Mound Road 106, Warren, MI 48090-9055

circumstances curvilinear coordinates fitted on the body are currently used even if most of the efficiency of the solution procedure is lost. In addition, the complexity of the computer code as well as the number of operations per node and storage requirements are increased. Therefore, given the finite amount of memory available on each computer, the maximum number of nodes over which the flow can be computed is reduced.

Another factor increasing the complexity of the numerical simulations is the presence of moving boundaries. In fact, when boundary fitted meshes are employed, the grid must be recomputed as the geometry changes, thus considerably increasing the computational time. Unfortunately in industrial flows the presence of boundaries in relative motion is the rule rather than the exception, making the computations very time consuming.

The last point to be considered is the Reynolds number, which in real applications is usually far too high to make the flow affordable by direct numerical simulation (DNS). Industrial flows, in fact, are usually turbulent, and their resolution must rely on turbulence modeling such as the large-eddy simulation (LES) approach or the Reynolds averaged Navier-Stokes equations (RANS).

From this scenario it appears that flows of practical interest, owing to the combination of complex geometries, moving boundaries, and high Reynolds numbers, make their computation extremely expensive, and the use of an alternative approach is very much desirable.

In this report we illustrate an alternative procedure for simulating complex flows while retaining the advantages of orthogonal fixed grids. Specifically, we will test and validate a method in which boundary conditions are assigned independently of the grid by prescribing suitable body forces. These forces are such as to yield a desired velocity value $\overline{\mathbf{v}}$ on a given surface, which in general will not coincide with the coordinate lines and will move in time. Indeed this idea is not new since Peskin (1972) already used a similar approach. More recently Goldstein, Handler & Sirovich (1993) and Saiki & Biringen (1996), have shown further examples in which complex boundaries were mimicked using body forces on a Cartesian mesh. The main drawback of all these procedures was the largely reduced stability limit of the time integration scheme. Goldstein Handler & Sirovich (1993), for example, point out that when computing the flow around a circular cylinder their time step could not be bigger than $5\cdot10^{-5}$-$5\cdot10^{-4}$, which yielded a CFL between $4\cdot10^{-3}$-$4\cdot10^{-2}$. It is clear that with this restriction this technique is mainly limited to two-dimensional flows and its validity is largely compromised. A different expression for the forcing was suggested by Mohd-Yusof (1996,1997) and Mohd-Yusof & Lumley (1994,1996), who, by computing the laminar flow over a riblet and the flow around cylinders, showed the stability limit of the integration scheme to be essentially unaffected by the forcing. This new forcing was used by Fadlun, Verzicco & Orlandi (1998), who showed that, though the results are essentially the same as those obtained by the old method, the time step remains large enough to make three-dimensional simulations affordable. In that work the results were validated by an ad hoc experiment.

Although the method is in principle very general, to our knowledge it was never

applied before to a real flow of practical interest in which complex geometries, moving boundaries, and turbulence models are required. The main aim of this report is to show some results obtained for the computation of a motored piston-cylinder assembly whose Reynolds number is high enough to require the use of an LES approach. The results are compared with an experiment performed in exactly the same conditions (Morse, Whitelaw & Yianneskis, 1978), indicating that the present method is a good candidate to simulate industrial flows in an inexpensive way.

2. The problem

The configuration chosen to validate the present numerical procedure is a simplified axisymmetric piston-cylinder assembly with a fixed central valve. Both, cylinder head and piston are flat (pancake chamber), and a sketch of the geometry is given in Fig. 1.

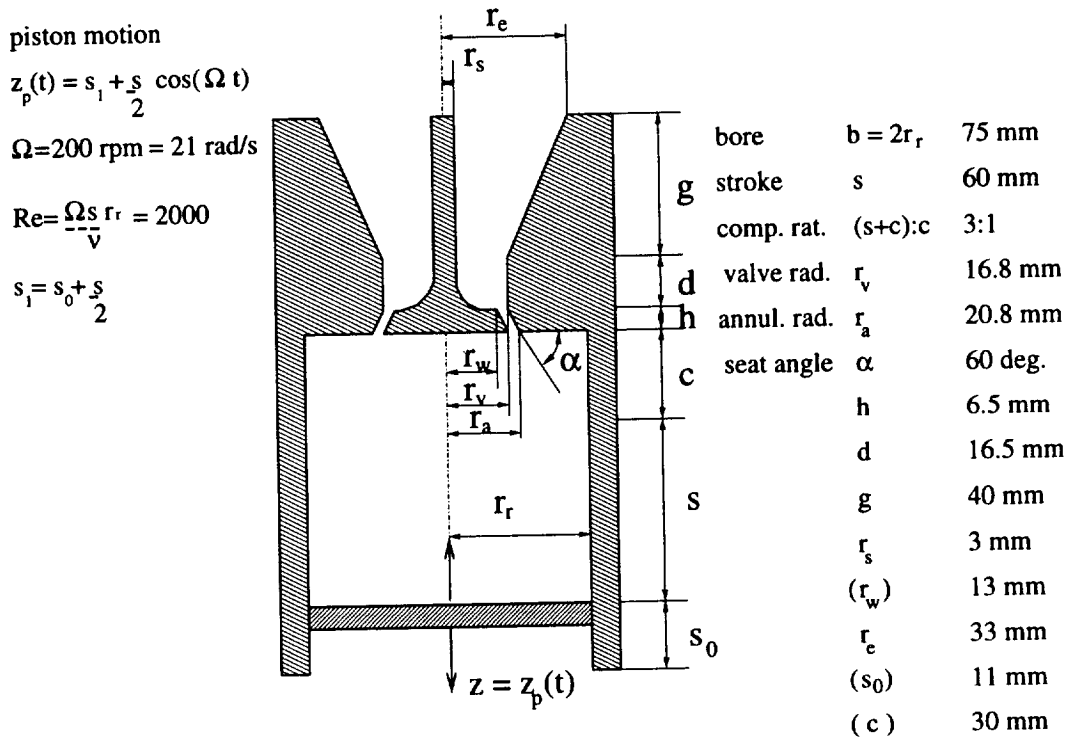

FIGURE 1. Sketch of the problem.

In the experiment the piston was externally motored so that the fluid flowed into the cylinder from outside during the downward piston motion and vice-versa when the piston was moved up. Since the valve was fixed and a tiny annular gap was left open between the valve and the cylinder head, no compression phase was included in the flow dynamics. The piston was driven by a simple harmonic motion at a

speed of 200rpm $\simeq$ 21rad/s, which for the present geometry yields a mean piston speed of $\overline{V}_p = 0.4$m/s (when averaged over half cycle).

Experimental measurements were available for the validation of the numerical results. In particular, Morse *et al.* (1978) used Laser-Doppler anemometry to measure phase-averaged mean and rms radial profiles of axial velocity. The profiles were available at 10mm increments starting from the cylinder head for crank angles 36° and 144° after top dead center.

3. Equations, solution procedure, and simulation set-up

The governing equations for the LES of the piston-cylinder assembly are the filtered Navier-Stokes equations with the boundary body force **f**:

$$\frac{D\overline{\mathbf{u}}}{Dt} = -\nabla\overline{P} + \nabla\cdot\{\tilde{\nu}[\nabla\overline{\mathbf{u}} + (\nabla\overline{\mathbf{u}})^T]\} + \mathbf{f}, \tag{1a}$$

$$\nabla\cdot\overline{\mathbf{u}} = 0. \tag{1b}$$

Here $\overline{\mathbf{u}}$ is the filtered velocity, $\overline{P}$ is the sum of the filtered pressure and the trace of the sub-grid scale stress tensor while its anisotropic part q_{ij} has been parametrized by the dynamic sub-grid scale model through $q_{ij} = -2\nu_t\overline{S}_{ij}$ with ν_t the turbulent viscosity and $\overline{S}_{ij}$ the filtered rate of strain tensor. With this notation $\tilde{\nu}$ is defined as $\tilde{\nu} = \nu_t + 1/Re$, and the Reynolds number is $Re = \Omega s r_r/\nu$ (see figure 1) with ν the kinematic viscosity of the fluid. The turbulent viscosity ν_t was determined by a dynamic procedure (Germano *et al.*1991 and Lilly 1992) that does not require external constants. Since the flow is unsteady and inhomogeneous in time, the averaging in the computation of the constant C in the expression of the turbulent viscosity ($\nu_t = C\Delta^2(2\overline{S}_{ij}\overline{S}_{ij})^{1/2}$, with Δ the local grid spacing) was performed only in the azimuthal direction and among the closest neighbors in the radial and axial directions. All the points with total viscosity $\tilde{\nu}$ smaller than zero were then clipped, and they never exceeded 3% of the total points.

The boundary body force **f** is prescribed at each time step on a given surface so that the desired velocity $\overline{\mathbf{v}}$ is obtained on that boundary. As shown by Mohd-Yusof (1996), considering the time-discretized version of Eq. (1a), one can write

$$\overline{\mathbf{u}}^{n+1} - \overline{\mathbf{u}}^n = \Delta t(RHS + \mathbf{f}), \tag{2}$$

where RHS contains the nonlinear, pressure, and viscous terms. If we want $\overline{\mathbf{u}}^{n+1} = \overline{\mathbf{v}}$ then **f** has to be

$$\mathbf{f} = -RHS + \frac{\overline{\mathbf{v}} - \overline{\mathbf{u}}^n}{\Delta t} \tag{3}$$

in the flow region where we want to mimic the body and zero elsewhere. Of course in general the surface of the region where we want $\overline{\mathbf{u}}^{n+1} = \overline{\mathbf{v}}$ will not coincide with a coordinate line (Fig. 2); therefore, the value of **f** on the cell node closest to the surface but outside the body is linearly interpolated between the actual value inside the body and the zero value in the flow. The interpolation procedure is consistent

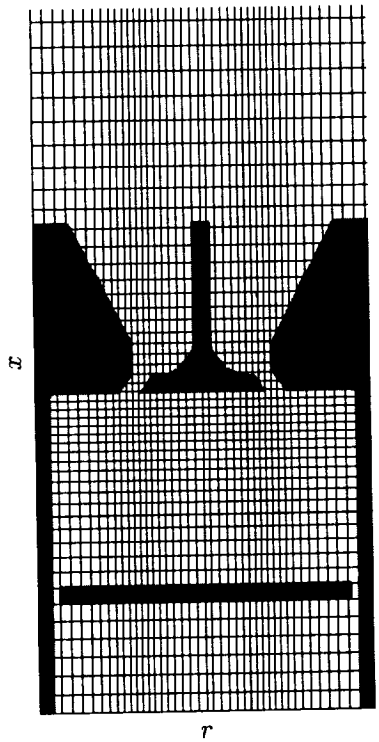

FIGURE 2. Vertical section through the meridional planes $\theta = 0$ and $\theta = \pi$ of the computational grid (only 1 every 4 grid points are shown) and the body force distribution to mimic the geometry of Fig. 1.

with the central finite-difference approximation since both of them are second-order accurate. Further details will be given in a forthcoming paper where this procedure is shown to be consistent with the second order accuracy of the scheme.

Equations (1) have been discretized in a cylindrical coordinate system by central second-order accurate finite-difference approximations on a staggered grid. Details of the numerical method are given in Verzicco & Orlandi (1996); therefore, only the main features are summarized here. In the three-dimensional case, in the limit of $\nu \rightarrow 0$, the energy is conserved and this holds in the discretized equations. The system is solved by a fractional-step method with the viscous terms computed implicitly and the convective terms explicitly; the large sparse matrix resulting from the implicit terms is inverted by an approximate factorization technique. At each time step the momentum equations are provisionally advanced using the pressure at the previous time step, giving an intermediate non-solenoidal velocity field. A scalar quantity Φ is then introduced to project the non-solenoidal field onto a solenoidal one. The large band matrix associated with the elliptic equation for Φ is reduced to a penta-tridiagonal matrix using trigonometric expansions (FFTs) in the azimuthal direction; the matrix is then inverted using the FISHPACK package. A hybrid low-storage third-order Runge-Kutta scheme is used to advance the equations in

time. Finally, in cylindrical coordinates the equations are singular at $r = 0$. The advantage of using staggered quantities is that only the radial component of the momentum equation needs to be evolved at the centerline ($r = 0$), and for this component we calculate the evolution of $q_r = ru_r$ instead of u_r since the former quantity clearly vanishes on the centerline.

The simulation set-up for the problem described in Section 1 is shown in Fig. 2. The lower boundary of the domain is inflow or outflow with a prescribed velocity profile depending on the phase of the piston motion. The upper boundary is also inflow or outflow, but a convective boundary condition for the velocities has been used. Thus if u_i is the i-th velocity component, the equation

$$\frac{\partial u_i}{\partial t} + C_i \frac{\partial u_i}{\partial x} = 0 \tag{3}$$

is solved at the boundary, and C_i is explicitly determined from the previous time step. The lateral wall of the computational domain is free-slip, and all of the no-slip boundary conditions at the body surfaces are enforced by **f**.

The axisymmetric simulations have been started from rest, and the transient (typically 2 cycles) has been discarded. In order to save computational time, the three-dimensional DNS and LES were restarted from the corresponding axisymmetric field, replicated in the azimuthal direction with a random azimuthal velocity field ($|u_\theta|_{\max} = 0.25\overline{V}_p$) superimposed. The initial transient was thus reduced to one cycle.

4. Results

Since the flow inside the piston engine is turbulent, unsteady, and fully three-dimensional, the numerical simulation must cope with all of these aspects. Nevertheless, in order to test the procedure, before considering the whole problem we have simulated the flow at a lower Reynolds number with the hypothesis of axisymmetry. This simulation served also as a guideline for the analysis of the large-scale dynamics, which in the fully turbulent case become less clear. The results are given in Fig. 3 where azimuthal vorticity maps at six instants within a cycle are shown. At $t = 0$ the piston starts its descent and the fluid is sucked from outside into the cylinder through the annular gap between the central valve and the cylinder head. This generates a high speed jet which impinges on the side wall and eventually separates owing to viscous effects. At $t = \pi/2$ the velocity of the jet is the highest, and the flow is completely dominated by the toroidal vortex, which grows in size as the piston moves down. It should be noted that if $V_p(t)$ is the piston speed, on account of mass conservation, the jet velocity should be about $10V_p(t)$; in reality, the jet velocity is even higher since the boundary layers developing on the walls of the annular gap reduce the effective area.

The interaction of the jet with the horizontal and vertical walls generates a variety of smaller structures already visible at $t = \pi/2$. Later on, when the piston decreases its speed, the jet does not have enough momentum to penetrate the flow down to the piston, but rather generates structures which remain localized close to the valve.

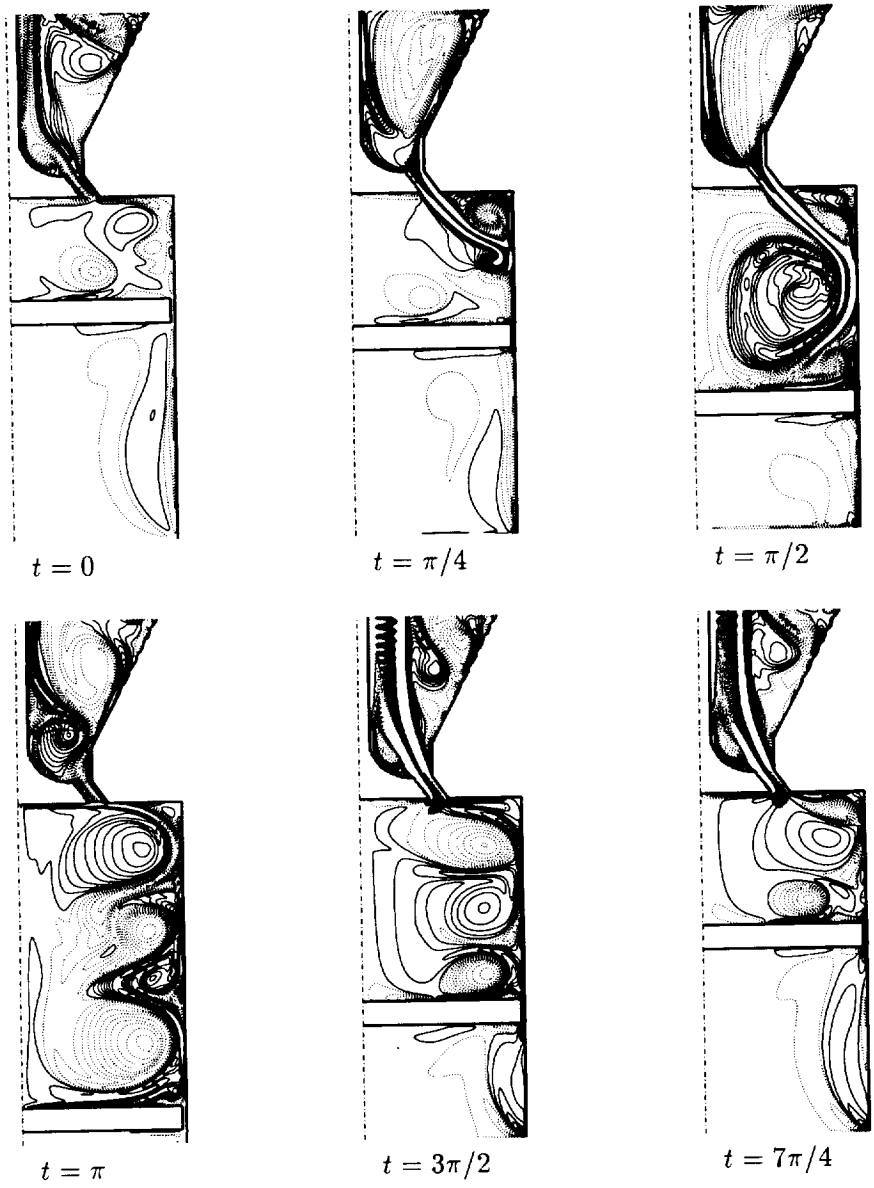

FIGURE 3. Contour plots of azimuthal vorticity at $Re = 625$, (129×385 grid). —— positive ····· negative values ($\Delta\omega = \pm 2.5$).

The complex flow structure emerging from the interaction of all the recirculating vortices is shown at $t = \pi$ when the piston is at its lowest position. As the piston starts moving up, the flow structures are pushed out of the cylinder through the tiny channel again, generating a high speed jet but now in the exhaust region. At $t = 7\pi/4$ the piston is slowly reaching the top-dead-center position, and only a residual motion is left inside the cylinder; a new cycle will start with similar features at $t = 2\pi$. Note that below the piston a secondary flow is generated by the piston

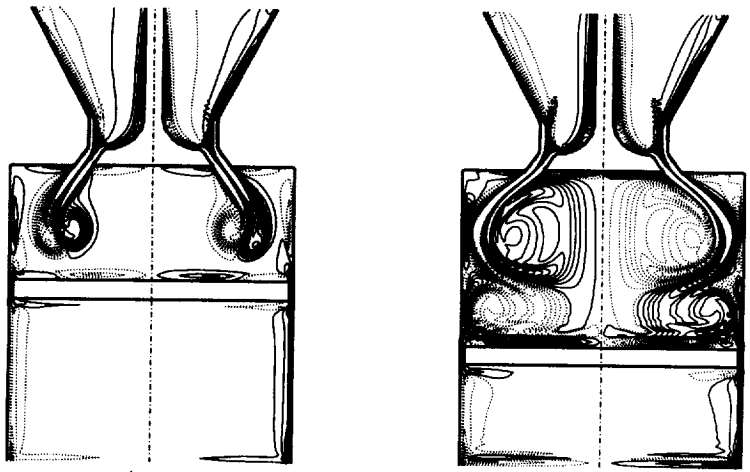

FIGURE 4. Contour plots of azimuthal vorticity at $Re = 315$; three-dimensional simulation without azimuthal perturbation ($97 \times 85 \times 193$ grid). ——— positive ····· negative values ($\Delta\omega = \pm 2.5$).

motion and by the mass flow imposed at the lower boundary. This flow, however, does not interact with the primary flow since the piston moves as a solid body as confirmed by the absence of vorticity inside the body.

Very similar dynamics were observed by Eaton & Reynolds (1987, 1989), who by smoke visualization and high-speed photography were able to capture the flow dynamics in an axisymmetric motored piston-cylinder assembly. In their description, however, it is clearly stated that when the piston reaches the bottom-dead-center (BDC) position, the flow is complex and very three-dimensional in nature. Haworth & Jansen (1997) simulated the same flow described in this report and they also found the flow to be fully three-dimensional and turbulent. These observations motivated us to set as the ultimate goal the three-dimensional simulation at the same Reynolds number as the experiment of Morse *et al.* (1978). However, before proceeding to the full simulation a few intermediate steps are necessary.

The first is to verify that the boundary body forces do not introduce any unphysical perturbation making the flow artificially three-dimensional. For this reason we have performed a three-dimensional simulation without initial azimuthal perturbation and we have verified that indeed the flow remains axisymmetric at least during the first two cycles. In Fig. 4 two vertical sections are shown of the flow at $Re = 315$, confirming that the symmetry about the central axis is preserved. Note that the

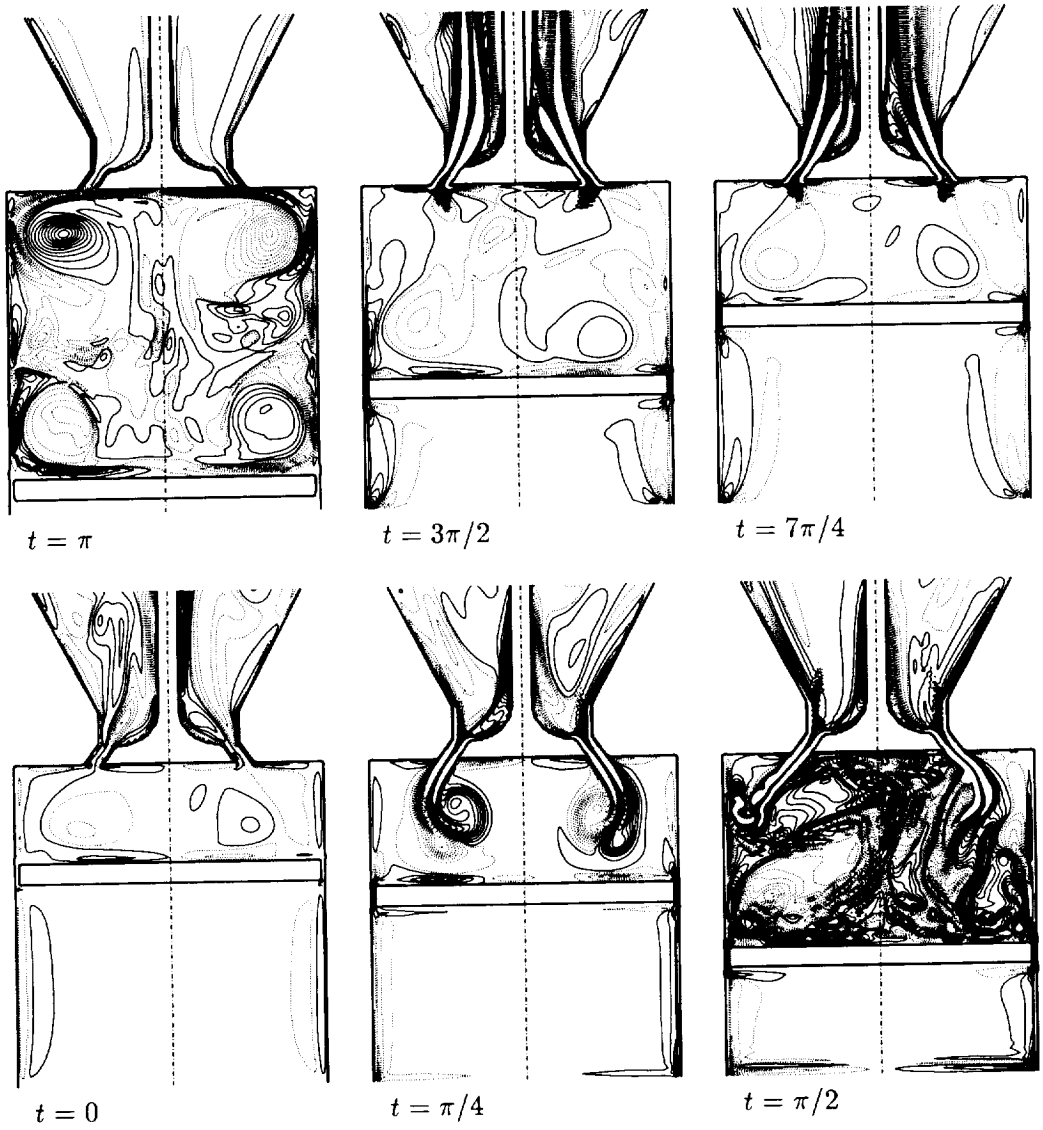

FIGURE 5. Contour plots of azimuthal vorticity at $Re = 315$; three-dimensional simulation with azimuthal perturbation ($97 \times 85 \times 193$ grid). —— positive ····· negative values ($\Delta\omega = \pm 2.5$).

Reynolds number of this simulation has been halved with respect to the axisymmetric case, and the reason is that the same radial and axial grid spacing could not be maintained with 97 grid points in the azimuthal direction. Given the reduced radial and axial resolution, we had to reduce the Reynolds number to fully resolve all the flow scales without resorting to a turbulence model. It could be argued that

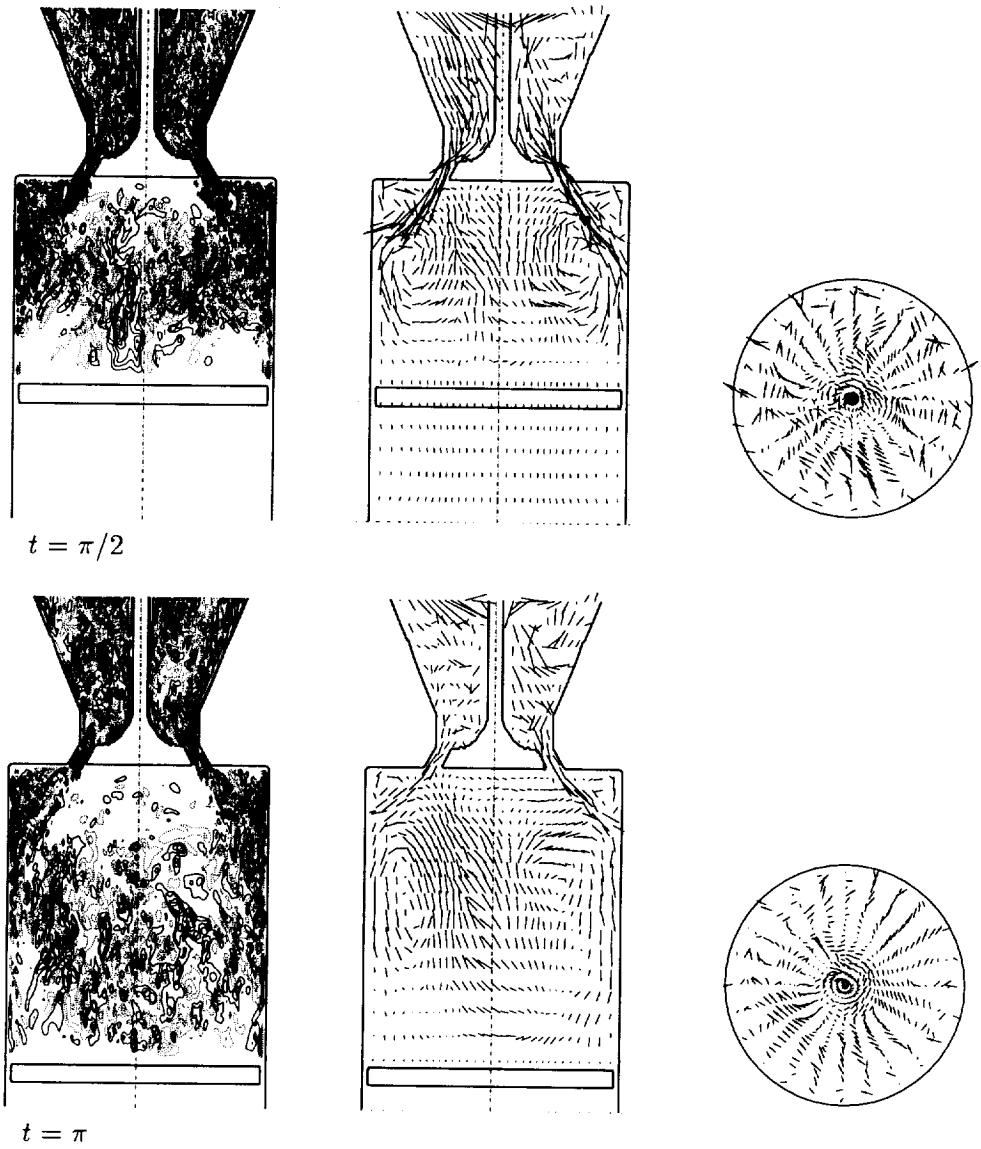

FIGURE 6. (Left) Contour plots of azimuthal vorticity at $Re = 2000$ ($65 \times 65 \times 151$ grid). —— positive ····· negative values ($\Delta\omega = \pm 2.5$). (Center) meridional velocity vectors. (Right) horizontal velocity vectors in a section 15mm below the cylinder head.

the reduced Reynolds number is the reason for the symmetry conservation; however, the same simulation with an initial azimuthal perturbation shows that indeed this is not the case. In Fig. 5 six vorticity snapshots taken across two consecutive cycles are reported showing that strong three-dimensionalities develop and that, differently from the axisymmetric case, the flow does not repeat itself after each

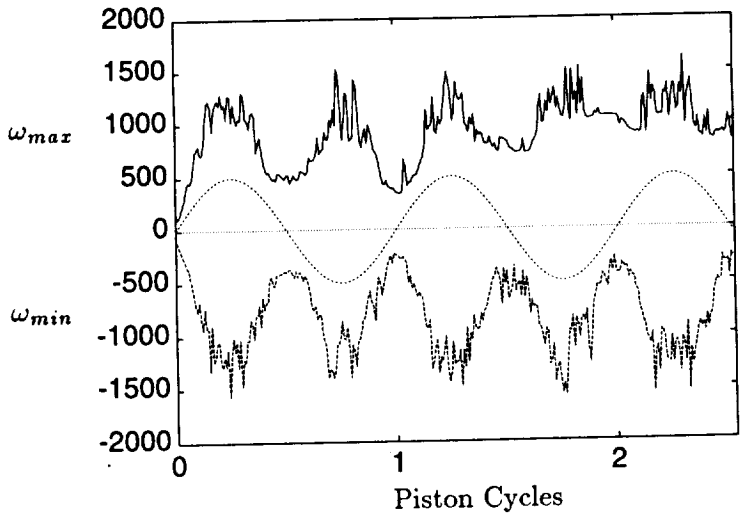

FIGURE 7. Time evolution of the azimuthal vorticity extrema for the large-eddy simulation at $Re = 2000$. The dotted line shows the time law of the piston displacement (in arbitrary units).

cycle. This implies that phase averages are needed to compute mean profiles and higher-order moments, thus requiring the simulation of the flow over several cycles. Additional information obtained by this simulation is that with this grid the DNS at the present Re is already at the resolution limit; therefore, a turbulence model is needed to simulate higher Re cases.

As stated in Section 2, the experiment performed by Morse *et al.* (1978) was at $Re = 2000$, which is definitely too high to be affordable with DNS. For this reason a large-eddy simulation with the dynamic subgrid-scale model was carried out, and some representative results are given in Fig. 6. A computer animation of the flow provided considerable information on the in-cylinder dynamics, which is impossible to summarize with a limited number of snapshots. From Fig. 6, however, it is already evident that the flow degenerates into small scale structures even if the underlying large-scale flow, already evidenced in the axisymmetric simulations, is still discernible from the meridional velocity vectors. The motion in the meridional planes is coupled with intense azimuthal velocity fluctuations whose magnitude is comparable with the vertical velocity. As already indicated by the DNS at low Re, this flow is time periodic only in a statistical sense; therefore, the calculation of the statistics requires phase averages in order to converge. This is confirmed by the time evolution of the azimuthal vorticity extrema over few cycles given in Fig. 7 where the piston motion is shown for reference. It can be noted that, while the low frequency dynamics follow the piston motion, the fluctuations are related to the small scales, thus reflecting the turbulent character of the flow.

In Fig. 8 is shown the comparison between the numerical and experimental mean and rms radial profiles of axial velocity at the crank angle 36° after TDC with the profiles 10mm axially spaced starting from the cylinder head. The numerical results

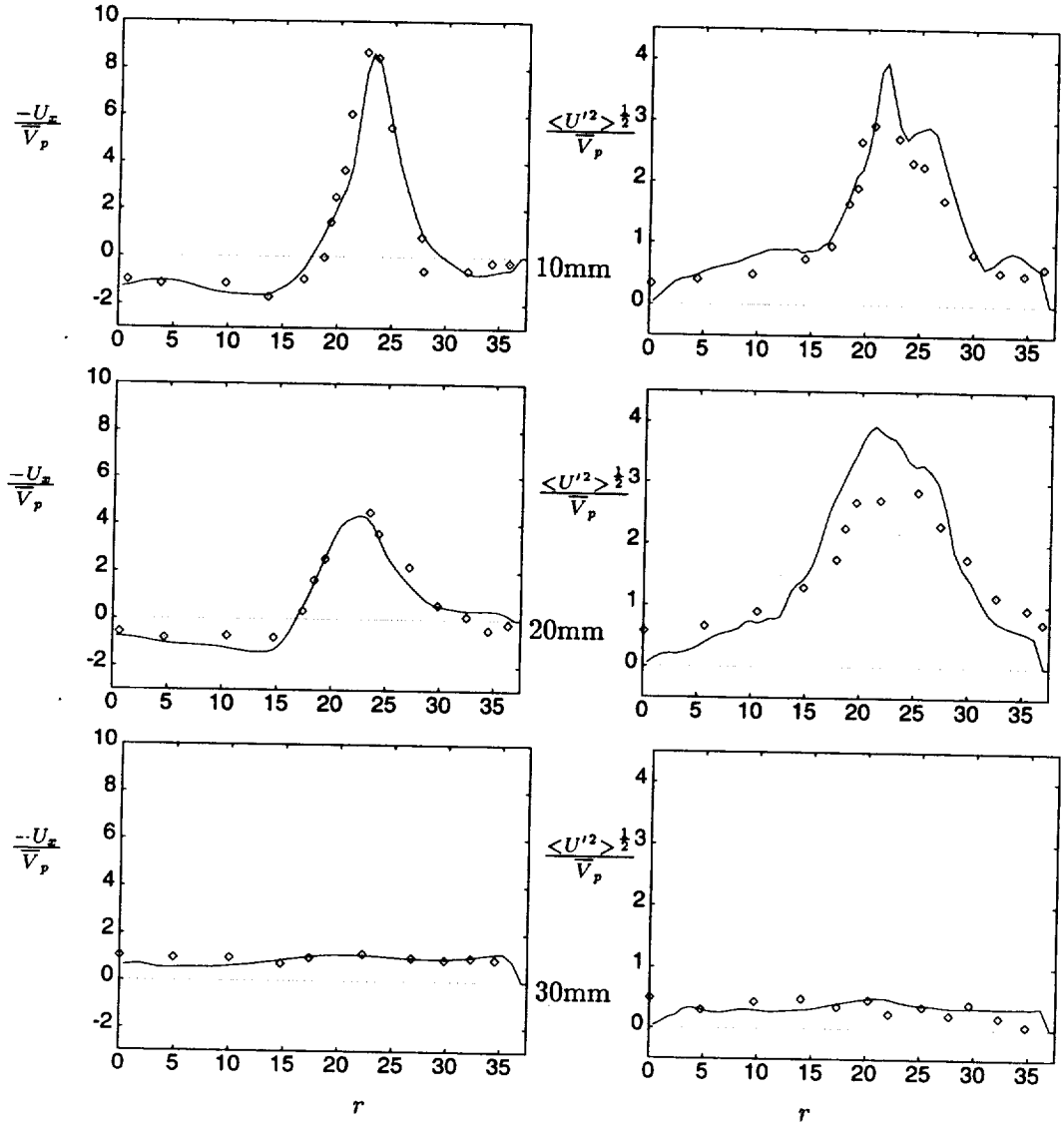

FIGURE 8. Mean (left) and rms (right) radial profiles of axial velocity at 36° after TDC for the flow at $Re = 2000$. —— numerical simulation; symbols for the experimental results.

are azimuthally and phase averaged over three piston cycles. While it is clear that the rms profiles would certainly benefit from some additional averaging, the mean profiles already show a good agreement with the experiment. Figure 9 shows the same profiles as Fig. 8 but for a crank angle of 144° after TDC, and again the results are very satisfactory. The same quality of agreement is obtained for the other profiles at 144° respectively at 40, 50, 60, and 70mm below the cylinder head, but they are not shown for the sake of conciseness.

As already mentioned the flow has very strong variation from cycle to cycle that

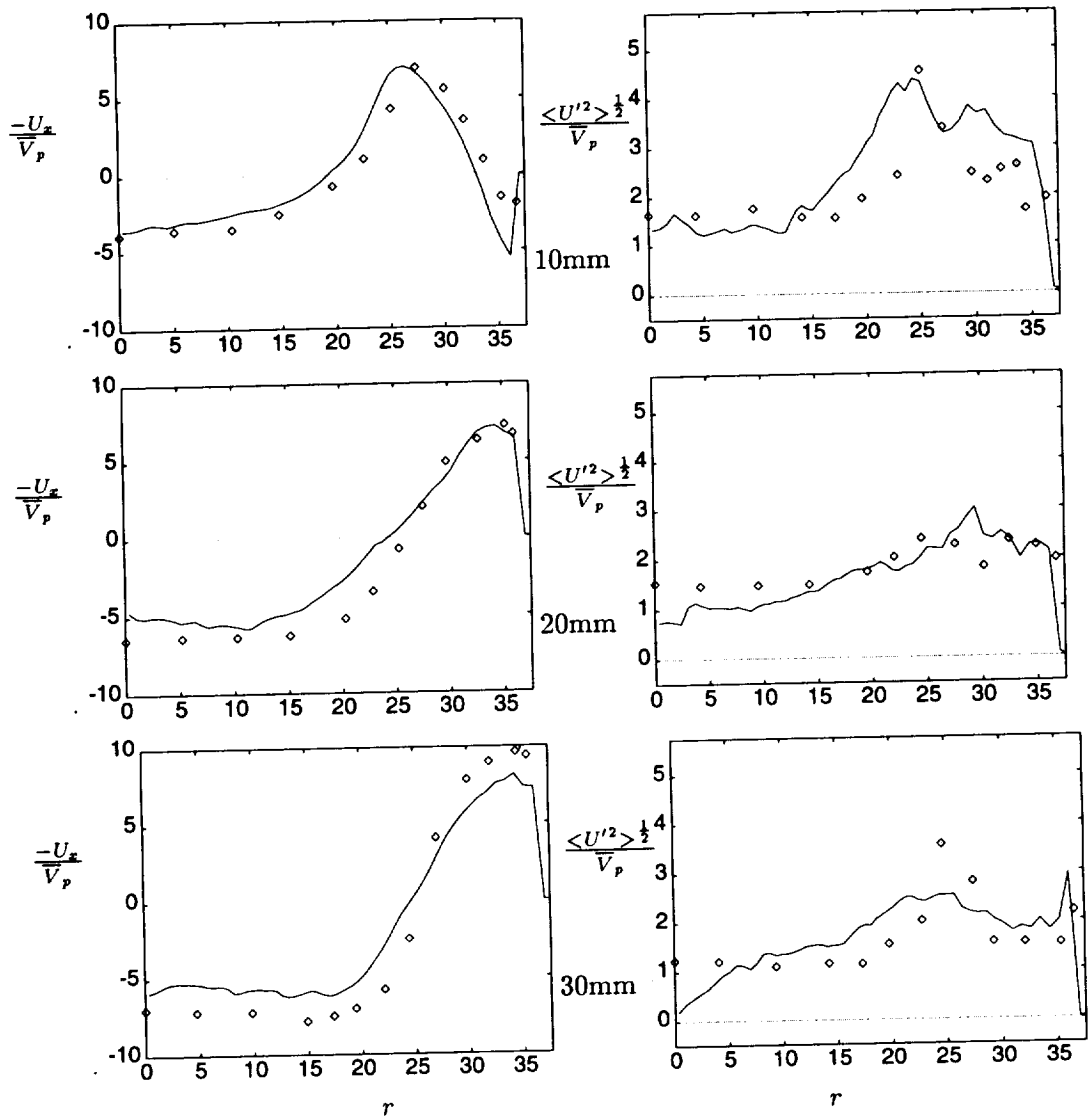

FIGURE 9. The same as Fig. 8 at 144° after TDC.

could be of some interest to engineers in determining how much the flow deviates from its average properties. In order to show these fluctuations we report in Fig. 10 some profiles at 36° ATDC and 10mm below the cylinder head for three different cycles. We can see that the mean profiles are quite smooth (note that these profiles are already azimuthally averaged, the instantaneous azimuthal section is less smooth); the radial shift of the peak is quite small and its intensity constant within 20%. The rms profiles, on the other hand, fluctuate more with oscillations up to 50%; these large fluctuations are likely to be the reason for the discrepancies observed in Figs. 8 and 9 between numerical and experimental rms profiles.

Before concluding this section we wish to briefly summarize the results of some

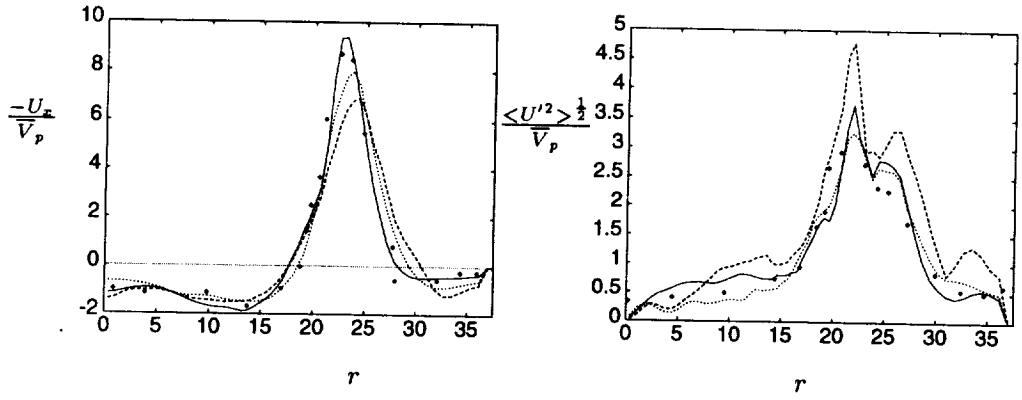

FIGURE 10. Mean (left) and rms (right) radial profiles of axial velocity at 36° after TDC for the flow at $Re = 2000$, 10mm below the cylinder head. ---- cycle 1, —— cycle 2, and ····· cycle 3. The symbols are the experimental results.

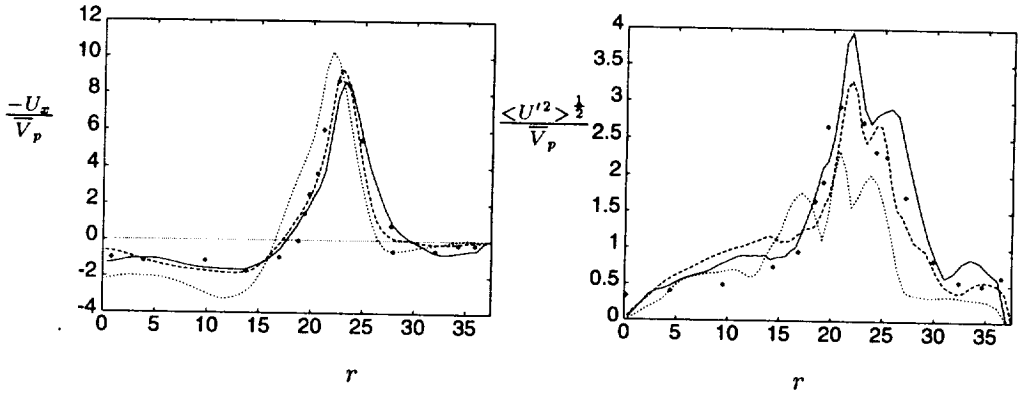

FIGURE 11. mean (left) and rms (right) radial profiles of axial velocity at 36° after TDC for the flow at $Re = 2000$, 10mm below the cylinder head. ---- dynamic model and fine grid, —— dynamic model and coarse grid, ····· Smagorinsky model and coarse grid. The symbols are the experimental results.

further comparisons. In particular, LES of this piston flow has also been carried out on a coarser grid using both the dynamic and the Smagorinsky models. The results for the same quantities as Fig. 10 are shown in Fig. 11. The profiles obtained by the coarser grid show fairly good agreement with the experiments and the fine-grid case, and the dynamic model behaves consistently with the expectations, i.e. it is more active as the grid becomes coarser. The Smagorinsky model (with the constant set equal to 0.2) shows bigger discrepancies with the experiments, yielding a more peaked jet and reduced velocity fluctuations. This behavior is also consistent with the more dissipative nature of this turbulence model, which tends to smooth all velocity gradients independently of their laminar or turbulent character. It should be noted that this result was obtained for one particular value of the constant C, and a tuning of this constant could improve the results. However, Fig. 5 shows that

the flow is very inhomogeneous in space, thus a single value of the constant might not be sufficient for the description of the flow dynamics.

5. Conclusions

In this report we have described an alternative procedure for simulating complex flow of industrial interest in a very inexpensive way. This technique is based on the use of body forces which allow the assignment of boundary conditions independently of the grid. The main advantage of this procedure is that the above forces can be prescribed on a simple cylindrical mesh so that all the advantages and the efficiency of solving the Navier-Stokes equations in simple constant-metric coordinates are retained when dealing with complex geometries.

In order to validate this procedure the flow in a motored axisymmetric piston-cylinder assembly has been simulated and the results have shown a very good agreement with the experiments. The selected flow was particularly suitable for testing the numerical procedure since it has complex geometries with moving boundaries and its Reynolds number is high enough to require a turbulence model. These are standard requirements for industrial flows and a robust numerical procedure must efficiently cope with all of them.

Results have shown that the dynamic subgrid-scale model is particularly suitable; in fact this model automatically switches off close to the walls without requiring *ad hoc* damping functions (like the van Driest function for the Smagorinsky model). This feature is very useful in the present numerical method since the body surface in general is not a coordinate line and the computation of the wall distance becomes difficult and time consuming. In addition, in the presence of moving boundaries this distance should be recomputed every time step with a further increase of the CPU time.

The efficiency of the proposed method can be illustrated by considering that most of the results were obtained from simulations run on a PC workstation with 128MB of RAM in about a week using a grid of about $6 \cdot 10^5$ gridpoints (about 24 hours per engine cycle). Comparative results for the same flow were obtained by Haworth & Jansen (1997), using the fully compressible formulation on an unstructured deforming mesh of about $1.5 \cdot 10^5$ gridpoints running on a single processor Cray T-90, or 8-processor SGI Origin 2000, occupying 600MB of RAM for a time of 30-40 CPU hours per engine cycle.

We are indebted to M. Fatica for countless suggestions and for providing his help in the numerical simulations and çomputer animations. We acknowledge W. H. Cabot for the advice in the implementation of the LES model in the code. R. V. wishes to acknowledge the ERO-US Army (European Research Office US Army) for a partial support under contract n. N68171-98-M-5645.

REFERENCES

EATON, A. R. & REYNOLDS, W. C. 1987 High-Speed Photography of Smoke-Marked Flow in a Motored Axisymmetric Engine. *ASME Paper 87-FE-10.*

EATON, A. R. & REYNOLDS, W. C. 1989 Flow Structure and Mixing in a Motored Axisymmetric Engine. *SAE Paper 890321.*

EL THARY, S. H. & HAWORTH D. C. 1996 A perspective on the state-of-the-art in IC engine combustion modeling. *SIAM* Sixth International Conference on Combustion, New Orleans.

FADLUN, E. A., VERZICCO, R. & ORLANDI, P. 1998 Flussi in geometrie complesse con forze di massa su griglie Cartesiane: simulazioni numeriche e validazione sperimentale. *Master Thesis* Dept. Meccanica & Aeronautica (1998) (in italian).

GERMANO, M., PIOMELLI, U., MOIN, P. & CABOT, W. H. 1991 A dynamic subgrid-scale eddy viscosity model. *Phys. of Fluids A.* **3,** 1760-1765.

GOLDSTEIN, D., HANDLER, R. & SIROVICH, L. 1993 Modeling a no-slip flow boundary with an external force field. *J. Comp. Phys.* **105,** 354-366.

HAWORTH, D. C. & JANSEN, K. 1997 Large-Eddy Simulation on Unstructured Deforming Meshes: Towards Reciprocating IC Engines. Submitted to *Computer and Fluids.*

LILLY, D. K. 1992 A proposed modification of the Germano subgrid-scale closure method. *Phys. of Fluids A.* **4,** 633-635.

MOHD-YUSOF, J. 1996 Interaction of Massive Particles with Turbulence. *Ph. D. Thesis,* Cornell University.

MOHD-YUSOF, J. 1997 Combined immerse-boundary/B-spline methods for simulations of flows in complex geometries. *CTR Annual Research Briefs 1997.* NASA Ames/Stanford Univ., 317-327.

MOHD-YUSOF, J. & LUMLEY, J. L. 1994 Simulation of Flow Around Cylinders Using Boundary Forcing. *Bulletin of the Am. Phys. Soc.* **39**(9).

MOHD-YUSOF, J. & LUMLEY, J. L. 1996 Improved Immersed Boundary Techniques for Complex Flows. *Bulletin of the Am. Phys. Soc.* **41**(9).

MORSE, A. P., WHITELAW, J. H. & YIANNESKIS, M. 1978 Turbulent flow measurement by Laser Doppler Anemometry in a motored reciprocating engine. *Report FS/78/24.* Imperial College Dept. Mech Eng.

PESKIN, C. S. 1972 Flow patterns around hearth valves: a numerical method . *J. Comp. Phys.* **10,** 252-271.

SAIKI, E. M. & BIRINGEN, S. 1996 Numerical simulation of a cylinder in uniform flow: application of a virtual boundary method. *J. Comp. Phys.* **123,** 450-465.

VERZICCO, R. & ORLANDI, P. 1996 A finite-difference scheme for three-dimensional incompressible flow in cylindrical coordinates. *J. Comp. Phys.* **123,** 402-413.

Center for Turbulence Research
Proceedings of the Summer Program 1998

DNS study of stability of trailing vortices

By P. Orlandi[1], G. F. Carnevale[2], S. K. Lele AND K. Shariff

Three-dimensional numerical simulations are used to investigate the possibility of diminishing the strength of trailing vortices. Direct numerical simulation is first used to reproduce results of recent laboratory experiments on the short-wave co-operative instability for two counter-rotating vortices. The effect of perturbing the vortices by internal and external density perturbations is considered. It is found that perturbing trailing vortices with temperature variations may be a useful means of initiating the short-wave instability and ultimately causing the cross diffusion of vorticity necessary to destroy the coherence and strength of the trailing vortices.

1. Introduction

Vortices in the wake of heavy aircraft pose a serious threat to following aircraft. The danger is particularly severe during landings and take-offs for two reasons. First, the extension of the flaps of the leading aircraft may create trailing vortices that are even stronger than the wing tip vortices. Second, the proximity of the following aircraft to the ground means that a small perturbation in its trajectory may be disastrous. Thus sufficient separation between planes must be maintained to allow time for the dispersal of trailing vortices. If it were not for this requirement, intervals between landings and take-offs could be reduced significantly with obvious economic benefit. There are two strategies being pursued to ameliorate this situation. One involves attempting to better quantify the time interval needed for safety given current plane designs. The other considers the possibility of modifying and controlling the vortices to accelerate their dispersal. In either case, an improved knowledge of the possible instabilities of trailing vortices is essential. Thus, in an age of jumbo jets and congested airports, the evolution of vortices shed from the airplanes is a pressing issue and recently has received a great deal of attention. There have been several experimental studies in real flight conditions and in wind tunnels, as discussed in the review article by Spalart (1998). Also, in the last few years direct numerical simulations have been performed to study aspects of this problem. For example, the influence of atmospheric turbulence on creating instabilities with a wavelength on the order of the diameter of the vortex cores was studied by Risso, Corjon & Stoessel *et al.* (1996) in a relatively small computational domain. It is also possible to simulate the Crow (1972) instability, which is of much longer scale.

1 Università di Roma "La Sapienza" Dipartimento di Meccanica e Aeronautica, via Eudossiana 18 00184 Roma, Italy.

2 Scripps Institution of Oceanography, University of California San Diego, 9500 Gilman Dr., La Jolla, CA 92093

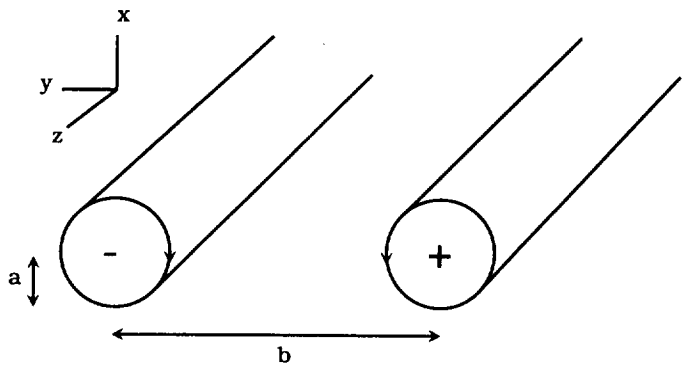

FIGURE 1. Schematic diagram of a pair of counter-rotating trailing vortices. In this configuration the mutual advection causes the vortices to move in the downward direction (the negative x direction). The spanwise separation of the centers of the vortices is b and the core size is a. The orientation of the axis is also displayed. Note that the z axis points out of the page.

The effects of the Crow instability can be seen on clear days when airplanes fly at high altitudes and their contrails are visible. As the instability unfolds, the contrails merge at places to form elongated rings or loops.

Trailing vortices come in counter-rotating pairs (see Fig. 1). The wing tips of the plane each shed one vortex in such a pair. Also the flaps when extended shed pairs of vortices. The diagram in Fig. 1 shows the separation distance b between the centers of the vortices, the core size or radius a, and the orientation of our coordinate system. The y direction, pointing from the center of one vortex to the other, we will call the spanwise direction. The direction along the core, the z direction, we will refer to as axial. The signs associated with the centers of the vortices in the figure refer to the sign of the z component of vorticity, ω_z. For the orientation of the pair of counter-rotating vortices shown in the figure, the propagation by mutual advection is in the negative x direction.

We can consider two relevant processes for decreasing the dangerous effects of trailing vortices. The maximum velocity due to a vortex of given strength or circulation Γ scales as Γ/a. Thus the dangerous effects of the vortex can be decreased by increasing its core radius, which can be accomplished most efficiently by turbulent diffusion. This will not, however, diminish the circulation. Decreasing the circulation can be accomplished by cross diffusion and cancellation between the two-counter rotating vortices. Although the Crow instability can lead to a decrease in Γ by cross diffusion, it appears that it proceeds too slowly and over too long a distance. We will focus here instead on the so called 'elliptical cooperative instability, which has a length scale comparable to the vortex core size and a growth rate that can exceed that of the Crow instability. This short-wavelength instability has been the subject of a number of theoretical studies (c.f. Widnall *et al.*1974; Pierrehumbert, 1986; Bayly, 1986; Landman and Saffman, 1987; and Waleffe 1990). The basic mechanism involved in the instability is that strain produced by one of

the vortices on the other amplifies bends in the vortex profile, creating a sinusoidal modulation on the core shape and position along the axial direction. The instability has been demonstrated in laboratory experiments by Thomas and Auerbach (1994) and Leweke and Williamson (1998). These laboratory experiments verified many of the predictions of linear instability theory. In these experiments, the Reynolds number, $Re_\Gamma = \Gamma/\nu$, ranged from 2500 to 12000. At least at the lower end of this range, the values of Re_Γ are sufficiently low to permit direct numerical simulation of the experimental flows with a reasonable number of grid points. Believing that there will be many similarities between the instability as observed in the laboratory and that which may occur for the much higher Reynolds number flows caused by the trailing vortices in airplane wakes, we began our investigation with a numerical study of the laboratory experiment. In Section 2, we describe simulations in which we applied a random velocity perturbation to two counter-rotating vortices. The evolution in these simulations showed a short-wave cooperative instability closely reproducing that observed in the laboratory. In all of the simulations presented here the initial Reynolds number was fixed at $Re_\Gamma = 3400$.

Our investigation of the laboratory experiments leads to the conclusion that, in order for the short-wave cooperative instability to be of practical use in dispersing trailing vortices, the fastest growing mode of the instability should be selectively and strongly forced. One method of forcing that may be feasible would be to apply a strong temperature variation to the trailing vortices with a wavelength matched to the faster growing cooperative instability. Following this idea, we performed a series of simulations in which temperature perturbations were applied either in the cores of the vortices or in the vicinity of the vortices. The results showed that this method can indeed be used to force the destruction of the vortices much more rapidly than by the application of random velocity perturbations. This is discussed in Section 3.

2. Simulation of the laboratory experiments

The appropriate evolution equations are the Navier-Stokes equations for a uniform density incompressible fluid. Our numerical model is based on the momentum equation which can be written as

$$\frac{\partial u_i}{\partial t} + \frac{\partial u_i u_j}{\partial x_j} = -\frac{\partial p}{\partial x_i} + \nu \frac{\partial^2 u_i}{\partial {x_j}^2}, \tag{1}$$

with $\nabla \cdot \mathbf{u} = 0$. Our numerical scheme uses a staggered mesh with the velocity components located on the faces of the cell and the pressure at the center, and it uses a fractional step method (Kim & Moin 1985). This scheme is described in detail in Verzicco and Orlandi (1996).

The complicated mechanism by which vortices are created in the laboratory would be rather difficult to simulate and, in any case, not of prime concern in this study. Thus we are content to perform simulations in which the initial state is a pair of counter-rotating vortices. The choice of the structure of the initial vortices requires some care. If one starts with vortices whose vorticity distributions in an $x - y$

cross section are radially symmetric, then there will be a transition period in which fluid is shed in the wake of the vortices during the period in which the structure of each vortex adjusts to the presence of the other vortex. This adjustment is a purely two-dimensional process (cf. Carnevale & Kloosterziel 1994) and is of little interest to the present study. We could wait for this adjustment period to pass and then use the resulting adjusted vortices as the initial vortices for our study. As an alternate approach, we found that the adjustment phase could be mostly eliminated by using vortices whose structure is given by the analytical formula for the vortices of the Lamb dipole (1945, section 165). This is a vortex structure in which there are two counter-rotating vortices with the entire dipolar vorticity distribution confined in a circular region whose radius we will denote by $a_{\mathcal{L}}$. When unperturbed, the Lamb dipole propagates at a constant speed $U_{\mathcal{L}}$ without change. For sufficiently high resolution, this form-preserving motion can be readily simulated. Taking as an initial condition the two semicircular halves of the Lamb dipole separated by some distance, we found that in the subsequent evolution the two vortices adjusted the presence of each other more smoothly and without the large amount of vorticity shedding observed in the case initialized with two circularly symmetric vortices. In all of the simulations presented below, the unperturbed basic state is taken as the two halves of the Lamb dipole with the vorticity extrema separated by some distance b, and the initial condition is prepared by adding perturbations to this.

To initialize our simulations of the laboratory experiments, the perturbation used was a randomly generated three-dimensional velocity field. This perturbation was localized to the region were the axial vorticity ω_{z0} was greater in magnitude than a given threshold (set arbitrarily at 20% of the unperturbed vorticity maximum). The random velocity thus generated was not solenoidal, but this defect is remedied automatically by the first time step of the simulation, which projects the initial velocity onto a solenoidal field. The perturbed field is then found to have pointwise fluctuations in the cross vorticity components, ω_x and ω_y of at most 20% of $|\omega_{z0}|_{max}$. The basic simulation then consisted of the interaction of the pair of the counter-rotating vortices for a fixed period of time. Three different values were used for the separation between the vortices to see how the growth of the instability varied with separation. We began by comparing the results of a set of runs with resolution $N_x = N_y = N_z = 64$ and domain size $(L_x, L_y, L_z) = (2\pi, 2\pi, \pi)$ where N_x is the number of grid points in the x direction and L is the size of the computational domain in the x-direction in units of the unperturbed Lamb dipole radius $a_{\mathcal{L}}$. These runs produced velocity fields that seemed under-resolved, lacking features evident in the experimental visualizations. A further set of runs with $N_x = N_y = N_z = 128$ was then performed. These simulations resembled those in the laboratory experiments very well, and it seemed that this resolution was sufficient to resolve the structures that were important to the short-wave cooperative instability. However, when we checked the speed of the dipole, we found it fell significantly short of the speed of the theoretical dipole. We obtained some improvement by increasing the domain size and resolution in the spanwise direction. This is because, in periodic geometry, if the vortices are not sufficiently far from the boundaries in the spanwise direction,

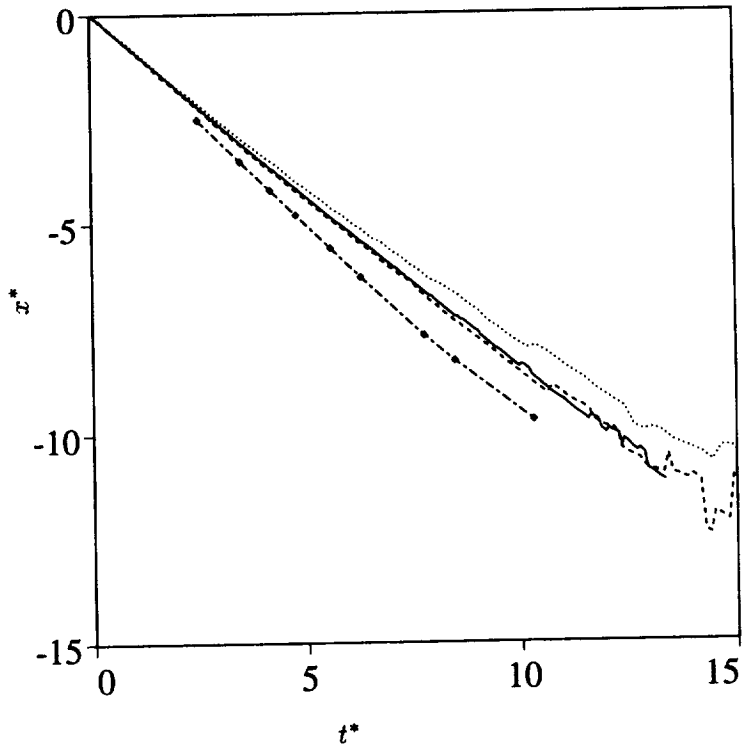

FIGURE 2. History of the positions of the vorticity maxima. The line with symbols corresponds to the experimental data of Leweke and Williamson (1998). The other curves correspond to the numerical simulations with —— $b = 1.9$, ---- $b + 1.4$, and ····· $b = 1$.

they will strongly feel the presence of the periodic replicas. As discussed below, we found that $L_y = 3\pi$ was a reasonable choice for our simulations. Also we found that $L_z = \pi$ was sufficient to allow two full wavelengths of the most unstable mode. Thus our final set of simulations was performed with (N_x, N_y, N_z)=(128,192,128) and $(L_x, L_y, L_z) = (2\pi, 3\pi, \pi)$.

A theoretical estimate of the speed of the dipole can be made based on the speed of a dipole composed of two line vortices. The azimuthal velocity field created by a straight line vortex of circulation Γ at a distance b from the vortex is $v_\theta = \Gamma/(2\pi b)$, where θ is taken as the azimuthal angular coordinate in a cylindrical coordinate system centered on the vortex. Thus, two mutually advecting line vortices of equal strength separated by a distance b will propagate at this speed. For the problem of trailing vortices, it is often convenient to nondimensionalize length by b, the separation between centers of the vortices, and time by $\tau = 2\pi b^2/\Gamma$, the time it takes the dipole to travel a distance b. In these units, which we shall refer to as τ units, the speed of the idealized dipole of line vortices is 1. This system of scaling will be denoted by an asterisk superscript. Another system that is useful here is the

advective time scaling based on the unperturbed Lamb dipole with zero separation between the halves of the Lamb dipole. The length unit in this system is $a_{\mathcal{L}}$ and the time unit is $a_{\mathcal{L}}/U_{\mathcal{L}}$. This system we will refer to as advective scaling. All quantities without the asterisk superscript will be in these units.

In Fig. 2, we show histories of the position of the maximum of the vorticity for three simulations with different values of b. The circulation in advective units was the same in each case: $\Gamma = 6.83$. The values of b were measured a short time after the initial adjustment of the dipole. In units of $a_{\mathcal{L}}$ the values of b were 1.0, 1.4, and 1.9. In Fig. 2, the position is in units of b, and time is in units of τ. Also shown in the diagram are the results from one of the laboratory experiments as given by Leweke and Williamson (1998). The laboratory experiments for the early evolution show a speed almost precisely equal to 1 in τ units. Our simulations, however, show speeds of about 0.85. There are two reasons for the reduced speed. First of all, since the vortices involved here are not circularly symmetric, there is some ambiguity about how b should be chosen. We simply measured the distance between the extrema of vorticity. For the Lamb dipole, with no separation between the halves of the dipole, the theoretical speed in units of b and τ is, in fact, approximately 0.87 (cf. Carnevale, Kloosterziel and Philippe, 1993). Thus some of the error may be due to our definition of b when b is close to 1. This cause for discrepancy should diminish as b increases due to the fact that the vorticity distributions for each vortex would then become more circularly symmetric. Unfortunately, in a periodic domain a second problem then arises. As b increases, the effect of the periodic replica of the vortices on the speed of the dipole increases. For example, on a domain with $L_y = 3\pi$ (in units of $a_{\mathcal{L}}$) and with $b = 2$, there would be approximately a 15% decrease in speed due to this effect. We had to make a decision about choosing the domain size that would be large enough to give reasonable values for the speed and yet with a high enough resolution to observe small structures during the breakdown of the vortices. Some experimentation suggested that $L_y = 3\pi$ was a reasonable compromise.

There are various quantities that can be used to measure the progress of the cooperative instability. For the unperturbed pair of vortices, the only nonzero component of the vorticity is the axial vorticity ω_z. Thus a good indicator of the growth of an instability would be the evolution of the maximum value of the magnitude of one of the other components of vorticity. In Fig. 3a we plot the evolution of the maximum value of the spanwise vorticity ω_y for the three simulations with different values of b. Vorticity and time have been nondimensionalized using τ as defined above. Also plotted is the history of the maximum value of the axial vorticity (chain-dashed line) for one of the simulations. The curves for ω_y each have a section that is roughly linear on this linear-logarithmic plot, indicating exponential growth in time. In the inviscid theory, the growth rate for the short-wave instability is constant when measured in τ units. Thus, the approximate collapse of the data for the three values of b also suggests that this exponential growth is the result of the short-wave cooperative instability.

The viscous theory of the instability does introduce some dependence on b which does not seem correctly reproduced in our simulations. As discussed above, there is

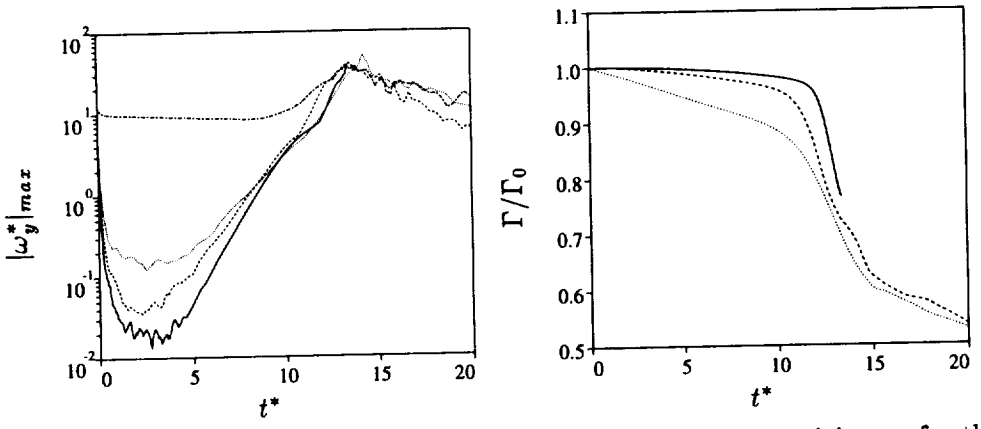

FIGURE 3. a) History of the maximum value of the spanwise vorticity ω_y for three cases: —— $b = 1.9$, ---- $b + 1.4$, and ····· $b = 1.0$. For comparison, the history of the maximum value of ω_z (— —) for $b = 1$ is also plotted. b) History of the circulation normalized by its initial value. The line types for the different values of b are as in panel (a)

some ambiguity in the definition of b especially when the vortices are close together. For the case of the largest b represented (solid line), the growth rate is approximately $\sigma^* = 0.91$ while the theoretical prediction, taking viscous decay into account, is $\sigma^* = 0.99$. We found some improvement in the correspondence in a simulation in which the spanwise domain size was increased to $4\pi a_{\mathcal{L}}$. In that case $\sigma^* = 0.96$. However, the viscous theory predicts that σ^* should decrease with b (cf. Leweke and Williamson, 1998) while here we find just the opposite.

Note that the value of ω_y becomes comparable to ω_z for $t^* \approx 13$. The evolution of ω_x (not shown) is similar to that of ω_y. The vorticity components in x and y directions becoming comparable in magnitude to the axial vorticity indicates that the dipolar structure of the vortices may be breaking down. As we will see, the ω_x and ω_y components produce strong deformations associated with small scales as would occur in a transition to turbulent flow. One indication of the destruction of the vortices is the history of the circulation which is shown in Fig. 3b. This circulation Γ was obtained by integrating the spanwise vorticity in each xy plane for $0 \leq y \leq L_y/2$ and then separately for $-L_y/2 \leq y \leq 0$, and then finally averaging over z. By $t^* \approx 13$, in all cases, there is a significant drop in Γ, and this occurs at approximately the same time as the values of ω_x and ω_y become comparable to that of ω_z. Actually, this Γ is not an ideal measure of the circulation or strength of the vortices. The circulation around a material circuit is changed by viscosity only, but due to lack of symmetry of the sinuous mode, the decay of Γ as defined here is not necessarily a measure of the destruction of circulation by viscosity. The present measure could decrease even in the inviscid case: at a cross-section where there is a rightward bend, the circulation in the right half decreases due to transport of opposite sign vorticity from the left half; at a cross-section where there is a leftward bend, the circulation in the right half also decreases because it is being transported

into the left half. For future work, a better measure might be the circulation around a suitable ensemble of material circuits.

To visualize the three-dimensional character of the shortwave instability, we produced isosurface plots of vorticity and velocity. For each of the three simulations with different values of b, the vorticity structures observed were qualitatively similar once time was scaled with τ. Visualization by this method shows some structures that are very similar to those observed by dye visualization in the experiments by Leweke & Williamson (see the top panel of Fig. 4). In Fig. 4, we show the isosurface plots of the magnitude of the vorticity $|\omega|$ for the case $b = 1.9$. The isosurface value is the same at each time shown and is $|\omega/\omega_0| = 0.4$ where $|\omega_0|$ is the maximum magnitude of the unperturbed dipole vorticity field. Note that in both the laboratory experiments and the simulations the instability is sinuous; that is, the sinusoidal bending of the vortex cores are in phase. This is interesting because when one considers the effect of one vortex upon the other to be a pure strain, there is no mechanism for choosing the phase relationship between the distortions of each vortex. The isosurface plot for $t^* = 9.0$ represents the field at a time in the exponentially growing phase indicated in Fig. 3a. As we will see below, the perturbation vorticity and velocity fields at this point match the predictions of linear theory well. By time $t^* = 10.5$, nonlinear effects are evident. The formation of 'caps' on the points where the isosurface is most curved results from vortex stretching in the spanwise direction. This is followed by the production of the vortices seen at $t^* = 12.0$, which span the two original cores and which begin the cross-diffusion of circulation.

It is interesting to consider the form of the perturbation during the exponential phase of the growth. Theoretical predictions for the fastest growing unstable mode can be found in Leweke and Williamson (1998) and Waleffe (1990). In Fig. 5 we show contour plots of the axial velocity and vorticity perturbation fields in an $x-y$ cross section at time $t^* = 9.0$. The cores of the vortices are marked by the thick solid lines, which are vorticity magnitude contours at a level that is a factor of e^{-1} less than the instantaneous maximum. The perturbation fields are qualitatively as predicted by the linear theory. The asymmetry here is probably due to the asymmetry in the original random forcing. According to the theory, there should be a $\pm 45°$ angular difference in the orientation of the the dipolar perturbation structures on the two vortices. In addition, the orientation of the dipolar velocity perturbation field should be perpendicular to that of the perturbation vorticity field. We see that these relationships hold approximately in this cross section.

As for the wavelength of the fastest growing mode, theory based on a Rankine vortex (uniform vorticity core) predicts a wavelength $\lambda = 2.51 a_R$, where a_R is the radius of the core. Unfortunately, since our vortices are not circularly symmetric in cross section and do not have a uniform distribution of ω_z, it is not clear what distance to use for a_R in making a comparison with the theory. Since the Rankine vortex achieves its maximum vorticity at the radial position a_R, we can try to substitute the radius where the maximum value of velocity is achieved along some direction for the value of a_R. At $t_* = 9.0$, for the case $b = 1.9$ shown in Fig. 5, the

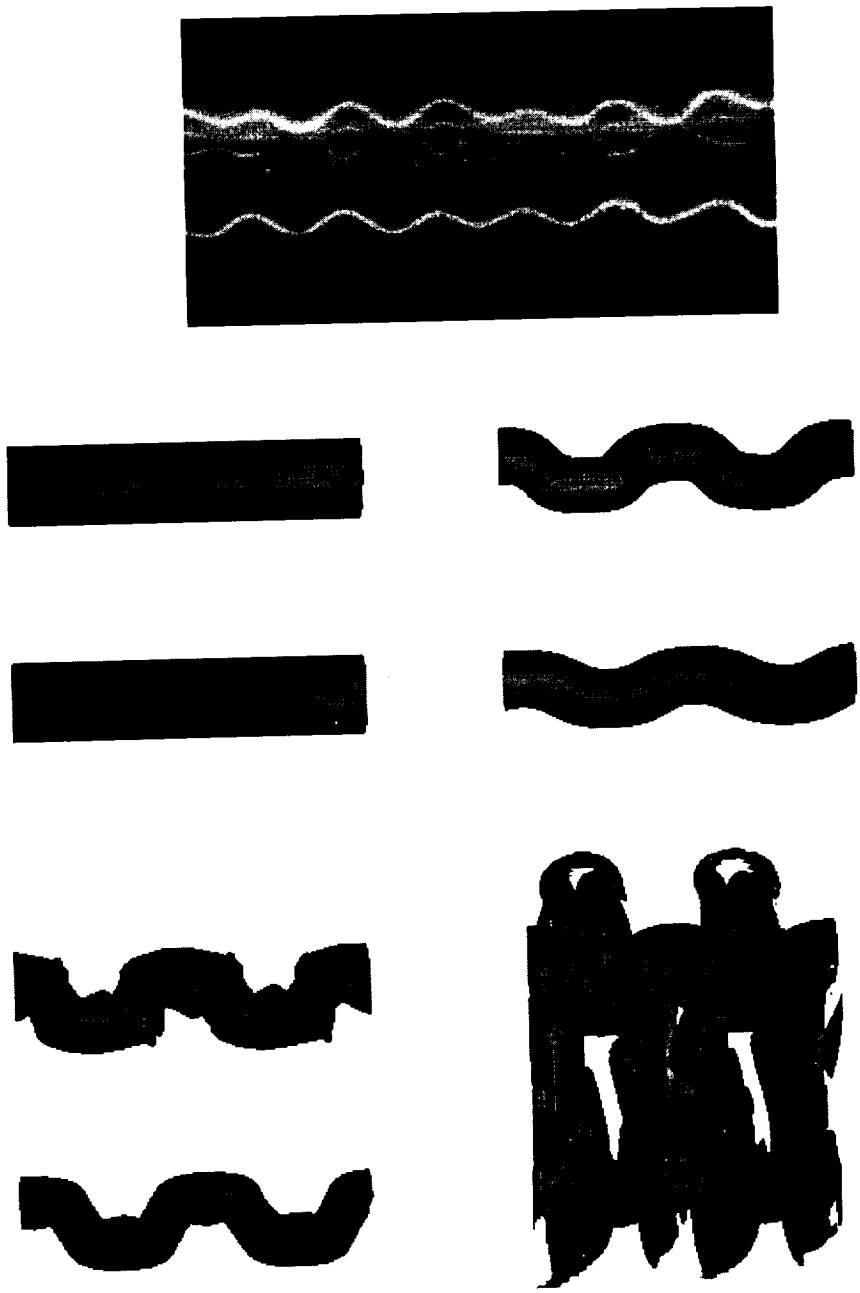

FIGURE 4. Top: dye visualization of the short-wave instability in the laboratory by Leweke & Williamson (1998). Four lower panels: isosurface plots of $|\omega/\omega_0| = 0.4$ for the case of the two vortices separated by $b = 1.9$. The times represented from left to right, top to bottom, are $t^* = 1.5$, 9.0, 10.5, and 12.0.

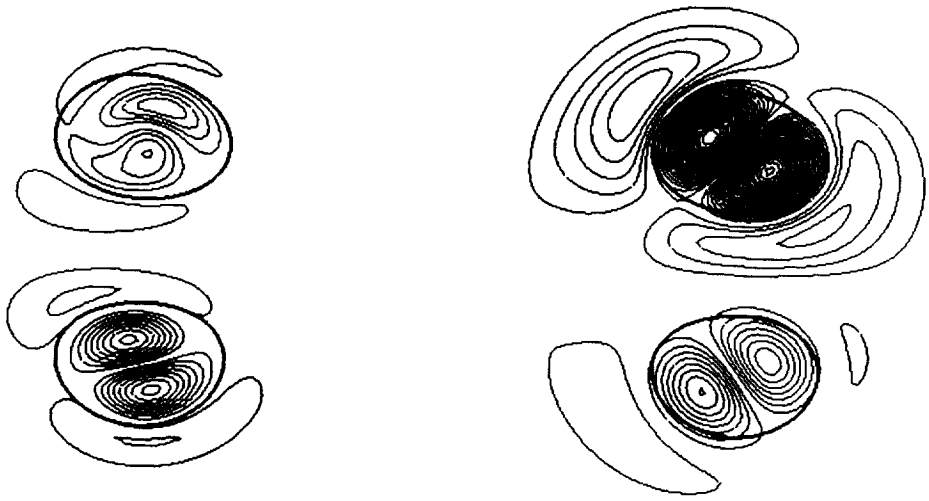

FIGURE 5. Contours of ω_z' (left) and of u_z' (right) in an x-y cross section of one vortex in the dipole shown in Fig. 4 ($b = 1.9$). The time is $t^* = 9$. The thick solid curves indicate the contour of total vorticity magnitude $|\omega|$ at a level of e^{-1} times the maximum value.

distance between the point of minimum velocity and maximum v_y for one of the vortices is approximately $0.69a_{\mathcal{L}}$. This is an upper bound on the velocity induced by the core given the elongation of the core in the x-direction. Substituting this value for a_R, the wavelength should be $\lambda = 1.73a_{\mathcal{L}}$, whereas, in the simulation the wavelength is $\lambda = 0.5\pi a_{\mathcal{L}} \approx 1.57a_{\mathcal{L}}$ instead, which is within about 10% of the predicted value. The wavelengths in the periodic domain are discrete and so the instability cannot pick out a wavelength that is not one of the discrete set. We tried varying L_z by 10% to allow the wavelength to better match the theoretical prediction and found the results to be substantially the same as those given above.

From a practical standpoint, it seems from Fig. 3a that random perturbations applied to the vortices is an inefficient way of initiating the cooperative instability. The initial perturbation has maximum vorticity amplitude of about 10% that of the unperturbed vortices. However, this decays greatly in the initial transient period, and importantly, we see that the larger the value of b, the more profound is the initial decay. It took about 5τ periods for the exponential growth to become evident. If we imagine linearizing the equations of motion about the unperturbed vortices and considering the eigenmodes of the resultant differential operator, it appears that our initial perturbation is made of a superposition of eigenmodes, many of which are decaying. The projection of the initial perturbation on the growing eigenmodes must be very small. If a 10% perturbation could be applied in the pure fastest growing normal mode, then the transient phase could be avoided. With an inviscid theoretical maximum growth rate of $\sigma^* = 9/8$, the period of growth would only need

to be 2τ. We attempted to initialize the flow field with the dipole perturbed by the fastest growing eigenmode predicted by theory based on the Rankine vortex. This reduced the transient period by about half, but that still left a significant period of decay. Given the distortion of each vortex due to the presence of the other, it is not surprising that the theoretical normal mode based on the Rankine vortex is not a pure normal mode for the actual dipole. In addition, it is probably not practical from the viewpoint of aircraft design to consider the application of a perturbation exactly designed to match the velocity field of the pure normal mode. Thus, in the next section, we turn to the question of finding a perturbation or forcing which is more readily applied to the destruction of the dipole.

3. Density perturbations

As a practical method for strongly perturbing trailing vortices, we considered the application of density perturbations both within and exterior to the vortex cores. Such perturbations could be achieved through heating. If the perturbation is applied with a variation in intensity along the axial direction, then a buoyancy force of varying strength will be felt along the length of the vortex. If the wavelength of the spatial variation of the perturbation is tuned to that of the cooperative instability, then not only will the vortex be disturbed by the buoyancy forcing, but also by the interaction of the neighboring vortex through the cooperative instability.

The simplest approximation that captures the buoyancy force due to small density variations is the Boussinesq approximation. If the acceleration of gravity is taken to be in the negative x-direction, which is the direction of our dipole motion, then the Boussinesq approximation for the momentum equation can be written as

$$\frac{\partial u_i}{\partial t} + \frac{\partial u_i u_j}{\partial x_j} = -\frac{\partial p'}{\partial x_i} + \frac{1}{Re}\frac{\partial^2 u_i}{\partial {x_j}^2} - \theta\delta_{i1}, \tag{2}$$

and the equation for the density is

$$\frac{\partial \theta}{\partial t} + \frac{\partial \theta u_j}{\partial x_j} = +\frac{1}{ReSc}\frac{\partial^2 \theta}{\partial {x_j}^2}. \tag{3}$$

The notation assumes the directions x, y, z are numbered sequentially from 1 to 3, and δ_{ij} is the Kronecker delta. In these equations we nondimensionalize length by $a_{\mathcal{L}}$ and time by $a_{\mathcal{L}}/U_{\mathcal{L}}$ where $a_{\mathcal{L}}$ and $U_{\mathcal{L}}$ are the radius and speed of the unperturbed Lamb dipole. The dimensionless density θ is given by

$$\hat{\theta} = \frac{\rho' g a_{\mathcal{L}}}{\rho_0 U_{\mathcal{L}}^2}, \tag{4}$$

where ρ' is the perturbation to the background density ρ_0 and g is the acceleration of gravity. Note that p' is the pressure less the background pressure $-\rho_0 g x$. The Reynolds number is given by $Re = U_{\mathcal{L}} a_{\mathcal{L}}/\nu$, and Sc is the Schmidt number given by $Sc = \nu/\kappa$ where κ is the thermal diffusivity.

In deriving the Boussinesq approximation, one assumes that ρ'/ρ is sufficiently small. In particular, a term equal to

$$\left(\frac{\rho'}{\rho}\right)\left(\frac{1}{\rho_0}\frac{\partial p'}{\partial x}\right)$$

has been neglected. Thus the approximation is strictly valid only if this term is small compared to the retained term θ. This can be translated into the statement that the centripetal acceleration within the trailing vortex, which is on the order of U^2/a, should be much less than the acceleration due to gravity. Assuming a vortex circulation of $100\text{m}^2/\text{s}$ and a core radius of about 5m would make the ratio of centripetal to gravitational acceleration about 1/2. Thus it may be necessary to use the full Navier Stokes equations for accurate predications, but we can get some first insights by using the simpler Boussinesq approximation.

To see how buoyancy forcing affects a pair of counter-rotating vortices, we began with a simple test. We used the same basic vorticity distributions as in the previous section; that is, the vortices are initially taken as the separated halves of a Lamb dipole. To these vortices we added an initial distribution of θ that was taken to be independent of the axial coordinate x and proportional to the magnitude of the vorticity in each of the vortices with the maximum amplitude set at θ_0. In one case we took $\theta_0 = +1$ and in the other $\theta_0 = -1$. Since there was no variation in the axial direction, two-dimensional numerical simulations sufficed to show the evolution. In Fig. 6, where we have plotted the trajectories of the extrema of vorticity for these two simulations, we see the interesting effect of the temperature perturbation. As predicted by Turner (1959), the speed of the 'heavy' vortices which are originally moving in the $-x$ direction decreases and the separation of the vortices increases. It may seem counterintuitive that adding weight to the downward propagating vortices can slow them down, but, in fact, the total momentum does increase as the vortices separate and entrain more fluid in their motion. The tendency for the 'heavy' vortices to slow and move apart and the 'light' vortices to move together and speed up could be used to distort the vortices and perhaps destroy their coherence by modulating the density distribution in the axial direction. Given the impracticality of cooling trailing aircraft vortices and the advantage of light vortices being forced to move closer together, we shall mainly consider perturbations with $\theta < 0$.

On the question of the size of the density perturbation to use, we can use some order of magnitude estimates. First we must estimate the values to use for $a_{\mathcal{L}}$ and $U_{\mathcal{L}}$ in formula (4). The radius of the vortices in the unperturbed Lamb dipole cannot be related easily to the radius of actual trailing vortices. Recall that in the case of the randomly perturbed dipole with $b = 1.9$, we found a maximum velocity at a distance of about $0.7a_{\mathcal{L}}$. Thus if we take a core radius for a trailing vortex as say $a = 5\text{m}$, then we would estimate $a_{\mathcal{L}}$ to be somewhat larger, say $a_{\mathcal{L}} = a/0.7 \approx 7\text{m}$. The speed $U_{\mathcal{L}}$ of a Lamb dipole in terms of the circulation of its vortices and $a_{\mathcal{L}}$ is given approximately by $U_{\mathcal{L}} = \Gamma/(2.2\pi a_{\mathcal{L}})$ (see Kloosterziel and Carnevale, 1993). Thus if we take $\Gamma = 100\ \text{m}^2/\text{s}$, this would give $U_{\mathcal{L}} \approx 2\ \text{m/s}$. Thus for $|\theta_0| = 1$ the magnitude to the density variation as a percentage of the background would be 6%

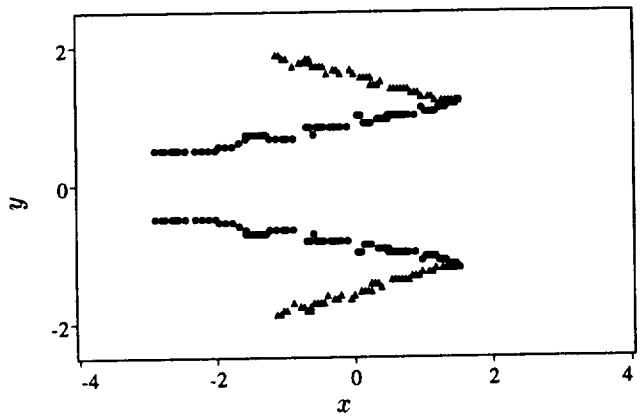

FIGURE 6. Trajectories of the vorticity extrema for $\theta_0 = -1$ ($\bullet$) and $\theta_0 = +1$ ($\blacktriangle$). The vortices propagate in the negative x-direction.

according to formula (4). In terms of temperature, this would correspond to a 20% variation on a background of 300°K.

It is interesting to consider how the temperature variation forces the growth of the non-axial vorticity. Taking the curl of the momentum equation, we obtain the vorticity equation,

$$\frac{\partial \omega_i}{\partial t} + u_j \frac{\partial \omega_i}{\partial x_j} = \omega_j \frac{\partial u_i}{\partial x_j} + \frac{1}{Re} \frac{\partial^2 \omega_i}{\partial {x_j}^2} - \epsilon_{ij1} \frac{\partial \theta}{\partial x_j}, \tag{5}$$

from which we can see how the buoyancy term directly forces the vorticity components ω_y and ω_z. In particular, a modulation of θ in the z direction will directly force the growth of ω_y, which is the field that we used to monitor the progress of the cooperative instability in the random initial velocity perturbation cases. There we found that when ω_y became comparable to ω_z, strong cross diffusion between the counter-rotating vortices occurred. Thus if we can accelerate the growth of ω_y through modulating θ in the axial direction, we may achieve a more rapid destruction of the coherent vortices. Since the rate of growth of ω_y will be directly proportional to $\partial\theta/\partial z$, we can expect that the early growth will be linear in time. This linear growth will dominate the exponential growth of an eigenmode perturbation of the cooperative instability if $\partial\theta/\partial z$ is sufficiently large.

With the hope of combining both the effects of temperature forcing and the cooperative instability, we decided to modulate the temperature field with the same wavelength that was observed to be the wavelength of the fastest growing mode in the experiments with random initial velocity perturbations. With the idea of implementing this kind of perturbation by heating, we chose to modulate the density by multiplying by a factor given by $(1 - \sin(k_\theta 2\pi z/L_z)) * 0.5$. With $L_z = \pi a_\mathcal{L}$, the appropriate wavenumber k_θ is 2. We performed a series of simulations with different amplitudes for θ_0 (the maximum value of the initial perturbation). For $\theta_0 = 1$, we found that the values of $|\omega_y|_{max}$ grew to the same levels as in the random perturbations cases but in a much shorter time. This is shown in Fig. 7 where we

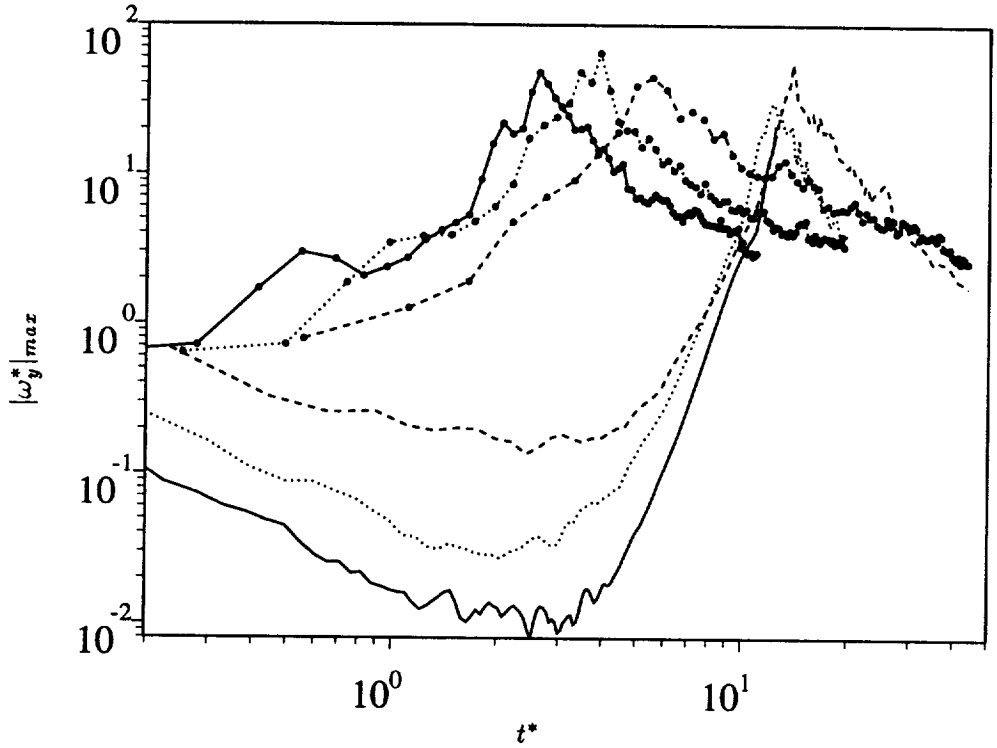

FIGURE 7. History of $|\omega_y|_{max}$ for the dipoles separated by $b = 1.9$ ——— , $b = 1.4$ ---- and $b = 1$ ····· . The curves without symbols correspond to the cases perturbed initially with the random velocity field, while those with circles correspond to the cases initially perturbed with spatially-periodic density variations ($\theta_0 = -1$).

plot the results for the same three values of the separation b as used in the previous simulations. We also plot the results from the random velocity perturbation runs for comparison. As before, the time scale is in τ units. Thus we see that for θ_0, levels of $|\omega_y|_{max}$ sufficient to destroy the coherence of the vortices are reached in a period of a few τ units. Also it is encouraging that as the distance b between the vortices increases, the time at which the peak in $|\omega_y|_{max}$ is reached decreases. To what extent this tendency will hold up for much larger values of b will be explored below.

That the early evolution is dominated by the buoyancy forcing can be seen by scaling the time differently. If we scale time according to $\hat{t} = \sqrt{\theta}t$ where t is in advective time units, then we find that the vorticity perturbations grow nearly linearly in $\hat{t}$ at early times, and the growth rate is independent of θ_0. This is shown in Fig. 8. We display the results for three different values of θ_0. This linear growth and scaling with the buoyancy time scale and not the τ time scale indicates that at early times the dynamics is dominated by buoyancy and not by the cooperative instability.

In Fig. 9, we show the evolution an isosurface of vorticity magnitude of the

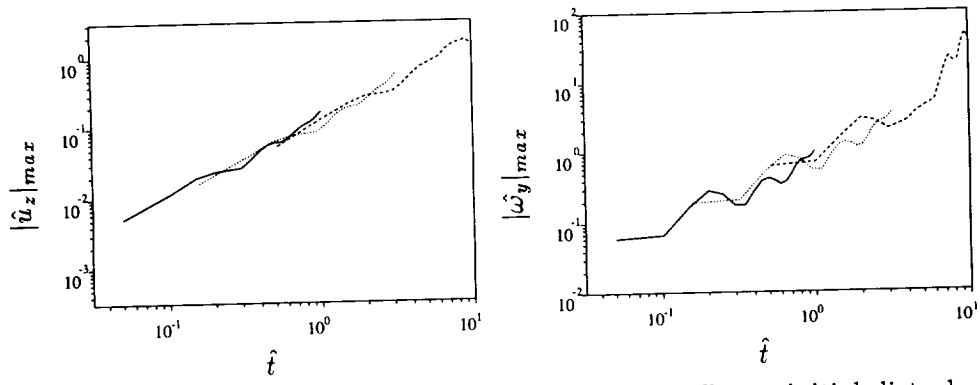

FIGURE 8. History of a)$|\hat{u}_z|_{max}$ and b) $|\hat{\omega}_y|_{max}$ for different initial disturbances (—— $\theta_0 = 1.$, ---- $\theta_0 = 0.1$, and ····· $\theta_0 = 0.01$).

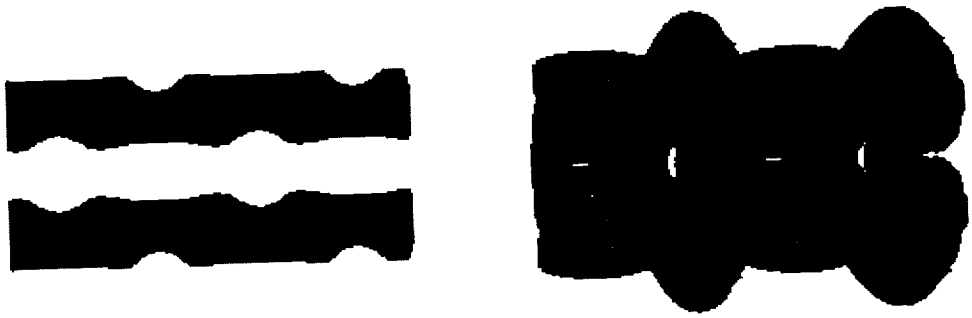

FIGURE 9. Plots of the iso-surface $|\omega|/\omega_0 = 0.64$ at $t^* = 1$ (left) and $t^* = 2$ (right).

thermally perturbed vortex pair for the case $b = 1.9$, $\theta_0 = -1$. Note that since the vortices will be drawn together where the density is lowest and since temperature is distributed with the same phase on each vortex, the pair is forced into the varicose mode. Recall that in the case of the random velocity perturbations, the fastest growing mode appeared to be a sinuous mode. This suggested that it may be possible to increase the growth rate of the instability by shifting the phase of the temperature on one vortex relative to the other in the temperature modulation in the axial direction. We performed two additional simulations with phase shifts $\alpha = \pi/8$ and $\pi/4$. The resulting graphs of the evolution of $|\omega_y|_{max}$ are shown in Fig. 10a along with the graph for the $\alpha = 0$ case. Although there does not appear to be much difference in the growth during the early phase, which is dominated by buoyancy forcing, ultimately the shift by $\pi/4$ does yield an increase in the peak amplitude by a factor greater than 2. Thus it seems that the phase shift does enhance the growth in the period of the evolution that we suppose to be dominated by cooperative instability. Figure 10b shows the history of Γ, which is calculated by summing all of the axial vorticity separately for $y < 0$. This shows that the

introduction of the phase shift causes the circulation to decay earlier and more rapidly. Unfortunately, it does not seem possible by using heating alone to force the two vortices into the sinuous mode that previous work indicates is the fastest growing mode.

Before proceeding to larger values of the separation, we will introduce another perturbation strategy. Although it is possible to construct heaters or burners near the source of trailing vortices on a wing or to inject jet exhaust directly into them, this may be inconvenient or impractical. As an alternative, with the idea of using jet exhaust for heating, we also considered the effect of heating in between the two vortices. Preliminary to performing simulations in three dimensions for larger values of b, we ran a series of two-dimensional tests. The two-dimensional simulations can show us the early effects of the thermal forcing and provide some idea of the resolution that will be needed in the three-dimensional simulations. In Figs. 11 and 12, we compare the results from three simulations. The left-hand panels in Fig. 11 show contour plots of ω_z at two times during the evolution in which the density distribution, with $\theta_0 = -1$, was proportional to the magnitude of the vorticity as in our earlier simulations. The initial density distribution is shown in the upper left panel of Fig. 12. Here we have used a separation of approximately $b = 6$ and $L_y = 6\pi$. With this density distribution and such a large separation, the vortices soon roll up into roughly circularly symmetric structures, and these tend to move toward each other by the Turner (1959) effect. In the center panels of Figs. 11 and 12, we illustrate the evolution in a case in which the heating (i.e. low density) is introduced in between the two vortices. The density distributions are initially exactly the same as in the simulation illustrated in the left-hand panels, except that the density patches are displaced a distance $a_\mathcal{L}$ away from the center of the vortices. In the early evolution, the gradients of density produce vorticity according to Eq. 5. Since the vorticity generated is proportional to $\partial\theta/\partial y$ (in these figures the y direction is toward the left), two dipolar vortices are formed. These newly generated dipoles move downward both due to self advection and due to the advection of the nearby primary vortices. Then from each secondary dipole, the vortex that has the same sign vorticity as the nearer primary vortex soon merges with the primary vortex. The remaining secondary vortex is partly sheared out around the primary vortex and partly rolled up to form a dipolar vortex with the primary. The case with $\theta_0 = +1$ is shown in the right-hand panels in Figs. 11 and 12. Here, the primary vortices again merge with the like signed secondary vortices, but the surviving secondary vortices are entirely sheared out to surround the primary vortices. Notice that in both cases, $\theta_0 = -1$ and $+1$, the production of thin filaments of density that are in some places parallel to the x-axis must be accompanied by the production of even thinner filaments of vorticity. This poses a resolution problem. Comparing grids with resolution 128×384 with 192×512, we found that there was not a significant difference in the evolution of the vorticity fields except on the smallest scales. Thus we were able to proceed with three-dimensional simulations of these 'experiments' with resolutions $128 \times 384 \times 64$. We were able to reduce the number of grid points in the z direction by taking only one full wavelength for the

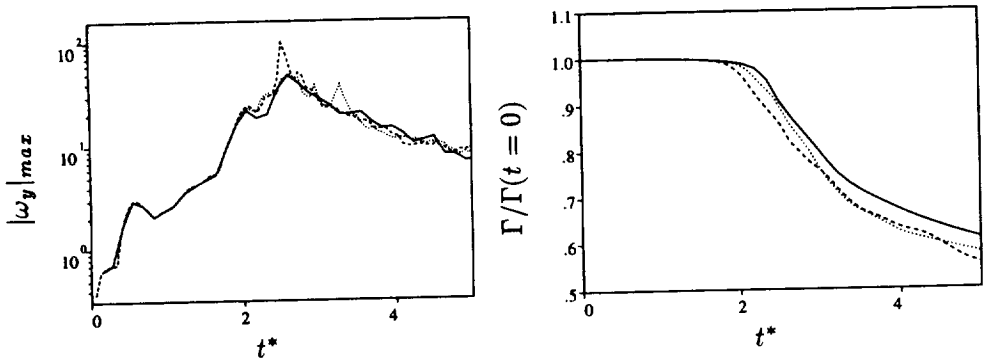

FIGURE 10. History of a) spanwise vorticity and b) circulation for —— $\alpha = 0$, ... $\alpha = \pi/8$ and ---- $\alpha = \pi/4$.

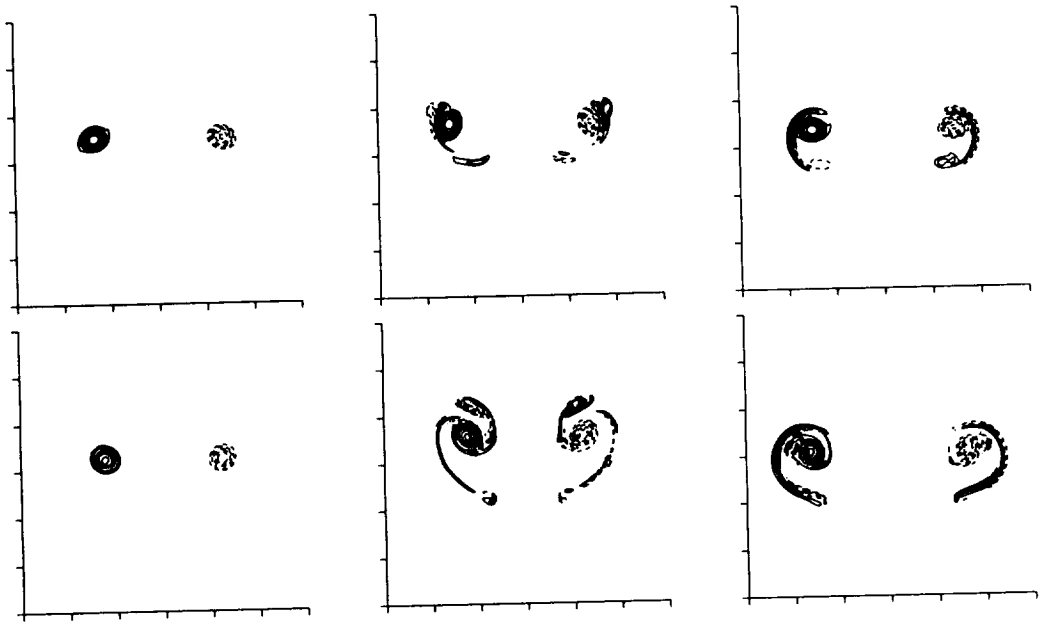

FIGURE 11. Contours of the vorticity in the two-dimensional simulations with the dipole halves separated by a distance of $8b$. The top/bottom panels correspond to early/late times. The left panels correspond to the case in which the density perturbation with peak magnitude $\theta_0 = -1$ is applied within the vortex. The middle (right) panels correspond to the case in which the patches of density are outside the initial vortices and are separated by $4b$ and have peak amplitude $\theta_0 = -1$ ($\theta_0 = +1$).

modulation of θ in that direction. This resolution is sufficient to observe the growth of the instability and to follow the initial stages of cross diffusion, but is inadequate to follow the evolution of fully developed turbulence. Hence, all of the runs to be presented will end somewhat short of this stage.

In Fig. 13a, we show the growth of $|\omega_y|_{max}$ for the three-dimensional simulations corresponding to the two-dimensional simulations just discussed. In order to make

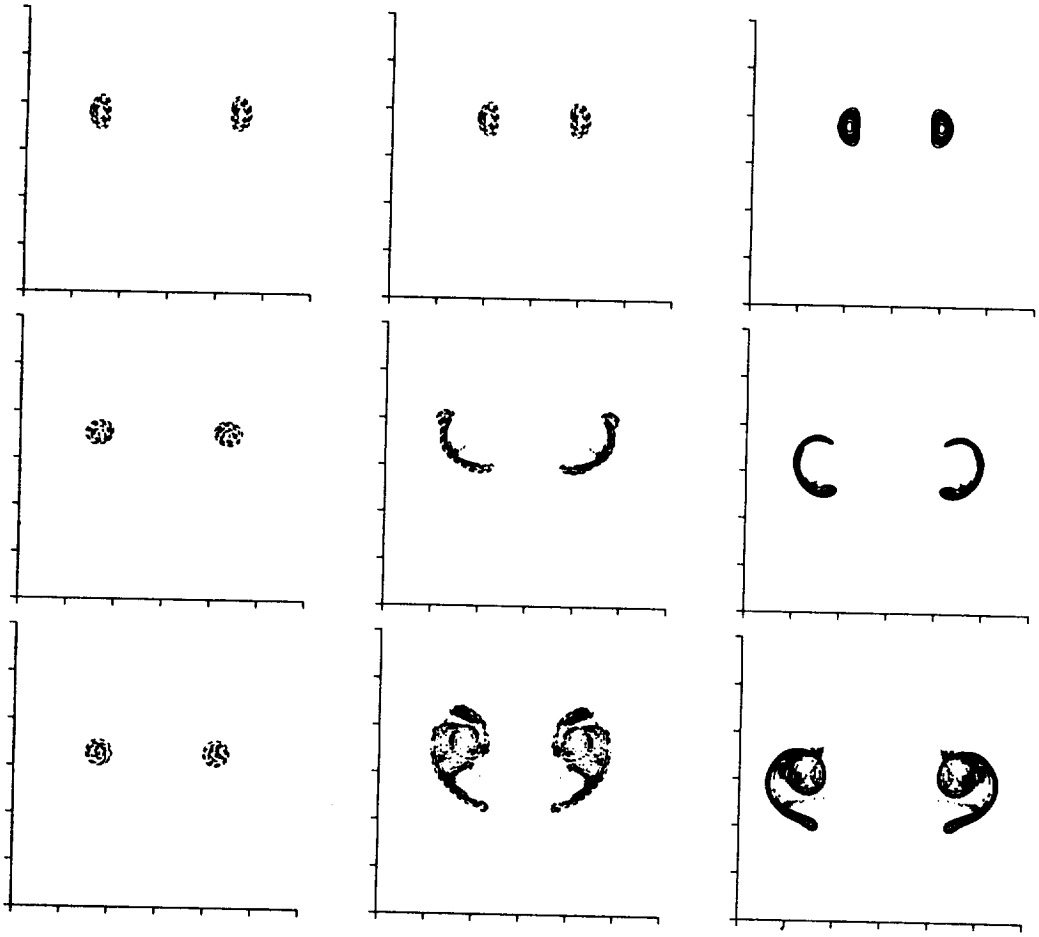

FIGURE 12. Density contours in two-dimensional simulations of the dipole with vortices separated by a distance $6b$. The panels in the left ($\theta_0 = -1$) column are for the case with the distribution of density initially coincident with the vorticity. In the cases represented by the center ($\theta_0 = -1$) and right ($\theta_0 = +1$) columns, the initial density patches are separated by $4b$. In each column, time advances from top to bottom.

some comparisons with the amplitude of the perturbation vorticity $|\omega_y|$ and the unperturbed peak value ω_{z0}, we will use advective time units in this and subsequent graphs. In Fig. 13a, we find that in the case with the density variation internal to the vortices, the peak for $|\omega_y|_{max}$ is reached by time $t = 2$ in advective time units. In τ units this would be approximately $t^* = 0.06$, which is remarkably short. This is much earlier than the time for the peak to be reached for smaller values of b. Thus the trend that we observed in Fig. 7 does continue for larger separations. Unfortunately, the value reached by $|\omega_y|_{max}$ is far short of the unperturbed vorticity value ω_{z0}, which is approximately 11.1 with advective time scaling. For smaller values of b, the value of $|\omega_y|_{max}$ peaked above ω_{z0} just before all vorticity components began

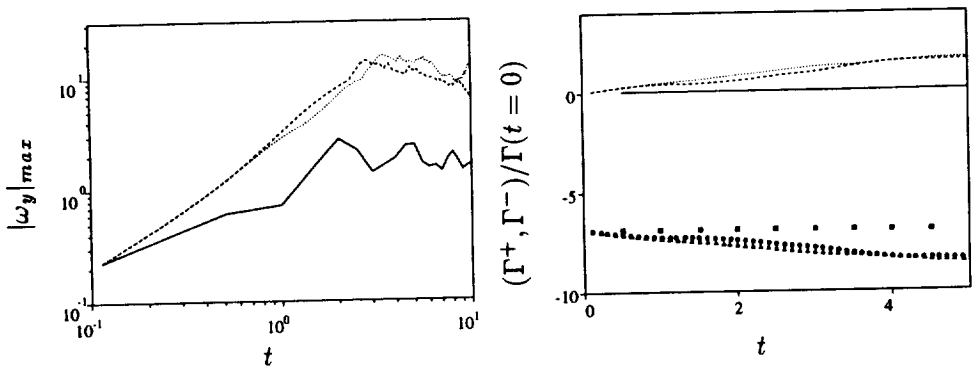

FIGURE 13. History of (a) $|\omega_y|_{max}$ and (b) $\Gamma^{\pm}$ for three cases. In both panels the solid curve corresponds to the case in which the density perturbation with peak amplitude $\theta_0 = -1$ is applied within the vortex, while the broken curves correspond to the cases for which the density variations were applied in between the vortices (---- $\theta_0 = -1$ and ····· $\theta_0 = +1$). The evolution of Γ^- is represented by symbols (▪ interior perturbation with $\theta_0 = -1$, • exterior perturbation with $\theta_0 = -1$, and ▲ exterior perturbation with $\theta_0 = +1$). $\Gamma^{\pm}$ is the sum of all $\pm$ values of ω_z for $y > 0$.

to decay rapidly (see Fig. 7). For this case with $b = 6$, it seems that the values of the perturbation ω do not grow sufficiently to reach a point of strong turbulent mixing, and hence the decay subsequent to $|\omega_y|_{max}$ reaching its peak is not strong. Also from Fig. 13a, we learn that for the cases with $b = 6$ and the density perturbation between the vortices, $|\omega_y|_{max}$ grows much more rapidly and peaks at a much higher value than in the case with internal density perturbation. In these cases $|\omega_y|_{max}$ does surpass ω_{z0}. The time to peak is about 0.1 in τ units. In advective time units, the decay of the circulation appears rather slow.

Over the course of the three simulations discussed in the previous paragraph, we computed the total circulation for each vortex; that is, we summed ω_z for all $y > 0$ and for $y < 0$ separately. The circulation for each vortex was conserved over the time span of these simulations. Also, for $y > 0$, we calculated Γ^+ (Γ^-), which is the sum of all values of ω_z for which $\omega_z > 0$ ($\omega_z < 0$). The history of Γ^+ and Γ^- is shown in Fig. 13b. For the case with internal heating, there is relatively less variation in Γ^+ and Γ^- over time than for the case with external heating. For the external heating case there is significant growth of Γ^+, indicating strong deformations of the vortex. However, the fact that in each case the sum of Γ^+ and Γ^- is conserved in time tells us that the vortices are not so strongly deformed as to allow any mixing between the two primary vortices by $t = 5$ in advective time units. Due to lack of computational resources, we were not able to run these cases to much longer times, so we do not know how much the circulation would decay on the τ time-scale. We recall that for the cases with small b, a decay of about 25% of the circulation took from about two to four τ units. For $b = 6$, $\tau \approx 33$ advective time units, which is much longer than the timespan represented here. Thus it may be that the decay in circulation has just not begun on the short timescale represented by Fig. 13.

To further compare the results for large and small separations, we plot the history

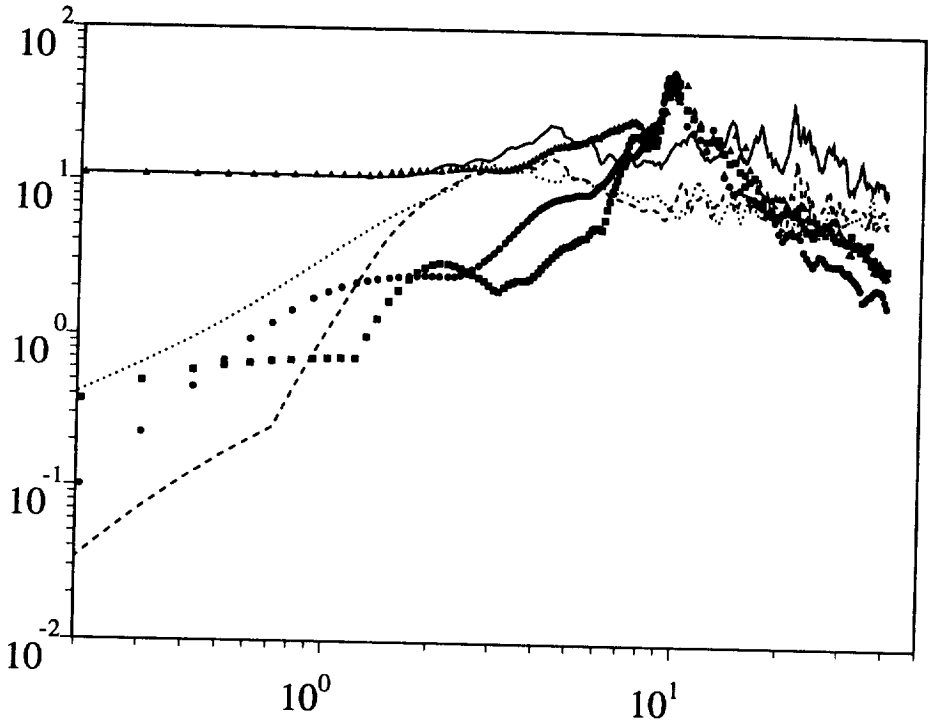

FIGURE 14. History of the three vorticity components for two cases: for the case with $b = 6$ with the density variation in between the vortices ($|\omega_x|_{max}$ ---- , $|\omega_y|_{max}$ ····· , $|\omega_x|_{max}$ ——), and for the case with $b = 2$ and density variation in the interior of the vortices ($|\omega_x|_{max}$ • , $|\omega_y|_{max}$ ■ , $|\omega_x|_{max}$ ▲).

of all three vorticity components in Fig. 14 for both $b = 6$ and $b = 1.9$. The unit of time for this graph is taken as the advective time units. For $b = 1.9$, all vorticity components rapidly decay after the perturbation vortices surpass the axial vorticity, while for $b = 6$ all component remain relatively strong after peaking.

4. Conclusions

With the first series of simulations that we presented, we were able to reproduce the results of the laboratory studies of the short-wave cooperative instability. The numerical simulations provide the possibility of analyzing the evolution of the velocity and vorticity fields far more accurately than is possible with current diagnostic techniques in the laboratory. In particular, measurement of the non-axial components of vorticity, which are key to the instability, is very difficult in the laboratory. Here we were able to analyze the growth of the non-axial vorticity components and show how they led to the cross diffusion of circulation between the two primary vortices. In addition, the degree of control over initial conditions in the simulations allows far more precise testing of hypotheses than is possible in the laboratory. The main drawback of the numerical simulations is the problem of insufficient resolution for simulations in which the separation is large.

Having analyzed the basic short-wave instability, we turned to the problem of finding a practical way of perturbing the pair of counter rotating vortices so as to accelerate the short-wave cooperative instability. We suggested that variations of density along the axial direction may be used to excite the cooperative instability. These density variations result in buoyancy forcing that persists beyond the initial addition of the perturbation. There is an initial period dominated by the thermal forcing in which the perturbation vorticity begins to grow. If the wavelength of the axial modulation of the density perturbation is chosen to match that of the fastest growing cooperative instability mode, then this proves an efficient mechanism for initiating the short wave instability.

We were able to demonstrate the effectiveness of density perturbations in initiating instability and producing rapid cross diffusion for separations up to about $b/a = 2$. Beyond this, problems of numerical resolution make the situation less clear. We presented some evidence at $b/a \approx 6$ that similar effect could be found, but we were not able to simulate long enough at high enough resolution to see whether the cross diffusion would occur on the same time scale in τ units as at smaller b. Thus we are led to suggest that this would be a fertile area for laboratory experimentation.

As for the practicality of using density perturbations, we can say a few words here. We imagine that the method of producing the density variation for aircraft trailing vortices would be by heating either within the vortices or between them. This could be accomplished either by redirecting and modulating the existing jet exhaust or by adding auxiliary burners in the vicinity of the points where the vortices roll up (e.g. wing tips, and flap edges). This heating would only be required during take-offs and landings. Consider the problem of modulating the temperature of a vortex with a sinusoidal perturbation of wavelength about twice the vortex core radius with an amplitude 30°C over say a 10km span. If we take the estimates of $a \doteq 5$m for the core radius and 300km/hr for the plane speed, we calculate that the total amount of kerosene that would need to be burned from such a perturbation would be only about 140kg. This would seem a reasonable cost if the result were to minimize the effect of the trailing vortices.

Acknowledgments

The authors gratefully acknowledge the important contribution of W. C. Reynolds in suggesting the use of temperature perturbations to drive the instability of the vortices. The authors are very grateful to the Center for Turbulence Research for making their collaboration possible. GFC and PO received additional support from the National Science Foundation (INT-9511552) and the Office of Naval Research (N00014-97-1-0095). In addition, GFC acknowledges support from the San Diego Supercomputer Center under an NPACI award. The top panel of Fig. 4 was reproduced with the kind permission of C. H. K. Williamson.

REFERENCES

BATCHELOR, G. K. 1991 *An introduction to fluid dynamics*, Cambridge; New York: Cambridge University Press.

BAYLY, B. J. 1986 Three-dimensional instability of elliptical flow. *Phys. Rev. Lett.* **57,** 2160-2163.

CARNEVALE, G. F. & KLOOSTERZIEL, R. C. 1994 Lobe shedding from propagating vortices. *Physica D.* **76,** 147-167.

KLOOSTERZIEL R. C., CARNEVALE G. F. & PHILIPPE D. 1993 Propagation of barotropic dipoles over topography in a rotating tank. *Dynamics of Atmospheres and Oceans.* **19,** 65-100.

LAMB, HORACE, SIR 1945 *Hydrodynamics*, New York, Dover.

LEWEKE, T. & WILLIAMSON, C. H. K. 1998 Cooperative elliptic instability of a vortex pair. *J. Fluid Mech.* **360,** 85-119.

LANDMAN, M. J. & SAFFMAN, P. G. 1987 The three-dimensional instability of strained vortices in a viscous fluid. *Phys. Fluids.* **30,** 2339-2342.

PIERREHUMBERT, R. T. 1986 Universal short-wave instability of two-dimensional eddies in an inviscid fluid. *Phys. Rev. Lett.* **57,** 2157-2159.

RISSO, F., CORJON, A., & STOESSEL, A. 1997 Direct numerical simulations of wake vortices in intense homogeneous turbulence. *AIAA J.* **35,** 1030-1040.

SHARIFF, K., VERZICCO, R. & ORLANDI, P. 1994 A numerical study of three-dimensional vortex ring instabilities: Viscous corrections and early nonlinear stage. *J. Fluid Mech.* **279,** 351-375.

SPALART, P. R. 1996 On the motion of laminar wing wakes in a stratified fluid. *J. Fluid Mech.* **327,** 139-160.

SPALART, P. R. 1998 Airplane trailing vortices. *Ann. Rev. Fluid Mech.* **30,** 107-138.

THOMAS, P. J. & AUERBACH, D. 1994 The observation of the simultaneous development of a long- and a short-wave instability mode on a vortex pair. *J. Fluid Mech.* **265,** 289-302.

VERZICCO, R. & ORLANDI P. 1996 A finite difference scheme for direct simulation in cylindrical coordinates. *J. Comp. Phys.* **123,** 402-414.

WALEFFE, F. 1990 On the three-dimensional instability of strained vortices. *Phys. Fluids A (Fluid Dynamics).* **2,** 76-80.

WIDNALL, S. E., BLISS, D. B. & TSAI, C.-Y. 1974 The instability of short waves on a vortex ring. *J. Fluid Mech.* **66,** 35-47.

Evaluation of the statistical Rayleigh-Ritz method in isotropic turbulence decay

By G. L. Eyink [1] AND A. Wray

A Rayleigh-Ritz method for calculating the statistics of nonlinear dynamical systems is tested against LES data for homogeneous and isotropic decay of turbulence. The comparisons in this work are of 2-point, 2-time Eulerian velocity correlators. At this level, the Rayleigh-Ritz predictions are formally realized by a linear Langevin model for the fluctuation variables. We study how well standard K-ε models that are adequate to describe the decay of ensemble means can also predict the decay of fluctuations. In addition to such standard *RANS* closures, we also consider some spatially nonlocal and temporally non-Markovian models, which include scale-dependent eddy viscosities and convective sweeping in Fourier space.

1. Introduction

This work investigates a Rayleigh-Ritz variational method to solve for the statistics of nonlinear dynamics, which was earlier proposed (Eyink, 1996). Formally, the method provides an approximate solution of the Liouville-Hopf equation for the time-evolution of probability distributions in phase-space by the method of weighted residuals (Finlayson, 1972). The Rayleigh-Ritz method can be understood most simply as the classical moment-closure method extended to give a description, not merely of averages, but also of fluctuations. The ordinary moment-closure equation for a set of ensemble-averages $m_i(t) = \langle \psi_i(t) \rangle$, which we may write as

$$\dot{m}_i(t) = V_i(\mathbf{m}, t), \tag{1}$$

can be obtained as an Euler-Lagrange equation in a variational solution of the Liouville-Hopf equation by the method of weighted residuals. On the other hand, the Euler-Lagrange equation for a *constrained variation* under a constraint on the mean moment histories is a *perturbed closure equation* of the form

$$\dot{m}_i(t) = V_i(\mathbf{m}, t) + \sum_j C_{ij}(\mathbf{m}, t) h_j(t). \tag{2}$$

Here, $h_j(t)$ is a Lagrange multiplier function to incorporate the constraint. The function $\mathbf{C}(\mathbf{m}, t)$ represents the statistical *covariance matrix* of the closure variables at a single time t, or $C_{ij}(\mathbf{m}, t) := \langle \psi_i'(t) \psi_j'(t) \rangle_{\mathbf{m}}$, given as a function of the moment averages $\mathbf{m}$. As usual, $\psi_i' = \psi_i - m_i$ represents a fluctuation variable.

1 University of Arizona

Any of the closure schemes ordinarily applied to the modeling of Eq. (1) for the averages can also be applied to Eq. (2), providing thereby predictions for fluctuations. Intuitively, the imposition of constraints should give information about fluctuations by the principle that the probability of a fluctuation is determined by the cost to produce it under a constraint. This may be called the "Cramér principle", see (Frisch, 1995). In fact, it may be shown (Eyink, 1996) that the solution of Eq. (2) contains complete information about the statistical distribution of the random histories $\psi_i'(t)$. In particular, it can be shown that the *2-time covariance matrix* $C_{ij}(t,t_0) := \langle \psi_i'(t)\psi_j'(t_0)\rangle$ is obtained in the Rayleigh-Ritz method from a simple *fluctuation-response relation*:

$$C_{ij}(t,t_0) = R_{ij}(t,t_0) + R_{ji}(t_0,t) \tag{3}$$

where $\mathbf{R}(t,t_0)$ is the response $R_{ij}(t,t_0) := \frac{\delta m_i(t)}{\delta h_j(t_0)}\Big|_{\mathbf{h}=0}$ of the solution $m_i(t)$ of Eq. (2) to an infinitesimal change of the control field $h_j(t)$, see (Eyink, 1998).

It is the purpose of this work to investigate the success of standard closures to predict fluctuations when employed in the constrained variational equation (2). We shall consider here only the simplest situation for a turbulent fluid governed by the Navier-Stokes equations, namely, homogeneous, isotropic decay at high Reynolds number. It is well-known that *RANS* closures such as the standard K-ε model are adequate to reproduce the ensemble-averages in such an equilibrium turbulence. The main issue to be addressed here is the success of such closures to predict the lowest-order statistic for the fluctuations, the 2-time covariance matrix of the closure variables. The Rayleigh-Ritz method also gives predictions for all higher-order multi-time statistics, e.g. transition probabilities, but we shall confine ourselves here to a check only at the lowest-order. The 2-time correlations already have some direct interest in terms of the *predictability problem* for meteorology and climatology since they give the statistical correlation between successive states, e.g. the correlation between the weather today and weather tomorrow. In addition, information about fluctuations is essential in engineering problems such as the turbulence *control problem* or the LES-RANS *matching problem* for wall-bounded flows.

The method of our investigation is to compare the Rayleigh-Ritz predictions with those of an Ensemble LES calculation for isotropic decay. The use of LES rather than DNS allows our study to be made, in principle, at infinite Reynolds number and, hence, to avoid the issue of viscous corrections to the closures. The Ensemble LES method is discussed in detail in (Carati, 1997). Our study uses a dynamical Smagorinsky subgrid stress model with the dynamical coefficient calculated for a sharp spectral filter by an average over 64 different ensemble realizations on a 64^3 lattice. The single-time spectrum is obtained for the resolved velocity field $\mathbf{v}(\mathbf{x},t)$ by averaging over the space domain as well as the ensemble realizations. In addition to the single-time statistics, we obtain the *2-time cospectra* of the velocities $\mathbf{v}(\mathbf{x},t)$ at each time t with the velocities $\mathbf{v}(\mathbf{x},t_0)$ at the initial time t_0. This allows us to make a direct check on the Rayleigh-Ritz predictions. To avoid issues of modeling the single-time correlations, we directly input the LES results for the single-time

correlations at the initial time t_0. Then, the Rayleigh-Ritz method is used to integrate these input correlations forward in one time variable to obtain the 2-time correlations at the pair of times t, t_0. These predictions are finally compared with the LES results for the same quantities as the basic check on the method. The Rayleigh-Ritz calculations are carried out primarily for the K-ε closure. It is a main objective of this work to determine what temporal statistics may be correctly predicted with such a standard 1-point closure. However, based upon the results of the comparison of those predictions with the LES results, improved Rayleigh-Ritz approximations are also developed exploiting more refined closure assumptions.

2. Comparison of Rayleigh-Ritz with LES

2.1 The single-time LES results

Let us first describe the results of our LES calculations for the velocity spectrum $E(k,t)$, which is graphed in Fig. 1 for several times t over the LES run, including the initial time $t_0 = 0.2295$. As may be seen, the peak wavenumber at the initial time t_0 is approximately $k_P = 9$, but this decreases in time to a value of about $k_P = 6$ at the end of the run. At each time t, the spectrum beyond the peak is an inertial-range power-law. Graphing compensated spectra reveals that the power-law is, to a reasonably good approximation, given by the Kolmogorov $\frac{5}{3}$ law. As time advances, the spectra are degraded rapidly in the high wavenumber range, while at wavenumbers well below the peak the spectrum is nearly unchanged in time. The low-wavenumber range can also be reasonably well fit by a power-law $\propto k^m$ with $m \approx 6$. This power-law is transient due to backscatter of energy into the low-wavenumbers, which leads to a slow decrease in the effective m value over time.

2.2 Comparison of the K-ε Rayleigh-Ritz with LES

The most popular engineering closure for the ensemble-averages is $\overline{v}_i, \overline{K}$, and $\overline{\varepsilon}$ is the K-ε RANS model. As a reminder, its equations have the form:

$$\partial_t \overline{v}_i + (\overline{\mathbf{v}} \cdot \nabla)\overline{v}_i = -\nabla_i \overline{p} - \nabla_j \tau_{ij} + \nu \triangle \overline{v}_i, \tag{4}$$

$$\partial_t \overline{K} + (\overline{\mathbf{v}} \cdot \nabla)\overline{K} = -\tau_{ij}\nabla_j \overline{v}_i - \overline{\varepsilon} - \nabla_i J_i + \nu \triangle \overline{K}, \tag{5}$$

$$\partial_t \overline{\varepsilon} + (\overline{\mathbf{v}} \cdot \nabla)\overline{\varepsilon} = \nu \triangle \overline{\varepsilon} + \nabla_i \mathcal{D}_i + \mathcal{P} - \Phi. \tag{6}$$

Here, $\tau_{ij} = \overline{v_i' v_j'}$ is the Reynolds stress. J_i is the space transport of kinetic energy by turbulent diffusion and molecular viscosity. Likewise, $\mathcal{D}_i$ is the space transport of dissipation, and $\mathcal{P}, \Phi$ are production and destruction of dissipation, respectively. The equations are exact as written, but the terms $\tau_{ij}, J_i, \mathcal{D}_i, \mathcal{P}$, and Φ are all higher-order moments that must be modeled. In the standard K-ε closure, the Reynolds stress is modeled as:

$$\tau_{ij} = \frac{2}{3}\overline{K}\delta_{ij} - \nu_T(\nabla_j \overline{v}_i + \nabla_i \overline{v}_j), \tag{7}$$

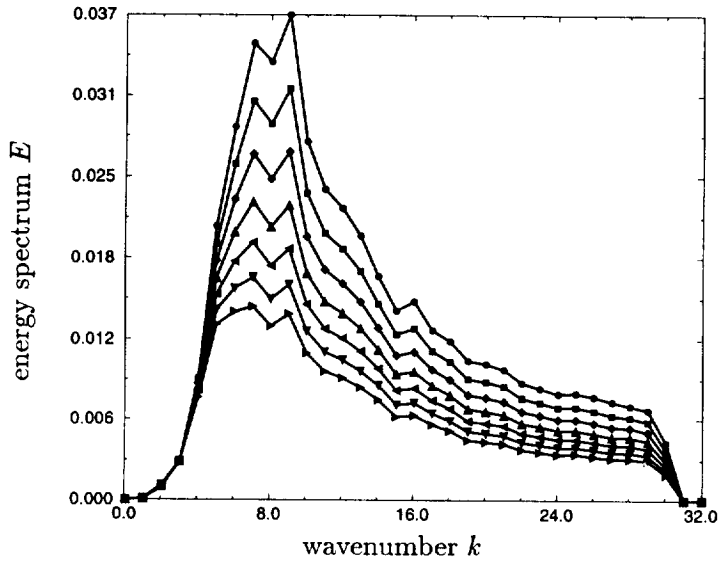

FIGURE 1. Velocity spectrum $E(k,t)$. • : t=0.2295, ■: t=0.3299, ♦: t=0.4183, ▲: t=0.5262, ◄: t=0.6407, ▼: t=0.7647, ►: t=0.8940

where the eddy viscosity is given by $\nu_T = C_\mu \frac{\overline{K}^2}{\overline{\varepsilon}}$, with $C_\mu = 0.09$ the conventional value of the constant. Similar gradient-diffusion models are made for the other transport terms in the K-ε closure equations, but these do not concern us here.

As reviewed in the Introduction, the Rayleigh-Ritz method gives predictions for statistics of the fluctuations v_i' by means of a perturbation of the moment-equations (4)-(6). At the level of 2nd-order statistics, the predictions are the same as those of a linear Langevin model (Eyink, 1998). For the K-ε Rayleigh-Ritz, the corresponding Langevin equations are obtained by linearizing (4)-(6) around the homogeneous state $\overline{v}_i \equiv 0, \overline{K}(t), \overline{\varepsilon}(t)$ and by then adding suitable white-noise forces. In the case of isotropic decay, the Langevin models for the two sets of variables v_i' and K', ε' are completely uncoupled, and they can be analyzed separately. Results on the K-ε fluctuations will be given elsewhere. The equation for the velocity fluctuations is $\partial_t v_i' = \nu_T \triangle v_i' + q_i$. Because all of the coefficients in the Langevin model are independent of space, it is advantageous to take a Fourier transform. The fluctuations at distinct wavenumbers then also completely decouple. In the Fourier representation

$$\frac{d}{dt}\widehat{v}_i(\mathbf{k},t) = -\nu_T k^2 \widehat{v}_i(\mathbf{k},t) + \widehat{q}_i(\mathbf{k},t), \tag{8}$$

It is clear that this equation cannot be accurate at all wavenumbers. In particular, K-ε modeling is not intended to apply to inertial-range wavenumbers and higher. The principle that the dynamics of fluctuations should be governed by the same equations which determine the evolution of the mean values is known in statistical physics as the "Onsager regression hypothesis" (Onsager, 1931). For the hydrodynamic variables of molecular dynamical systems, the hypothesis is asymptotically exact in the limit of wavenumbers small compared to the inverse mean-free-length

and frequencies small compared to the inverse mean-free-time. Likewise, we anticipate here that a K-ε Rayleigh-Ritz can be accurate—at most—for some range of low wavenumber modes.

In general, one should expect that a model superior to standard K-ε will allow for a wavenumber- and time-dependent dynamics as in the velocity sector

$$\frac{d}{dt}\widehat{v}_i(\mathbf{k},t) = A(k,t)\widehat{v}_i(\mathbf{k},t) + \widehat{q}_i(\mathbf{k},t). \tag{9}$$

Without loss of generality, this may be represented by a scale-dependent eddy-viscosity as $A(k,t) = -\nu_T(k,t)k^2$. Standard Kolmogorov dimensional reasoning would give $\nu_T(k,t) \propto \varepsilon^{1/3}(t)k^{-4/3}$ in the inertial range. In fact, we may note that a Langevin model for the velocity of the form of (24) was proposed by Kraichnan in his "Distant-Interaction Algorithm" (DSTA) (Kraichnan, 1987). However, Kraichnan's model was proposed for *Lagrangian* time-correlations rather than the *Eulerian* ones considered here. There is nothing that prevents the Rayleigh-Ritz method being applied to Lagrangian variables of the fluid system. However, for the moment we wish to study the ability of the standard K-ε closure to make correct predictions for Eulerian statistics within the variational apparatus.

Our basic test of the K-ε Rayleigh-Ritz scheme is to calculate the 2-time spectrum $E(k;t,t_0)$. Although the predictions are the same as those of the Langevin model in Eq. (8), we shall not calculate the 2-time correlations directly from that stochastic equation. Instead, we make use of the fluctuation-response relation (3). A direct application would involve calculating a numerical derivative with respect to the h-field of the solution of the perturbed closure equation, for $h(t) = h\delta(t - t_0)$. However, this algorithm turns out to be numerically unstable, and its accuracy degrades rapidly in time. Instead, our numerical procedure, for each wavenumber k, is to solve in conjunction with the ODE for the ensemble-means a linearized K-ε closure equation for the 2-time cospectra with the LES 1-time cospectra at time t_0 as initial data. Although the Langevin equations are not directly employed to calculate the 2-time cospectra, it is still important to determine whether these Rayleigh-Ritz predictions have a model realization. To investigate this we have also calculated the noise spectra of the Langevin white-noise forces $Q(k,t)$. These are obtained from a *fluctuation-dissipation relation* (Eyink, 1998)

$$Q(k,t) = \nu_T k^2 E(k,t) + \frac{1}{2}\dot{E}(k,t), \tag{10}$$

by inputting for each time t the single-time spectra discussed in Section 2.1. Realizability requires that $Q(k,t)$ be nonnegative for each wavenumber k.

In Fig. 2 the 2-time spectra $E(k;t,t_0)$ are graphed as functions of wavenumber k, for both the LES and the K-ε Rayleigh-Ritz, at a sequence of times t starting with t_0. Several points of comparison become immediately apparent. At wavenumbers much less than the peak, the LES and Rayleigh-Ritz spectra are almost indistinguishable. Around the peak wavenumber there is a close agreement for a short time, but later on the Rayleigh-Ritz spectrum decays slower than the LES. At wavenumbers higher than the peak, the opposite is initially true: the LES spectrum decays

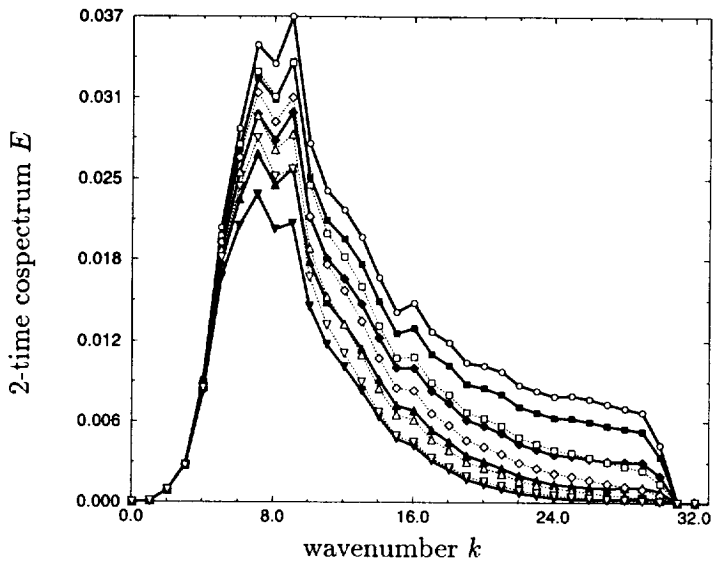

FIGURE 2. Comparison of 2-time velocity cospectra $E(k;t,t_0)$. t=0.2295: • - LES, ○ - $K\varepsilon$RR; t=0.3299: ■- LES, □- $K\varepsilon$RR; t=0.4183: ♦- LES, ◇- $K\varepsilon$RR; t=0.5262: ▲- LES, △- $K\varepsilon$RR; t=0.6407: ▼- LES, ▽- $K\varepsilon$RR.

slower initially and persists at larger magnitude than the Rayleigh-Ritz spectrum. However, as time passes, the decay rate of the LES spectrum increases, and it first equals in magnitude and then dips below the Rayleigh-Ritz spectrum.

These observations are reasonably explained. At the low wavenumbers, the rate of change of both spectra is very slight so that the close agreement is automatic. The agreement at early times near the energy peak is presumably an indication that the K-ε model with the standard choice of constants is an excellent model of the intrinsic dynamics at those scales. This is the range of wavenumbers in which the "regression hypothesis" appears to be valid. In other words, for early times the decay of correlations is due primarily to the space diffusion of fluctuations by turbulent viscosity, well-described by the standard K-ε model. However, since we are dealing with *Eulerian* time-correlations, this decay mechanism is overwhelmed at later times by *convective dephasing* (Kraichnan, 1964b). The phase shift $e^{-i\mathbf{v}\cdot\mathbf{k}(t-t_0)}$ in Fourier amplitudes due to advection by a random velocity $\mathbf{v}$ leads to a decay rate of correlations which goes roughly as $\sim v_0^2 k^2 (t-t_0)$, where v_0 is an rms velocity. This grows faster in k than an eddy-damping rate such as appears in Eq. (9), which goes as $\nu(k,t)k^2 \sim k^{2/3}$ in the inertial range. At the same time, the decay rate from convection grows in time proportional to $t-t_0$. Hence, it is negligible at short times but rapidly grows to dominate the intrinsic decay from eddy-damping. This leads to the later overestimation of the spectrum around the peak wavenumber by K-ε Rayleigh-Ritz since the latter incorporates no such convective effects. The same physical considerations explain the observations in the high wavenumber range beyond the peak. At early times when convective effects are negligible, the constant eddy-viscosity in the standard K-ε model overestimates the eddy-damping in the

higher wavenumbers. Hence, the early decay of the Rayleigh-Ritz spectrum is too rapid. At the same time, the K-ε modeling includes no convective dephasing effects, which rapidly grow to dominate the decay of the Eulerian time-correlations. Hence, the early decay of the LES 2-time spectra lags behind the Rayleigh-Ritz predictions, but at later times it exceeds the Rayleigh-Ritz decay.

We do not have space here for a complete discussion of the realizability of the K-ε Rayleigh-Ritz, but it is important to make a few remarks. The noise spectrum $Q(k,t)$ of the Langevin force in Eq. (12) calculated from the FDT Eq. (10) is not strictly realizable. Indeed, it takes on negative values for large wavenumbers $k > 36$ and also slightly negative values for a range of small wavenumbers $k = 5-8$. The breakdown at large wavenumbers is not really a great surprise because the K-ε modeling is not expected to be valid there. However, the breakdown for the wavenumbers $k = 5-8$ is more serious. The reason for the realizability violation, as we shall see below, is the K-ε model's underestimation of the eddy-viscosity in those wavenumber modes. On the other hand, the wavenumber which corresponds to the spectral peak at the initial time, $k = 9$, has a *marginally realizable* noise covariance. That is, to within numerical precision, the noise vanishes at that wavenumber initially. This is not an accident, as we see below.

2.3 Improved Rayleigh-Ritz and comparison with LES

We now consider various strategies to develop an improved Rayleigh-Ritz. As a first step, we shall carry out a *POP analysis*, which, as described in (Penland, 1989), is a technique to obtain models for $A(k,t_0)$ and $Q(k,t_0)$ directly from empirical 2-time data. The time-dependent POP method we use is a "zero-lag" prescription discussed in (Eyink, 1998). In principle, the POP analysis gives the best possible such linear Langevin model although there is an important issue about the "optimum lag" to be used in this analysis. If it is realizable, then the best one could hope is that the Rayleigh-Ritz *Ansatz* should reproduce the POP model. This is always possible if the the Rayleigh-Ritz *Ansatz* goes beyond the standard K-ε model by allowing a wavenumber and time-dependent eddy-viscosity $\nu_T(k,t)$, as in Eq. (9). In addition to the POP analysis, we shall also determine a "zero-lag K-ε model" by insisting that the Rayleigh-Ritz produce $Q(k,t) \equiv 0$ for all k,t. We may enforce in this way some agreement with the zero-lag POP result since the latter always has vanishing noise initially when the input 2-time covariance is continuously differentiable (Eyink, 1998). Thus, we may use this condition as a means to extract k,t-dependent values of the K-ε closure constant $C_\mu(k,t)$. This "zero-lag" Rayleigh-Ritz procedure differs from POP in using only single-time LES data.

We shall determine below both zero-lag POP models and "zero-lag" K-ε Rayleigh-Ritz models and compare these to one another. From the discussion in Section 3.2, we may anticipate that these models should give a good short-time description of the Eulerian 2-time correlations but a much better long-time description of Lagrangian 2-time correlations. Of course, there is nothing to prevent application of both the POP and Rayleigh-Ritz methods to Lagrangian dynamical variables. Furthermore, one should not expect the zero-lag POP models to differ substantially between the two cases. The reason has to do with the physics of the convective dephasing.

We have seen above that the decay rate from convective dephasing should vanish $\propto (t - t_0)$ for short times. In that case, any difference in the time derivative of Eulerian and Lagrangian correlators should *vanish* in the zero-lag limit $t \to t_0$. Needless to say, while the POP models are not expected to differ for the two sets of variables, the *validity* of the POP models will depend upon the choice. In agreement with earlier workers such as (Kraichnan, 1987), we expect the POP Langevin models to give a much better representation of the Lagrangian dynamics.

In principle, therefore, we should compare the predictions of our POP and "zero-lag" Rayleigh-Ritz models to Lagrangian 2-time data from the LES. We hope to do so later on, but, at the moment, such data are not available. Below we have attempted instead to add into the Rayleigh-Ritz equations the "convective dephasing" in order to make a more meaningful comparison with the Eulerian 2-time data at our disposal. We have added the convection effects in a relatively crude way by supplying to the derivative of the 2-time correlations in each wavenumber shell a new term

$$\partial_t E(k;t,t_0) = \cdots - \left[2C_\eta k^2 \int_{t_0}^{t} ds \int_0^k dq\ E(q,s)\right] E(k;t,t_0). \qquad (11)$$

Note that $2\int_0^k dq\ E(q,t)$ represents the mean-square velocity $v^2_{\rm rms}(k,t)$ of all the wavenumbers smaller than the given wavenumber. This is natural for a term to represent advection by the larger eddies. The constant C_η represents the "efficiency" of the dephasing. Clearly, this should in reality be wavenumber dependent. Because the smaller eddies are more random and more rapidly evolving, the phase shifts they induce in Fourier amplitudes will suffer much destructive interference before averaging over the ensemble of velocities. Hence, their contribution to correlation decay will be reduced. On the contrary, the larger eddies are much more coherent and slowly evolving so that there will be mostly constructive addition to the Fourier phase shift. The constant value $C_\eta \equiv 1$ would hold for perfect "efficiency" of the dephasing, as is true for a frozen-in-time, uniform Gaussian velocity, with perfect coherence in space-time (Kraichnan, 1964b). Thus, we adopt a value, somewhat arbitrarily, of an order of magnitude less than unity: $C_\eta = 0.1$. This is likely to be an overestimate at high wavenumbers and an underestimate at low wavenumbers. The above crude model can be regarded as a simplified form of the DIA model for the convection effects as discussed in (Kraichnan, 1959), Section 5, and (Kraichnan, 1964a).

Our POP results are presented in the form of a "dimensionless eddy-viscosity" $C_\mu(k,t_0) := \frac{\nu_T(k,t_0)}{\overline{K}^2(t_0)/\overline{\varepsilon}(t_0)}$.

In agreement with our earlier observations, there is a "negative eddy-viscosity" in the lowest wavenumbers $k = 1-3$, the most negative value -1.9333 occurring at $k = 1$. Thereafter, the eddy viscosity grows to a maximum 1.1760 at wavenumber $k = 6$ and beyond the maximum decays in a roughly power-law fashion, consistent with expectations for an inertial range. The value at the energy peak wavenumber $k = 9$ is 0.0858, remarkably close to the standard K-ε value of $C_\mu = 0.09$. We

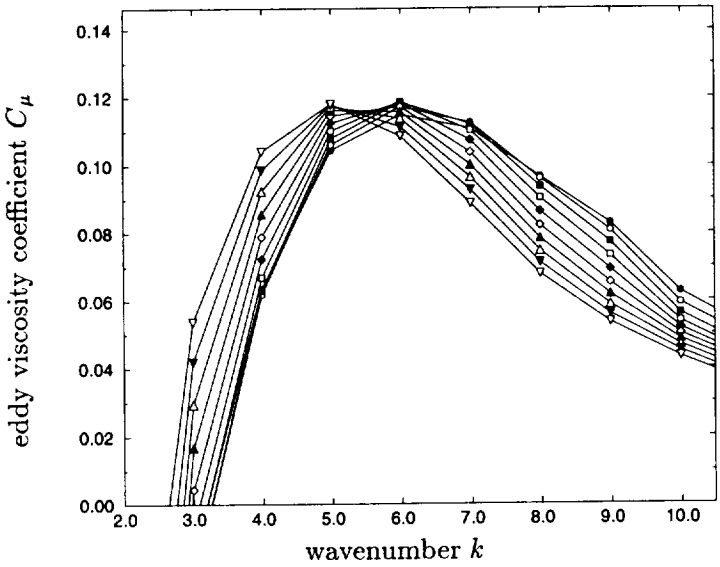

FIGURE 3. Dimensionless eddy-viscosity spectrum $C_\mu(k,t)$ at several times. t=0.2295: • , t=0.3299: ○ , t=0.4183: ■, t=0.5262: □, t=0.6407: ♦, t=0.7647: ◊, t=0.8940: ▲, t=1.0318: △, t=1.1788: ▼, t=1.3354: ▽.

emphasize that this value is obtained here from the decay of *fluctuations* and not, as usual, from the diffusive decay of *mean* values. The close agreement supports the idea that something like the "regression hypothesis" should hold for wavenumbers around the energy peak.

The results of the "zero-lag" Rayleigh-Ritz analysis are entirely consistent with those for the zero-lag POP. In fact, the results for $C_\mu(k,t_0)$ are so close numerically that a plot of them together would show no difference between them. The "zero-lag" Rayleigh-Ritz values $C_\mu(k,t)$ are plotted in Fig. 3 for the low wavenumbers $k = 2-10$ at a sequence of times. There is seen to be a slight drift to the left in time. Remarkably, this is consistent with the slow decrease of the energy peak wavenumber k_P over that same time from $k_P = 9$ initially to $k_P = 6$ at the final time. The wavenumber at which $C_\mu(k,t) \approx 0.09$ tracks along with the peak wavenumber k_P over the whole period of the decay. This a further verification of the "regression hypothesis" for the energy peak wavenumbers.

A realizability check on the POP model helps to explain the close agreement of the POP and "zero-lag" Rayleigh-Ritz results at early times. Shown in Fig. 4 are the POP noise spectral values for the first fourteen nonzero wavenumber modes, $k = 1-14$, plotted as a function of time up to $t = 1.4$. It may be seen that the noise spectra all start at zero at the initial time t_0, to numerical precision, and thereafter rise to positive values. Most importantly, this result establishes the realizability of the Langevin model with the POP coefficients. In agreement with the results of the previous section, the standard value $C_\mu = 0.09$ leads to a noise spectrum indistinguishable from zero initially at the peak wavenumber.

We are now in possession of a fully realizable Langevin model of the form of Eq. (9)

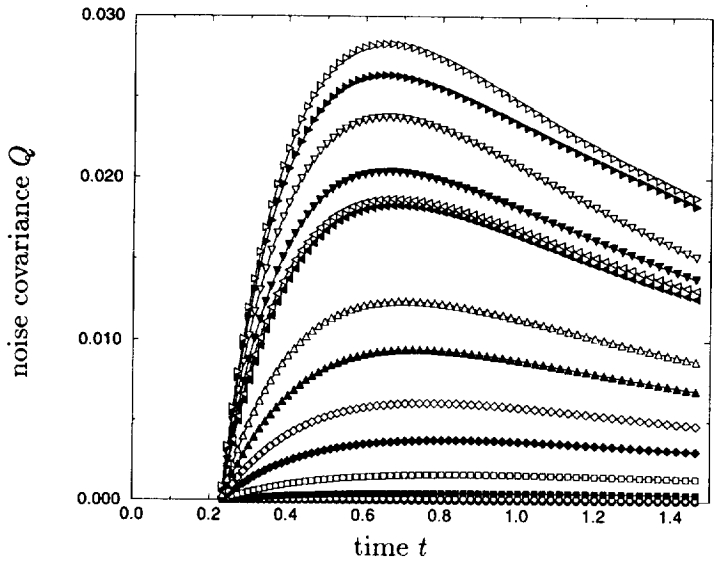

FIGURE 4. POP noise covariance $Q(k,t)$ in low wavenumbers. k=1: • , k=2: ○ , k=3: ■, k=4: □, k=5: ♦, k=6, ◊, k=7: ▲, k=8: △, k=9: ◀, k=10: ◁, k=11: ▼, k=12: ▽, k=13: ▶, k=14: ▷.

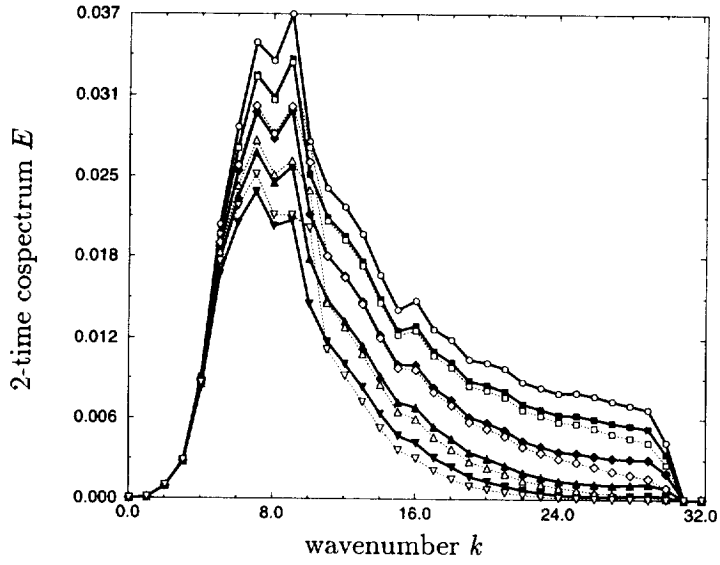

FIGURE 5. Comparison of 2-time velocity cospectra $E(k;t,t_0)$. t=0.2295: • - LES, ○ - RRC; t=0.3299: ■- LES, □- RRC; ; t=0.4183: ♦- LES, ◊- RRC; t=0.5262: ▲- LES, △- RRC; t=0.6407: ▼- LES, ▽- RRC;

with the coefficients therein determined either from POP or "zero-lag" Rayleigh-Ritz. The model is very similar in form to the DTSA model (Kraichnan, 1987). As has been discussed earlier, the same model will presumably arise for either Eulerian or Lagrangian variables. However, it is probably a much more accurate, long-term predictor for Lagrangian time-correlations than it is for Eulerian. Unfortunately, we have no such Lagrangian data with which to compare. Instead, we shall correct the "zero-lag" Rayleigh-Ritz model to include convective dephasing effects as described previously. In Fig. 5 we show plotted together as functions of wavenumber k the LES results for the 2-time velocity spectrum $E(k;t,t_0)$ and those obtained from the "zero-lag" Rayleigh-Ritz with the convective correction in Eq. (11), for several times over the run. As may be seen, there is a much improved agreement for all times. The only defect is at the later times when the Rayleigh-Ritz calculation gives a slightly too great decay at high wavenumbers and a slightly too slow decay at low wavenumbers. This is in agreement with our earlier remark that the "efficiency" $C_\eta = 0.1$ we used in the convective correction is likely too large at high wavenumbers and too small at low wavenumbers.

4. Conclusions

The results of this work allow us to draw the following tentative, general conclusions:

(i) The standard K-ε model gives a very good quantitative account of fluctuations at the energy peak wavenumber and a rather good one at lower wavenumbers. This supports the idea that a proper application of Onsager's "regression hypothesis" for turbulent flow is to fluctuations in the peak wavenumber range. Presumably, an "optimal" POP analysis would recover something very close to the standard K-ε model in that regime. Because this range of wavenumbers makes a dominant contribution to integrations over k, the single-point, 2-times statistics will be rather well captured by such modeling.

(ii) However, the agreement of the predicted and measured statistics is restricted to a short time for Eulerian correlations. The success in reproducing those correlations at longer time separations by making a simple convective correction suggests that much better long-term predictability will be obtained for Lagrangian variables with a standard $RANS$-type model.

(iii) Further improved predictions can be obtained in the Rayleigh-Ritz framework by going beyond the K-ε modeling. Even the simple expedient of taking the $RANS$ model coefficients to be functions of wavenumber k—and thus nonlocal kernels in physical space—can give much better results. In the case of the velocity sector, a "zero-lag" model of this type is very similar to the DSTA model of Kraichnan (1987). Such models can presumably give good long-term predictions for Lagrangian variables. To predict Eulerian time-correlations at large time-separations seems to require a non-Markovian or history-dependent *Ansatz* in the Rayleigh-Ritz formalism to properly capture the convective dephasing effects.

The final verification of these conclusions will require some more work. In particular, a POP analysis based upon a complete set of 2-time correlation functions ought

to be performed. This would allow a systematic investigation of lag-dependence, which is particularly important in the K-ϵ sector. Furthermore, a proper comparison of the predictions with LES or other data would require Lagrangian time-correlations.

Acknowledgments

We thank all of the participants at the CTR Summer Program for useful interactions, but, in particular, Bill Reynolds and Daniele Carati. G. E. thanks V. Yakhot for some stimulating discussions.

REFERENCES

CARATI, D. 1997 Perspectives for ensemble average LES. *1997 Annual Res. Briefs*, Center for Turbulence Research, NASA Ames/Stanford University, 107-112.

EYINK, G. L. 1996 Action principle in nonequilibrium statistical dynamics. *Phys. Rev. E.* **54**, 3419-3435.

EYINK, G. L. 1997 Fluctuations in the irreversible decay of turbulent energy. *Phys. Rev. E.* **56**, 5413-5422.

EYINK, G. L. 1998 Linear stochastic models of nonlinear dynamical systems. *Phys. Rev. E,* to appear.

EYINK, G. L. & ALEXANDER, F. 1998 Predictive turbulence modeling by variational closure. *J. Stat. Phys.* **91**, 221-283.

FINLAYSON, B. A. 1972 *The method of weighted residuals and variational principles, with applications in fluid mechanics, heat and mass transfer.* Academic Press.

FRISCH, U. 1995 *Turbulence: the legacy of A. N. Kolmogorov.* Cambridge University Press.

KRAICHNAN, R. H. 1959 The structure of isotropic turbulence at very high Reynolds numbers. *J. Fluid Mech.* **5**, 497-543.

KRAICHNAN, R. H. 1964a Decay of isotropic turbulence in the direct interaction approximation. *Phys. Fluids.* **7**, 1030-1048.

KRAICHNAN, R. H. 1964b Kolmogorov's hypotheses and Eulerian turbulence theory. *Phys. Fluids.* **7**, 1723-1734.

KRAICHNAN, R. H. 1987 An interpretation of the Yakhot-Orszag turbulence theory. *Phys. Fluids.* **30**, 2400-2405.

ONSAGER, L. 1931 Reciprocal relations in irreversible processes. I. *Phys. Rev.* **37**, 405-426.

PENLAND, C. 1989 Random forcing and forecasting using principal oscillation pattern analysis. *Mon. Weath. Rev.* **117**, 2165-2185.

515-34

Center for Turbulence Research
Proceedings of the Summer Program 1998

Group analysis, DNS and modeling of a turbulent channel flow with streamwise rotation

By M. Oberlack[1], W. Cabot, AND M. M. Rogers

The turbulent channel flow with streamwise rotation has been investigated by means of several different analytical, numerical, and modeling approaches. Lie group analysis of the two-point correlation equations led to linear scaling laws for the streamwise mean velocity. In addition it was found that a cross flow in spanwise direction is induced, which may also exhibit a linear region. By further analysis of the two-point correlation equation, it is shown that all six components of the Reynolds stress tensor are non-zero. In addition certain symmetries and skew-symmetries about the centerline have been established for all flow quantities. All the latter findings of the analysis have been very well verified by means of direct numerical calculations. The flow has also been tackled by LES and second-moment closure models. The dynamic LES captured most of the theoretical and DNS findings quantitatively. The second-moment closure model was able to capture most of the basic trends, but any quantitative agreement could not be achieved.

1. Introduction

During the development of the symmetry theory in Oberlack (1997a), it was noticed that there may be one additional turbulent scaling law which was not mentioned since no experimental or DNS data were available. This is the turbulent channel flow rotating about the streamwise direction. A sketch of the flow geometry is given in Fig. 1.

The flow appears to have several common features with the classical rotating channel flow (Johnston *et al.* 1972) but also has some very distinct characteristics. The classical case considers the rotation of a turbulent channel flow about the spanwise direction (x_3). In this flow the mean stream lines follow plane spirals. In contrast to this, mean stream lines of the present flow exhibit corkscrew-like spirals. However, the most obvious difference between the two cases may be the induction of a mean velocity in x_3-direction. This cross flow can be deduced by investigating the mean momentum equation and the Reynolds stress transport equation.

It is interesting to note that the induced cross flow is a property of the turbulent flow and may not be deduced from the equations for laminar flows.

Similar to the classical case, it will be shown that the only self-similar mean velocity profiles are linear functions

$$\bar{u}_1 = A_1\Omega_1 x_2 + B_1 \quad \text{and} \quad \bar{u}_3 = A_2\Omega_1 x_2 + B_2$$

1 Inst. für Technische Mechanik, RWTH-Aachen, Germany

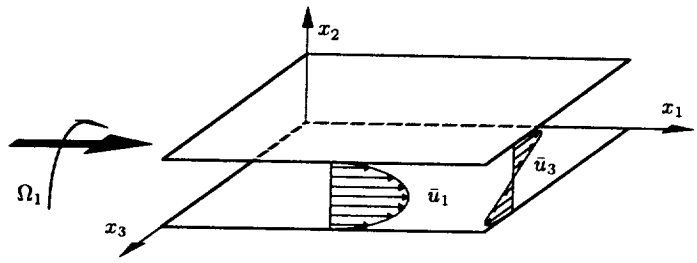

FIGURE 1. Sketch of the flow geometry of a turbulent channel flow with streamwise rotating.

to be derived in the subsequent sections. In both the present and the classical case, the mean velocities scale on the rotation rate.

Nevertheless, it is anticipated that the general appearance of the mean velocity profile in x_1-direction is very different from the classical case. Since the reflection symmetry about the center line is not broken, the mean velocity may stay symmetrical. In Oberlack (1997a) it was observed that, except for the log-law, the highest degree of symmetry is usually obtained in flow regions with the weakest wall influence. Hence, it is expected that two linear regions may emerge near the center region. To the best knowledge of the authors, it appears that the above mentioned test case has never been described in the literature.

The paper is organized as follows. In the next section three different analyses are presented. The one which actually initiated the project is Lie group analysis of the present flow, which suggested the linear velocity profiles. Besides the latter analysis, global time scales of the flow will be investigated which indicate the location of the linear regions. In the final analysis, it will be examined which flow quantity is symmetric or antisymmetric about the centerline of the channel. In the section thereafter, a DNS of the rotating channel flow is presented. Mean velocities and statistical quantities for different rotation rates will be established. Finally, the present test case is to be tackled with turbulence models. Results from second-moment closure models and LES are shown.

2. Analysis

The basis for the analysis of the present flow geometry in Subsections 2.2 and 2.3 is the mean momentum equation and the two-point velocity correlation equation in a rotating frame of reference, which are given respectively by

$$0 = -\frac{1}{\rho}\frac{\partial \bar{p}}{\partial x_1} - \frac{\partial \overline{u_1 u_2}}{\partial x_2} + \nu \frac{\partial^2 \bar{u}_1}{\partial x_2^2} \tag{1a}$$

$$0 = -\frac{1}{\rho}\frac{\partial \bar{p}}{\partial x_2} - \frac{\partial \overline{u_2 u_2}}{\partial x_2} - 2\,\Omega_1 \bar{u}_3 \tag{1b}$$

$$0 = -\frac{\partial \overline{u_2 u_3}}{\partial x_2} + \nu \frac{\partial^2 \bar{u}_3}{\partial x_2^2} \tag{1c}$$

and

$$
\begin{aligned}
0 = & -R_{2j}\delta_{i1}\frac{d\bar{u}_1(x_2)}{dx_2} - R_{2j}\delta_{i3}\frac{d\bar{u}_3(x_2)}{dx_2} - R_{i2}\delta_{j1}\frac{d\bar{u}_1(x_2+r_2)}{d(x_2+r_2)} - R_{i2}\delta_{j3}\frac{d\bar{u}_3(x_2+r_2)}{d(x_2+r_2)} \\
& - [\bar{u}_1(x_2+r_2) - \bar{u}_1(x_2)]\,\frac{\partial R_{ij}}{\partial r_1} - [\bar{u}_3(x_2+r_2) - \bar{u}_3(x_2)]\,\frac{\partial R_{ij}}{\partial r_3} \\
& - \frac{1}{\rho}\left[\delta_{i2}\frac{\partial \overline{pu_j}}{\partial x_2} - \frac{\partial \overline{pu_j}}{\partial r_i} + \frac{\partial \overline{u_i p}}{\partial r_j}\right] + \nu\left[\frac{\partial^2 R_{ij}}{\partial x_2 \partial x_2} - 2\,\frac{\partial^2 R_{ij}}{\partial x_2 \partial r_2} + 2\,\frac{\partial^2 R_{ij}}{\partial r_k \partial r_k}\right] \\
& - \frac{\partial R_{(i2)j}}{\partial x_2} + \frac{\partial}{\partial r_k}\left[R_{(ik)j} - R_{i(jk)}\right] - 2\,\Omega_1\left[e_{1li}R_{lj} + e_{1lj}R_{il}\right]
\end{aligned}
\tag{2}
$$

(see, e.g., Rotta 1972 and Hinze 1959); $\bar{u}_i$, $\bar{p}$, $\overline{u_i u_j}$, ν, Ω_1, and e_{ijk} are the respectively the mean velocity, the mean pressure, the Reynolds stress tensor, the dynamic viscosity, the rotation rate in x_1-direction, and the alternation tensor. The five two-point correlation tensor functions which appear in Eq. (2) are defined as

$$
R_{ij}(\boldsymbol{x},\boldsymbol{r};t) = \overline{u_i(\boldsymbol{x},t)\,u_j(\boldsymbol{x}^{(1)},t)}\ , \tag{3a}
$$

$$
\overline{pu_j}(\boldsymbol{x},\boldsymbol{r};t) = \overline{p(\boldsymbol{x},t)\,u_j(\boldsymbol{x}^{(1)},t)}\ , \quad \overline{u_j p}(\boldsymbol{x},\boldsymbol{r};t) = \overline{u_j(\boldsymbol{x},t)\,p(\boldsymbol{x}^{(1)},t)}\ , \tag{3b}
$$

$$
\begin{aligned}
R_{(ik)j}(\boldsymbol{x},\boldsymbol{r};t) &= \overline{u_i(\boldsymbol{x},t)\,u_k(\boldsymbol{x},t)\,u_j(\boldsymbol{x}^{(1)},t)}\ , \\
R_{i(jk)}(\boldsymbol{x},\boldsymbol{r};t) &= \overline{u_i(\boldsymbol{x},t)\,u_j(\boldsymbol{x}^{(1)},t)\,u_k(\boldsymbol{x}^{(1)},t)}\ ,
\end{aligned}
\tag{3c}
$$

where u_i and p correspond to the fluctuating quantities. The tensors (3a-c) are functions of the physical and the correlation space coordinates $\boldsymbol{x}$ and $\boldsymbol{r} = \boldsymbol{x}^{(1)} - \boldsymbol{x}$ respectively. For the present case all statistical quantities only depend on the wall-normal coordinate x_2 and the correlation coordinate $\boldsymbol{r}$. The double two-point correlation tensor R_{ij}, later on simply referred to as two-point correlation, converges to the Reynolds stress tensor $\overline{u_i u_j}$ in the limit of zero separation $|\boldsymbol{r}|$:

$$
\overline{u_i u_j}(\boldsymbol{x}) = \lim_{r\to 0} R_{ij}(\boldsymbol{x},\boldsymbol{r})\ . \tag{4}
$$

It should be noted that the two-point correlation equation only contains the triple correlations as unknown terms. For both two-point velocity-pressure correlations, $\overline{u_i p}$ and $\overline{pu_j}$ a Poisson equation may be derived (see, e.g., Oberlack 1994, 1995). In addition, all dependent variables in (2) must satisfy the continuity conditions

$$
\frac{\partial R_{ij}}{\partial x_i} - \frac{\partial R_{ij}}{\partial r_i} = 0\ , \quad \frac{\partial R_{ij}}{\partial r_j} = 0\ , \quad \frac{\partial \overline{pu_j}}{\partial r_j} = 0 \quad \text{and} \quad \frac{\partial \overline{u_i p}}{\partial x_i} - \frac{\partial \overline{u_i p}}{\partial r_i} = 0\ . \tag{5}
$$

For the understanding of the self-similarity of the two-point correlation equation given further below, two identities may give some interesting insight in the structure

of the two-point correlation function. They can easily be derived from a geometrical consideration by interchanging the two points $\boldsymbol{x}$ and $\boldsymbol{x}^{(1)} = \boldsymbol{x} + \boldsymbol{r}$:

$$R_{ij}(\boldsymbol{x}, \boldsymbol{r}) = R_{ji}(\boldsymbol{x} + \boldsymbol{r}, -\boldsymbol{r}) \ , \ \overline{u_i p}(\boldsymbol{x}, \boldsymbol{r}) = \overline{p u_i}(\boldsymbol{x} + \boldsymbol{r}, -\boldsymbol{r}) \ . \tag{6}$$

The former is particularly interesting for the trace elements of R_{ij} since it defines a functional equation in real- and correlation-space. There exists a similar identity to (6) for the triple correlation, which will not be utilized here.

Some fundamental properties of the flow can already be read from Eq. (1a-c). For high Reynolds number flows, viscous transport terms are only significant in the near-wall region. In regions sufficiently apart from solid walls, the viscous terms may be neglected to leading order, and the balance is dominated by the pressure and the turbulent stresses.

From Eq. (1a) the usual linear turbulent shear stress profile for $\overline{u_1 u_2}$ may be derived because the pressure-gradient in the streamwise (x_1) direction is constant. Since no pressure-gradient in the spanwise (x_3) direction is present, it can be deduced from Eq. (1c) that the shear stress $\overline{u_2 u_3}$ is uniform. Equation (1b) only determines the pressure-gradient in wall-normal direction. Though it is the only mean momentum equation containing the Coriolis force, it has no influence on the mean velocity. It will be seen later that the mean velocity is only determined by the turbulent stresses. This is similar to the usual non-rotating channel flow in which no information for the mean flow can be determined from the mean momentum equation.

At this point it will be anticipated that besides the shear stress $\overline{u_2 u_3}$ the additional shear stress $\overline{u_1 u_3}$ is induced due the rotation. This can be taken from Eq. (2) in which a Coriolis term appears in the R_{13}-equation. From the structure of the "13" equation, it appears that the Coriolis term may not be solely balanced by the pressure-velocity correlation and by the triple correlation. One may naturally expect that the term $[\bar{u}_k(x_2 + r_2) - \bar{u}_k(x_2)] \, \partial R_{13}/\partial r_k$ may also contribute to the balance in the equation. Hence $\overline{u_1 u_3}$ may be non-zero though this stress has no counterpart in the mean velocities in an eddy-viscosity sense.

2.1 Time-scale analysis

In the present subsection the characteristic time scales of the viscous sublayer and the universal logarithmic region will be compared with the characteristic time scale of the rotation rate. The latter is defined as

$$t_\Omega \equiv \frac{1}{\Omega} \tag{7}$$

where Ω is the rotation rate about the x_1-direction, also denoted by Ω_1.

The characteristic time scale of the viscous sublayer and the universal logarithmic region are

$$t_\nu \equiv \frac{\nu}{u_\tau^2} \quad \text{and} \quad t_{\log} \equiv \frac{y}{u_\tau} \tag{8}$$

respectively where u_τ is the "friction velocity" defined as $u_\tau = \sqrt{\nu \left.\frac{\partial \bar{u}_1}{\partial x_2}\right|_{\text{wall}}}$. For sufficiently high Reynolds number, t_ν is a fixed small quantity while $t_{\log}$ increases with the distance from the wall. Comparing the ratio of the latter flow time scales with the rotation time scale we respectively obtain

$$T_1 = \frac{t_\nu}{t_\Omega} = \frac{\nu\Omega}{u_\tau^2} = \frac{\text{Ro}}{2\text{Re}} \tag{9}$$

and

$$T_2 = \frac{t_{\log}}{t_\Omega} = \frac{y\Omega}{u_\tau} = \text{Ro}\frac{y}{h} \ , \tag{10}$$

where $\text{Re}_\tau = hu_\tau/2\nu$ and $\text{Ro} = \Omega h/u_\tau$.

For zero rotation rate both quantities are exactly zero. However, assuming Ro of the order $\mathcal{O}(1)$ and supposing Re to be a large parameter, the time scale ratio T_1 is a small quantity. Hence it is concluded that the rotation only perturbs the viscous sublayer, and a significant change may not be observed.

Considering the same order of magnitude assumptions for Ro as above, it can be concluded that T_2 may only be a small parameter for small y/h. This is the flow region close to the wall and next to the viscous sublayer. In contrast, if y/h is of order $\mathcal{O}(1)$, T_2 may become an order $\mathcal{O}(1)$ parameter. Consequently, we conclude that this is the flow region which is affected most by the system rotation. In this region system rotation is a leading order effect. In addition we conclude that the region which is affected most by the rotation extends further to the wall with increasing rotation rate. The mean velocity of a turbulent channel flow is only weakly affected by the system rotation in the near-wall region. However, system rotation has a substantial effect on regions sufficiently far from the wall such as the logarithmic region up to the centerline.

In fact this global effect has been observed both in experiments and in DNS for the classical rotating channel flow with x_3 as the rotation axis (see e.g. Johnston *et al.* 1972, Kristoffersen & Andersson 1993). In contrast to the present case the classical rotating channel case does not reveal a symmetric mean velocity profile about the centerline. Instead a skewed mean velocity profile in the center part of the channel is observed.

2.2 Reflection symmetry of statistical flow quantities about the centerline

Reflection symmetries can be obtained by finding transformations of the form $\tilde{\phi} = -\phi$ where ϕ may represent any dependent and independent variable. The following is observed in a variety of different channel type of flows such as the usual turbulent Poiseuille and the turbulent Couette flow. If the corresponding equations and boundary conditions admit a certain reflection symmetry about the centerline, this is also verified for all statistical quantities.

For the present problem the system (2) and (5) admits the reflection symmetry where the variables are respectively separated as independent variables, mean quantities, and statistical quantities

$$\tilde{x}_1 = x_1 \ , \ \tilde{x}_2 = -x_2 \ , \ \tilde{x}_3 = -x_3 \ , \ \tilde{r}_1 = r_1 \ , \ \tilde{r}_2 = -r_2 \ , \ \tilde{r}_3 = -r_3 \ , \tag{11a}$$

$$\tilde{\bar{u}}_1 = \bar{u}_1 \ , \quad \tilde{\bar{u}}_3 = -\bar{u}_3 \ , \quad \tilde{\bar{p}} = \bar{p} \ , \tag{11b}$$

$$\begin{pmatrix} \tilde{R}_{11} & \tilde{R}_{12} & \tilde{R}_{13} \\ \tilde{R}_{21} & \tilde{R}_{22} & \tilde{R}_{23} \\ \tilde{R}_{31} & \tilde{R}_{32} & \tilde{R}_{33} \end{pmatrix} = \begin{pmatrix} R_{11} & -R_{12} & -R_{13} \\ -R_{21} & R_{22} & R_{23} \\ -R_{31} & R_{32} & R_{33} \end{pmatrix} \ , \tag{11c}$$

$$\begin{pmatrix} \widetilde{\overline{pu_1}} \\ \widetilde{\overline{pu_2}} \\ \widetilde{\overline{pu_3}} \end{pmatrix} = \begin{pmatrix} \overline{pu_1} \\ -\overline{pu_2} \\ -\overline{pu_3} \end{pmatrix} \quad \text{and} \quad \begin{pmatrix} \widetilde{\overline{u_1 p}} \\ \widetilde{\overline{u_2 p}} \\ \widetilde{\overline{u_3 p}} \end{pmatrix} = \begin{pmatrix} \overline{u_1 p} \\ -\overline{u_2 p} \\ -\overline{u_3 p} \end{pmatrix} \ . \tag{11d}$$

The latter reflection symmetries can be generalized as such that any other statistical one-, two-, and multi-point quantity can be determined from the fluctuation quantities according to the transformation for the fluctuations

$$\tilde{u}_1 = u_1 \ , \quad \tilde{u}_2 = -u_2 \ , \quad \tilde{u}_3 = -u_3 \ , \quad \tilde{p} = p \ . \tag{12}$$

For example, the transformation of the two-point triple correlations $R_{(ik)j}$ and $R_{i(jk)}$ which are not stated above can be determined in a similar manner.

From (11b) it can be determined that $\bar{u}_1$ is symmetric about the centerline and $\bar{u}_3$ is antisymmetric about the centerline.

The transformation of the Reynolds stress tensor can also be obtained by employing Eq. (4) in the transformation (11c). The consequences for the stresses are such that all normal stresses and $\overline{u_2 u_3}$ are symmetric about the centerline. In contrast $\overline{u_1 u_2}$ and $\overline{u_1 u_3}$ are antisymmetric about the centerline. It should be noted that the results for $\overline{u_1 u_2}$ and $\overline{u_2 u_3}$ can also be obtained from the mean momentum Eqs. (1a) and (1c). The reflection properties of other one-point quantities such as the pressure-strain correlation and the dissipation tensor can also be determined by (12).

2.3 Lie group analysis of the two-point correlation equation

For simplicity it will be assumed in the following analysis that the Reynolds number tends to infinity so that the viscous terms in the two-point correlation equation (2) may be neglected. The basis for this assumption is the fact that, to leading order only, the large scales determine the mean velocity. Viscosity only affects the small scales of the order $\mathcal{O}(\eta)$ where η is the Kolmogorov length scale. Hence neglecting viscosity is only valid for $|\boldsymbol{r}| > \eta$. If $|\boldsymbol{r}| < \eta$, the last term of the third line in Eq. (2) corresponds to the dissipation and cannot be neglected.

The general purpose of Lie group analysis, also called symmetry analysis, is twofold. First, the symmetry transformations are to be determined, which give profound knowledge of the flow physics. Second, the symmetries may be used to achieve self-similarity or reduction of the two-point correlation equation. The first step to accomplish this objective is to find symmetry transformations which do not change the form of the equation under investigation. In fact, this is analogous to the analysis presented in the previous subsection where reflection symmetries have been investigated which do not alter the equations. However, the main difference in the present subsection is that the transformations considered therein are *finite* groups.

In order to obtain a reduction, *continuous* groups of transformations need to be considered. The method to find the desired continuous groups of transformations is called Lie group analysis. A good introduction to this method is given in Bluman and Kumei (1989) and Stephani (1989). In the present subsection only a heuristic approach will be presented while some more mathematical details on group methods are presented in Appendix B in Oberlack (1997a).

Self-similarity or reduction is always associated with the decrease of the number of independent variables. It is important to note that the independent variables are not necessarily restricted to the usual variables such as space and time. Instead any parameter in the equation under investigation may be considered as independent variable as long as it does not implicitly depend on any other independent parameter in the problem.

Hence, in the first step a reduction will be achieved by rewriting the two-point correlation equation as such that $\Omega_1 \equiv \Omega$ is absorbed into all the remaining independent and dependent variables. The most general form of transformation allowing this reduction is

$$x_i = \tilde{x}_i\gamma(\Omega) \ , \quad r_i = \tilde{r}_i\gamma(\Omega) \ , \quad \bar{u}_i = \tilde{\bar{u}}_i\gamma(\Omega)\Omega \ , \tag{13a}$$

$$R_{ij} = \tilde{R}_{ij}\gamma(\Omega)^2\Omega^2 \ , \quad \overline{pu_i} = \widetilde{\overline{pu_i}}\gamma(\Omega)^3\Omega^3 \ , \quad \overline{u_ip} = \widetilde{\overline{u_ip}}\gamma(\Omega)^3\Omega^3 \ , \tag{13b}$$

$$R_{(ik)j} = \tilde{R}_{(ik)j}\gamma(\Omega)^3\Omega^3 \ , \quad R_{i(jk)} = \tilde{R}_{i(jk)}\gamma(\Omega)^3\Omega^3 \ , \tag{13c}$$

where the new variables are denoted by tilde, and $\gamma(\Omega)$ is an arbitrary function of Ω. After employing (13a-c) and imposing the high Reynolds number limit, the two-point correlation equations read

$$\begin{aligned} 0 = &-\tilde{R}_{2j}\delta_{i1}\frac{d\tilde{\bar{u}}_1(\tilde{x}_2)}{d\tilde{x}_2} - \tilde{R}_{2j}\delta_{i3}\frac{d\tilde{\bar{u}}_3(\tilde{x}_2)}{d\tilde{x}_2} - \tilde{R}_{i2}\delta_{j1}\frac{d\tilde{\bar{u}}_1(\tilde{x}_2+r_2)}{d(\tilde{x}_2+\tilde{r}_2)} - \tilde{R}_{i2}\delta_{j3}\frac{d\tilde{\bar{u}}_3(\tilde{x}_2+r_2)}{d(\tilde{x}_2+\tilde{r}_2)} \\ &- [\tilde{\bar{u}}_1(\tilde{x}_2+\tilde{r}_2) - \tilde{\bar{u}}_1(\tilde{x}_2)]\frac{\partial\tilde{R}_{ij}}{\partial\tilde{r}_1} - [\tilde{\bar{u}}_3(\tilde{x}_2+\tilde{r}_2) - \tilde{\bar{u}}_3(\tilde{x}_2)]\frac{\partial\tilde{R}_{ij}}{\partial\tilde{r}_3} \\ &- \frac{1}{\rho}\left[\delta_{i2}\frac{\partial\widetilde{\overline{pu_j}}}{\partial\tilde{x}_2} - \frac{\partial\widetilde{\overline{pu_j}}}{\partial\tilde{r}_i} + \frac{\partial\widetilde{\overline{u_ip}}}{\partial\tilde{r}_j}\right] \\ &- \frac{\partial\tilde{R}_{(i2)j}}{\partial\tilde{x}_2} + \frac{\partial}{\partial\tilde{r}_k}\left[\tilde{R}_{(ik)j} - \tilde{R}_{i(jk)}\right] - 2\left[e_{1li}\tilde{R}_{lj} + e_{1lj}\tilde{R}_{il}\right] \ . \end{aligned} \tag{14}$$

Obviously the set of independent variables x_2, r_i, and Ω has been reduced by one. From group theory it follows (see Appendix B in Oberlack 1997a) that the latter equation admits a further similarity reduction only for certain mean velocities which obey the equations

$$\begin{aligned} &[a_1(\tilde{x}_2+\tilde{r}_2) + a_3 + a_5]\frac{d\tilde{\bar{u}}_1(\tilde{x}_2+\tilde{r}_2)}{d(\tilde{x}_2+\tilde{r}_2)} - a_1\tilde{\bar{u}}_1(\tilde{x}_2+\tilde{r}_2) \\ =&[a_1\tilde{x}_2 + a_5]\frac{d\tilde{\bar{u}}_1(\tilde{x}_2)}{d\tilde{x}_2} - a_1\tilde{\bar{u}}_1(\tilde{x}_2) \ , \end{aligned} \tag{15a}$$

$$[a_1(\tilde{x}_2+\tilde{r}_2)+a_3+a_5]\frac{d\tilde{\bar{u}}_3(\tilde{x}_2+\tilde{r}_2)}{d(\tilde{x}_2+\tilde{r}_2)}-a_1\tilde{\bar{u}}_3(\tilde{x}_2+\tilde{r}_2)$$

$$=[a_1\tilde{x}_2+a_5]\frac{d\tilde{\bar{u}}_3(\tilde{x}_2)}{d\tilde{x}_2}-a_1\tilde{\bar{u}}_3(\tilde{x}_2)\ , \tag{15b}$$

The corresponding similarity variables are to be obtained from the invariant surface condition (see e.g. Bluman & Kumei 1989)

$$\frac{d\tilde{r}_1}{a_1\tilde{r}_1+a_2}=\frac{d\tilde{r}_2}{a_1\tilde{r}_2+a_3}=\frac{d\tilde{r}_3}{a_1\tilde{r}_3+a_4}=\frac{d\tilde{x}_2}{a_1\tilde{x}_2+a_5}$$

$$=\frac{d\tilde{R}_{ij}}{2a_1\tilde{R}_{ij}}=\frac{d\widetilde{\overline{pu_i}}}{3a_1\widetilde{\overline{pu_i}}}=\frac{d\widetilde{\overline{u_jp}}}{3a_1\widetilde{\overline{u_jp}}}=\frac{d\tilde{R}_{(ik)j}}{3a_1\tilde{R}_{(ik)j}}=\frac{d\tilde{R}_{i(jk)}}{3a_1\tilde{R}_{i(jk)}} \tag{16}$$

where the constants of integration are taken as the new variables. The equations for the mean velocities above (15a,b) can only have a unique solution if

$$a_3=0. \tag{17}$$

Since each Eq. (15a-b) on the left-hand side depends on x_2+r_2 and on the right-hand side on x_2, they can only be equal if they are both equal to a constant. Hence, (15a,b) uniquely transfer to

$$[a_1\tilde{x}_2+a_5]\frac{d\tilde{\bar{u}}_1(\tilde{x}_2)}{d\tilde{x}_2}-a_1\tilde{\bar{u}}_1(\tilde{x}_2)=c_1\ , \tag{18a}$$

$$[a_1\tilde{x}_2+a_5]\frac{d\tilde{\bar{u}}_3(\tilde{x}_2)}{d\tilde{x}_2}-a_1\tilde{\bar{u}}_3(\tilde{x}_2)=c_3\ , \tag{18b}$$

Each of the parameters a_1-a_5 have a distinct physical meaning. The parameter a_1 corresponds to the scaling group; i.e. Eq. (14) admits a transformation of the form

$$\tilde{x}_2^*=\mathrm{e}^{a_1}\tilde{x}_2\ ,\quad \tilde{r}_i^*=\mathrm{e}^{a_1}\tilde{r}_i\ ,\quad \tilde{\bar{u}}_i^*=\mathrm{e}^{a_1}\tilde{\bar{u}}_i\ , \tag{19a}$$

$$\tilde{R}_{ij}^*=\mathrm{e}^{2a_1}\tilde{R}_{ij}\ ,\quad \widetilde{\overline{pu_i}}^*=\mathrm{e}^{3a_1}\widetilde{\overline{pu_i}}\ ,\quad \widetilde{\overline{u_ip}}^*=\mathrm{e}^{3a_1}\widetilde{\overline{u_ip}}\ , \tag{19b}$$

$$\tilde{R}_{(ik)j}^*=\mathrm{e}^{3a_1}\tilde{R}_{(ik)j}\ ,\quad \tilde{R}_{i(jk)}^*=\mathrm{e}^{3a_1}\tilde{R}_{i(jk)}\ , \tag{19c}$$

which does not alter the functional form of the equation written in the new coordinates. The parameters a_2-a_5 correspond to the translation groups which conform to the fact that (14) is autonomous with respect to $\tilde{x}_2$ and $\tilde{r}_i$. As a result (14) is invariant under transformations such as

$$\tilde{x}_2^*=\tilde{x}_2+a_5\ . \tag{20}$$

However, for physical reasons the translation invariance of $\tilde{r}_i$ is not meaningful, and a_2-a_4 must be zero. In order to understand the problem with these "artificial" invariances, one has to call to mind that the translation invariance with respect to $\tilde{r}_i$ gives rise to a new solution where the correlation function is shifted in correlation space. Since R_{ij} reaches its finite maximum at $|\tilde{\boldsymbol{r}}|=0$ and tends to zero for $|\tilde{\boldsymbol{r}}|\to\pm\infty$, a shift in the correlation space cannot be a new solution.

Depending on the value of a_1, two fundamentally different cases are to be distinguished for which a similarity reduction may be obtained.

2.2.1 $a_1 \neq 0$

The present case corresponds to the fact that scaling with respect to space is not inhibited and (18a,b) integrate to

$$\tilde{\bar{u}}_1 = C_1 \left(\bar{x}_2 + \frac{a_5}{a_1} \right) - \frac{c_1}{a_1} \ , \tag{21a}$$

$$\tilde{\bar{u}}_3 = C_3 \left(\bar{x}_2 + \frac{a_5}{a_1} \right) - \frac{c_3}{a_1} \ , \tag{21b}$$

where C_1 and C_3 are integration constants. If the transformation (13a) to the original coordinates is inferred, the latter equations read

$$\bar{u}_1 = C_1 \, \Omega \, x_2 + \Omega \, \gamma(\Omega) \left(C_1 \frac{a_5}{a_1} - \frac{c_1}{a_1} \right) \ , \tag{22a}$$

$$\bar{u}_3 = C_3 \, \Omega \, x_2 + \Omega \, \gamma(\Omega) \left(C_3 \frac{a_5}{a_1} - \frac{c_3}{a_1} \right) \ . \tag{22b}$$

It appears that the additive constants may depend on the rotation rate in an unknown manner. In order to resolve this problem, it is helpful to investigate the two-point correlation function.

Though a solid theoretical basis on first principles is still lacking, it appears that to leading order the two-point correlation function does not scale with the rotation rate Ω. Hence it can be concluded from Eq. (13b) that, in order to have no Ω dependence of R_{ij}, the function γ behaves as $\gamma \sim 1/\Omega$. As a result, the two additive constants appearing in the scaling laws (22a,b) do not depend on Ω either. Only the slope of the linear scaling laws depends on the rotation rate.

The similarity variables for the case $a_1 \neq 0$ corresponding to the mean velocities (21a,b) are to be obtained from the characteristic Eqs. (16). Employing $a_2 = a_3 = a_4 = 0$, the integration yields

$$\eta_1 = \frac{\tilde{r}_1}{\tilde{x}_2 + \frac{a5}{a_1}} \ , \quad \eta_2 = \frac{\tilde{r}_2}{\tilde{x}_2 + \frac{a5}{a_1}} \ , \quad \eta_3 = \frac{\tilde{r}_3}{\tilde{x}_2 + \frac{a5}{a_1}} \ , \tag{23a}$$

$$\tilde{R}_{ij} = F_{ij} \left(\tilde{x}_2 + \frac{a_5}{a_1} \right)^2 \ , \ \widetilde{\overline{pu_i}} = G_i \left(\tilde{x}_2 + \frac{a_5}{a_1} \right)^3 \ , \ \widetilde{\overline{u_j p}} = H_j \left(\tilde{x}_2 + \frac{a_5}{a_1} \right)^3 \ , \tag{23b}$$

$$\tilde{R}_{(ik)j} = F_{(ik)j} \left(\tilde{x}_2 + \frac{a_5}{a_1} \right)^3 \ , \quad \tilde{R}_{i(jk)} = F_{i(jk)} \left(\tilde{x}_2 + \frac{a_5}{a_1} \right)^3 \ , \tag{23c}$$

where the integration constants η_i, F_{ij}, G_i, H_i, $F_{(ik)j}$, and $F_{i(jk)}$ are the new similarity variables. In order to verify the similarity reduction of Eq. (14), the quantities F_{ij}, G_i, H_i, $F_{(ik)j}$, and $F_{i(jk)}$ are introduced as new dependent variables only depending on η_i.

In order to obtain a new identity in similarity space, the latter scaling is substituted into Eq. (6) for R_{ij}. For this purpose the origin of $\tilde{x}_2$ may be chosen as such

$$\tilde{x}_2' = \tilde{x}_2 + \frac{a_5}{a_1} \tag{24}$$

that the similarity variable simplifies to

$$\eta_i = \frac{\tilde{r}_i}{\tilde{x}_2'} \tag{25}$$

Introducing the transformation (23) into Eq. (6), we obtain the relation $F_{ij}(\tilde{x}_2', \tilde{x}_2'\boldsymbol{\eta}) \cdot (\tilde{x}_2')^2 = F_{ji}(\tilde{x}_2'(1+\eta_2), -\tilde{x}_2'\boldsymbol{\eta})(\tilde{x}_2')^2$. Since it was previously assumed that all two-point correlation functions are solely functions of $\boldsymbol{\eta}$, only the ratio of the first and the second parameter can appear in F_{ij}. Thus, we finally obtain

$$F_{ij}(\boldsymbol{\eta}) = F_{ji}\left(\frac{-\boldsymbol{\eta}}{1+\eta_2}\right) \ . \tag{26}$$

The latter relation gives valuable insight into the structure of the solution. Relation (26) connects different $\tilde{\boldsymbol{r}}$ domains to each other.

Interestingly enough, relation (26) gives raise to a new symmetry transformation

$$\tilde{\eta}_i = \frac{-\eta_i}{1+\eta_2} \tag{27}$$

which is neither a reflection symmetry in the classical sense nor a continuous transformation (Lie group) since it does not contain a continuous parameter. Its validity can be verified by substituting (27) into Eq. (14) after the similarity coordinate (25) and the linear profiles (21a,b) have been employed.

One interesting feature of (26) is that it can be considered as a algebraic functional equation for the trace element of F_{ij} or R_{ij} in the following denoted as $F_{[ii]}$ with $i = 1,2,3$. The "equilibrium" plane for Eq. (26) is $\eta_2 = -2$ with arbitrary η_1 and η_3 where both the argument as well as the value of F_{ij} are the same. In addition $\boldsymbol{\eta} = 0$ is an "equilibrium" point. Apart from these two regions, Eq. (26) defines a mapping between different $\boldsymbol{\eta}$-domains. There are two pairs of η_2-regions which map into each other, namely

$$\eta_2: \ (-\infty,-2) \leftrightarrow (-2,-1) \quad \text{and} \quad (-1,0) \leftrightarrow (0,\infty) \ . \tag{28}$$

The latter nomenclature refers to the fact that, once the functional values for $F_{[ii]}$ in the η_2 region $(-2,-1)$ are known, the corresponding values in the region $(-\infty,-2)$ are uniquely determined and vice versa. After a value for η_2 is chosen, the values for η_1 and η_3 map according to

$$\frac{-\eta_1}{1+\eta_2} \rightarrow \eta_1 \quad \text{and} \quad \frac{-\eta_3}{1+\eta_2} \rightarrow \eta_3 \tag{29}$$

A graphical mapping scheme is given in Fig. 2. For clarity only the η_1-η_2 domain is depicted where connected mapping-regions are indicated by arrows. The extension to the entire $\boldsymbol{\eta}$-domain is straightforward.

Besides the above symmetry relation for $F_{[ii]}$ with $i = 1,2,3$, (26) provides solutions for any off-diagonal F_{ij} element with $(i \neq j)$ if F_{ji} is known. Of course, similar features can be given for the pressure-velocity correlation and for the triple-correlation.

For the present case $a_1 \neq 0$, the statistical variables scale with the wall distance. This is different in the following subsection.

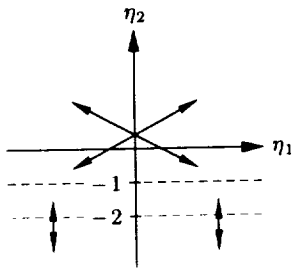

FIGURE 2. Non-locally related correlations in the η_1-η_2 plane according to Eq. (26).

2.2.2 $a_1 = 0$

The present subsection corresponds to the fact that scaling with respect to space is broken as can also be read from Eq. (19). As a result Eqs. (18a) and (18b) may be integrated to

$$\tilde{\bar{u}}_1 = \frac{c_1}{a_5}\tilde{x}_2 + C_3 \ , \tag{27a}$$

$$\tilde{\bar{u}}_3 = \frac{c_3}{a_5}\tilde{x}_2 + C_4 \ , \tag{27b}$$

where C_3 and C_4 are integration constants. The characteristic Eqs. (16) can not be integrated in the usual way. However, a reduction may still be possible since the correlation equation is autonomous in x_2. Due to the linear profile all statistical functions in (14) may not depend on the spatial coordinate $\tilde{x}_2$. Obviously, the present case corresponds to a homogeneous shear flow. Even though this does not appear to be a reduction in the usual sense from a group theoretical point of view, this is similar to the case $a_1 \neq 0$. In Section 2.2.1 a reduction was conducted by the scaling group (a_1) while in the present case the reduction may be conducted by the translation group (a_5). In both cases the dimensionality of the problem is reduced.

It should be noted that for physical reasons the case $a_1 \neq 0$ appears to be more likely to be applicable to the rotating channel flow for the following reason. One of the key observations in Oberlack (1997a) was that turbulence has a tendency to establish a maximum degree of symmetry transformations. For the different channel flow cases, the highest degree of symmetry has been observed where the least wall influence is present, namely in the core region of the channel. Hence it may be expected that the same maximum principle applies for the present flow.

It is very important to note that the present analyses and, in particular, the one in Subsections 2.2.2 and 2.2.3 are not limited to the two-point correlation equation. The results regarding all the symmetries and scaling laws hold for all multi-point correlation equations up to any arbitrary order. Hence the closure problem of turbulence which usually precludes exact results do not form an obstacle for the present analysis.

More mathematical details on group methods and how to obtain the latter results can be found in appendix B of Oberlack (1997a).

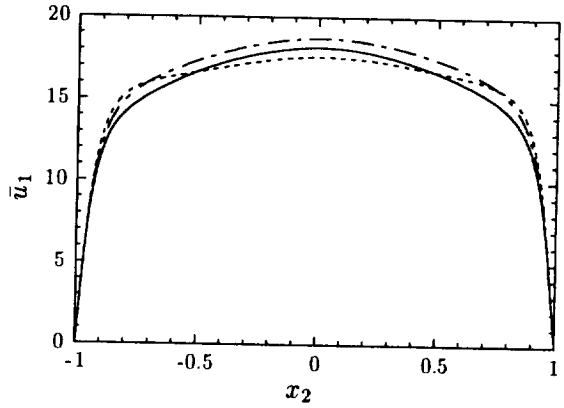

FIGURE 3. Streamwise mean velocity at Ro = 0 ——— , Ro = 3.2 —·— and Ro = 10 ---- .

To conclude from the analysis, it is to be expected that a cone-shaped mean velocity in the streamwise direction will appear as such that the two flanks of the cone are linear. Furthermore, linear profiles for the cross flow will also establish on both sides of the centerline.

3. Direct numerical simulation of the flow

A DNS of the rotating channel flow has be conducted. The utilized numerical technique is a standard spectral method with a Fourier decomposition in streamwise and spanwise direction and a Chebyshev decomposition in wall-normal direction. The flow quantities are non-dimensionalized by $h/2$ and u_τ where h is the channel width and u_τ is the friction velocity of the non-rotating case, which is defined as

$$\tau = u_\tau^2 = \left| \frac{1}{\rho} \frac{\partial \bar{p}}{\partial x_1} \right| \frac{h}{2} \ .$$

The density ρ is set to unity. The definition of the Reynolds number and its numerical value for all subsequent calculations below are

$$\mathrm{Re}_\tau = \frac{h u_\tau}{2\nu} = 180 \ .$$

The rotation number is defined as

$$\mathrm{Ro} = \frac{\Omega h}{u_\tau} \ .$$

The boundary conditions are non-slip at $x_2 = \pm 1$ and periodic in x_1- and x_3-direction. The pressure-gradient is held constant for all computations. Further details on the numerical scheme may be obtained in Kim, Moin & Moser (1987).

Two computations at rotation numbers of Ro = 3.2 and Ro = 10 have been conducted. All presented results for Ro = 0 have been taken from Kim, Moin &

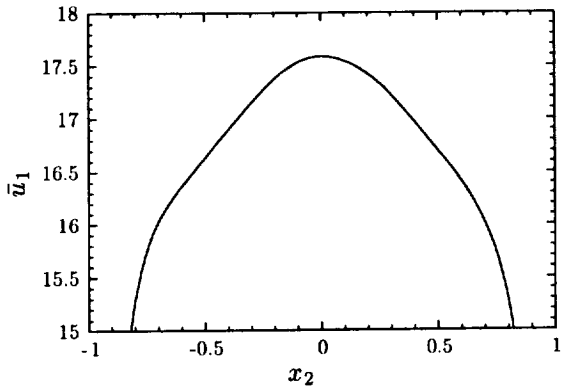

FIGURE 4. Streamwise mean velocity at Ro = 10 in the core region.

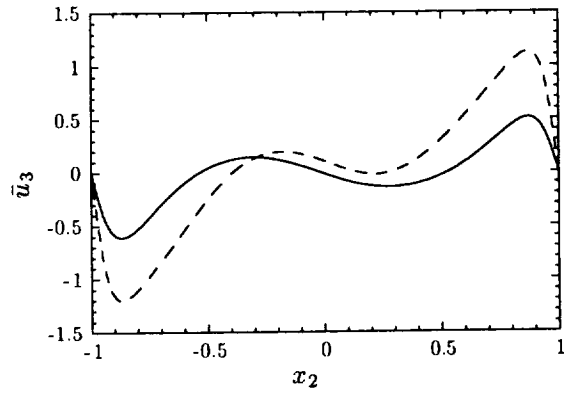

FIGURE 5. Spanwise mean velocity at Ro = 3.2 —— and Ro = 10 ---- .

Moser (1987). The domain sizes used in the x_1, x_2, and x_3 directions are 4π, 2, and $4\pi/3$ on $128 \times 129 \times 128$ grids, respectively, for the Ro = 0 and 3.2 cases, and 8π, 2, and 2π on a $256 \times 129 \times 128$ grid for the Ro = 10 case. In Fig. 3 the streamwise mean velocity profiles at Ro = 0, Ro = 3.2, and Ro = 10 are compared. As expected from the global time scale analysis, the near-wall region up to $x_2 = \pm 0.9$ is only marginally perturbed. Approaching the core region of the flow, a significant change in the mean velocity profile is visible with a very pronounced shoulder at $x_2 = \pm 0.8$ for Ro = 10. In addition, a much flatter center region is noticeable. For the lower rotation rate no linear region is noticeable. It is interesting to note that an increase of mass flow is induced by the low rotation, which seems to disappear by increasing the rotation rate.

As predicted by the group analysis, two linear regions emerge on each side of the centerline for the high rotation rate. A more detailed perspective of the linear region is given in Fig. 4 where only the "head" of the profile for Ro = 10 is depicted. The linear regions cover the wide range $x_2 = 0.2 - 0.6$ on both sides of the center

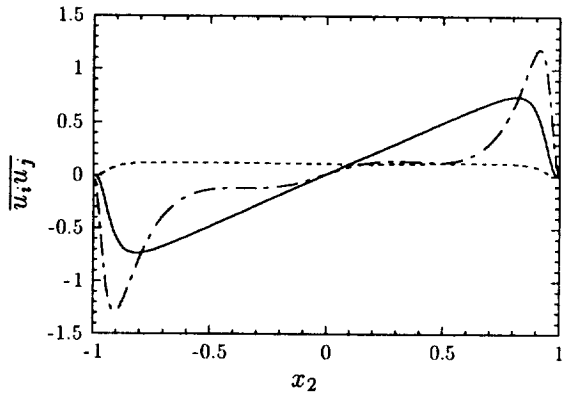

FIGURE 6. Shear stresses at Ro = 10: $\overline{u_1u_2}$ ——— , $\overline{u_2u_3}$ ---- , $\overline{u_1u_3}$ —·— .

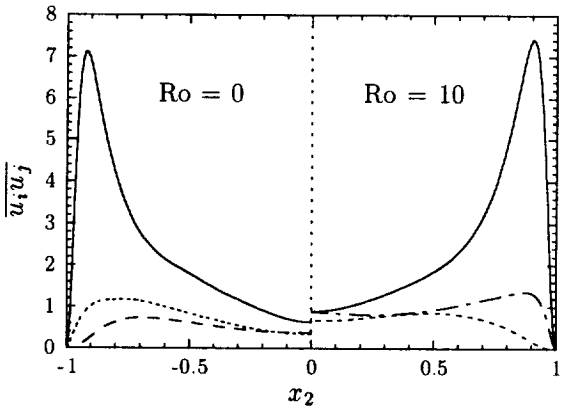

FIGURE 7. Normal stresses at Ro = 0 on the left and Ro = 10 on the right hand side: $\overline{u_1u_1}$ ——— , $\overline{u_2u_2}$ ---- , $\overline{u_3u_3}$ —·— .

line.

As already mentioned in Section 2, a mean cross flow denoted by $\bar{u}_3$ is induced by the rotation. In Subsection 2.2 it was prognosticated that the flow is skew-symmetric about the centerline as shown in Fig. 5.

Though a still clearer verification is still lacking, it appears that the predicted linear profile is also visible in the induced crossflow. The location of the linear region is slightly shifted towards the wall region compared to the linear region of the streamwise velocity. One of the most interesting feature of the cross flow is the region near the centerline. Therein the cross flow has opposite sign compared to the flow regions closer to the channel walls. This large scale property of the flow may correspond to certain coherent structures; however, no such flow pattern could clearly be extracted from the flow so far.

From the statistical one-point quantities, only the Reynolds stress tensor has been computed. In Fig. 6 the Reynolds shear stresses at Ro = 10 are displayed. Both the linear and the constant curves for $\overline{u_1u_2}$ and $\overline{u_2u_3}$ respectively can be derived from

the Eqs. (1a) and (1c) by neglecting the viscous terms, which are only significant in the near-wall region. One of the most intriguing features of the shear stresses is the induced $\overline{u_1 u_3}$ component. The two other cross stresses can both be interpreted in terms of a simplified eddy-viscosity type of sense from its corresponding mean velocities. However, this cannot be done for the $\overline{u_1 u_3}$ shear stress. Hence $\overline{u_1 u_3}$ can only be modeled with the aid of more elaborate turbulence models such as LES or Reynolds stress transport models, to be presented in the next subsection.

In a corresponding DNS at Ro = 0, only the Reynolds shear stress $\overline{u_1 u_2}$ is non-zero. The latter curve is not shown in Fig. 6 since both $\overline{u_1 u_2}$ stress curves are very close to each other and only differ slightly in the near-wall region where viscosity is dominating the flow. All statistical curves exhibit the reflection symmetry properties about the centerline as has been found in Subsection 2.2.

The normal stresses for both the rotating and the non-rotating case are depicted in Fig. 7. Obviously, only very weak differences are noticeable compared to the strong change in the mean streamwise mean velocity induced by the rotation. Though the shape and magnitude of each set of curves for Ro = 0 and Ro = 10 are very similar, there are some distinct qualitative differences in the core region of the flow. We recall that the largest changes should be visible towards the core region of the flow as to be expected from the time scale analysis.

Many of the DNS results have to be considered as preliminary. For both the mean velocities and the stresses in Figs. 3-7, it is noticeable that the statistics is not fully converged. All cases presented previously bear the problem that the curves are not fully symmetric or skew-symmetric about the centerline. There are several problems leading to this deficiency.

A general problem with rotating flows is the fact that in order to get good statistics the required integration time of the computation is considerably longer than for the corresponding non-rotating case. This also appears to be an important issue for the present computation. Second, it is observed in the rotating pipe flow computation by Orlandi & Fatica (1998) and Eggels, Boersma & Nieuwstadt (1996) that very long coherent structures in the streamwise direction appear. This requires a very large computational box in order to ensure a sufficient decay to zero for the two-point correlation functions. In fact, for the present computation it was also noticed that the box in the spanwise direction needs to be larger than for the non-rotating channel flow. In Figs. 8-10 two-point correlations in both the streamwise and spanwise directions are shown. In Fig. 8 the two-point correlations in the streamwise direction for all normal stresses are shown at mid-plane ($x_2 = 0$). Particularly, the spanwise component differs significantly from zero at $x_1 = 5\pi$. In Figs. 9 and 10 a wavy kind of two-point correlation is noticeable in the spanwise direction both at mid-plane ($x_2 = 0$) as well as in the near-wall region at $x_2 = -0.71$. Except for the streamwise component at mid-plane, a substantial deviation from zero at $x_3 = \pi$ is evident. From the latter findings it is apparent that a larger computation box both in the streamwise as well as in the spanwise direction is imperative to obtain more reliable, i.e. box independent results.

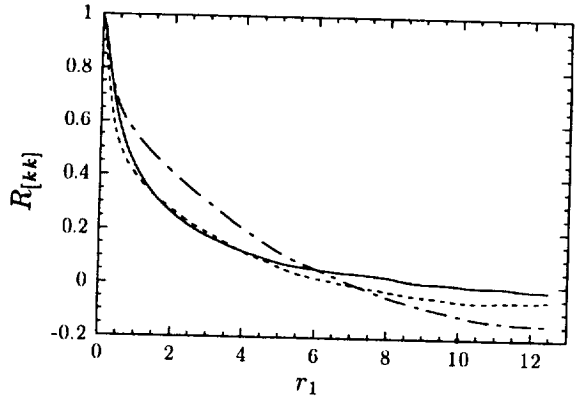

FIGURE 8. Two-point correlations in streamwise direction at mid-plane ($x_2 = 0$) for Ro = 10: R_{11} ——— , R_{22} ---- , R_{33} —·—·— .

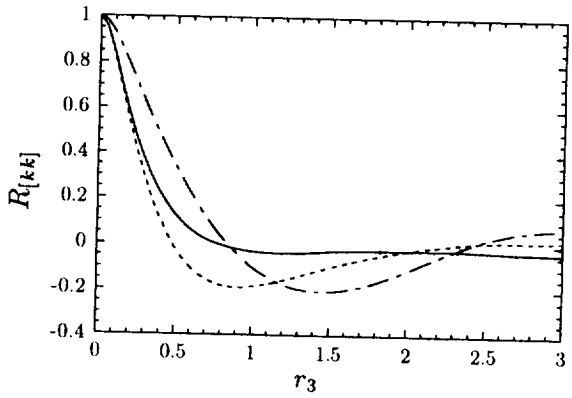

FIGURE 9. Two-point correlations in spanwise direction at mid-plane ($x_2 = 0$) for Ro = 10: R_{11} ——— , R_{22} ---- , R_{33} —·—·— .

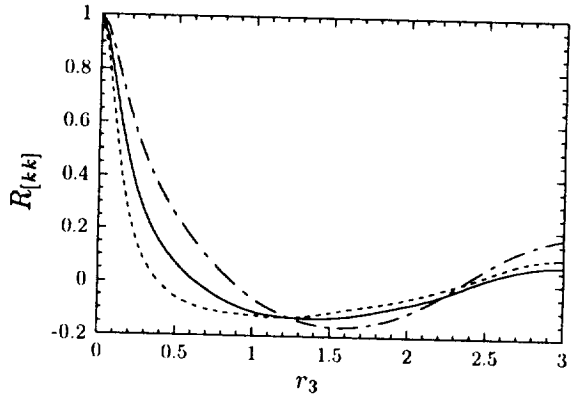

FIGURE 10. Two-point correlations in spanwise direction in the near-wall region ($x_2 = -0.71$) for Ro = 10: R_{11} ——— , R_{22} ---- , R_{33} —·—·— .

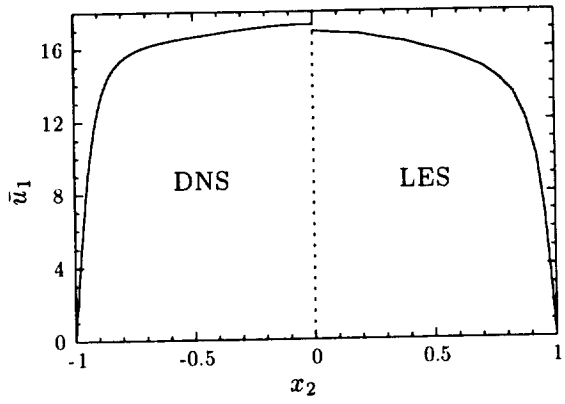

FIGURE 11. Streamwise mean velocity from DNS on the left- and LES on the right-hand side at Ro = 10.

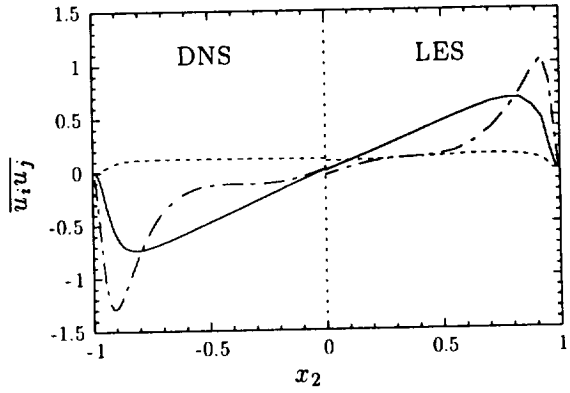

FIGURE 12. Shear stresses from the DNS on the left- and LES on the right-hand side at Ro = 10: $\overline{u_1u_2}$ ——— , $\overline{u_2u_3}$ ---- , $\overline{u_1u_3}$ —·— .

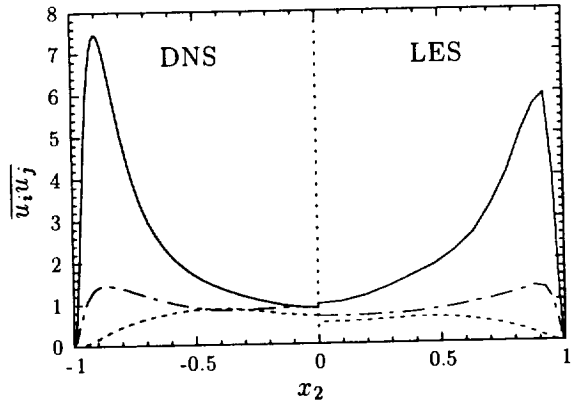

FIGURE 13. Normal stresses from the DNS on the left- and LES on the right-hand side at Ro = 10: $\overline{u_1u_1}$ ——— , $\overline{u_2u_2}$ ---- , $\overline{u_3u_3}$ —·— .

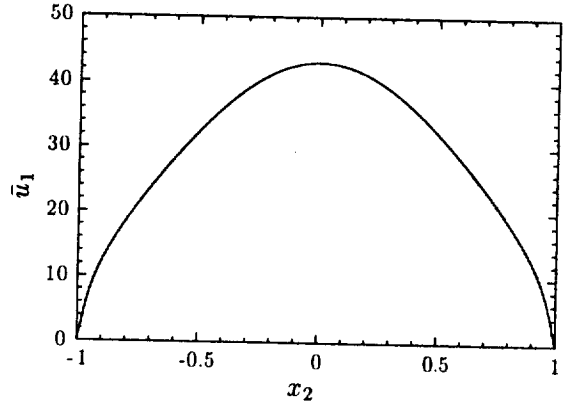

FIGURE 14. Streamwise velocity from the RANS model at Ro = 28.

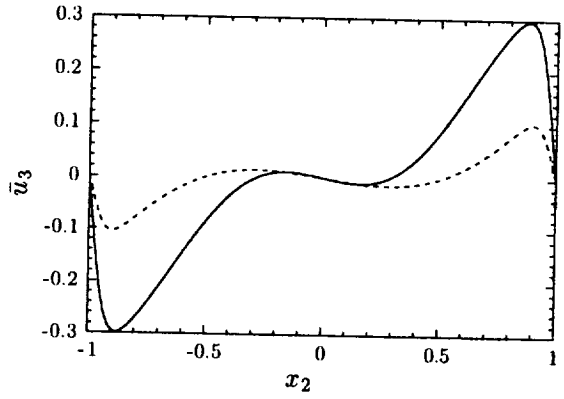

FIGURE 15. Spanwise velocity from the RANS model at Ro = 3.2: IP model ——— , SSG model - - - - .

4. LES and second-moment closure models

System rotation is not a singular influence on the flow, but belongs to a wider class of benchmarks which mimics mean streamline curvature. This is very important for almost any application. Since system rotation is a challenging measure for turbulence models, we have investigated the response of two classes of turbulence models on the influence of streamwise rotation on the turbulent channel flow. First, LES of turbulence has be investigated. Thereafter, second-moment closure has been employed to test its ability to model the flow. Classical two-equation models such as the k-ε or the k-ω model have not been examined since they exhibit no reaction on system rotation. This inability can directly read off from the model equations since no Coriolis type of term appears in the transport equation for the statistical quantities.

The first turbulence model to be investigated is the dynamic subgrid-scale model (Germano *et al.* 1991, Lilly 1992) used in LES. Since the dynamic model is "2D

material-frame indifferent" (see Speziale 1981 and Oberlack 1997b), one may expect that at least in the limit of large rotation numbers the model should capture the trends observed in the DNS. Interestingly enough, it will be seen subsequently that the dynamic model captures very well most of the trends in the flow even quantitatively except for the linear regions in the streamwise mean velocity. The flow parameters and the numerical scheme are the same as for the DNS. The grid sizes in x_1, x_3, and x_4 direction are 48, 32, and 32 respectively for the Ro = 0 and 3.2 cases, and $96 \times 33 \times 48$ for the Ro = 10 case.

In Fig. 11 the streamwise mean velocities from DNS and LES are compared. Even though the LES profile changes significantly due to the system rotation it does not exhibit a clear linear region as was observed in the DNS. In addition, the mass flux is marginally smaller than in the DNS.

In Fig. 12 the shear stresses from the DNS are very well represented by the LES calculation. Even quantitative results show close agreements with the DNS. The normal stresses in Fig. 13 exhibit less good agreement with the DNS, but a correct qualitative agreement is clearly visible. In particular, the near-wall peak of $\overline{u_1 u_1}$ is too low compared to the DNS. A general trend is that all Reynolds stress profiles in the LES are somewhat lower than in the DNS. Apparently, the sub-grid scale model produces slightly too much damping, which is particularly noticeable in the $\overline{u_1 u_1}$ and $\overline{u_1 u_3}$ stress component.

The second turbulence model to be investigated for the present type of flow is a second-moment closure model. The equations are based on the IP model (see Launder, Reece & Rodi 1975) and the SSG model (see Speziale, Sarkar & Gatsi 1989) for the pressure-strain term. The near-wall behavior of the pressure-strain term is modeled by the elliptic-relaxation approach developed by Durbin (1991,1993). The equation for the dissipation of turbulent kinetic energy is taken from the Launder-Reece-Rodi model. Model parameters have been taken from the original publications and have not been altered for the present computation.

Some general remarks should be made before some results from the second-moment model will be presented. Investigating the structure of the model equations, it appears that the linear region of the mean velocities may lead to a reduction of variables and hence to self-similarity. This is essentially due to the fact that the model equations contain Coriolis type of terms. This is in clear contrast to classical two-equation models. Besides the usual Coriolis terms, the rotation rate only appears in the pressure-strain model and not in the dissipation equation. Since the cross flow and the stress components $\overline{u_2 u_3}$ and $\overline{u_1 u_3}$ are solely induced by the rotation, it is the pressure-strain model in particular which determines these quantities. As a result it will subsequently be seen that the cross flow is particularly sensitive to the pressure-strain model though the general flow pattern is captured with all models.

The turbulent diffusion terms have a very strong influence on the model results. Hence the linear regions in the streamwise velocity are only visible at very high rotation rates for which DNS results have not been obtained yet. In Fig. 14 the streamwise velocity is shown for the very high rotation number Ro = 28 obtained

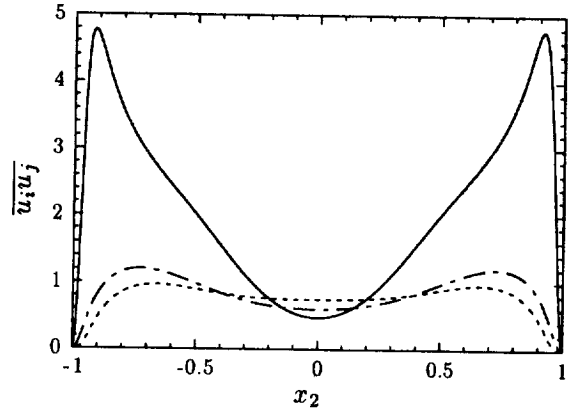

FIGURE 16. Normal stresses from the SSG model at Ro = 10: $\overline{u_1 u_1}$ ——— , $\overline{u_2 u_2}$ - - - - , $\overline{u_3 u_3}$ — — — .

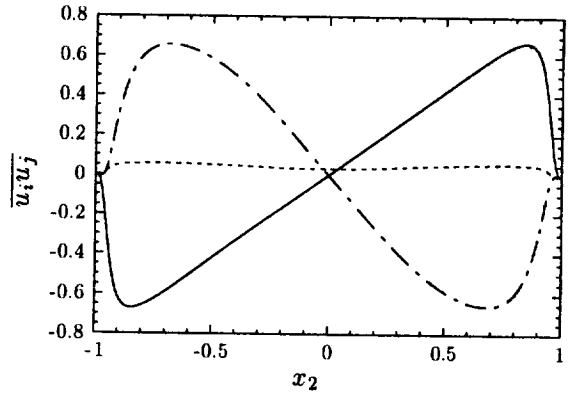

FIGURE 17. Shear stresses from the SSG model at Ro = 10: $\overline{u_1 u_2}$ ——— , $\overline{u_2 u_3}$ - - - - , $\overline{u_1 u_3}$ — — — .

with the IP model. Almost identical results are obtained with the SSG model not presented here.

In contrast to this, the cross flow is extremely sensitive to the implemented pressure-strain model. In Fig. 15 the spanwise velocities for the IP and the SSG model are compared at Ro = 3.2. Apparently the shape of the DNS curve in Fig. 5 is represented by both models. However, both absolute values of the $\bar{u}_3$ velocities are very much underpredicted. Even the maximum of the SSG model is underpredicted by a factor of two.

Much less sensitive to the pressure-strain model are the normal stresses. In Fig. 16 the normal stress from the SSG model are presented. It is interesting to note that not only the overall property of the DNS data are modeled quite well represented, but also that a quantitative agreement within 30% is obtained. This has been obtained without adjusting any model coefficients.

In contrast to this, it can be seen in Fig. 17 that from the shear stresses only

$\overline{u_1 u_2}$ is obtained with reasonable agreement compared to the DNS results. Of course, this is due to fact that $\overline{u_1 u_2}$ is merely determined by the mean momentum equation, which does not contain any modeled terms. Though an almost constant $\overline{u_2 u_3}$ component is obtained in the center region of the flow as predicted by the DNS, its value is much too small. Regarding the $\overline{u_1 u_3}$ stress component, one has to conclude that the model equation is not even able to model the proper tends of the DNS results. The sign of $\overline{u_1 u_3}$ disagrees with the result from the DNS.

5. Summary and conclusions

The general purpose of the present work is to establish a new but still very simple canonical test case to study basic turbulence physics. It has been confirmed by DNS that there are linear regions in both the streamwise and the spanwise mean velocity as was suggested by Lie group analysis of the two-point correlation equations. Additional scaling properties of the two-point correlation functions have been established.

Beside the mean flow, all Reynolds stress quantities have been computed. It is interesting to note that, in contrast to the classical rotating channel flow, all six Reynolds stress components are non-zero. The stress components from the DNS have the expected symmetry properties about the centerline as predicted by the symmetry analysis.

The flow is very challenging for turbulence models since common two-equation models can not account for the rotation effects. Both LES with the dynamic subgrid-scale model and second-moment models have been tested for the present flow geometry. The LES captures most of the DNS results very well. Only the linear regions in the streamwise velocity were not visible. Employing a second-moment model, some basic trends of the flow have been captured. However, several serious drawbacks have been encountered. This is, in particular, that the linear region in the streamwise velocity was only visible for very high rotation rates. In addition, the induced cross flow had the proper shape but was extremely sensitive to the employed pressure-strain model. Finally, most of the qualitative tendencies in the Reynolds stresses were captured except for the $\overline{u_1 u_3}$ component, which showed the opposite sign to that obtained by the DNS.

Future extensions of the project may be manyfold. First, a larger computational domain need to be utilized to obtain more reliable results for the two-point correlation functions. Second, a much longer time integration time is mandatory in order to obtain better turbulence statistics. In addition, a higher rotation rate may be investigated to verify certain trends such as the linear scaling. Also, other scaling and symmetry properties described in Section 2 may be verified by the numerical data. Finally, other turbulence properties such as statistical quantities or coherent structures can also be analyzed from the data.

REFERENCES

BLUMAN, G. W. & KUMEI, S. 1989 *Symmetries and Differential Equations.* Applied mathematical sciences, vol. 81, Springer.

DURBIN, P. 1991 Near-wall turbulence closure modeling without 'damping functions'. *Theoret. Comput. Fluid Dyn.* **3,** 1-13.

DURBIN, P. 1993 A Reynolds stress model for near-wall turbulence. *J. Fluid Mech.* **249,** 465-498.

EGGELS, J. G. M., BOERSMA, B. J. & NIEUWSTADT, F. T. M. 1996 Direct and large eddy simulation of turbulent flow in an axially rotating pipe. Submitted to *J. Fluid Mech.*

GERMANO, M., PIOMELLI, U., MOIN, P., & CABOT, W. H. 1991 A dynamic subgrid-scale eddy viscosity model. *Phys. Fluids A.* **3,** 1760-1765. Erratum: *Phys. Fluids A* **3**, 3128.

HINZE, J. O. 1959 *Turbulence*, McGraw-Hill, NY, reissued 1975 and 1987.

JOHNSTON, J. P., HALLEEN, R. M. & LAZIUS, D. K. 1972 Effects of spanwise rotation on the structure of two-dimensional fully developed turbulent channel flow. *J. Fluid Mech.* **56,** 533-557.

KIM, J., MOIN, P. & MOSER, R. 1987 Turbulence statistics in fully developed channel flow at low Reynolds number. *J. Fluid Mech.* **177,** 133-166.

KRISTOFFERSEN, R. & ANDERSSON, H. I. 1993 Direct simulations of low-Reynolds-number turbulent flow in a rotating channel. *J. Fluid Mech.* **256,** 163-197.

LILLY, D. 1992 A proposed modification of the Germano subgrid-scale closure method. *Phys. Fluids A.* **4,** 633-635.

OBERLACK M. 1994 Derivation and Solution of a New Length Scale- and Dissipation-Tensor Equation for Turbulent Flows, *Doctor's Thesis RWTH Aachen, Germany.*

OBERLACK M. 1995 Analysis of the Two-Point Velocity Correlations in Turbulent Boundary Layer Flows, *Annual Research Briefs.* Center for Turbulence Research, NASA Ames/Stanford Univ., 209-220.

OBERLACK, M. 1997a Unified Theory for Symmetries in Plane Parallel Turbulent Shear Flows, *Manuscript no. 163*, Center for Turbulence Research, NASA Ames/Stanford Univ., under review in *J. Fluid Mech.*

OBERLACK, M. 1997b Invariant modeling in large-eddy simulation of turbulence, *Annual Research Briefs*, Center for Turbulence Research, NASA Ames/Stanford Univ., 3-22.

ORLANDI, P. & FATICA M. 1997 Direct simulations of turbulent flow in a pipe rotating about its axis. *J. Fluid Mech.* **343,** 43-72.

ROTTA, J. C. 1972 *Turbulente Strömungen*, Teubner Stuttgart.

SPEZIALE, C. G. 1981 Some Interesting Properties of Two-Dimensional Turbulence. *Phys. Fluids A.* **28**(8), 1425-1427.

STEPHANI, H. 1989 *Differential Equations: Their Solution using Symmetries.* edited by Malcolm MacCallum, Cambridge University Press.

The RANS modeling group

There were four project areas: rocket motor internal flows (Cucci, Iaccarino, Najjar, Moser); compressible and transitional flow (Lien, Kalitzin); buoyant heat transfer (Tieszen, Ooi); and non-local pressure effects (Manceau, Wang).

The rocket internal flow is treated as duct flow with mass injection through the wall. The regime of interest is high injection rate, so the near-wall region is far from equilibrium. Turbulence in the injection flow is thought to have a significant effect. RANS computations of channel flow with wall injection do a good job of predicting the significant departures from equilibrium. RANS simulations of a nozzleless rocket are complicated by the transitional nature of the flow.

The rocket group also preformed an initial DNS of channel flow with injection through both walls. A force was added to the momentum equation to obtain streamwise homogeneity. High injection velocities were found to produce large near-wall structures, that are not present with impermeable walls.

The question of whether elliptic relaxation is applicable to transonic flow with shock waves was answered in the affirmative by Lien and Kalitzin. In the $v^2 - f$ model, the elliptic f-equation affects the mean flow only indirectly through the eddy viscosity; so it is no more implausible to use elliptic relaxation than to use other turbulence closures in transonic flow.

Transition from laminar to turbulent flow occurs in many experiments to which RANS is applied. Lien and Kalitzin looked into modifications of the turbulence model that might simulate transition. The idea is that the model bifurcates from a laminar to a turbulent solution branch at some point in the flow. The model coefficients control that locations. Transition is notoriously present in buoyancy driven flows. Tieszen and Ooi have examined the effect of adding buoyant production terms to the turbulent kinetic energy equation. In some cases the main effect of such terms was to control the location of transition. Good predictions of the boundary layer on a vertical plate and of recirculation in a closed cavity were obtained — provided that transition occurred at the correct position.

Non-local pressure effects are associated with velocity-pressure gradient correlations in the Reynolds stress transport equations. Closing these correlations is a primary focus of Second Moment Closure. Elliptic relaxation is a non-local treatment of such terms. There is a degree of arbitrariness in the derivation of the Yukawa type of equation for elliptic relaxation. Manceau and Wang have exploited a DNS database in order to evaluate the assumptions inherent in this derivation. Although the basic method was found consistent with DNS data, it does not account for several sources of anisotropy. Modifications of elliptic relaxation that might treat these effects are discussed.

Paul Durbin

Simulation of rocket motor internal flows with turbulent mass injection

By A. Ciucci[1], G. Iaccarino, R. Moser[2], F. Najjar[2] AND P. Durbin

A study of flows subject to strong, turbulent fluid injection has been conducted in this work. The study included both RANS simulations of a nozzleless rocket motor to investigate the applicability of closure models to this type of flows and a DNS analysis aiming at gaining a better understanding of the flow structure near a wall with strong blowing. For the nozzleless motor simulations, both a k-ϵ and the $v^2 - f$ turbulence models were adopted. Results indicated a strong dependence on turbulent transition; large overpredictions were obtained with free transition, but a much better agreement with the experimental data was achieved when transition was fixed. Also, a parametric study indicated only a weak dependence of the solution, in particular of the turbulent kinetic energy profiles, on the turbulent fluctuations at the wall. The DNS analysis of a "periodic" motor with injection from two opposite walls has revealed that the streaks dominant in the conventional near-wall turbulence are not visible. Also, simulations of a channel flow with injection from one wall and suction from the other wall have been performed using the $v^2 - f$ turbulence model; comparison with available DNS data is very good.

1. Introduction

The internal flow development inside the combustion chamber of a solid rocket plays a key role both in motor design and during motor operation. In particular, the mean velocity field and the turbulence characteristics have a strong, direct impact on many physical processes occurring within the motor such as the internal ballistics and erosive burning, the convective heat transfer to the thermal protection, the motion of alumina droplets and subsequent slag deposition at motor aft-end.

Turbulence effects significantly influence the flow processes in proximity of the combustion surface. A full treatment of this region would include the modeling and resolution of complex physical and chemical phenomena which take place during the solid propellant combustion process. This process occurs in a very thin layer at the grain surface and are usually the subject of dedicated, detailed investigations. Therefore, both in experimental studies and in CFD simulations, the burning surface is simply treated as a porous wall through which mass injection occurs at a given total temperature.

Experimental studies of the boundary layer in pipes with uniform mass injection were carried out by Olson and Eckert in 1966, by Simpson *et al.* in 1969 and, in the

1 CIRA, via Maiorise 81043 Capua (CE), Italy

2 University of Illinois at Urbana-Champaign, 1304 West Springfield Avenue, Urbana, IL 61801

70's, by Julien *et al.* (1971), Andersen *et al.* (1975), and Kays and Moffat (1975). Mean velocity profiles, skin friction, and heat transfer measurements were performed in turbulent boundary layers with and without acceleration. These measurements showed good agreement with the theoretical results of Stevenson (1963), who derived a modified law of the wall in which injection velocity effects were taken into account through the definition of an "effective" velocity. In all these works, low values of injection velocity were investigated.

The injection-driven flow in a cylindrical port rocket motor (i.e., with a closed end) is significantly different from the flow in a pipe with or without porous walls. Mass addition from the wall in injection-driven flows is usually quite large; as a result, the velocity profile for an injection-driven flow comes essentially from a balance between the pressure gradient and inertial forces, in contrast with a pipe flow where the velocity profile is determined by a balance of viscous stresses and pressure forces.

The experiments performed by Dunlap *et al.* (1974) and by Yamada *et al.* (1976) showed that the mean flow field is accurately represented by a cosine distribution for the axial velocity (Culick, 1996) in the forward region of a cylindrical port rocket chamber; however, these investigations, performed at large injection rates, revealed that the flow was highly turbulent over most of the chamber.

Later, Traineau *et al.* conducted cold flow simulations of a two-dimensional nozzleless motor, and Dunlap *et al.* (1990) investigated the internal flow in a cylindrical port rocket chamber; in both cases, injection rates were considerably high.

Several numerical investigations of flows with fluid injection at the wall have been performed in the past. Sabnis *et al.* (1989a) carried out a simulation of the test motor geometry employed by Dunlap *et al.* (1974), using the k-ϵ turbulence model of Jones and Launder (1972); a large overprediction of the turbulence intensity profiles was obtained. Later, Sabnis *et al.* (1989b) adopted a modified form of the same turbulence model and compared their results with the data of Traineau *et al.* (1986); some improvements were achieved, but a considerable discrepancy in the turbulence data remained.

Beddini (1986) performed numerical studies of the injection-driven flow in a duct using a parabolic form of the Navier-Stokes equations together with a full Reynolds stress turbulence model. In this work, turbulent fluctuations at the surface, described as "pseudoturbulence", were introduced for the first time.

With the increase in computer power and advancements in CFD in recent years, both LES and DNS analyses of turbulent flows with wall transpiration have been performed. Moin (1982) and Piomelli *et al.* (1989) applied LES to compute the flow in a channel with a uniform injection at the lower wall and an equal suction at the opposite wall, reproducing the experiment by Andersen *et al.* (1975); low injection rates were considered.

In the DNS study of Nicoud *et al.* (1995), a somewhat similar geometry was considered; instead of suction, a free-stream boundary condition with a fixed pressure gradient was applied at the boundary opposite to the injecting wall. Strong

(but uniform) injection rates were assumed in the attempt to reproduce flow conditions representative of a solid rocket motor. Despite the high injection velocity, the law-of-the-wall as modified by Stevenson (1963) was recovered.

Liou and Lien (1995) and Liou *et al.* (1998) performed a numerical simulation of a more realistic geometry using an LES approach without sub-grid-scale modeling. Although their results were in general in good agreement with the experimental data of Traineau *et al.* (1986), turbulence intensities were somewhat underpredicted in the second half of the channel.

The majority of the works on flows with mass injection through a porous wall has involved the investigation of weak injection rates. The injection rate is commonly characterized by the value of the dimensionless parameter $V_{inj}{}^{+}$, defined as the ratio between the injection velocity and the friction velocity.

For *weak* injection rates characterized by values of $V_{inj}{}^{+}$ up to O(1/10), the two-layer structure of the turbulent boundary layer is retained and a (modified) universal law-of the-wall seems to exist (Stevenson, 1963).

On the other hand, as the injection velocity increases to values of $V_{inj}{}^{+}$ of O(1), the turbulent fluctuations of the injected fluid become probably appreciable and should be taken into account. In this case, both the *strong* blowing and the velocity fluctuations may induce a change in the structure of the boundary layer.

In the LES and DNS approaches to this type of turbulent flow, low injection rates were considered by Piomelli *et al.* (1989) ($V_{inj}{}^{+}$ equal to 0.0516 and 0.154), and Sumitani and Kasagi (1995) ($V_{inj}{}^{+}$ equal to 0.05). In the DNS study of Nicoud *et al.* , strong injection rates were assumed ($V_{inj}{}^{+}$=1.4), but no velocity fluctuations were introduced at the wall. Liou and Lien (1995) and Liou *et al.* (1998) adopted an LES approach without SGS modeling to simulate the internal flow in a nozzleless motor and compared their results with the experimental data of Traineau *et al.* (1986); values of $V_{inj}{}^{+}$ were in the range 1.5-6. To the best of the authors' knowledge, no DNS work has taken into account the turbulent fluctuations of the injected fluid at the wall; however, this approach seems the most promising to gather some physical insights of the near wall physical processes for flows with strong injection.

Near-wall flow behavior is also an open issue in turbulence modeling for RANS applications. When low Reynolds number formulations are employed, suitable damping functions are employed to account for the attenuation of the turbulent effects close to a solid wall. These functions should be appropriately modified to account for the damping reduction due to fluid injection. Furthermore, the standard boundary conditions adopted for no-slip walls (k=0) would be inappropriate for surfaces with strong mass injection where velocity fluctuations seem to exist at the wall.

2. Approach

The main aim of this work was to investigate the flows subject to strong injection from a porous wall. In particular, the objectives of the study were twofold: to assess the applicability and potential accuracy improvement of advance turbulence models, such as the *v2f* model, to the simulation of this class of flows; and to improve the understanding of the fluid physics governing this turbulent flow and obtain some physical insights on the near- wall turbulent structures.

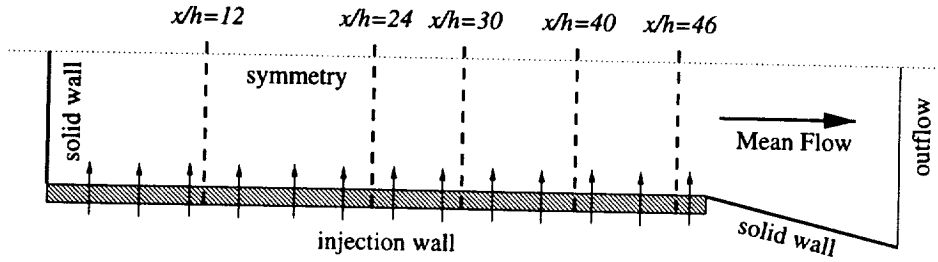

FIGURE 1. Nozzleless rocket motor. Broken lines indicate cross-sections where experimental measurements are taken.

To this end, the research work has comprised two separate but complementary activities. In the first activity, numerical simulations of a rocket chamber with realistic flow conditions have been performed using the RANS equations and the v^2-f turbulence model developed by Durbin (1991). The nozzleless motor geometry tested by Traineau *et al.* (1986), for which experimental data were readily available, has been selected for this computational investigation.

The second activity concerned a DNS analysis of a planar channel with mass injection from both upper and lower walls, and periodic boundary conditions on the four planes perpendicular to the walls, in the streamwise and transverse direction; this configuration will be referred to as "periodic" motor. No DNS study of this flow configuration has been performed thus far.

Finally, a third part of the work regarded the simulations of a channel flow with injection from one wall and an equal suction at the opposite wall, for which DNS data are available for comparison (Piomelli *et al.* , 1989; Sumitani and Kasagi, 1995). these three activities is given in the following.

2.1 Nozzleless motor

A schematic representation of the nozzleless rocket motor considered in this activity is shown in Fig. 1. This is a 2-D planar, porous walled duct close at one end and with a divergent section with impermeable walls at the other end. The cylindrical port chamber has a length of 48 cm, a height of 2 cm, and wall porosity equal to 50 micron; the diverging part has a length of 3.2 cm and a semi-angle equal to 15 degrees; the expansion area ratio is 1.86. Air at a temperature of 260 K and a pressure of 8 bar was used in the experiments of Traineau *et al.* Large injection flow rates were attained in these tests: the injection mass flux was equal to 13 kg/sec/m^2 while the injection Reynolds number was 7840; these represent typical values for solid rocket motors; the mean flow Reynolds number based on throat conditions was approximately $1.5\,10^6$. Experimental data available at five axial stations along the cylindrical duct (shown in Fig. 1) include: static pressure measurements, mean velocity profiles, turbulence intensity, and Reynolds stress profiles.

Computations of the flow in this nozzleless duct were performed using the full compressible Navier-Stokes equations together with the $v^2 - f$ turbulence model; simulations with a low Reynolds k-ϵ model in standard form were also carried out for comparison. The *v2f* turbulence model uses the standard k- ϵ equations together

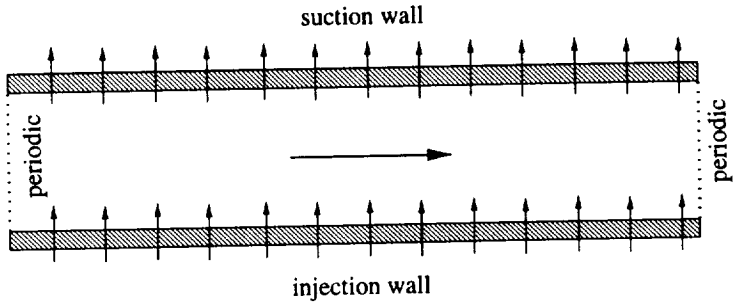

FIGURE 2. Channel flow with injection and suction.

with a third transport equation for $\overline{v^2}$, which can be interpreted as the velocity component normal to the streamlines, and an elliptic relaxation equation for f, representing the production of $\overline{v^2}$. More details on this model are available in the literature (Durbin, 1991; Durbin, 1995). The v^2-f model appears to be a promising approach because it is based on elliptic relaxation rather than on algebraic damping functions for predicting the near-wall turbulence. Wall turbulent injection can be accounted for through assigned values of k and v^2 at the surface.

The computer code CFL3D has been used for the simulations. The value of the mass flux as well as appropriate values of k and v^2 have been prescribed at the porous wall together with a $u = 0$ condition; no-slip conditions have been assigned on all solid walls, and symmetry conditions have been imposed at the symmetry plane; extrapolation was employed at the outflow (supersonic) boundary. It must be noted that a value of f must be specified at the boundaries; most of the calculations have been performed imposing f=*constant* on both injecting and impermeable walls. However, this condition is strictly applicable to solid walls. Thus, some computations with the boundary condition df/dn=0 have also been performed to check the effects of this condition of the flow solution. Furthermore, all computations have been carried out using the standard values of the constants which appear in the model.

A grid dependence study has been initially conducted to determine the grid resolution necessary to resolve the flow field with sufficient accuracy; three grid levels have been used with 57x49, 113x97, and 233x165 grid points in the axial and radial direction, respectively. Then, computations have been performed using both the k-ϵ and the $v2f$ turbulence models and imposing different turbulent boundary conditions at the porous wall, with free transition. Afterwards, some of the computations have been repeated imposing a fixed transition, again with both turbulence models, to investigate turbulent transition effects.

2.2 Channel flow with injection and suction

A analysis of the flow in a channel with injection from one wall and equal suction on the other wall (Fig. 2) was carried out to test the $v^2 - f$ turbulence model. A 1D channel flow code was used and no modifications to the original formulation were employed to run the test cases except for the necessary changes to implement

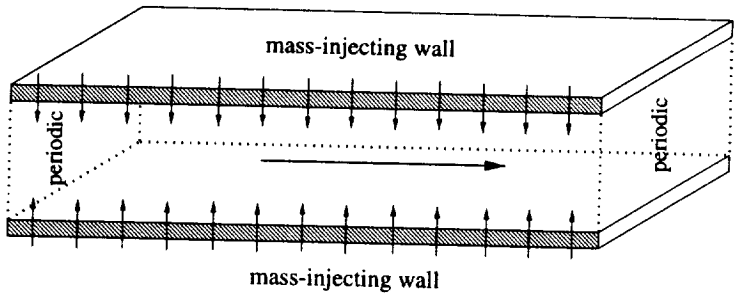

FIGURE 3. Schematic representation of "periodic" motor with injection from both walls.

the fluid transpiration boundary conditions. Cases with no wall transpiration and with both weak ($v^+ = 0.04$) and strong ($v^+ = 1.4$) injection/suction have been simulated.

2.3 DNS of "periodic" motor

Direct Numerical Simulations (DNS) of a turbulent channel flow with strong wall injection are performed as a model for the flow in a solid rocket motor. The spectral code of Kim *et al.* (1987), initially formulated for the turbulent channel flow simulations, was modified to include mass injection on both walls. The spectral formulation is based on Fourier series in the streamwise and spanwise directions with Chebyshev polynomial expansions in the wall-normal direction. Since the flow in a rocket motor accelerates in the axial (streamwise) direction due to the mass injection, this results in streamwise inhomogeneity. To allow the use of periodic boundary conditions through the Fourier representation, the rocket problem must be reformulated so that the streamwise homogeneity is preserved. This is accomplished using a multiscale asymptotic representation of the streamwise acceleration similar to the formulation used by Spalart (1988) for DNS of turbulent boundary layers. To this end, we define the ratio of the injected mass flow rate over the mass-averaged core flow rate, $\epsilon = V_{inj}/U_m$, to be a small parameter. The mean velocity in the vicinity of a streamwise location $x = \tilde{x}$ can be written as $U(x,y) = \tilde{U}(\tilde{x},y)(1+\epsilon(x-\tilde{x}))$. Similarly, a multiscale representation of the velocity fluctuations is given by $u_i'(x,y,z,t) \approx A(X)\tilde{u}_i'(\tilde{x},y,z,t)$ where $\tilde{u}_i'$ is now assumed to be homogeneous and $A = 1+\epsilon(x-\tilde{x})$. The resulting equations for the evolution of u_i in the vicinity of $x = \tilde{x}$ are then:

$$\frac{\partial u_i}{\partial x_i} = -\epsilon\, U$$

$$\frac{\partial u_i}{\partial t} + \epsilon u_1\,(u_i - \delta_{2i}U_2) + u_i\frac{\partial u_i}{\partial x_i} = -\frac{\partial p}{\partial x_i} + \frac{1}{Re}\frac{\partial^2 u_i}{\partial {x_i}^2}$$

In the derivation of the above equation, the following assumptions have been imposed $dA/dx \approx \epsilon$, $A(X) = 1$, $d^2A/dx^2 = 0$, and $1/A\ \tilde{u}\ dA/dx = 0$.

For each location of the rocket motor, a separate simulation is performed using the above equations with periodic boundary conditions in the streamwise and spanwise directions. Similar to Spalart (1988), the additional terms present in the fluctuating continuity equation are set to zero (see the above mentioned assumptions), resulting in the usual continuity equation, $\partial u_i'/\partial x_i = 0$. The flow variables have been non-dimensionalized by the transverse (y) injection velocity, V_{inj}, and the channel half-height, h, with the Reynolds number defined as $Re_{inj} = V_{inj}h/\nu$.

Simulations are performed for two values of ϵ, $\epsilon = 0.04$ and $\epsilon = 0.1$, representing distinct regimes in the solid rocket motor and corresponding to non-dimensional streamwise locations of 50 and 20, respectively. These two cases will be referred to as Case A and Case B with the corresponding Reynolds numbers of 400 and 1000. A grid resolution study has shown that a $128 \times 129 \times 128$ Fourier- Chebyshev representation is marginally adequate to capture the turbulence. The streamwise and spanwise computational domain periods are set at $4\pi h$ and $2\pi h$, respectively. The resulting streamwise and spanwise grid spacings are $\Delta x = 0.0982$ and $\Delta z = 0.0491$, respectively. A non-uniform Gauss-Lobatto distribution applied in the transverse direction results in a minimum wall-normal grid spacing of $\Delta y_{min} = 3.012 \times 10^{-4}$ for the first point located away from the wall and a maximum value of $\Delta y_{max} = 2.454 \times 10^{-2}$ at the channel centerline. The adequacy of the grid resolution and the size of the computational domain have been assessed by examining the two-point correlations and the one- dimensional energy spectra and are found to be appropriate for the present study. Further, 3/2-dealiasing is used in the streamwise and spanwise directions while a variable time-stepping procedure is applied to maintain a CFL number less than 2.8 (Spalart *et al.* , 1991). The computations are integrated in time until the flow reaches a statistical steady state. The progress towards the steady state is identified by monitoring the temporal evolution of the normal Reynolds stress components till they reach their stationary values. Periodicity is applied in x and z while the boundary conditions in the transverse direction are a uniform wall-normal velocity of $v(y = \pm 1) = \mp 1$ and no-slip for the tangential velocity components.

3. Results

The results of the numerical simulations of the nozzleless motor, the channel flow studies, and the DNS analysis of the "periodic" motor are reported in sections 3.1, 3.2, and 3.3, respectively. A synthesis of all results is provided in the subsequent section 3.4.

3.1 Nozzleless motor

The results of the grid dependence analysis are shown in Fig. 4 both for the k-ϵ and *v2f* turbulence models. The velocity profiles of Figs. 4a and 4c clearly indicate that the coarse grid does not provide enough spatial resolution to capture the velocity field; both medium and fine grids give much better results even though some small discrepancy is observed with the $v^2 - f$ model. However, the analysis of the turbulence kinetic energy profiles reveals a considerable increase of k values with increasing grid spacing, indicating that grid independence is not achieved. It must

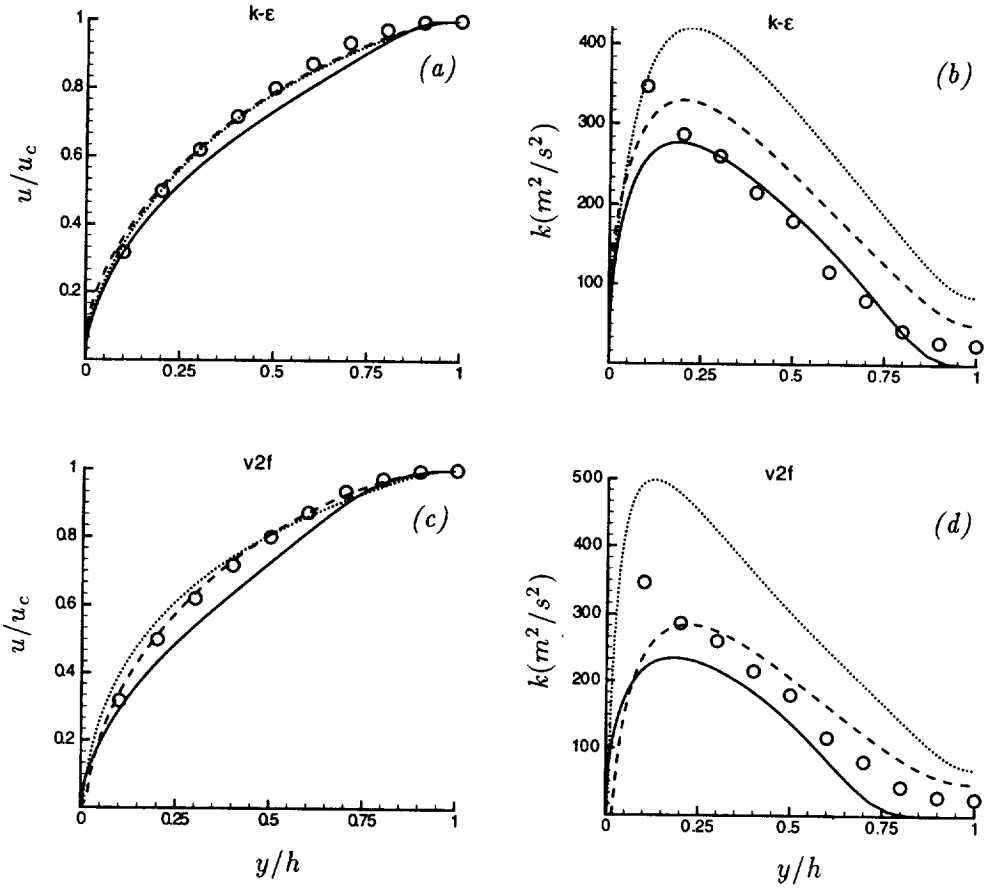

FIGURE 4. Grid dependence analysis, $y/h = 30$. ——— : coarse grid (57x49); ---- : medium grid (113x97); ····· : fine grid (233x165); o : experimental data.

be observed that no further refinement of the computational grid was performed due to the extremely high computational time required. Therefore, all of the results presented here have been obtained with the finer grid (233x165).

The computed pressure distributions along the motor centerline are compared with the experimental values in Fig. 5; a strong pressure gradient is present in the duct, and compressibility effects become relevant in the second half of the channel. The small discrepancy observed in the pressure data is reflected in the u velocity axial distributions shown in Fig. 6. differences are observed between the two turbulence models.

A comparison of the velocity profiles with the experimental data of Traineau *et al.* (1986) is reported in Fig. 7a-e. The computed results are obtained under free transition conditions and with no fluctuations at the wall. In the two initial stations, predicted profiles lie below the experimental values: at $x/h = 12$ the computed velocity profile approximates very well Culick's inviscid distribution while at $x/h =$

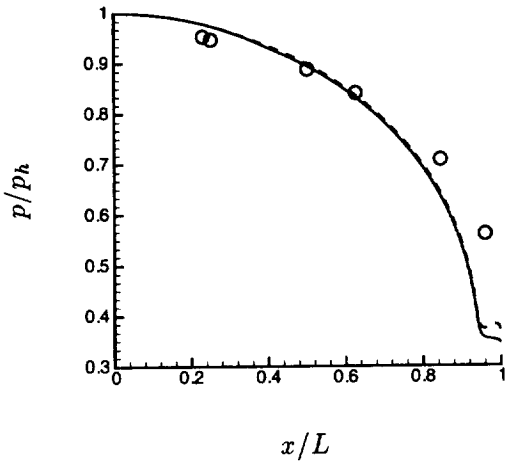

FIGURE 5. Pressure axial distribution. ——— : k-ϵ; - - - - : v^2-f; o : experimental data.

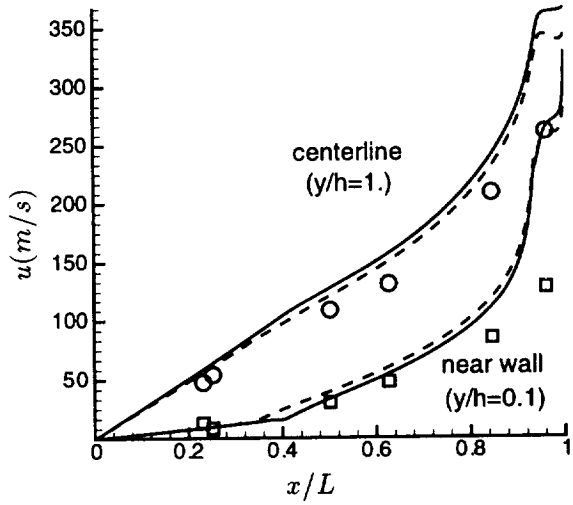

FIGURE 6. Axial distribution of u velocity component. ——— : k-ϵ; - - - - : v^2-f; o : experimental data.

24 the profiles start to transition toward a "fuller" profile; a full transition has occurred at $x/h = 30$ and a turbulent velocity profile is attained more downstream. The *v2f* model predicts slightly larger values than those computed with the k-ϵ model.

Larger discrepancies are observed in the turbulent kinetic energy profiles illustrated in Fig. 8a-e. The higher experimental levels observed in the initial part of the channel are probably due to the "pseudoturbulence" of the injected flow; as reported by Traineau *et al.* (1986), transition to turbulence occurs between $x/h = 20$

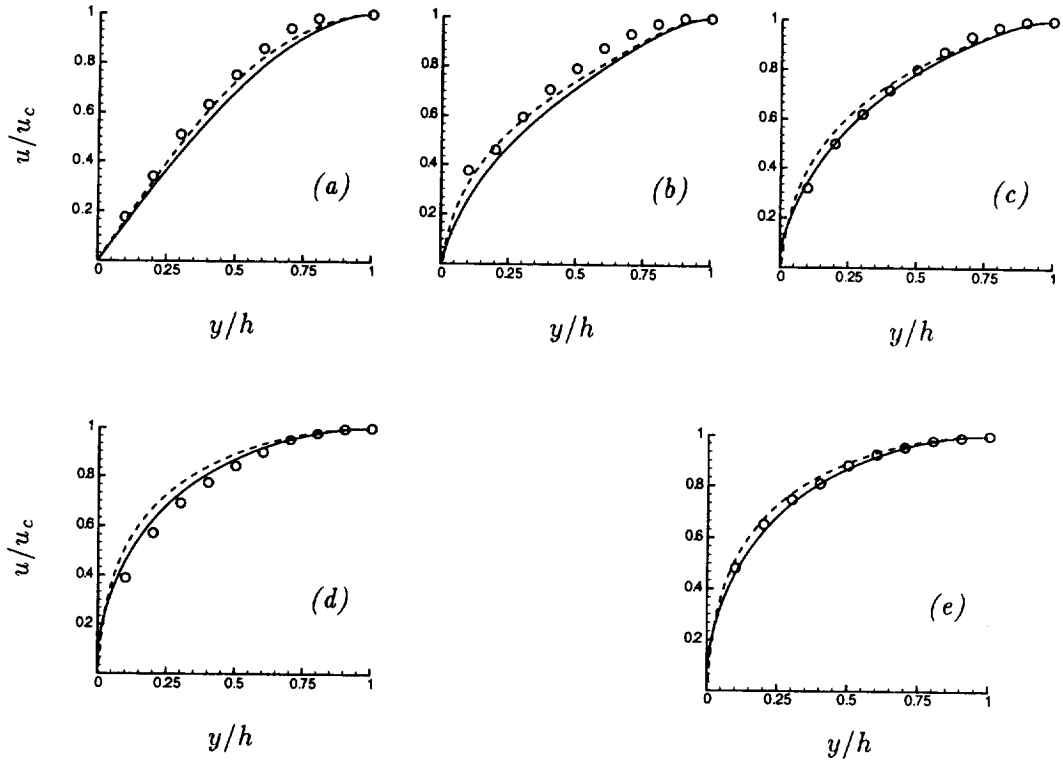

FIGURE 7. Comparison of computed velocity profiles with experimental measurements at five axial stations - *(a)* $x/h = 12$; *(b)* $x/h = 24$; *(c)* $x/h = 30$; *(d)* $x/h = 40$; *(e)* $x/h = 46$. ——— : k-ϵ; ---- : $v^2 - f$; o : experimental data.

and $x/h = 30$, and the flow becomes fully turbulent beyond this location. The computations predict a somewhat faster transition with higher k values within most of the channel: an overprediction slightly less than 100% is observed in the middle of the channel; this overprediction tends to decrease at locations more downstream. The $v^2 - f$ model predicts higher peak values and closer to the wall than the k-ϵ model.

The differences between computed and measured values may be due both to the turbulence of the injected fluid and to transition effects. Fig. 9 shows the change in the turbulent kinetic energy profile at $x/h = 30$ obtained with fluctuations at the wall such that $k = 75\% V_{inj}^2$. The *v2f* prediction gives a reduction, although rather limited, of the k peak; the levels predicted with the k-ϵ model remain the same, but the peak moves closer to the wall. The different results obtained with the $v^2 - f$ and k-ϵ models may be related to the different transitional behavior of the two models. A turbulent kinetic energy contour map is illustrated in Fig. 10; turbulence transition is clearly revealed, indicating that the $v^2 - f$ model predicts an earlier transition that the k-ϵ model. This may explain the higher k values computed with the *v2f* model. Computations were repeated fixing transition at $x/h = 25$;

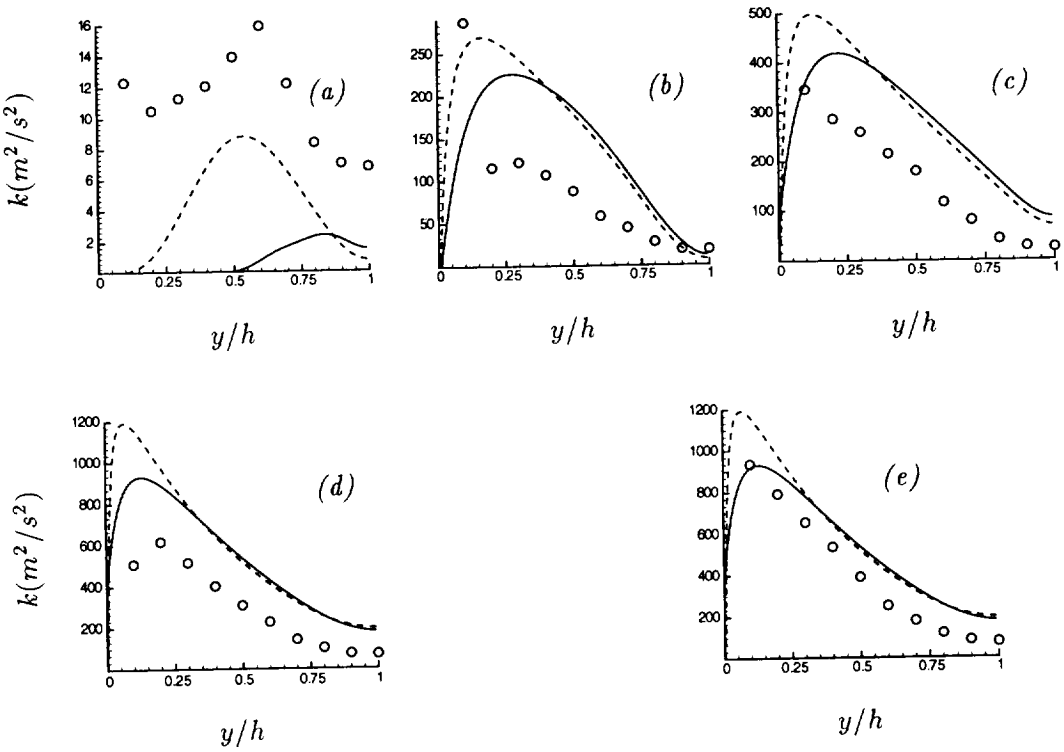

FIGURE 8. Comparison of computed turbulent kinetic energy profiles with experimental measurements at five axial stations - *(a)* $x/h = 12$; *(b)* $x/h = 24$; *(c)* $x/h = 30$; *(d)* $x/h = 40$; *(e)* $x/h = 46$. ——— : k-ϵ; ---- : $v^2 - f$; o : experimental data.

Fig. 11 shows the k profiles at two axial stations for the $k = 75\%V_{inj}^2$ injection case. A much better agreement with the experimental data is now attained, indicating that transition is indeed a major effect in the prediction of the turbulence levels. Both turbulence models provide a rather good accuracy; it must be noted that the values obtained in this work with the k-ϵ model are considerably better than those reported in the literature (Sabnis *et al.* , 1989a; Sabnis *et al.* , 1989b). This could be related to a grid effect on the transitional behavior of this flow.

The effects of the turbulent boundary condition on the flow solution are illustrated in Fig. 12. The fluctuations at the injection surface have some effects on the velocity profile (Fig. 12a); however, the u velocity is basically the same regardless of the fluctuation level. On the contrary, increasing the fluctuation level and, in particular, the v^2 fluctuations tends to decrease the predicted k values, thus improving the agreement with the experimental data (Fig. 12b). However, these effects are rather limited. Also, the location of the k peak remains the same. Finally, Fig. 13 shows the effects of the boundary condition imposed on the f variable, that is, $f = 0$ vs. $df/dn = 0$; also in this case only small improvements are attained.

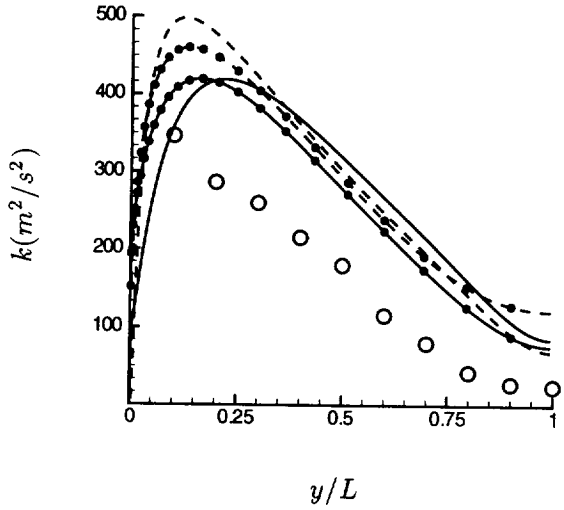

FIGURE 9. Effects of fluctuations at the wall on turbulent kinetic energy profiles, $x/h = 30$. ——— : k-ϵ; ---- : $v^2 - f$; • : results with fluctuations at the wall; o : experimental data.

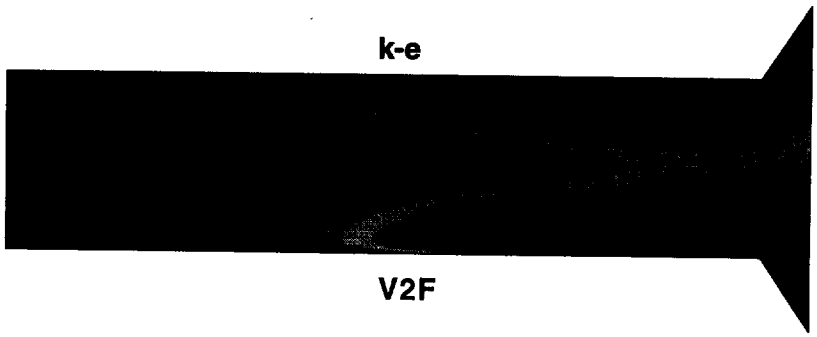

FIGURE 10. Comparison of k-ϵ and $v^2 - f$ turbulent kinetic energy contour maps.

3.2 "Periodic" motor with injection and suction

In Fig. 14a the flow in a channel with no wall transpiration is reported while in Fig. 14b an injection/suction velocity corresponding to $v^+ = 0.04$ was applied (the left side of the picture corresponds to the injection side while the right side corresponds to the suction side). The agreement is remarkably good for both cases, proving that the near-wall region is captured with a good accuracy by the $v^2 - f$ model in both cases. In particular, the strong asymmetry of the mean velocity profile and the increased turbulent kinetic energy peak in the proximity of the

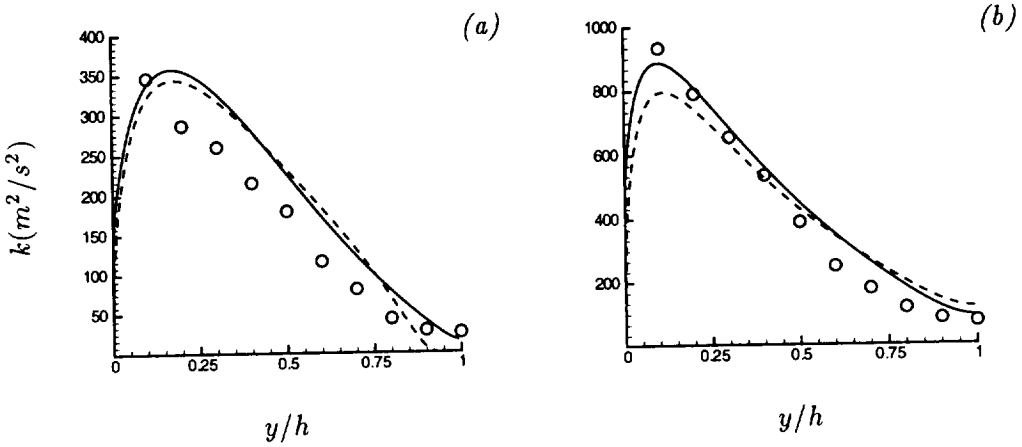

FIGURE 11. Comparison of computed turbulent kinetic energy profiles with experimental measurements for fixed transition at $x/h = 25$ - *(a)* $x/h = 30$; *(b)* $x/h = 46$. ——— : k-ϵ; ---- : $v^2 - f$; o : experimental data.

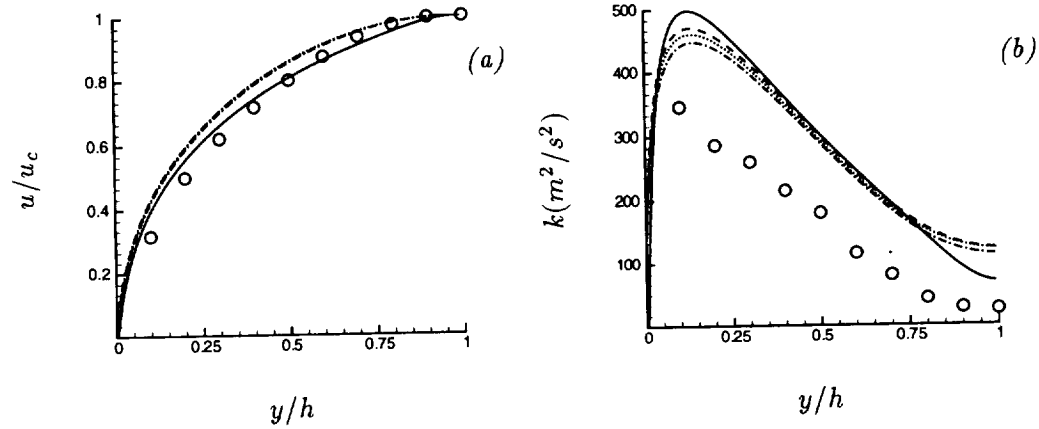

FIGURE 12. Effects of turbulent boundary condition on $v^2 - f$ computed results; $x/h = 30$ - *(a)* velocity profiles; *(b)* turbulent kinetic energy profiles. ——— : $k = 0(nofluct.)$; ---- : $k = 25\%V_{inj}^2$ $v^2 = 2/3k$; ····· : $k = 75\%V_{inj}^2$ $v^2 = 2/3k$; —·— : $k = 75\%V_{inj}^2$; $v^2 = k$; o : experimental data.

injecting wall are captured very well by the model.

3.3 "Periodic" motor with injection from both sides

As mentioned before, earlier experimental and numerical studies have shown that the mean velocity does not differ significantly from the laminar inviscid similarity profile obtained by Culick (1966). This solution is found to hold in the first half portion of the rocket motor. In agreement with these previous results, the mean

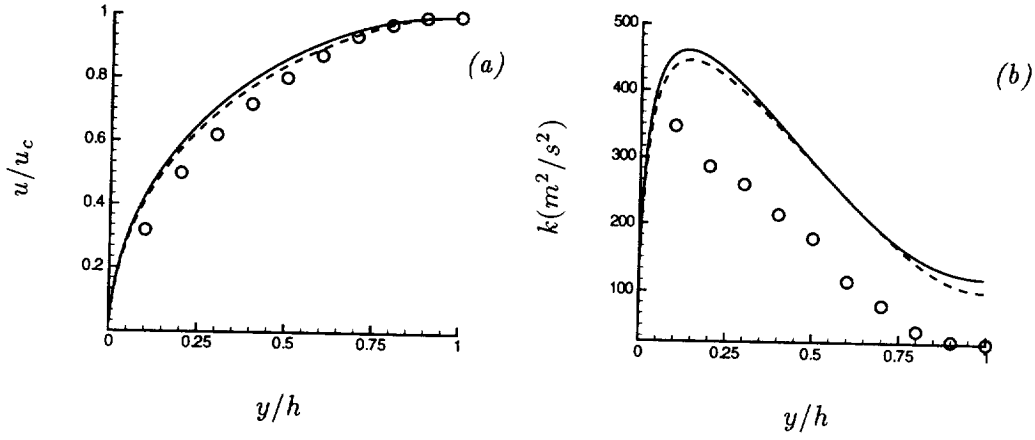

FIGURE 13. Effects of f boundary condition on $v^2 - f$ computed results; $x/h = 30$ - *(a)* velocity profiles; *(b)* turbulent kinetic energy profiles. ——— : $f = 0$; ---- : $df/dn = 0$; o : experimental data.

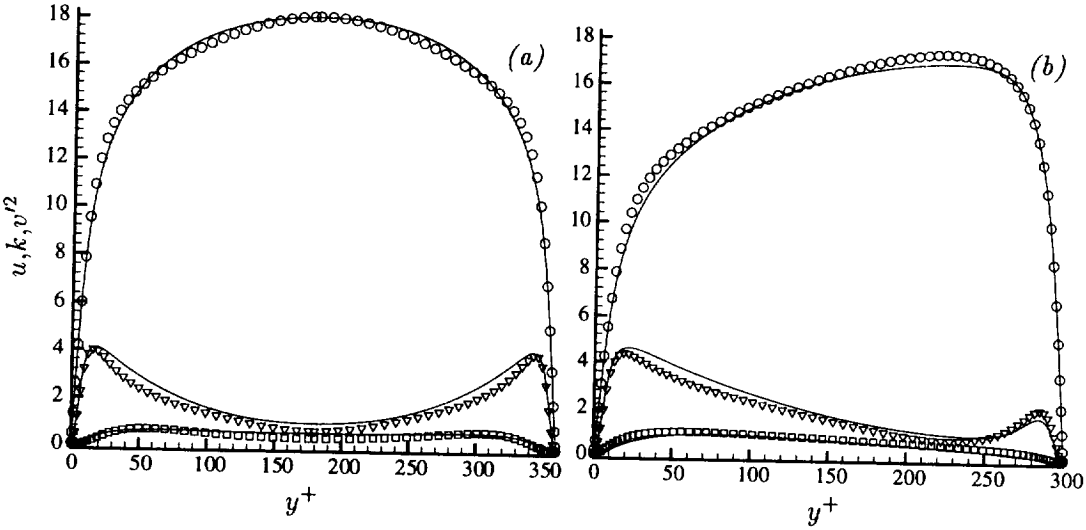

FIGURE 14. Channel flow results: *(a)* Re_τ =180, v^+_{inj}=0; *(b)* Re_τ =150, v^+_{inj}=0.05. —: Numerical results; o : DNS-mean velocity; ▽ : turbulent kinetic energy; □ : v'^2.

streamwise (Fig. 15a) and transverse (Fig. 15b) velocity profiles determined from the DNS are seen to depart only mildly from the inviscid solution.

However, the departures from the analytical solution introduce inflection points in the velocity profile located at $y/h = 0.023$ and $y/h = 9.75 \times 10^{-4}$ for Cases A and B, respectively; whereas the inflections in the similarity solution are at the boundaries. The DNS computations performed by Nicoud (1997) reveal an inflection point located at $y/h \simeq 0.07$. This aspect may introduce stability consequence though the presence of the wall injection makes it less clear.

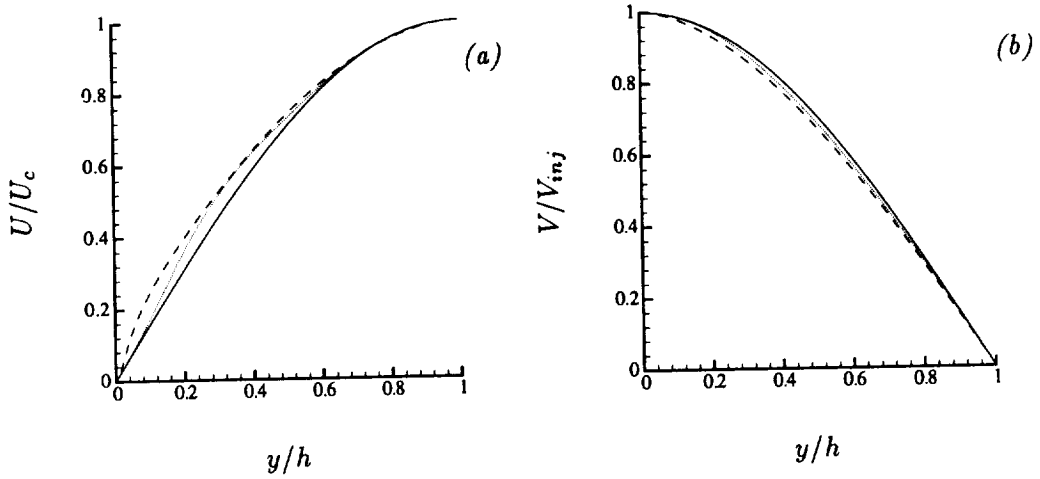

FIGURE 15. Distribution of mean velocity profiles; *(a)* streamwise component; *(b)* cross-stream component. ---- : Case A; ····· : Case B; ——— : Inviscid Solution (Culick, 1966).

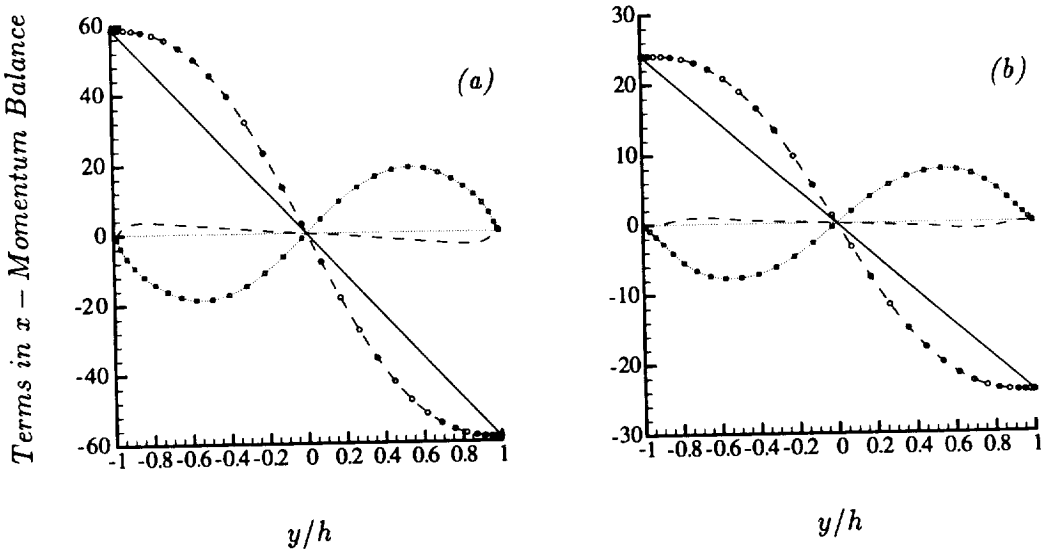

FIGURE 16. Distribution of streamwise momentum transport terms; *(a)* Case A; *(b)* Case B. ···: $\frac{1}{Re}\frac{\partial U}{\partial y}$; - - -: $-\overline{u'v'}$; □ : $-VU$; o : $-2\int \epsilon U^2 dy$; —: *Balance.*

Dunlap *et al.* (1990) as well as several researchers (e.g. Liou & Lien, 1995) have discussed the fact that, for injection-driven flows, the mean velocity distribution is insensitive to the presence of turbulence and that the turbulent stresses have a

second-order contribution to the mean momentum balance. Integrating the mean streamwise momentum equation, we obtain:

$$\frac{1}{Re}\frac{\partial U}{\partial y} - \overline{u'v'} - VU - 2\int \epsilon U^2 dy = \frac{\Delta P}{\Delta x} y$$

Hence, the mean pressure gradient term is balanced by the Reynolds and viscous shear stresses (similar to the turbulent channel flow) with two new terms: the vertical convection, VU, and the streamwise acceleration, $\int \epsilon U^2 dy$. For the two cases considered, the total shear stress is observed to make a small contribution (of less than 20%) to the overall momentum transport balance, as is shown in Fig. 16. This behavior is clearly different from that observed in turbulent channel flows where the mean flow is established from the balance between the turbulent shear stress and the pressure gradient. Further, it is seen from Figs. 16a and 16b that the magnitudes of the individual terms in the momentum balance are nearly twice as large in Case A compared to those for Case B, signifying the increased contribution of the convection and acceleration terms as the flow moves down the rocket motor.

Since the mean flow dynamics in the current injection-driven configuration have been shown to be vastly different from those present in the turbulent channel flow, it is not surprising that the distributions of the rms velocity fluctuations have significant departures from the channel, as seen in Fig. 17. Although the profiles for Case A are similar to the ones found for the turbulent channel flow, the stresses reach a peak farther from the channel walls, e.g. at a location of $y/h \simeq \pm 0.83$. Further, it is observed that the cross-stream velocity rms, v_{rms}, has the lowest magnitude amongst the three components and has a peak value twice as high as that observed for a turbulent channel flow, e.g 2.2 compared to 1.0. However, this behavior differs significantly from the normal stresses obtained for Case B, where the peaks in the streamwise and spanwise velocity rms are observed to move farther from the channel walls at $y/h = \pm 0.63$ while the cross-stream velocity rms shows a parabolic profile with a peak in the channel core.

It is quite clear based on the results presented above that the statistical quantities differ significantly from those of the turbulent channel flow and are highly dependent on the ratio of the injection to the axial velocity (i.e. the axial location in a rocket) through the variable ϵ. To gain further insight, the structural characteristics dominant in the current flow configuration are investigated. It is observed that, for the low injection ratio computed ($\epsilon = 0.04$) corresponding to Case A, the flow has a turbulent signature in which the small- scale structures are dominant, as seen in Fig. 18a. However, at the higher injection ratio considered of $\epsilon = 0.1$ for Case B, the flow is characterized by near-wall large-scale coherent structures inclined at an angle opposite to the mean flow direction, shown in Fig. 18b. These inclined near-wall structures have a streamwise separation distance of π, as computed from the streamwise correlation coefficient, and are spanwise coherent. The coherence of these spanwise structures is clearly captured in Fig. 19 where the contours of ω_z are plotted in a xz-plane parallel to the wall at $y/h = +0.96$. It is quite evident that the streaks dominant in conventional near-wall turbulence have been eradicated in

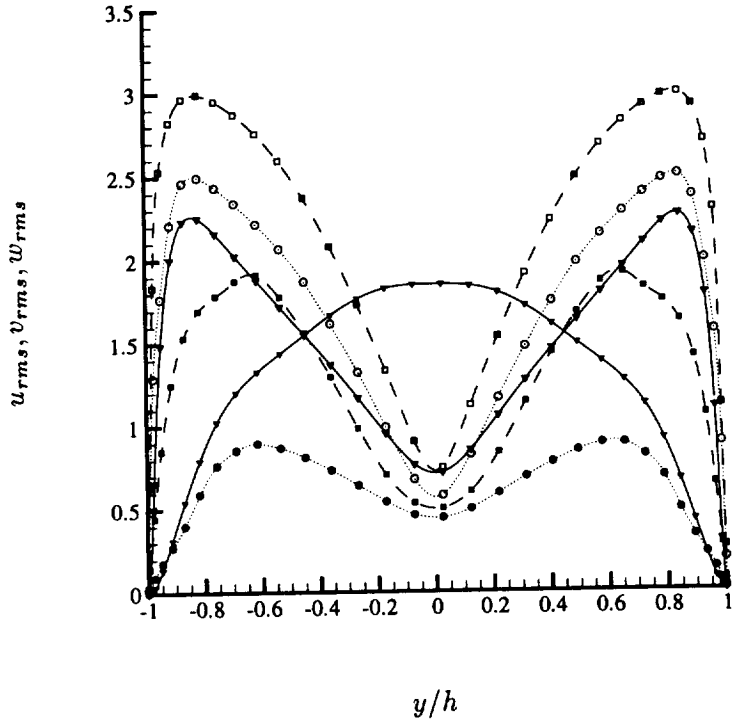

FIGURE 17. Distribution of the normal Reynolds stresses. Closed and open symbols refer to Case A and B, respectively. □ : u_{rms}; ▽ : v_{rms}; ○ : w_{rms}.

the present flow. Instead, roller-like vortical structures dominate the near-wall signature. For Case A, although the near-wall streaks are also absent, the flow does not reveal any near-wall coherent structures as in Case B. As a matter of fact, the spanwise correlation coefficient is observed to drop sharply to zero for a location close to the wall.

Another interesting flow feature observed in the high injection ratio case, Case B, is the presence of two-dimensional convection cells captured in the span-averaged stream-function, ψ, contours, shown in Fig. 20. These cells are seen to alternate in sign as they convect through the periodic computational domain. It is conjectured that their presence is set up by a mechanism similar to the Benard convection cells in buoyancy-driven flows since there is a large mean vertical acceleration at the center of this flow.

3.4 Synthesis of results

In the attempt to perform a synthesis of the results, some comparisons among the results obtained with the different methods have been made. Fig. 21a illustrates the velocity profile in wall units at the injection surface for a strong injection parameter, $V_{inj}{}^{+} = 1.4$; the results computed with the $v^2 - f$ turbulence model compare well

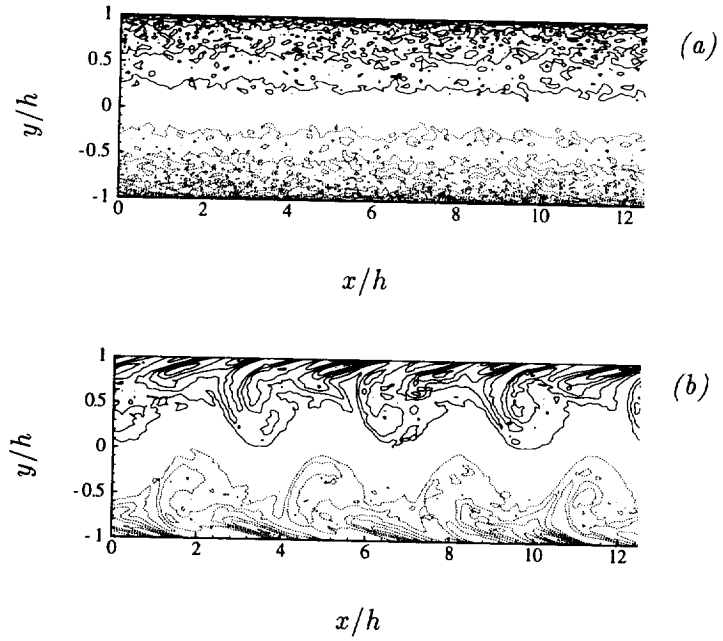

FIGURE 18. Contours of instantaneous spanwise vorticity, ω_z, of the fluctuating field averaged in the z-direction; *(a)* Case A; *(b)* Case B. Dashed (solid) contours represent clockwise (counter-clockwise) rotation with contours levels of $(\omega_{z_{min}}, \omega_{z_{max}}, \Delta\omega_z) = (-120, +120, 20)$, and $(-60, +60, 10)$ for cases A and B, respectively.

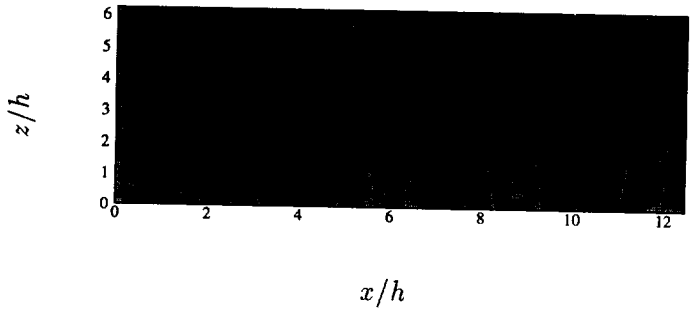

FIGURE 19. Contours of instantaneous spanwise vorticity, ω_z, of the fluctuating field at $y = +0.96$ for Case B. Dashed (solid) contours represent clockwise (counter-clockwise) rotation with contours levels of $(\omega_{z_{min}}, \omega_{z_{max}}, \Delta\omega_z) = (-60, -5, 5)$.

with the DNS data of Nicoud *et al.* (1995) while the values obtained in the present DNS investigation appear to be somewhat lower. It must be remembered that this flow geometry differs from that of the other two cases. All three curves differ from the standard law-of-the-wall for no slip surfaces. The distribution of k^+ along the

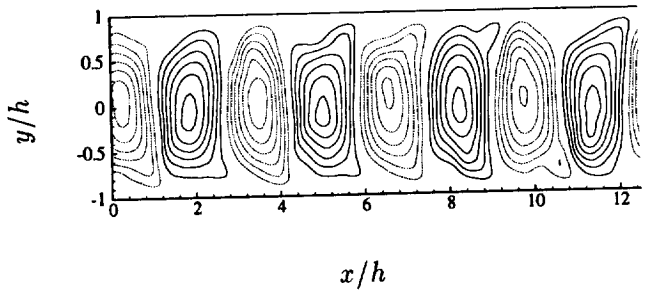

FIGURE 20. Contours of instantaneous stream-function, ψ, of the fluctuating field averaged in the z-direction for Case B. Solid (dashed) contours represent clockwise (counter-clockwise) rotation with contours levels of $(\psi_{min}, \psi_{max}, \Delta\psi) = (-1.2, +1.2, 0.2)$.

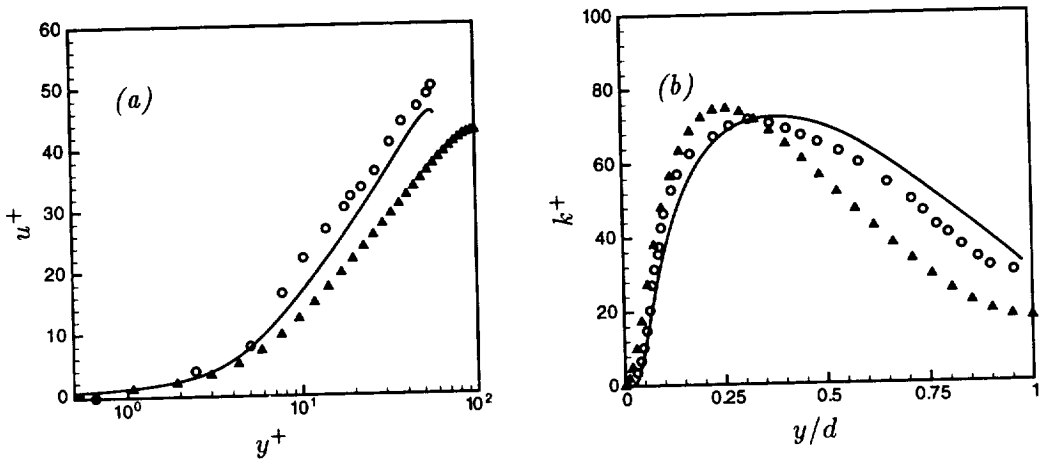

FIGURE 21. Effects of strong blowing on velocity and turbulence kinetic energy in wall units - ${V_{inj}}^+ = 1.4$. ——— : $v^2 - f$; ▽ : DNS (Nicoud *et al.*); ○ : DNS (present results).

height of the channel is shown in Fig. 21b. A rather good agreement in the peak values is observed with a larger discrepancy in the peak distance from the wall where blowing is applied. However, the model prediction is rather surprising.

A more comprehensive comparison of results is shown in Fig. 22, in which the ratio of the skin friction coefficient with injection to the skin friction coefficient for no slip conditions is plotted vs. a blowing parameter B_0. Three regions can be identified on this plot; a low injection region (${V_{inj}}^+ = 0.05$), a strong injection region (${V_{inj}}^+ = 1.4$), and a very strong injection region (${V_{inj}}^+ = 4.$). In all cases, results follow the experimental correlation derived by Andersen *et al.* (1975); some spreading of the present DNS data is observed. This correlation was indeed derived from tests with very low blowing. These results seem to suggest that this correlation may hold also for high injection rates.

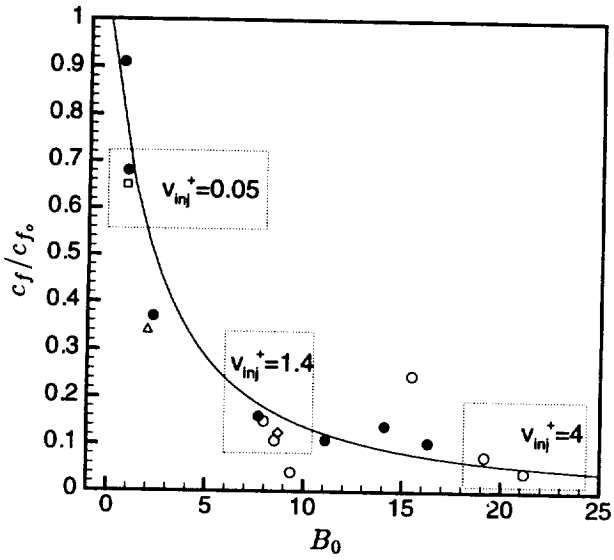

FIGURE 22. Distribution of dimensionless skin friction coefficient vs. blowing parameter. ——— : Exp. correlation of Andersen *et al.* ; △ : LES, Piomelli *et al.* ; □ : DNS, Sumitani *et al.* ; ◇ : DNS, Nicoud *et al.* ; ○ : DNS, present results; ● : v2f, present results.

4. Conclusions

A study of internal flows with strong turbulent injection from the wall has been performed. The work has comprised three main activities. RANS simulations of a nozzleless rocket motor have been carried out using both a k-ϵ and the $v^2 - f$ turbulence models; results have been compared with the experimental data of Traineau *et al.* (1986). Both models largely overpredicted the measured values when computations are performed with free transition. The correct capture of transition explains most of the discrepancy observed as well as the difference in the predictions of the two turbulence models. Compressibility effects also play a non-trivial role. When transition is fixed (at $x/h = 25$) a much better agreement is recovered. Furthermore, the present investigation has indicated a rather weak effect of the turbulent fluctuations at the wall on the flow solution. The effects of the f boundary condition for the $v^2 - f$ model have also been investigated with very small changes in the results. More extensive investigation of the applicability of the $v^2 - f$ turbulence model to this kind of flow is needed before any definite conclusion may be drawn. 1-D simulations of a channel flow with injection from one wall and equal suction from the opposite wall have also been performed. Results are in very good agreement with the DNS data available for no or weak injection. The results obtained for strong fluid injection appear to fall along the correlation curve derived by Andersen *et al.* (1975). No fluctuations at the wall were introduced in this channel flow study. Finally, a DNS analysis of a "periodic" motor with mass addition from two opposite walls has been conducted with the aim of obtaining some physical insights on the complex shear layer characteristics and turbulence

structure near a wall with strong blowing. Results are presented for two cases with different ratio of injection and centerline velocity. In both cases the near-wall coherent structures present in channel flows without mass-injection have been eradicated; in particular, at higher injection ratio the flow is characterized by large-scale coherent structures inclined at an angle opposite to the mean flow direction. Budgets of the streamwise momentum transport equation are also presented to shed light on the role of the acceleration term (due to the mass-injection) on the flow field establishment. The activities conducted in this work represent a first step toward the understanding and improved modeling of the near-wall processes for this class of flows. Results achieved are very encouraging, which should foster a more extensive research in this field.

REFERENCES

ANDERSEN, P. S., KAYS, W. M., & MOFFAT, R., J. 1975 Experimental results for the transpired turbulent boundary layer in an adverse pressure gradient. *J. Fluid Mech.* **69,** 353-375.

BEDDINI, R. A. 1986 Injection-induced flows in porous-walled ducts. *AIAA J.* **24**(11), 1766-1773.

CULICK, F. E. C. 1966 Rotational axisymmetric mean flow and damping of acoustic waves in solid propellant rocket motors. *AIAA J.* **4**(8), 1462-1464.

DUNLAP, R., WILLOUGHBY, P. G., & HERMSEN, R. W. 1974 Flowfield in the combustion chamber of a solid propellant rocket motor. *AIAA J.* **12**(10), 1440-1442

DUNLAP, R., BLACKNER, A. M., WAUGH, R. C., BROWN, R. S., & WILLOUGHBY, P. G. 1990 Internal flow field studies in a simulated cylindrical port rocket chamber. *J. Prop. and Power.* **6**(6), 690-704.

DURBIN, P. A. 1991 Near-wall turbulence closure modeling without "damping functions". *Theoret. Comput. Fluid Dyn.* **3,** 1-13.

DURBIN, P. A. 1995 Separated flow computations with the k-ϵ-v^2 model. *AIAA J.* **33**(4), 659-664.

JONES, W. P., AND LAUNDER, B. E. 1972 The prediction of laminarization with a two-equation model of turbulence. *Intl. J. of Heat and Mass Trans.* **15,** 301-314.

JULIEN, H. L., KAYS, W. M., & MOFFAT, R. J. 1971 Experimental hydrodynamics of the accelerated boundary layer with and without mass injection. *J. Heat Transfer.* **93,** 373-379.

KAYS, W. M., & MOFFAT, R., J. 1975 The behavior of transpired turbulent boundary layers. *Rept. HMT-20.* Stanford Univ, Stanford, CA.

KIM, J., MOIN, P., & MOSER, R. 1987 Turbulence statistics in fully developed channel flow at low Reynolds number. *J. Fluid Mech.* **177,** 133-166.

LIOU, T-M., & LIEN, W-Y. 1995 Numerical simulations of injection-driven flows in a two-dimensional nozzleless solid rocket motor. *J. Prop. and Power.* **11**(4), 600-606.

LIOU, T-M., LIEN, W-Y., & HWANG P-W. 1998 Transition characteristics of flowfield in a simulated solid rocket motor. *J. Prop. and Power.* **14**(3), 282-289.

MOIN, P. 1982 Numerical simulation of wall-bounded turbulent shear flows. *Proceedings of the 8th International Conference on Numerical Methods in Fluid Dynamics.* Edited by E. Krause, Springer-Verlag, New York, 55-76.

NICOUD, F., POINSOT, T. J., & MINH, H. H. 1995 Direct numerical simulation of a turbulent flow with massive uniform injection. *X Symposium on Turbulent Shear Flows.* **3**, 29.13-29.18.

OLSON, R. M., & ECKERT, E. R. G. 1966 Experimental studies of turbulent flow in a porous circular tube with uniform fluid injection through the tube wall. *J. Appl. Mech* (March 66), 7-17.

PIOMELLI, U., MOIN, P., & FERZIGER, J. 1991 Large eddy simulation of the flow in a transpired channel. *J. Thermophysics.* **5**(1), 124-128.

SABNIS, J. S., GIBELING, H. J., & MCDONALDS H. 1989a Navier-Stokes analysis of solid propellant rocket motor internal flows. *J. Propulsion and Power.* **5**(6), 567-664.

SABNIS, J. S., MADABHUSHI, R., GIBELING, H. J., & MCDONALDS, H. 1989b On the use of k-ϵ turbulence model for computation of solid rocket internal flows. *AIAA 89-2558.* 25th Joint Propulsion Conference, Monterey, CA.

SIMPSON, R. L., MOFFAT, R. J., & KAYS, W. M. 1969 The turbulent boundary layer on a porous plate: experimental skin friction with variable injection and suction. *Int. J. Heat and Mass Trans.* **12**(7), 771-789.

SPALART, P. 1988 Direct simulation of a turbulent boundary layer up to R_θ = 1410. . *J. Fluid Mech.* **187**, 61-98.

SPALART, P., MOSER, R., ROGERS, M. 1991 Spectral Methods for the Navier-Stokes equations with one infinite and two periodic directions. *J. Comp. Phys.* **96**(2), 297-324.

STEVENSON, T. 1963 A law of the wall for turbulent boundary layers with suction or injection. *J. Thermophysics.* **5**(1), 124-128.

SUMITANI, Y., & KASAGI, N. 1995 direct numerical simulation of turbulent transport with uniform wall injection and suction. *AIAA J.* **33**(7), 1220-1228.

TRAINEAU, J-C., HERVAT, P., & KUENTZMANN, P. 1986 Cold-flow simulation of a two-dimensional nozzleless solid rocket motor. *AIAA 86-1447.* 22nd Joint Propulsion Conference, Huntsville, AL.

YAMADA, K., GOTO, M., & ISHIKAWA, N. 1976 Simulative study on the erosive burning of solid rocket motors. *AIAA J.* **14**(9), 1170-1176.

Center for Turbulence Research
Proceedings of the Summer Program 1998

RANS modeling for compressible and transitional flows

By F. S. Lien[1], G. Kalitzin AND P. A. Durbin

Recent LES suggested that the turbulence fluctuation in the wall-normal direction v' plays an important role in the evolution of transition. This motivates the use of $v^2 - f$ model for turbomachinery flows, in which different types of transition co-exist. An 'ad hoc' Reynolds-number-dependent term is added to $C_{\epsilon 1}$ in the ε-equation in order to reduce the level of near-wall dissipation rate. As a result, the onset and length of transition are greatly improved for a moderate level of free-stream turbulence intensity. However, the peak of streamwise turbulence intensity within the transition zone is underestimated. The implication of this is that the intermittency effect needs to be incorporated into the model – for example, based on the 'conditioned Navier-Stokes equation' which splits the equation into turbulent and nonturbulent parts – in order to capture the correct physical mechanism of transition. Another objective of this study is to resolve the issue of whether the 'elliptic relaxation' model can be used for supersonic flows. The results for the RAE2822 transonic airfoil will demonstrate that a good agreement with experimental data has been achieved. This is because the pressure-strain term ($\sim f$), though elliptic in nature, acts simply as a source term in the $\overline{v^2}$-equation, which is not associated with the convection process.

1. Introduction

Turbomachinery flows, even in simple linear cascades, pose a range of physical, geometrical, and numerical challenges. The former includes the passing-wake/boundary-layer interaction, shock/boundary-layer interaction, rotation, tip and passage vortices, impingement, separation, and transition. Because the turbulence level in compressors and turbines is typically about $5 - 10\%$ (except in the wakes, where the turbulence level can be as high as $15 - 20\%$), three types of transition are commonly observed in gas turbine engines. The first is called 'bypass transition', in which Tollmien-Schlichting waves are completely bypassed and turbulent spots are directly produced within the boundary layer by the influence of free-stream turbulence. The second, termed 'separated-flow' transition, often occurs in the free shear layer close to the reattachment point of a laminar separation bubble. The third, caused by the periodic passing of wakes from upstream airfoils, is called 'wake-induced' transition. Moreover, pressure gradients due to curvatures of blade surfaces also influence the evolution of transition. For example, favorable pressure gradient tends to delay transition and, when the acceleration parameter $K = \nu/U_\infty^2(dU_\infty/dx) > 3 \times 10^{-6}$,

1 University of Waterloo, Canada

results in 'relaminarization'. On the other hand, adverse pressure gradient tends to promote transition. Only the first two types of transition will be investigated here.

Modeling transition within the RANS approach was mostly based on the low-Reynolds-number eddy-viscosity formulation. Examples include Launder & Sharma's $k-\varepsilon$ model (1974) and Craft's *et al.* $k-\varepsilon-A_2$ model (1995). Although these two models can give credible results for a flow over a flat plate with a sharp leading edge at zero pressure gradient, the transition was predicted too early when the flow is accelerated/decelerated, and in certain circumstances numerical instabilities also occurred (see Chen *et al.*, 1998a & 1998b, for details). In order to improve these deficiencies, several researchers introduced the intermittency factor γ into the expression of turbulent viscosity:

$$\nu_t = \gamma \nu_t^*, \tag{1}$$

where ν_t^* is the turbulent viscosity from one of the conventional eddy-viscosity models, in order to control the growth of transition through the level of turbulent shear stress and, consequently, the production of turbulence. For example, Huang & Xiong (1998) chose the γ experimentally correlated by Dhawan & Narasimha (1958) and combined it with Menter's SST model (1993) for low-speed turbine flows. Steeland & Dick (1996), on the other hand, performed the 'conditioned-averaging' on the Navier-Stokes equation, which was split into turbulent and nonturbulent parts. Both parts together with a transport equation for γ were solved simultaneously for flows subjected to favorable/adverse pressure gradients. Recent LES for bypass transitional flow (Yang *et al.*, 1994) suggested that v' – the turbulence fluctuation in the wall-normal direction – plays an important role within the transition process. This motivates us to apply the v^2-f model (Durbin, 1995), without the inclusion of γ at the present stage, to transitional flows, in which both bypass transition and separated-flow transition involve.

The v^2-f model consists of three transport equations for the turbulent kinetic energy k, the dissipation of the turbulent kinetic energy ϵ, and a transport equation for the energy of the fluctuations normal to the streamlines $\overline{v}^2$. In addition, the model includes a Helmholz type equation for a quantity f which models the pressure-strain term. This equation is elliptic in nature, and as a consequence information from all spatial directions is used to compute the variable f at a given point. In regions of transonic flows where the velocity exceeds the speed of sound, only information from the upstream direction is needed to compute mean flow parameters. In addition, any shock waves appearing in the flow may induce strong spatial gradients in the source terms of the turbulent model. This raises the questions of whether the elliptic relaxation model is able to represent transonic flows and how accurate it is in predicting the shock location in flows involving shock-boundary layer interactions. This forms the second part of the present investigation.

2. Unified approach of v^2-f model

The turbulent velocity and time scales, L and T, are determined from the standard $k-\varepsilon$ equations:

$$\partial_t k + U \cdot \nabla k = P_k - \varepsilon + \nabla \cdot [(\nu + \frac{\nu_t}{\sigma_k})\nabla k], \tag{2}$$

$$\partial_t \varepsilon + U \cdot \nabla \varepsilon = \frac{C_{\varepsilon 1} P_k - C_{\varepsilon 2}\varepsilon}{T} + \nabla \cdot [(\nu + \frac{\nu_t}{\sigma_\varepsilon})\nabla \varepsilon]. \tag{3}$$

where T and L (to be used later) are:

$$T = \max\left[\frac{k}{\varepsilon}, 6(\frac{\nu}{\varepsilon})^{1/2}\right], \; L = C_L \max\left[\frac{k^{3/2}}{\varepsilon}, C_\eta(\frac{\nu^3}{\varepsilon})^{1/4}\right]. \tag{4}$$

In order to avoid the stagnation anomaly, the realizability constraints are imposed on both scales (Durbin, 1996):

$$T \leq \frac{k}{\sqrt{3}\,\overline{v^2}C_\mu}\frac{1}{\sqrt{2S_{ij}S_{ij}}}, \quad L \leq \frac{k^{3/2}}{\sqrt{3}\,\overline{v^2}C_\mu}\frac{1}{\sqrt{2S_{ij}S_{ij}}} \tag{5}$$

where $S_{ij} = \frac{1}{2}(\frac{\partial U_i}{\partial x_j} + \frac{\partial U_j}{\partial x_i})$. On no-slip boundaries, $y \to 0$,

$$k = 0, \; \varepsilon \to 2\nu\frac{k}{y^2}. \tag{6}$$

The $\overline{v^2}$ transport equation is

$$\partial_t \overline{v^2} + U \cdot \nabla \overline{v^2} = \underline{kf - \overline{v^2}\frac{\varepsilon}{k}} + \nabla \cdot [(\nu + \frac{\nu_t}{\sigma_k})\nabla \overline{v^2}], \tag{7}$$

where

$$kf = \phi_{22} - \varepsilon_{22} + \frac{\overline{v^2}}{k}\varepsilon \tag{8}$$

represents redistribution of turbulence energy from the streamwise component. Non-locality is represented by solving an *elliptic relaxation* equation for f:

$$L^2\nabla^2 f - f = \frac{1}{T}(C_1 - 1)\left[\frac{\overline{v^2}}{k} - \frac{2}{3}\right] - C_2\frac{P_k}{k}, \tag{9}$$

The asymptotic behavior of ϕ_{22} and ε_{22} near a wall are (see, for example, Mansour *et al.*,1988):

$$\phi_{22} = -2\frac{\overline{v^2}}{k}\varepsilon, \quad \varepsilon_{22} = 4\frac{\overline{v^2}}{k}\varepsilon. \tag{10}$$

where y is minimum distance to walls. This yields the boundary condition for f:

$$kf(0) \to -5\frac{\overline{v^2}}{k}\varepsilon \;\text{ or }\; f(0) \to -\frac{20\nu^2\overline{v^2}}{\varepsilon(0)y^4} \tag{11}$$

(Durbin, 1995)

The Boussinesq approximation is used for the stress-strain relation:

$$\frac{\overline{u_i u_j}}{k} - \frac{2}{3}\delta_{ij} = -\frac{\nu_t}{k}\left(\frac{\partial U_i}{\partial x_j} + \frac{\partial U_j}{\partial x_i}\right), \tag{12}$$

where the eddy viscosity is given by

$$\nu_t = C_\mu \overline{v^2} T. \tag{13}$$

The original boundary condition for f, i.e. Eq. (11), involves $\varepsilon(0)$ in the denominator, which is ill-defined in the laminar and transitional regions. This causes oscillations for $f(0)$ in those regions as illustrated in Fig. 1 for a boundary-layer flow over a flat plate. As the flow becomes fully turbulent further downstream, $f(0)$ is well-defined and its distribution becomes fairly smooth. Note that the oscillatory behavior of $f(0)$ does not in any way influence the laminar flow solution, which is governed mainly by the molecular viscosity of the fluid. This problem, most often encountered when a segregated numerical procedure is adopted, can be overcome by reformulating the underlined term of Eq. (7) as follows:

$$\underbrace{\phi_{22} - \varepsilon_{22} + 6\frac{\overline{v^2}}{k}\varepsilon}_{=kf} - 6\frac{\overline{v^2}}{k}\varepsilon, \tag{14}$$

which changes slightly the definition of f. Important to know here is that such a modification also ensures that $\overline{v^2} \sim y^4$ as $y \to 0$. As $y \to \infty$, the kinematic blocking effect arising from 'elliptic relaxation' should disappear, i.e. both $kf - \frac{\overline{v^2}}{k}\varepsilon$ in Eq. (7) and $kf - 6\frac{\overline{v^2}}{k}\varepsilon$ in Eq. (14) should be identical and equal to

$$-C_1\frac{\varepsilon}{k}\left(\overline{v^2} - \frac{2}{3}k\right) - C_2 P_k. \tag{15}$$

Therefore, the use of $kf - 6\frac{\overline{v^2}}{k}\varepsilon$ requires the source term of Eq. (9) to be changed to:

$$\frac{1}{T}\left[(C_1 - 6)\frac{\overline{v^2}}{k} - \frac{2}{3}(C_1 - 1)\right] - C_2\frac{P_k}{k}. \tag{16}$$

To facilitate the coding, two variants of the $v^2 - f$ model are combined into the same set of equations:

$$\partial_t \overline{v^2} + U \cdot \nabla \overline{v^2} = kf - n\overline{v^2}\frac{\varepsilon}{k} + \nabla \cdot \left[\left(\nu + \frac{\nu_t}{\sigma_k}\right)\nabla \overline{v^2}\right], \tag{17}$$

$$L^2 \nabla^2 f - f = \frac{1}{T}\left[(C_1 - n)\frac{\overline{v^2}}{k} - \frac{2}{3}(C_1 - 1)\right] - C_2\frac{P_k}{k}, \tag{18}$$

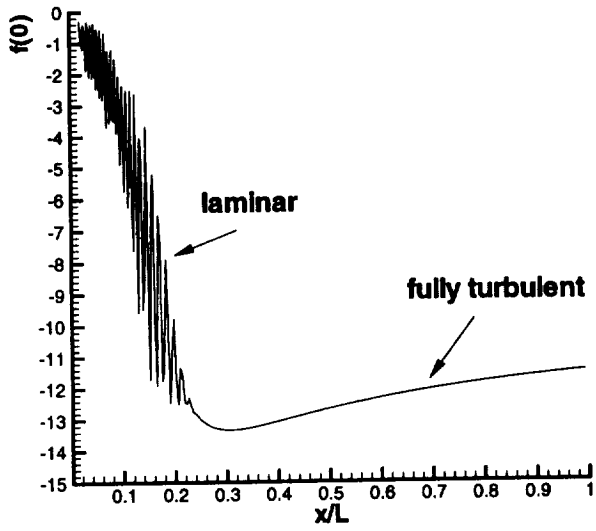

FIGURE 1. Distribution of $f(0)$ for a flow over a flat plate.

where $n = 1$ corresponds to the original $v^2 - f$ model and $n = 6$ relates to the variant of the model discussed in Lien & Durbin (1996). The constants of the original model (i.e. $n = 1$) are:

$$C_\mu = 0.22,\ \sigma_k = 1,\ \sigma_\varepsilon = 1.3,$$

$$C_{\varepsilon 2} = 1.9,\ C_1 = 1.4,\ C_2 = 0.3 \tag{19}$$

$$C_{\varepsilon 1} = 1.4(1 + 0.045\sqrt{k/\overline{v^2}}),\ C_L = 0.25,\ C_\eta = 80. \tag{20}$$

For $n = 6$, $C_{\varepsilon 1}$, C_L, C_η needs a slight adjustment:

$$C_{\varepsilon 1} = 1.4(1 + 0.050\sqrt{k/\overline{v^2}}) + \underline{0.4\exp(-0.1R_t)},\quad C_L = 0.23,\quad C_\eta = 70, \tag{21}$$

where $R_t = k^2/\varepsilon\nu$. The underlined term above is introduced to improve the prediction of bypass transition (see Section 4.1 for details), and its effect on the solution in the fully turbulent region is insignificant as illustrated in Fig. 2 for a fully-developed channel flow at $Re_\tau = 395$ (Kim *et al.*, 1987).

3. Numerical method

All transitional flows in Sections 4.1 and 4.2 have been computed with the STREAM general geometry, block-structured, finite-volume code (Lien *et al.*, 1996). Advection is approximated by a TVD scheme with the UMIST limiter (Lien & Leschziner, 1994). To avoid checkerboard oscillations within the co-located storage

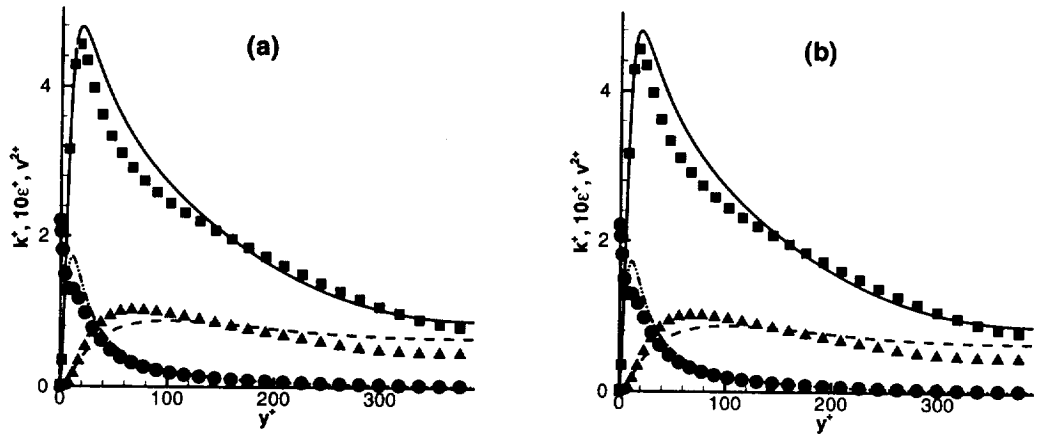

FIGURE 2. Channel flow: (a) with $0.4\exp(-0,1R_t)$ in $C_{\epsilon 1}$; (b) without $0.4\exp(-0,1R_t)$ in $C_{\epsilon 1}$; —— k^+(comp); —·— $10\varepsilon^+$(comp); ---- $\overline{v^2}^+$(comp); ■ k^+(DNS); • $10\varepsilon^+$(DNS); ▲ $\overline{v^2}^+$(DNS).

arrangement, the "Rhie and Chow" interpolation method (1983) is used. The solution is effected by an iterative pressure-correction SIMPLE algorithm applicable to both subsonic and transonic conditions.

The transonic computations in Section 4.3 were performed with the CFL3D computer code (Krist *et al.*, 1998), which solves the time-dependent thin-layer Reynolds-averaged Navier Stokes equations using multi-block structured grids. A semi-discrete finite-volume approach is used for the spatial discretization. The convective and diffusion terms are discretized with a third order upwind and a central difference stencil, respectively. The code uses flux-difference splitting based on the Roe-scheme. Time advancement is implicit. Approximate factorization is used to invert the mean flow system of equations. The steady-state computations have been performed by marching in time from an initial guess. Multigrid and local time stepping are used for convergence acceleration.

The $v^2 - f$ model is solved separately from the mean flow. The k and ϵ equations as well as the $\overline{v^2}$ and f equations are solved pairwise simultaneously. First-order upwind discretization of the convective terms has been employed. The time integration of the equations is implicit. The boundary conditions are also treated implicitly. Approximate Factorization (AF) and the Generalized Minimum Residual (GMRES) (Saad, 1986) algorithm are used to invert the resulting matrices. While the latter is more robust, it requires more computational memory. The AF method decomposes the matrices formed by the implicit operator into 1D tridiagonal matrices. This allows a very fast inversion of the matrices with very low memory requirements. The splitting, however, is an approximation and introduces error terms which necessitate smaller timesteps.

4. Results and discussion

4.1 Flow over a flat plate with a sharp leading edge at zero pressure gradient

The first problem investigated here is the simplest (though fundamentally important) transitional-flow test cases proposed in the European Research Community On Flow Turbulence And Combustion (ERCOFTAC) Special Interest Group on Transitional Modeling, which include cases T3A, T3A-, T3B, T3B+ and T3B_{DNS} (see Savill, 1993, for details). Two cases, namely T3A and T3A-, will be presented and the corresponding initial conditions are given in the following table:

T3A	$Tu = 3\%$	U_∞ =19.6 m/s	$l_{\varepsilon\infty}$ =5.2 mm	at x=-150 mm
T3A-	$Tu = 0.9\%$	U_∞ =5.2 m/s	$l_{\varepsilon\infty}$ =10.4 mm	at x=-150 mm

The computation domain extends to 0.15 m upstream of leading edge, allowing the free-stream turbulence quantities to be specified as the in-flow condition:

$$k_{in} = 1.5(Tu\, U_\infty)^2, \quad \varepsilon_{in} = \frac{k_{in}^{3/2}}{l_{\varepsilon\infty}} \tag{22}$$

The computational mesh for T3A, containing 200 × 50 nodes, is employed here, in which sufficient number of grid lines are clustered towards the leading edge. As the turbulence transport plays an important role in triggering the bypass transition, it is crucial to use a second-order convection scheme for both momentum and turbulence quantities (Chen *et al.*, 1998a).

Predicted skin-friction distributions for T3A and the corresponding profiles of mean-velocity and turbulence-intensity u' at three locations across the laminar, transitional, and fully-turbulent regions are given in Figs. 3-5. As seen from Fig. 3, the introduction of the transition-correction term $0.4\exp(-0.1R_t)$ to $C_{\varepsilon 1}$ significantly improves the prediction of the onset of transition. As a result, the U-profile within the transition zone (x=595 mm) is better predicted in comparison with the original model. Although the new R_t-dependent term in $C_{\varepsilon 1}$ does better predict the location of the peak value of u', the level of turbulence intensity is too low, particularly at x=595 mm. This discrepancy is partially due to the use of Boussinesq stress-strain relation, in which turbulence intensities are assumed to be locally isotropic ($\sim \frac{2}{3}k$). The new R_t-dependent term also acts to further suppress the u' level by increasing slightly the value of $C_{\varepsilon 1}$ near the wall, which suppresses the generation of turbulence energy and, consequently, delays the onset of transition. It is clear that the mechanisms of triggering and controlling the evolution of transition process are different in the experiment and in the model. The LES work of Yang *et al.* (1994) suggested that u' and v' are not well correlated within the transition region. So far only the LES results are able to predict the correct peak of u' within the laminar and transition regions.

The skin-friction distribution for T3A- case, of which the level of free-stream turbulence intensity and dissipation-rate length scale are lower than T3A, is given in Fig. 6. As seen, the onset of transition is too early, and the sensitivity of the

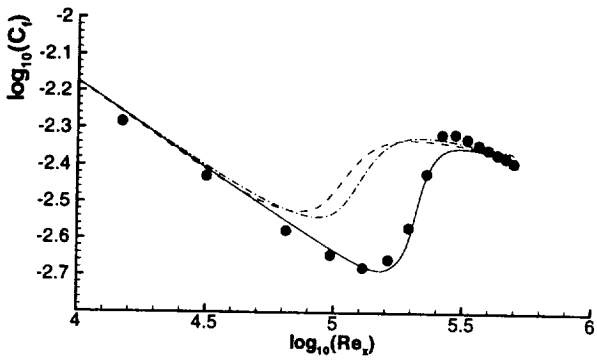

FIGURE 3. Flat plate (T3A): skin-friction distributions. ——— n=6 with R_t correction; —·— n=6 without R_t correction; ---- n=1 (original model); • expt.

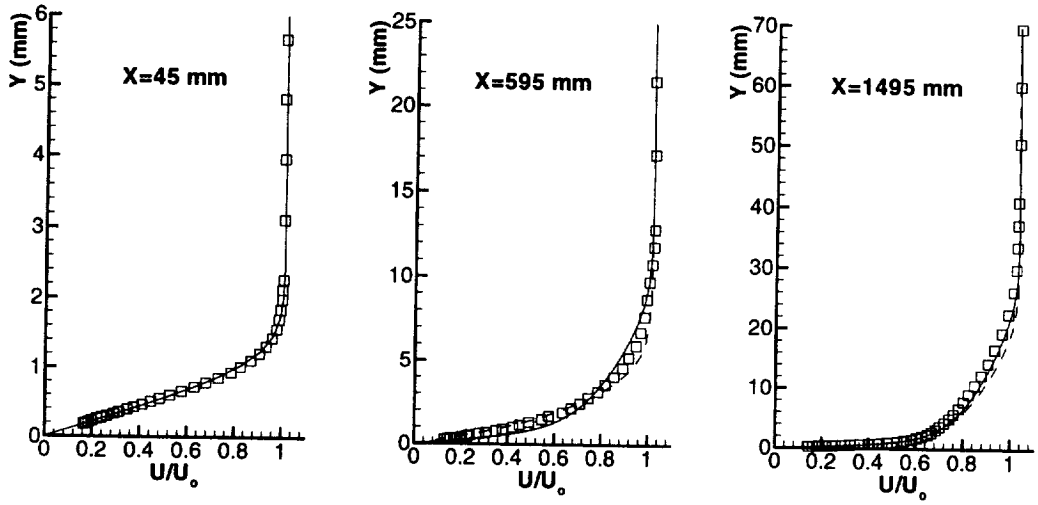

FIGURE 4. Flat plate (T3A): streamwise velocity profiles. ---- n=6 with R_t correction; ——— n=1 (original model); □ expt.

R_t-dependent term to very low turbulence intensity is too weak. One possible reason for this is that at $Tu = 0.9\%$ the influence of Tollmien-Schlichting waves might not be entirely negligible. The results suggest that the dissipation equation and, likely, the 'elliptic relaxation' equation, which is responsible for energy redistribution among different Reynolds-stress components, require further re-calibration, particularly within the transition region. The introduction of intermittency factor γ into the model will increase the model's sensitivity to a number of flow features such as pressure gradients and free-stream turbulence level, depending on how γ is correlated. To pursue this modeling approach further, the provision of DNS data is indispensable.

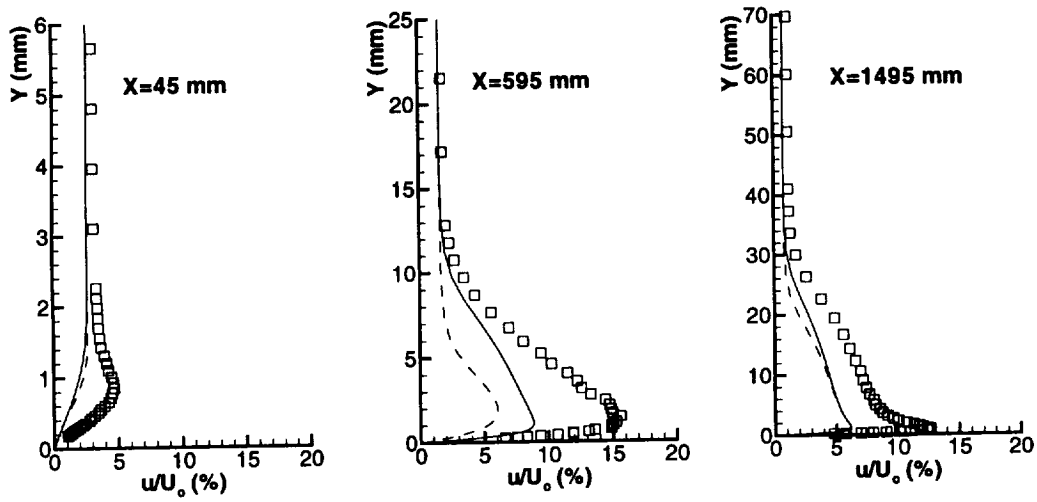

FIGURE 5. Flat plate (T3A): streamwise turbulence-intensity profiles. ---- n=6 with R_t correction; —— n=1 (original model); □ expt.

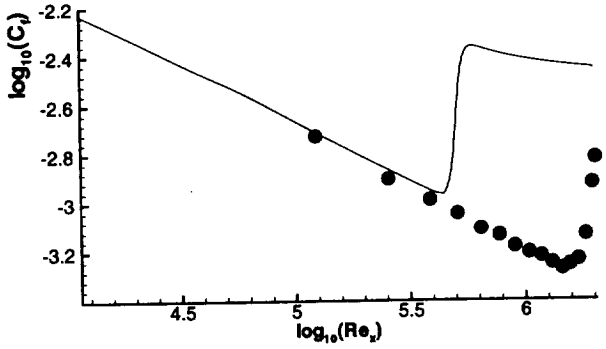

FIGURE 6. Flat plate (T3A-): skin-friction distributions. —— n=6 with R_t correction; • expt.

4.2 Double-circular-arc (DCA) compressor blade

The experimental data for DCA compressor blade was obtained by Deutsch & Zierke (1988) using one-component LDV system. The blade is formed by two circular arcs and has a 65° camber angle, a 20.5° stagger angle, a solidity of 2.14, and a 228.6 mm chord length. Three incidence angles were measured and only $i = +5°$ – the one with massive trailing-edge separation as illustrated in Fig. 7 – is considered here. The Reynolds number, based on the inlet velocity and blade chord length, is 505,000. The turbulence intensity and length scale, recommended by Chen *et al.* (1998b) and used herein, are $Tu = 2\%$ and $l_{\epsilon\infty}= 4.5$ mm, which give the correct turbulence level at the edges of boundary layers in accord with the experimental

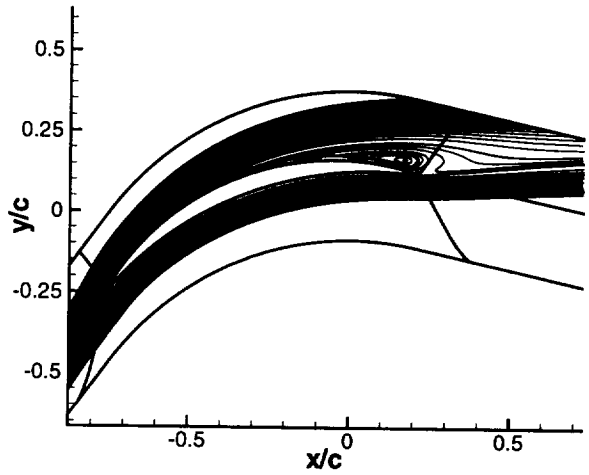

FIGURE 7. DCA compressor blade: massive trailing separation.

data. An 8-block computational mesh of 25,000 nodes, which surrounds the blade and extends in the cross-stream direction from the middle of one passage to the middle of the adjacent ones, is employed.

Experimental data suggests the existence of a large separation bubble near the leading edge. To resolve this feature, it is important to impose the realizability constraint on turbulence time and length scales in order to reduce excessive turbulence energy close to the stagnation region. The turbulence-energy contours obtained with and without the realizability constraint are shown in Fig. 8, and its impact on the size of leading-edge separation bubble are given in Fig. 9. As seen from Figs. 8 and 9, the separation bubble obtained with the realizability constraint is considerably larger than that obtained without the constraint. This is because without the constraint the turbulent mixing along the curved shear layer is too high, which entrains too much fluid into the bubble and, as a result, causes a too early reattachment.

The differences in the fluid displacement close to the leading edge also affect the development of the boundary layer further downstream. This is illustrated by the streamwise velocity profiles at two locations, $x/c = 12.7\%$ and $x/c = 94.9\%$, given in Fig. 10. The model without the realizability constraint appears to predict well the velocity profile at $x/c = 12.7\%$. However, the flow is too turbulent, which tends to resist separation. As a result, the boundary layer at $x/c = 94.9\%$ is slightly too thin. On the other hand, the use of realizability constraint overpredicts the size of leading-edge separation bubble, which results in slightly too thick boundary layers at both $x/c = 12.7\%$ and $x/c = 94.9\%$.

The distributions of pressure coefficient C_p on both sides of the blade are given in Fig. 11. The pressure plateau, clearly seen on the suction side beyond 80% of the chord, indicates that a massive trailing-edge separation exists. The model without including the realizability constraint predicts a too early pressure recovery on the

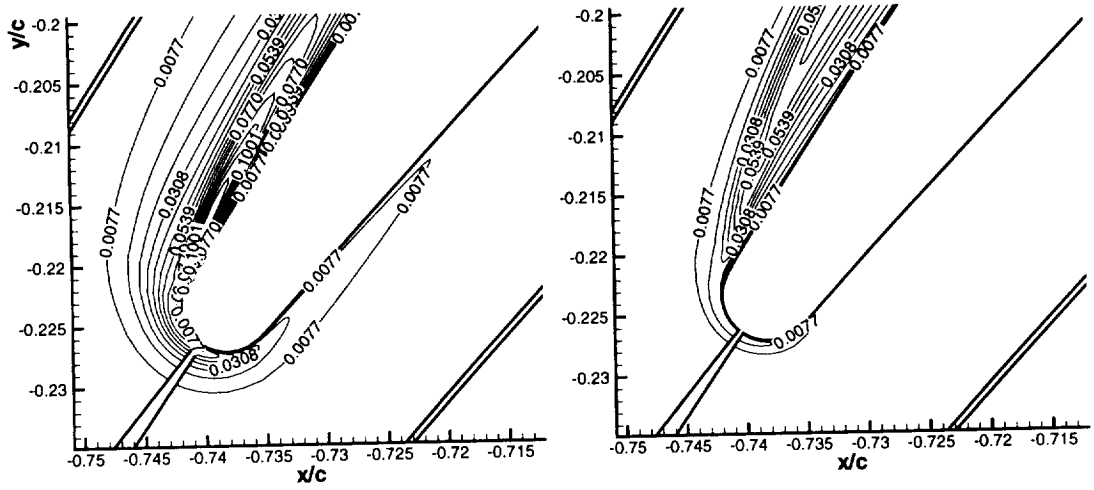

FIGURE 8. DCA compressor blade: turbulence-energy contours near the leading edge obtained without (left) and with (right) realizability constraint.

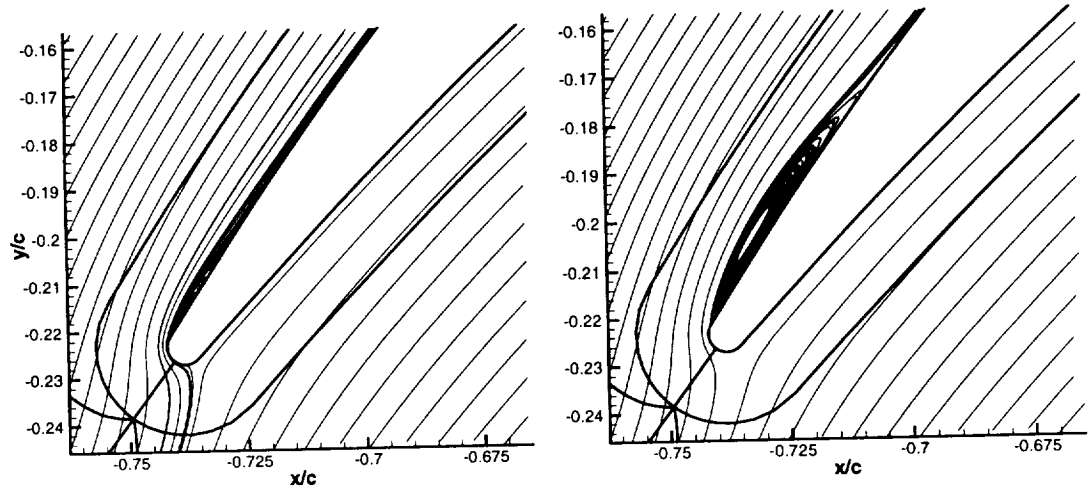

FIGURE 9. DCA compressor blade: leading-edge separation bubbles obtained without (left) and with (right) realizability constraint.

suction side, which is consistent with a too thin boundary layer at $x/c = 94.9\%$ observed in Fig. 10. Overall, it is fair to say that the results returned by the $v^2 - f$ model variants agree reasonably well with the measurement even in this complex flow involving impingement, transition, and massive separation.

4.3 RAE2822 transonic airfoil

Flow around the transonic RAE2822-airfoil has been chosen to study the performance of the $v^2 - f$ model in predicting shock-boundary layer interaction. Two test cases, case 9 and case 10, from the experiments by Cook *et al.* (1979) have been considered. The flow conditions for these cases differ only slightly in Mach and

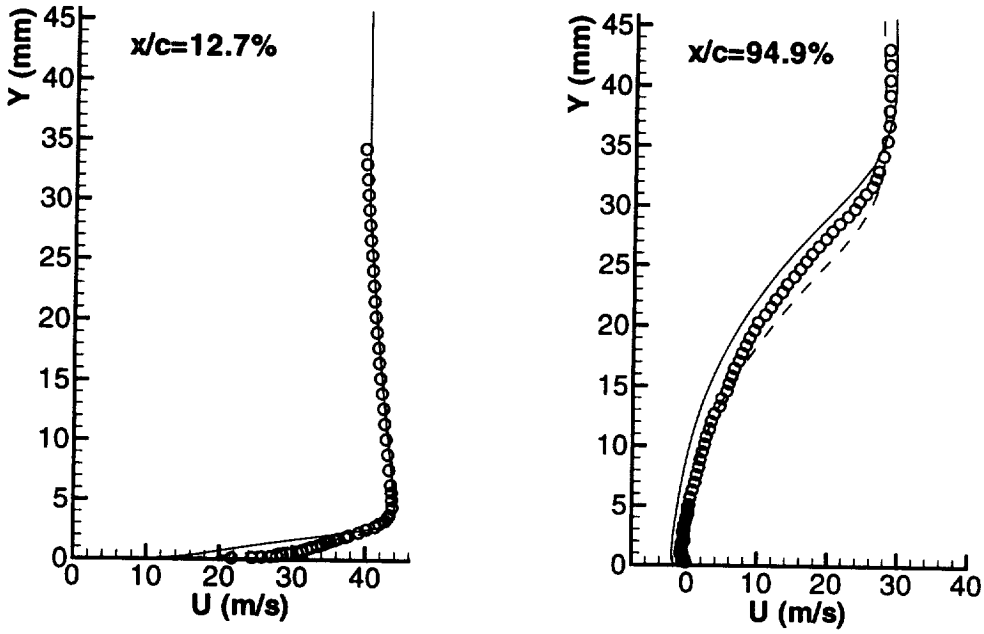

FIGURE 10. DCA compressor blade: streamwise velocity profiles. —— n=6 with R_t correction; ---- n=1 (original model); o expt.

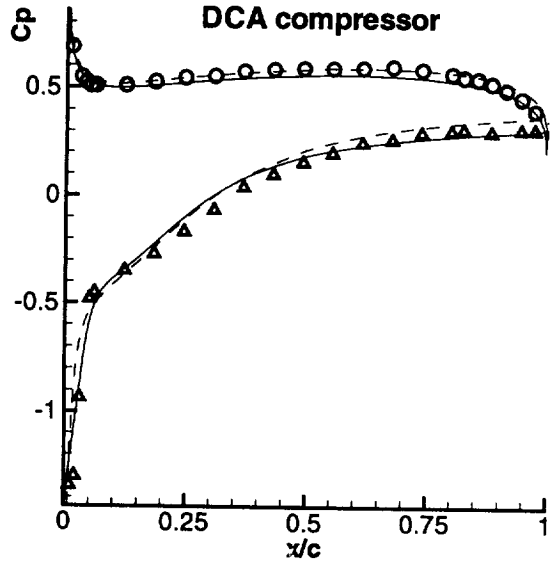

FIGURE 11. DCA compressor blade: pressure coefficient. —— n=6 with R_t correction; ---- n=1 (original model); o expt (pressure side); △ expt (suction side).

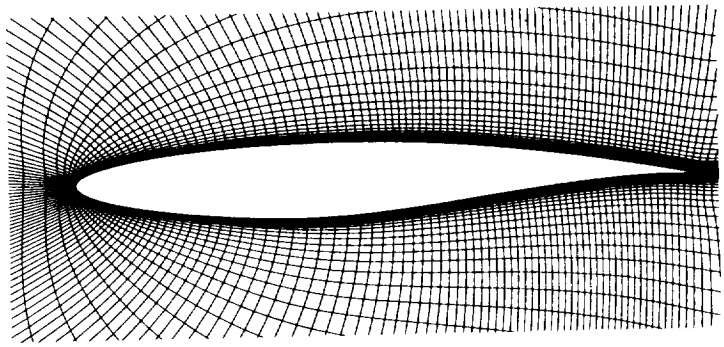

FIGURE 12. RAE2822 airfoil: computational mesh 256x64.

Reynolds number. While in case 9 the shock is too weak to induce separation, for case 10 the flow separates at the shock. The amount of separation and the position of the shock is very dependent on the turbulence model used.

The experimental data was obtained in the wind tunnel for the flow conditions: case 9: $M = 0.73, Re = 6.50\ 10^6, \alpha = 3.19^o$; and case 10: $M = 0.75, Re = 6.20\ 10^6, \alpha = 3.19^o$. Transition has been tripped in the experiments near the leading edge of the airfoil at $x/c = 0.03$ on both the upper and lower surface of the airfoil.

To compare the experimental data with the computed flow around the airfoil in free-flight conditions, corrections to the tunnel data are required. Different wind tunnel corrections have been used in the various studies published in the literature (see Haase *et al.*, 1992, Krist *et al.*, 1998, and others). The flow conditions used in the EUROVAL-project are adopted here. They are for case 9: $M = 0.734, Re = 6.50\ 10^6, \alpha = 2.54$; and for case 10: $M = 0.754, Re = 6.20\ 10^6, \alpha = 2.57$. Note that for case 10 in particular, researchers tend to compute the flow with a slightly larger angle of attack. Clearly, this influences the location of the shock. The shock location and the pressure distribution, particularly on the suction side, are influenced by the outer extent of the computational domain. The finite far field boundary causes a lower circulation around the airfoil, leading to an underprediction of lift. A vortex correction to the far-field boundary condition adjusts the circulation around the airfoil and has, therefore, been employed for the present computations.

In addition, computations have been carried out with the Spalart-Allmaras (1992) and Menter SST (1993) models to allow a comparison of results computed with the same flow solver. Both these models are included in the standard release of CFL3D, version 5.0. The $v^2 - f$ model has been implemented in CFL3D in its original form. This corresponds to setting $n = 1$ in Eqs. (17) and (18). Transition has been fixed by switching of the production terms in the equations as described in Kalitzin (1997).

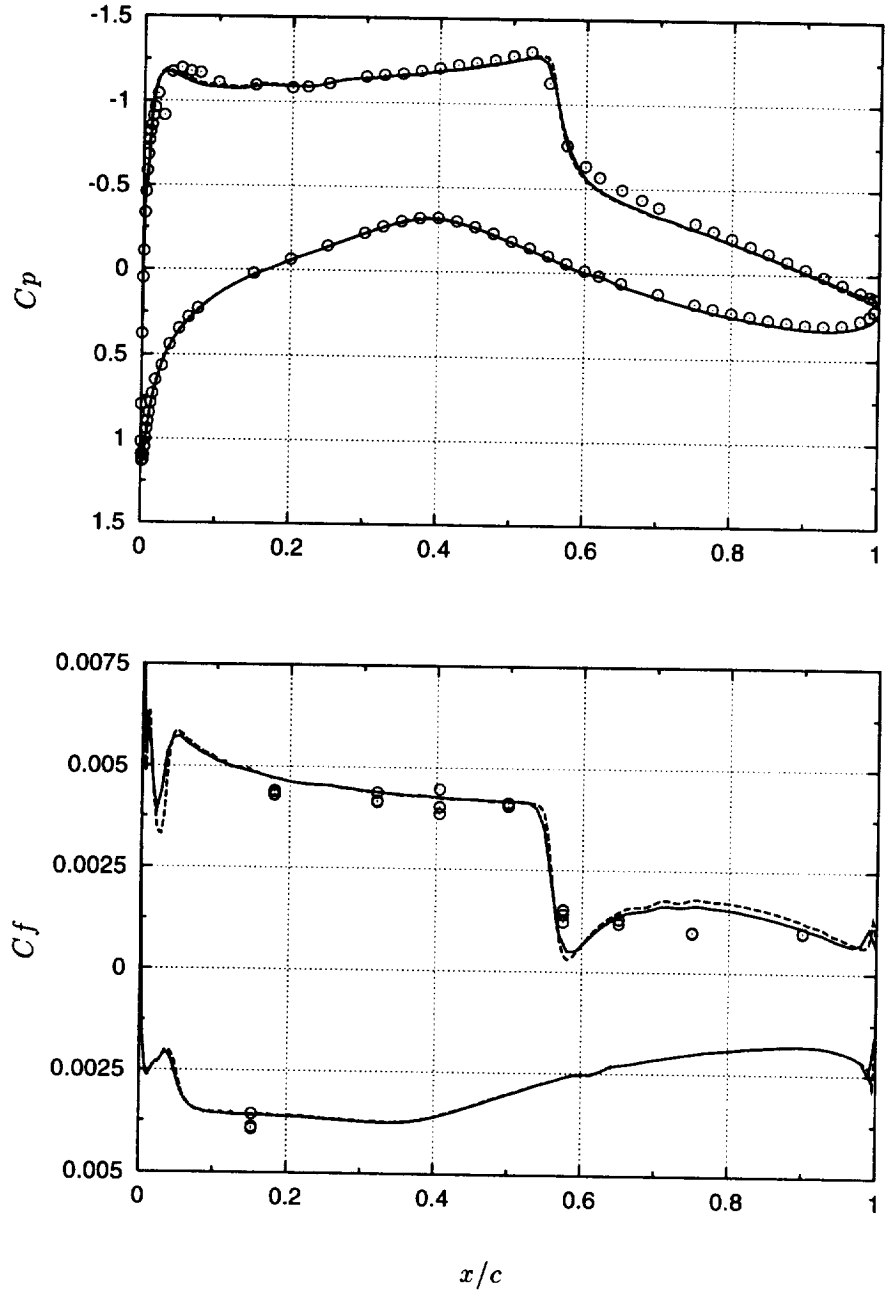

FIGURE 13. RAE2822 airfoil: pressure and skin friction distribution; case 9, ——— : $v^2 - f$ 256x64, ---- : $v^2 - f$ 512x128, o : expt.

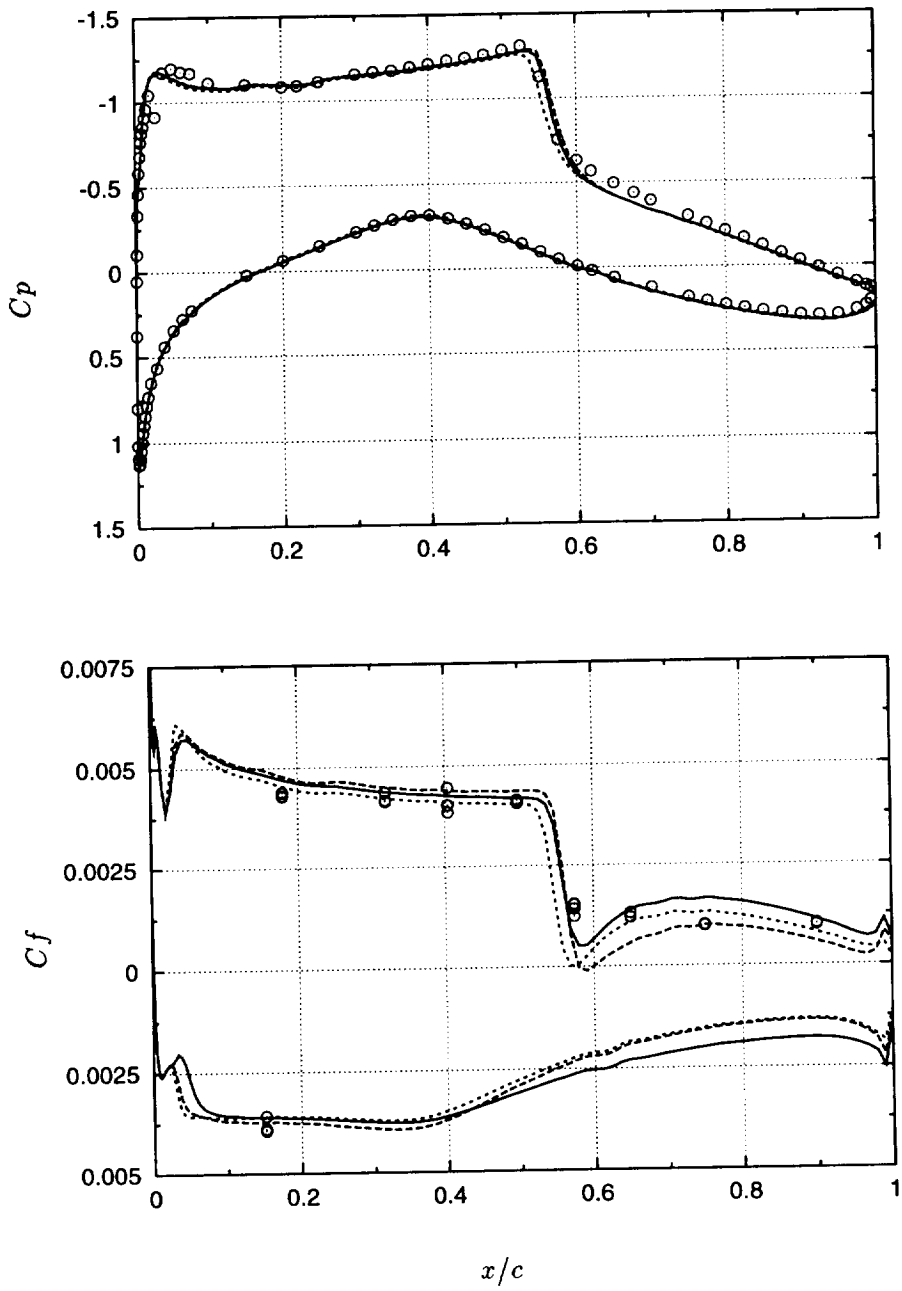

FIGURE 14. RAE2822 airfoil: pressure and skin friction distribution; case 9, ——— : $v^2 - f$, - - - - : Spalart-Allmaras, ····· : Menter SST, o : expt.

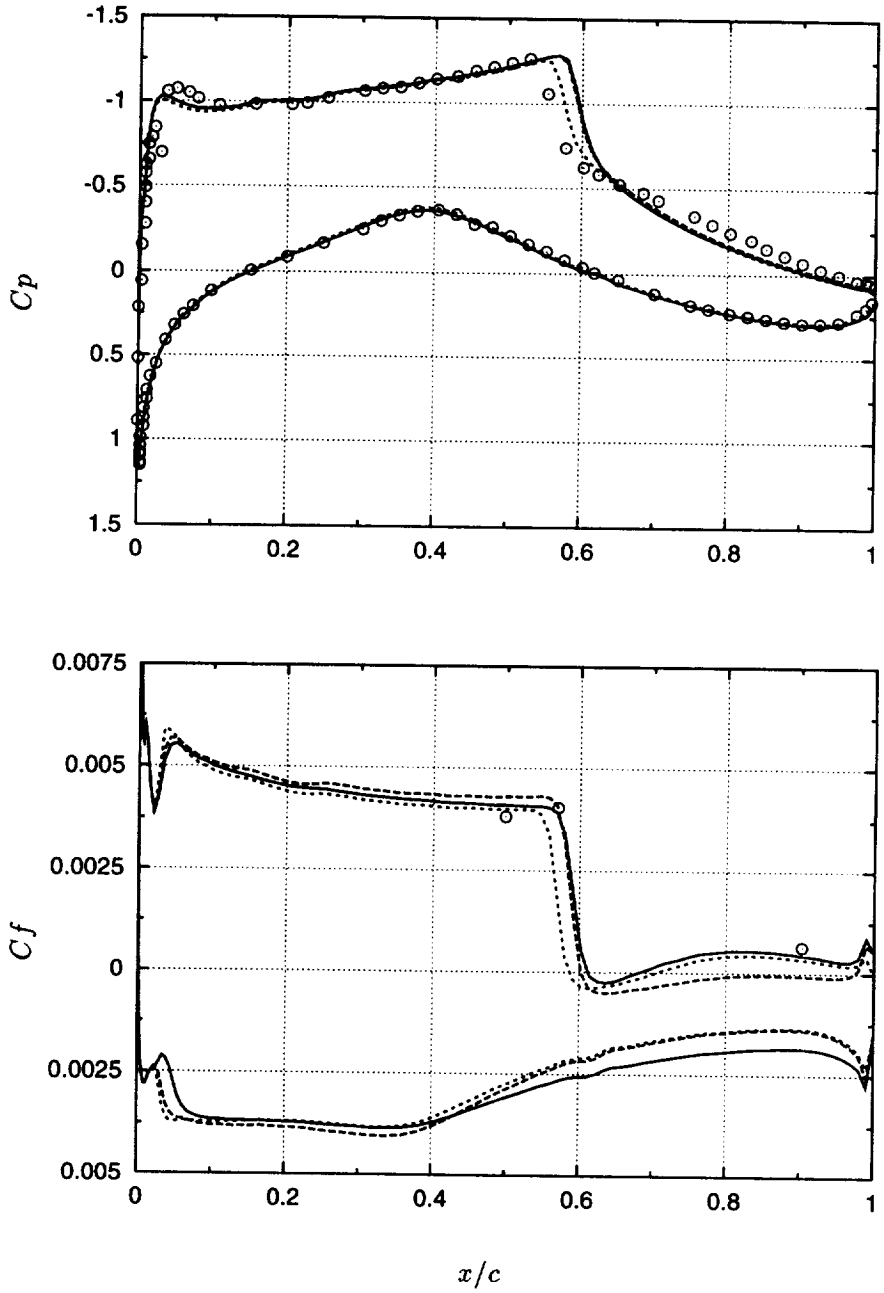

FIGURE 15. RAE2822 airfoil: pressure and skin friction distribution; case 10, ——— : $v^2 - f$, - - - - : Spalart-Allmaras, ····· : Menter SST, o : expt.

The present computations were carried out using the EUROVAL mesh, which consists of 256x64 cells. 192 cells are located on the airfoil surface. The far field is about 15 cord lengths from the airfoil. The average y^+ value of the first cell above the wall is about 1. The airfoil is represented in this mesh along the measured (not the designed) airfoil contours. The mesh is shown in Fig. 12.

A grid dependency study has been carried out with the $v^2 - f$ model for case 9 on a mesh with twice as many cells in each direction. The average y^+ value of the first cell above the wall is for this mesh about 0.5. The pressure and skin friction distribution is almost mesh independent as indicated by the results shown in Fig. (13).

A comparison of the pressure and skin friction distribution computed with the $v^2 - f$, the Spalart-Allmaras and the Menter SST models are shown in Figs. 14 and 15 for case 9 and 10, respectively. While the pressure distribution agrees quite well with the experimental data for all models for case 9, the shock location is generally too far downstream for case 10. The $v^2 - f$ model predicts the shock location very similarly to the Spalart-Allmaras model in both cases. It is, however, interesting to note that the skin friction computed with the Spalart-Allmaras model for case 10 reveals a fully separated flow from the shock downstream to the trailing edge. One would expect that this separation would lead to a thicker boundary layer with the consequence of a shock location further upstream. The SST model, in contrast, predicts the shock further upstream while the separation bubble is of similar size as with the $v^2 - f$ model. It is also interesting to note the similarity in the skin friction on the pressure side of the airfoil for the Menter SST and the Spalart-Allmaras models. The skin friction predicted with the $v^2 - f$ model is slightly larger here than with the other two models.

The lift and drag coefficients for case 9 and 10 are given in the table below. For the $v^2 - f$ model the predicted force coefficients lie somewhere in between the ones obtained with the Menter SST and Spalart-Allmaras models.

	$v^2 - f$ (512x128)	$v^2 - f$	Spalart-Allmaras	Menter SST	Expt
case 9					
C_L	.7983	.7995	.8066	.7789	.803
C_D	.01645	.01733	.01738	.01611	.0168
case 10					
C_L		.7570	.7628	.7262	.743
C_D		.02587	.02645	.02407	.0242

The convergence of all three models investigated for case 9 required about 1000 iterations for a 5-order magnitude drop in the L2 norm of the residual of the mean flow and turbulence quantities. In the $v^2 - f$ computation of case 10, however, small unsteady oscillations in $\overline{v^2}$ and f were observed between the shock and the trailing edge. These oscillations are caused by the use of local timesteps for the turbulence equations. The computation fully converged when a constant timestep was used throughout the boundary layer. The results presented were achieved by using local

timesteps for the mean flow and constant timesteps for the turbulence equations. This finding requires further investigation.

5. Conclusions

A unified formulation of the $v^2 - f$ model, which allows two types of boundary conditions at walls depending on the value of integer 'n', is adopted here with application to both transitional and compressible flows, the latter involving shock waves. The outcome of the present study permits the following conclusions to be drawn:

(1) In most cases (some of the results are not included here for brevity), both variants have very similar performance. The 'code-friendly' version (i.e. n=6) is numerically more robust for transitional flows when an uncoupled solution procedure is adopted.

(2) The performance of the $v^2 - f$ model for a flow over compressor-cascade blades, involving both the leading-edge and trailing-edge separation, are very encouraging. The imposition of realizability constraint on turbulence scales significantly reduces the level of turbulence energy at the stagnation region. Although the size of the resulting laminar separation bubble is slightly too large, the velocity profiles close to the trailing edge are in good agreement with the experimental data.

(3) In order to model the transition mechanism on the basis of physical ground, the intermittency effect needs to be incorporated into RANS models. The DNS data, once available, will provide detailed information in terms of the Reynolds-stress budget and intermittency factor, which can be used to re-calibrate the pressure-strain term and turbulence-dissipation equation within the transition region.

(4) Combining Dhawan & Narasimha's intermittency factor with the $v^2 - f$ model based on the conditioned Navier-Stokes equation approach is currently under investigation.

(5) The results obtained with the $v^2 - f$ model for the RAE2822 airfoil demonstrate the capability of predicting transonic flows around airfoils. The present computations were carried out with the original model setting $n = 1$. Generally, the model converges well even on the finer mesh. This is attributed to a pairwise implicit solution of the model's equations and an implicit treatment of the boundary conditions.

Acknowledgments

The first author would like to express his gratitude to CTR and University of Waterloo in Canada for their financial support.

REFERENCES

CHEN, W. L., LIEN, F. S. & LESCHZINER, M. A. 1998a Non-linear eddy-viscosity modeling of transitional boundary layers pertinent to turbomachine aerodynamics. *Int. J. Heat Fluid Flow.* **19,** 297-306.

CHEN, W. L., LIEN, F. S. & LESCHZINER, M. A. 1998b Computational prediction of flow around highly loaded compressor-cascade blades with non-linear eddy-viscosity models. *Int. J. Heat Fluid Flow.* **19,** 307-319.

CRAFT, T. J., LAUNDER, B. E. & SUGA, K. 1995 A non-linear eddy viscosity model including sensitivity to stress anisotropy. *Proc. 10th Symp. on Turbulent Shear Flows.* **2,** 23.19-23.24.

COOK, P. H., MCDONALD, M. A. & FIRMIN, M. C. P. 1979 Aerofoil 2822 - pressure distributions, boundary layer and wake measurements. *AGARD AR 138.*

DEUTSCH, S. & ZIERKE, W. C. 1988 The measurement of boundary layers on a compressor blade in cascade: part 2 – suction surface boundary layers. *ASME J. Turbomach..* **110,** 138-145.

DHAWAN, S. & NARASIMHA, R. 1958 Some properties of boundary layer during the transition from laminar to turbulent flow motion. *J. Fluid Mech.* **3,** 418-436.

DURBIN, P. A. 1995 Separated flow computations with the $k-\epsilon-\overline{v^2}$ model. *AIAA J.* **33,** 659-664.

DURBIN, P. A. 1996 On the $k-\epsilon$ stagnation point anomaly. *Int. J. Heat and Fluid Flow.* **17,** 89-90.

HAASE, W., BRADSMA F., ELSHOLZ E., LESCHZINER M., & SCHWAMBORN D. 1993 EUROVAL-an European Initiative on Validation of CFD Codes. *Notes on Numerical Fluid Mechanics, Volume 42, Vieweg.*

HUANG, P. G. & XIONG, G. 1998 Transition and turbulence modeling of low pressure turbine flows. *AIAA Paper No. 98-0339.*

KALITZIN G. 1997 Application of turbulence models to high-lift airfoils. *CTR-Annual Research Briefs, Center for Turbulence Research, NASA Ames/Stanford Univ., 165-177.*

KIM, J., MOIN, P. & MOSER, R. D. 1987 Turbulence statistics in fully-developed channel flow at low Reynolds number. *J. Fluid Mech.* **177,** 133-166.

KRIST, S., BIEDRON, R. & RUMSEY, C. 1998 CFL3D User's Manual (Version 5.0). *NASA/TM-1998-208444.*

LAUNDER, B. E. & SHARMA, B. I. 1974 Application of the energy dissipation model of turbulence to the calculation of flow near a spinning disc. *Letters in Heat and Mass Transfer.* **1,** 131-138.

LIEN, F. S. & DURBIN, P. A. 1996 Non-linear $k-\varepsilon-v^2$ modeling with application to high-lift. *CTR summer proceedings*

LIEN, F. S. & LESCHZINER, M. A. 1994 Upstream monotonic interpolation for scalar transport with application to complex turbulent flows. *Int. J. Num. Methods Fluids.* **19,** 527-548.

LIEN, F. S., CHEN, W. L. & LESCHZINER, M. A. 1996 A multiblock implementation of a non-orthogonal collocated finite volume algorithm for complex turbulent flows. *Int. J. Num. Methods Fluids.* **23,** 567-588.

MANSOUR, N. N., KIM, J. & MOIN, P. 1988 Reynolds-stress and dissipation-rate budgets in a turbulent channel flow. *J. Fluid Mech.* **194,** 15-44.

MENTER, F. R. 1993 Zonal two equation $k-\omega$ turbulence model predictions. *AIAA Paper No. 93-2906.*

RHIE, C. M. & CHOW, W. L. 1983 Numerical study of the turbulent flow past an airfoil with trailing edge separation. *AIAA J.* **21,** 1525-1532.

SAAD, Y. & SCHULTZ M. H. 1986 GMRES: a generalized minimal residual algorithm for solving nonsymmetric linear systems. *SIAM J. Sci. Stat. Comp.* **7,** 856-869.

SAVILL, A. M. 1993 Some recent progress in the turbulence modeling of bypass transition. *Near-Wall Turbulent Flows. R. M. C. So, C. G. Speziale & B. E. Launder (eds.) 829-848, Elsevier Science Publishers.*

STEELANT, J. & DICK, E. 1996 Modeling of bypass transition with conditioned Navier-Stokes equations coupled to an intermittency transport equation. *Int. J. Num. Methods Fluids.* **23,** 193-220.

SPALART, P. R. & ALLMARAS, S. R. 1992 A one-equation turbulence model for aerodynamic flows. *AIAA Paper No. 92-439.*

YANG, Z., VOKE, P. R. & SAVILL, A. M. 1994 Mechanism and models of boundary layer receptivity deduced from large-eddy simulation of bypass transition. *Direction and Large-Eddy Simulation.* **1,** P. R. Voke, L. Kleiser & J. Chollet (eds.) 225-236, Kluwer Academic Publishers.

Modeling of natural convection heat transfer

By S. Tieszen, A. Ooi, P. Durbin AND M. Behnia

Results from two-dimensional calculations using the $v^2 - f$ and a $k - \epsilon$ model are compared with data for two geometries, the vertical flat plate and the 5:1 height:width box with a constant temperature hot and cold side wall. The results show that the $v^2 - f$ model is at least as good as a $k - \epsilon$ model with a two-layer wall treatment. The nature of buoyancy/turbulence coupling is discussed, and three different treatments of it are compared. Preliminary results show that all three treatments have little effect on the heat transfer in fully turbulent conditions but that the generalized gradient diffusion hypothesis can make a large difference in the location of transition with the $v^2 - f$ model.

1. Introduction

The progress reported in this study is part of a continuing effort to explore the predictive capability of the $v^2 - f$ elliptic relaxation approach (c.f. Durbin 1991, Durbin 1993, and Lien & Durbin 1996) as a wall treatment. Of particular interest to the current study is the determination of the usefulness of the $v^2 - f$ approach in predicting heat transfer in flows in which buoyancy plays a large role. The $v^2 - f$ approach has proven useful in predicting heat transfer in forced convective flows (Durbin 1993, Behnia *et al.* 1996, 1997).

The prediction of heat transfer in buoyancy influenced flows is important for a number of engineering applications, including cooling of electronics, heating and cooling of buildings, process heat transfer (e.g., heat exchangers), and safety applications (e.g., heat transfer from fires). In many of these applications, mixed convection exists in which both forced and free convection contribute to the heat transfer. As a precursor to attempting the complexities of mixed convection heat transfer, the current study will focus on heat transfer in purely buoyant flows. However, since our ultimate objective is mixed convection, we will limit our scope of natural convection to those scenarios that are associated with some definable average mean flow. Thus, we will not look at turbulent natural convection in boxes that are uniformly heated from below.

Buoyant flows differ from forced convective flows in some significant aspects. In particular, in subsonic forced convective flows, the coupling between the momentum and energy equations tends to be one-way with momentum affecting the advection term in the energy equation. The energy equation typically does not feed back into the momentum equation directly. In buoyant flows, the coupling is direct and two-way with the density gradient in a gravity field appearing in the momentum equations. There is little disagreement about the effect of buoyancy on the mean flow.

On the other hand, the nature of the coupling between buoyancy and turbulence generation is a matter of considerable speculation (Tieszen *et al.* 1996). Take a vertical plume as an example. Vortex dynamicists tend to view buoyancy in terms of baroclinic vorticity generation (BVG). BVG is proportional to the density gradients that are normal (perpendicular) to the pressure gradients. Hence, in a gravitational field, temperature gradients perpendicular to gravity (i.e., horizontal) tend to result in generation of vorticity. The resulting vorticity field is the gradient of velocity in which the hot fluid rises and is replaced by transverse inflow. The interaction of these vortical structures is chaotic and turbulence results. In the more traditional perspective, density gradients produce vertical momentum. Conservation of mass requires a transverse inflow to replace the vertically accelerating low-density (high temperature) fluid. Large-scale instabilities occur as the flow accelerates and a turbulent cascade results.

In either view, turbulence is not a direct result of buoyancy, but of instabilities (traditional view) or chaotic interactions among vortical structures (vortex dynamics view). The fundamental question underlying the effect of buoyancy on turbulence is at what length scales does buoyancy express itself. If buoyancy expresses itself at the global length scales, then it need only be represented in the mean flow equations. If buoyancy is responsible (in part) for the large-scale instabilities, then perhaps its coupling to the turbulence is present but weak since flow instabilities will result in a cascade independent of buoyancy. On the other hand, if buoyancy produces small-scale instabilities (or vortical structures, depending on your viewpoint) then the buoyancy-produced structures interact directly with the existing turbulence and the coupling may be strong. The length scales over which buoyancy expresses itself are not currently well understood. Hence, the difficulty in modeling their interaction with turbulent momentum.

Turbulence expresses itself in the Reynolds Averaged Navier Stokes (RANS) equations as long time or ensemble averages of unresolved temporal fluctuations. In the mean flow equations, these are the Reynold stresses in the momentum equations, $\rho\langle u_i u_j\rangle$, and turbulent flux in the energy equation, $\rho\langle u_i h\rangle$. In either case, buoyancy does not change this result, i.e., the buoyant term is linear so does not show up as a non-linear cascade requiring an independent closure term. In RANS modeling, buoyant-turbulence interaction expresses itself as a production term in the turbulence equations. In the context of the current study, this is in the k, ϵ, and f equations. Therefore, in the current modeling strategy, the buoyancy/turbulence interaction question becomes one of modeling the production term in these equations.

Hanjalic (1994) gives a good overview of the different levels of buoyancy modeling that have been attempted. He begins with a second order closure and shows successive simplifications that can be made through algebraic stress models to models compatible with $k-\epsilon$ level approaches. To represent flows without a steady mean flow, such as the bottom heated box, it is necessary to include temperature fluctuations as a source term. Hence a transport equation for temperature variance and, in some cases, its dissipation need to be modeled. Since this set of problems is beyond

the current study's interest, simpler closures (simple and generalized gradient) will be adopted as well as leaving the buoyancy only in the mean flow equations. This approach is more recently justified by the DNS study of Boudjemadi *et al.* (1998). For studying heat transfer, the velocity and temperature gradients in the near wall region are important. The velocity profile in a natural convection boundary layer is somewhat similar to a wall jet (Tsuji & Nagano 1988). However, the natural convection boundary layer has an interesting feature in the near wall region not found in momentum driven flows. From the wall to the velocity maximum, buoyant production offsets viscous production of u_1u_2 so that in the near wall region the absolute value of u_1u_2 is lower than would be found in a wall jet – nearly zero. As a result, u_1u_2 is not correlated well with the mean velocity gradient ($\partial U/\partial x_2$). Hence the gradient diffusion approximation for momentum (eddy viscosity) breaks down in this region. The gradient diffusion approximation is still good for the turbulent thermal flux, however, in the same region. In the outer flow, from the velocity peak outward, the turbulence values are similar to those in a wall jet. This near wall feature indicates that buoyancy does have an effect on the turbulence at small length scales, sufficiently strong to cause a qualitative difference in the flow.

Since the near wall region is important to heat transfer, it has been found that the wall treatment is very important to modeling the heat transfer (Ince & Launder 1989, Henkes 1990, Henkes & Hoogendoorn 1989, 1995). For example, Henkes (1990) found that for a hot plate at $Ra = 10^{11}$, standard $k - \epsilon$ without a wall treatment resulted in a prediction 52% over experimental values. With the wall treatments he tried, the discrepancy was about $\pm$ 17%.

Therefore, even though the $v^2 - f$ approach for wall treatments has proven successful, because of the physical differences between buoyant flow and forced convection flows, and the sensitivity of heat transfer to wall treatments, it is necessary to test the $v^2 - f$ model in these flows. Two standard tests cases were chosen and will be discussed in the next section. The models and numerics will be discussed following the description of the test cases, followed by results and conclusions.

2. Benchmark problems

Two benchmark problems, shown schematically in Fig. 1, were chosen: the first is the heated vertical plate; the second is the hot wall - cold wall box. These flows have been studied both experimentally and numerically. As a consequence, comparisons can be made with both the data and other models.

There are two difficulties with buoyant flows that affect to one degree or another all the data. The first difficulty is that purely buoyant flows that have been studied experimentally undergo a laminar to turbulent transition (other than the box heated from below). Transition is not a challenge experimentally, but computationally it is difficult because of the complex physics and small scale structures involved. In the boundary layer problem, numerical transition is usually handled by artificially tripping the boundary layer at the experimentally determined location. However, in the box problem, which is elliptic in nature, it is difficult to artificially trip the solution. Therefore, the comparison is complicated by uncertainties in both the

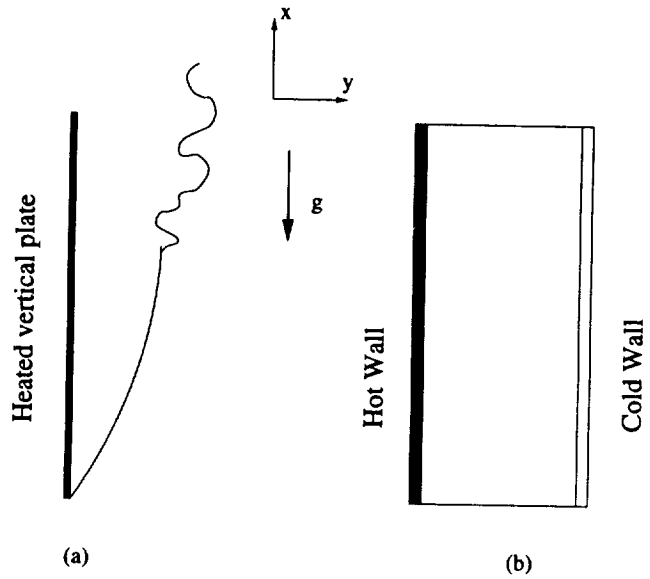

FIGURE 1. Benchmark problems for comparison with $v^2 - f$ results. (a) is a schematic of the vertical flat plate boundary layer problem and (b) is the heated rectangular box.

turbulent heat transfer prediction and the location of transition, which strongly affects the flow pattern.

The second difficulty with natural convection flows is that they are generally low velocity (low momentum) and coupled into the energy equation so they are difficult to stabilize into a prescribed flow pattern. The experimental studies selected for benchmarks all attempted to produce two-dimensional flow patterns so as to facilitate comparison with numerical data. It has proved particularly difficult to produce a truly two-dimensional flow in the box geometry. Numerically, the low momentum and tight coupling with the energy equation expresses itself in long iteration times to reach steady state.

The heated vertical plate is the simplest canonical flow for buoyant heat transfer. As such it has been studied experimentally by a number of investigators including Warner & Arpaci (1968), Cheesewright (1968), Pirovanov *et al.* (1970), Siebers, Schwind & Moffat (1983), and Tsuji & Nagano (1988a, 1988b). Numerical simulations of the heated plate include Lin & Churchill (1978), Henkes & Hoodendoorn (1989), and Peeters & Henkes (1992).

The hot wall - cold wall box is more complex than the boundary layer in that it has a temperature gradient along the vertical centerline and adverse pressure gradients as the flows approach the corners. Data for box geometries include Cheesewright, King & Ziai (1986), Cheesewright & Ziai (1986) and King (1989) for a 5:1 vertical to horizontal aspect ratio and Betts & Bokhari (1995) and Dafa'Alla & Betts (1996) for a 28.6:1 aspect ratio. Numerical simulations of the hot wall - cold wall box include Henkes & Hoogendoorn (1995) for the 5:1 box and Bassina *et al.* (1998),

for the 28.6:1 aspect ratio.

3. Computational models

For the problems studied, variable density was allowed only in the buoyancy term (Boussinesq approximation). With this simplification, the RANS mean-flow equations are:

$$\frac{\partial}{\partial t}(\rho U_i)+\frac{\partial}{\partial x_j}(\rho U_i U_j) = \frac{\partial}{\partial x_j}\left(\mu\left(\frac{\partial U_i}{\partial x_j}+\frac{\partial U_j}{\partial x_i}\right)\right)-\frac{\partial P}{\partial x_i}-g_i\beta(\Theta-\Theta_\infty)+\frac{\partial}{\partial x_j}(-\rho\langle u_i u_j\rangle) \tag{1}$$

$$\frac{\partial}{\partial t}(\rho c_p\Theta)+\frac{\partial}{\partial x_i}(\rho U_i c_p\Theta) = \frac{\partial}{\partial x_i}\left(k\frac{\partial\Theta}{\partial x_i}\right)+\frac{\partial}{\partial x_j}(-\rho c_p\langle u_j\theta\rangle) \tag{2}$$

where $\langle\rangle$ denote ensemble averaging. Θ and θ are the mean temperature and its fluctuating part respectively. All other symbols have their usual meaning. For the vertical flat plate, the standard boundary layer approximations are used and the parabolic equations are solved.

For the momentum equations, the Reynold stress term $\langle u_i u_j\rangle$ is closed with the usual simple gradient assumption.

$$\rho\langle u_i u_j\rangle = \rho\left(\frac{2}{3}\right)k\delta_{ij}-\mu_t\left(\frac{\partial U_i}{\partial x_j}+\frac{\partial U_j}{\partial x_i}\right) \tag{3}$$

This assumption is made for convenience only. The data of Tsuji & Nagano (1988b) show that from y^+ of about 20 to 100 that $\langle u_1 u_2\rangle$ is not correlated with the mean velocity gradient (in this paper 1 & 2 are the streamwise and cross-stream indices respectively). To correctly model this trend in the data, a more general algebraic or second order closure model for momentum would be required (Peeters & Henkes 1992). It may be expected that ignoring this trend will produce a difference in the calculated skin friction. However, for this study, we will assume that the effect of modeling the momentum transfer in the boundary layer with the simple gradient diffusion approximation will have little effect on the heat transfer predicted. To validate this assumption, comparison with experimental data must be made.

The v^2-f model of Durbin (1995) is used to obtain the eddy viscosity and provide a wall treatment. The eddy viscosity is given by:

$$\mu_t = \rho C_\mu v^2 T \tag{4}$$

where k, ϵ, v^2, and f are given by the solutions of

$$\frac{\partial v^2}{\partial t}+U_j\frac{\partial v^2}{\partial x_j} = kf-v^2\frac{\epsilon}{k}+\frac{\partial}{\partial x_j}\left[\left(\nu+\frac{\nu_t}{\sigma_k}\right)\frac{\partial v^2}{\partial x_j}\right] \tag{5}$$

$$L^2\frac{\partial^2 f}{\partial x_j\partial x_j}-f = (1-C_1)\frac{[(2/3)-v^2/k]}{T}-C_2\frac{P}{k} \tag{6}$$

$$\frac{\partial k}{\partial t} + U_j \frac{\partial k}{\partial x_j} = P - \epsilon + \frac{\partial}{\partial x_j}\left[\left(\nu + \frac{\nu_t}{\sigma_k}\right)\frac{\partial k}{\partial x_j}\right] \tag{7}$$

$$\frac{\partial \epsilon}{\partial t} + U_j \frac{\partial \epsilon}{\partial x_j} = \frac{C_{\epsilon_1} P - C_{\epsilon_2}\epsilon}{T} + \frac{\partial}{\partial x_j}\left[\left(\nu + \frac{\nu_t}{\sigma_\epsilon}\right)\frac{\partial \epsilon}{\partial x_j}\right], \tag{8}$$

with time and length scales given by

$$L^2 = C_L \max\left[\frac{k^3}{\epsilon^2}, C_\eta^2\left(\frac{\nu^3}{\epsilon}\right)^{1/2}\right] \tag{9}$$

$$T = \max\left[\frac{k}{\epsilon}, 6\left(\frac{\nu}{\epsilon}\right)^{1/2}\right]. \tag{10}$$

The model constants are

$$C_\mu = 0.22, C_{\epsilon_2} = 1.9, C_1 = 1.4$$

$$C_2 = 0.3, C_L = 0.3, C_\eta = 70 \tag{11}$$

$$\sigma_k = 1.0, \sigma_\epsilon = 1.3$$

In Eqs. (6), (7), and (8) the production term is given by

$$P = \nu_t\left(\frac{\partial U_j}{\partial x_i} + \frac{\partial U_i}{\partial x_j}\right)\frac{\partial U_j}{\partial x_i} + G \tag{12}$$

where G is the buoyant production term and will be subject to several treatments as described below.

The standard $k - \epsilon$ model is given by Eqs. (7) & (8) with time scale $T = k/\epsilon$. The buoyant production term is not included in the ϵ equation (Eq. (8)). The eddy viscosity is given by

$$\mu_t = \rho C_\mu \frac{k^2}{\epsilon} \tag{13}$$

The two-layer wall treatment is the one-equation model of Wolfstein (1969). In the inner layer where

$$Re_y = \frac{k^{1/2} y \rho}{\mu} < 200,$$

the eddy viscosity is given by

$$\mu_t = \rho C_\mu k^{1/2} l_\mu \tag{14}$$

and

$$\epsilon = \frac{k^{3/2}}{l_\epsilon} \tag{15}$$

$$l_\mu = c_l y \left(1 - exp\left(-\frac{Re_y}{A_\mu}\right)\right) \tag{16}$$

$$l_\epsilon = c_l y \left(1 - exp\left(-\frac{Re_y}{A_\epsilon}\right)\right) \tag{17}$$

The constants used to simulate this model can be found in Chen & Patel (1988).

Specification of the turbulent thermal flux is required to close the mean energy equation (Eq. (2)). In the current study, $\langle u_i\theta\rangle$ is closed by the simple mean gradient assumption consistent with the eddy viscosity closure for momentum. The ratio of turbulent to thermal eddy viscosity is the turbulent Prandtl number, Pr_t. Its value is 0.9 for the current study. The closure term is

$$\langle u_i\theta\rangle = -\frac{\nu_t}{Pr_t}\frac{\partial\Theta}{\partial x_i} \tag{18}$$

Tsuji & Nagano (1988b) show that the cross-stream thermal flux is correlated with the mean cross-stream temperature gradient (i.e., it remains positive with a negative temperature gradient) for a large part of the boundary layer. The turbulent Prandtl number ranges from 0.9 to about 1.1 before it becomes ill defined from the velocity peak to the wall, suggesting that this assumption might not be valid in the inner region of the boundary layer.

In keeping with the uncertainty in the physical coupling of buoyancy and turbulence, several treatments are employed to close the buoyant production term in Eqs. (6), (7), and (8). In all cases, the buoyant production term is given by,

$$G = -\beta g \langle u_1\theta\rangle , \tag{19}$$

where β is the thermal expansion coefficient. $\beta = 1/T$ for the cases studied here (air as the fluid).

In the first level of treatment, G is set equal to zero. This level of treatment is consistent with the assumption that buoyancy affects only the global length scales of the problem and expresses itself in turbulence only through velocity gradients that produce the Reynold stresses.

The second level of treatment is to employ the simple gradient diffusion approximation for $\langle u_i\theta\rangle$ consistent with the approximations used in the mean flow equations. This approximation gives

$$G = -\frac{g}{T}\frac{\nu_t}{Pr_t}\frac{\partial\Theta}{\partial x_1} \tag{20}$$

This approximation is the most common, and perhaps its use is more for consistency of approximation in all equations than in its physics representation. In Eq. (20), the production term is proportional to the temperature gradient in the direction

of gravity. Therefore, this mechanism only allows buoyancy to be represented by streamwise temperature gradients. In stratified flows, clearly the vertical temperature gradient will affect the flow (Rodi 1987). However, Eq. (20) suggests that stratification strongly affects the length scale at which buoyancy expresses itself. If the flows are not stratified, then buoyancy expresses itself only in the mean flow equations (global problem length scales). If it is stratified, then buoyancy expresses itself in turbulent production (length scales within the turbulent spectrum). Typically, the vertical stratification in many flow situations is small compared to cross-stream gradients such as in the problems studied here. It is not clear how shallow vertical temperature gradients could reduce the scale of the buoyant instabilities to create turbulent production, yet sharp horizontal gradients express themselves only at global problem length scales (i.e., no production from cross-stream derivatives).

The third level of treatment is to employ the generalized gradient diffusion approximation (Daly & Harlow 1970 and Ince & Launder 1989) for $\langle u_i\theta\rangle$. This is the simplest closure known to the authors for which temperature gradients perpendicular to gravity result in buoyant production. The generalized gradient diffusion hypothesis (GGDH) is

$$G = -g_i\beta c_\theta \frac{k}{\epsilon}\langle u_i u_j\rangle \frac{\partial\Theta}{\partial x_j}, \tag{21}$$

with the Reynold stresses given by Eq. (3). In the boundary layer implementation, the streamwise derivatives are dropped.

For the vertical plate, a parabolic marching solver is used. The first mesh point is located at $y^+ \approx 1$, with 200 mesh points in the cross-stream direction. The mesh is not evenly distributed, but stretched in the cross-stream direction using a hyperbolic tangent function. For selected calculations, the mesh was doubled and no significant changes were found. For the box problem, a commercial code (FLUENT 4.4) is used. The solver employed was uses the SIMPLE algorithm and the QUICK second order interpolation scheme. The first mesh point was located at $y^+ = 5$ with a 150 $\times$ 150 mesh grid. The mesh is not evenly distributed. Fine mesh is used close to the wall and gets coarser towards the center plane of the box. For selected cases, a 75 $\times$ 75 mesh grid was employed and small changes were noted in the solutions, so subsequent runs were all made at 150 $\times$ 150.

4. Results

Solutions using the $v^2 - f$ model are compared with experimental data in Figs. 2-4 for the vertical plate benchmark. Figure 2 shows the $v^2 - f$ model and data sets for local Nusselt number versus Rayleigh number, where

$$Ra_x = \frac{g\beta\Delta\Theta x^3 Pr}{\nu^2} = Gr_x Pr \tag{22}$$

and Gr_x is the Grashof number. The calculation used the level 1 treatment for buoyancy, i.e., it was not included in the production terms. The calculation was started with a laminar profile as the inlet boundary condition and marched up

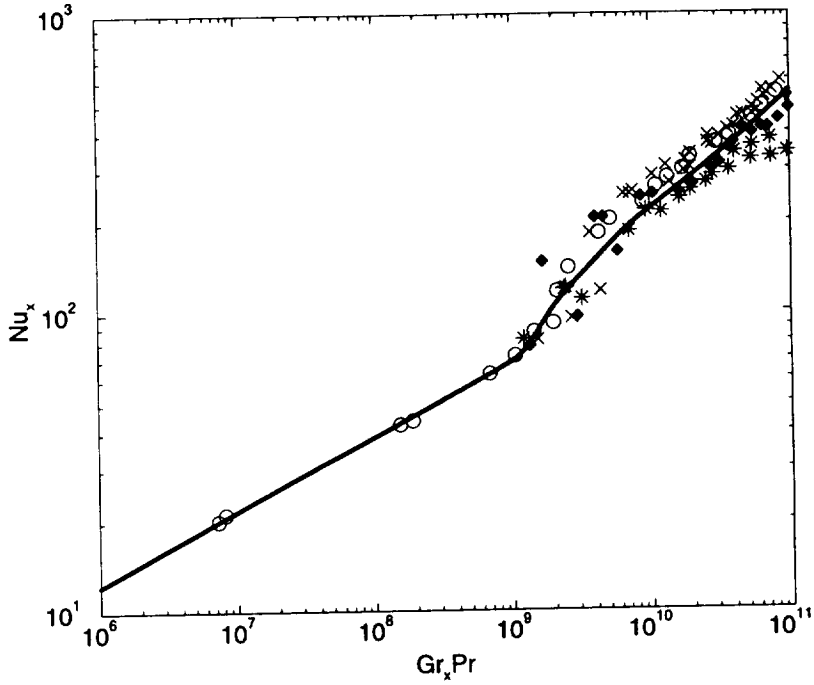

FIGURE 2. Nu_x *vs.* Ra_x for the vertical flat plate boundary layer. —— $v^2 - f$ turbulence model, × Cheesewright (1968), ♦Pirvano *et al.* (1970), ○ Tsuji & Nagano (1988), * Warner & Arpaci (1968).

the plate. At $Gr_x \approx 10^9$ the computation was deliberately tripped to turbulence by initializing k, ϵ, and v^2 to some small values, and Eqs. (5)-(8) were solved to simulate the development of the turbulence quantities in the boundary layer.

As is evident from Fig. 2, the $v^2 - f$ turbulence model agrees very well with experimental data. The predictions are well within the scatter of the data from various experiments. Note that the scatter of the data within each experiment is less than between experiments. This error indicates that apparatus/measurement technique dependency (bias error) dominates the uncertainty. Tsuji and Nagano, (1988a), suspect small gradients in the ambient air temperature.

The mean streamwise velocity profiles at various Gr_x are shown in Fig. 3. The $v^2 - f$ model calculation and the experiments of Tsuji & Nagano (1988) are shown. Data have been non-dimensionalized by standard wall units. The $v^2 - f$ calculation used the level 3 treatment for buoyancy. As will be discussed below, little effect was noted for the vertical plate problem for the different buoyancy treatments. The comparison between the $v^2 - f$ model and the data is again very good with the velocity peak predicted in location and amplitude quite closely.

In general, the effect of the different buoyancy treatments was small. Figure 4 shows the comparison of level 1 and level 3 treatments on the thermal eddy viscosity

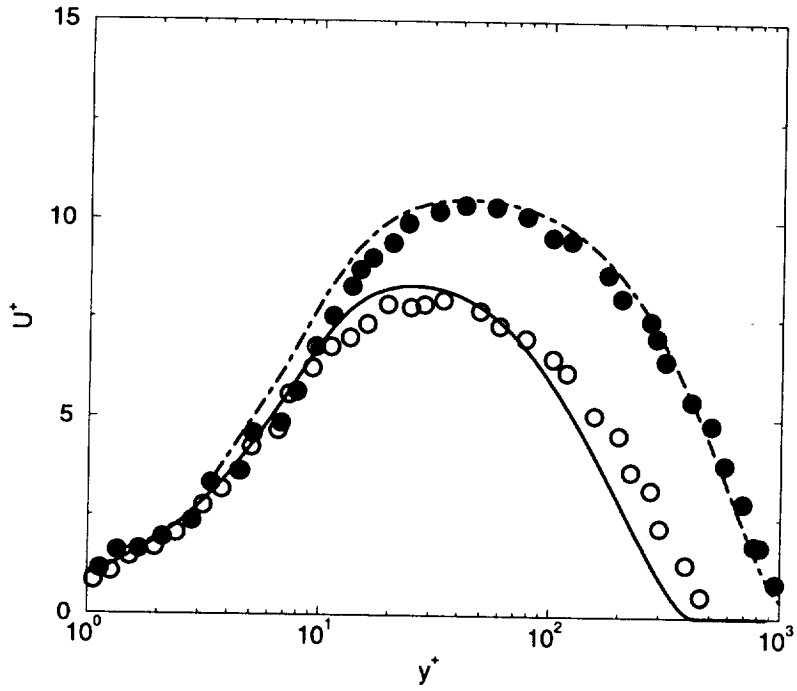

FIGURE 3. U^+ *vs* y^+ for the vertical flat plate boundary layer. Lines are data from the $v^2 - f$ numerical model (—— $Gr_x = 1.56 \times 10^{10}$, — — — $Gr_x = 1.80 \times 10^{11}$) and symbols are from experimental data of Tsuji & Nagano (1988a) (o $Gr_x = 1.56 \times 10^{10}$, • $Gr_x = 1.80 \times 10^{11}$).

as a function of non-dimensional distance from the wall. The GGDH model has an adjustable constant that was set at 0.05 in Fig. 4. This value is about 1/3 that used by Ince & Launder (1989). Further adjustment upward would result in a better fit of the data in the outer part of the boundary layer from y^+ of 100 to 1000 but would degrade the comparison in the inner part of the boundary layer from y^+ of 25 to 100. As will be noted later, the value at 0.05 resulted in a good comparison with the box data. Hence, the constant was left at 0.05.

The small effect of the three treatments on the results that could be interpreted to mean buoyancy is unimportant as a source of turbulence. However, there is still a significant discrepancy in the thermal eddy viscosity between the $v^2 - f$ results and the data. Another interpretation is that the treatments attempted in this study are insufficient to represent the effects of buoyancy, and perhaps a more general treatment such as proposed by Hanjalic (1994), is required. It was reported by Tsuji & Nagano (1988b) that the eddy viscosity, defined by

$$\nu_t = -\langle uv \rangle / \partial_y U, \tag{23}$$

has an unusual form (going to $\pm\infty$) as a function of y_+ for the thermal boundary

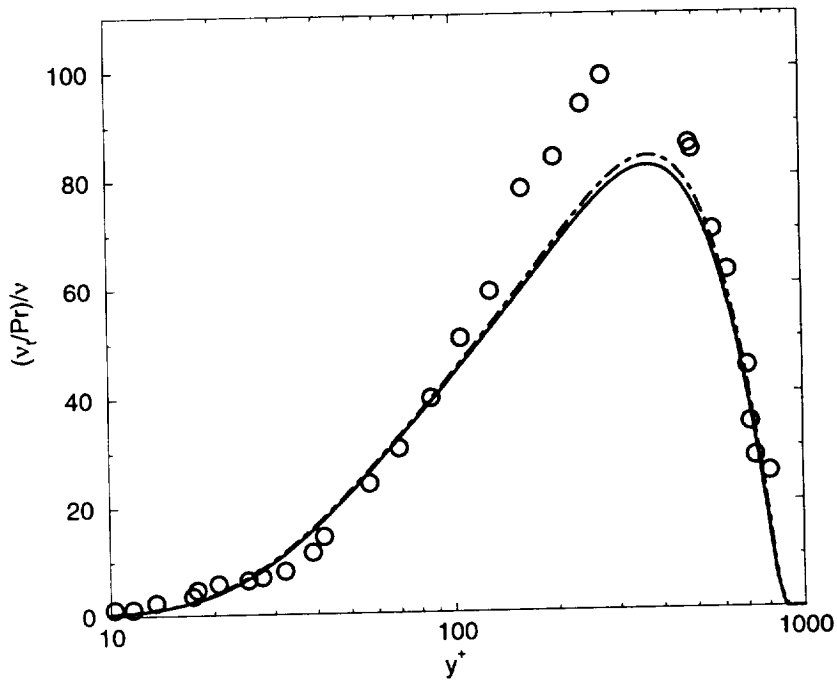

FIGURE 4. Normalized turbulent thermal viscosity vs. y^+. —— standard $v^2 - f$ model, —·— $v^2 - f$ model with GGDH and $C_g = 0.05$, o Tsuji & Nagano (1988). Data compared at $Gr_x = 9 \times 10^{10}$.

layer. This behavior cannot be represented with a simple gradient diffusion model for eddy viscosity that has been used in the current study.

The $v^2 - f$ model results are compared with data in Figs. 5-8 for the 5:1 vertical box. Figure 5 shows streamlines of the flow in the box from the $v^2 - f$ model with level 1 buoyancy treatment. The flow pattern is basically two separate wall boundary layers that are not interacting. In the experiment by Cheesewright, King & Ziai (1986), it was noted that the effects of the hot and cold walls were not symmetric and that there was re-laminarization as the flow passed across the floor of the cavity followed by a new transition approximately 20% of the way up the hot wall. In Fig. 5, the broadening of the boundary layers just past the mid-height of the box indicated for the level 1 buoyancy treatment that the transition was delayed in the calculation relative to the experiments.

Figure 6 shows the $v^2 - f$ model with two levels of buoyancy treatment (1 and 3), the $k - \epsilon$ model (buoyancy treatment 2) with a two layer wall treatment, and data sets for $Nu_x/Ra_x{}^{1/3}$ vs. x/H. Comparing the $v^2 - f$ model with level 1 buoyancy and the $k - \epsilon$ model against the hot wall data (King 1989) shows that the heat transfer is slightly underpredicted by the $k - \epsilon$ model and significantly underpredicted by the $v^2 - f$ model. However, the $v^2 - f$ results with GGDH

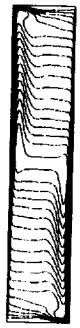

FIGURE 5. Contours of the stream function.

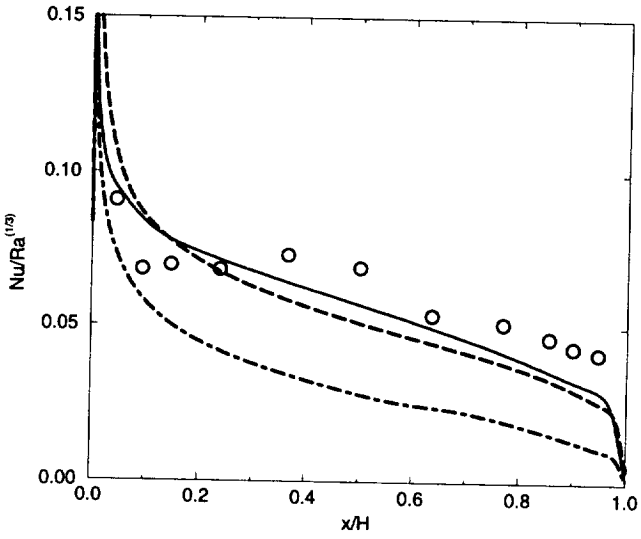

FIGURE 6. This figure shows the local Nusselt number divided by the cube root of the local Rayleigh number vs. non-dimensional height up the wall. o Experimental data (King 1989), ---- KEPS (level 2), —·— $v^2 - f$ (level 1), —— $v^2 - f$ (level 3).

buoyancy treatment provides the best comparison.

The underprediction by the $v^2 - f$ model without the GGDH buoyancy treatment is a result of a late transition to turbulence by the model. This can be seen by the change in slope of the curve around a y/H = 0.6. It is seen more clearly in Fig. 7, which shows the vertical velocity distribution in the horizontal (cross-stream) direction. The $v^2 - f$ model with the level 1 treatment has a very narrow distribution, which is characteristic of a laminar boundary layer. With the introduction of the generalized gradient diffusion term (level 3 buoyancy) into the $v^2 - f$ model, the boundary layer transitions much earlier, thus broadening the profile as seen in Fig. 7

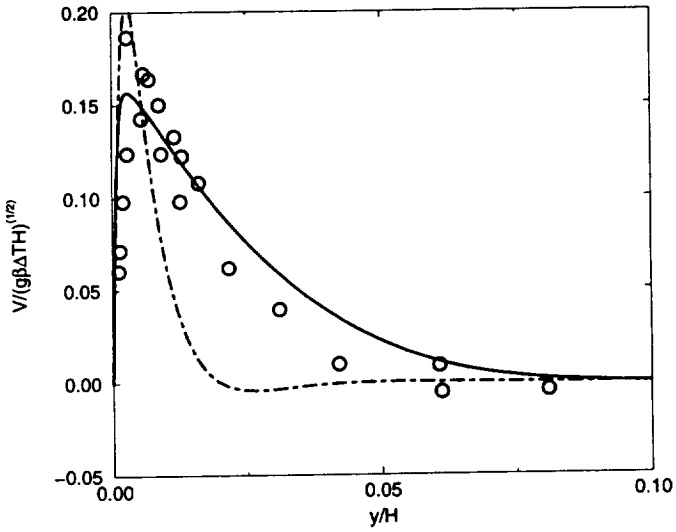

FIGURE 7. Mean vertical velocity profiles at $x = H/2$. o Experimental data of Cheesewright (1986), —·— level 1 treatment of the $v^2 - f$ model, ——— $v^2 - f$ model with GGDH.

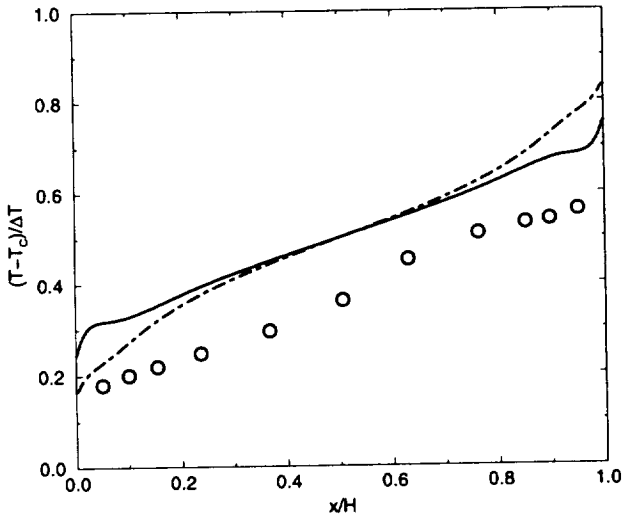

FIGURE 8. This figure shows the $(\Theta - \Theta_c)/\Delta\Theta$ vs. non-dimensional height up the wall. o Experimental data (Cheesewright & Ziai, 1986), ——— $v^2 - f$ model with GGDH, —·— level 1 treatment of the $v^2 - f$ model.

and matching the vertical heat transfer profile much better as seen in Fig. 6.

Experimental data for natural convection in a box is hard to obtain because small amounts of heat loss have a large effect on the outcome. Figure 8 shows the center-plane temperature profile versus elevation. The variables are non-dimensionalized such that at mid-height the temperature should be 0.5. In both calculations it is, but in the data it is lower. This is due to heat loss from the box. In general, the slope of the curve with elevation is better predicted with the $v^2 - f$ model with the level 3 buoyancy treatment than the $v^2 - f$ with level 1 buoyancy treatment.

5. Conclusions

The $v^2 - f$ model compared well with the vertical flat plate data without changes. However, in the hot-wall, cold-wall box, it had a delayed transition with respect to the data and significantly underpredicted the heat transfer. With the addition of the generalized gradient diffusion term to the model, the transition occurred near that in the data and the overall heat transfer comparisons were excellent. Since a coefficient was set in the generalized gradient diffusion term, substantially more comparisons are needed to establish whether or not it is generally useful in transitionally buoyant flows. From the vertical plate data, it seems to have little effect on the heat transfer in fully developed turbulent flows.

The nature of buoyancy/turbulence interactions is not well known. Hence, the ability to model it is not universally agreed upon. Of the three levels of treatment of the buoyant production term tested, none produced any large effect (outside of the location of transition) on the heat transfer. It is not clear whether this outcome means that buoyancy has little effect, or a more sophisticated model is required to delineate the effects. Certainly the good agreement between the models and the test results indicate that if the effect is large, it is being masked by other modeled terms.

REFERENCES

BASSINA, I. A., LOMAKIN, S. A., NIKULIN, D. A., STRELETS, M. KH. & SHUR, M. L. 1998 Assessment of Applicability of Modern Models of Turbulence for Calculation of Natural-Convection Flows and Heat Transfer. *High Temperature.* **36**(2), 230-238.

BEHNIA, M., PARNEIX, S. & DURBIN, P. 1996 Simulation of jet impingement heat transfer with the $k - \epsilon - v2$ model. *Annual Research Briefs.* Center for Turbulence Research, NASA Ames/Stanford University. 3-16.

BEHNIA, M., PARNEIX, S., & DURBIN, P. 1997 Accurate modeling of imping-ing jet heat transfer. *Annual Research Briefs.* Center for Turbulence Research, NASA Ames/Stanford University. 149-163.

BETTS, P. L. & BOKHARI, H. 1995 New experiments on turbulent natural convec-tion of air in a tall cavity. *IMechE Conference Transactions.* 4th UK National Conference on Heat Transfer. Paper C510/091 213-217.

BOUDJEMADI, R., MAUPU, V., LAURENCE D., LE. QUERE P. 1998 Budgets of turbulent stresses and fluxes in a vertical slot natural convection flow at Rayleigh $Ra = 10^5$ and 5.410^5. *Intl. J. of Heat & Fluid Flow.* **18**(1), 70-79.

CHEESEWRIGHT, R. 1968 Turbulent Natural Convection From a Vertical Plane Surface. *ASME J. Heat Transfer.* **90,** 1-8.

CHEESEWRIGHT, R., KING, K. J. & ZIAI, S. 1986 Experimental Data for the Validation of Computer Codes for the Prediction of Two-Dimensional Buoyant Cavity Flows. *Proceedings of the ASME Meeting, HTD.* **60,** 75-81.

CHEESEWRIGHT, R., & ZIAI, S. 1986 Distributions of Temperature and Local Heat-Transfer Rate In Turbulent Natural Convection in a Large Rectangular Cavity. *Proceedings of the 8th International Heat Transfer Conference, San Fransisco.* 1465-1470.

CHEN, H. C. & PATEL, V. C. 1988 Near-Wall Turbulence Models for Complex Flows Including Separation. *AIAA J.* **26(6),** 641-648.

DAFA'ALLA, A. & BETTS, P. L. 1996 Experimental Study of Turbulent Natural Convection in a Tall Air Cavity. *Exp. Heat Transfer.* **9,** 15-194.

DALY, B. J. & HARLOW, F. H. 1970 Transport Equations in Turbulence. *Phys. Fluids.* **13**(11), 2634-2649.

DURBIN, P. A. 1991 Near-wall turbulence closure modeling without "damping functions". *Theor. & Comp. Fluid Dynamics.* **3,** 1-13.

DURBIN, P. A. 1993 Application of a near-wall turbulence model to boundary layers and heat transfer. *International J. Heat & Fluid Flow.* **14,** 316-323.

DURBIN, P. A. 1995 Separated Flow Computations with the $k - \epsilon - v^2$ model. *AIAA J.* **33**(2), 659-664.

HANJALIC, K. 1994 Achievements and Limitations in Modeling and Computation of Buoyant Turbulent Flows and Heat Transfer. *10th International Heat Transfer Conference,* Brighton, UK.

HENKES, R. A. W. M. 1990 Natural-Convection Boundary Layers. *Ph. D. Thesis,* Delft University of Technology, Delft, The Netherlands.

HENKES, R. A. W. M. & HOOGENDOORN, C. J. 1989 Comparison of turbulence models for the natural convection boundary layer along a heated vertical plate. *International J. Heat & Mass Transfer.* **32**(1), 157-169.

HENKES, R. A. W. M. & HOODENDOORN, C. J. 1995 Comparison Exercise for Computations of Turbulent Natural Convection in Enclosures. *Numerical Heat Transfer, Part B.* **28,** 59-78.

INCE, N. Z. & LAUNDER, B. E. 1989 On the computation of buoyancy-driven turbulent flows in rectangular enclosures. *Intl. J. Heat & Fluid Flow.* **10**(2), 110-117.

KING, K. J. 1989 *Turbulent Natural Convection In Rectangular Air Cavities.* Ph.D. thesis, Queen Mary College, London, UK.

LIEN, F. S.& DURBIN, P. A. 1996 Non-linear $k-\epsilon-v^2$ modeling with application to high-lift. *Proceedings of the 1996 Summer Program.* Center for Turbulence Research NASA Ames/Stanford University, 5-22.

LIN, S. J. & CHURCHILL, S. W. 1978 Turbulent Free Convection From A Vertical, Isothermal Plate. *Numerical Heat Transfer.* **1,** 129-145.

OSTRACH, S. 1953 An Analysis of Laminar Free Convection Flow and Heat Transfer about a Flat Plate Parallel to the Direction of the Generating Body Force. *NACA Report 1111.*

PEETERS, T. W. J. & HENKES, R. A. W. M. 1992 The Reynolds-stress model of turbulence applied to the natural-convection boundary layer along a heated vertical plate. *Intl. J. Heat & Mass Transfer.* **35**(2), 403-420.

PIROVANO, A., VIANNAY, S. & JANNOT, M. 1970 Convection Naturelle En Regime Turbulent Le Long D'Une Plaque Plane Vertical. *Proceedings of the 4th International Heat Transfer Conference,* Paris-Versailles, France, 1-12.

RODI, W. 1987 Examples of Calculation Methods for Flow and Mixing in Stratified Fluids. *J. Geophysical Res.* **92**(C5), 5305-5328.

SIEBERS, D. L., MOFFAT, R. F. & SCHWIND, R. G. 1985 Experimental, Variable Properties Natural Convection From a Large, Vertical, Flat Surface. *ASME J. Heat Transfer.* **107,** 124-132.

TIESZEN, S. R., NICOLETTE, V. F., GRITZO, L. A., HOLEN, J. K., MURRAY, D. & MOYA, J. L. 1996 Vortical Structures in Pool Fires: Observation, Speculation, and Simulation, Sandia National Laboratories, Albuquerque, NM. *SAND96-2607, November.*

TSUJI, T. & NAGANO, Y. 1988a Characteristics of a turbulent natural convection boundary layer along a vertical flat plate. *Intl. J. Heat & Mass Transfer.* **31**(8), 1723-1734.

TSUJI, T. & NAGANO, Y. 1988b Turbulence measurements in a natural convection boundary layer along a vertical flat plate. *Intl. J. Heat & Mass Transfer.* **31**(10), 2101-2111.

WARNER, C. Y. & ARPACI, V. S. 1968 An Experimental Investigation of Turbulent Natural Convection in Air along a Vertical Heated Flat Plate. *Intl. J. Heat & Mass Transfer.* **11,** 397-406.

WOLFSTEIN, M. 1969 The Velocity and Temperature Distribution of One-Dimensional Flow with Turbulence Augmentation and Pressure Gradient. *Intl. J. Heat & Mass Transfer.* **12,** 301-318.

Assessment of non-local effect on pressure term in RANS modeling using a DNS database

By R. Manceau[1], M. Wang AND P. Durbin

A DNS database for the channel flow at $Re_\tau = 590$ is used to investigate the validity of the hypotheses used to model the pressure term in the Reynolds stress transport equations by elliptic relaxation. It is shown that the correlation function involving the fluctuating velocity and the Laplacian of the pressure gradient, which is modeled by an exponential function, is actually not isotropic. It is not only elongated in the streamwise direction but also asymmetric in the direction normal to the wall. This feature is the main cause for the slight amplification of the redistribution between the Reynolds stress components in the log layer as predicted by the elliptic relaxation operator. The expected reduction in redistribution is predicted by a new formulation of the model, which can be derived by accounting for the asymmetry in the correlation function, without using any wall echo correction terms. The belief that this reduction is due to the wall echo effect is called into question through the present DNS analysis.

1. Introduction

During the past few decades, turbulence modelers mainly focussed on the pressure term in the Reynolds stress transport equations. In second moment closures, the production is exact and, accordingly, the pressure term is one of the most important terms to be modeled. Indeed, in a channel flow, this term is the main productive term in the equations for the diagonal Reynolds stresses except for the component in the streamwise direction, and balances the production term in the Reynolds shear stress equation (Mansour, Kim & Moin 1988).

Chou (1945) was the first to derive the integral equation of the pressure term from the Poisson equation for the pressure fluctuations and to distinguish between the slow part, rapid part and surface term (even though he did not use this terminology). For the rapid part, which involves the mean velocity gradient, he proposed to consider that the latter is locally a constant in order to be taken outside the integral. Since Chou's pioneering work, this approach has become very popular in the turbulence modeling community and the starting-point of all second moment closure models (e.g. Launder, Reece & Rodi 1975).

Bradshaw, Mansour & Piomelli (1987) assessed the validity of this local approximation for the rapid pressure using a DNS database. They showed that in the channel flow at $Re_\tau = 180$ (Kim, Moin & Moser 1987), this hypothesis is valid only

1 Laboratoire National d'Hydraulique, Electricité de France, 6 quai Watier 78 401 Chatou, France

for $y^+ \geq 40$. As a result, models based on it cannot be integrated down to the wall without modifications such as the introduction of damping functions.

In order to avoid the *ad hoc* damping functions, which are usually calibrated on experimental or DNS data with little theoretical basis, Durbin (1991) introduced a novel method. He proposed to model directly the two-point correlation in the integral equation of the pressure term, which preserves the non-local effect in the Reynolds stress transport equations. Then, he introduced the so-called elliptic relaxation approach, allowing the derivation of second moment closure models which can be integrated down to the wall without any damping functions.

While this method has led to very encouraging results, some room for improvement remains. One purpose of the present work is to assess the validity of the two-point correlation approximation, which was originally derived on an intuitive basis. Secondly, this work aims to assess the influence of the anisotropy of the two-point correlation on the pressure term in order to support future modifications of the model. Durbin's model assumes an isotropic shape for the correlation function, which may be the main improvable point of the method. These modeling issues will be examined using a channel flow DNS database at $Re_\tau = 590$ (Moser, Kim & Mansour 1998). In particular, the anisotropy of the correlation function will be explored, and the evolution of the length scale across the channel evaluated.

2. The pressure term in a channel

2.1. Integral equation of the pressure term

The pressure term which appears in the Reynolds stress equations is

$$\phi_{ij} = -\frac{1}{\rho}\left(\overline{u_j p_{,i}} + \overline{u_i p_{,j}}\right) \ , \tag{1}$$

where ρ is the density, p is the fluctuating pressure, u_i are the fluctuating velocity components and $.,_i$ denotes derivative with respect to the x_i coordinate. The overline indicates ensemble average. Usually, ϕ_{ij} is split into two terms: the pressure-strain correlation and the pressure diffusion (Launder, Reece & Rodi 1975). However, the original form (1) of ϕ_{ij} will be used for the following reasons: first, Lumley (1975) showed that the decomposition is not unique and that this particular one is not the best one ; secondly, in the vicinity of a wall, the asymptotic behavior is not preserved for certain components. For instance, if $i = 1$ and 2 correspond respectively to the streamwise direction and the direction normal to the wall, the component ϕ_{12} behaves as y, whereas the pressure-strain and the pressure diffusion take a non-zero value at the wall. Therefore, in order to model correctly the total pressure term, it is necessary to model both terms of the decomposition such that their sum decreases as y in the vicinity of the wall.

The pressure fluctuation is the solution of the Poisson equation obtained by taking the divergence of the fluctuating part of the Navier-Stokes equations:

$$\nabla^2 p = -2\rho U_{i,j}\, u_{j,i} + \rho\left(\overline{u_i u_j} - u_i u_j\right)_{,ij} \ , \tag{2}$$

where ∇^2 denotes the Laplacian operator and U_i the i^{th} component of the mean velocity. Since the differentiations are commutative, the gradient of the pressure fluctuation is also the solution of a Poisson equation:

$$\nabla^2 p_{,k} = -2\rho \left(U_{i,j}\, u_{j,i}\right)_{,k} + \rho \left(\overline{u_i u_j} - u_i u_j\right)_{,ijk} \ . \tag{3}$$

In the following, the gradient of the pressure fluctuation will be assumed to satisfy the boundary condition $\partial p_{,k}/\partial \mathbf{n} = 0$, where $\mathbf{n}$ is the outgoing unit vector normal to the wall. This condition is not exact, but Kim (1989) uses this type of hypothesis for the pressure itself and showed that this is valid in the channel flow at $Re_\tau = 180$. In the present case, the same hypothesis can be applied to the pressure gradient, considering that its "Stokes part", i.e. the part produced by the inhomogeneous boundary condition, can be neglected.

The general solution of Eqs. (3) is

$$p_{,k}(\mathbf{x}) = -\int_\Omega \frac{\nabla^2 p_{,k}(\mathbf{x}')}{4\pi\|\mathbf{x}'-\mathbf{x}\|}\, dV(\mathbf{x}') - \int_{\partial\Omega} p_{,k}(\mathbf{x}') \frac{\partial}{\partial \mathbf{n}'}\left(\frac{1}{4\pi\|\mathbf{x}'-\mathbf{x}\|}\right) dS(\mathbf{x}') \ , \tag{4}$$

where bold letters $\mathbf{x}$ and $\mathbf{x}'$ denote position vectors, dV and dS the elementary volume and surface and $\partial\Omega$ the domain boundary.

Multiplying (4) by the fluctuating velocity and taking ensemble averaging, one can derive an integral equation for $\overline{u_j p_{,i}}$ and hence ϕ_{ij},

$$\rho\phi_{ij}(\mathbf{x}) = -\int_\Omega \left(\overline{u_j(\mathbf{x})\nabla^2 p_{,i}(\mathbf{x}')} + \overline{u_i(\mathbf{x})\nabla^2 p_{,j}(\mathbf{x}')}\right) \frac{dV(\mathbf{x}')}{4\pi\|\mathbf{x}'-\mathbf{x}\|} -$$
$$\int_{\partial\Omega} \left(\overline{u_j(\mathbf{x})p_{,i}(\mathbf{x}')} + \overline{u_i(\mathbf{x})p_{,j}(\mathbf{x}')}\right) \frac{\partial}{\partial \mathbf{n}'}\left(\frac{1}{4\pi\|\mathbf{x}'-\mathbf{x}\|}\right) dS(\mathbf{x}') \ . \tag{5}$$

This equation will henceforth be referred to as the integral equation of the pressure term. It involves two-point correlations such as $\overline{u_j(\mathbf{x})\nabla^2 p_{,i}(\mathbf{x}')}$, which need to be modeled and are the main concern of this work.

In some situations, the surface integral in (4) can be transformed into a volume integral. For instance, in a semi-infinite space, bounded by an infinite plane, as considered by Launder, Reece & Rodi (1975), Eq. (4) can be written as

$$p_{,k}(\mathbf{x}) = -\int_\Omega \nabla^2 p_{,k}(\mathbf{x}') \left(\frac{1}{4\pi\|\mathbf{x}'-\mathbf{x}\|} + \frac{1}{4\pi\|\mathbf{x}'^*-\mathbf{x}\|}\right) dV(\mathbf{x}') \ , \tag{6}$$

where $\mathbf{x}'^*$ is the image term of $\mathbf{x}'$ by symmetry with respect to the plane. The function

$$G_\Omega(\mathbf{x},\mathbf{x}') = -\frac{1}{4\pi\|\mathbf{x}'-\mathbf{x}\|} - \frac{1}{4\pi\|\mathbf{x}'^*-\mathbf{x}\|} \tag{7}$$

is then called the Green function of the domain Ω.

In more general geometries, the Green function is unknown. In the particular case of a channel, the Green function is easy to derive only after taking Fourier transforms in x- and z-directions (Kim 1989). This spectral Green function is not useful for the present purpose: however, a form of (4) without surface integral will be needed in the following analysis, especially in §5.1, where the question of the wall echo effect will be investigated. The purpose of the next section is to derive a sufficiently good approximation of (4) which does not involve any surface integral.

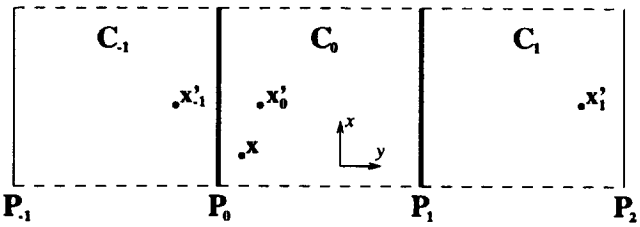

FIGURE 1. Sketch of a channel (C_0) and its images.

2.2. Approximation of the Green function in a channel

The simplest solution to eliminate the surface integral in (4) is to neglect it. Chou (1945) used this approximation but emphasized that all the conclusions which can be drawn are thus valid only at locations "not too close to the boundary of the moving fluid" because, in the vicinity of the wall, the weight of the surface integral has the same order of magnitude as the volume integral. This can be easily seen in the case of a semi-infinite domain bounded by a plane. In this case, Eq. (4) can be written as (6), which shows that if the fixed point $\mathbf{x}$ is sufficiently close to the wall, the principal term and the image term are almost equal. If $\mathbf{x}$ is exactly on the wall, the two terms are identical. Furthermore, Bradshaw (1973) noted that the order of magnitude of the image term is still 15% of the total when the correlation length scale is $L = \kappa y$, where κ is the Karman constant. The influence of this term will be assessed in §5.1. At this point, the surface integral cannot be neglected and therefore, in order to allow the following DNS analysis to be valid down to the wall, a less crude approximation than that used by Chou is needed.

Let us consider a channel C_0 bounded by two infinite planes P_0 and P_1 (Fig. 1). In this domain, the problem to solve is

$$\nabla^2 f = g \ , \tag{8}$$

with $f_{,\mathbf{n}} = 0$ on ∂C_0. Let us now consider the image channels C_{-1} and C_1 shown in Fig. 1, which are symmetrical to C_0 with respect to P_0 and P_1, respectively. Extending g by symmetry in C_{-1} and C_1, solving Eq. (8) in the domain $C_{-1} \cup C_0 \cup C_1$ and using all the symmetries, the solution can be shown to take the form

$$f(\mathbf{x}) = -\int_{C_0} H(\mathbf{x},\mathbf{x'}_0)\ g(\mathbf{x'}_0)\ dV(\mathbf{x'}_0) \ - \int_{\partial C_0} \frac{\partial H(\mathbf{x},\mathbf{x'}_0)}{\partial \mathbf{n'}}\ f(\mathbf{x'}_0)\ dS(\mathbf{x'}_0) \ , \tag{9}$$

with

$$H(\mathbf{x},\mathbf{x'}_0) = \frac{1}{4\pi\|\mathbf{x'}_{-1} - \mathbf{x}\|} + \frac{1}{4\pi\|\mathbf{x'}_0 - \mathbf{x}\|} + \frac{1}{4\pi\|\mathbf{x'}_1 - \mathbf{x}\|} \ , \tag{10}$$

where $\mathbf{x'}_{-1}$ and $\mathbf{x}_1$ are the specular images of $\mathbf{x'}_0$ in P_0 and P_1 (Fig. 1), respectively. The surface integral in this expression can now be neglected. Indeed, on P_0, the derivative of $H(\mathbf{x},\mathbf{x'}_0)$ can be evaluated:

$$\frac{\partial}{\partial \mathbf{n'}} H(\mathbf{x},\mathbf{x'}_0) = \frac{\|\mathbf{x'}_{-1} - \mathbf{x}\| \cdot \mathbf{n'}}{4\pi\|\mathbf{x'}_{-1} - \mathbf{x}\|^3} - \frac{\|\mathbf{x'}_0 - \mathbf{x}\| \cdot \mathbf{n'}}{4\pi\|\mathbf{x'}_0 - \mathbf{x}\|^3} + \frac{\|\mathbf{x'}_1 - \mathbf{x}\| \cdot \mathbf{n'}}{4\pi\|\mathbf{x'}_1 - \mathbf{x}\|^3} \ . \tag{11}$$

Since $\mathbf{x'}_{-1} = \mathbf{x'}_0$, the sum of the two first terms is zero and hence the surface integral only involves the contribution of the image $\mathbf{x'}_1$, which is far from the point $\mathbf{x}$. Likewise, on the other wall P_1, the surface integral only contains the contribution of the image point on P_{-1}. This is in contrast to Chou's approximation, where the derivative in the neglected surface integral is equal to the second term of (11). It goes to infinity when $\mathbf{x'}_0 = \mathbf{x}$, giving to the surface integral the same weight as the volume integral. In the following analysis, the function $H(\mathbf{x}, \mathbf{x'}_0)$ will be used, considering it as a sufficiently good approximation of the Green function, even in the vicinity of the walls.

3. The elliptic relaxation method

By using the approximate Green function, the integral equation of the pressure term (5) can be written as

$$\rho\phi_{ij}(\mathbf{x}) = -\int_\Omega \left(\overline{u_j(\mathbf{x})\nabla^2 p_{,i}(\mathbf{x'})} + \overline{u_i(\mathbf{x})\nabla^2 p_{,j}(\mathbf{x'})}\right) H(\mathbf{x},\mathbf{x'})\, dV(\mathbf{x'}) \ . \tag{12}$$

In this equation, two-point correlations between the fluctuating velocity and the Laplacian of the pressure gradient appear. Following Durbin (1991), in order to preserve the non-local effect, they can be modeled as

$$\overline{u_n(\mathbf{x})\nabla^2 p_{,m}(\mathbf{x'})} = \overline{u_n(\mathbf{x'})\nabla^2 p_{,m}(\mathbf{x'})} \exp\left(-\frac{\|\mathbf{x'}-\mathbf{x}\|}{L}\right) \ , \tag{13}$$

where L is the correlation length scale. The validity of this hypothesis will be scrutinized in §5.2 using a DNS database. Here, the rationalization of the elliptic relaxation equation is analyzed in the context of channel flow.

Durbin (1991) used Chou's approximation, which excludes the image terms in $H(\mathbf{x},\mathbf{x'})$. The integral equation of the pressure term, combined with the model (13), becomes

$$\rho\phi_{ij}(\mathbf{x}) = -\int_\Omega (\overline{u_j(\mathbf{x'})\nabla^2 p_{,i}(\mathbf{x'})} + \overline{u_i(\mathbf{x'})\nabla^2 p_{,j}(\mathbf{x'})}) \underbrace{\frac{\exp\left[-\dfrac{\|\mathbf{x'}-\mathbf{x}\|}{L}\right]}{4\pi\|\mathbf{x'}-\mathbf{x}\|}}_{E(\mathbf{x},\mathbf{x'})} dV(\mathbf{x'}) \ . \tag{14}$$

The function $E(\mathbf{x},\mathbf{x'})$ is the free-space Green function associated with the operator $-\nabla^2 + 1/L^2$. Hence, (14) is the solution of the following Yukawa equation*:

$$\phi_{ij} - L^2\nabla^2\phi_{ij} = -\frac{L^2}{\rho}(\overline{u_j\nabla^2 p_{,i}} + \overline{u_i\nabla^2 p_{,j}}) \ . \tag{15}$$

* In 1935, Yukawa was the first to apply this inversion in physics to solve the equation of interaction potential between particles.

Noting that in quasi-homogeneous situations, the second term on the LHS of this equation vanishes, Durbin proposed to use a quasi-homogeneous model ϕ_{ij}^h instead of the RHS. This leads to the following elliptic relaxation model for ϕ_{ij}:

$$\phi_{ij} - L^2\nabla^2\phi_{ij} = \phi_{ij}^h \ . \tag{16}$$

Any quasi-homogeneous model, such as LRR model or SSG model, can be used for ϕ_{ij}^h, thus allowing the extension of these models down to solid boundaries. Indeed, (16) is valid down to the wall, when appropriate boundary conditions for ϕ_{ij} are provided (Durbin 1993).

However, Eq. (14) does not give rigorously the solution of (15) in a plane channel. Analogous to the Green function for the Laplacian operator, the Green function associated with the Yukawa operator must at least be approximated using the image points with respect to the walls. Thus, a better approximation to the solution of (15) is

$$\rho\phi_{ij}(\mathbf{x}) = -\int_\Omega (\overline{u_j(\mathbf{x'}_0)\nabla^2 p_{,i}(\mathbf{x'}_0)} + \overline{u_i(\mathbf{x'}_0)\nabla^2 p_{,j}(\mathbf{x'}_0)})$$

$$\left(\frac{\exp\left[-\dfrac{\|\mathbf{x'}_{-1}-\mathbf{x}\|}{L}\right]}{4\pi\|\mathbf{x'}_{-1}-\mathbf{x}\|} + \frac{\exp\left[-\dfrac{\|\mathbf{x'}_0-\mathbf{x}\|}{L}\right]}{4\pi\|\mathbf{x'}_0-\mathbf{x}\|} + \frac{\exp\left[-\dfrac{\|\mathbf{x'}_1-\mathbf{x}\|}{L}\right]}{4\pi\|\mathbf{x'}_1-\mathbf{x}\|} \right) dV(\mathbf{x'}_0) \ . \tag{17}$$

Now, using the approximation (13) for the two-point correlations, the integral equation of the pressure term (12) does not lead to (17) but to the following equation:

$$\rho\phi_{ij}(\mathbf{x}) = -\int_\Omega (\overline{u_j(\mathbf{x'}_0)\nabla^2 p_{,i}(\mathbf{x'}_0)} + \overline{u_i(\mathbf{x'}_0)\nabla^2 p_{,j}(\mathbf{x'}_0)})$$

$$\left(\frac{\exp\left[-\dfrac{\|\mathbf{x'}_0-\mathbf{x}\|}{L}\right]}{4\pi\|\mathbf{x'}_{-1}-\mathbf{x}\|} + \frac{\exp\left[-\dfrac{\|\mathbf{x'}_0-\mathbf{x}\|}{L}\right]}{4\pi\|\mathbf{x'}_0-\mathbf{x}\|} + \frac{\exp\left[-\dfrac{\|\mathbf{x'}_0-\mathbf{x}\|}{L}\right]}{4\pi\|\mathbf{x'}_1-\mathbf{x}\|} \right) dV(\mathbf{x'}_0) \ . \tag{18}$$

Hence, the modeled pressure term (18) does not rigorously satisfy the Yukawa Eq. (15). However, the main contribution of the image terms to the integral corresponds to point $\mathbf{x'}_0$ near the walls. For instance, the weight of the first image term is important when $1/4\pi\|\mathbf{x'}_{-1}-\mathbf{x}\|$ has the same order of magnitude as $1/4\pi\|\mathbf{x'}_0-\mathbf{x}\|$, i.e., very close to the wall, where $\mathbf{x'}_{-1} \simeq \mathbf{x'}_0$. Then, the exponential factors $\exp(-\|\mathbf{x'}_{-1}-\mathbf{x}\|/L)$ and $\exp(-\|\mathbf{x'}_0-\mathbf{x}\|/L)$ are almost equal as well. Therefore, even considering that the Green function in a channel must be at least approximated by $H(\mathbf{x},\mathbf{x'})$, rather than using Chou's approximation, the elliptic relaxation model for the pressure term (16) can be considered as valid, as long as the model for the two-point correlations (13) is valid itself.

4. Focus and description of the DNS assessment

4.1 Issues to examine in the elliptic relaxation method

The elliptic relaxation approach is based on a unique hypothesis, namely the approximation (13) of the two-point correlations. This approximation was originally introduced intuitively by Durbin (1991) in order to preserve the dependence of the pressure term on all the points of the domain, leading to the well known non-local effect in the Reynolds stress equations.

The standard way (Monin & Yaglom 1975) of defining a correlation function f to be used in (12) is by writing the two-point correlations as

$$\overline{u_j(\mathbf{x})\nabla^2 p_{,i}(\mathbf{x}')} + \overline{u_i(\mathbf{x})\nabla^2 p_{,j}(\mathbf{x}')} = \left(\overline{u_j(\mathbf{x})\nabla^2 p_{,i}(\mathbf{x})} + \overline{u_i(\mathbf{x})\nabla^2 p_{,j}(\mathbf{x})}\right) f(\mathbf{x},\mathbf{x}') \ . \tag{19}$$

In this expression, the one-point correlation is expressed in $\mathbf{x}$, i.e., the point where the velocities are evaluated in the two-point correlation. Then, it can be moved outside the integral in (12), which leads to the loss of the non-locality of the pressure term. However, this formulation allows the definition of the following length scale:

$$L(\mathbf{x})^2 = \int_\Omega f(\mathbf{x},\mathbf{x}')H(\mathbf{x},\mathbf{x}')dV(\mathbf{x}') \ , \tag{20}$$

which is an integral scale, since it provides the ratio between the integral and the correlation at zero separation:

$$\rho\phi_{ij} = -L^2\left(\overline{u_j(\mathbf{x})\nabla^2 p_{,i}(\mathbf{x})} + \overline{u_i(\mathbf{x})\nabla^2 p_{,j}(\mathbf{x})}\right) \ . \tag{21}$$

In order to preserve the non-local effect, the correlation function must be defined in the following way:

$$\overline{u_j(\mathbf{x})\nabla^2 p_{,i}(\mathbf{x}')} + \overline{u_i(\mathbf{x})\nabla^2 p_{,j}(\mathbf{x}')} = \left(\overline{u_j(\mathbf{x}')\nabla^2 p_{,i}(\mathbf{x}')} + \overline{u_i(\mathbf{x}')\nabla^2 p_{,j}(\mathbf{x}')}\right) f(\mathbf{x},\mathbf{x}') \ . \tag{22}$$

The only difference between (19) and (22) is the point where the one-point correlation is evaluated. If (22) is used in (12), the single-point correlation cannot be taken outside the integral. But the decomposition of the two-point correlation into the one-point correlation evaluated at $\mathbf{x}'$ and the correlation function, and the modeling of the latter as a function which solely depends on the difference $\mathbf{x}' - \mathbf{x}$, allows the conversion of the integral to a convolution product. Thus, Eq. (12) can be inverted, leading to (15). The feature which is used here is that $-\nabla^2\delta + \delta/L^2$, where δ is the Dirac function, is equal to the inverse of $\exp(-r/L)/r$ for the convolution product. Hence, the non-local effect is preserved through the Yukawa operator.

The shape of the correlation function defined by (22) has never been assessed before. The first purpose of this work is then to check if the approximation $f(\mathbf{x},\mathbf{x}') = \exp(-\|\mathbf{x}'-\mathbf{x}\|/L)$ is consistent with the DNS data. For instance, the correlation function in (22) is not prevented from being larger than 1. If the root-mean square of the velocity fluctuation u_n varies rapidly in one direction, $\overline{u_n(\mathbf{x})\nabla^2 p_{,m}(\mathbf{x}')}$

can become larger than $\overline{u_n(\mathbf{x}')\nabla^2 p_{,m}(\mathbf{x}')}$. On the other hand, the correlation between the velocity and the Laplacian of the pressure gradient should decrease very rapidly with increasing separations and hence, the correlation function should remain smaller or only slightly larger than one.

The length scale used in the approximation (13) is not rigorously an integral scale because it does not satisfy (21). Nevertheless, it is the integral of the function $\exp(-r/L)$ from zero to infinity. One may attempt to evaluate this length scale as the integral of the correlation function $f(\mathbf{x}, \mathbf{x}')$. However, as will be shown in §5.4, this definition is not satisfactory. Thus, another purpose of the present work is to evaluate alternative definitions of the length scale, and compare it with the turbulent length scale $k^{3/2}/\varepsilon$, which is used in elliptic relaxation models.

The ultimate objective of the evaluations of the correlation function and the length scale is to find ways to improve the elliptic relaxation approach. As pointed out by Wizman *et al.* (1996), the elliptic relaxation equation does not act in the right direction in the log layer. For instance, if the IP and Rotta models are used as the source term in (16), since the anisotropy is fairly constant in the log layer, ϕ_{ij} has the same behavior in $1/y$ as ε and P. Then, it can be easily shown that the solution of (16) is

$$\phi_{ij} = \frac{1}{1 - 2C^2\kappa^2}\phi_{ij}^h \ , \tag{23}$$

if the length scale is $L = C\kappa y$, where κ is the Karman constant. Hence, in the log layer, the redistribution of energy between the components of the Reynolds stress tensor is amplified, while a damping due to the presence of the wall is expected.

Therefore, Wizman *et al.* (1996) introduced other formulations of the elliptic relaxation equation. The first one, the so-called *neutral formulation*, is defined as

$$\phi_{ij} - \nabla^2(L^2\phi_{ij}) = \phi_{ij}^h \ . \tag{24}$$

It produces neither amplification nor reduction of the redistribution in the log layer, since it leads to $\phi_{ij} = \phi_{ij}^h$. The second one, which yields the best agreement with DNS data, is given by

$$\phi_{ij} - L^2\nabla\left(\frac{1}{L^2}\nabla(L^2\phi_{ij})\right) = \phi_{ij}^h \ . \tag{25}$$

It exhibits a damping of the redistribution in the log layer.

These empirically derived new formulations require further justifications. What is suspected here is that the approximation of the correlation function f by an exponential function is not appropriate. Indeed, the latter is isotropic, whereas the former may decrease more rapidly when the point $\mathbf{x}'$ is moving towards the wall than when it is moving away from it. Experiments from Sabot (1976) in a pipe show that the contours of the two-point correlations of velocities are tightly packed between the point of zero separation and the wall. It is suspected that the same phenomenon occurs for correlations between velocity and Laplacian of the pressure gradient. Moreover, this feature is closely linked to the variation of the

length scale in the near wall region. When the correlation function is modeled by an isotropic function, the same weight is given to points towards the wall and those away from it. Since the source term decreases in the log layer, it results in an over-prediction of the integral. This phenomenon can be suspected to be the reason for the erroneous behavior of the elliptic relaxation equation in the log layer. This idea will be carefully explored in the following DNS analysis, in order to support modifications of the model such as those proposed by Wizman *et al.* (1996).

In addition, some general improvements of the model can be expected from such reformulations. Because of the erroneous behavior described above, it is difficult to reproduce accurately both the viscous sublayer and log layer. For instance, the coefficients of the V2F model have been tuned as a compromise between the boundary layer and the channel flow, since it is impossible to predict perfectly both flows with the same set of coefficients. Furthermore, this type of compromise limits the influence of the elliptic relaxation equation to a region very close to the wall. Parneix, Laurence & Durbin (1998) showed that in the case of the backstep flow, the turbulent force $-\overline{uv}_{,y}$ in the mean streamwise velocity equation is over-predicted in the backflow region, which acts to slow down the flow, leading to an under-prediction of the intensity of the recirculation. All modifications of the coefficients attempted by them proved ineffective, and they only managed to reduce the error by 50% by including terms involving the gradient of the mean flow in the turbulent transport term. In this case some improvement can be expected too by extending the influence of the elliptic relaxation equation in the backflow region and particularly by reformulating this equation in order to account for the variations of the length scale.

4.2 Channel flow database and post-processing

Since the Laplacian of the pressure gradient, which involves three spatial derivatives, will be calculated, a very accurate DNS database is needed. The database used in this study is the most recent channel flow simulation of Moser, Kim & Mansour (1998) at $Re_\tau = 590$. This flow was computed on a grid of $384 \times 257 \times 384$ points in streamwise (x), wall normal (y) and spanwise (z) directions, respectively. The computational domain is given by $2\pi\delta$, 2δ and $\pi\delta$ in x, y and z, where δ denotes the channel half-width. The simulation code employed a spectral method (Fourier series in x and z, and Chebychev polynomial in y) for spatial derivatives, and a semi-implicit scheme for time integration. A total of 75 fields (restart files) are available for statistical averaging.

In order to assess the shape of the correlation function f defined by (22), the two-point correlations between the fluctuating velocities and the Laplacian of the pressure gradient must be calculated. They are evaluated in the following manner:

- First, the Laplacian of the total pressure gradient is evaluated directly from the velocity field, $\nabla^2\widetilde{p} = -\widetilde{u}_{i,j}\widetilde{u}_{j,i}$ where $\widetilde{\cdot}$ denotes total quantities. The spatial derivatives are calculated using the same Fourier/Chebychev spectral method as for the DNS.
- The one-point and two-point correlations between the gradient of the Laplacian of the total pressure and the velocity components $\overline{\widetilde{u}_j(\mathbf{x}')\nabla^2\widetilde{p}_{,i}(\mathbf{x}')}$ and $\overline{\widetilde{u}_j(\mathbf{x})\nabla^2\widetilde{p}_{,i}(\mathbf{x}')}$

are then computed. The gradient is calculated using Fourier spectral derivatives in x and z, and fourth order finite differences in y.

- The corresponding mean quantities involving U_i and $\nabla^2 P_{,i}$ are calculated. They are finally subtracted out from correlations between total quantities in order to obtain the correlations between fluctuating quantities.

The ensemble averages are replaced by averaging in the homogeneous directions and over the 75 restart fields. The computations are very expensive. As a practical matter, calculations are performed at 7 representative y-locations only, for separations in x-y, x-z, y-z planes.

5. Results and discussion

5.1 The wall echo

Since the paper of Launder, Reece & Rodi (1975), it has been widely accepted in the turbulence community that, in a semi-infinite space bounded by a plane at $y = 0$, the image term in the integral equation of ϕ_{ij} represents the so-called wall echo effect, responsible for the reduction of the amplitude of the energy redistribution between components of the Reynolds stress tensor. Consequently, in second moment closure models, extra terms are frequently incorporated to account for this effect (Gibson & Launder 1978). These wall echo terms depend on the distance to the wall, which is often not well defined in complex geometries. The inclusion of wall echo terms often worsen the predictions in engineering applications even though they have proven to be effective in simple flows.

The physical reasoning behind this is that the pressure fluctuations are reflected by the wall, introducing an "echo" contribution which can be considered as instantaneous in an incompressible flow. Considering each point of the domain as a source of pressure fluctuations, the echo can be represented by an image source of fluctuations. The contribution of this echo actually increases the pressure fluctuations (in a closed room, the echo increases the noise). This feature is linked to the homogeneous Neumann boundary condition at the wall. Mathematically, this can be related to the fact that the presence of the wall induces the presence of an image term in the Green function (7). On account of the homogeneous Neumann boundary condition, the image term appears with the same sign as the principal term, whereas if a homogeneous Dirichlet boundary condition was satisfied at the wall, it should have an opposite sign.

Thus, the wall echo effect cannot be responsible for the damping of the energy redistribution. Figure 2 shows a comparison among the three source terms in the integral Eq. (12) of the pressure term, corresponding to the three parts in $H(\mathbf{x}, \mathbf{x'}_0)$ (cf. (10)), for the components ϕ_{11} and ϕ_{22}. The magnitudes of these source terms have been arbitrarily normalized such that the maximum of the first image term ($n = -1$) is 1. The solid line, representing the principal term ($n = 0$), has been truncated because it approaches infinity at $y^+ = y'^+ = 30$. It is clear that the first image term ($n = -1$), associated with the closer wall located at $y^+ = 0$, is always of the same sign as the principal term. It can also be noticed that this term gives more weight to the region very close to the wall, where it becomes equal to the

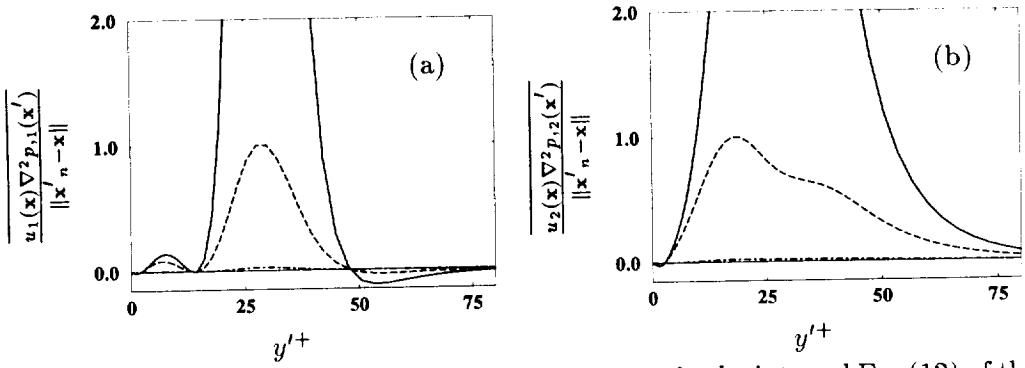

FIGURE 2. Comparisons of the different source terms in the integral Eq. (12) of the pressure term with $H(\mathbf{x}, \mathbf{x'}_0)$ given by (10) at location $y^+ = 30$. Separations in x- and z-directions are zero. (a) ϕ_{11}; (b) ϕ_{22}. ——— n=0 (principal term); ---- n=-1 (first image term); —·— n=1 (second image term). The vertical coordinate is arbitrarily normalized such that the maximum of $n = -1$ term is 1.

principal term and the two-point correlation changes sign for the component ϕ_{22}, as shown in Fig. 2b. However, this feature is not present in Fig. 2a and, moreover, the contribution of this part of the domain to the integral is rather small. It must be emphasized that even though the $n = -1$ source term appears negligible near the point of zero separation relative to the $n = 0$ term, which goes to infinity, its contribution to the integral is significant. Indeed, the value of the volume integral of $1/r$ between $r = 0$ and $r = 1$ is only 2π. Thus, Figs. 2a and 2b clearly show that the contributions of the image terms to the integral are of the same sign as the contribution of the principal term. Unfortunately, it is not possible here to evaluate quantitatively the relative weight of each term because it involves two-point correlations with separations in the whole 3D-domain, which have not been calculated.

At this point a very interesting conclusion can be drawn. The image terms in the integral Eq. (12) with $H(\mathbf{x}, \mathbf{x'})$ defined by (10), which account for the wall echo, actually have an amplification effect on the redistribution of turbulent energy between the different component of the Reynolds stress. Thus, it is time to abandon the traditional way of modeling the damping of the redistribution, which consists of introducing Gibson & Launder (1978) type terms involving functions of the geometry. This damping can only be caused by the damping of the two-point correlation itself, which is a consequence of the no-slip boundary conditions and the wall-blocking effect.

This phenomenon is an inhomogeneity effect, which can only be accounted for by non-local models, such as the elliptic relaxation model. However, it has been shown in §4.1 that the behavior of the latter is not satisfactory in the log layer. The following sections will show that this flaw is due to the fact that the model does not account for the asymmetry of the correlation function in the direction normal to the wall, which is a consequence of the variation of the length scale in inhomogeneous regions. By reformulating the elliptic relaxation equation, the damping of

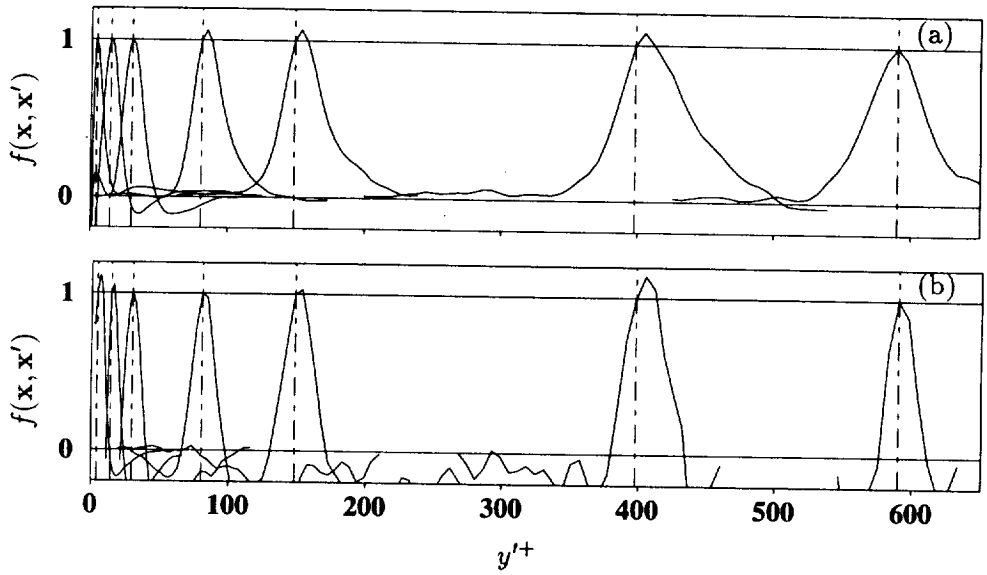

FIGURE 3. Correlation function defined by (26) calculated from the DNS data at different y locations: $y^+ = 4$; $y^+ = 14$; $y^+ = 30$; $y^+ = 80$; $y^+ = 150$; $y^+ = 400$; $y^+ = 590$. Separations in x- and z-directions are zero. (a) $f(\mathbf{x},\mathbf{x}') = \overline{u_1(\mathbf{x})\nabla^2 p_{,1}(\mathbf{x}')}/\overline{u_1(\mathbf{x}')\nabla^2 p_{,1}(\mathbf{x}')}$; (b) $f(\mathbf{x},\mathbf{x}') = \overline{u_2(\mathbf{x})\nabla^2 p_{,2}(\mathbf{x}')}/\overline{u_2(\mathbf{x}')\nabla^2 p_{,2}(\mathbf{x}')}$.

the redistribution in the log layer can be reproduced, without introducing any "wall echo" correction term (§6.2).

5.2 Asymmetry of the correlation function in y-direction

The main purpose of this study is to investigate through DNS data the shape of the correlation function defined by (22), which is modeled by an exponential function in the elliptic relaxation method. First, it must be emphasized that this model function is unique, i.e., it does not depend on the component of ϕ_{ij}. This feature is not supported by any theoretical result, but is necessary to warrant the frame independence of the model. On the other hand, using DNS data, a correlation function $f(\mathbf{x},\mathbf{x}')$ can be calculated for each component of ϕ_{ij}:

$$f(\mathbf{x},\mathbf{x}') = \frac{\overline{u_\alpha(\mathbf{x})\nabla^2 p_{,\beta}(\mathbf{x}')} + \overline{u_\beta(\mathbf{x})\nabla^2 p_{,\alpha}(\mathbf{x}')}}{\overline{u_\alpha(\mathbf{x}')\nabla^2 p_{,\beta}(\mathbf{x}')} + \overline{u_\beta(\mathbf{x}')\nabla^2 p_{,\alpha}(\mathbf{x}')}}\ , \tag{26}$$

without summation over Greek indices. It is obviously impossible to derive a model of f which matches the DNS results for all the components. Hence, the following analysis should be interpreted in a qualitative rather than quantitative sense.

Figure 3 shows the correlation function $f(\mathbf{x},\mathbf{x}')$ corresponding to components ϕ_{11} (Fig. 3a) and ϕ_{22} (Fig. 3b) for 7 different y locations, at zero x- and z-separation. Each curve has been truncated for clarity, since the ratio (26) becomes rather "noisy" for large separations. Several observations can be made from the figure:

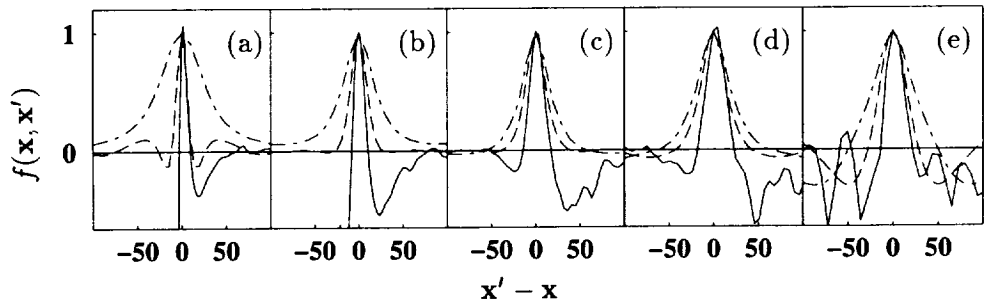

FIGURE 4. Comparison of shapes of the correlation function corresponding to ϕ_{22} for separations in the 3 principal directions at different locations. (a) $y^+ = 14$, (b) $y^+ = 30$, (c) $y^+ = 80$, (d) $y^+ = 150$, (e) $y^+ = 590$. Separations: —·— , x-direction, ($\Delta y = \Delta z = 0$); ——— , y-direction, ($\Delta x = \Delta z = 0$); ---- , z-direction, ($\Delta x = \Delta y = 0$).

- The correlation functions corresponding to ϕ_{11} and ϕ_{22} are quite different. In particular, the correlation length scale appears to be significantly larger at every location for the 11 component than for the 22 component.
- The correlation function becomes negative at certain separations, particularly for the 22 component.
- The correlation length scale varies with location. It increases rapidly when the fixed point $\mathbf{x}$ moves away from the wall. Then, it seems to reach a maximum level and decreases slightly as the center of the channel is approached. This behavior seems to be qualitatively the same for both components.
- These functions have asymmetrical shapes, particularly in the log layer. As pointed out in §4.1, the correlation function defined by (26) is not restricted to values less than or equal to 1. It can be observed in Fig. 3b that this is indeed the case. For instance, the correlation function at $y^+ = 400$ reaches a maximum value of approximately 1.15 at $y'^+ \simeq 405$.

The main conclusion which can be drawn from the figures is that the correlation function is very asymmetric. This feature is linked to the rapid variation of the length scale, which increases with distance from the wall. Modeling the correlation function by an exponential function leads to too much weight being placed in the region between the point and the wall. Therefore, as will be described below, the over-estimation of the pressure term in the log layer can be corrected by introducing some asymmetry in the model for $f(\mathbf{x},\mathbf{x}')$.

5.3 Anisotropy of the correlation function

Figure 4 shows the correlation function corresponding to ϕ_{22}, evaluated from (26) with $\alpha = \beta = 2$, for separations in the principal directions. Note that for separations in y-direction the correlation function goes to $-\infty$ when the point y' approaches the wall, as can be seen in Figs. 4a and 4b. This is because in the ratio (26), the one-point correlation involves $u_2(y')$, which behaves as y'^2 in the vicinity of the wall, whereas the two-point correlation only contains $u_2(y)$ which is constant with respect to y'. Accordingly, the ratio behaves as y'^{-2} near the wall.

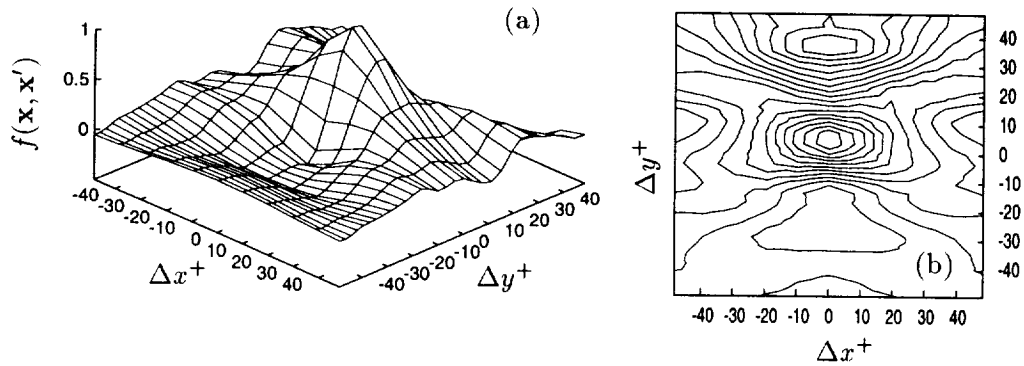

FIGURE 5. Correlation function corresponding to ϕ_{22} at $y^+ = 80$ for separations in the x-y plane ($\Delta z = 0$). (a) $f(\mathbf{x},\mathbf{x}')$, (b) Iso-correlation contours. Contour levels from -0.5 to 1 are separated by 0.1.

All the Figs. 4a-e show that the velocity u_2 and the y-derivative of the Laplacian of the pressure are correlated over a longer distance in the streamwise direction than in other two principal directions. This feature is consistent with the streamwise elongation of the turbulent structures observed in the experiments. This anisotropy is very important near the wall (Fig. 4a) and becomes less pronounced away from it (Figs. 4b-e). Note that at the center of the channel, the correlation function is still anisotropic.

The anisotropy of the correlation function at location $y^+ = 80$, corresponding to Fig. 4c, can also be observed in Fig. 5. In 5a, $f(\mathbf{x},\mathbf{x}')$ is plotted as a function of separation in the x-y plane ($\Delta z = 0$). Figure 5b shows the contour levels of this surface. One can observe that near the point of zero separation, the highest contour, which corresponds to $f(\mathbf{x},\mathbf{x}') = 1$, is almost round. The shape of the contours becomes more elongated in the x-direction as the level decreases.

The asymmetry of the correlation function in y-direction, emphasized in §5.2, appears in Fig. 5b as well. When looking only at the spacing between consecutive contours, the function may seem somewhat symmetric. But it must be noted that the contours are not centered at the point of zero separation. Actually, the highest contour level plotted, $f(\mathbf{x},\mathbf{x}') = 1$, contains this point. This asymmetry is clearly observed as well in the regions of negative contour values. First, they are not symmetrical with respect to zero, since they are approximately centered at $\Delta y^+ = -25$ and $\Delta y^+ = 35$. Secondly, the extremum of the region corresponding to positive separations is much lower than the other one.

The above observations demonstrate that the correlation function is not only asymmetric in the y-direction but also anisotropic, especially in the very near-wall region ($y^+ < 30$). Consequently, it calls into question the use of the exponential function, which does not distinguish between streamwise, wall-normal and spanwise directions. However, this anisotropy cannot be considered as being responsible for the defects noted in §4.1, since in the case of channel flow, the non-local effect obviously does not act in the homogeneous directions. Nevertheless, this points out

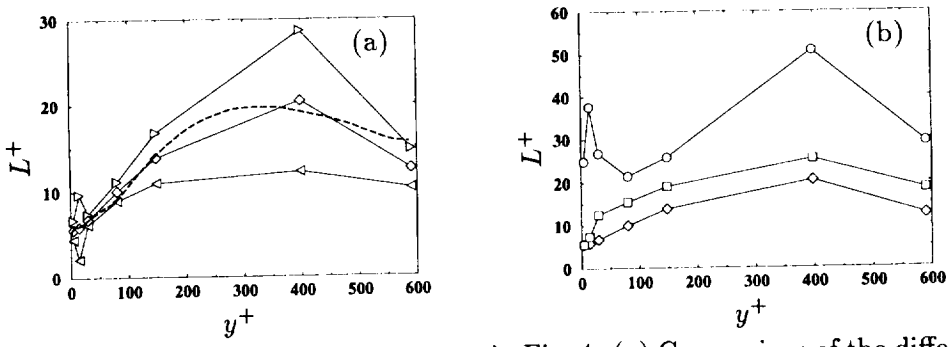

FIGURE 6. Length scales based on curves in Fig. 4. (a) Comparison of the different length scales in y-direction: ◂ Left length scale; ◇ Central length scale; ▸ Right length scale; ---- $L = C_L \max\left(k^{3/2}\varepsilon^{-1}, C_\eta \nu^{3/4}\varepsilon^{-1/4}\right)$ with $C_L = 0.045; C_\eta = 80.0$. (b) Comparison of the length scale in the 3 directions: ◇ Central length scale in y-direction; ○ Length scale in x-direction; □ Length scale in z-direction.

a feature of the correlation function which can become important in more complex flows.

5.4 The correlation length scale

The length scale L entering the model of the two-point correlations (13) is not easy to determine in DNS data. As emphasized in §4.1, it does not correspond rigorously to the integral scale (20).

It is noted that L is the integral of the function $\exp(-r/L)$ from zero to infinity. This property allows one to evaluate a length scale in each direction, but it is unfortunately not satisfactory. Since the x-direction is homogeneous, the integral over x of quantities involving x-derivatives is zero. Hence, the evaluation of the length scale in x-direction of the correlation function associated to ϕ_{11}, i.e., the function defined by (26) with $\alpha = \beta = 1$, gives exactly zero. This is due to the fact that it does not give the right weights to the different regions. Indeed, considering isotropic turbulence and ignoring the image terms, it can be seen that the 3-D integral (20) reduces to the 1-D integral $\int_0^\infty r f(\mathbf{x}, r) dr$, which increases the relative weight of the large separations.

The method which will be used in the following is not an integral method. It can be noted that the function $\exp(-r/L)$ takes the value $1/e$ for $r = L$. Thus, a length scale can be defined by the separation where the correlation function takes this value. Although this method is very simple, it provides a measure of the width of the function in each direction. The drawback is that it only characterizes the shape of the function at small separations and, in particular, it does not account for the negative excursions.

Nevertheless, this method allows the evaluation of the qualitative behavior of the length scale across the channel and distinguishes between the length scales evaluated at the left and right of the zero separation point, characterizing the asymmetry of the function. Figure 6 shows the different length scales which can be evaluated from the correlation functions depicted in Fig. 4. Figure 6a compares the different length

scales defined in the y-direction: the left (right) length scale corresponds to the value of negative (positive) separation at which the correlation function is equal to $1/e$, and the "central" length scale is the mean of the left and right length scales. It can be observed that, except for the peculiar behavior at $y^+ = 14$, the asymmetry is weak close to the wall and becomes more pronounced away from it. This trend is reversed when the center of the channel is approached.

The growth of the central length scale with y is nearly linear up to $y^+ = 200$. In Fig. 6a, the length scale used in the elliptic relaxation model is also plotted. It can be seen that the global shape is very satisfactory, although the coefficient C_L has been reduced by a factor of 4. This value of C_L cannot be considered as the value which must be used in the model, since it only corresponds to the component ϕ_{22}.

Figure 6b shows the evolution across the channel of the length scale in the 3 principal directions. Although their amplitudes are different, their behaviors appear quite similar, except for $y^+ < 100$, where a spike appears in the streamwise length scale.

These results indicate that the length scale used in the model, which is the standard turbulent length scale bounded by the Kolmogorov length scale, represents quite satisfactorily the variations of the correlation length in the channel. The coefficient C_L is likely over-estimated, but the results presented here are mainly qualitative and therefore, the coefficient tuned by computer optimization must be preferred. Overall, these results justify the way the length scale is modeled in the elliptic relaxation method. The use of the Kolmogorov length scale as a lower bound, which was originally introduced only to avoid singularities in the model, has proved important to improving the predictions of the model. This is due to the behavior of the correlation length described above, which does not go to zero and varies linearly in the vicinity of the wall.

6. Proposed modification to the model

6.1 Correction to the model of the correlation function

The results presented in the previous section show that the model of the correlation function can be improved. For the present study, whose main purpose is to find ways to correct the wrong behavior in the log layer as detailed in §4.1, the most noteworthy feature of the correlation function is its asymmetry in the y-direction. Indeed, Fig. 7 shows that, when the original correlation function model is used, the two-point correlation obtained by multiplying the model function by the one-point correlation from the DNS data (cf. (26)), is larger toward the wall than away from it. This is very different from the two-point correlation computed directly from the DNS fields, which is quite symmetrical. Consequently, the integral of the two-point correlation is over-estimated, leading to the incorrect amplification of the pressure term pointed out in §4.1.

This work does not attempt to find the best way to modify the model. Rather, it presents a direction in which an improvement of the model can be sought. An example of modification is presented in Fig. 7. The asymmetrical correlation function shown in 7b is obtained by introducing a dependence on the gradient of the

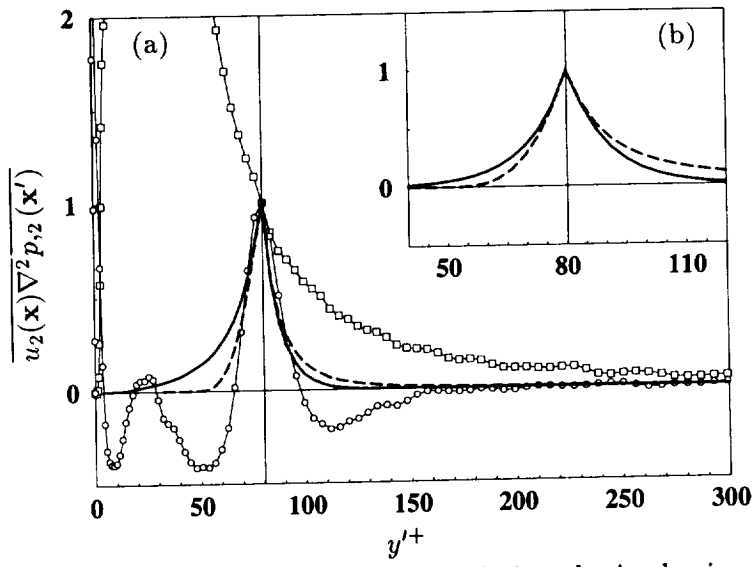

FIGURE 7. *A priori* test of the two-point correlation obtained using two different correlation functions. (a) One- and two-point correlations. All quantities are normalized by the value of the two-point correlation at zero separation. □ One-point correlation from DNS ($\mathbf{x} = \mathbf{x}'$); ○ Two-point correlation from DNS; —— Two-point correlation obtained using the symmetrical exponential correlation function shown in (b) and the one-point correlation from DNS; ---- Two-point correlation obtained using the asymmetrical exponential correlation function shown in (b) and the one-point correlation from DNS. (b) Model of the correlation function. —— Symmetrical correlation function: $f(y,y') = \exp(-|y'-y|/L)$; ---- Asymmetrical correlation function: $f(y,y') = \exp(-|y'-y|/(L+(y'-y)dL/dy)$.

length scale: $f(y,y') = \exp(-|y'-y|/(L+(y'-y)dL/dy)$. The resulting two-point correlation, shown in 7a, is much closer to the DNS value than the one obtained using the original model. In particular, the new function corrects the erroneous shape observed between the point and the wall. The next section will detail the consequence of this new model on the form of the elliptic relaxation equation.

6.2 Reformulation of the elliptic relaxation equation

The simple modification of the correlation function model proposed above can easily lead to a new form of the elliptic relaxation model. The correlation function is henceforth modeled by

$$f(\mathbf{x},\mathbf{x}') = \exp\left(-\frac{r}{L + r\mathbf{u}\cdot\nabla L}\right) , \tag{27}$$

where r and $\mathbf{u}$ denote respectively $\|\mathbf{x}'-\mathbf{x}\|$ and $(\mathbf{x}'-\mathbf{x})/\|\mathbf{x}'-\mathbf{x}\|$. Considering the new term $r\mathbf{u}\cdot\nabla L$ as a small correction, a Taylor expansion of (27) leads to the following expression:

$$f(\mathbf{x},\mathbf{x}') = \exp\left(-\frac{r}{L}\right) + \frac{r^2}{L^2}\exp\left(-\frac{r}{L}\right)\mathbf{u}\cdot\nabla L \ . \tag{28}$$

Using (28), the integral equation of the pressure term leads to two terms ϕ^a_{ij} and ϕ^b_{ij}. The first term is the same as the original one and satisfies

$$\phi^a_{ij} - L^2\nabla^2\phi^a_{ij} = -\frac{L^2}{\rho}g_{ij} \ , \tag{29}$$

where g_{ij} denotes the one-point correlation $\overline{u_j\nabla^2 p_{,i}} + \overline{u_i\nabla^2 p_{,j}}$. The second term

$$\phi^b_{ij} = 8\frac{L^3}{\rho}\nabla L\cdot\nabla g_{ij} \tag{30}$$

is a correction term. Following Durbin (1991), the RHS of (29) can be replaced by any quasi-homogeneous model, which corresponds to modeling g_{ij} by $\rho\phi^h_{ij}/L^2$. There are two possible ways to take into account the correction term in the model. First, it can be considered as an explicit correction as

$$\phi^a_{ij} - L^2\nabla^2\phi^a_{ij} = \phi^h_{ij} \ ; \tag{31}$$

$$\phi^b_{ij} = 8L^3\nabla L\cdot\nabla\frac{\phi^a_{ij}}{L^2} \ . \tag{32}$$

Here, (31) gives exactly the same solution as the original model, while (32) provides an explicit correction. The second possibility is to introduce the correction directly into the elliptic relaxation equation in the following manner:

$$\phi_{ij} - L^2\nabla^2\phi_{ij} - 8L^3\nabla L\cdot\nabla\frac{\phi_{ij}}{L^2} = \phi^h_{ij} \ . \tag{33}$$

The same analysis as in §4.1 can be conducted in the log layer, which yields the following results:

(a) with the explicit formulation (31) and (32): $\phi_{ij} = \dfrac{1-24C^2\kappa^2}{1-2C^2\kappa^2}\phi^h_{ij}$;

(b) with the implicit formulation (33): $\phi_{ij} = \dfrac{1}{1+22C^2\kappa^2}\phi^h_{ij}$.

Both new formulations give a reduction of the redistribution, in contrast to the original one, which gave an amplification, as pointed out in §4.1. Note that the reductions are identical up to the third order in the small parameter $C\kappa$.

Thus, the simple modification of the model for the correlation function proposed above overcomes the deficiencies of the original model in the log layer. The so-called "wall echo effect", called into question in §5.1, can be obtained only by accounting for the asymmetry of the correlation function in the direction normal to the wall, i.e., by introducing a dependence on the gradient of the length scale in the model. This can be compared to the correction applied by Launder & Tselepidakis (1991), who sought to avoid the use of wall echo terms by introducing an "effective velocity gradient" in their pressure term model, defined as

$$\nabla U_i^{eff} = \nabla U_i + c^{eff}L(\nabla L\cdot\nabla)\nabla U_i \tag{34}$$

(see Wizman *et al.* (1996) for more details). This approach accounts for the inhomogeneity of the flow in the near-wall region, which is very similar to the present work.

7. Conclusions

A DNS database for a channel flow at $Re_\tau = 590$ has been used to assess the validity of the model assumptions in the elliptic relaxation method. Several conclusions can be drawn:

- The method, which is based on the approximation of the correlation function (26) by an exponential function, is consistent with DNS data, although some refinements are necessary. In particular, the length scale used in the model, defined by the standard turbulent length scale bounded by the Kolmogorov length scale, reproduces rather surprisingly the overall shape of that obtained from DNS data.
- The shape of the correlation function depends on the component of the two-point correlation tensor used to evaluate it. Therefore, one can not expect an accurate reproduction of all the two-point correlations. Only a global accounting of the non-local effect is possible.
- An analysis of the image terms entering the approximate Green function of the channel shows that they actually lead to an amplification, rather than reduction, of the redistribution between the components of the Reynolds stress, in contrast to the common belief. The reduction can only be due to the damping of the source term in the integral equation, especially for the diagonal component normal to the wall. Accordingly, this is not a wall echo effect, but a wall blocking effect.
- The correlation function computed from DNS data is strongly asymmetric in the direction normal to the wall, particularly in the log layer. Modeling it by a simple exponential function gives too much weight to the region between the point and the wall. Since the one-point correlation increases rapidly toward the wall, it yields an over-estimation of the pressure term. This is the reason for the observed erroneous amplification of the redistribution in the log layer.
- The correlation function is anisotropic. In particular, very close to the wall, the iso-correlation contours are strongly elongated in the streamwise direction. This feature has no influence on the channel flow, and its effect on complex flows cannot be determined in the present study.
- A simple modification to the correlation function model, accounting for the observed asymmetry in the direction normal to the wall, allows the derivation of a new formulation of the elliptic relaxation equation which does not possess the same defect as the original version. This result shows that the reduction of the redistribution in the log layer can be reproduced by introducing inhomogeneity effects and avoiding the use of any wall echo correction terms.

Based on the physical insight gained through this study, effort will continue to be directed toward the improvement of the elliptic relaxation method. Different formulations of the model will be tested in simple flows, in order to assess the improvement of the predictions. The new model will be calibrated on the channel flow and the boundary layer flow to allow its application in more complex configurations.

Acknowledgments

The authors gratefully acknowledge William Cabot, Javier Jimenez, and Robert

Moser for assistance with the DNS database and useful discussions.

REFERENCES

BRADSHAW, P. 1973 The Strategy of Calculation Methods for Complex Turbulent Flows. *Imperial College, Dept. of Aero. Report.* **73-05,** 1-56.

BRADSHAW, P., MANSOUR, N. N. & PIOMELLI, U. 1987 On Local Approximations of the Pressure-Strain Term in Turbulence Models. *Proc. Summer Program,* Center for Turbulence Research, NASA Ames/Stanford Univ., 159-164.

CHOU, P. Y. 1945 On velocity correlations and the solutions of the equations of turbulent fluctuation. *Qrtly. of Appl. Math.* **3,** 38-54.

DURBIN, P. A. 1991 Near-wall turbulence closure modeling without "damping functions". *Theoret. Comput. Fluid Dynamics.* **3,** 1-13.

DURBIN, P. A. 1993 A Reynolds stress model for near-wall turbulence. *J. Fluid Mech.* **249,** 465-498.

GIBSON, M. M. & LAUNDER, B. E. 1978 Ground effects on pressure fluctuations in the atmospheric boundary layer. *J. Fluid Mech.* **86,** 3.

KIM, J. 1989 On the structure of pressure fluctuations in simulated turbulent channel flow. *J. Fluid Mech.* **205,** 421-451.

KIM, J., MOIN, P. & MOSER, R. 1987 Turbulence statistics in fully developed channel flow at low Reynolds number. *J. Fluid Mech.* **177,** 133-166.

LAUNDER, B. E., REECE, G. J. & RODI, W. 1975 Progress in the development of a Reynolds-stress turbulence closure. *J. Fluid Mech.* **68-3,** 537-566.

LAUNDER, B. E. & TSELEPIDAKIS, D. P. 1991 Progress and paradoxes in modelling near-wall turbulence. *8th Symp. Turb. Shear Flows.* **29-1,** 1-6.

LUMLEY, J. L. 1975 Pressure-strain correlation. *Phys. Fluids.* **18**(6), 750-750.

MANSOUR, N. N., KIM, J. & MOIN, P. 1988 Reynolds-stress and dissipation-rate budgets in a turbulent channel flow. *J. Fluid Mech.* **194,** 15-44.

MONIN, A. S. & YAGLOM, A. M. 1975 *Statistical Fluid Mechanics.* MIT Press, English version of the original Russian version (1965).

MOSER, R., KIM, J. & MANSOUR, N. N. 1998 Manuscript in preparation.

PARNEIX, S., LAURENCE, D. & DURBIN, P. A. 1998 A procedure for using DNS databases. *J. Fluid Eng.* **120,** 40-47.

SABOT, J. 1976 *Etude de la cohérence spatiale et temporelle de la turbulence établie en conduite circulaire.* PhD thesis, Université de Lyon.

WIZMAN, V., LAURENCE, D., KANNICHE, M., DURBIN, P. & DEMUREN, A. 1996 Modeling near-wall effects in second-moment closures by elliptic relaxation. *Int. J. Heat and Fluid Flow.* **17,** 255-266.

The LES group

The 1998 Summer Program contained seven projects in LES involving fifteen scientists. The interest in LES continues to grow, and the findings from the Summer Programs have found increased utility in setting the direction for research in LES.

The project by Carati and Rogers was the first application of the 'Ensemble Averaged LES' concept developed at the 1996 Summer Program to an inhomogeneous flow, the time evolving plane wake. In this procedure, one executes several realizations of a turbulent flow on the same number of computer processors simultaneously. Thus, at each time step the ensemble averaged field is available, which could be used in parameterization of the subgrid scale stresses. Such parameterization can lead to improved and economical models as well as being useful for building a bridge between LES and Reynolds averaged approach, RANS. As with homogeneous flows, it appears that only about sixteen realizations are sufficient. Interestingly, the three models tested led to similar results for low order turbulence statistics which were in good agreement with the DNS data.

One of the important and relatively unattended areas for research in subgrid scale modeling is for high speed compressible flows. The LES equations contain several terms without counterparts in incompressible flows. Adams *et al* used DNS data of a $M = 3$ compression corner with a shock to compute and evaluate the relative importance of the subgrid scale terms. In addition, as with numerous other studies, they demonstrated that scale similarity type models perform better in *a priori* tests. An important issue addressed in this report is the treatment of shock wave as a subgrid scale entity. A new and very promising approach for subgrid scale modeling, in general, and for the treatment of shocks, in particular, was introduced. This is an algorithmic procedure, as opposed to phenomenological modeling, which uses regularized deconvolution of the velocity field to estimate the unfiltered flow field. If this methodology turns out to be robust, especially when applied to high Reynolds number flows, it will have far reaching consequences in the development of modern LES in the years to come.

The deconvolution strategy is very similar to Domaradzki's subgrid scale estimation model and is also related to Leonard's (*AIAA Paper 97-0204*) estimate of the filtered advection term in the Navier Stokes equations. Domaradzki's approach, which was extended to compressible turbulence during the Summer Program, appears to be a bit more involved than the deconvolution approach and has an adjustable model parameter, but its results appear to be equally impressive. Like the scale similarity models, the estimation model yields high correlations with the DNS data and, additionally, appears to provide correct level of subgrid scale dissipation which the scale similarity models tend to be incapable of. Winckelmans *et. al* conducted a thorough evaluation of Leonard's model in both the isotropic decay problem and turbulent channel flow. It was quickly discovered that the model does not provide sufficient dissipation, and hence the Smagorinsky model was added to the model. The model coefficient was computed using the dynamic procedure, which is now

much better behaved in terms of lower variability in space and positive values. The principal deficiency of the Leonard model without the Smagorinsky component is manifested in incorrect distribution in the energy spectrum. Another improved feature of the Leonard model is the higher values of subgrid scale shear stress near walls. Cottet & Vasilyev implemented an integral formulation of Leonard's model. This formulation allows for a simple method to distinguish forward and backscatter of energy and allows for a more rigorous control of backscatter, which is essential for stabilization of the computations. Apparently, the backscatter control feature is the reason for not requiring additional dissipation through added Smagorinsky model or other means.

An important pacing item for application of LES to complex flows is the resolution of the wall layer. For high Reynolds number *attached* boundary layers, the resolution of the wall layer is too demanding of computer resources, and development of lower dimensional modeling approaches for this region is an active area of research in LES. The wall modeling problem is divided into two parts: the actual modeling of the wall layer by a lower dimensional dynamic system, and the transfer of the appropriate information to the outer layer LES. In an attempt to focus on the mathematical boundary condition aspect of the problem and to avoid the particular complications of the wall region, Jiménez and Vasco considered a novel simulation of a channel half by prescribing boundary conditions on the centerline. They confirmed the earlier results by Baggett and the previous experience from the prescription of inflow conditions in LES, that prescription of random fluctuations, even with correct second order statistics, is inadequate as boundary conditions. They attribute the difficulty to large pressure fluctuations at the boundary which induce artificial energy fluxes across it. Nicoud *et al.* use the scaled velocity field at an interior plane in LES of channel flow to supply turbulence structures at the boundary. A dynamic procedure was developed to relate the time scales of the velocity in the interior plane and at the boundary. The ratio of the two time scales appear to be near one rather than that deduced from the log layer scaling. The results are encouraging, but further refinements are needed.

Parviz Moin

Center for Turbulence Research
Proceedings of the Summer Program 1998

Ensemble-averaged LES of a time-evolving plane wake

By D. Carati[1] AND M. M. Rogers

The ensemble-averaged dynamic procedure (EADP) introduced during the 1996 CTR Summer Program is tested on a time-evolving plane wake, an inhomogeneous flow that is statistically non-stationary. Convergence of the results with respect to the LES ensemble size is investigated, and it is found that an ensemble of as few as 16 realizations yields accurate converged results. New modeling concepts are tested in which quantities that explicitly require the knowledge of several realizations of the same flow are included.

1. Introduction

The idea of using a set of LES's for developing new concepts in subgrid-scale modeling was introduced during the 1996 CTR Summer Program (Carati, Wray & Cabot 1996). This method consists of generating several statistically equivalent LES's simultaneously, evaluating the subgrid-scale model constant by using information derived from the set of resolved velocity fields. Each of these fields evolves according to

$$\partial_t \overline{u}_i^r + \partial_j \overline{u}_j^r \overline{u}_i^r = -\partial_i \overline{p}^r + \nu_0 \nabla^2 \overline{u}_i^r - \partial_j \tau_{ij}^r \qquad r = 1, \ldots, R\,, \tag{1.1}$$

where r is an index corresponding to the realization being considered and R is the total number of realizations. Utilizing these R realizations, an ensemble-averaged dynamic procedure (EADP) can be developed as an alternative to the volume-averaged (or plane-averaged) dynamic procedure. There are several advantages of the EADP. Foremost of these is that the method does not rely on any homogeneous flow directions for the computation of model terms. Hence, there is no theoretical limitation preventing its use in a fully inhomogeneous and non-stationary flow. Also, the EADP is well suited for parallel computing since the R simulations only interact through the computation of the subgrid-scale model (see Fig. 1). The other terms in the equation can then be computed independently from the other realizations. It should also be noted that for statistically stationary flows the EADP is not more expensive than traditional LES because the ensemble greatly reduces the averaging time period required for converged statistics. In fact, if the different realizations are really independent, the CPU time required for collecting the statistics could even be reduced by using an ensemble of LES's. Finally, the EADP is theoretically

1 Université Libre de Bruxelles, (Brussels, Belgium).

appealing because it could provide useful information on the statistics of resolved velocity fields that might be used for building a bridge between LES and RANS.

Prior to this work, the EADP had only been tested in detail on homogeneous turbulence (both forced and decaying) with the Smagorinsky (1963) model. The feasibility of the method has been demonstrated, but its robustness for more complex flows and its potential advantages were not explored thoroughly. For homogeneous turbulence it was shown that good results were obtained with only $R = 16$ realizations. It is, of course, crucial to show that the number of realizations required for implementing this method does not increase dramatically for flows of greater complexity. Also, the knowledge of several realizations could be used not only to compute the Smagorinsky constant through the EADP, but also to explore new subgrid-scale models. The motivations for this work are thus to check the robustness of the method in an inhomogeneous flow and to demonstrate that new ensemble-based modeling concepts can be proposed and tested easily with the EADP.

The flow considered here is a time-evolving plane wake for which data from both direct numerical simulations (Moser & Rogers 1994, Moser, Rogers & Ewing 1997) and large-eddy simulations (Ghosal & Rogers 1997) are available. This flow is both statistically non-stationary and inhomogeneous and should thus be a more demanding test of the EADP than the homogeneous flows studied previously.

2. Subgrid-scale modeling

Subgrid-scale modeling for an ensemble of LES's is not more complicated than that for a single LES. As usual in LES, the model terms are assumed to depend both on instantaneous local quantities (such as the resolved strain-rate tensor) and universal parameters. In the context of an ensemble of LES's, it is natural to suppose that the instantaneous and local dependence of the model will also be realization dependent, while the universal parameter should be independent of the realization. Thus the model for the subgrid-scale tensor in each realization, $\tau_{ij}^r = \overline{u_i^r u_j^r} - \overline{u}_i^r\ \overline{u}_j^r$, can be expressed as

$$\tau_{ij}^r - \frac{1}{3}\tau_{kk}^r \delta_{ij} \approx C \mathcal{T}_{ij}^r[\overline{u}_l^r; \overline{G}]\ , \tag{2.1}$$

where $\mathcal{T}_{ij}^r$ is a tensorial functional of both the resolved field corresponding to the same realization index r and the LES filter $\overline{G}$. In contrast, the parameter C should be the same for all the realizations in the ensemble. The EADP prediction (Carati, Wray & Cabot 1996) C_d for the parameter C is given by

$$C_d = \frac{\sum_r L_{ij}^r \mathcal{M}_{ij}^r}{\sum_r \mathcal{M}_{ij}^r \mathcal{M}_{ij}^r}\ , \tag{2.2}$$

where $\mathcal{M}_{ij}^r = \widehat{\mathcal{T}_{ij}^r[\overline{u}_l^r; \overline{G}]} - \mathcal{T}_{ij}^r[\widehat{\overline{u}}_l^r; \widehat{\overline{G}}]$ and $L_{ij}^r = \widehat{u_i^r u_j^r} - \widehat{\overline{u}}_i^r \widehat{\overline{u}}_j^r$. Here, $\widehat{\overline{G}}$ is the filter obtained by successively applying the LES filter and a test filter $\widehat{G}$. In the present study, we have investigated three different models, all based on the eddy-viscosity concept. The first one is the classical Smagorinsky model.

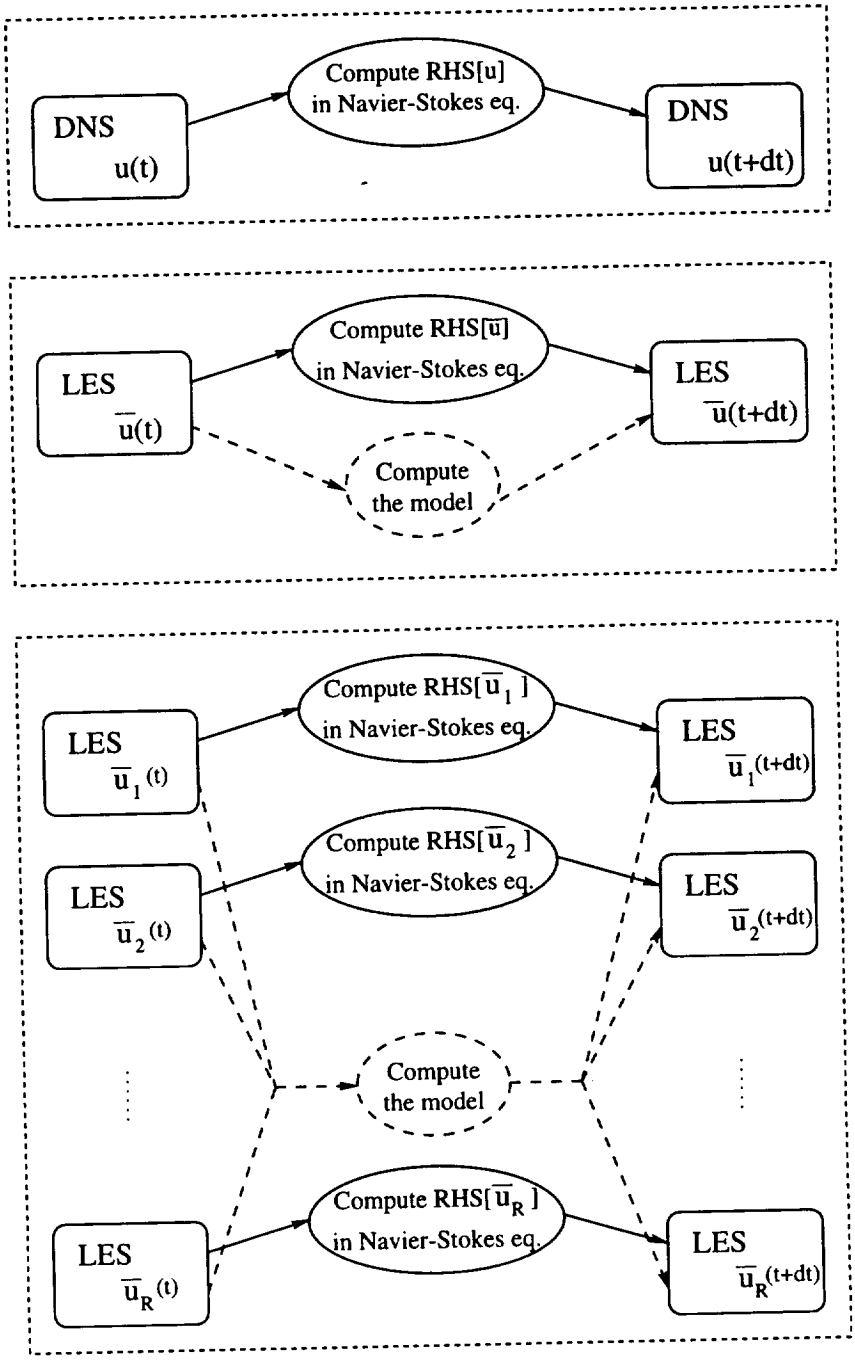

FIGURE 1. When a set of LES's are generated simultaneously, the different LES's are advanced in time through two types of terms. The first type, like in DNS (top) and traditional LES (middle), is given by the right-hand-side of the Navier-Stokes equation. For these terms no information is needed from the other fields. Information from the other fields is only required for the subgrid-scale model terms (bottom).

$$\textbf{Smagorinsky model:} \quad \mathcal{T}_{ij}^r[\overline{u}_l^r;\overline{G}] = -2\overline{\Delta}^2 \left(2\overline{S}_{kl}^r\overline{S}_{kl}^r\right)^{1/2} \overline{S}_{ij}^r \tag{2.3}$$

In the Smagorinsky model (2.3), the inertial range scaling for the eddy-viscosity $\nu_t \sim \overline{\Delta}^{4/3}\bar{\epsilon}^{1/3}$ has been expressed in terms of the resolved strain-rate tensor by using the approximation for the dissipation rate $\bar{\epsilon} \sim \nu_t \overline{S}_{kl}^r \overline{S}_{kl}^r$. This approximation is required in traditional LES because a separate equation for the dissipation rate is not usually computed. However, in LES based on the dynamic procedure, the product of C and $\bar{\epsilon}^{1/3}$ can be predicted through the expression (2.2). This has motivated the use of models directly based on the inertial range scaling such as

$$\textbf{Model A:} \quad \mathcal{T}_{ij}^r[\overline{u}_l^r;\overline{G}] = -2\overline{\Delta}^{4/3} \overline{S}_{ij}^r \,. \tag{2.4}$$

The model parameter predicted by the dynamic procedure with model A (2.4) is not dimensionless, but this does not cause any difficulties. Finally, we have considered a third model for which the tensorial functional $\mathcal{T}_{ij}^r[\overline{u}_l^r;\overline{G}]$ not only depends on the particular realization $\overline{u}_l^r$, but also on the ensemble-averaged velocity field.

$$\textbf{Model B:} \quad \mathcal{T}_{ij}^r[\overline{u}_l^r;\overline{G}] = -2\overline{\Delta}^{4/3} \left(\overline{S}_{ij}^r - \langle\overline{S}_{ij}\rangle\right) , \tag{2.5}$$

where the brackets indicate ensemble-averaging over all realizations. The advantage of this last model is that it can represent the effects of backscatter in some realizations while maintaining an overall average dissipative effect (provided that the parameter C is positive). In each realization the subgrid-scale dissipation is proportional to $\overline{S}_{kl}^r(\overline{S}_{kl}^r - \langle\overline{S}_{kl}\rangle)$, which can be either positive or negative. However, the mean of this quantity is $(\overline{S}_{kl}^r - \langle\overline{S}_{kl}\rangle)^2$, which is always positive.

Of course, the sign of C will also determine the sign of the subgrid-scale dissipation since a negative C corresponds to a negative eddy-viscosity. In order to avoid numerical instabilities, C must then be set equal to a minimal positive value (clipping procedure, see Ghosal *et al.*, 1995) at points where the total viscosity (eddy plus molecular) is negative. For the Smagorinsky model, the stability condition

$$C\overline{\Delta}^2 \left(2\overline{S}_{kl}^r\overline{S}_{kl}^r\right)^{1/2} + \nu_0 > 0 \tag{2.6}$$

depends on the realization. This is an undesirable property since C is supposed to be a universal flow characteristic for all members of the ensemble. An alternative formulation in which C is indeed the same for all realizations results from the following stability condition

$$C\overline{\Delta}^2 \max_r \left\{ \left(2\overline{S}_{kl}^r\overline{S}_{kl}^r\right)^{1/2} \right\} + \nu_0 > 0 \,. \tag{2.7}$$

In the limit of an infinite number of realizations, the maximum of the resolved strain-rate tensor amplitude would be almost unbounded. Hence, for the Smagorinsky model, it is reasonable to simply impose $C > 0$. For model A, however, the situation is different. The stability condition is the same in each realization

$$C\overline{\Delta}^{4/3} + \nu_0 > 0 \,, \tag{2.8}$$

resulting in the model parameter C being given by $C = \max\{C_d, -\nu_0 \overline{\Delta}^{-4/3}\}$. For simplicity, the same condition has been used for model B.

3. Application of the EADP to a time-evolving plane wake

In a previous study, the EADP has been successfully implemented for homogeneous turbulence in both forced (stationary) and decaying (non-stationary) situations. Here, we propose to investigate a flow with the added complexity of an inhomogeneous direction. The pseudospectral direct numerical simulation of the plane wake considered here has been described in detail by Moser & Rogers (1994) and Moser, Rogers & Ewing (1997). The spatial dependence of the independent variables is represented in the periodic streamwise and spanwise directions by Fourier basis functions and the cross-stream dependence is represented by a class of Jacobi polynomials on a mapped infinite domain. Up to $512 \times 195 \times 128$ modes are required to accurately resolve the turbulence. The Reynolds number based on the integrated mass flux deficit,

$$\mu = -\int_{-\infty}^{+\infty} (U(y) - U_\infty)\, dy, \tag{3.1}$$

is $R_e = \mu/\nu = 2000$. In a time-evolving plane wake, the integrated mass flux deficit is constant.

LES's of the same flow using the dynamic procedure and a filtered DNS field as an initial condition have been reported by Ghosal & Rogers (1997). The simulations were pseudospectral like the DNS, but the spatial dependence of the vorticity in the inhomogeneous cross-stream direction is represented in terms of Fourier modes on a finite domain. The appropriate non-periodic velocity field is then calculated using the method of Corral & Jimenez (1995). The number of modes used in the LES's was $64 \times 48 \times 16$ and the same number of modes and same numerical method have been adopted for the LES's examined here. Thus each LES mode represents up to 260 DNS modes.

3.1 The initial conditions

In order to justify ensemble-averaging, the R velocity fields should be *statistically equivalent* and *statistically independent*. Carati *et al.* (1996) have proposed that acceptable initial conditions for LES $v(\mathbf{x}, 0) = v_0(\mathbf{x}; w_l)$ should be generated using random numbers w_l and should satisfy some constraints: $P_s[v_0] = p_s, \quad s = 1, \ldots S$. For example, the constraints could be obtained by matching the mean velocity profile, the energy spectrum, etc. Proposed definitions for "statistically equivalent" and "statistically independent" were also given. Two LES's are statistically equivalent if the domain of the flow and the boundary conditions are exactly the same and if the initial conditions satisfy the same set of constraints. Two LES's are statistically independent if the initial conditions are generated with uncorrelated random numbers w_l. For the time-evolving plane wake, a large number of quantities are measured, and any number of them might be considered as constraints that need to be maintained by all realizations (e.g. profiles of mean velocity, turbulent kinetic energy, enstrophy, etc.). The question then becomes: is it possible to create R independent

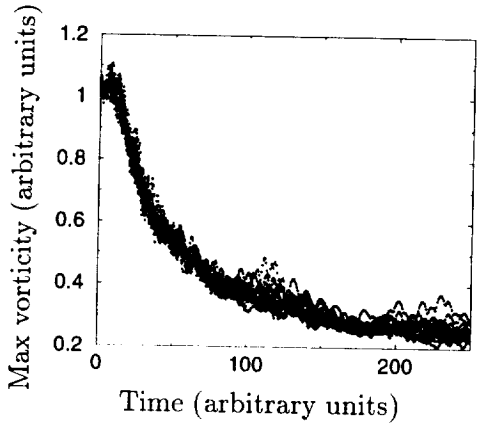

FIGURE 2. Maximum grid-point value of the x-component of the resolved vorticity, $\omega_{x\,\mathrm{max}}^{r}$, as a function of time for each of the 16 realizations.

initial LES fields that maintain all the relevant quantities in the plane wake from one single filtered DNS field? Since the observed quantities of interest are obtained through $(x-z)$-plane averaging, they are invariant under the transformation

$$\overline{u}_i(x,y,z,t_0) \longrightarrow \overline{u}_i(x+\delta_x,y,z+\delta_z,t_0)\,. \tag{3.2}$$

Thus by using R values of (δ_x^r,δ_z^r), R different (but statistically identical) initial velocity fields can be produced from the filtered DNS field by shifting in the $(x-z)$ plane. These initial fields clearly satisfy the requirement that the LES realizations be statistically equivalent because the initial values of any plane-averaged quantity are identical. However, this procedure does not produce statistically independent initial conditions, even with random choices for (δ_x^r,δ_z^r), because the two fields are identical and simply shifted in space. Without the subgrid model terms, this correlation would maintain itself in time. However, the model terms will have the desirable effect of de-correlating the different members of the ensemble. This results because the universal model terms act at the same $(x-z)$ location in all the realizations, not at the same relative position in the shifted flows. An example of this de-correlation is given in Fig. 2, where the maximum grid-point value of the streamwise vorticity component $\omega_{x\,\mathrm{max}}^{r}$ for each of the 16 realizations is plotted as a function of time (model A has been used to generate this plot). Because this maximum is computed on a grid that has been shifted by a random (nonintegral multiple of the grid-spacing) shift, $\omega_{x\,\mathrm{max}}^{r}$ is not the same for all the realizations, even at $t=0$. The fairly rapid spreading of the values associated with the different realizations suggests that the different LES fields de-correlate fairly quickly.

If a very large number of realizations is used, the coefficient C obtained through the EADP is independent of x and z. It reduces to the value of C obtained by the plane-averaged dynamic procedure. In this limit, the various realizations will not diverge and the EADP, with the peculiar construction of the initial conditions presented above, will degenerate into a collection of LES based on the plane-averaged dynamic procedure. A more sophisticated procedure for building the initial conditions would then be needed if a large number of realizations were required for

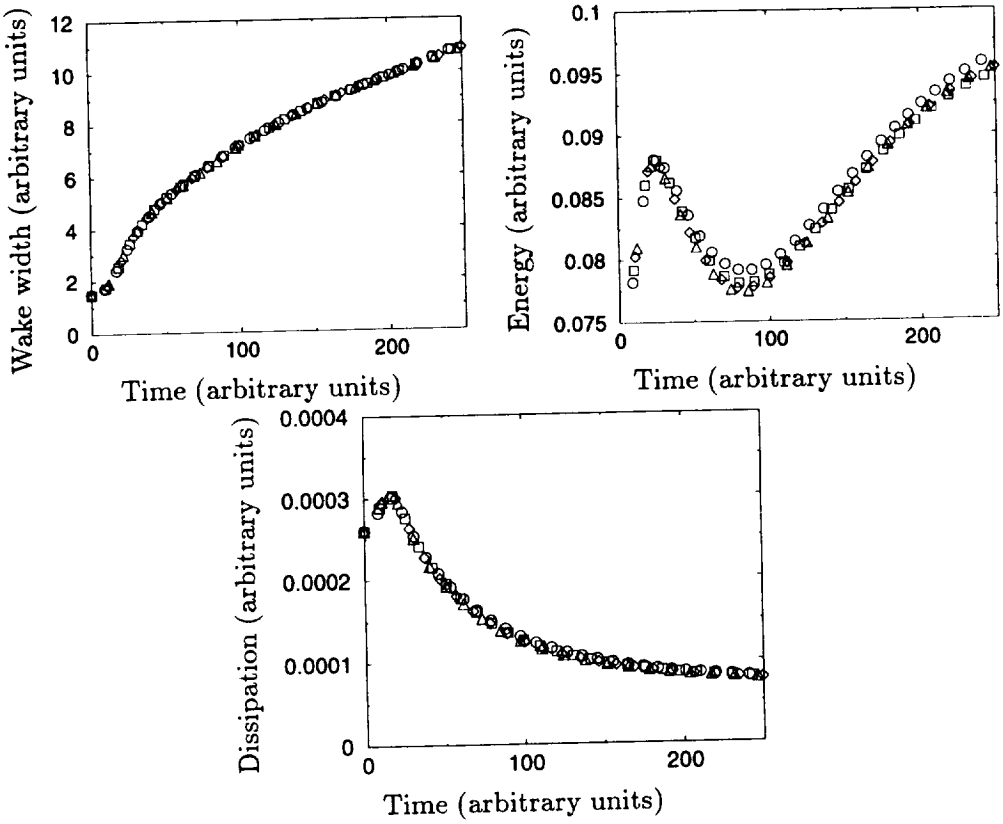

FIGURE 3. Convergence of the ensemble-averaged evolutions of the wake width (top-left), resolved turbulent kinetic energy density integrated in y (top-right) and resolved turbulent kinetic energy dissipation integrated in y (bottom). Various ensemble sizes are compared: $R = 4$, ○ ; $R = 8$ □ ; $R = 16$, ◇ ; and $R = 32$, △ .

statistical convergence. However, it will be seen that $R = 16$ realizations are adequate for satisfactorily converged statistics, and this issue is irrelevant in the present study.

3.2 Tests of convergence

In order to test the convergence of the EADP results for increasing values of R, two types of tests were performed. First, the ensemble-averaged values of several relevant quantities in the time-evolving wake flow have been compared for various ensemble sizes. In particular, the results for *i*) the wake width, *ii*) the turbulent kinetic energy density integrated in y, and *iii*) the turbulent kinetic energy dissipation integrated in y are compared for $R = 4$, 8, 16, and 32. As can be seen from Fig. 3, the values obtained with 16 and 32 realizations are almost indistinguishable for all three quantities.

Second, the influence of the ensemble size on the computed eddy-viscosity has been examined. The profile of the mean eddy-viscosity and the fraction of grid points for which the eddy-viscosity has been clipped according to the criterion (2.8)

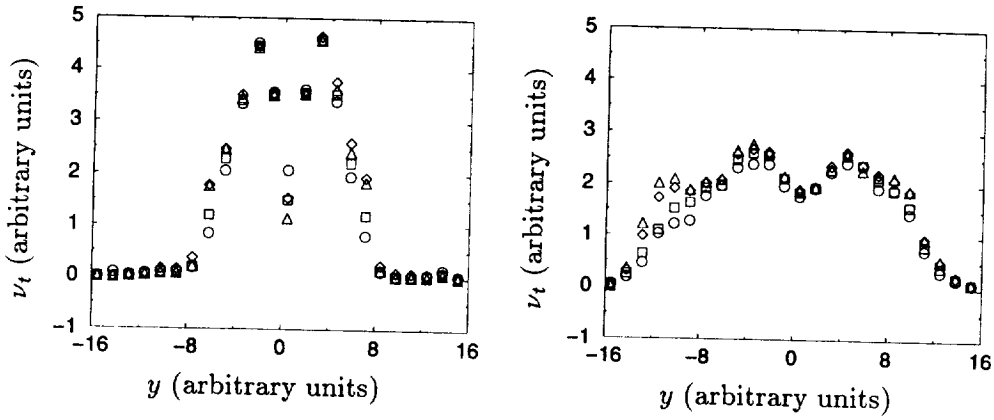

FIGURE 4. Convergence of the eddy-viscosity profile for $t = 0$ (left) and $t = 250$ (right). Various ensemble sizes are compared: $R = 4$, ○ ; $R = 8$, □ ; $R = 16$, ◇ ; and $R = 32$, △ . The eddy-viscosity is normalized by the molecular viscosity.

are compared for the same values of R in Figs. 4 and 5. As seen in Fig. 4, the eddy-viscosity profile depends only weakly on the number of realizations for values of R between 4 and 32, and the profiles are nearly identical for $R = 16$ and $R = 32$. As expected, the fraction of grid points requiring clipping of the model coefficient C rapidly decreases with R (Fig. 5). The total fraction of clipped points integrated in y is less than 1% for $R = 16$ during the entire simulation. This, combined with the very small change in most of the ensemble-averaged quantities as R is increased from 16 to 32, supports the adoption of $R = 16$ as a reasonable ensemble size for both model testing and production LES. Because this value of R is the same as that required for the simulation of homogeneous turbulence, it seems reasonable to hope that $R = 16$ provides an adequate ensemble size for the EADP in even more complicated geometries.

The comparison between various ensemble sizes is presented here only for model A (2.4). However, the same conclusions concerning the convergence of the results and the appropriate value of R are obtained when either the Smagorinsky model or model B (2.5) is used as well.

3.3 Comparison of models

As mentioned in the introduction, an important motivation for developing the EADP is the possibility of investigating new concepts in subgrid-scale modeling. Here, the filtered DNS of Moser, Rogers, & Ewing (1997) is compared with the LES predictions of Ghosal & Rogers (1997) and the predictions of the models presented in Section 2. We have also added the results of a LES without a subgrid-scale model. In all cases, and in agreement with the conclusion of the preceding section, the simulations for the EADP have been performed with $R = 16$.

The first important conclusion is that the plane-averaged and ensemble-averaged dynamic procedures lead to indistinguishable results when they are applied with the same model. For instance, in the LES of Ghosal & Rogers (1997), the plane-averaged dynamic procedure has been implemented with the standard Smagorinsky

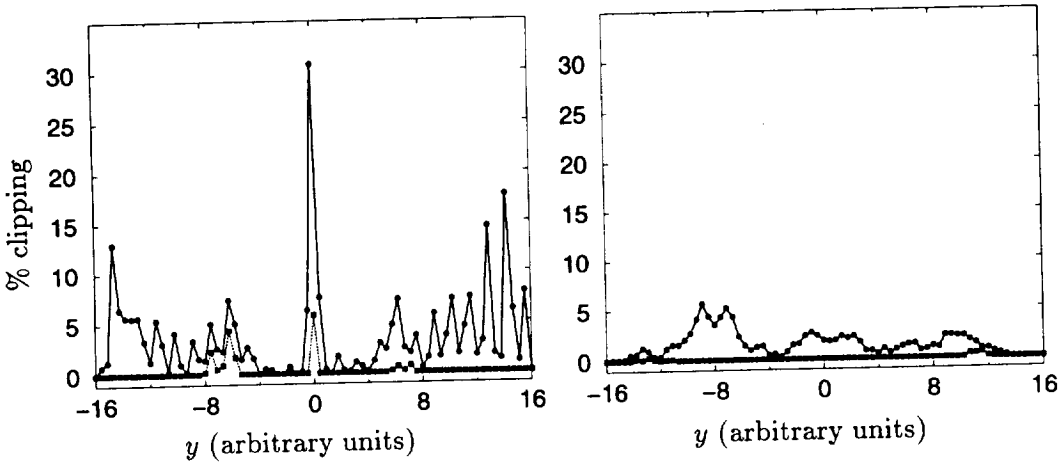

FIGURE 5. Profile of the fraction of grid points requiring clipping of the coefficient C at $t = 0$ (left) and $t = 250$ (right). Two ensemble sizes are compared: $R = 4$, • ; and $R = 32$, ▪ .

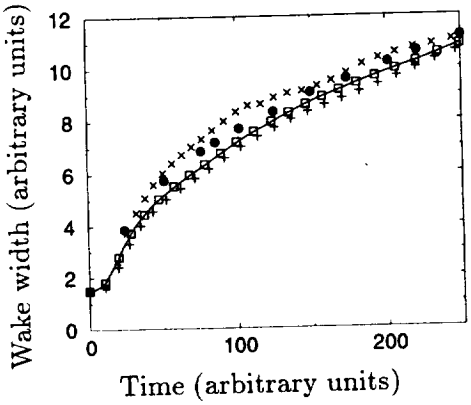

FIGURE 6. The wake width evolution obtained from the filtered DNS, •; the Smagorinsky model, —; Model A, □ ; Model B, +; and no model, ×.

model. Their results are identical to those obtained when the Smagorinsky model is used with the EADP. In the following comparison, the Smagorinsky case will refer to both the EADP and the plane-averaged LES of Ghosal & Rogers.

The evolution of the wake width is illustrated in Fig. 6. This quantity is dominated by large-scale flow features and consequently is not strongly affected by the models. Actually, the prediction of the LES without a subgrid-scale model (an under-resolved DNS) provides a reasonable approximation to the value obtained by filtering the DNS data.

The turbulent kinetic energy density integrated in y is more difficult to predict using LES. As can be seen in Fig. 7, not using a subgrid-scale model results in poor prediction of resolved energy density. Model A leads to almost the same result as the Smagorinsky model. This is a general feature of the dynamic procedure

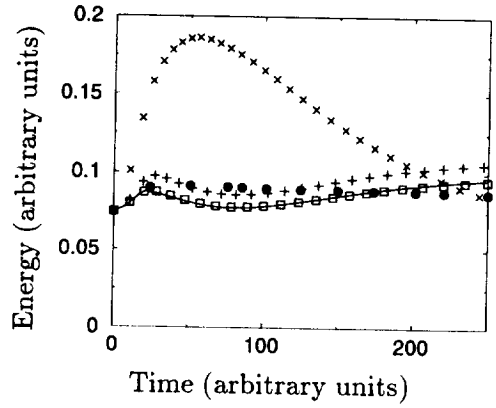

FIGURE 7. The evolution of the resolved turbulent kinetic energy density integrated in y obtained from the filtered DNS •; the Smagorinsky model, —; Model A, □ ; Model B, +; and no model, ×.

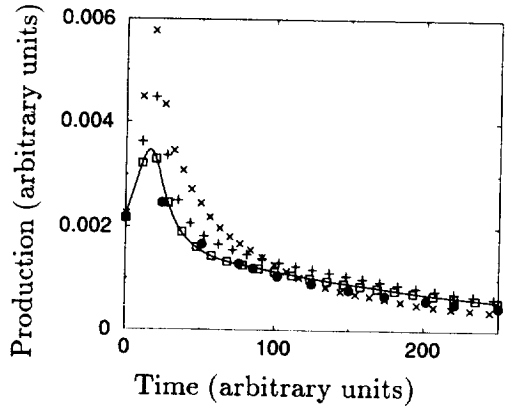

FIGURE 8. The evolution of the resolved turbulent kinetic energy production integrated in y obtained from the filtered DNS •; the Smagorinsky model, —; Model A, □ ; Model B, +; and no model, ×.

that has been noted previously (Wong & Lilly 1994; Carati, Jansen & Lund 1995). However, within the dynamic procedure approach the model A is computationally much cheaper to implement than the Smagorinsky model, and this motivates the use of the scaling (2.4) for the eddy-viscosity instead of (2.3). The model B, from which the ensemble-averaged resolved strain-rate has been removed, leads to results that better fit the DNS data in the early stages of the simulation. At later times, however, this model is further from the filtered DNS values than model A and the Smagorinsky model. In general the predictions of all three models seem comparable.

The evolution of the turbulent kinetic energy production integrated in y is presented in Fig. 8. The no-model LES prediction for the resolved energy production is much too high in the early stage and too low at later times. Again, model A

leads to almost the same result as the Smagorinsky model. Model B systematically over-predicts the energy production. However, it would be rather speculative to draw any definitive conclusion regarding which model (A or B) is better from the results presented here.

4. Conclusions

The motivations for the present study were *i*) the determination of the required number of realizations for ensemble-averaged determination of subgrid LES terms and *ii*) the demonstration of new modeling concepts than can be implemented within the framework of the EADP.

Simulations with $R = 16$ lead to results that do not differ significantly from those obtained with $R = 32$. Hence, $R = 16$ is a reasonable choice for the ensemble size. This is the same value recommended by Carati *et al.* (1996) for homogeneous turbulence, suggesting that this might be an adequate ensemble size for converged results even in more complex flows. This is, of course, a major encouragement for further developing the EADP methodology.

All three subgrid-scale models employed with the EADP procedure resulted in comparable predictions of various filtered DNS statistics, whereas not using any model provided inadequate estimates of quantities other than the mean velocity profile. Predictions using the Smagorinsky model and the EADP procedure are identical to those made by conventional plane-averaged evaluation of the Smagorinsky model terms. Model A leads to results that are very similar to those predicted by the Smagorinsky model. Hence the present study suggests that, in the context of the dynamic procedure, the Smagorinsky model should be abandoned in favor of model A, which is computationally much cheaper. We have also introduced a new model (model B), which explicitly requires ensemble-averaged statistics to predict the subgrid terms (although the same model could be implemented without an ensemble if the flow has a homogeneous direction for averaging). Having an ensemble of LES's opens up many new possibilities for subgrid-scale modeling. The subgrid-scale tensor has traditionally been modeled in terms of the resolved strain-rate tensor $\overline{S}_{ij}^r$. With an ensemble of LES realizations, it is possible to build up new models based on quantities that explicitly require an averaging procedure such as the ensemble-averaged resolved strain-rate tensor $\langle \overline{S}_{ij}^r \rangle$ (as in model B). Another tensor that could be an interesting ingredient in subgrid-scale modeling is the second-order velocity correlation $\langle (\overline{u}_i^r - \langle \overline{u}_i^r \rangle)(\overline{u}_j^r - \langle \overline{u}_j^r \rangle) \rangle$.

Considering the rapid development of parallel computers, the use of an ensemble of statistically equivalent and independent LES's can be regarded as a very promising technique. This technique can be implemented with fairly small ensemble sizes. Original modeling concepts that cannot be implemented in fully inhomogeneous flows by conventional LES techniques are possible within the framework of the EADP and warrant further examination.

REFERENCES

CARATI, D., JANSEN K. & LUND, L. 1995 A family of dynamic models for large-eddy simulation, in *CTR Annual Research Briefs 1995*, Center for Turbulence Research, NASA Ames/Stanford Univ., 35-40.

CARATI, D., WRAY, A. & CABOT, W. 1996 Ensemble-averaged dynamic modeling, in the *Proceedings of the 1996 Summer Program*, Center for Turbulence Research, NASA Ames/Stanford Univ., 237-248.

CORRAL, R. & JIMENEZ, J. 1995 Fourier/Chebyshev methods for the incompressible Navier–Stokes equations in infinite domains. *J. Comput. Phys.* **121,** 261-270.

GHOSAL, S., LUND, T., MOIN, P. & AKSELVOLL, K. 1995 The Dynamic Localization Model for large eddy simulation of turbulent flows. *J. Fluid Mech.* **286,** 229-255.

GHOSAL, S. & ROGERS, M.M. 1997 A numerical study of self-similarity in a turbulent plane wake using large-eddy simulation. *Phys. Fluids.* **9,** 1729-1739.

MOSER, R.D. & ROGERS, M.M. 1994 Direct simulation of a self-similar plane wake. *NASA Tech. Memo 108815.*

MOSER, R.D., ROGERS, M.M. & EWING, D.W. 1997 Self-similarity of time evolving plane wakes. *J. Fluid Mech.* **367,** 255-289.

SMAGORINSKY, J. S. 1963 General circulation experiments with the primitive equations: I. The basic experiment. *Mon. Weather Rev.* **91,** 99-164.

WONG, V. C. & LILLY, D. 1994 A comparison of two subgrid closure methods for turbulent thermal convection. *Phys. Fluids.* **6,** 1016-1023.

Center for Turbulence Research
Proceedings of the Summer Program 1998

Analysis and subgrid modeling of shock-wave/boundary-layer interaction

By N. A. Adams[1], S. Stolz[1], A. Honein AND K. Mahesh

This paper considers two different issues that arise in LES of supersonic wall bounded flows. First, an *a priori* analysis of subgrid-scale models in a highly compressible environment is conducted. DNS data from a Mach 3 compression-corner are used for this purpose. Models of the scale-similarity type correlate best with filtered DNS data. Lower correlations are obtained with the dynamic mixed model, the dynamic Smagorinsky model, and the fixed-coefficient Smagorinsky model. Second, the possibility of treating the shock as a subgrid scale is investigated. It is found that a straightforward application of dynamic eddy-viscosity models is unsuccessful. A direct deconvolution is found to give a proper agreement between a 6th order spectral-like finite-difference scheme and a 5th order ENO shock-capturing scheme for the simple case of a 1D convected $M = 3$ shock.

1. Introduction

Large-eddy simulation (LES) is now a viable tool for studying moderately complex turbulent flows at Reynolds numbers for which direct numerical simulation (DNS) is infeasible. Most LES performed have been in incompressible flows. This paper considers LES of a highly compressible flow – the interaction of a shock wave with a Mach 3 turbulent boundary layer along a compression corner. Two issues relevant to the LES of this flow are studied: the accuracy of subgrid models, and the effect of subgrid models on the shock, which itself can be a subgrid-scale entity.

In this paper we conduct an *a priori* analysis of DNS data for supersonic compression ramp flow. Several models are considered. Of particular concern are SGS terms in the energy equation, where compressibility effects are significant. Next, we briefly address the question of whether and how a shock can be treated as a subgrid-scale structure.

2. Part 1: Analysis of compression-corner data

In this section, we focus on *a priori* analysis of data from DNS of a compression ramp at $M = 3$, $Re_\theta = 1685$ and a deflection angle of 18°. The numerical method used in the DNS is described by Adams (1998; results are analyzed and reported by Adams & Kleiser (1998).

1 ETH Zürich, Institute of Fluid Dynamics, CH-8092 Zürich, Switzerland.

2.1 Mathematical model

Considering the conservative Navier-Stokes equations in curvilinear coordinates, we apply a filter operation with filter width Δ in computational space ξ to the dependent variables

$$\overline{\phi}(\xi) = G(\xi - \xi') \otimes \phi(\xi') = \int_\Omega G(\xi - \xi')\phi(\xi')d\xi' \quad .$$

We obtain the fundamental equations for the resolved conservative variables $\{\overline{\rho},\ \tilde{u}_i,\ \tilde{E}\}$. Favre-filtered quantities are denoted by "$\tilde{\bullet}$". They are computed from a mass-weighted filtering operation

$$\tilde{\phi} = \frac{\overline{\rho\phi}}{\overline{\rho}} \quad .$$

The nomenclature of the following equations may be found in Vreman (1995) and Adams (1998). The filtered continuity equation becomes

$$\tfrac{1}{J}\tfrac{\partial \bar{\rho}}{\partial t} + \tfrac{\partial}{\partial \xi_i}\left(\tfrac{\bar{\rho}\tilde{u}_j}{J}\tfrac{\partial \xi_i}{\partial x_j}\right) = \gamma_{C1} + \gamma_{C2}, \quad \text{where}$$

$$\begin{aligned} \gamma_{C1} &= \tfrac{\partial}{\partial \xi_k}\left(\tfrac{\overline{\rho u_j}}{J}\tfrac{\partial \xi_k}{\partial x_j}\right) - \tfrac{\partial}{\partial \xi_k}\left(\tfrac{\overline{\rho u_j}}{J}\tfrac{\partial \xi_k}{\partial x_j}\right) \\ \gamma_{C2} &= \tfrac{\partial}{\partial \xi_k}\left(\tfrac{\overline{\rho u_j}}{J}\tfrac{\partial \xi_k}{\partial x_j}\right) - \overline{\tfrac{\partial}{\partial \xi_k}\left(\tfrac{\rho u_j}{J}\tfrac{\partial \xi_k}{\partial x_j}\right)} \end{aligned} \quad . \tag{1}$$

γ_{C1} is an $\mathcal{O}(\Delta^2)$ error term, which results from the non-identity mapping between computational space ξ_i and physical space x_i. γ_{C2} is an error due to a variable filter width (commutation error). This error vanishes since in our case the filter G is not an explicit function of ξ_i and filtering is peformed in computational space.

The filtered momentum equations are

$$\begin{aligned} &\tfrac{1}{J}\tfrac{\partial \bar{\rho}\tilde{u}_i}{\partial t} + \tfrac{\partial}{\partial \xi_k}\left(\tfrac{\bar{\rho}\tilde{u}_i\tilde{u}_j}{J}\tfrac{\partial \xi_k}{\partial x_j} + \tfrac{\bar{p}}{J}\delta_{ij}\tfrac{\partial \xi_k}{\partial x_j}\right) - \tfrac{\partial}{\partial \xi_k}\left(\tfrac{\check{\sigma}_{ij}}{J}\tfrac{\partial \xi_k}{\partial x_j}\right) = \\ &= -\tfrac{\partial}{\partial \xi_k}\left(\tfrac{\bar{\rho}\tau_{ij}}{J}\tfrac{\partial \xi_k}{\partial x_j}\right) + \beta_i + \gamma_{I1i} + \gamma_{I2i} \end{aligned}$$

$$\bar{\rho}\tau_{ij} = \bar{\rho}(\widetilde{u_i u_j} - \tilde{u}_i\tilde{u}_j)$$

$$\sigma_{ij} = \tfrac{\mu}{Re}S_{ij}$$

$$S_{ij} = \tfrac{\partial \xi_k}{\partial x_j}\tfrac{\partial u_i}{\partial \xi_k} + \tfrac{\partial \xi_k}{\partial x_i}\tfrac{\partial u_j}{\partial \xi_k} - \tfrac{2}{3}\tfrac{\partial \xi_k}{\partial x_l}\tfrac{\partial u_l}{\partial \xi_k}\delta_{ij} \quad . \tag{2}$$

$$\beta_i = \tfrac{\partial}{\partial \xi_k}\left(\tfrac{\bar{\sigma}_{ij} - \check{\sigma}_{ij}}{J}\tfrac{\partial \xi_k}{\partial x_j}\right)$$

$$\begin{aligned} \gamma_{I1i} &= \tfrac{\partial}{\partial \xi_k}\left(\tfrac{\overline{\rho u_i u_j + p\delta_{ij} - \sigma_{ij}}}{J}\tfrac{\partial \xi_k}{\partial x_j}\right) - \tfrac{\partial}{\partial \xi_k}\left(\tfrac{\overline{\rho u_i u_j + p\delta_{ij} - \sigma_{ij}}}{J}\tfrac{\partial \xi_k}{\partial x_j}\right) \\ \gamma_{I2i} &= \tfrac{\partial}{\partial \xi_k}\left(\tfrac{\overline{\rho u_i u_j + p\delta_{ij} - \sigma_{ij}}}{J}\tfrac{\partial \xi_k}{\partial x_j}\right) - \overline{\tfrac{\partial}{\partial \xi_k}\left(\tfrac{\rho u_i u_j + p\delta_{ij} - \sigma_{ij}}{J}\tfrac{\partial \xi_k}{\partial x_j}\right)} \end{aligned}$$

The term β_i arises from the non-linearity of the viscous stresses. γ_{I1} and γ_{I2} are error terms analogous to γ_{C1} and γ_{C2}.

The resolved-energy equation is obtained by filtering the enthalpy equation and by adding the filtered momentum equation, multiplied by $\tilde{u}_i$:

$$\frac{1}{J}\frac{\partial \check{E}}{\partial t} + \frac{\partial}{\partial \xi_k}\left(\frac{\check{E}+\check{p}}{J}\tilde{u}_j\frac{\partial \xi_k}{\partial x_j}\right) - \frac{\partial}{\partial \xi_k}\left(\frac{\check{\sigma}_{ij}\tilde{u}_i}{J}\frac{\partial \xi_k}{\partial x_j}\right) + \frac{\partial}{\partial \xi_k}\left(\frac{\check{q}_j}{J}\frac{\partial \xi_k}{\partial x_j}\right) =$$
$$= -\alpha_1 - \alpha_2 - \alpha_3 + \alpha_4 + \alpha_5 - \alpha_6 + \gamma_{E1} + \gamma_{E2}$$

$$\begin{aligned}
q_j &= \frac{\mu}{(\gamma-1)RePrM^2}\frac{\partial \xi_k}{\partial x_j}\frac{\partial T}{\partial \xi_k} \\
\alpha_1 &= \tilde{u}_i\frac{\partial}{\partial \xi_k}\left(\frac{\bar{\rho}\tau_{ij}}{J}\frac{\partial \xi_k}{\partial x_j}\right) \\
\alpha_2 &= \frac{1}{\gamma-1}\frac{\partial}{\partial \xi_k}\left(\frac{\overline{pu_j}-\bar{p}\tilde{u}_j}{J}\frac{\partial \xi_k}{\partial x_j}\right) \\
\alpha_3 &= \frac{1}{J}\left(\overline{p\frac{\partial u_j}{\partial \xi_k}} - \bar{p}\frac{\partial \tilde{u}_j}{\partial \xi_k}\right)\frac{\partial \xi_k}{\partial x_j} \\
\alpha_4 &= \frac{1}{J}\left(\overline{\sigma_{ij}\frac{\partial u_i}{\partial \xi_k}} - \bar{\sigma}_{ij}\frac{\partial \tilde{u}_i}{\partial \xi_k}\right)\frac{\partial \xi_k}{\partial x_j} \\
\alpha_5 &= \frac{\partial}{\partial \xi_k}\left(\frac{\tilde{u}_i\bar{\sigma}_{ij}-\tilde{u}_i\check{\sigma}_{ij}}{J}\frac{\partial \xi_k}{\partial x_j}\right) \\
\alpha_6 &= \frac{\partial}{\partial \xi_k}\left(\frac{\bar{q}_j-\check{q}_j}{J}\frac{\partial \xi_k}{\partial x_j}\right)
\end{aligned} \tag{3}$$

$$\gamma_{H1} = \frac{\partial}{\partial \xi_k}\left[\left(\frac{\overline{pu_j}}{\gamma-1}+q_j\right)\frac{1}{J}\frac{\partial \xi_k}{\partial x_j}\right] - \frac{\partial}{\partial \xi_k}\left[\overline{\left(\frac{pu_j}{\gamma-1}+q_j\right)\frac{1}{J}\frac{\partial \xi_k}{\partial x_j}}\right] + \frac{1}{J}\overline{p\frac{\partial u_j}{\partial \xi_k}}\frac{\partial \xi_k}{\partial x_j} -$$
$$-\overline{\frac{p}{J}\frac{\partial u_j}{\partial \xi_k}\frac{\partial \xi_k}{\partial x_j}} + \overline{\frac{\sigma_{ij}}{J}\frac{\partial u_i}{\partial \xi_k}\frac{\partial \xi_k}{\partial x_j}} - \frac{1}{J}\overline{\sigma_{ij}\frac{\partial u_i}{\partial \xi_k}}\frac{\partial \xi_k}{\partial x_j}$$

$$\gamma_{H2} = \frac{\partial}{\partial \xi_k}\left[\overline{\left(\frac{pu_j}{\gamma-1}+q_j\right)\frac{1}{J}\frac{\partial \xi_k}{\partial x_j}}\right] - \overline{\frac{\partial}{\partial \xi_k}\left[\left(\frac{pu_j}{\gamma-1}+q_j\right)\frac{1}{J}\frac{\partial \xi_k}{\partial x_j}\right]}$$

$$\gamma_{E1} = \tilde{u}_i\gamma_{I1i} + \gamma_{H1}$$

$$\gamma_{E2} = \tilde{u}_i\gamma_{I2i} + \gamma_{H2}$$

A "$\check{\bullet}$" indicates that the respective quantities are computed according to their definition but with resolved primitive variables, e.g., $\check{E} = \bar{p}/(\gamma-1) + \overline{\bar{\rho}\tilde{u}_i\tilde{u}_i/2}$, which we call the total resolved energy. Note that the filtered Jacobian $\overline{\partial \xi_i/\partial x_j}$ has been replaced by the unfiltered $\partial \xi_i/\partial x_j$. This contributes another error of order $\mathcal{O}(\Delta^2)$, which is on the order of the leading error terms. Whereas subgrid-scale stresses formally are analogous to the incompressible case, additional terms appear in Eqs. (1) - (3) due to the non-vanishing velocity-field divergence and due to variable viscosity. Some of these additional subgrid-scale terms have an intuitive physical interpretation as shown in Table 1.

$SGS-term$	physical interpretation
α_1	SGS-dissipation.
α_2	Pressure-velocity correlation; reversible transfer between internal and kinetic energy; by rearrangement an expression similar to the turbulent heat flux in RANS-modeling is found: $\alpha_2 = \frac{1}{(\gamma-1)\gamma M^2}\frac{\partial}{\partial \xi_k}\left(\frac{\overline{\rho T u_j}-\bar{\rho}\tilde{T}\tilde{u}_j}{J}\frac{\partial \xi_k}{\partial x_j}\right)$.
α_3	Pressure-dilatation correlation.
α_4	SGS-molecular dissipation.

TABLE 1. Physical interpretation of SGS-terms.

2.2 A priori analysis

For an assessment of the correlation between modeled and exact data, an *a priori* analysis of a DNS data base for a turbulent supersonic compression ramp (Adams and Kleiser, 1998) was performed. The filter used here is a Padé filter of 2^{nd} order (Lele, 1992) where the advantage of having a continuous parameter to change the effective filter width is used to tune the filter in order to best approximate a Gauß transfer function in wavenumber space. The cut-off wavenumber is $k_c = \pi/4$ for the *grid filter* and $k_c' = \pi/8$ for the *test filter* where required. The filter formula is

$$\alpha \bar{f}_{i-1} + \bar{f}_i + \alpha \bar{f}_{i+1} = a f_i + \frac{b}{2}(f_{i-1} + f_{i+1}) \tag{4}$$

where $b = a = 1/2 + \alpha$. The effective cutoff wavenumber is given by Δ in the exact Gauß transfer function

$$\hat{G}(\xi) = \mathrm{e}^{-(\Delta\xi/2)^2/8}$$

where ξ is the wavenumber normalized with the grid-spacing h. By approximating the Gauß transfer function by the transfer function of filter (4), one finds the best matches for $\alpha = -0.2$ for an effective filter width $\Delta = 4h$ and $\alpha = -0.43$ for an effective filter width $\Delta = 8h$.

We refer to three different subdomains of the compression corner geometry, the locations of which are indicated in Fig. 1. The first (A) is located ahead of the shock, the second (B) around the corner, and the last (C) behind the shock. All blocks span the domain in y-direction. The streamwise extent of block A is about 2.7 mean-boundary-layer thicknesses (at inflow) δ_0, and it has a height of about $1.2\delta_0$. Block B is about $2\delta_0$ long and is about $1.2\delta_0$ high (above the plate); the extents of block C are about $2.7\delta_0$ and $1.4\delta_0$, respectively.

By a comparison of the L_2-norms (see Table 2) of the SGS-terms in the momentum equation, the subgrid-scale stresses τ_{ij} and related terms in the energy equation are found to be dominant.

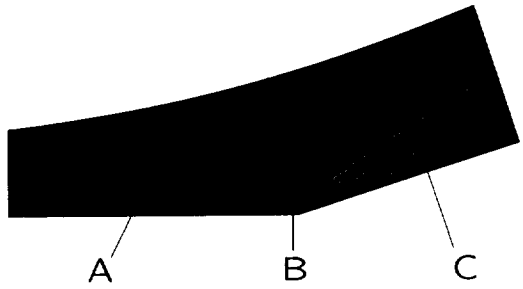

FIGURE 1. Location of subdomains for the compression corner geometry.

SGS-	L_2-norm				SGS-	L_2-norm			
term	global	A	B	C	term	global	A	B	C
$\tau_{xx} \cdot 10^3$	5.908	3.611	10.297	14.769	α_1	5.190	0.885	4.497	7.401
$\tau_{xy} \cdot 10^3$	1.330	0.424	3.124	3.143	α_2	3.255	0.694	3.329	5.535
$\tau_{xz} \cdot 10^3$	1.745	0.338	2.363	4.293	α_3	1.901	0.430	2.254	3.450
$\tau_{yy} \cdot 10^3$	2.615	0.708	5.955	6.202	α_4	0.480	0.113	0.717	1.407
$\tau_{yz} \cdot 10^3$	0.753	0.219	1.613	1.786	α_5	0.070	0.038	0.092	0.206
$\tau_{zz} \cdot 10^3$	2.512	0.507	4.637	5.149	α_6	0.114	0.127	0.181	0.229
$\frac{\partial \tau_{1j}}{\partial x_j}$	17.123	1.132	16.336	54.340	β_1	0.033	0.013	0.055	0.079
$\frac{\partial \tau_{2j}}{\partial x_j}$	4.980	1.297	9.599	12.960	β_2	0.049	0.045	0.105	0.099
$\frac{\partial \tau_{3j}}{\partial x_j}$	16.254	1.167	13.089	51.517	β_3	0.536	0.230	1.188	1.238

TABLE 2. L_2-norms of SGS-terms calculated from DNS-data.

The terms β_i (see Eq. 2) are smaller by at least a factor of 5 in subdomain A than the respective components of the divergence of the SGS-stress tensor. In the subdomains B and C the β_i are even smaller. They vanish in an isothermal flow since there $\bar{\mu} = \check{\mu} = \mu(\tilde{T}) = const$ and accordingly $\bar{\sigma} = \check{\sigma}$. The most significant terms in the energy equation are α_1 through α_4. The magnitude of α_5 and α_6 is about one to two orders of magnitude smaller.

In order to evaluate the performance of the models, a correlation coefficient C and a ratio A between model predictions and filtered DNS data are computed:

$$C(E,M) = \frac{\langle EM \rangle - \langle E \rangle \langle M \rangle}{\sqrt{\langle E^2 \rangle - \langle E \rangle^2} \sqrt{\langle M^2 \rangle - \langle M \rangle^2}}$$

and

$$A(E,M) = \sqrt{\frac{\langle (E(\mathbf{x}))^2 \rangle}{\langle (M(\mathbf{x}))^2 \rangle}} \ .$$

Herein, $\langle \cdot \rangle$ denotes an average over all points of the subdomain; E is the filtered DNS data and M is the SGS model data. If C is 1, both filtered DNS and approximation are perfectly correlated. Their magnitude is the same if $A = 1$.

2.2.1 Momentum equation

In Table 3 we show A and C for τ_{ij} and α_1 for subdomain B and different subgrid models. The different models used are the Smagorinsky model with Yoshizawa's extension (Yoshizawa, 1986)

$$m_{ij} = -\overline{\rho} C_S^2 \Delta^2 \sqrt{\frac{1}{2} S_{ij} S_{ij}} \left(S_{ij} - \frac{2}{3} \delta_{ij} \frac{\partial u_k}{\partial x_k} \right) + \frac{2}{3} C_k \delta_{ij} \Delta^2 \sqrt{\frac{1}{2} S_{ij} S_{ij}}$$

$$\text{with} \quad S_{ij} = \frac{\partial u_i}{\partial x_j} + \frac{\partial u_j}{\partial x_i} \ , \quad C_S = 0.16 \quad \text{and} \quad C_k = 0.0886 \ ,$$

the dynamic mixed model (DMM, Zang *et al.*, 1993, Vreman *et al.*, 1994)

$$m_{ij} = \widetilde{\overline{\rho u_i}\ \overline{\rho u_j} \ / \ \overline{\rho}} - \widetilde{\overline{\rho u_i}}\ \widetilde{\overline{\rho u_j}} \ / \ \widetilde{\overline{\rho}} - \overline{\rho} C_d \Delta^2 \sqrt{\frac{1}{2} S_{ij} S_{ij}} \left(S_{ij} - \frac{2}{3} \delta_{ij} \frac{\partial u_k}{\partial x_k} \right)$$

where C_d is a dynamic coefficient, the scale-similarity model (SSM, Bardina *et al.*, 1983)

$$m_{ij} = \widetilde{\overline{\rho u_i}\ \overline{\rho u_j} \ / \ \overline{\rho}} - \widetilde{\overline{\rho u_i}}\ \widetilde{\overline{\rho u_j}} \ / \ \widetilde{\overline{\rho}} \ ,$$

and the resolved turbulent stresses with $r = \hat{\Delta}/\Delta = 2$ (Pruett, 1997)

$$m_{ij} = \frac{1}{r^2} \left((\overline{\rho u_i}\ \overline{\rho u_j} \ / \ \overline{\rho})\hat{} - \widehat{\overline{\rho u_i}}\ \widehat{\overline{\rho u_j}} \ / \ \hat{\overline{\rho}} \right) \ .$$

model		τ_{xx}	τ_{xy}	τ_{xz}	τ_{yy}	τ_{yz}	τ_{zz}	α_1
Smagorinsky/	C	0.813	0.514	-0.227	0.721	-0.092	0.660	0.215
Yoshizawa	A	2.113	7.430	2.470	1.160	4.328	1.289	2.116
dynamic	C	0.947	0.850	0.696	0.849	0.578	0.695	0.592
mixed-model	A	1.481	1.364	1.055	2.186	1.542	1.827	0.934
scale-simi-	C	0.967	0.918	0.862	0.949	0.846	0.945	0.854
larity model	A	1.554	1.906	1.628	2.943	2.509	2.902	2.875
resolved	C	0.914	0.784	0.632	0.907	0.694	0.904	0.670
	A	2.872	4.731	3.326	6.509	6.775	5.961	9.515

TABLE 3. Correlation coefficient C and ratio A of the L_2-norms over subdomain B for different SGS models.

FIGURE 2A. τ_{xz}, filtered DNS data

FIGURE 2B. τ_{xz}, scale - similarity model

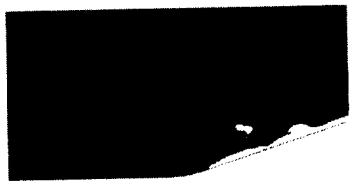

FIGURE 2C. τ_{xz}, dynamic mixed model

FIGURE 2D. τ_{xz}, resolved turbulent stress

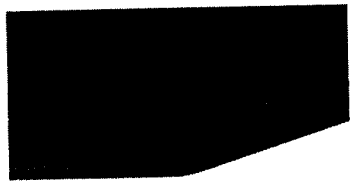

FIGURE 2E. τ_{xz}, Smagorinsky / Yoshizawa

The correlation coefficient C and the ratio A show that the Smagorinsky model correlates poorly with the filtered DNS data, see also Fig. 2E. The correlation of the turbulent resolved stresses is good for $\hat{\Delta}/\Delta = 2$ (Fig. 2D), but the magnitude is considerably under-predicted. For $\hat{\Delta}/\Delta = 1$, which coincides with the SSM, correlation and magnitude are improved (Fig. 2B). This agrees with the analytical predictions of Pruett (1997), who showed that the SSM should approximate SGS-stresses better than the turbulent resolved stresses with $\hat{\Delta}/\Delta = 2$. The DMM performs reasonably well (Fig. 2C, Table 3), but not as well as the SSM.

2.22 Energy equation

Three different models have been tested for the most significant SGS-terms of the energy equation. These models are the full dynamic mixed model (FDMM, Vreman, 1995), a scale-similarity-approach (SSM), and the resolved SGS quantities.

The SSM-approach for M_i amounts to computing the SGS-terms from the filtered variables,

$$\alpha_i = F(\mathbf{w}) \ , \qquad \beta_i = F(\mathbf{w}) \ ,$$

$$M_i = F(\overline{\mathbf{w}})$$

$$\text{with} \quad \mathbf{w} = (\rho,\ \rho u,\ \rho v,\ \rho w,\ p)^T \ .$$

The resolved SGS quantities M_i of the respective α_i are computed in the following way, using resolved and test-filtered data:

$$\alpha_i = \overline{f_i(\mathbf{w})} - f_i(\overline{\mathbf{w}}) \ ,$$

$$M_i = \frac{1}{r^2}\left(\widehat{f_i(\overline{\mathbf{w}})} - f_i(\hat{\overline{\mathbf{w}}})\right) \ .$$

Figure 4C shows that α_4 of the FDMM does not agree well with filtered DNS data. $\alpha_2 + \alpha_3$, as predicted by FDMM, correlates better with the filtered DNS data since it contains a scale-similarity part, Fig. 3D. The agreement between resolved SGS quantities and filtered DNS data is moderate, Fig. 3C. The SSM-approach gives much better correlation with filtered DNS data, Figs. 3B and 4B, and can furthermore provide predictions for all other SGS-terms as well, see Table 4.

model		α_2	α_3	α_4	α_5	α_6	β_1	β_2	β_3
dynamic	C	0.510		0.137	—	—	—	—	—
mixed model	A	0.762		0.628	—	—	—	—	—
scale-simi-	C	0.838	0.781	0.944	0.805	0.573	0.836	0.830	0.924
larity-model	A	3.001	2.926	5.127	2.981	0.932	3.320	1.847	3.467
resolved	C	0.330	0.552	—	—	—	—	—	—
	A	5.759	10.754	—	—	—	—	—	—

TABLE 4. Correlation coefficient C and ratio A of the L_2-norms over subdomain B for different SGS-terms of the energy equation and for β_i of the momentum equations.

3. Part 2: Treatment of shock wave

The numerical diffusion introduced by shock-capturing schemes interacts with subgrid-scale turbulence. In the recent past it has been attempted to make use of this feature by so-called MILES (monotonically integrated LES, i.e. using a monotone scheme which suppresses subgrid-scales) to model turbulent subgrid correlations, see Boris *et al.* (1992).

The question arises whether one can model non-turbulent subgrid-scales such as shocks by appropriate subgrid-scale models. This would allow for a unified approach to LES of shock-turbulence interaction similarly as with MILES but with full control of subgrid-scale modeling. Also the conservation equations could be advanced with a non-dissipative scheme such as spectral collocation or central finite-differences.

In this section, we briefly report on ongoing work on how to properly treat a shock as subgrid-scale entity in LES.

FIGURE 3A. $\alpha_2+\alpha_3$, filtered DNS data

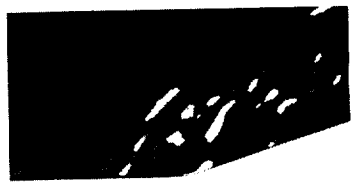

FIGURE 3B. $\alpha_2+\alpha_3$, scale-similarity model

FIGURE 3C. $\alpha_2+\alpha_3$, resolved turbulent quantities

FIGURE 3D. $\alpha_2 + \alpha_3$, dynamic mixed model

FIGURE 4A. α_4, filtered DNS data

FIGURE 4B. α_4, scale - similarity model

FIGURE 4C. α_4, dynamic mixed model

3.1 Shock as a sub-grid scale

If the filtering concept is interpreted strictly, then a shock, which is a discontinuity for an inviscid fluid, becomes a subgrid scale. Its resolved form can be represented by a filtered Heavyside function which is the error function. For simplicity we consider the one-dimensional filtered Euler equations

$$\frac{\partial \bar{u}}{\partial t} + \frac{\partial F(\bar{u})}{\partial x} = \mathcal{E} \tag{5}$$

with

$$\mathcal{E} = \frac{\partial F(\bar{u})}{\partial x} - \overline{\frac{\partial F(u)}{\partial x}} \tag{6}$$

where $\bar{u} = \{\bar{\rho},\ \tilde{u},\ \check{E}\}$ and $F(\bar{u}) = \{\bar{\rho}\tilde{u},\ \bar{\rho}\tilde{u}^2 + \bar{p},\ (\check{E} + \bar{p})\tilde{u}\}$. The right-hand side term $\mathcal{E}$ which is introduced by the filtering we will here call the error term. The filtered solution satisfies the modified differential Eq. (5), and $\mathcal{E}$ can have dissipative and dispersive character. If (5) could be solved exactly with an exact $\mathcal{E}$, then at any (t, x) the solution of (5) would correspond to the filtered solution of the unfiltered equation. The nonlinearity in both the filtered and the unfiltered equation is responsible for the wave steepening which generates the shock. The approximation of $\mathcal{E}$ needs be to sufficiently accurate in order to avoid that SGS-structures appear (it needs to "dissipate" the small scales generated by the nonlinearity) and to ensure the correct shock convection (it needs to compensate for the dispersive error to some extent). Concerning subgrid-scale approximation theory, a shock is a generic subgrid-scale with the advantage that one knows the exact and the filtered solution analytically.

3.2 Dynamic model

An obvious attempt is to approximate $\mathcal{E}$ by a standard SGS-model. Here we chose the dynamic Smagorinsky model since it has the basic form of a diffusion term, which benefits stabilization of the nonlinear term in Eq. (5). On the other hand it should be kept in mind that, as we have seen in Part 1, this model gives a poor approximation to $\mathcal{E}$. In our case the modeled term in the one-dimensional momentum equation is

$$m_2 = -\Delta_a C \bar{\rho} \left| \frac{\partial \tilde{u}}{\partial x} \right| \frac{\partial \tilde{u}}{\partial x}$$

and in the energy equation it is

$$m_3 = \tilde{u} \frac{\partial \bar{\rho} m_2}{\partial x} - \frac{\Delta_a^2}{(\gamma - 1) M^2} \frac{\partial}{\partial x} \left(\bar{\rho} C' \frac{\partial \tilde{u}}{\partial x} \frac{\partial \tilde{T}}{\partial x} \right) .$$

The constants C and C' are computed dynamically from a comparison with the test filtered Leonard expression for $\mathcal{E}$. Δ_a is the filter width. The main ingredients of standard dynamic modeling are the hypotheses of same SGS structure on grid and test filter levels and a dynamic constant being unaffected by the filtering. The

constants are filtered with the test filter of width Δ_b to avoid subgrid-scale contributions stemming from the ill-posedness of the coefficient-determination procedure.

Several variants of the dynamic procedure have been tried, also a form that emerges when the non-linear terms are explicitly filtered. It turned out, however, that if the explicit filtering formulation is applied consistently, terms of different character are forced to match by the dynamic procedure. A Taylor-series expansion shows that to leading order the approximation for the second component of $\mathcal{E}$,

$$L_2 \doteq \Delta_b^2 \mu_2 \bar{u}\bar{u}''$$

is forced to match

$$m_2 \doteq \Delta_a^2 \mu_2 |\bar{u}'|\bar{u}' \ ,$$

where the primes denote partial derivatives with respect to x, and μ_2 is the second moment of the filter kernel. For the generic filtered shock solution, it was shown that these terms have different character.

The test case where the model has been applied is the 1D $M = 3$ test case of Adams & Shariff (1996) without incoming perturbations. As underlying numerical schemes, an explicit 2^{nd} order finite difference scheme with 3rd order Runge-Kutta time integration and a 6th order Padé scheme (Lele, 1992) with same time integration were used. The former scheme can be stabilized by using a von Neumann-Richtmyer artificial viscosity for $\mathcal{E}$ (Hirsch, 1988) but not so the latter. None of the dynamic formulations we tried gave a stable solution of Eq. (5), so the concept of a standard dynamic model for shock computation was not pursued.

3.3 Deconvolution

From the notion that $\mathcal{E}$ can be understood not as a term to be modeled but as an error term which requires proper approximation, one can try to recover $\mathcal{E}$ by a deconvolution of the filter operation at each time instant to obtain u from $\bar{u}$. If this could be done exactly, $\mathcal{E}$ of Eq. (6) would vanish. Since a regularization of the deconvolution operation is required, a small error remains in practice. The filter used here is the same 2^{nd} order Padé filter as in section 3.2. The parameter α is chosen as $\alpha = -0.2$ in order to resemble a Gauß filter with effective width $\Delta = 4h$ (h is the grid spacing) and $\alpha = -0.43$ for $\Delta = 8h$. Note that the the smallest resolved wave number is assumed to be half the Nyquist wave number. It cannot be expected that at $\Delta = 2h$ a finite-difference scheme has any useful resolution properties and even a spectral scheme's error is of order one at this wave number.

For the abovementioned test case, a simple deconvolution by inverting the filter operation (4) has shown remarkably good agreement with filtered data obtained from a direct simulation with a high-order shock-capturing scheme, Fig. 5. Due to the ill-conditioned character of the deconvolution procedure the non-regularized deconvolution became unstable when perturbations were added to the shock-convection problem as in Adams & Shariff (1996). Indeed, the filter operation (4) is only invertible in its discretized form, a continuous Gauß filter is not invertible as can be shown by a brief argument in Fourier dual-space. Extending the work on deconvolution approaches for shock-turbulence interaction regularization procedures will be

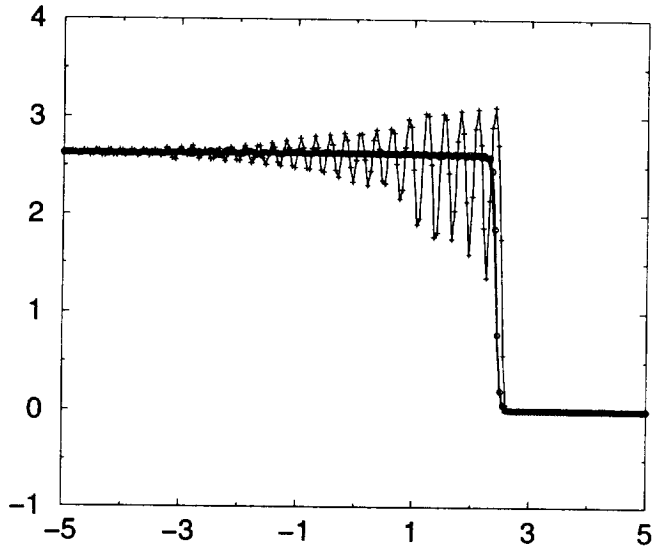

FIGURE 5. Shock simulation, velocity distribution, ——— : filtered 5th order ENO scheme, o———o : deconvolved 6th order Padé scheme, +———+ : artificial viscosity and 2nd order central scheme.

considered. It is expected that with regularized deconvolution methods an efficient treatment of any subgrid-scale entity, such as shocks or turbulent eddies, will be possible.

4. Concluding remarks and outlook

We have shown that standard subgrid-scale models require improvement before they can be expected to reliably represent subgrid-scale effects in physically complex flow. Nor did a straightforward application of a standard dynamic modeling procedure to treat a generic non-turbulent subgrid-scale, in our case a shock, prove to be applicable. A promising alternative appears to be (approximate) deconvolution strategies, also called de-filtering or estimation models (see the contribution of A. Domaradzki in this volume). They show in *a priori* tests a considerably higher correlation with filtered DNS data. Also often deemed misleading, in our understanding *a priori* tests constitute a necessary criterion for a SGS approximation to work, very much as a finite-difference discretization is supposed to give a good approximation to the, say, spatial derivatives in a PDE before anyone would expect that time-integration would make any sense. The traditional dynamic procedure, in fact, tries to alleviate some of these problems by making the Smagorinsky model more variable and by measuring this variability by a term of scale-similarity type (the test filtered Leonard term). The brief treatise on LES shock-treatment suggests that regularized deconvolution can be considered as a promising way for an accurate representation of subgrid-scales. It seems that many problems in the application of LES models come from the fact that LES practically always operates at the numerical resolution limits of the underlying schemes. An LES model needs

to correct what is not resolved numerically, and, obviously, then an LES model becomes related to the numerical scheme.

Acknowledgments

The first author wants to acknowledge enlightening discussions with Dr. C. D. Pruett before and during the course of this project.

REFERENCES

ADAMS, N. A. 1998 Direct numerical simulation of turbulent compression corner flow. *Theor. Comp. Fluid Dyn.* **12**, 109-129.

ADAMS, N. A., KLEISER L. 1998 Direct simulation of the turbulent boundary layer along a compression ramp at $M = 3$ and $Re_\theta = 1685$. *Report in preparation.*

ADAMS, N. A., SHARIFF, K. 1996 A high-resolution hybrid compact-ENO scheme for shock-turbulence interaction problems. *J. Comput. Phys.* **127**, 27-51.

BARDINA, J., FERZIGER, J. H. & REYNOLDS W. C. 1983 Improved turbulence models based on LES of homogeneous incompressible turbulent flows. Department of Mechanical Engineering, *Report No. TF-19*, Stanford University, Stanford, California.

BORIS, J. P., GRINSTEIN, F. F. ORAN E. S. & KOLBE R. L. 1992 New insights into large-eddy simulation, *Fluid Dyn. Res.* **10**, 199-228.

HIRSCH, C. 1988 Numerical Computation of Internal and External Flows. Vol. 2. *John Wiley and Sons.*

LELE, S. K. 1992 Compact Finite Difference Schemes with Spectral-like Resolution. *J. Comp. Phys.*, 103, 16-42.

PRUETT, C. D. 1997 Toward Simpilification of Dynamic Subgrid-Scale Models. In *Advances in DNS / LES*, 291-298.

VREMAN, B., GEURTS, B. & KUERTEN, H. 1994b On the formulation of the dynamic mixed subgrid-scale model. *Phys. Fluids* **6**, 4057-4059.

VREMAN, B. 1995 Direct and Large-Eddy Simulation of the Compressible Turbulent Mixing Layer. Ph.D. Thesis, Dept. of. Applied Mathematics, University of Twente.

YOSHIZAWA, A. 1986 Statistical theory for compressible turbulent shear flows, with the application to subgrid modeling. *Phys. Fluids* **29**(7), 2152-2164.

ZANG, Y., STREET, R. L. & KOSEFF J. R. 1993 A dynamic mixed subgrid-scale model and its application to turbulent recirculating flows. *Phys. Fluids A* **5**, 3187-3196.

A subgrid-scale estimation model applied to large eddy simulations of compressible turbulence

By J. A. Domaradzki[1], T. Dubois AND A. Honein

A subgrid-scale estimation procedure investigated previously for incompressible turbulence is extended to compressible flows. The procedure provides an estimate of the unfiltered velocity field and temperature appearing in the expressions for the subgrid-scale stress tensor and heat flux. The procedure in the physical space representation is applied to the compressible equations, which are written in a conservative form using sixth-order finite difference compact schemes for the approximation of the spatial derivatives. Two compressible flows are considered in this investigation: spatially decaying turbulence and shock/turbulence interaction. *A priori* analysis and actual large eddy simulations for both flows have been performed and a good agreement with filtered direct numerical simulations results has been obtained.

1. Introduction

Subgrid-scale (SGS) models commonly used in large eddy simulations (LES) of turbulent flows fall into three general categories: eddy viscosity models, similarity models, and so-called mixed models which combine eddy viscosity and similarity expressions. For review see Lesieur and Métais (1995) and Galperin and Orszag (1993). In recent years major advances in SGS modeling were made using the dynamic procedure (Germano *et al.* 1991, Lilly 1992, and Ghosal *et al.* 1995), which allows computation of model coefficients from a resolved LES field rather than prescribing them as constants. Despite evident progress in the field of SGS modeling, the existing models fail to capture some physical features of the actual SGS interactions. For instance, the eddy viscosity models properly model global SGS dissipation, *i.e.* the net energy flux from the resolved to the unresolved subgrid-scales, but predict very low correlations between the actual and modeled SGS quantities (Clark *et al.* 1979, Lund 1991, Kerr *et al.* 1996, O'Neil and Meneveau 1997). On the other hand, the similarity models correlate very well with the exact stresses in *a priori* analyses but significantly under predict SGS dissipation in actual large eddy simulations. Such difficulties motivate continuing search for better SGS models, and this effort is reflected in several articles in these Proceedings.

One such alternative approach to SGS modeling was proposed recently by Domaradzki *et al.* (1997, 1998). The proposed approach provides an estimate of the unfiltered velocity field appearing in the definition of the subgrid-scale stress tensor.

1 Department of Aerospace and Mechanical Engineering, University of Southern California, Los Angeles, California 90089-1191

Once the unfiltered velocity is found, it is used to compute all SGS quantities directly from the definitions. The estimation model was implemented and evaluated for incompressible channel flow at low and moderate Reynolds numbers, providing very good agreement with the DNS and experimental results. However, further work is needed to evaluate, document, and improve the performance of the model for higher Reynolds numbers and different flows. In this report we extend the SGS estimation model to compressible flows and evaluate its performance for spatially decaying compressible turbulence and shock/turbulence interaction.

2. Formulation

2.1 The large eddy simulation equations

The LES equations are obtained by spatial filtering of Navier-Stokes equations for compressible flows. The result is rewritten in terms of Favre (or density-weighted) filtering, which for a function f is defined as

$$\tilde{f} = \frac{\overline{\rho f}}{\bar{\rho}},$$

where the overbar denotes spatial filtering with a top-hat filter with the filter width Δ_f and ρ is the density. We follow Moin *et al.* (1991) and Erlebacher *et al.* (1992) in neglecting several terms in the equations that are considered small. Resulting continuity and momentum equations for spatially filtered density $\bar{\rho}$ and Favre filtered velocity $\tilde{u}_i$ are

$$\frac{\partial \bar{\rho}}{\partial t} + \frac{\partial}{\partial x_i}(\bar{\rho}\tilde{u}_i) = 0, \tag{1a}$$

$$\frac{\partial \bar{\rho}\tilde{u}_i}{\partial t} + \frac{\partial}{\partial x_j}(\bar{\rho}\tilde{u}_i\tilde{u}_j + \bar{p}\delta_{ij}) = \frac{\partial \tilde{\sigma}_{ij}}{\partial x_j} - \frac{\partial \tau_{ij}}{\partial x_j}. \tag{1b}$$

In Eq. (1) $\tilde{\sigma}_{ij}$ is the viscous stress, that is

$$\tilde{\sigma}_{ij} = \overline{\mu}\left(\frac{\partial \tilde{u}_i}{\partial x_j} + \frac{\partial \tilde{u}_j}{\partial x_i} - \frac{2}{3}\frac{\partial \tilde{u}_k}{\partial x_k}\delta_{ij}\right), \tag{2}$$

where μ is the viscosity and τ_{ij} represents the subgrid-scale (SGS) stress,

$$\tau_{ij} = \bar{\rho}(\widetilde{u_i u_j} - \tilde{u}_i\tilde{u}_j) = \overline{\rho u_i u_j} - \overline{\rho u_i}\,\overline{\rho u_j}/\bar{\rho}. \tag{3}$$

According to Lee (1992), a conservative formulation for the energy equation is required in the computation of shock/turbulence interaction. Following Mahesh (1998), the conservative energy equation is written as,

$$\frac{\partial E_T}{\partial t} + \frac{\partial}{\partial x_i}\left[(E_T + p)u_i\right] = \frac{\partial}{\partial x_j}(u_i\sigma_{ij}) - \frac{\partial}{\partial x_i}\left(\kappa\frac{\partial T}{\partial x_i}\right), \tag{4}$$

where the total energy is given by $E_T = \rho C_v T + \rho u_k u_k/2$, κ is the thermal conductivity, and C_v is the specific heat at constant volume.

Using the definition of the Favre filtering and of the total energy, the term $\overline{E_T u_i}$ in (4) can be rewritten as

$$\begin{aligned}\overline{E_T u_i} &= \bar{\rho} C_v \tilde{T} \tilde{u}_i + C_v q_i + \frac{1}{2}\widetilde{\rho u_k u_k} \tilde{u}_i + \frac{1}{2}\bar{\rho}\left(\widetilde{u_k u_k u_i} - \widetilde{u_k u_k}\tilde{u}_i\right) \\ &= \bar{E}_T \tilde{u}_i + C_v q_i + \frac{1}{2}\bar{\rho}\left(\widetilde{u_k u_k u_i} - \widetilde{u_k u_k}\tilde{u}_i\right),\end{aligned} \tag{5}$$

where the subgrid-scale heat flux q_i is

$$q_i = \bar{\rho}\left(\widetilde{T u_i} - \tilde{T}\tilde{u}_i\right) = \overline{\rho u_i T} - \overline{\rho u_i}\,\overline{\rho T}/\bar{\rho} \tag{6}$$

The last term in (5), corresponding to convection of SGS kinetic energy by SGS velocity, is expected to be small and is neglected. The other nonlinear term on the left-hand side of (4), involving pu_i, is rewritten after filtering as follows,

$$\overline{pu_i} = \overline{\rho R T u_i} = \bar{\rho}\widetilde{R T u_i} = \bar{\rho} R \tilde{T}\tilde{u}_i + R q_i,$$

In the last formula the equation of state for ideal gas $p = \rho R T$ was used, where R is the gas constant. The filtered r.h.s. of Eq. (4) is treated as in Moin *et al.* (1991), leading to the final form of the filtered total energy equation

$$\begin{aligned}\frac{\partial \bar{E}_T}{\partial t} + \frac{\partial}{\partial x_i}\left((\bar{E}_T + \bar{\rho} R \tilde{T})\tilde{u}_i\right) = &-\frac{\partial}{\partial x_i}(C_p q_i) \\ &+ \frac{\partial}{\partial x_i}\left(\overline{\kappa}\frac{\partial \tilde{T}}{\partial x_i}\right) + \frac{\partial}{\partial x_i}(\tilde{\sigma}_{ij}\tilde{u}_i).\end{aligned} \tag{7}$$

In deriving (7) the filtered equation of state was used, $\bar{p} = \bar{\rho} R \tilde{T}$, and the relation $C_p = C_v + R$, where C_p is the specific heat at constant pressure. Finally, note that the resolved temperature and total energy are related by

$$\bar{E}_T = \bar{\rho} C_v \tilde{T} + \frac{1}{2}\bar{\rho}\tilde{u}_k\tilde{u}_k + \frac{1}{2}\tau_{kk}. \tag{8}$$

To close the above equations for the primitive variables $\bar{\rho}, \tilde{u}_i, \tilde{T}$, the SGS stress (3) and the SGS heat flux (6) must be expressed in terms of those variables using an SGS model.

2.2 The subgrid scale estimation procedure

Consider a velocity field u_i which is a continuous function of variable x on the interval $[0, L_x]$. For the purpose of numerical simulations, u_i may be approximated in terms of its values at discrete points using sufficiently small mesh size Δ_{DNS}. Assume that the continuous function u_i is filtered with a top hat filter Δ_f. In general, the filtered velocity $\overline{u}_i$ is smoother than the unfiltered field u_i, and it can

be accurately represented by sampling it on a coarser mesh $\Delta_{LES} \approx \Delta_f \ll \Delta_{DNS}$. Specifically, we will choose $\Delta_{LES} = \Delta_f/2$.

The SGS estimation procedure consists of two steps. In the kinematic step we seek a function $u_i^0(x)$ such that

$$\overline{u_i^0}(x_n) = \overline{u}_i(x_n), \tag{9}$$

on the LES mesh points $x_n = n\Delta_{LES}$, $(n = 0, 1, \ldots, N)$. Note that the right-hand side of Eq. (9) are the values of the resolved field, assumed to be known on the LES mesh. Clearly, without additional assumptions the above condition does not provide a unique solution for $u_i^0(x)$. To further specify the problem we assume that $u_i^0(x)$ may be accurately represented by N nodal values, $u_i^0(x_n)$. Then, the filtering on the left-hand side of Eq. (9) involves integration over interval Δ_f spanning three neighboring points. We use the Simpson's rule for the integration, which results in a tridiagonal system of equations for the values of $u_i^0(x_n)$

$$\frac{1}{6}\left[u_i^0(x_{n-1}) + 4u_i^0(x_n) + u_i^0(x_{n+1})\right] = \overline{u}_i^{(N)}(x_n). \tag{10}$$

The system can be solved if values for the end points are provided. In this work we apply the procedure to periodic functions only.

The subgrid scales are generated in the nonlinear step on a fine mesh with the mesh size $\Delta_{LES}/2$

$$x_j = j\Delta_{LES}/2, \ (j = 0, 1, \ldots, 2N). \tag{11}$$

First, we interpolate previously computed u_j^0 from the coarse LES mesh to the fine mesh using cubic splines. Next, the small scales are produced as a result of nonlinear interactions among large scales. To this end the advection effects by the large scales are removed from the nonlinear term

$$N_i^0 = -(u_j^0 - \overline{u_j^0})\frac{\partial}{\partial x_j}u_i^0, \tag{12}$$

and the growth rate of subgrid scales by the nonlinear interactions among resolved scales is obtained as

$$N_i' = N_i^0 - \overline{N_i^0}. \tag{13}$$

If the nonlinear interactions are maintained over time θ, the small scales become

$$u_i' = \theta N_i', \tag{14}$$

and the estimated velocity field is

$$u_i^e = u_i^0 + u_i'. \tag{15}$$

To fully determine the small scales using the nonlinear correction term Eq. (14), the time scale θ is needed. Physically θ can be interpreted as the large eddy turnover

time. Its value may vary with the position in a flow to reflect local conditions of turbulence. We estimate θ, assuming that locally in space the energy of subgrid scales Eq. (14) is proportional to the energy of the smallest resolved scales. This provides the following expression

$$\theta = C\sqrt{\frac{(u_i^0 - \overline{u_i^0})^2}{N_i'^2}}, \tag{16}$$

where the constant of proportionality C is found to be approximately $1/2$ for the inertial range spectral form.

For applications to compressible flows the following changes are made. First, the deconvolution for ρ is performed providing unfiltered ρ^0. To avoid violating the conservation of mass, no attempt is made to use the nonlinear correction for SGS density scales. Next the deconvolution is performed for spatially filtered velocities, $\overline{\rho u_i} = \bar{\rho}\tilde{u}_i$. The resulting quantities are divided by ρ^0 to provide u_i^0 for use in the nonlinear correction step as described above. Similarly, the deconvolution for $\overline{E}_T$ is performed, and the relation for E_T^0 in terms of ρ^0, u_i^0, and T^0 is solved for the temperature T^0. The nonlinear correction to T^0 is found as for the velocity by replacing the nonlinear term for the velocity by the nonlinear term for the temperature. Estimated density $\rho^e = \rho^0$, velocity $u_i^e = u_i^0 + u_i'$, and temperature $T^e = T^0 + T'$ are used to calculate the SGS stress and the SGS heat flux from formulas (3) and (6), respectively.

3. Numerical implementation

Two test cases have been considered, namely spatially decaying turbulence and the interaction of isotropic turbulence with a shock wave. For both cases, DNS data are available and were used for *a priori* tests and comparisons with large eddy simulations. The DNS code uses modified sixth-order Padé (compact) scheme for discretization of the spatial derivatives and a third order (low storage) Runge-Kutta scheme for the time discretization. In the shock/turbulence interaction case, a sixth-order ENO scheme is used in the vicinity of the shock wave, i.e. $x \simeq 2$; it is applied only in the streamwise (shock-normal) direction.

The cubic computational domain has dimensions L_x, L_y, and L_z in three Cartesian directions. The grid points are clustered around the shock in the streamwise direction while a uniform mesh is used in the cross-stream directions y and z. Approximately non-reflecting boundary conditions are specified at the exit, i.e. $x \simeq L_x$. In the cross-stream directions periodic boundary conditions are imposed. The mean flow is in the x direction. In spatial simulation, a uniform mesh is used in all spatial directions. Moreover, the flow is supersonic so that the primitive variables are specified at the inflow boundary $x = 0$ and no boundary conditions are needed at the outflow $x = L_x$.

The generation of inflow conditions is described in Mahesh *et al.* (1996). First, a temporal (decaying) simulation of isotropic turbulence is conducted. The resolution and domain size are the same as used for the spatial simulation and are listed in

Table 1. The Reynolds number based on the Taylor microscale and the turbulent Mach number at the initial time are $Re_\lambda = 30$ and $M_t = 0.17$, respectively. The simulation is advanced until a state of fully developed turbulence is reached. Turbulent fluctuations obtained in such a simulation are then superimposed on spatially uniform mean values of the velocity, pressure, and density at the inflow. Inflow turbulence is advected through the computational domain by the mean velocity and decays with the increasing distance from the inflow plane.

The estimation model was implemented only in the cross-stream directions y and z, and the full DNS resolution was used in the streamwise x direction. Parameters for all simulated cases are summarized in Table 1 for the spatial simulations (prefix SP) and in Table 2 for the shock/turbulence interaction case (prefix SH). For both flows *a priori* tests were performed using high resolution DNS databases hiDNS. After that the model was implemented in time evolving large eddy simulations, cases SPLES-1 and SHLES-1, for the respective spanwise resolutions in each direction a factor of three and four less than the full DNS resolution. Additionally, for the compressible turbulence case a simulation without a model was performed (case SPloDNS) with the same low resolution as the case SPLES-1. Comparing these two cases allows assessment of the relative importance of the model in the flow evolution.

Table 1. Parameters of the spatially decaying turbulence.

Case	Grid	$L_x \times L_y \times L_z$	Re_λ	M_t
SPhiDNS	$97 \times 97 \times 97$	$2\pi \times 2\pi \times 2\pi$	30	0.17
SPloDNS	$97 \times 33 \times 33$	$2\pi \times 2\pi \times 2\pi$	30	0.17
SPLES-1	$97 \times 33 \times 33$	$2\pi \times 2\pi \times 2\pi$	30	0.17

Table 2. Parameters of the simulations of shock/turbulence interaction.

Case	Grid	$L_x \times L_y \times L_z$	Re_λ	M	M_t
SHhiDNS	$231 \times 81 \times 81$	$10 \times 2\pi \times 2\pi$	19.1	1.29	0.14
SHLES-1	$231 \times 21 \times 21$	$10 \times 2\pi \times 2\pi$	19.1	1.29	0.14

A number of physical quantities are available from the numerical simulation results. In addition to SGS stress (3) and SGS heat flux (6), an important quantity is the SGS dissipation per unit mass

$$\epsilon_{SGS} = \frac{1}{\bar{\rho}} \tau_{ij} \frac{\partial \tilde{u}_i}{\partial x_j}, \tag{17}$$

which affects the resolved kinetic energy $K = \frac{1}{2}\tilde{u}_i\tilde{u}_i$. The SGS kinetic energy is $K_{SGS} = \frac{1}{2}(u_iu_i - \tilde{u}_i\tilde{u}_i)$. For plotting purposes all computed fields are reduced

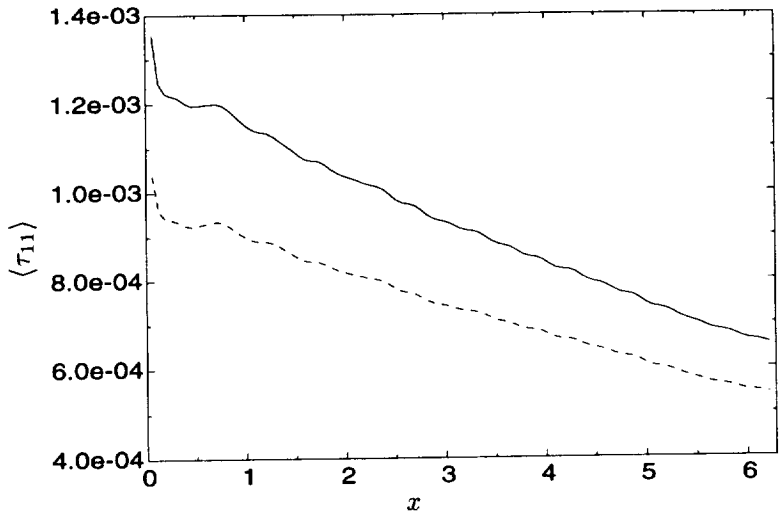

FIGURE 1. The plane average component of the streamwise component of the SGS stress tensor $\langle \tau_{11} \rangle$. ——— : case SPhiDNS; ------ : value predicted by the estimation procedure.

to functions of the streamwise variable x by averaging over spanwise planes and over several realizations. Such averages are signified by brackets $< \ldots >$. To assess predictions of the backscatter by the model, the SGS dissipation is decomposed in each cross-stream plane into forward transfer (negative values, $< \epsilon^{-}_{SGS} > = < (\epsilon_{SGS} - |\epsilon_{SGS}|)/2 >$) and inverse transfer or backscatter (positive values, $< \epsilon^{+}_{SGS} > = < (\epsilon_{SGS} + |\epsilon_{SGS}|)/2 >$).

3.1 Spatially decaying turbulence

In *a priori* tests the exact SGS quantities computed from the fully resolved DNS fields were compared with the SGS quantities predicted by the estimation model. Spanwise resolution was reduced from 97×97 mesh points in DNS to 33×33 points for the model. Calculated correlation coefficients between the exact and the modeled SGS quantities were found to always exceed 90%. These values are much higher than for the eddy viscosity based models and comparable to values observed for the similarity models.

In Fig. 1 we plot the averaged τ_{11} component of the SGS stress tensor computed exactly and using the estimation model. The error in the model prediction is about 25% at the inflow, decreasing to 15% at the outflow. It is well known that a success of a SGS model critically depends on its ability to correctly predict the SGS dissipation. In Fig. 2 we plot the actual and the model SGS dissipation decomposed into forward transfer (negative curves) and backscatter (positive curves). The agreement between the exact and the modeled quantities is now much better than for the SGS stresses. However, the forward transfer is slightly under predicted by the model. This may be a cause for concern because even small errors in the SGS dissipation may accumulate in actual LES, leading to incorrect long time dynamics. This is the problem commonly encountered by pure similarity models. In order to fully

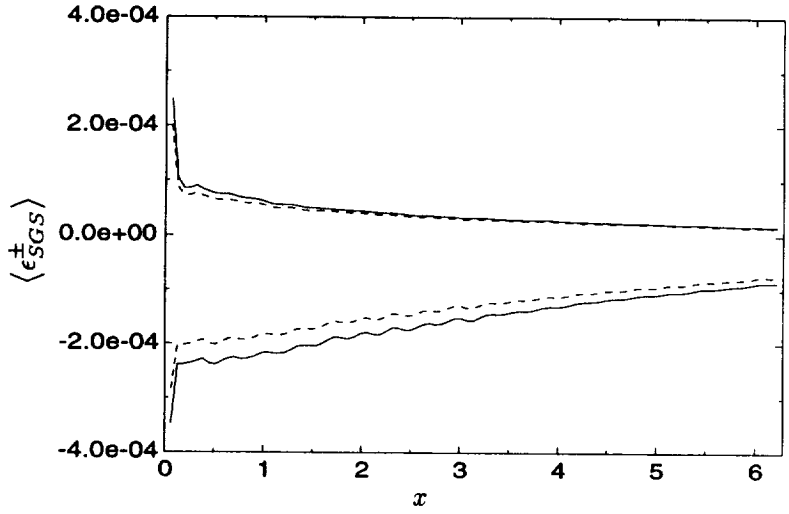

FIGURE 2. Negative and positive values of local SGS dissipation averaged over the cross-stream directions $\langle \epsilon^{\pm}_{SGS} \rangle$. ——— : case SPhiDNS; ------ : value predicted by the estimation procedure.

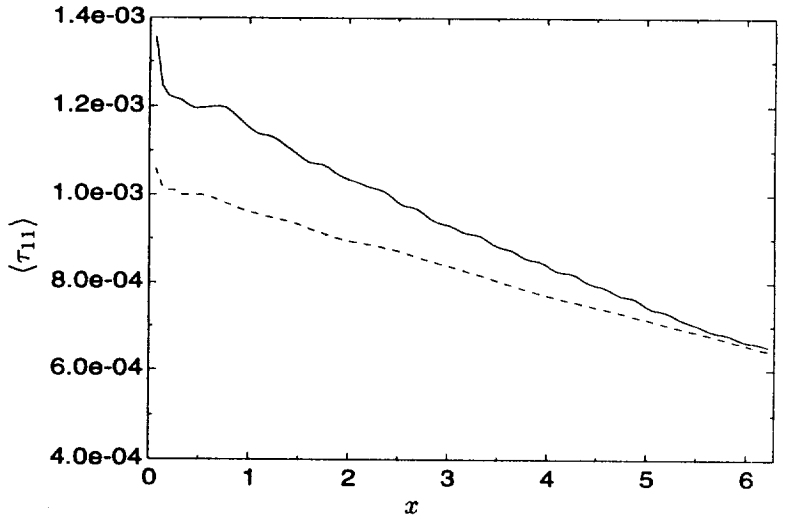

FIGURE 3. The plane averaged component of the streamwise component of the SGS stress tensor $\langle \tau_{11} \rangle$. ——— : case SPhiDNS; ------ : case SPLES-1.

assess a SGS model, actual LES must be performed over sufficiently long evolution times. Such LES with the estimation model have been performed, and the results are reported below.

In Fig. 3 we compare the exact value of τ_{11} component of the SGS stress tensor with the value it has in the well developed large eddy simulation run SPLES-1. It is interesting to note that the agreement is now better than in *a priori* test. We offer the following explanation. If SGS quantities are under predicted by the model at

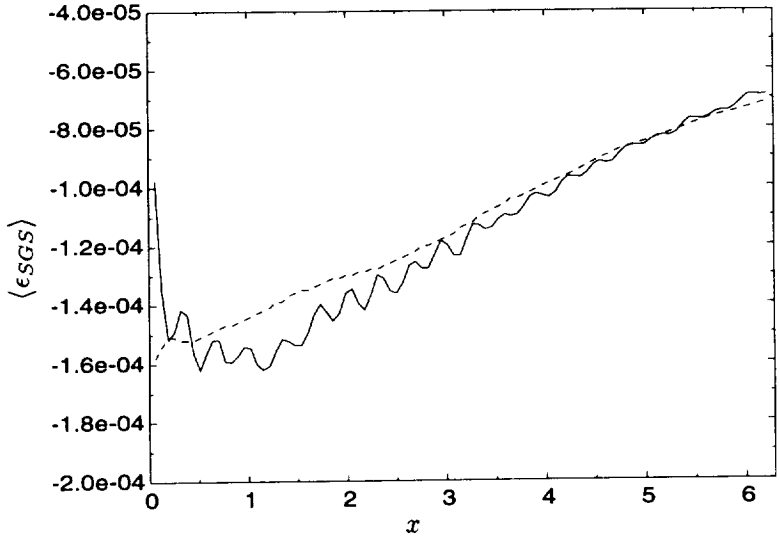

FIGURE 4. The plane averaged SGS dissipation $\langle \epsilon_{SGS} \rangle$. ——— : case SPhiDNS; ------ : case SPLES-1.

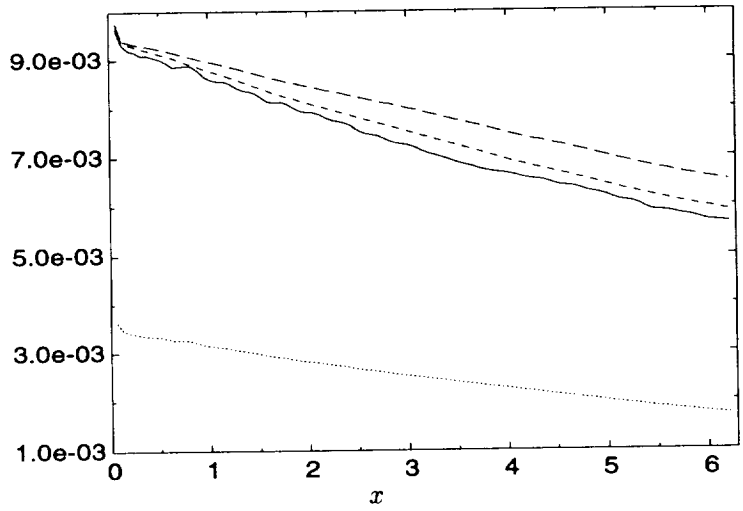

FIGURE 5. Plane averaged resolved kinetic energy $\frac{1}{2}\langle \bar{u}_i \bar{u}_i \rangle$. ——— : case SPhiDNS; ------ : case SPLES-1; - - - - : case SPloDNS; ····· : SGS kinetic energy $\frac{1}{2}\langle u_i u_i - \bar{u}_i \bar{u}_i \rangle$.

the initial time, the energy levels of the resolved scales will start increasing in the simulations. Because of the dependence of the estimation procedure on the resolved scales, this will lead to the increase of the SGS quantities until a balance is reached.

The total SGS dissipation for the run SPLES-1 averaged over time is plotted in Fig. 4 where it is compared with the exact SGS dissipation in the run SPhiDNS. There is more variability present in the DNS results because fewer fields were available for time averaging than for the LES run. The model appears to slightly under

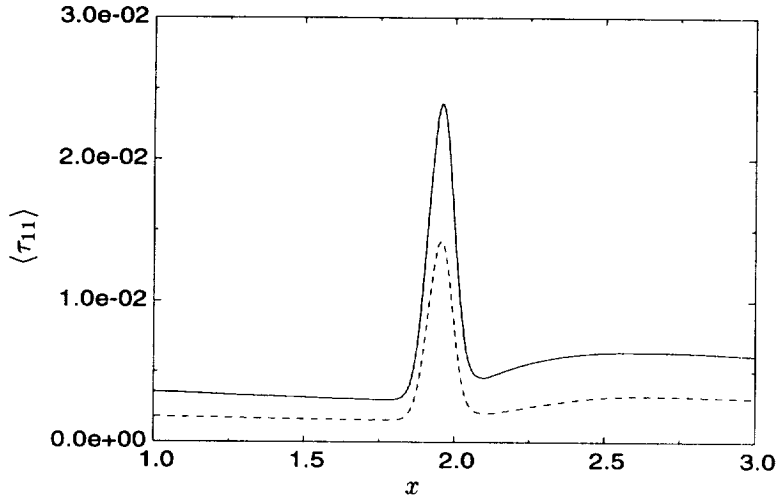

FIGURE 6. The plane averaged component of the streamwise component of the SGS stress tensor $\langle \tau_{11} \rangle$. ——— : case SHhiDNS; ------ : value predicted by the estimation procedure.

predict the exact quantity in the vicinity of the inlet $x < 2$, but the prediction becomes progressively better as the flow evolves away from the inlet. These results are entirely consistent with the results of the *a priori* analysis. We thus conclude that the estimation model maintains correct levels of the SGS dissipation in the actual LES. This feature clearly differentiates it from the classical similarity models. It should also allow proper prediction of the evolution of the turbulent kinetic energy.

In Fig. 5 we plot the dependence of the kinetic energy on the streamwise distance from the inlet. The resolved kinetic energy in LES decays somewhat more slowly than the corresponding quantity obtained from high resolution DNS, consistent with the under prediction of the SGS dissipation by the estimation model in run SPLES-1. However, if no model is used the energy prediction deteriorates markedly (case SPloDNS), indicating that the estimation model has a significant effect on the simulations. This conclusion is further confirmed by noting that in the simulation the SGS kinetic energy is not negligible and constitutes about 25% of the total kinetic energy in DNS.

3.2 Shock/turbulence interaction

For the shock/turbulence interaction problem, the low spanwise resolution of 21×21 mesh points provides a more severe test of the model since a run without the model at this resolution quickly became unstable. All SGS quantities for this problem have much larger values in the vicinity of the shock location $x = 2$ than away from the shock, and that region is emphasized in the plots. In Figs. 6, 7, and 8 we compare the exact and modeled SGS stress component τ_{11}, SGS heat flux q_1, and SGS dissipation ϵ_{SGS}, respectively, obtained in *a priori* analysis. We observe that all SGS quantities are predicted in a qualitative agreement with the exact data, in particular the peak locations, but the model values are not quantitatively

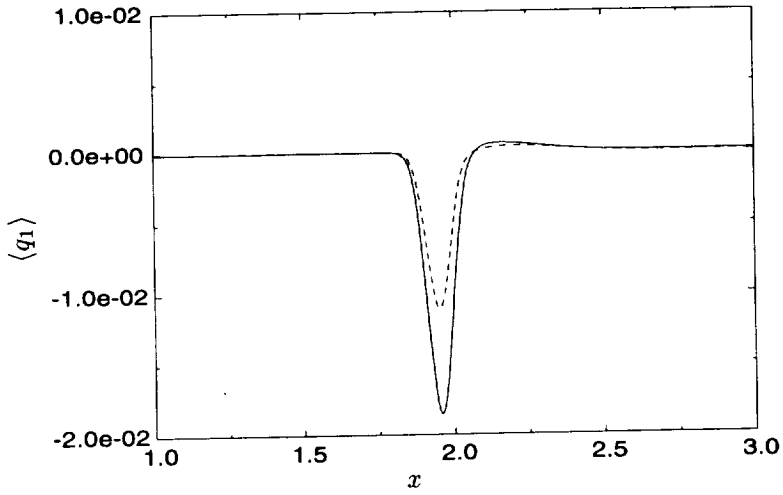

FIGURE 7. The plane averaged component of the streamwise component of the SGS heat flux $\langle q_1 \rangle$. ——— : case SHDNS; ------ : value predicted by the estimation procedure.

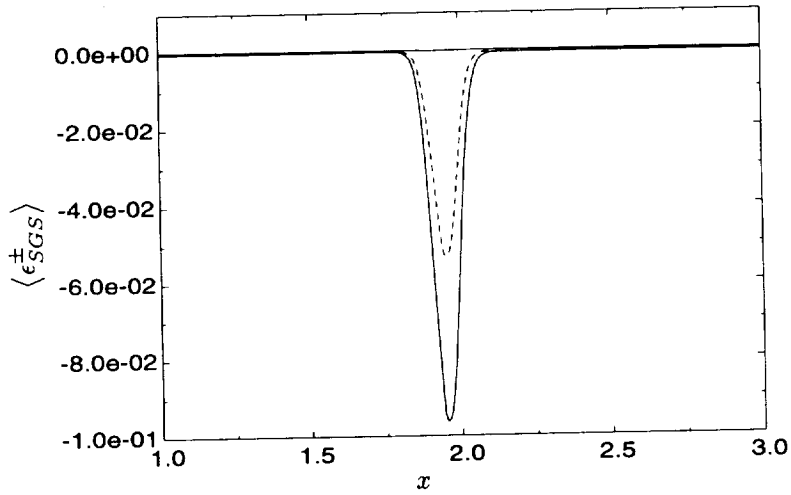

FIGURE 8. Negative and positive values of local SGS dissipation averaged over the cross-stream directions $\langle \epsilon^{\pm}_{SGS} \rangle$. ——— : case SHDNS; ------ : value predicted by the estimation procedure.

accurate. We also find that for this problem the backscatter component of the SGS dissipation is negligible compared with the forward transfer (Fig. 8). When the estimation model is implemented in time evolving LES, the agreement between the LES and exact SGS data improves. This is illustrated in Figs. 9 - 11 and is consistent with the similar behavior observed for the decaying turbulence case.

While good predictions of SGS quantities are an important test of an SGS model,

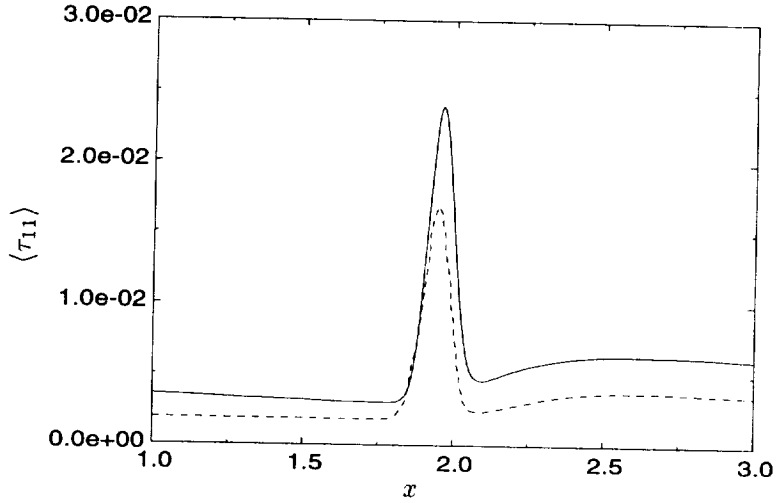

FIGURE 9. The plane averaged component of the streamwise component of the SGS stress tensor $\langle \tau_{11} \rangle$. ——— : case SHhiDNS; ------ : case SHLES-1.

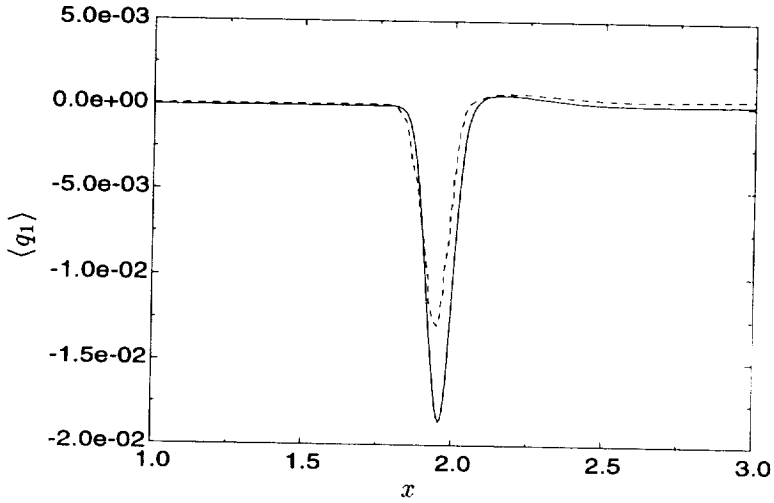

FIGURE 10. The plane averaged component of the streamwise component of the SGS heat flux $\langle q_1 \rangle$. ——— : case SHhiDNS; ------ : case SHLES-1.

the LES practice is concerned with predictions of physical quantities that are accessible to experimental measurements. Two such quantities are the turbulent kinetic energy and the mean velocity. In Fig. 12 we compare the mean velocity obtained in the LES case SHLES-1 with the mean velocity for the case SHhiDNS. The comparison is very good though the location of the shock in LES is slightly shifted upstream. A similar shift is observed for the kinetic energy in Fig. 13 (see the inset). The resolved energy decays before and after the shock, and the estimation model is clearly capable of capturing that decay though it over estimates the energy levels in those regions. In the shock region, magnified in the inset, the energy levels

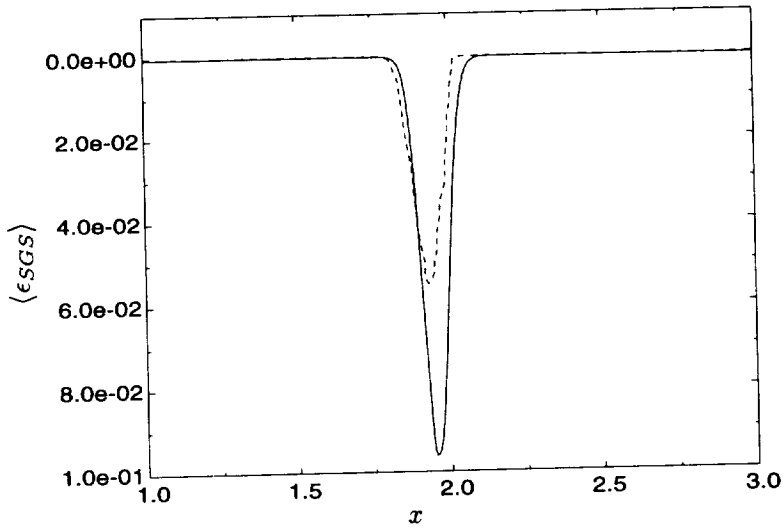

FIGURE 11. Plane averaged SGS dissipation: $\langle \epsilon_{SGS} \rangle$. ——— : case SHhiDNS; ------ : case SHLES-1.

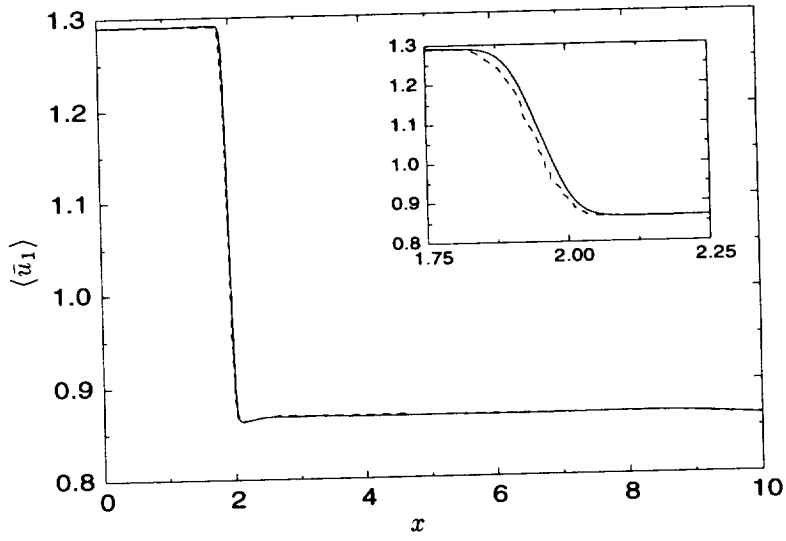

FIGURE 12. Mean velocity profile $\langle \bar{u}_1 \rangle$. ——— : case SHhiDNS; ------ : case SHLES-1.

in LES are in excellent agreement with the resolved energy in DNS. Overall, for all x the SGS energy component is of the same order as the resolved energy, pointing to a significant effect of the model on the LES. Similar behavior was observed for other LES quantities such as density, pressure, and temperature, i.e. uniformly good agreement with the DNS results and a slight upstream shift of the LES curves with respect to the DNS curves.

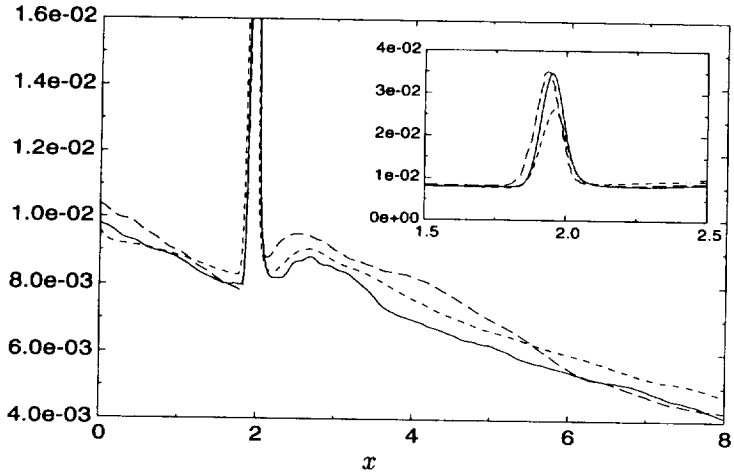

FIGURE 13. Plane averaged resolved kinetic energy $\frac{1}{2}\langle \bar{u}_i \bar{u}_i \rangle$. ——— : case SHhiDNS; ---- : case SHLES-1; ------ : plane averaged SGS kinetic energy $\frac{1}{2}\langle u_i u_i - \bar{u}_i \bar{u}_i \rangle$.

4. Conclusions

The subgrid-scale estimation model developed previously for incompressible flows was extended to compressible turbulence. The basic modeling principle is to recover unfiltered, resolved scales from a filtered LES field using the deconvolution procedure and to generate a range of smaller subgrid-scales through nonlinear interactions among resolved ones. In principle, the technique should be applicable to filtered evolution equations for any system whose dynamics are governed by nonlinear interactions which produce local energy cascade. In compressible turbulence both the velocity and temperature (or energy) dynamics have this property. Consequently, the estimation procedure used for incompressible turbulence could be applied with only minor modifications to the velocity and temperature fields in compressible turbulence. The performance of the estimation procedure was evaluated by comparing model results with high resolution DNS databases for two flows: spatially decaying compressible turbulence and shock/turbulence interaction. In both cases SGS quantities obtained using the estimation model showed high correlations with the exact DNS results in *a priori* tests. However, the values of the modeled quantities were generally less than the exact values. This feature of *a priori* tests indicates that either the modeled SGS scales do not provide a perfect approximation to the actual SGS scales or that more nonlocal interactions than accounted for by the model should be included. At low Reynolds numbers considered here, the latter explanation is unlikely. Therefore, we believe that further work on improving the quality of the estimated SGS scales is needed. Deficiencies of the modeled scales had negligible effect on the quality of the results in actual LES, which showed much better agreement with the DNS results than *a priori* tests. This was explained by the dynamic coupling between the model and the resolved scales, which in the time evolving LES increases the SGS quantities over their *a priori* values.

Overall, the results presented in this report strongly support the claim that the estimation model accounts properly for the SGS interactions in compressible turbulence. However, it must be noted that only low Reynolds number flows were considered. We cannot exclude a possibility that any deficiencies of the estimated scales, which did not appear to be significant at low Reynolds numbers, will become amplified at high Reynolds numbers. Also, neglecting the nonlocal transfers may no longer be a valid approximation at high Reynolds numbers. The former deficiencies would need to be corrected by developing better approximations to the subgrid scales at high Reynolds numbers while the latter effects are amenable to eddy viscosity modeling. Moreover, because of the particular geometry for both problems, the model could be applied only in two cross-stream directions. For more general problems, e.g. flows with more complex shock patterns, the model will have to be applied in all three spatial directions. An extension of the procedure to incorporate filtering in all three directions is straigthforward and is currently being tested on the channel flow problem.

Acknowledgments

JAD was partially supported by the NSF Grant CTS-9704728, and by CTR.

REFERENCES

CLARK, R. A. & FERZIGER J. H. & REYNOLDS, W. C. 1979 Evaluation of subgrid-scale models using an accurately simulated turbulent flow. *J. Fluid Mech.* **91,** 1.

DOMARADZKI, J. A. & SAIKI, E. M. 1997 A subgrid-scale model based on the estimation of unresolved scales of turbulence. *Phys. Fluids.* **9**(7), 2148-2164.

DOMARADZKI, J. A. & LOH, K. 1998 The subgrid-scale estimation model in the physical space representation. *Phys. Fluids.* (Submitted).

ERLEBACHER, G. & HUSSAINI, M. Y. & SPEZIALE, C. G. & ZANG, T. A. 1992 Toward the large-eddy simulation of compressible turbulent flows. *J. Fluid Mech.* **238,** 155-185.

GALPERIN, B. & ORSZAG, S. A. EDS. 1993 Large eddy simulation of complex engineering and geophysical flows. Cambridge University Press, Cambridge.

GERMANO, M. & PIOMELLI, U. & MOIN, P. & CABOT, W. H. 1991 A dynamic subgrid-scale eddy viscosity model. *Phys. Fluids A.* **3**(7), 1760-1765.

GHOSAL, S. & LUND, T. S. & MOIN, P. & AKSELVOLL, K. 1995 A dynamic localization model for large-eddy simulation of turbulent flows. *J. Fluid Mech.* **286,** 229-255.

KERR, R. M. & DOMARADZKI, J. A. & BARBIER, G. 1996 Small-scale properties of nonlinear interactions and subgrid-scale energy transfer in isotropic turbulence. *Phys. Fluids.* **8,** 197.

LEE, S. 1992 Large eddy simulation of shock turbulence interaction. *Annual Research Briefs*. Center for Turbulence Research, NASA Ames/Stanford Univ., 73-84.

LESIEUR, M. & MÉTAIS, O. 1996 New trends in large-eddy simulations of turbulence. *Ann. Rev. Fluid Mech.* **28**, 45.

LILLY, D. K. 1992 A proposed modification of the Germano subgrid-scale closure method. *Phys. Fluids A.* 4(3), 633-635.

LUND, T. S. 1991 On dynamic models for large eddy simulations. *Annual Research Briefs*. Center for Turbulence Research, NASA Ames/Stanford Univ., 177-190.

MAHESH, K. 1998 Private communication.

MAHESH, K. & LELE, S. K. & MOIN, P. 1997 The influence of entropy fluctuations on the interaction of turbulence with a shock wave. *J. Fluid Mech.* **334**, 353-379.

MOIN, P. & SQUIRES, K. & CABOT, W. & LEE, S. 1991 A dynamic subgrid-scale model for compressible turbulence and scalar transport. *Phys. Fluids A.* **3**(11), 2746-2757.

O'NEIL, J. & MENEVEAU, C. 1997 Subgrid-scale stresses and their modeling in a turbulent wake. *J. Fluid Mech.* **349**, 253.

Testing of a new mixed model for LES: the Leonard model supplemented by a dynamic Smagorinsky term

By G. S. Winckelmans[1], A. A. Wray AND O. V. Vasilyev[2]

A new mixed model which uses the Leonard expansion (truncated to one term) supplemented by a purely dissipative term (dynamic Smagorinsky) has been developed and tested in actual Large Eddy Simulations (LES) of decaying homogeneous turbulence and of channel flow. This model assumes that the LES filter is smooth in wave space, which is the case of most filters defined in physical space (*e.g.*, top hat, Gaussian, discrete filters). The dynamic procedure has been extended for the mixed model. It is used to determine the model coefficient, C, for the added Smagorinsky term. The one-term Leonard model provides significant local backscatter while remaining globally dissipative. In *a priori* testing, its correlation with DNS is greater than 0.9. However, when used on its own in actual LES, this model is found to provide too little dissipation. Hence the need for added dissipation, here provided by the dynamic Smagorinsky term. In 64^3 LES of decaying homogeneous turbulence started from Gaussian filtered 256^3 DNS at $Re_\lambda \simeq 90$, the new mixed dynamic model performs significantly better than the dynamic Smagorinsky model with same Gaussian filtering; it also outperforms the dynamic Smagorinsky model with sharp cutoff filtering: much better energy spectra, much better energy and enstrophy decay. For the preliminary 48^3 LES runs on the channel flow at $Re_\tau = 395$ done with smooth LES filtering (Gaussian in the homogeneous directions, top hat in the non-homogeneous direction), the mixed dynamic model is also superior to the dynamic Smagorinsky model. However, the dynamic Smagorinsky model with sharp cutoff test filtering in the homogeneous directions still produces a better mean velocity profile. This result calls for further investigations.

1. Introduction and model development

We consider incompressible flows ($\partial_i u_i = 0$). Upon applying a spatial filter, $\overline{G}$,

$$\overline{f}(\mathbf{x}) = \int \overline{G}(\mathbf{x}-\mathbf{y})\, f(\mathbf{y})\, d\mathbf{y} \ , \tag{1}$$

to the Navier-Stokes (NS) equations written in the velocity-pressure formulation, one obtains the evolution equation for the filtered velocity field (with $\partial_i \overline{u}_i = 0$):

$$\partial_t \overline{u}_i + \partial_j \left(\overline{u}_i\, \overline{u}_j\right) + \partial_i \overline{P} = \partial_j \left(2\nu\, \overline{S}_{ij}\right) - \partial_j \tau_{ij} \ , \tag{2}$$

1 Mechanical Engineering, Center for Systems Engineering and Applied Mechanics, Université catholique de Louvain, Belgium.

2 Current address: Mechanical and Aerospace Engineering, University of Missouri-Columbia.

with $\overline{P} = \overline{p}/\rho$ the pressure divided by the density, $\overline{S}_{ij} = (\partial_j \overline{u}_i + \partial_i \overline{u}_j)/2$ the symmetric rate of strain tensor, and $\tau_{ij} = \overline{u_i u_j} - \overline{u}_i \overline{u}_j$ the symmetric stress tensor due to the filtering. This tensor is often called "subgrid-scales" stress tensor. This name is misleading because the filtering above is defined independently of a numerical grid. A better term would be "filtered-scales" stress tensor.

We here consider non-linear models of the family derived from Leonard (1974, 1997). Consider the Gaussian filter, $\overline{\Delta}\,\overline{G}(x) = \exp\left(-x^2/2\overline{\Delta}^2\right)/\sqrt{2\pi}$, $\overline{G}(k) = \exp\left(-k^2\,\overline{\Delta}^2/2\right)$. The Leonard expansion is then obtained as:

$$\overline{f\,g} \simeq \overline{f}\,\overline{g} + \overline{\Delta}^2\,\partial_x\overline{f}\,\partial_x\overline{g} + \frac{\overline{\Delta}^4}{2!}\,\partial_x\partial_x\overline{f}\,\partial_x\partial_x\overline{g} + \frac{\overline{\Delta}^6}{3!}\,\partial_x\partial_x\partial_x\overline{f}\,\partial_x\partial_x\partial_x\overline{g} + \ldots \,. \quad (3)$$

This result is remarkable because, at least in principle, it provides a means of evaluating the filter of a product of variables from the filtered variables and their derivatives. In 3-D, the filter is taken as the product of 1-D filters. One then obtains for the stress (Leonard, 1997):

$$\tau_{ij} = \overline{\Delta}^2\,\partial_k\overline{u}_i\,\partial_k\overline{u}_j + \frac{\overline{\Delta}^4}{2!}\,\partial_k\partial_l\overline{u}_i\,\partial_k\partial_l\overline{u}_j + \frac{\overline{\Delta}^6}{3!}\,\partial_k\partial_l\partial_m\overline{u}_i\,\partial_k\partial_l\partial_m\overline{u}_j + \ldots \,. \quad (4)$$

For 3-D LES, it would be very expensive (both in terms of memory and CPU requirements) to keep many terms in this expansion. In that respect, an already very interesting candidate model for LES is the one corresponding to truncation of the expansion to the first term:

$$\tau_{ij}^M = \overline{\Delta}^2\,\partial_k\overline{u}_i\,\partial_k\overline{u}_j \,. \quad (5)$$

This non-linear isotropic model was not included in the LES models evaluated in *a priori* tests in Clark *et al.* (1979), McMillan & Ferziger (1979), Bardina *et al.* (1983), Lund & Novikov (1992), Salvetti & Banerjee (1995), some of which were revisited in Winckelmans *et al.* (1996). It has, however, already been tested *a priori* against experimental data (unfortunately, 2-D cuts) in Liu *et al.* (1994) with correlation levels of about 0.7, and against DNS data in Borue & Orszag (1998) with correlation levels between 0.83 and 0.97 (*i.e.*, very high!) depending on the type of smooth filter used and on the filter size. It is also argued in Liu *et al.* (1994) that this model has some ties with the Bardina (1983) scale-similarity model, $\tau_{ij}^M = L_{ij} = \overline{\overline{u}_i\overline{u}_j} - \overline{\overline{u}}_i\overline{\overline{u}}_j$. The link also appears in an appendix in Horiuti (1997) where we observe that the first term in the approximate expansion of L_{ij} is indeed the same as the first term in the exact Leonard expansion. The other terms are, however, very different. The Leonard model (truncated to one term or more) is thus not identical to the Bardina model. Nevertheless, we recall that, for smooth filtering such as the Gaussian or the top hat, the Bardina model also exhibits a high level of correlation with the exact stress: *e.g.*, 0.8 in Liu *et al.* (1994), 0.7 in Gaussian filtered DNS in Winckelmans *et al.* (1996), but only 0.5-0.6 in Liu *et al.*

(1994) when "approximating" the Bardina model by using $\tau_{ij}^M \simeq L_{ij} = \widehat{\overline{u}_i \overline{u}_j} - \widehat{\overline{u}}_i \widehat{\overline{u}}_j$ where the second filter width, $\widehat{\Delta}$, is now taken as twice the original filter width, $\overline{\Delta}$. In *a priori* tests with smooth filters, it thus appears that the one-term Leonard model consistently produces higher levels of correlation than the Bardina model.

Finally, it can also be shown (Carati *et al.*, 1998) that, for all filters that are C^∞ in wave space and have non-zero second moment (that is most of the filters defined in physical space, such as the Gaussian, the top hat, all discrete filters, etc.), there exists a generalized Leonard expansion that always starts with

$$\tau_{ij} = \overline{\Delta}^2 \, \partial_k \overline{u}_i \, \partial_k \overline{u}_j + \dots \, . \tag{6}$$

where the filter width is normalized as follows:

$$\overline{\Delta}^2 = \int_{\infty}^{\infty} x^2 \, \overline{G}(x) \, dx = -\frac{d^2 \overline{G}}{dk^2}|_{k=0} \, . \tag{7}$$

Hence, the present investigation (theoretical and numerical) using the one-term Leonard model is not limited to the Gaussian filter; this model is truly generic. An important exception (because it is still used so often in spectral LES) is the sharp cutoff "filter" applied in wave space. This "filter" has very poor properties in physical space; it doesn't even have a second order moment. It does not allow for any kind of generalized Leonard expansion, or even any kind of one-term Leonard model, because it totally removes all information beyond the sharp cutoff. We also recall that no significant correlation with DNS data are obtained when testing the Bardina model with the sharp cutoff filter.

It should also be noted that an original integral formulation of the one-term Leonard model has been developed and tested by Cottet (1997a,b), following developments in vortex methods (Cottet, 1996). Its further investigation was the object of parallel study during this Summer Program.

When used in the filtered NS equations, the one-term Leonard model behaves as a non-linear diffusion/antidiffusion model. Indeed, it is easily seen (Leonard, 1997) that

$$-\partial_j \tau_{ij}^M = -\overline{\Delta}^2 \, \overline{S}_{jk} \, \partial_j \partial_k \overline{u}_i \, , \tag{8}$$

so that $\overline{S}_{jk}$ plays the role of a tensorial viscosity for the filtered velocity field. This tensor is not positive-definite. Transforming to the principal coordinates, $\mathbf{x}'$, of $\overline{S}_{jk}$, one obtains (Leonard 1997):

$$-\overline{S}_{jk} \, \partial_j \partial_k \overline{f} = -\left(\alpha_1 \, \partial_{1'} \partial_{1'} + \alpha_2 \, \partial_{2'} \partial_{2'} + \alpha_3 \, \partial_{3'} \partial_{3'}\right) \overline{f} \, . \tag{9}$$

Since the eigenvalues of $\overline{S}_{jk}$, $(\alpha_1, \alpha_2, \alpha_3)$, satisfy $\alpha_1 + \alpha_2 + \alpha_3 = 0$, one has effectively negative diffusion along the stretching direction(s). This corresponds to local directional backscatter.

Let's examine the energy transfer and the dissipation. One easily obtains:

$$\partial_t \left(\frac{\overline{u}_i \overline{u}_i}{2} \right) + \partial_j \left(\left(\overline{P} + \frac{\overline{u}_i \overline{u}_i}{2} \right) \overline{u}_j + \overline{u}_i \left(\tau_{ij} - 2\nu \, \overline{S}_{ij} \right) \right) = -\epsilon \, , \tag{10}$$

with $\epsilon = -\tau_{ij}\overline{S}_{ij} + 2\nu\,\overline{S}_{ij}\overline{S}_{ij}$. The term $\partial_j(\cdots)$ represents the convective contribution to the energy flux, while ϵ represents the local energy flux: (1) the flux from large (and less filtered) scales to small (and more filtered) scales: effective dissipation if positive, effective backscatter if negative; and (2) the dissipation due to the molecular viscosity: clearly always positive. For homogeneous turbulence, the convective contribution has no net effect. We then write, for the global dissipation rate,

$$\frac{d\overline{E}}{dt} = \frac{d}{dt}\langle\frac{\overline{u}_i\overline{u}_i}{2}\rangle = -\langle\epsilon\rangle\ . \tag{11}$$

For uniform ν, the global dissipation due to viscosity is also obtained as

$$\langle\epsilon^\nu\rangle = \nu\,\langle 2\overline{S}_{ij}\overline{S}_{ij}\rangle = 2\nu\,\langle\frac{\overline{\omega}_i\overline{\omega}_i}{2}\rangle = 2\nu\,\overline{\mathcal{E}} \tag{12}$$

where $\overline{\omega}_i = \epsilon_{ijk}\partial_j\overline{u}_k$ (with ϵ_{ijk} the permutation tensor) is the filtered vorticity field and $\overline{\mathcal{E}}$ is the global enstrophy.

The contribution of the Leonard model to the local energy flux (dissipation or backscatter) is (Leonard, 1997; Borue & Orszag, 1998):

$$\begin{aligned}\epsilon^M = -\tau_{ij}^M\,\overline{S}_{ij} &= -\overline{\Delta}^2\,\partial_k\overline{u}_i\,\partial_k\overline{u}_j\overline{S}_{ij}\\ &= -\overline{\Delta}^2\,\left(\overline{S}_{ki}\overline{S}_{ij}\overline{S}_{jk} - \overline{R}_{ki}\overline{S}_{ij}\overline{S}_{jk}\right)\\ &= \overline{\Delta}^2\,\left(\frac{1}{4}\overline{\omega}_i\overline{S}_{ij}\overline{\omega}_j - \mathrm{tr}\left(\overline{S}^3\right)\right)\ .\end{aligned} \tag{13}$$

where $\overline{R}_{ij} = \left(\partial_j\overline{u}_i - \partial_i\overline{u}_j\right)/2 = -\epsilon_{ijk}\overline{\omega}_k/2$ is the antisymmetric rate of rotation tensor. This contribution is not necessarily positive, hence the natural backscatter provided by the model.

For homogeneous turbulence, the global contribution of the model is, however, dissipative as $\langle\epsilon^M\rangle$ is proportional to the negative of the global skewness. A sufficient condition to ensure global dissipation is thus that the global skewness of the LES field remains negative (the necessary condition being that $\langle\epsilon^\nu + \epsilon^M\rangle \geq 0$). The skewness is indeed negative in homogeneous turbulence and its DNS. It should also be negative in good LES. It was indeed found to remain negative in all LES's of decaying homogeneous turbulence that we conducted during the present investigation, these LES's being started from a filtered DNS field and thus having a negative global skewness initially. If one starts a DNS or a LES from a random field with Gaussian statistics, then the skewness is initially zero. However, as the simulation proceeds, it quickly becomes negative because the flow develops into "real" turbulence.

The one-term Leonard model could be constrained locally by putting a limiter on the directional negative diffusion: find the eigenvalues and eigenvectors of the local strain rate tensor, express the forcing term, $-C\,\overline{\Delta}^2\,\overline{S}_{jk}\partial_j\partial_k\overline{u}_i$ in this system of coordinates, and ignore (*i.e.*, clip) the direction(s) corresponding to negative diffusion. This certainly makes the model anisotropic. Notice that there is now a need for a new unknown parameter C. Indeed, since this "clipping" corresponds to a

major alteration of the original Leonard model, there is no reason to expect, *a priori*, that $C = 1$. Of course, this clipping approach can be refined further by enforcing that the total forcing term $\left(\nu\partial_j\partial_j - C\,\overline{\Delta}^2\,\overline{S}_{jk}\partial_j\partial_k\right)\overline{u}_i$ be clipped in the direction(s) corresponding to net negative diffusion. We notice, in passing, that the integral formulation developed by Cottet (1996, 1997a,b) essentially allows for convenient directional clipping without having to compute eigenvalues and eigenvectors.

Alternatively, one could clip the Leonard model isotropically by enforcing that $\epsilon^M \geq 0$ at each point. Defining $m_{ij} = \overline{\Delta}^2\,\partial_k\overline{u}_i\partial_k\overline{u}_j$, the model could be written as

$$\begin{aligned} \tau_{ij}^M &= C\,m_{ij} \qquad \text{if} \qquad -m_{ij}\overline{S}_{ij} \geq 0\,, \\ \tau_{ij}^M &= C\left[m_{ij} - \frac{(m_{kl}\overline{S}_{kl})}{(\overline{S}_{kl}\overline{S}_{kl})}\,\overline{S}_{ij}\right] \qquad \text{otherwise}\,. \end{aligned} \tag{14}$$

Again, there is a parameter C, and one can also refine this approach. For both clipping approaches, the determination of the parameter could be done using a dynamic procedure.

In any case, "clipping" guarantees pure dissipation (and hence numerical stability), but it isn't justified theoretically. Here, we wish to first investigate the unaltered model: no clipping. With good numerics, and assuming that the computation doesn't blow up, the hope is that such a model could indeed provide for reasonable local backscatter while remaining globally sufficiently dissipative. One could argue that, in principle, the unclipped one-term Leonard model is numerically ill-conditioned. Our numerical experience so far (decaying homogeneous turbulence and channel flow) is that the simulations do not blow up, confirming our hope that LES's with that model and without limiter (*i.e.*, with local backscatter) can indeed be carried out successfully. This is very good news. This result is probably due, in part, to the fact that the direction(s) of negative diffusion evolve in space and time while the simulation proceeds. The negative diffusion (which is certainly numerically unstable if applied forever) here constantly changes direction and is counterbalanced by positive diffusion. In a way, the simulation corresponds to dynamic dissipation events happening together with dynamic backscatter events, the mean remaining globally dissipative.

However, in our pseudo-spectral LES of decaying isotropic turbulence at high Re_λ, the one-term Leonard model, when used on its own, is found to provide too little global dissipation, see Figs. 3 to 5 (even though the simulation doesn't blow up). This is seen even more clearly when comparing the evolution of the LES energy spectrum with the DNS, see Figs. 7 to 9. Thus, we find that the one-term Leonard model does not suffice in actual LES runs. Hence, it was decided to develop and test a mixed model: add to the one-term Leonard model a purely dissipative term such as the dynamic Smagorinsky term:

$$\tau_{ij}^M = \overline{\Delta}^2\,\partial_k\overline{u}_i\,\partial_k\overline{u}_j - 2\,C\,\overline{\Delta}^2\,\left(2\overline{S}_{kl}\overline{S}_{kl}\right)^{1/2}\,\overline{S}_{ij}\,. \tag{15}$$

This is done in the same spirit as Zang *et al.* (1993) for the mixed model constructed by adding a dynamic Smagorinsky term to the Bardina model. See also

Horiuti (1997) for yet another two-parameter dynamic mixed model. This mixed model proposed here is still isotropic as opposed to non-isotropic models such as Carati & Cabot (1996) or Cottet (1997a,b). The first term is expected to be "the good filtered-scales model" because (1) it has some solid mathematical basis (see above) and (2) it naturally provides for local backscatter (as LES models should, see also Carati *et al.*, 1995a). On its own, however, it does not provide for enough dissipation. Conversely, the second term (with the classical Smagorinsky, 1963, $1/T$ scaling, $\left(2\overline{S}_{kl}\overline{S}_{kl}\right)^{1/2}$, such as above; or with the Kolmogorov scaling proposed by Carati *et al.*, 1995b, and tested in actual LES, *e.g.*, Dantinne *et al.*, 1998; or with other scalings,*e.g.*, see a review in Winckelmans *et al.*, 1996) has long been known to be a poor model that always produces local dissipation (when C is constrained to remain positive). For the proposed mixed model, we now have:

$$\epsilon^M = -\tau_{ij}^M \overline{S}_{ij} = -\overline{\Delta}^2 \, \partial_k \overline{u}_i \, \partial_k \overline{u}_j \, \overline{S}_{ij} + C \, \overline{\Delta}^2 \, \left(2\overline{S}_{ij}\overline{S}_{ij}\right)^{3/2} \; . \tag{16}$$

When the Smagorinsky term is used on its own as a LES model together with the dynamic procedure (Germano *et al.*, 1991; Ghosal *et al.*, 1992, 1995; Moin *et al.*, 1994), it doesn't necessarily lead to the correct dissipation as compared to the DNS; it very much depends on the filter used, see the results below, Figs. 3 to 5. We here wish to stress that, in the present approach, we really consider the one-term Leonard model as "the filtered-scales model" and the dynamic Smagorinsky term as an added numerical aid for enhancing the local dissipation. Although there is some similarity between the second possible clipped model presented above and the present mixed model, there are significant differences. The formulation of the mixed model is continuous (no "if" statement). Moreover, in the mixed model, the added term with dynamic C is not a clipping of the first term as C does not multiply both terms. As a consequence, the new mixed model is still isotropic, and it still allows for local backscatter; ϵ^M is not necessarily positive. Of course, the amount of local backscatter allowed is now less than for the pure Leonard model, and the dissipation is now more. Notice that the first term (the "model") still has the known coefficient coming from the Leonard expansion with the chosen smooth LES filter (e.g., Gaussian). In all we do here, it is with that same chosen LES filter that we filter the DNS results in order to compare them with the LES results (or, conversely, that we de-filter the LES results to compare them with the DNS results).

Whether the dynamically obtained C in this new mixed model will lead to the proper amount of dissipation as compared to DN, remains to be seen (see the results section). In that respect, for identical LES filters, it had better be that the dynamic C obtained in the mixed model turns out to be smaller than the dynamic C obtained when using the Smagorinsky term on its own as LES model. As mentioned above, C is here obtained through the dynamic procedure (Germano *et al.*, 1991; Ghosal *et al.*, 1992, 1995; Moin *et al.*, 1994) by (1) applying an additional test filter, $\widehat{G}$, which is such that the combined "LES + test" filter, $\widehat{\overline{G}}$, is similar the original LES filter, $\overline{G}$; (2) assuming similarity of the LES models at both levels, τ_{ij}^M similar to T_{ij}^M, with the same C; and (3) satisfying Germano's identity, $T_{ij} - \widehat{\tau}_{ij} = L_{ij} = \widehat{\overline{u}_i \overline{u}_j} - \widehat{\overline{u}}_i \widehat{\overline{u}}_j$, in

the least-square sense: $\langle E_{ij} E_{ij} \rangle$, where $E_{ij} = \left(T_{ij}^M - \widehat{\tau}_{ij}^M\right) - L_{ij}$, is minimized, with integration $\langle \ldots \rangle$ done over the homogeneous direction(s). C is thus uniform along the homogeneous direction(s). Moreover, along the non-homogeneous direction(s) (if any), it is also assumed that the spatial variation of C with respect to the test filter can be factored out, *i.e.*, that $\widehat{C\,a_{ij}} \simeq C\,\widehat{a}_{ij}$. This requirement is trivially satisfied if the test filter is only applied along the homogeneous direction(s), as is often the case in practice (but then the assumed similarity between the LES and LES+test filters is not strictly correct). Otherwise, it is only a (poor) assumption that should be validated *a posteriori* (at least statistically, when averaged over time).

Here, working in wave space, we take $\widehat{\overline{G}}(k) = \exp\left(-\alpha^2\, k^2 \overline{\Delta}^2/2\right)$, *i.e.*, $\widehat{\overline{\Delta}}/\overline{\Delta} = \alpha > 1$, which is indeed similar to $\overline{G}(k) = \exp\left(-k^2\overline{\Delta}^2/2\right)$. The required test filter is also Gaussian: $\widehat{G}(k) = \widehat{\overline{G}}(k)/\overline{G}(k) = \exp\left(-\left(\alpha^2-1\right)\, k^2\overline{\Delta}^2/2\right)$, *i.e.*, $\widehat{\Delta}/\overline{\Delta} = \sqrt{\alpha^2-1}$. Typically, we use $\alpha = 2$. Another filter is the top hat filter: $\overline{G}(k) = \sin\left(\sqrt{3}\,k\overline{\Delta}\right) / \left(\sqrt{3}\,k\overline{\Delta}\right)$, and thus $\widehat{\overline{G}}(k) = \sin\left(\sqrt{3}\,k\widehat{\overline{\Delta}}\right) / \left(\sqrt{3}\,k\widehat{\overline{\Delta}}\right)$. If we choose $\alpha = 2$, the test filter becomes $\widehat{G}(k) = \widehat{\overline{G}}(k)/\overline{G}(k) = \cos\left(\sqrt{3}\,k\widehat{\overline{\Delta}}\right)$ (Carati, 1997). This test filter is also easily applied in physical space using only grid values as it is the discrete "arithmetic mean": $\widehat{G}(x) = \left(\delta\left(x+\sqrt{3}\overline{\Delta}\right) + \delta\left(x-\sqrt{3}\overline{\Delta}\right)\right)/2$. Of course, one needs to choose $\overline{\Delta}$ so that $\sqrt{3}\overline{\Delta}$ is a multiple of the grid size Δ.

The dynamic procedure for the mixed model is summarized here as:

$$m_{ij} = \overline{\Delta}^2\, \partial_k \overline{u}_i\, \partial_k \overline{u}_j\ , \quad a_{ij} = 2\overline{\Delta}^2\, \left(2\overline{S}_{kl}\overline{S}_{kl}\right)^{1/2}\, \overline{S}_{ij}\ , \quad \tau_{ij}^M = m_{ij} - C\,a_{ij}\ ,$$

$$M_{ij} = \widehat{\overline{\Delta}}^2\, \partial_k \widehat{\overline{u}}_i\, \partial_k \widehat{\overline{u}}_j\ , \quad A_{ij} = 2\widehat{\overline{\Delta}}^2\, \left(2\widehat{\overline{S}}_{kl}\widehat{\overline{S}}_{kl}\right)^{1/2}\, \widehat{\overline{S}}_{ij}\ , \quad T_{ij}^M = M_{ij} - C\,A_{ij}\ ,$$

$$p_{ij} = L_{ij} + \left(\widehat{m}_{ij} - M_{ij}\right)\ , \quad q_{ij} = \left(\widehat{a}_{ij} - A_{ij}\right)\ , \quad C = \frac{\langle p_{ij}\, q_{ij}\rangle}{\langle q_{ij}\, q_{ij}\rangle}\ . \tag{17}$$

For homogeneous turbulence, all three directions are homogeneous so that $C = C(t)$. For the channel flow, two directions are homogeneous so that $C = C(y,t)$. Since the channel flow dynamical LES eventually reaches statistical equilibrium, time averaging can also be done at some point, and one ends up with a profile, $C = C(y)$. Then the dynamic procedure assumption above is statistically better verified.

Notice that the added dissipative term in the mixed model is formally of the same order as the one-term Leonard model: both involve product of first derivatives of the LES field. Since dynamic hyper-viscosity models such as

$$\tau_{ij}^M = 2\,C\,\overline{\Delta}^4\, \left(2\overline{S}_{kl}\overline{S}_{kl}\right)^{1/2}\, \partial_m\partial_m\overline{S}_{ij} \tag{18}$$

have also been used with some success in LES (*e.g.*, Winckelmans *et al.*, 1996, in *a priori* tests; Dantinne *et al.*, 1998, in actual LES with sharp cutoff test filtering), we also investigated the following possibility of mixed model:

$$\tau_{ij}^M = \overline{\Delta}^2\, \partial_k \overline{u}_i\, \partial_k \overline{u}_j + 2\,C\,\overline{\Delta}^4\, \left(2\overline{S}_{kl}\overline{S}_{kl}\right)^{1/2}\, \partial_m\partial_m\overline{S}_{ij}\ , \tag{19}$$

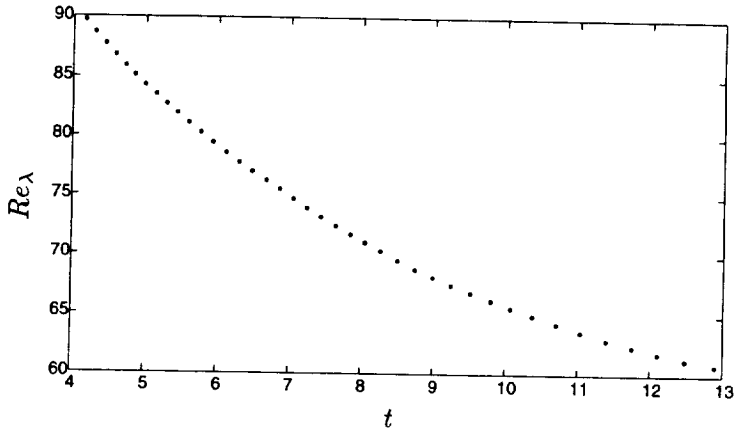

FIGURE 1. $Re_\lambda(t)$ for the reference 256^3 DNS.

where the added term now clearly involves higher order derivatives and is thus expected to only affect the high-end of the energy spectrum. When tested numerically with Gaussian filtering, this mixed model did not dissipate enough energy.

2. Results for decaying homogeneous turbulence

For the LES tests on decaying homogeneous turbulence, the solver is a dealiased pseudo-spectral code. The reference data is a 256^3 DNS at high Re_λ that was run using the same spectral code. The DNS was started using a field with given spectra and random phases. This initial condition then evolved into real turbulence. The usable reference DNS data then covers the window of Re_λ shown in Fig. 1. At the begining ($t = 4.17$, $Re_\lambda \approx 90$), the Kolmogorov scale, $\eta = \left(\nu^3/\langle\epsilon\rangle\right)^{1/4}$, is such that $k_{\max}\,\eta \approx 2$; the DNS is thus well-resolved. At the end ($t = 13.32$), $k_{\max}\,\eta \approx 4$. The $t = 4.17$ DNS was Gaussian filtered using $\overline{\Delta} = 2\sqrt{2}\,\Delta_{256}$, and was then further truncated to 64^3 (*i.e.*, $\overline{\Delta} = \Delta_{64}/\sqrt{2}$) to be used as an initial condition for the LES runs. Hence, at the maximum wavenumber of the truncated set, we have $\overline{G} = \exp\left(-\pi^2/4\right) = 0.085$; the 64^3 grid used to resolve the LES thus covers well the range where the LES filter is significant while not overkilling it. At half the maximum wavenumber, we have $\overline{G} = 0.54$. For the dynamic procedure, we used the classical value $\alpha = 2$. We also tried $\alpha = \sqrt{2}$, but the results were consistently slightly better with $\alpha = 2$.

As a first test of the one-term Leonard model, the correlation between the model, $\tau_{ij}^M = \overline{\Delta}^2 \partial_k \overline{u}_i \partial_k \overline{u}_j$, and the exact stress, τ_{ij}, was evaluated using the filtered DNS data. It came out very high, 0.92, in good agreement with correlations in Borue & Orszag (1998). That is certainly a victory for the one-term Leonard model, at least in such *a priori* testing. It shows that the expansion truncated to one term already contains most of the stress.

Notice that the correlation measures the alignement between the two stresses. It doesn't say anything about the "best" coefficient to use in front of the model. Since the original Leonard expansion has been truncated to one term, it is valid

to ask if this term shouldn't be rescaled somehow. Hence, as a second test of the one-term Leonard model, the dynamic procedure was applied to an assumed $\tau_{ij}^M = C\overline{\Delta}^2 \partial_k \overline{u}_i \partial_k \overline{u}_j$. The result came out to be $C = 1.0050$, pretty close to $C = 1$ indeed (difference of 0.5%). This is a double victory: one for the theoretical developments that claim that the good value is $C = 1$, and one for the dynamic procedure that indeed finds that value.

Filtering the DNS even more was also considered. With $\overline{\Delta}$ twice as large as above, the correlation came out as 0.89 and the dynamic C came out as $C = 0.9536$ (difference of 5%: not as good, but still very close. This filter size is probably too large with respect to the Kolmogorov scale of this high Re_λ turbulence.

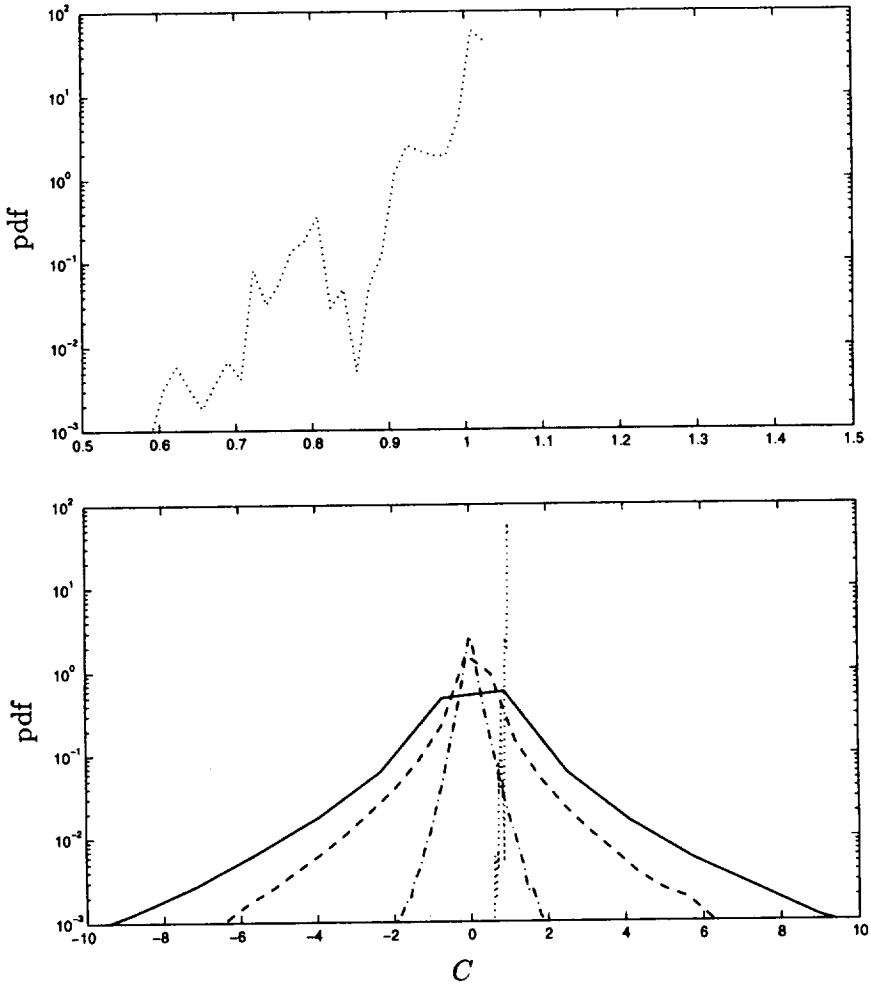

FIGURE 2. Pdf of the model coefficient, C: dynamic Leonard model, Gaussian: ····· ; Leonard model + dynamic Smagorinsky term, Gaussian: —— ; dynamic Smagorinsky model, Gaussian: ---- ; dynamic Smagorinsky model, sharp cutoff: —·— .

Finally, as a third test of the one-term Leonard model, the dynamic procedure was applied but this time locally (*i.e.*, no averaging over the homogeneous directions). The obtained pdf of C is given in Fig. 2. The striking result is that the pdf is extremely sharp, with prefered value: $C \approx 1$. Notice that the pdf is not symmetric; it is skewed to the left. Notice also that there are no negative C. Again, this is a victory of the model and of the local dynamic procedure. For comparison, we also provide the pdf of the Smagorinsky term when used as the LES model. Two cases are examined: Gaussian filtering and sharp cutoff filtering. In both cases, the obtained pdf is very wide with many negative C values, confirming that the Smagorinsky term is indeed a poor LES model.

From this *a priori* study, it certainly appears that there is no point in having something other than $C = 1$ in front of the one-term Leonard model. This is why the mixed model presented above only has one parameter: the one in front of the added dynamic Smagorinsky term. Notice that Fig. 2 also provides the pdf of that C; as expected, it is very wide, even wider than when the Smagorinsky term is used as LES model. This is to be expected since the Leonard term in the hybrid model is "the LES model", the remainder dynamic Smagorinsky term being added for enhancing dissipation with little pretention on actual LES modeling.

The results obtained when using the mixed model (Leonard model + dynamic Smagorinsky term) with Gaussian filtering are presented in Figs. 3 to 10. They are compared with (1) the DNS, (2) the Leonard model with Gaussian filtering, (3) the dynamic Smagorinsky model with Gaussian filtering, and (4) the dynamic Smagorinsky model with sharp cutoff filtering (often used in spectral LES). For fair comparison (quality versus computational cost), all LES's are run using the same resolution: 64^3. Moreover, for the LES's with Gaussian filtering, the quantities such as resolved energy spectra, $E(k)$, resolved energy, $E = \int_0^{k_{max}} E(k)\,dk$, and resolved enstrophy, $\mathcal{E} = \int_0^{k_{max}} k^2\,E(k)\,dk$, are evaluated by "defiltering" the LES results, i.e., by using $E(k) = \overline{E}(k)\,\exp\left(k^2\overline{\Delta}^2\right)$. This allows for straighforward comparison with the DNS and the sharp cutoff Smagorinsky LES. (Of course, another way would be to Gaussian filter the DNS and the sharp cutoff LES.)

The Leonard model with Gaussian filtering, when used on its own, does not blow up. However, it provides too little dissipation, see Figs. 3 and 5, even at the start. Thus, although the initial correlation between τ_{ij}^M and τ_{ij} is very high (0.92), the global model dissipation, $-\langle\tau_{ij}^M\overline{S}_{ij}\rangle$, is substantially lower than the exact filtered-scales dissipation, $-\langle\tau_{ij}\overline{S}_{ij}\rangle$ (here, at the start, 4.112 versus 6.773). As expected, the global model dissipation is positive since the global skewness of the LES fields is initially negative and remains so. The dynamic sharp cutoff Smagorinsky model leads to too much energy dissipation from the start, see Figs. 3 and 6. The dynamic Smagorinsky model with Gaussian filtering starts off with the correct slope, but it then quickly underdissipates, see Figs. 3 and 5. The mixed model starts off with the correct slope and follows well the energy decay curve, see Figs. 3 and 5. Initially, the total dissipation of the LES, model + viscous, is $(4.112+2.887)+1.5944 = 8.593$, to be compared to 8.367 for the 256^3 filtered DNS: only a 2.7% difference. Notice also

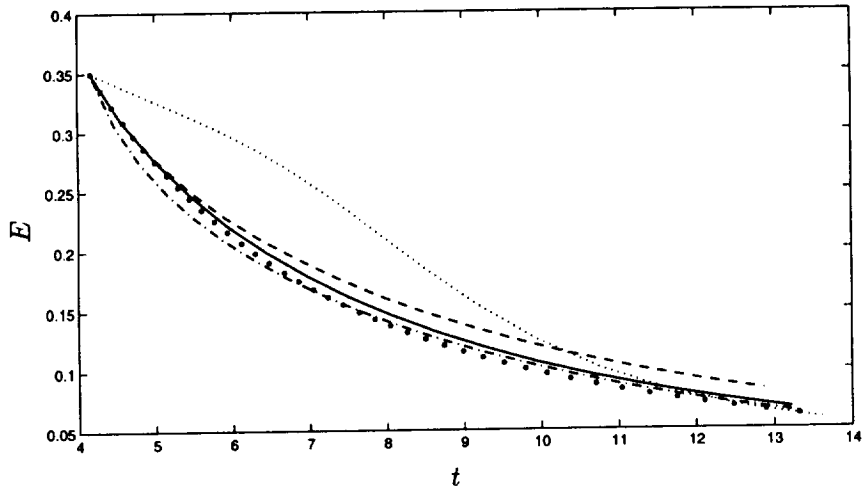

FIGURE 3. Resolved energy, $E(t)$: truncated DNS: • ; Leonard model, Gaussian: ····· ; Leonard model + dynamic Smagorinsky term, Gaussian: ——— ; dynamic Smagorinsky model, Gaussian: ---- ; dynamic Smagorinsky model, sharp cutoff: —·— .

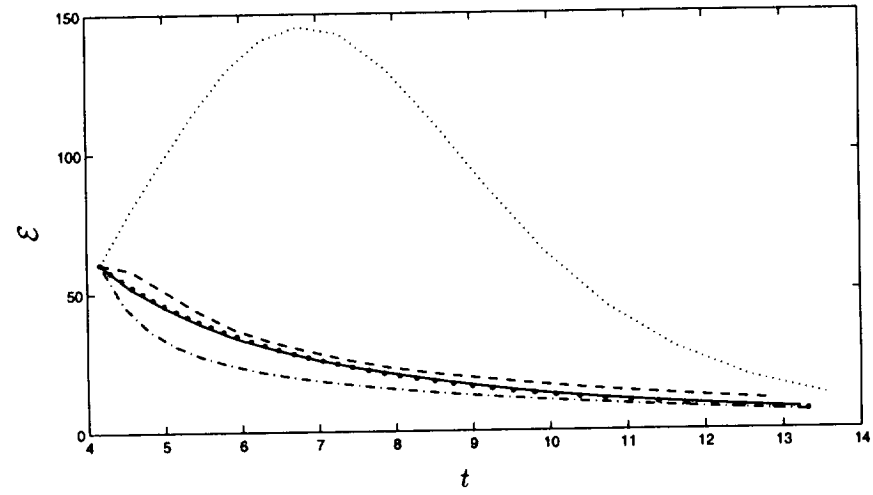

FIGURE 4. Resolved enstrophy, $\mathcal{E}(t)$: truncated DNS: • ; Leonard model, Gaussian: ····· ; Leonard model + dynamic Smagorinsky term, Gaussian: ——— ; dynamic Smagorinsky model, Gaussian: ---- ; dynamic Smagorinsky model, sharp cutoff: —·— .

the significant contribution of the Leonard term to the model global dissipation; it is larger than the contribution of the dynamic Smagorinsky term: 4.112 versus 2.887. As expected, it is positive since the global skewness of the LES fields is initially negative and remains so.

The differences between the investigated models are even more dramatic when

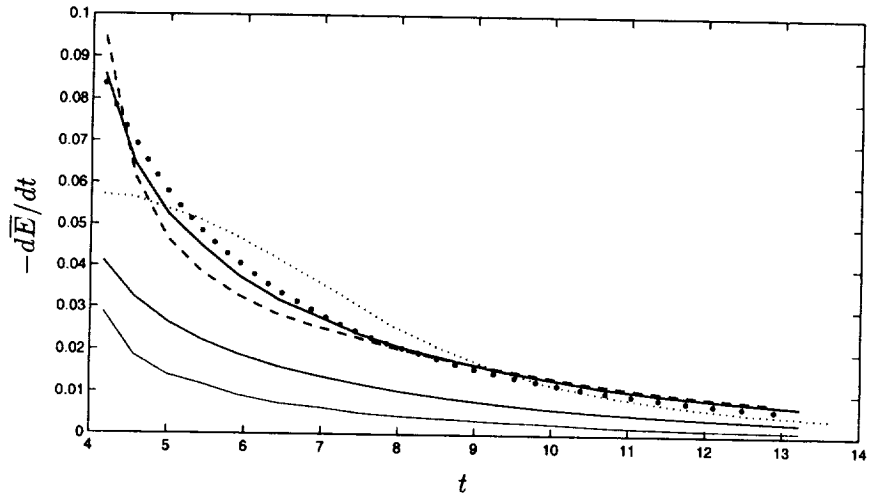

FIGURE 5. Dissipation of resolved energy, $-d\overline{E}/dt = -\langle \tau_{ij}^M \overline{S}_{ij} \rangle + 2\nu \langle \overline{S}_{ij} \overline{S}_{ij} \rangle$: truncated DNS, Gaussian: • ; Leonard model, Gaussian: ····· ; Leonard model + dynamic Smagorinsky term, Gaussian: ——— (Leonard: ——— (thin), Smagorinsky: ——— (thinner)); dynamic Smagorinsky model, Gaussian: ---- .

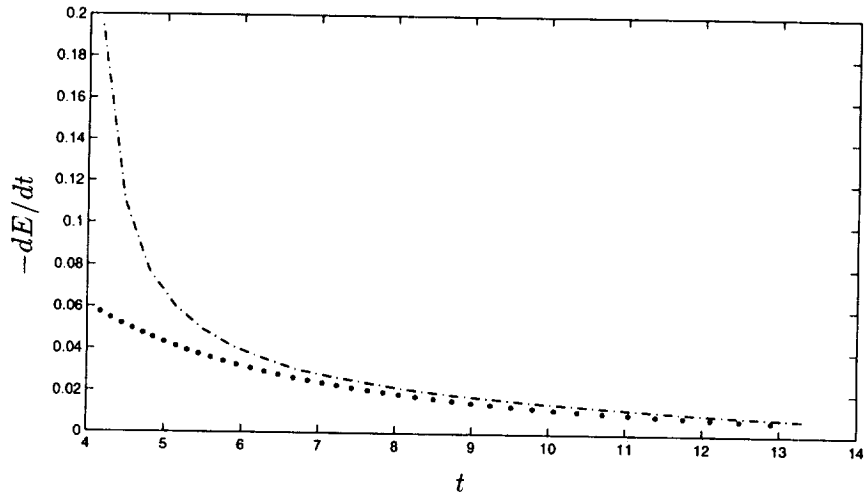

FIGURE 6. Dissipation of resolved energy, $-dE/dt$: truncated DNS, sharp cutoff: • ; dynamic Smagorinsky model, sharp cutoff: —·— .

considering the decay of the enstrophy (which puts more weight on the high-end of the spectrum), see Fig. 4: the dynamic sharp cutoff Smagorinsky model badly misses the initial slope of enstrophy decay (too much decay). Its Gaussian version also misses the initial slope, but on the other side (not enough decay). The mixed model performs very well not only initially, but for the whole course of the simulation; the LES decay curve is almost identical to the DNS curve.

The energy spectra produced by the mixed model are also clearly superior, see

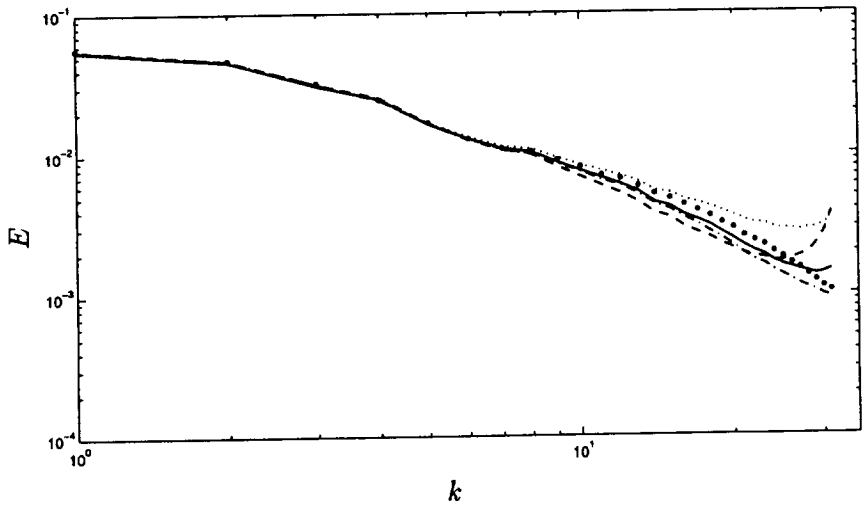

FIGURE 7. Resolved spectrum, $E(k)$, at $t \approx 4.5$: truncated DNS: • ; Leonard model, Gaussian: ····· ; Leonard model + dynamic Smagorinsky term, Gaussian: ——— ; dynamic Smagorinsky model, Gaussian: - - - - ; dynamic Smagorinsky model, sharp cutoff: —·— .

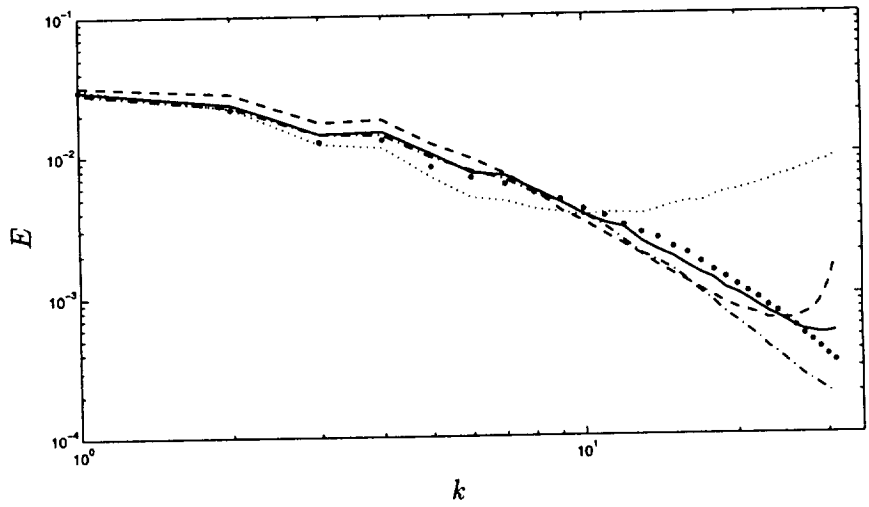

FIGURE 8. Resolved spectrum, $E(k)$, at $t \approx 7.5$: truncated DNS: • ; Leonard model, Gaussian: ····· ; Leonard model + dynamic Smagorinsky term, Gaussian: ——— ; dynamic Smagorinsky model, Gaussian: - - - - ; dynamic Smagorinsky model, sharp cutoff: —·— .

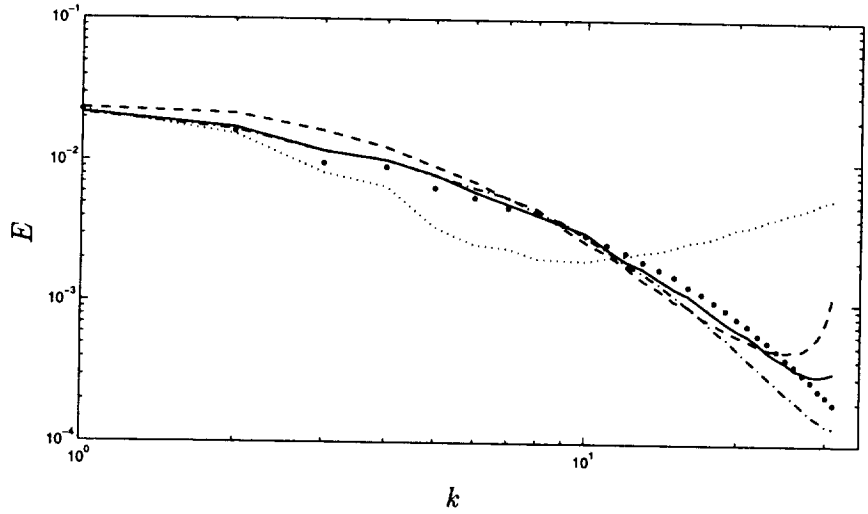

FIGURE 9. Resolved spectrum, $E(k)$, at $t \approx 9.0$: truncated DNS: • ; Leonard model, Gaussian: ····· ; Leonard model + dynamic Smagorinsky term, Gaussian: ——— ; dynamic Smagorinsky model, Gaussian: - - - - ; dynamic Smagorinsky model, sharp cutoff: —·— .

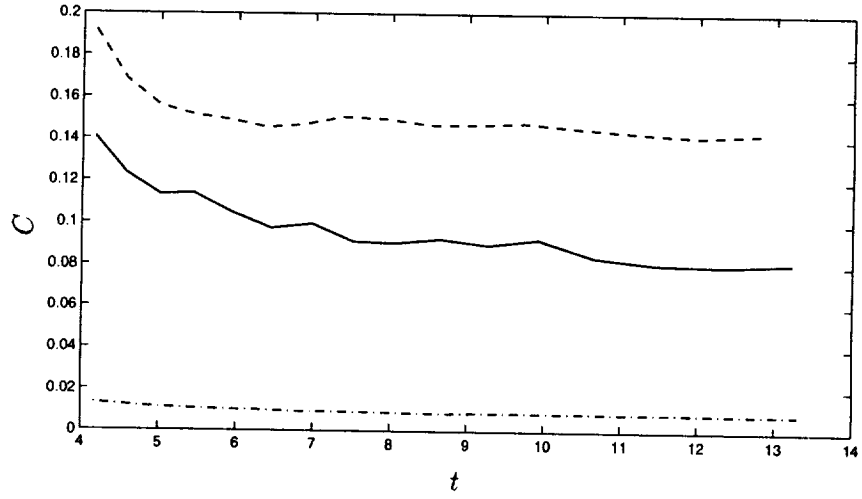

FIGURE 10. Model coefficient, $C(t)$: Leonard model + dynamic Smagorinsky term, Gaussian: ——— ; dynamic Smagorinsky model, Gaussian: - - - - ; dynamic Smagorinsky model, sharp cutoff: —·— .

Figs. 7 to 9; they closely match the DNS spectra over most of the range and for the whole course of the simulation except for the few last wavenumbers (that are here artificially enhanced on the graph because of the "defiltering" mentioned above). The sharp cutoff Smagorinsky model shows some discrepancy in the spectrum, starting at fairly low wavenumbers. Its Gaussian version doesn't perform significantly

better. As to the dynamic model coefficient, Fig. 10, it is seen that the C of the Smagorinsky term in the mixed model is indeed smaller than the C of the Smagorinsky model; the one-term Leonard model thus contributes significantly to the success of the mixed model.

3. Results for the channel flow

For the channel flow investigation, the solver is a fourth order finite difference code. The reference DNS is the AGARD database at $Re_\tau = h\,u_\tau/\nu = 395$ of Mansour *et al.* (1996) (see also Rodi & Mansour, 1993), where h is half the channel width and $u_\tau = \sqrt{\tau_w}$ is the friction velocity with τ_w the mean wall friction. The computational domain is $(L_x, L_y, L_z) = (2\pi, 2, 2\pi/3)h$. The LES filter is chosen as Gaussian in the homogeneous directions, x and z, and top hat in the non-homogeneous direction, y:

$$\overline{G} = \exp\left(-k_x^2\overline{\Delta}_x^2/2\right)\ \frac{\sin\left(\sqrt{3}\,k_y\overline{\Delta}_y\right)}{\left(\sqrt{3}\,k_y\overline{\Delta}_y\right)}\ \exp\left(-k_z^2\overline{\Delta}_z^2/2\right)\ . \tag{20}$$

Hence, the mixed model here becomes

$$\tau_{ij}^M = \overline{\Delta}_x^2\,\partial_x\overline{u}_i\,\partial_x\overline{u}_j + \overline{\Delta}_y^2\,\partial_y\overline{u}_i\,\partial_y\overline{u}_j + \overline{\Delta}_z^2\,\partial_z\overline{u}_i\,\partial_z\overline{u}_j - 2\,C\,\overline{\Delta}^2\ \left(2\overline{S}_{kl}\overline{S}_{kl}\right)^{1/2}\ \overline{S}_{ij}\ , \tag{21}$$

where the "effective" $\overline{\Delta}$ for the added dynamic Smagorinsky term is simply taken as $\left(\overline{\Delta}_x\,\overline{\Delta}_y\,\overline{\Delta}_z\right)^{1/3}$. Notice here another nice feature of the Leonard model: as opposed to the Smagorinsky model, there is no need to define an effective $\overline{\Delta}$. The dynamic procedure is done with $\alpha = 2$. Hence, the test filter here becomes:

$$\widehat{G} = \exp\left(-3\,k_x^2\overline{\Delta}_x^2/2\right)\ \cos\left(\sqrt{3}\,k_y\overline{\Delta}_y\right)\ \exp\left(-3\,k_z^2\overline{\Delta}_z^2/2\right)\ . \tag{22}$$

The test filter is applied in wave space in x and z and in physical space in y (using the arithmetic mean of the two neighbor grid points as explained previously).

For the preliminary runs done so far, the ratios of LES numerical grid to LES filter size are $\Delta_x/\overline{\Delta}_x = 2$, $\Delta_y/\overline{\Delta}_y = \sqrt{3}$ and $\Delta_z/\overline{\Delta}_z = 2$. The LES grid is 48x49x48.

Results on normalized mean profiles as a function of normalized distance to the wall are provided in Figs. 11 to 13: velocity, model stress and model dissipation. With the same smooth filtering, the mixed model outperforms the dynamic Smagorinky model: better mean velocity profile. Notice that the contribution of the Leonard part to the mixed model is significant; for the mean stress, it is higher than the contribution of the dynamic Smagorinsky term; for the mean dissipation, its contribution is higher close to the wall and slightly lower in the core flow. Notice also that the Leonard term contribution to the mean dissipation is indeed positive for all y although it is not necessarily positive locally because of the model backscatter. It is also found that the Leonard fraction of the model stress is essentially linear from the beginning of the log region to the channel center. This behavior is similar to what was obtained by Domaradzki & Saiki (1997) and Domaradzki & Loh (1998)

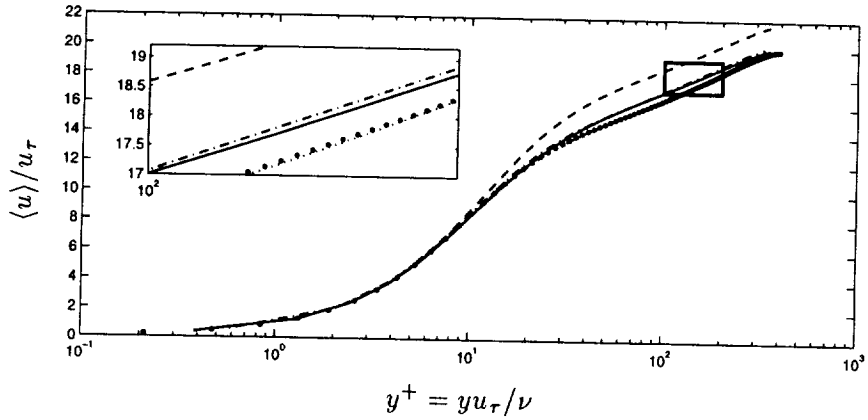

FIGURE 11. Mean velocity profile: DNS: • ; Leonard model + dynamic Smagorinsky term, 48x49x48, Gaussian and top hat: —— ; dynamic Smagorinsky model, 48x49x48, Gaussian and top hat: ---- ; dynamic Smagorinsky model, 32x33x32, sharp cutoff: —·— ; dynamic Smagorinsky model, 48x49x48, sharp cutoff: ····· .

using their LES subgrid-scale estimation model and comparing with filtered DNS data. This behavior is different from the behavior of the dynamic Smagorinky term (when used in the mixed model) or model (when used on its own), see Fig. 12.

However, when running a 48x49x48 LES using the Smagorinsky model with sharp cutoff test filtering in x and z and no test-filtering in y, the obtained mean velocity profile is closer to the DNS than for the mixed model with the smooth filtering and filter size used so far. That doesn't necessarily mean that the Smagorinsky model with sharp cutoff is superior. But it certainly calls for further study of the mixed model by investigating other ratios of numerical grid to filter size, other filters, and the effect of the y-grid non-uniformity (see, *e.g.*, Ghosal & Moin, 1995). It also calls for further *a priori* testing of the Leonard and mixed models using DNS of channel flows. This work is still in progress.

We provide in Fig. 14 the mean stress profile for the LES done using the mixed model. The different terms add up to the linear profile for the total stress as expected. Close to the wall, the main contribution is the one due to the viscous stress. Away from the wall, the main contribution is the "Reynolds" stress: $\langle \overline{u} \rangle \langle \overline{v} \rangle - \langle \overline{u}\,\overline{v} \rangle$. For the remainder (total stress minus Reynolds stress), the model contribution away from the wall is significantly higher than the viscous contribution, the Leonard contribution being itself higher than the Smagorinsky contribution. For comparison, Fig. 15 provides the mean stress profile when using the Smagorinsky model with same smooth filtering. Again, the model contribution is higher than the viscous contribution in the core flow.

Figures 16 and 17 provide the mean dissipation profiles: model contribution and viscous contribution. The viscous contribution is dominant close to the wall but is dominated by the model in the core flow. There are significant differences between the mixed model and the Smagorinky model as far as profiles of model versus viscous dissipation are concerned.

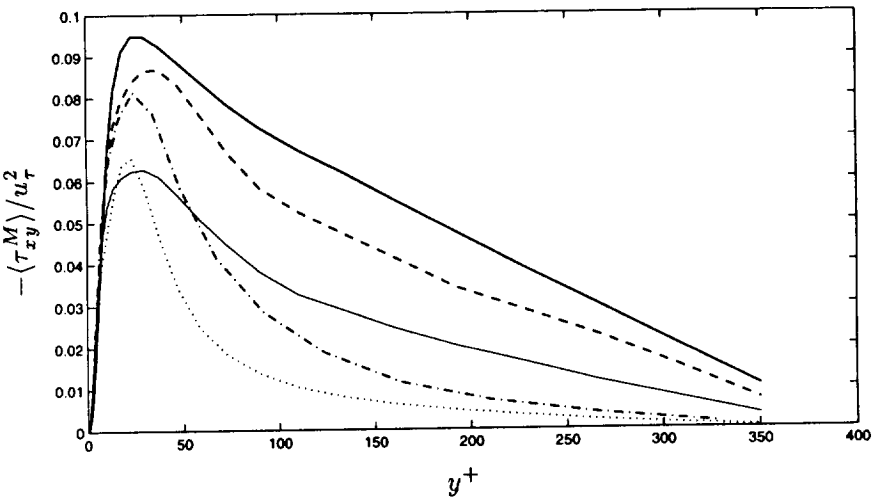

FIGURE 12. Mean model stress profile: Leonard model + dynamic Smagorinsky term, 48x49x48, Gaussian and top hat (Leonard: ——— , Smagorinsky: ———); dynamic Smagorinsky model, 48x49x48, Gaussian and top hat: ---- ; dynamic Smagorinsky model, 32x33x32, sharp cutoff: —·— ; dynamic Smagorinsky model, 48x49x48, sharp cutoff: ····· .

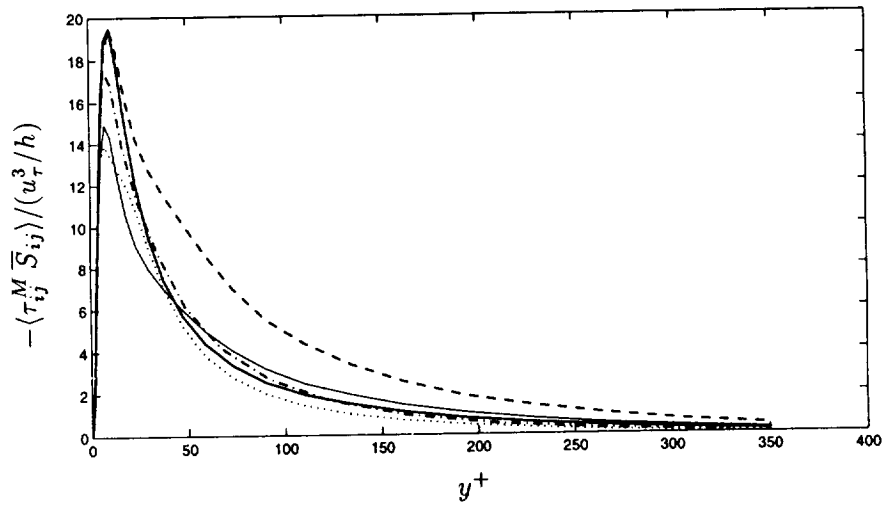

FIGURE 13. Mean model dissipation profile: Leonard model + dynamic Smagorinsky term, 48x49x48, Gaussian and top hat (Leonard: ——— , Smagorinsky: ———); dynamic Smagorinsky model, 48x49x48, Gaussian and top hat: ---- ; dynamic Smagorinsky model, 32x33x32, sharp cutoff: —·— ; dynamic Smagorinsky model, 48x49x48, sharp cutoff: ····· .

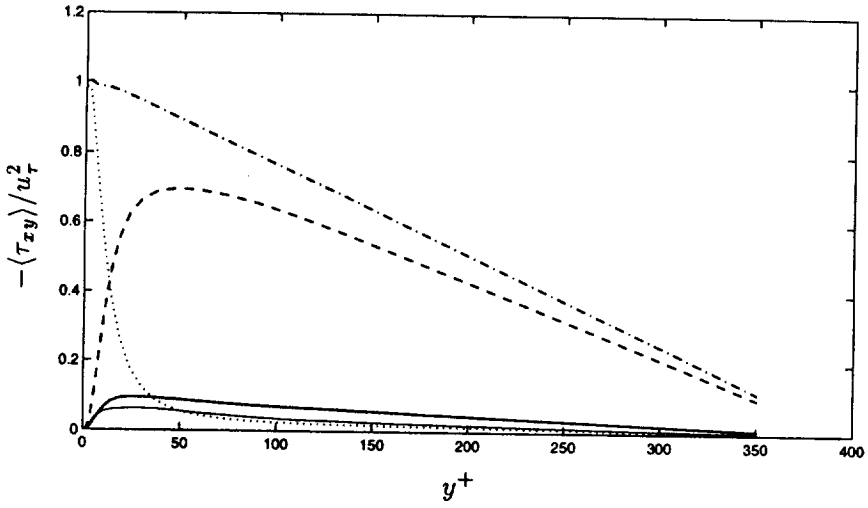

FIGURE 14. Mean stress profile for 48x49x48 LES using the Leonard model + dynamic Smagorinsky term, Gaussian and top hat: Leonard stress: ——, dynamic Smagorinsly stress: —— ; Reynolds stress, $(\langle \overline{u} \rangle \langle \overline{v} \rangle - \langle \overline{u}\,\overline{v} \rangle)/u_\tau^2$: ---- ; viscous stress, $2\nu \langle \overline{S}_{xy} \rangle / u_\tau^2$: ····· ; total stress: —·— .

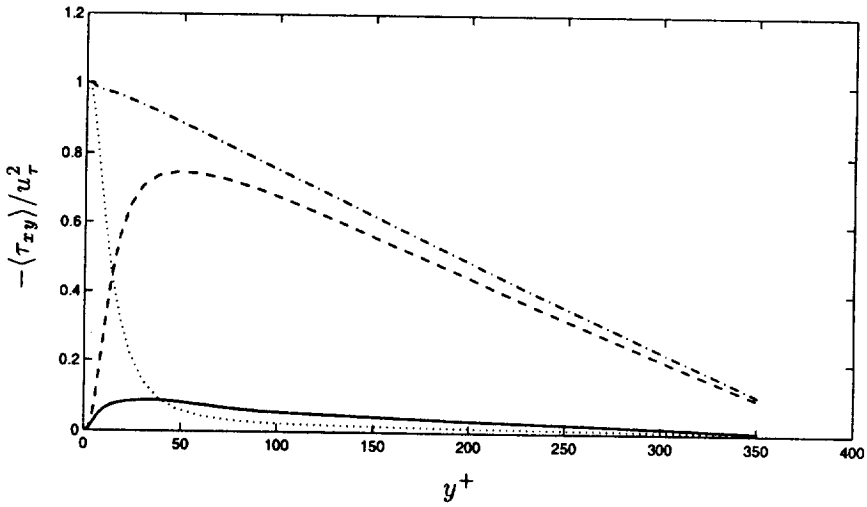

FIGURE 15. Mean stress profile for 48x49x48 LES using the dynamic Smagorinky model, Gaussian and top hat: model stress: ——; Reynolds stress, $(\langle \overline{u} \rangle \langle \overline{v} \rangle - \langle \overline{u}\,\overline{v} \rangle)/u_\tau^2$: ---- ; viscous stress, $2\nu \langle \overline{S}_{xy} \rangle / u_\tau^2$: ····· ; total stress: —·— .

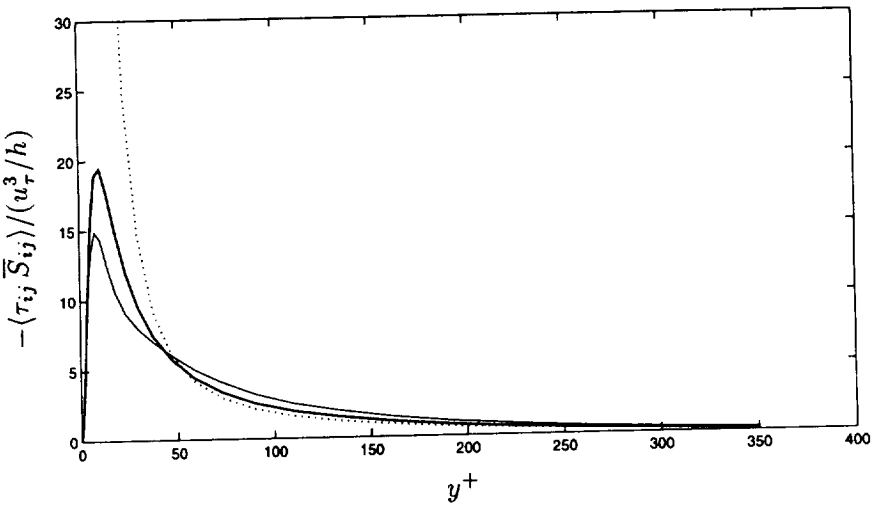

FIGURE 16. Mean dissipation profile for 48x49x48 LES using the Leonard model + dynamic Smagorinsky term, Gaussian and top hat: Leonard dissipation: ——— ; dynamic Smagorinsly dissipation: ——— ; viscous dissipation, $2\nu\,\langle\overline{S}_{ij}\overline{S}_{ij}\rangle/(u_\tau^3/h)$: ..... .

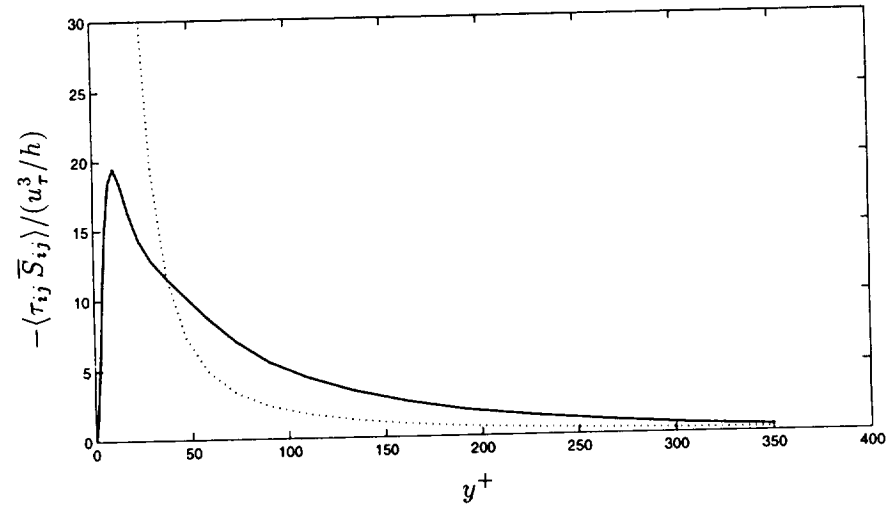

FIGURE 17. Mean dissipation profile for 48x49x48 LES using the dynamic Smagorinsky model, Gaussian and top hat: model dissipation: ——— ; viscous dissipation, $2\nu\,\langle\overline{S}_{ij}\overline{S}_{ij}\rangle/(u_\tau^3/h)$: ..... .

4. Conclusions

A new mixed model which uses the one-term Leonard model supplemented by a purely dissipative dynamic Smagorinsky term has been developed and tested in LES of decaying homogeneous turbulence and of channel flow. The dynamic procedure has been used to determine the coefficient of the Smagorinsky term. The one-term Leonard model provides for significant local backscatter while remaining globally dissipative. In *a priori* testing, its correlation with DNS was greater than 0.9. However, this model was found to provide too little dissipation in actual LES although it didn't blow up. Hence the need for the added dissipation provided by the dynamic Smagorinsky term in the mixed model. In 64^3 LES of decaying homogeneous turbulence started from Gaussian filtered 256^3 DNS at $Re_\lambda \simeq 90$, the new mixed dynamic model performed significantly better than the dynamic Smagorinsky model with same filtering; it also outperformed the dynamic Smagorinsky model with sharp cutoff filtering: much better energy spectra, energy decay, and enstrophy decay. For the preliminary 48^3 LES runs on the channel flow at $Re_\tau = 395$, the LES filter was Gaussian in the homogeneous directions and top hat in the non-homogeneous direction. The mixed dynamic model also outperformed the dynamic Smagorinsky model in that case. However, the dynamic Smagorinsky model with sharp cutoff test filtering in the homogeneous directions and no test filtering in the non-homogeneous direction still produced a better mean velocity profile. This result calls for further investigations.

REFERENCES

BARDINA, J., FERZIGER, J. H. & REYNOLDS, W. C. 1983 Improved turbulence models based on large eddy simulation of homogeneous incompressible turbulence. *Report TF-19*, Thermosciences Div., Dept. of Mech. Eng., Stanford University.

BORUE, V. & ORSZAG, A. 1998 Local energy flux and subgrid-scale statistics in three-dimensional turbulence. *J. Fluid Mech.* **366,** 1-31.

CARATI, D., GHOSAL, S. & MOIN, P. 1995 On the representation of backscatter in dynamic localization models. *Phys. Fluids.* **7**(3), 606-616.

CARATI, D., JANSEN, K. & LUND, T. 1995 A family of dynamic models for large-eddy simulation. *Annual Research Briefs*, Center for Turbulence Research, NASA Ames/Stanford Univ., 35-40.

CARATI, D. & CABOT, W. 1996 Anisotropic eddy viscosity models. *Proc. Summer Program*, Center for Turbulence Research, NASA Ames/Stanford Univ., 249-258.

CARATI, D.& VANDEN EIJNDEN, E. 1997 On the self-similarity assumption in dynamic models for large eddy simulations. *Phys. Fluids.* **9**(7), 2165-2167 (L).

CARATI, D., WINCKELMANS, G. S. & JEANMART, H. 1998 On reversibility in modeling for large eddy simulations. (In preparation.)

CLARK, R. A., FERZIGER, J. H. & REYNOLDS, W. C. 1979 Evaluation of subgrid-scale models using an accurately simulated turbulent flow. *J. Fluid Mech.* **91,** 1-16.

COTTET, G.-H. 1996 Artificial viscosity models for vortex and particle methods. *J. Comput. Phys.* **127,** 299-308.

COTTET, G.-H. 1997 Anisotropic subgrid-scale numerical schemes for Large Eddy Simulations of turbulent flows. (Submitted Sept. 1997.)

COTTET, G.-H. & WRAY, A. A. 1997 Anisotropic grid-based formulas for subgrid-scale models.*Annual Research Briefs*, Center for Turbulence Research, NASA Ames/Stanford Univ., 113-122.

DANTINNE, G., JEANMART, H., WINCKELMANS, G. S., LEGAT, V. & CARATI, C. 1998 Hyper-viscosity and vorticity-based models for subgrid-scale modeling. *Applied Scientific Research.* **59,** 409-420.

DOMARADZKI, J. A. & SAIKI, E. M. 1997 A subgrid-scale model based on the estimation of unresolved scales of turbulence. *Phys. Fluids.* **9,** 2148-2164.

DOMARADZKI, J. A. & LOH K.-C. 1998 The subgrid-scale estimation model in the physical space representation. submitted to Phys. Fluids.

GERMANO, M., PIOMELLI, U., MOIN, P. & CABOT, W. 1991 A dynamic subgrid-scale eddy-viscosity model. *Phys. Fluids A.* **3**(7), 1760-1765.

GHOSAL, S., LUND, T. S. & MOIN, P. 1992 A local dynamic model for large-eddy simulation. *Annual Research Briefs*, Center for Turbulence Research, NASA Ames/Stanford Univ., 3-25.

GHOSAL, S., LUND, T. S., MOIN, P. & AKSELVOLL, K. 1995 A dynamic localization model for large-eddy simulation of turbulent flows. *J. Fluid Mech.* **286,** 229-255.

GHOSAL, S. & MOIN, P. 1995 The basic equations for the large-eddy simulation of turbulent flows in complex geometry. *J. Comput. Phys.* **118,** 24-37.

HORIUTI, K. 1997 A new dynamic two-parameter mixed model for large-eddy simulation. *Phys. Fluid.* **9**(11), 3443-3464.

LEONARD, A. 1974 Energy cascade in large-eddy simulations of turbulent fluid flows. *Adv. Geophys.* **18,** 237.

LEONARD, A. 1997 Large-eddy simulation of chaotic convection and beyond. *AIAA Paper 97-0204, 35th Aerospaces Sciences Meeting & Exhibit*, Jan. 6-10, 1997, Reno, N.,

LIU, S., MENEVEAU, C. & KATZ, J. 1994 On the properties of similarity subgrid-scale models as deduced from measurements in a turbulent jet. *J. Fluid Mech.* **275,** 83-119.

LUND, T. S. & NOVIKOV, E. A. 1992 Parametrization of subgrid-scale stress by the velocity gradient tensor. *Annual Research Briefs*, Center for Turbulence Research, NASA Ames/Stanford Univ., 27-43.

MANSOUR, N. N., MOSER, R. D. & KIM, J. 1996 Reynolds number effects in low Reynolds number turbulent channels. (In preparation, data in AGARD database)

MCMILLAN, O. J. & FERZIGER, J. H. 1979 Direct testing of subgrid-scale models. *AIAA J.* **17,** 1340.

MOIN, P., CARATI, D., LUND, T., GHOSAL, S, & AKSELVOLL, K. 1994 Developments and applications of dynamic models for large eddy simulation of complex flows. *AGARD-CP-551, 74th Fluid Dynamics Symposium on Application of Direct and Large Eddy Simulation to Transition and Turbulence*, Chania, Crete, Greece, 1: 1-9.

PIOMELLI, U., MOIN, P. & FERZIGER, J. H. 1988 Model consistency in large eddy simulation of turbulent channel flows. *Phys. Fluids.* **31**(7), 1884-1891.

RODI, W. & MANSOUR, N. N. 1993 Low-Reynolds-number $\kappa - \epsilon$ modeling with the aid of direct simulation data. *J. Fluid Mech.* **250,** 509-529.

SALVETTI, M. V. & BANERJEE, S. 1995 *A priori* tests of a new dynamic subgrid-scale model for finite-difference large-eddy simulations. *Phys. Fluids.* **7**(11), 2831-2847.

SMAGORINSKY, J. 1963 General circulation experiments with the primitive equations. *Mon. Weather Rev.* **91,** 99-164.

WINCKELMANS, G. S., LUND, T. S., CARATI, D. & WRAY, A. A. 1996 *A priori* testing of subgrid-scale models in the velocity-pressure and the vorticity-velocity formulations, *Proc. Summer Program*, Center for Turbulence Research, NASA Ames/Stanford Univ., 309-328.

ZANG, Y., STREET, R. L. & KOSEFF, J. 1993 A dynamic mixed subgrid-scale model and its application to turbulent reciculating flows. *Phys. Fluids A.* **5,** 3186.

Center for Turbulence Research
Proceedings of the Summer Program 1998

Comparison of dynamic Smagorinsky and anisotropic subgrid-scale models

By Georges-Henri Cottet[1] AND Oleg V. Vasilyev[2]

1. Introduction

LES models using dynamically computed coefficient values have been extensively used since the pioneering work of Germano (Germano *et al.* 1991). Starting from the Smagorinsky subgrid-scale model, the common idea to all these models is to extrapolate the information on the resolved fields at two scale levels to compute optimal coefficient values.

A simple solution to the integral equations which follow from this approach can be obtained by restricting the test filter action to certain directions and assuming that the model coefficient only varies along the orthogonal directions. The coefficient values are then derived from simple least-square formulas.

The resulting global dynamic model has been successfully used for a number of flows having at least one direction of homogeneity. For more general flows, the brute force solution of the integral equations may lead to persistent local negative values, which have a destabilizing effect on the numerical solver. Clipping these values lead to discard up to 50% of the coefficients. Moreover, local large values of the coefficient require an implicit treatment of the eddy viscosity term to avoid prohibitively small time-steps. Ghosal *et al.* (1995) have proposed two models to address this issue. In the first one the positivity of the coefficient is rigorously constrained in the integral equation. In the second one, negative coefficient values are allowed, but the model is supplemented by a transport equation for the subgrid-scale kinetic energy. These techniques do alleviate the restrictions of the global dynamic model, but at the expanse of a significant computational overhead (Cabot, 1994).

Our work here has been motivated by practical considerations. It seems clear that the difficulties associated with the solution of integral equations in the dynamic Smagorinsky model would be avoided if the variations of the coefficient over a scale of the order of the grid-size could be assumed to be small. This, in turn, requires that the underlying subgrid-scale model is well-conditioned for the dynamic procedure, or, in other words, has good correlation properties. It is well known that this is not the case for the Smagorinsky model. Leonard's expansion of the subgrid-scale residual stress, by contrast, is known to have very good correlation properties. Its drawback in actual implementations is that it contains backscatter as well as dissipation. The backscatter control strategies which have been proposed so far do

1 LMC-IMAG, Université Joseph Fourier, BP 53 Grenoble Cédex 9, France

2 Present address: Department of Mechanical and Aerospace Engineering, University of Missouri, Columbia, MO 65211

not allow it to retain its anisotropic features and thus are inefficient (Vreman *et al.* 1997). This explains why this model is in general complemented by Smagorinsky model in so-called mixed models.

In Cottet (1997) we have proposed a simple grid-implementation of Leonard's expansion which enables a truly anisotropic backscatter control. Tests with constant coefficients for homogeneous isotropic turbulence as well as in channel flow geometry (Cottet and Wray, 1997) showed that this model performs better than the Smagorinsky model. In particular, unlike the Smagorinsky model, it has the property of vanishing in laminar regimes and solid boundaries. Moreover, the specific backscatter control enabled by the grid formulas overcomes the lack of dissipation in general observed in the implementation of Leonard's expansion (Vreman *et al.* 1997).

In view of these results, we believe that this model is a good candidate for simple local dynamic implementations. In the following section we summarize the key properties of the anisotropic subgrid scale formulas and present our approach for dynamic coefficient calculations. In Section 3 we then discuss results obtained for channel flows and draw some preliminary conclusions.

2. The dynamic anisotropic model

2.1 Anisotropic formulas

They are derived from Leonard's expansion of the self-similarity model, using integral approximations. Let ζ be a filter function satisfying

$$\int x_k x_l \zeta(\mathbf{x})\, d\mathbf{x} = \delta_{kl}\ , \qquad k,l = 1,\ldots,3. \tag{1}$$

If Δ is the filter width, then the formal Taylor series expansion gives

$$\Delta^2 D_{ik}\overline{\mathbf{u}}(\mathbf{x}) D_{jk}\overline{\mathbf{u}}(\mathbf{x}) = \frac{1}{\Delta^3}\left\{\int [\overline{u}_j(\mathbf{y}) - \overline{u}_j(\mathbf{x})][\overline{u}_i(\mathbf{y}) - \overline{u}_i(\mathbf{x})]\zeta(\frac{\mathbf{y}-\mathbf{x}}{\Delta})\, d\mathbf{y} + O(\Delta^2)\right\}, \tag{2}$$

where the notation $D_{ik}\overline{\mathbf{u}}$ stands for $\frac{\partial \overline{u}_i}{\partial x_k}$. Differentiating this expression we obtain the following SGS formula:

$$\partial_j \tau_{ij}(\mathbf{x}) \simeq -\frac{C}{\Delta^4}\int [u_j(\mathbf{y}) - u_j(\mathbf{x})][u_i(\mathbf{y}) - u_i(\mathbf{x})]\partial_j \zeta(\frac{\mathbf{y}-\mathbf{x}}{\Delta})\, d\mathbf{y}. \tag{3}$$

For the details of derivation we refer to Cottet (1997). The final SGS model is obtained by approximating Eq. (3), using numerical integration over the grid points close to $\mathbf{x}$. In other words, the filter function ζ is approximated by a discrete grid-based filter.

In the case of a non-uniform grid, a discrete grid-based filter cannot have the same filter widths in all three directions, and thus Eq. (2) can not be formally derived.

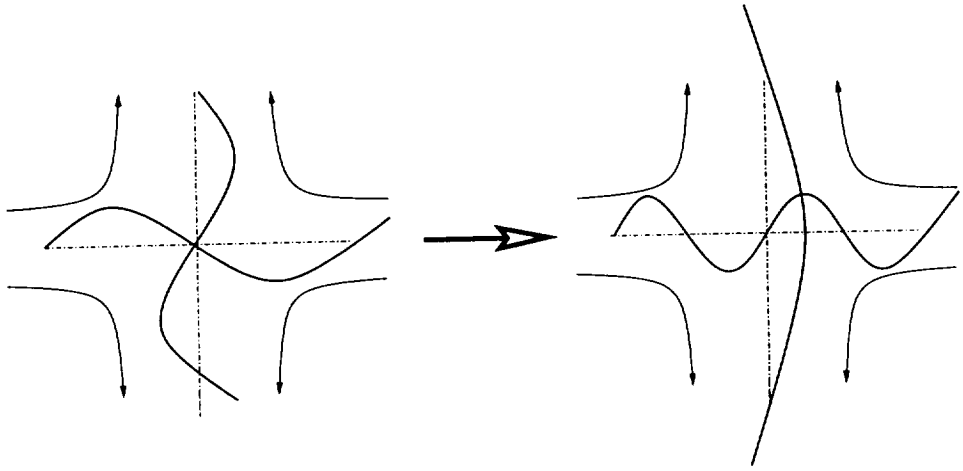

FIGURE 1. Flow around an hyperbolic point and production of small or large scale along the strain directions.

However, the integral in the right-hand side of Eq. (2) can be derived directly from the similarity model. It can be easily shown that

$$\frac{1}{\Delta^3}\int [\overline{u}_j(\mathbf{y})-\overline{u}_j(\mathbf{x})][\overline{u}_i(\mathbf{y})-\overline{u}_i(\mathbf{x})]\zeta(\frac{\mathbf{y}-\mathbf{x}}{\Delta})\,d\mathbf{y} = \widehat{\overline{u}_i\overline{u}_j}-\hat{\overline{u}}_i\hat{\overline{u}}_j+[\hat{\overline{u}}_i-\overline{u}_i][\hat{\overline{u}}_j-\overline{u}_j],$$

where $\widehat{(\cdot)}$ denotes the filtering operation with the filter function ζ. This observation, which shows that the anisotropic formulas are $O(\Delta^4)$ corrections over the similarity model, is true for any anisotropic discrete grid-based filter.

A nice feature of the integral formulas (2) and (3) is that they give a simple way to distinguish the backscatter and dissipation subgrid contributions. Multiplying Eq. (3) by $\overline{\mathbf{u}}$ leads to

$$\int \partial_j\tau_{ij}(\mathbf{x})\overline{u}_i(\mathbf{x})\,d\mathbf{x} \simeq \frac{C}{2}\Delta^{-4}\int [\overline{\mathbf{u}}(\mathbf{y})-\overline{\mathbf{u}}(\mathbf{x})]\cdot\nabla\zeta(\frac{\mathbf{y}-\mathbf{x}}{\Delta})|\overline{\mathbf{u}}(\mathbf{y})-\overline{\mathbf{u}}(\mathbf{x})|^2\,d\mathbf{x}\,d\mathbf{y}. \quad (4)$$

We illustrate the meaning of the Eq. (4) by considering spherically symmetric filters. In this case, $\nabla\zeta(\mathbf{x}) = \mathbf{x}\zeta'(|\mathbf{x}|)$ with $\zeta' \leq 0$. Therefore, dissipation or backscatter in the subgrid-scale model occurs respectively in the directions of compression or dilatation. The sketch in Fig. 1 shows the distinction among strain directions in the flow and illustrates the mechanism of small scales production. As a result, the following clipped model prevents backscatter and only dissipates in the direction of flow compression:

$$\partial_j\tau_{ij} \simeq \Delta^{-4}\int \left\{[\overline{\mathbf{u}}(\mathbf{x})-\overline{\mathbf{u}}(\mathbf{y})]\cdot\nabla\zeta(\frac{\mathbf{x}-\mathbf{y}}{\Delta})]\right\}_+ [\overline{\mathbf{u}}(\mathbf{x})-\overline{\mathbf{u}}(\mathbf{y})]\,d\mathbf{y}, \quad (5)$$

where $a_+ = \max(0,a)$.

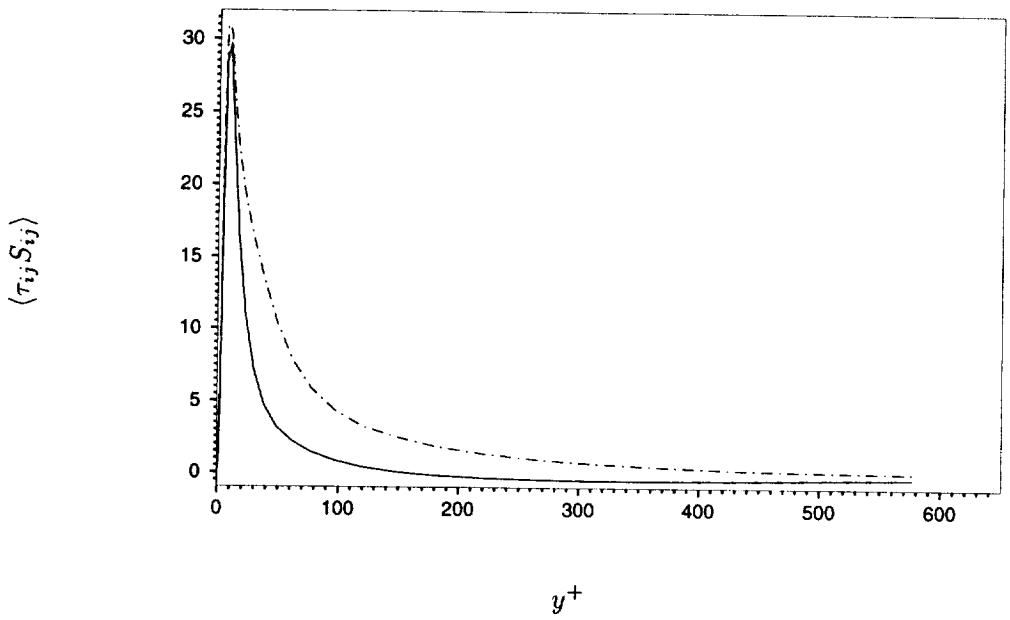

FIGURE 2. LES of plane channel flow at $Re_\tau = 650$. Subgrid-scale dissipation. $-\cdot-$: global dynamic Smagorinsky model; ——: global dynamic anisotropic model.

2.2 Dynamic procedure

Given their relationship with the similarity model, it is natural to view our subgrid-scale formulas as a model of the energy transfer between the scales Δ and $\Delta/2$. Note that this scale range is in general recognized to contain the essential part of the transfer between resolved and unresolved scales. Thus, in order to determine the model coefficient C, it is natural to compute the residual stress between the scales $\hat{\Delta} = 2\Delta$ and Δ explicitly and to match it with the model evaluated on the filtered field $\hat{\bar{\mathbf{u}}}$. In other words, the coefficient C should satisfy

$$\widehat{\bar{u}_i \bar{u}_j} - \hat{\bar{u}}_i \hat{\bar{u}}_j = C\{\sum_{\mathbf{y}\sim\mathbf{x}} [\hat{\bar{u}}_j(\mathbf{y}) - \hat{\bar{u}}_j(\mathbf{x})][\hat{\bar{u}}_i(\mathbf{y}) - \hat{\bar{u}}_i(\mathbf{x})]\zeta(\frac{\mathbf{y}-\mathbf{x}}{\hat{\Delta}}) \tag{6}$$

Following the standard dynamic formulation, a least square solution has to be sought to solve this system of six equations and, if one desired, to constrain variations of the coefficients only along specific directions. Note, that the approach we just described bypasses the Germano identity and instead uses the assumption that the models act in a limited scale range. One may object that replacing an exact identity by an assumption is not satisfactory. However, in our view the subgrid-scale models can never be expected to be very accurate (not speaking of the least square procedure used to adjust the coefficient to a number of equations); therefore, the exactness of the Germano identity is not of crucial importance in the dynamic determination of the coefficient.

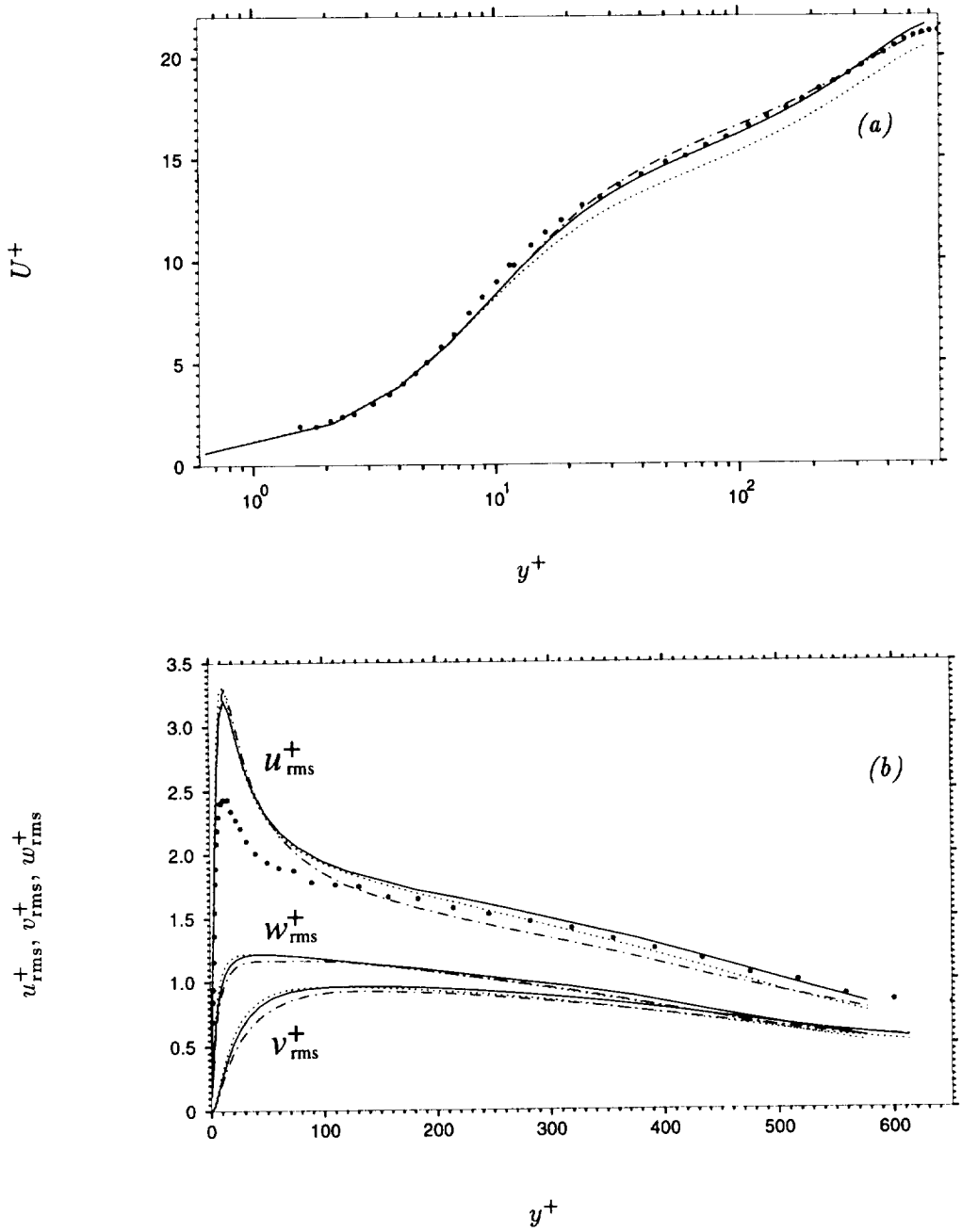

FIGURE 3. LES of plane channel flow at $Re_\tau = 650$. (a) Mean streamwise velocity; (b) Turbulence intensities. ·····: no-model; – · –: global dynamic Smagorinsky model; ——: global dynamic anisotropic model; •: experiment (Hussain and Reynolds, 1970).

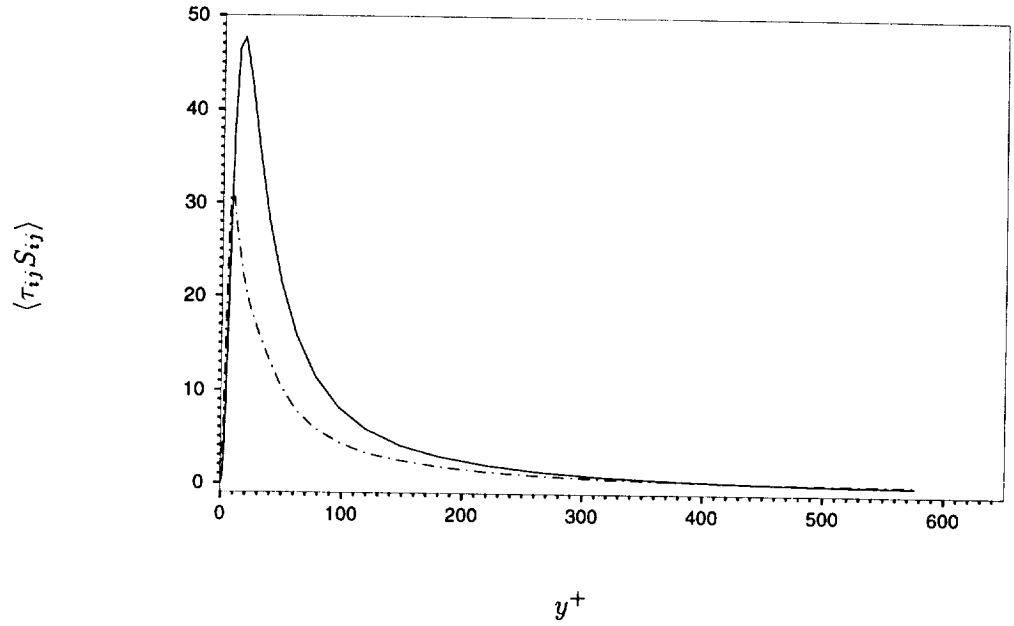

FIGURE 4. LES of plane channel flow at $Re_\tau = 650$. Subgrid-scale dissipation. – · –: global dynamic Smagorinsky model; ——: local dynamic anisotropic model.

3. Preliminary results

To validate our dynamic procedure, we have first implemented a *global* dynamic model. In this case the coefficient is constrained to vary only along the direction normal to the channel walls. A least square solution of Eq. (6) under this additional constraint is then given by

$$C = \frac{\langle L_{ij} M_{ij} \rangle}{\langle M_{kl} M_{kl} \rangle}$$

where L_{ij}, M_{ij} receptively denote the left- and right-hand side of Eq. (6), $\langle \cdot\,, \cdot \rangle$ means averaging in the wall parallel directions, and repeated indices mean the summation. This model has been compared to the classical global dynamic Smagorinsky model for a channel flow at Reynolds number of 650. The grid resolution is $48 \times 49 \times 48$. The numerical method is a fourth order finite-difference scheme on a staggered grid system; the grid is refined in the wall normal direction according to a hyperbolic tangent law (see Morinishi *et al.*, 1998, for details). In both methods, a sharp cut-off test filter was used along the homogeneous directions. Figure 2 shows the subgrid-scale dissipation produced by the models. They peak at about the same value. However, the anisotropic model seems to dissipate in a narrower region around the walls.

Figure 3a shows the mean velocity profiles. Both methods give a fair agreement with the experimental data when compared to the case where no-model is used. The similar fair agreement of the two models for the turbulent intensity profiles is

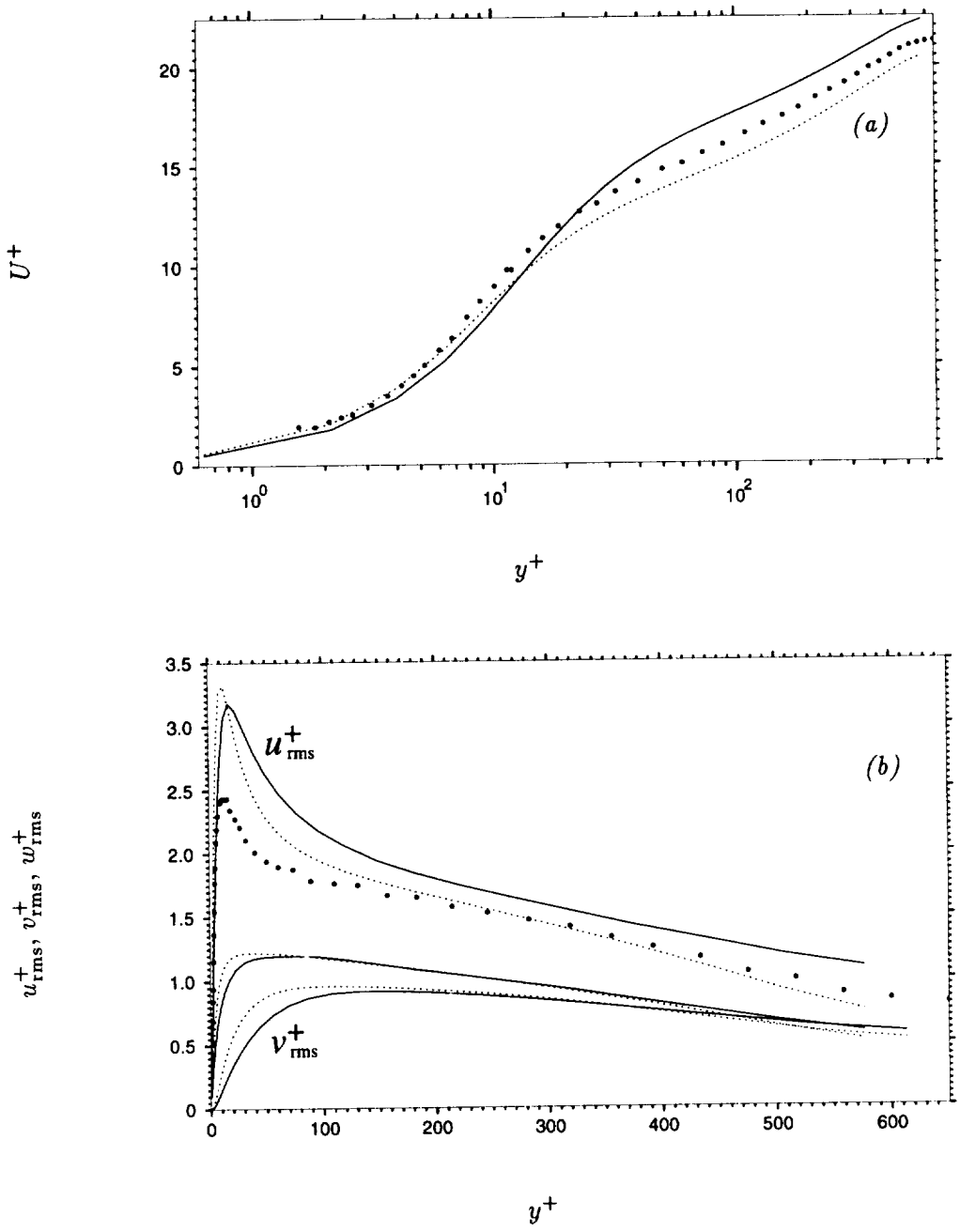

FIGURE 5. LES of plane channel flow at $Re_\tau = 650$. (a) Mean streamwise velocity; (b) Turbulence intensities. ·····: no-model; ——: local dynamic anisotropic model; •: experiment (Hussain and Reynolds, 1970).

observed in Fig. 3b.

Next we will discuss the implementation of *local* dynamic procedure for the anisotropic subgrid-scale model. There are several ways to implement local dynamic procedure. We decided to focus on the following approach: compute local coefficient C using Eq. (6), discard negative values of C, and use clipped formula (5) to evaluate subgrid-scale contribution.

Our first observation is that this model does not produce large local values of C and thus does not require an implicit treatment of the eddy viscosity term. This already contrasts with the behavior of local dynamic Smagorinsky model where the local model coefficient is found without solving an integral equation. In this case an explicit treatment of the eddy-viscosity term would lead to prohibitively small time-steps.

Figure 4 shows the comparison of the subgrid-scale dissipation of the local dynamic anisotropic model and global dynamic Smagorinsky model. Mean velocity and turbulence intensity profiles for local dynamic anisotropic model are presented in Fig. 5. The results of Fig. 5 show a reasonable agreement between the local dynamic anisotropic model and the experimental results. However, the excess dissipation in the near wall region causes the velocity profile to be overestimated in the middle of the channel.

We have also implemented a local dynamic model with a test filter in the physical space identical to the discrete grid-based filter. This option proved to produce too much dissipation. However, this model practically did not require any clipping: less then 1% of the model coefficients had negative values. This somehow substantiates our expectations that the anisotropic formulas are better conditioned than the Smagorinsky model for local dynamic coefficient calculations. However, more numerical experiments are certainly needed to fully assess the usefulness of these models in general geometries. In particular, we believe that a local model with a test filter adapted to the computational grid is the most natural extension of the method. It is well known that the choice of the test filter is a critical parameter in all dynamic formulations and has to be taken into account in the definition of the filter width. Note that even global dynamic models fail to give good results if the filter width issue is not properly defined (Lund 1997). This issue and its impact on local dynamic anisotropic calculations will be more systematically addressed in a future work.

REFERENCES

CABOT, W. 1994 Local dynamic subgrid-scale models in channel flow. *CTR Annual Research Briefs,* Center for Turbulence Research, NASA Ames/Stanford Univ., 143-160.

COTTET, G.-H. 1997 Anisotropic subgrid-scale models for Large Eddy Simulations of turbulent flows. *Preprint.*

COTTET, G.-H. & WRAY, A. A. 1997 Anisotropic grid-based formulas for subgrid-scales models. *CTR Annual Research Briefs,* Center for Turbulence Research, NASA Ames/Stanford Univ., 113-122.

GERMANO, M., PIOMELLI, U., MOIN, P. & CABOT, W. H. 1991 A dynamic subgrid-scale eddy viscosity model. *Phys. Fluids A.* **3,** 1760-1765.

GHOSAL, S., LUND, T.S, MOIN, P. & AKSELVOLL, K. 1995 A dynamic localization model for large-eddy simulation of turbulent flow. *J. Fluid Mech.* **286,** 229-255.

HUSSAIN, A. K. M. F. & REYNOLDS, W. C. 1970 *The mechanics of a perturbation wave in turbulent shear flow.* Rep.FM-6, Thermosciences Div., Dept. Mech. Eng., Stanford, CA.

LIU, S., MENEVEAU, C. & KATZ, J. 1994 The property of similarity subgrid-scale models. *J. Fluid Mech.* **275,** 83-119.

LUND, T. S. 1997 On the use of discrete filters for large eddy simulations. *CTR Annual Research Briefs,* Center for Turbulence Research, NASA Ames/Stanford Univ., 83-96.

MORINISHI, Y., LUND, T. S., VASILYEV, O. V., & MOIN, P 1998 Fully Conservative Higher Order Finite Difference Schemes for Incompressible Flow. *J. Comp. Phys.* **143,** 90-124.

VREMAN, V., GEURTS, B. & KUERTEN, H. 1997 Large-eddy simulations of the turbulent mixing layer. *J. Fluid Mech.* **339,** 357-390.

Center for Turbulence Research
Proceedings of the Summer Program 1998

Approximate lateral boundary conditions for turbulent simulations

By J. Jiménez AND C. Vasco[1]

Several synthetic lateral boundary conditions are tested on a direct numerical simulation in which only half of a turbulent channel is computed, with the boundary conditions being imposed at the central plane. This is motivated by the problem of matching large-eddy simulations to wall models. When the boundary contains no turbulent structure, a thin layer is created which decorrelates it from the flow, and the mean and fluctuating velocities are poorly represented. Introducing more structure, obtained by modifying velocity planes copied from the interior of the flow, improves the fluctuations, but the mean velocity profiles are still poor. This is traced to spurious pressure fluctuations which induce artificial energy fluxes, and can be partially avoided by approximately taking into account continuity in the generation of the boundary conditions. This third boundary condition gives good results for the velocity fluctuations, but some pressure and the mean velocity errors persist.

It is argued that the problem is related to that of imposing boundary conditions along characteristics in a hyperbolic system, and possible avenues for improvement are suggested.

1. Introduction

One of the problems of large-eddy simulations of complex flows is the high resolution required in the proximity of walls. The Reynolds shear stresses that determine the mean velocities are carried by the non-universal large turbulent scales. Sub-grid stresses in LES should be provided by the sub-grid model, but most present models do not reproduce the shear stresses well (Jiménez & Moser 1998). The simulations should therefore be designed so that most of the shear stresses are carried by the resolved eddies, and this implies that the filters should not be wider than a fixed small fraction of the local integral eddy scale. As the wall is approached the integral scale decreases and so does the necessary filter width. Baggett, Jiménez & Kravchenko (1997) estimated that the number of points required for a grid satisfying those requirements scales as $N \sim Re_\tau^2$, and increases without limit with the Reynolds number. Most of those points are concentrated in the near-wall region, and the resulting resolution requirements have for some time been the main roadblock for the practical application of LES (Chapman 1979).

To decrease the number of points, one possibility would be to use fully anisotropic subgrid models correctly representing the Reynolds stresses in all the regions of the

1 School of Aeronautics, U. Politécnica de Madrid.

flow, but, as mentioned above, such models are not available at present. Another possibility is to compute the wall region by some separate technique, usually RANS, while solving the LES equations only in an interior domain away from the wall. Variants of this approach are the various proposals to use subgrid models which smoothly merge into RANS near the wall (Schumann 1975, Sullivan *et al.* 1994, Spalart *et al.* 1997).

In implementing this second class of approximations, two problems arise. The first is to provide a good model for the wall region, while the second is to transfer to the outer simulation the information obtained in this way. This implies synthesizing instantaneous boundary conditions for which only a few low-order statistics are known, but which are realistic enough to minimize the formation of spurious layers as the simulated flow adapts to the synthetic boundary. Both problems are different and essentially independent of one another. Only the second one is addressed in this paper.

To separate our investigation as completely as possible from the particular requirements of modeling wall turbulence, we restrict our computations to the lower half of a plane channel and impose our boundary conditions at the central plane, trying to mimic the information coming from the other half of the channel. Within the limits of the summer program we also restrict ourselves to direct numerical simulations, thus making our conclusions independent of the particular sub-grid model used in real LES computations.

Our problem is then to find boundary conditions that can be imposed at a fully turbulent domain boundary, using only low order statistics of the flow outside the domain, such that a direct numerical simulation approximates the statistics of the turbulent flow within. Well-known subsets of this problem are the formulations of inflow and outflow boundary conditions for turbulent flows, which have been treated often. The techniques used are different for each of them and, while outflows are usually treated by advective boundary conditions in which information is allowed to leave the domain as smoothly as possible, inflows require information coming from outside, and therefore Dirichlet conditions. A general discussion of the boundary conditions required for incompressible viscous flows is Kreiss & Lorentz (1989), and examples of particular techniques used to generate synthetic incoming turbulence at inflows are Lee, Lele & Moin (1992), Le, Moin & Kim (1997), and Na & Moin (1998).

By choosing as our boundary the center of the channel we focus on the harder problem of lateral conditions, in which the average normal velocity is either zero or small with respect to the intensity of the turbulent fluctuations, and where weak inflows and outflows coexist at locations which are not known a-priori. This is also the problem relevant to imposing conditions near walls, where information, be it provided by a separate model running in the wall layer or by the smooth merging of LES and RANS, has to flow in both directions.

Baggett (1997) studied the same problem and tried several types of boundary conditions in which the three velocity components were prescribed at an off-wall plane in a channel. The information contained in his velocities ranged from purely

random numbers to fairly complete sets of structures corresponding to real channel turbulence at the same location. His experiments were in general not successful, but the location of his boundary plane was inside the near-wall region, where turbulence dynamics is known to be most complicated, and his numerical scheme was a low-order finite-difference scheme. It was not clear whether his lack of success was due to inappropriate boundary conditions or to any of those complicating factors. In this note we largely repeat, and extend, his experiments using higher order numerics and staying away from the wall region, in order to clarify the reasons for any failure.

The note is organized as follows. The numerical technique is described first, followed in §3 by a description of the results of three different synthetic boundary conditions. That section also contains a discussion of the errors introduced in the pressure field, and of their influence on other errors in the simulation. Finally the results and their relation to the general theory of hyperbolic equations are briefly discussed and suggestions for future work are offered.

2. Simulations

2.1 Flow description

The flow simulated is the lower half of a plane turbulent channel, between the lower wall at $y = 0$ and the central plane at $y = 1$. The Reynolds number is $Re_\tau = 190$, based on the friction velocity and on the half channel width. Since the full channel is nominally symmetric, all of the energy and momentum fluxes (i.e. the mean shear stress) should be zero at the central boundary. Other properties at the boundary, when needed, are taken from the comparable simulation by Kim, Moin & Moser (1987). Wall units are defined in the usual way in terms of the friction velocity at the wall, u_τ, and used throughout the paper.

2.2 Numerical scheme

The numerical method is essentially the one used by Kim, Moin & Moser (1987). The equations are integrated in a box which is doubly periodic in the streamwise and spanwise directions, of size $L_x \times L_z = 2.7 \times 1.58$, and bounded by the center of the channel and by one wall. The spatial discretization is Fourier spectral in x and z, and fourth-order B-splines in the wall-normal direction y (Jiménez, Pinelli & Uhlmann, 1998). The nonlinear terms are dealiased in the two Fourier directions by the 2/3 rule, but there is no dealiasing in y. Time discretization is third-order Runge-Kutta for the nonlinear convective terms and implicit Euler for the dissipative ones.

The numerical resolution in x, y, and z is $48 \times 97 \times 64$ before dealiasing, and the viscosity coefficient is $\nu = 1/3250$. The grid is stretched in the wall-normal direction according to the mapping

$$y_j = \frac{1}{2} + \frac{\tanh[2\pi\kappa(2j/N - 1)]}{2\tanh(2\pi\kappa)},$$

where $j = 0 \ldots N$ and $\kappa = 0.22$. This grid is stretched both at the wall and at the central plane, which was found necessary to accommodate the spurious thin

viscous layers generated by the boundary conditions. The stretching at the central boundary could probably be relaxed if better boundary conditions are found.

The equations are written in terms of the wall-normal vorticity ω_2 and of the Laplacian of the wall-normal velocity, $\Phi = \nabla^2 v$. The evolution equations to be solved are

$$\frac{\partial \Phi}{\partial t} = h_v + \frac{1}{Re}\nabla^2 \Phi, \tag{1}$$

$$\frac{\partial \omega_2}{\partial t} = h_g + \frac{1}{Re}\nabla^2 \omega_2, \tag{2}$$

where h_v and h_g are the nonlinear terms, as defined by Kim, Moin & Moser (1987). Continuity is imposed when obtaining the velocities from the evolution variables. Pressure is not used in the evolution of the flow and is obtained only as a post-processed variable. Nonlinear terms are discretized in the y-direction by means of a collocation method, and the linear ones by Galerkin projection.

The boundary conditions in the non-periodic direction are imposed at each time substep in the elliptic dissipative substep,

$$\left(1 - \frac{\Delta t}{Re}\nabla^2\right) \omega_2^{n+1} = \omega_2^n + \Delta t\, h_g^n, \tag{3}$$

$$\left(1 - \frac{\Delta t}{Re}\nabla^2\right) \Phi^{n+1} = \Phi^n + \Delta t\, h_v^n, \tag{4}$$

$$\nabla^2 v^{n+1} = \Phi^{n+1}. \tag{5}$$

At the wall, $y = 0$, the non-slip boundary conditions can be reduced to

$$v = \frac{\partial v}{\partial y} = \omega_2 = 0. \tag{6}$$

We give the boundary conditions at the center of the channel in the form of instantaneous planes of the three velocity components, which can be reduced to v, $\partial v/\partial y$, and ω_2 using continuity. The boundary conditions for (3) are therefore Dirichlet but, for (4)-(5), they are given in terms of v and $\partial v/\partial y$ rather than Φ. They are imposed by expressing the solution as a linear combination of the following Helmholtz problems, which refer only to the boundary condition at $y = 1$.

1) A particular solution (Φ_p, v_p) of the full system (4)-(5), with homogeneous Neumann boundary conditions for Φ_p and v_p at the central plane.

2) A solution Φ_1 of (4) with a homogeneous right-hand-side and $\Phi_1 = 1$ at $y = 1$, plus the associated solution for v_1, with Φ_1 as the right-hand side of (5) and $\partial v_1/\partial y = 1$ at $y = 1$.

3) A solution v_2 of (5) with Φ_1 in the right-hand-side and $v_2 = 1$ at $y = 1$.

The solution of (4)–(5) is then

$$v = v_p + a_1 v_1 + a_2 v_2, \tag{7}$$

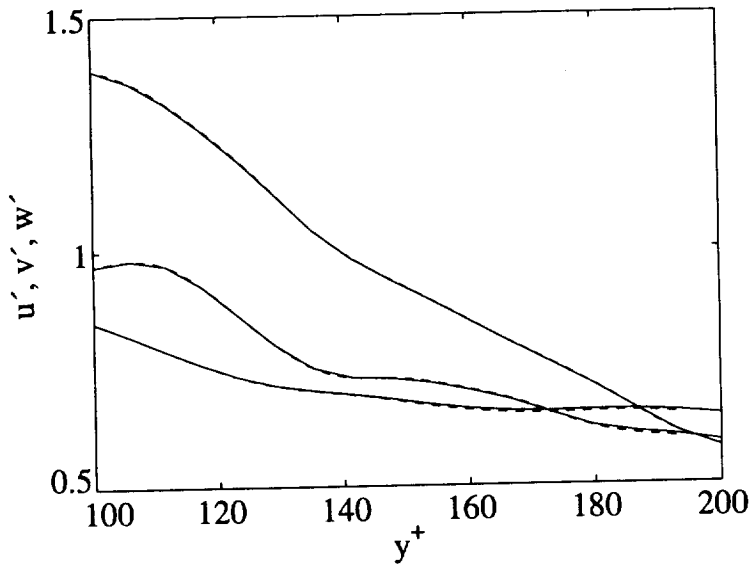

FIGURE 1. Validation of the code. ——— , full channel; ---- , half channel. Statistics taken over 2,000 time steps ($t^+ \approx 22$).

$$\Phi = \Phi_p + (a_1 + a_2)\Phi_1, \tag{8}$$

where a_1 and a_2 are chosen to satisfy the boundary conditions.

Pressure is obtained, whenever statistics are needed, by solving (Kim, 1989)

$$\nabla^2 p = -\nabla \cdot H, \tag{9}$$

where H is the nonlinear term of the Navier-Stokes equations. The boundary conditions for (9) are obtained from the y component of the momentum equation. At $y = 0$

$$\frac{\partial p}{\partial y} = \frac{1}{Re}\frac{\partial^2 v}{\partial y^2}, \tag{10}$$

and at the center of the channel

$$\frac{\partial p}{\partial y} = -\frac{Dv}{Dt} + \frac{1}{Re}\frac{\partial^2 v}{\partial y^2}. \tag{11}$$

These manipulations are done in Fourier space, where each coefficient is a function of two wavenumbers and of the physical location, y. To simplify the notation the dependence on the wavenumbers will not be made explicit in the following. Subindices refer to position in y and superindices to the time step.

The boundary condition for the mean streamwise velocity U at the center of the channel is either Dirichlet, taken from the full-channel DNS velocity profiles, or homogeneous Neumann, which uses the condition of symmetry. In all cases the mean spanwise velocity is set to zero.

The code was validated by running first a full channel, storing a time sequence of velocities at the central plane, and then running the half-channel code, using the previously saved planes as boundary conditions at $y = 1$. Very good agreement was obtained as shown in Fig. 1, even if the grids used in both cases were very different.

3. Approximate boundary conditions

The "exact" boundary conditions at the center of the channel were then replaced by several synthetic approximations.

3.1 Case A

The first approximate boundary condition was constructed as follows. We generated a plane of the velocity component u, with the same power spectrum and intensity as those in the interior plane $y \approx 0.9$ but with random phases. The v velocity component was generated using its own power spectrum from the same plane with phases such that the shear stress $|uv^* + u^*v|$ vanished for each Fourier mode. The asterisk stands for complex conjugation. The third velocity component was generated in a similar way, satisfying $|vw^* + v^*w| = 0$. This velocity plane was computed once at the beginning of the simulation and used at each time step after applying a translation by Ut where U is the mean velocity at the center of the channel, fixed through a Dirichlet boundary condition, and set equal to the constant mean value obtained in full-channel simulations.

Unsurprisingly, the results are bad (Fig. 2a). This case is similar to the severely scrambled one of Baggett (1997). The phases of his velocity fields were also random, and a linear combination was used to obtain the correct shear stress. The main difference was that his velocities were obtained from a full-channel run and then modified, thus maintaining the correct time scales. In both his and our cases the boundary conditions are completely uncorrelated from the rest of the domain, and a strong boundary layer is created between them and the first interior plane. This is due to the lack of turbulent structure of this boundary condition as will be shown by the next experiment.

Similar results were obtained in a previous test in which the boundary condition was built in the same way, but in which the phases of the velocities were regenerated independently for each time step.

3.2 Case B

In order to provide some turbulent structure for the boundary velocities, we used a velocity plane copied directly from the previous time step in the plane $y \approx 0.9$. The velocity u was rescaled to have the same r.m.s. fluctuation u' as in the statistics of the complete channel, and the other two velocities were linearly combined to have the correct intensities v', w' and shear stresses $\overline{uv} = 0$ and $\overline{vw} = 0$,

$$u_{bc}^{n+1} = \gamma_{00} u_{y=0.9}^{n}, \tag{12}$$

$$v_{bc}^{n+1} = \gamma_{11} u_{bc}^{n+1} + \gamma_{12} v_{y=0.9}^{n}, \tag{13}$$

$$w_{bc}^{n+1} = \gamma_{21} v_{bc}^{n+1} + \gamma_{22} w_{y=0.9}^{n}. \tag{14}$$

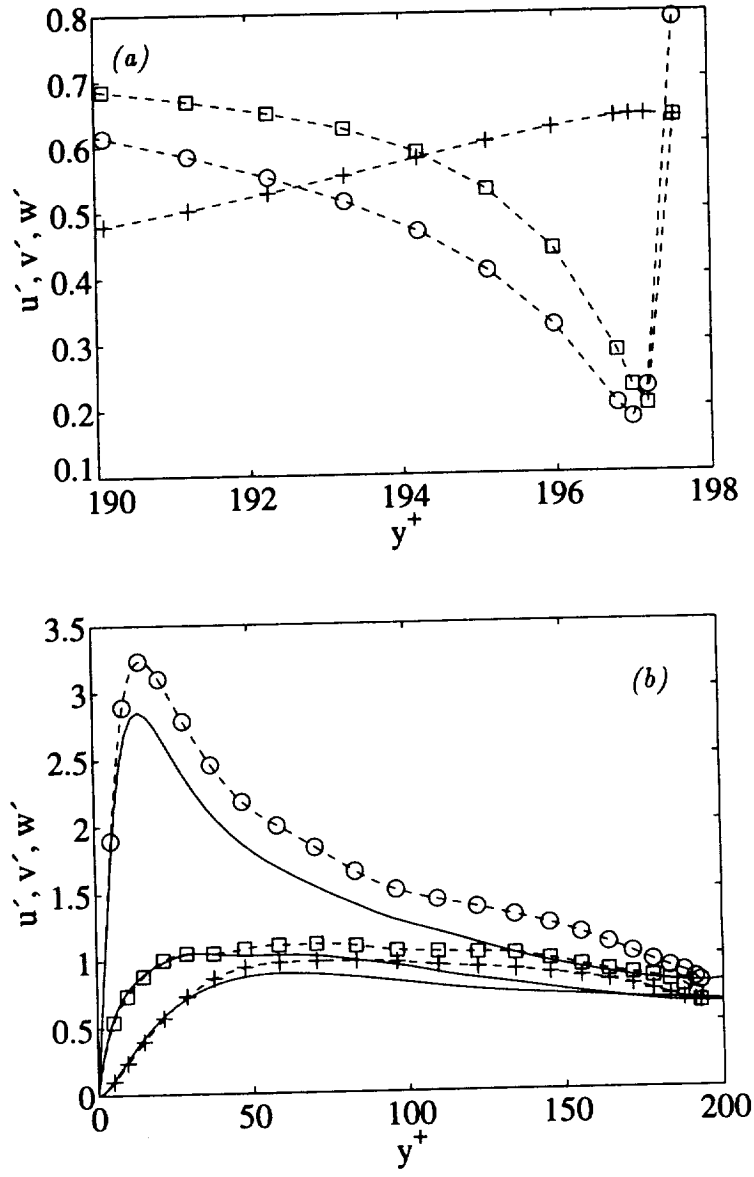

FIGURE 2. R.m.s. velocity fluctuations. o , u'; + , v'; □ , w'. *(a)* Case A. $t^+ \approx 72$. *(b)* Case B. $t^+ \approx 280$. ——— , full channel.

The same constants γ_{ik} were used for all of the Fourier modes. A Dirichlet boundary condition with the correct average velocity was used for U.

In this case (Fig. 2b), the strong boundary layer disappears as the boundary condition becomes correlated with the turbulent field. Nevertheless, u', v', and w' are not well reproduced, and the mean velocity profile (Fig. 4a) changes considerably,

increasing its slope in the vicinity of the center of the channel. This experiment was not run long enough to achieve fully converged statistics since it was clear that it was evolving in the wrong direction, especially for the mean velocity profile.

3.3 Pressure fluctuations

An interesting observation was that, in the last two cases, the structure of the pressure fluctuations was very different from that in a regular turbulent channel. A large peak appears near the center line (Fig. 3a), while the fluctuations of the full channel are minimum there (Kim, 1989). This was traced to large values of $\partial v/\partial y$ near the boundary, which enter the right-hand side of (9) as random delta-function pressure sources. Essentially this is a failure of continuity, which was not taken into account in any way in the previous experiments.

While it is clear that continuity cannot be imposed on a single plane and that the flow will react to any combination of boundary conditions for u and w by adjusting $\partial v/\partial y$, this derivative can conflict with the one implied by our boundary condition for v, resulting in very large values for the effective $\partial^2 v/\partial^2 y$, and in large pressures. The problem can be visualized by thinking of the boundary condition as an artificial wall, moving randomly and forcing the flow at the boundary. Whenever the moving wall and an interior eddy collide, high pressures are generated.

To further clarify the origin of the spurious pressure fluctuations, we present in Fig. 3b the pressure for an instantaneous flow field computed in three different ways. First we use the full equation, next we zero the right-hand side of (9) in the first eight planes near the center of the channel, and finally we keep the right-hand side but zero the boundary condition (11). The main contribution to the spurious pressure is seen to be the peak of the right-hand side of (9), and once it is removed the pressure fluctuations become consistent with those of a natural channel.

Since the spurious pressure derives from the solution of a Poisson equation, it permeates the channel to a depth which is of the order of the size of the largest eddies and has a global effect on the velocity profile.

Consider the integrated equation for the kinetic energy k of the velocity fluctuations

$$\phi(y) - \phi(0) = \int_0^y (P - \varepsilon + \nu \partial^2 k/\partial y^2)\,\mathrm{d}y, \tag{15}$$

where $P = -\overline{uv}\partial U/\partial y$ is the turbulent production, ε is the dissipation, and

$$\phi(y) = \overline{v(p+k)}, \tag{16}$$

is the diffusion energy flux. If an error Δp is made in the estimation of the pressure fluctuations at the boundary, it induces an error in the energy flux which is of order $\Delta\phi = O(v\Delta p) = O(u_\tau \Delta p)$. This extra energy has to be compensated in (15) by a change in the production since the dissipation is controlled by the turbulent cascade and is difficult to change. Since the stress $\overline{uv}$ is fixed by the momentum equation, only the velocity gradient $S = \partial U/\partial y$ is available to compensate the extra energy and its error is determined by the balance

$$|\overline{uv}| \int \Delta S\,\mathrm{d}y = u_\tau^2 O(\Delta U) = O(\Delta\phi). \tag{17}$$

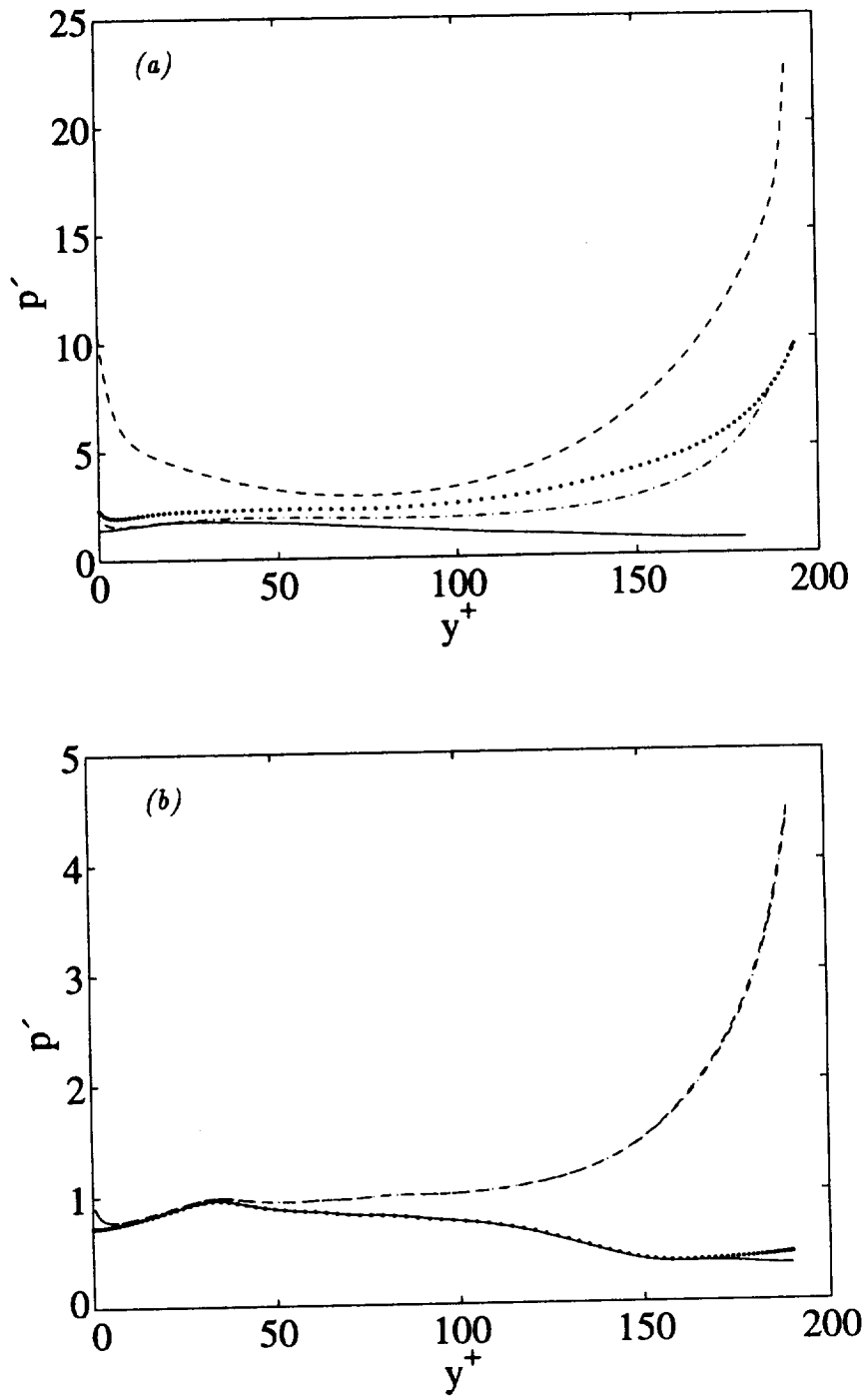

FIGURE 3. R.m.s. pressure fluctuations. *(a)* ——— , full channel; - - - - , case A; • • • , case B; —·— , case C. *(b)* Single field, case C. ——— , r.h.s. clipped and b.c. removed; • • • , r.h.s. clipped; - - - - , b.c. removed; —·— , full equation.

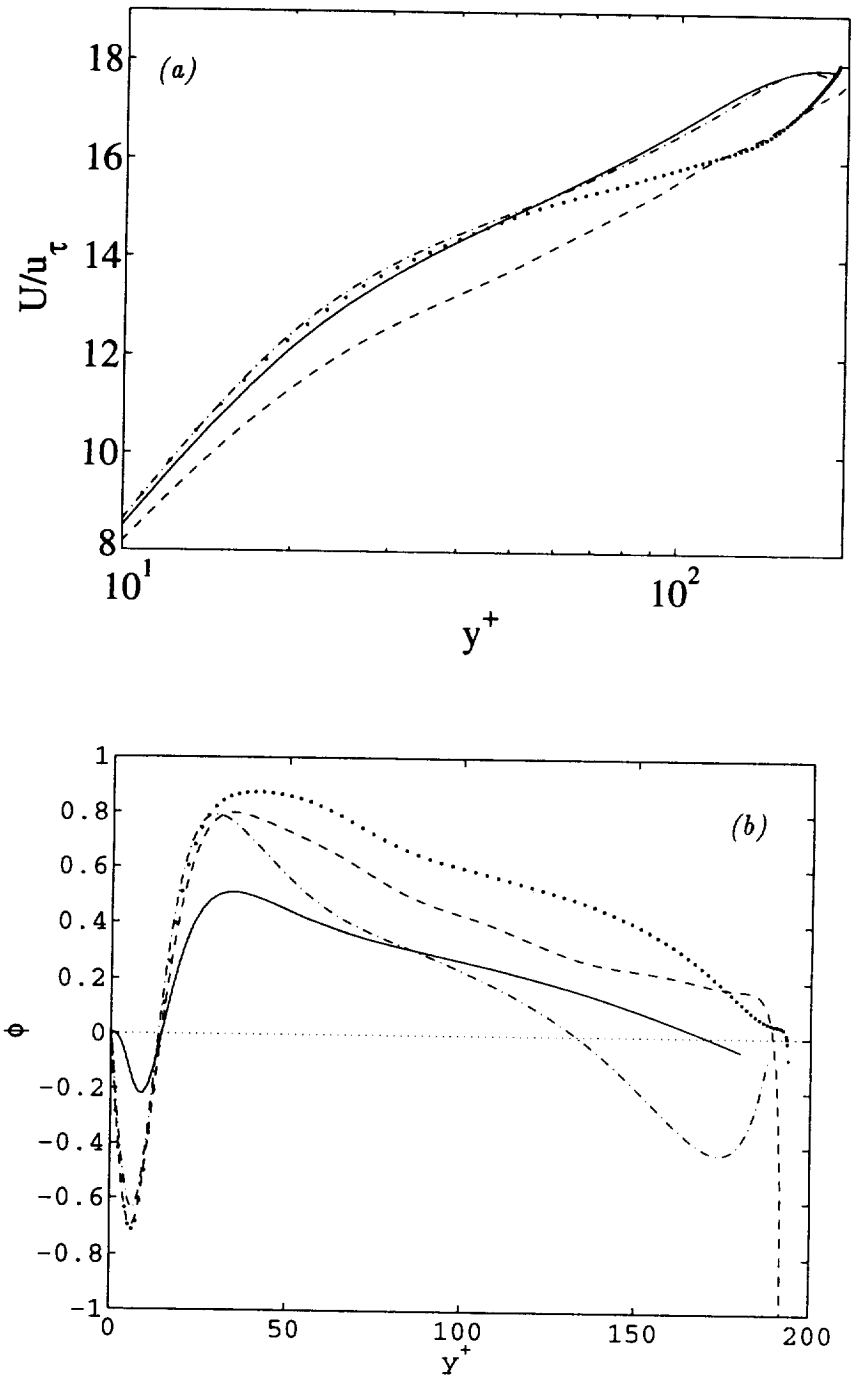

FIGURE 4. *(a)* Mean streamwise velocity. *(b)* Energy fluxes in the wall-normal direction. ——— , full channel; - - - - , case A; • • • , case B; —·— , case C.

The result is that $\Delta U^+ = O(\Delta p^+)$. Note that the effect on the mean profile can be expected to be largest near the center of the channel where the mean shear stress vanishes.

In case *A* where $\Delta p^+ \approx 20$, this gives errors comparable to the maximum velocity, as observed in Fig. 4a. In case *B* the errors in the pressure and in the mean profile, while milder, are still considerable. Note that in this figure as well as in Fig. 3, the different simulations have different values of Re_τ, both because of the errors introduced by the boundary conditions and because cases *A* and *B* were not run to full statistical convergence.

3.4 Case C

In an effort to decrease the velocity gradients at the boundary and, therefore, the magnitude of the spurious pressures and fluxes, a new condition was tried in which v at the boundary was obtained using an approximate continuity equation involving the velocities from the previous time step,

$$\frac{v_0^{n+1} - v_1^n}{\Delta y} = -\frac{\partial u_1^n}{\partial x} - \frac{\partial w_1^n}{\partial z}, \tag{18}$$

where the subindex $j = 0$ refers to the boundary plane and $j = 1$ to the first interior one. In this test u and w were copied from the plane $j = 1$ and then modified in the same way as in (12)-(14), using v in place of u and vice-versa. Previous tests had shown that the behavior of the boundary conditions was not very sensitive to the exact location of the plane from where the velocities were extracted. In this case the absolute values of the r.m.s. fluctuations were not given, and the intensities were forced to be equal in $j = 1$ and $j = 0$. This has the advantage that the correct intensities do not have to be known *a-priori* and is approximately equivalent to imposing zero derivatives for the intensities at the central plane and, therefore, to the condition of symmetry, but it should be emphasized that a Neumann condition was not imposed on individual Fourier components. A symmetry condition was also used for U, and the case was run to statistical equilibrium.

The results given in Fig. 5 are better than in the previous cases, with an agreement in the fluctuations which is particularly impressive given that their absolute values were not explicitly used at the boundary. The spurious peak pressure is also lower than before, but it is still substantial, and the Kármán constant of the mean velocity (Fig. 4a) is too low.

Figure 4b includes the energy flux for this case, which, contrary to the previous ones, is underestimated and becomes negative near the center. This means that energy is drained from the flow by the boundary condition rather than being injected as in the previous cases. It is interesting that, corresponding to this, the velocity overshoots the maximum near the central plane and then decreases slightly as the flow loses energy to the boundary. Note that the energy diffusion flux at the center of a full channel should be zero by symmetry.

4. Discussion and conclusions

We have tested several synthetic lateral boundary conditions at the central plane

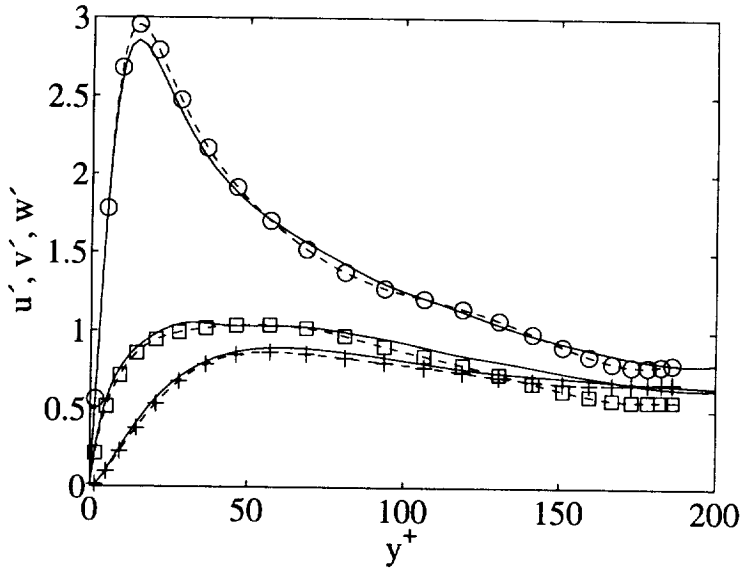

FIGURE 5. R.m.s. velocity fluctuations for case C. o , u'; + , v'; □ , w'; ——— , full channel. $\Delta t^+ \approx 2134$

of a channel flow with variable success. All of them are Dirichlet conditions for the three velocity components.

Conditions with no structure, even if they have an approximately correct power spectrum but random phases, develop a sharp boundary layer and become uncorrelated with the rest of the channel. Introducing information about the turbulent structure, which was done in our case by processing data from a different plane of the same computation, considerably decreases the intensity of the spurious boundary layer and leads to reasonably good results for some of the low order statistics, namely the r.m.s. intensities of the fluctuations of u, v, and w. This is especially true when the boundary conditions are tailored to take approximately into account the continuity constraint among the three velocity components.

Nevertheless the mean velocity profiles are poorly represented. This was traced to large errors in the pressure field and in the associated energy fluxes which, even if not explicitly used in our simulation code, have fluctuations near the boundary that are an order of magnitude larger than in regular channels. This is the result of a sharp peak in the right-hand side of the Poisson equation for the pressure, and derives from the attempts of the boundary conditions to locally violate continuity. Artificially removing that local peak restores the pressure fluctuations to their proper value. The peak in the source term is confined to the first few planes near the artificial boundary ($\Delta y \approx 0.04$), and can be approximated as $B(x, z)\delta(y-1)$, where δ is Dirac's delta function. The Poisson equation for the pressure sees this forcing as a spurious boundary condition for $\partial p/\partial y$, which overwhelms the real boundary condition (11). The errors in the pressure decay exponentially away from

the boundary with a scale length which is of the order of the energy-containing scales of the intensity B. That the scale length here is of the order of the channel width shows that the errors in the boundary condition are associated with the representation of the largest eddies.

The mathematical basis for the difficulty is easy to understand. For fully turbulent boundaries away from walls, viscosity can be neglected, and it is enough to analyze the problem for the Euler equations. Note that this would also be true in LES since the eddy viscosity of the subgrid terms would in that case be at most $O(u'\Delta x)$, and the Reynolds number based on it and on the macroscopic scales would still be large. The incompressible Euler equations, except for the pressure term, are hyperbolic with characteristics which coincide with the streamlines, and this fact is widely used in the design of inflow and outflow boundary conditions (see e.g. the discussion in Kreiss & Lorentz, 1989). Incoming flow needs Dirichlet conditions because the information is brought by the characteristics entering the domain, while outgoing flow does not for similar reasons. Lateral boundaries such as the one which occupies us here coincide with characteristics implied by the mean flow, and in that approximation no boundary conditions are needed or allowed along them.

Consider for example a two-dimensional flow in which the velocity is $(U+u_1, v_1)$, where $|u_1|, |v_1| \ll U$, and where the mean velocity U is constant. The equation for the perturbation is

$$\frac{\partial u_1}{\partial t} + U\frac{\partial u_1}{\partial x} + \frac{\partial p}{\partial x} = O(u_1^2/L), \tag{19}$$

where L is a characteristic eddy size, with a similar equation for v_1. Continuity is preserved automatically to lowest order, and in that approximation the pressure satisfies Laplace's equation and can be set to zero. The resulting equation for u_1 is hyperbolic and has no explicit dependence on y. Along boundaries on which y is constant, the solution is fully determined by the inflow at $x = 0$, and no further boundary condition is needed. In fact, a Galilean transformation to a frame of reference moving with the constant velocity U reduces (19) to

$$\frac{\partial u_1}{\partial t} + \frac{\partial p}{\partial x} = O(u_1^2/L). \tag{20}$$

This is an interesting equation which shows at once that the pressure fluctuations are $O(u_1^2)$ and that the Lagrangian accelerations are of the same order. It suggests that better boundary conditions for the general case could be constructed in the form

$$\frac{\partial u}{\partial t} + u\frac{\partial u}{\partial x} + w\frac{\partial u}{\partial z} = u_\tau^2 g_u, \quad \text{at} \quad y = 1, \tag{21}$$

where u_τ acts simply as a scale for the velocity fluctuations. The information in the boundary condition, including the external statistics and length scales, is contained in g_u, which should be $O(1)$, and it is easy to see that it can be interpreted as an applied stress. Such boundary conditions are presently being tested.

The work of C. V. was supported in part by the Spanish CICYT and by INTA. J. J. was supported by AFOSR under grant F49620-97-0210. We thank J. Baggett and W. Cabot for valuable suggestions on an earlier version of this manuscript.

REFERENCES

BAGGETT, J. S. 1997 Some modeling requirements for wall models in large eddy simulation. *CTR Research Briefs.* Center for Turbulence Research, NASA Ames/Stanford Univ., 123-134.

BAGGETT, J. S., JIMÉNEZ, J. & KRAVCHENKO, A. G. 1997 Resolution requirements in large-eddy simulations of shear flows. *CTR Research Briefs.* Center for Turbulence Research, NASA Ames/Stanford Univ., 51-66.

CHAPMAN, D. R. 1979 Computational aerodynamics development and outlook. *AIAA J.* **17,** 1293-1313.

JIMÉNEZ, J. & MOSER, R. 1998 LES: Where are we and what can we expect? *AIAA Paper 98-2891.*

JIMÉNEZ, J., PINELLI, A. & UHLMANN, M. 1998 Plane channel flow simulation over porous walls. *Tech. Note ETSIA/MF-9809,* School of Aeronautics, Madrid.

KIM, J. 1989 On the structure of pressure fluctuations in simulated turbulent channel flow. *J. Fluid Mech.* **205,** 421-451.

KIM, J., MOIN, P. & MOSER, R. 1987 Turbulence statistics in fully developed channel flow at low Reynolds number. *J. Fluid Mech.* **177,** 133-166.

KREISS, H. O. & LORENTZ, J. 1989 *Initial-boundary value problems and the Navier-Stokes equations.* Academic Press.

LE, H., MOIN, P. & KIM, J. 1997 Direct numerical simulation of turbulent flow over a backward-facing step. *J. Fluid Mech.* **330,** 349-374.

LEE, S., LELE, S. K. & MOIN, P. 1992 Simulation of spatially evolving turbulence and the applicability of Taylor's hypothesis in compressible flow. *Phys. Fluids A.* **4,** 1521-1530.

NA, Y., & MOIN, P. 1998 Direct numerical simulation of a separated turbulent boundary layer. *J. Fluid Mech.* **374,** 379-405.

SCHUMANN, U. 1975 Subgrid scale model for finite difference simulations of turbulent flows in plane channels and annuli. *J. Comput. Phys.* **18,** 376-404.

SPALART, P. R., JOU, W.-H., STRELETS, M. & ALLMARAS, S. R. 1997 Comments on the feasibility of LES for wings, and on a hybrid RANS/LES approach, in *Advances in DNS/LES, Proc. of the 1st AFOSR International Conference on DNS/LES,* Ruston LA, August 4-8, 1997 (C. Liu, Z. Liu and L. Sakell editors), Greyden Press, 137-148.

SULLIVAN, P. P., MCWILLIAMS, J. C. & MOENG, C.-H. 1994 A subgrid-scale model for large-eddy simulation of planetary boundary-layer flows. *Boundary-Layer Met.* **71,** 247-276.

Boundary conditions for LES away from the wall

By F. Nicoud, G. Winckelmans[1], D. Carati[2], J. Baggett AND W. Cabot

Artificial boundary conditions for LES away from the wall have been developed with the hope of avoiding the problem of grid refinement in the wall region of the LES. In the particular example of channel flow, the main idea is to replace the natural no-slip boundary conditions (at $y = 0$) by artificial boundary conditions at $y = y_1 > 0$. The one-point statistics (mean velocity and turbulence intensities) of the flow at y_1 are supposed to be provided externally. In practice, this information could be obtained from a RANS for the same flow. However, it is known that supplying only the one-point statistics of the velocity field is not sufficient for obtaining a reasonable core flow. The method developed here consists of building two-point statistics at the artificial boundary by using information from the core flow at $y = y_2 > y_1$. In particular, the time evolution of the velocity fields at $y = y_1$ and $y = y_2$ are assumed to be self-similar with a time scale ratio determined dynamically during the simulation. Encouraging results for the channel flow at $Re_\tau = 1000$ have been obtained when the domain removed from the simulation ($0 < y < y_1$) contains half of the grid points used in "full domain" LES of the channel flow.

1. Introduction

The grid refinement required in the near wall region has severely slowed the development of large-eddy simulation (LES) for flows of practical interest. Several techniques aimed at keeping the grid coarse in the near wall region have been investigated. Most of them supply artificial boundary conditions, either at the physical wall or inside the flow. In the latter case, the boundary conditions must compensate for the total absence of knowledge of the dynamics inside the unresolved wall region. In this preliminary study, we will only consider this type of off-wall boundary condition.

Previous studies (Baggett, 1997) have shown that providing the correct one-point statistics at the artificial boundary is not sufficient. Imposing only the mean velocity values and the mean turbulent stresses at the artificial boundary has been shown to lead to very poor results even in the simple geometry of the channel flow. Some information regarding the structure of turbulence should be imposed at the artificial boundary as well. In other words, at least the two-point statistics should have a reasonably correct value at the artificial boundary.

It is sometimes considered that going further than the second order statistics and trying to impose, for instance, third order moments of the velocity fluctuation is

1 Université catholique de Louvain, Louvain-la-Neuve, Belgium.

2 Université Libre de Bruxelles, Brussels, Belgium.

not necessary. As noted by Jiménez & Vasco (1998), this statement is debatable since some of the third order statistics of the velocity fluctuations correspond to the energy flux through the boundary. It might turn out that imposing this energy flux could be as important as imposing the wall stress. However, imposing the energy flux at the boundary is certainly quite difficult.

The purpose of this study is to investigate some new and very simple ideas for extrapolating from the core flow some information on the two-point statistics that should be imposed at the boundary. The artificial boundary conditions that we consider here only impose the first and second order statistics of the velocity fluctuations. In this first stage, we only consider LES of the channel flow for which we have a reference LES at Reynolds number $Re_\tau = 1000$ (Kravchenko, Moin & Moser, 1996).

2. Artificial boundary conditions

The underlying idea is to use some scaling law for reconstructing the velocity field at a certain distance from the solid boundary from the known velocity field in the core flow. For this reason, in this first study, we have focused on the channel flow for which a logarithmic profile is known to exist. In this domain, the size of the structures is supposed to grow linearly with the distance to the wall. In the channel flow at $Re_\tau = 1000$, both $y_1^+ = 100$ and $y_2^+ = 200$ are in the log-layer. We have thus considered several possibilities for reconstructing the velocity at y_1 from the velocity at y_2. First, we have considered the possibility of imposing a linear scaling law on the characteristic length scale for the velocity. However, we found that imposing the time scale of the velocity fluctuation is much easier and leads to better results. In practice, we have thus first assumed that the typical time-scale of the velocity fluctuation δv_i also follows a linear law in the log-layer. This can be expressed by:

$$\frac{1}{\langle(\delta v_i)^2\rangle} \left\langle \left(\frac{\partial \delta v_i}{\partial t}\right)^2 \right\rangle \propto y^{-2} \,. \tag{2.1}$$

This assumption is reasonable but it only relates statistical quantities at different values of y^+. The main assumption of our approach is to use this relation for connecting every point in the artificial boundary (y_1) with a point in another plane (y_2) which lies within the computed part of the flow:

$$\frac{1}{\sqrt{\langle(\delta v_i(y_1))^2\rangle}} \frac{\partial \delta v_i(y_1)}{\partial t} = \gamma_i \, \frac{1}{\sqrt{\langle(\delta v_i(y_2))^2\rangle}} \frac{\partial \delta v_i(y_2)}{\partial t} \tag{2.2}$$

where the γ_i should be equal to $y_2/y_1 = 2$ if the scaling law (2.1) were correct. In practice, $v_i'(y_1) \equiv \sqrt{\langle(\delta v_i(y_1))^2\rangle}$ is unknown and has to be provided as part of the boundary conditions while $v_i'(y_2) \equiv \sqrt{\langle(\delta v_i(y_2))^2\rangle}$ is directly measured from the computed part of the flow. Hence, the second order statistics must be provided at the boundary, as expected. The condition (2.2) will thus read:

$$\frac{\partial \delta v_i(y_1)}{\partial t} = \gamma_i \, \frac{v_i'(y_1)}{v_i'(y_2)} \frac{\partial \delta v_i(y_2)}{\partial t} \,. \tag{2.3}$$

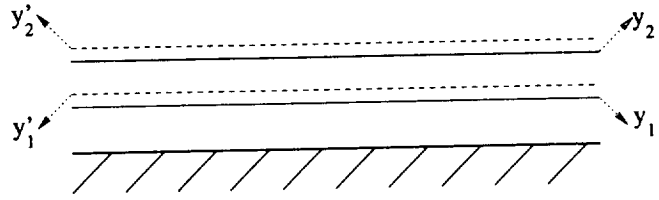

FIGURE 1. Schematic representation of the plane y_1, y_1', y_2, and y_2'.

In actual simulations, the condition has been implemented as follows:

$$\delta v_i(y_1, t + \Delta t) = \delta v_i(y_1, t) + \gamma_i \frac{v_i'(y_1)}{v_i'(y_2)} (\delta v_i(y_2, t) - \delta v_i(y_2, t - \Delta t)) \ . \tag{2.3}$$

Since the scaling (2.1) is not necessarily correct, we have also considered the possibility of estimating the value of the parameters γ_i during the course of the simulation. This dynamical estimation is done by using two additional planes inside the computed flow (see Fig. 1): plane y_1' just above y_1 and plane y_2' just above y_2 ($y_j' = y_j + \Delta y_j$, where Δy_j is the mesh size at plane j). The γ_i parameters measured for the pair (y_1', y_2') are used for connecting the planes (y_1, y_2).

Clearly, the artificial boundary conditions (2.3) do not determine the mean velocity value (first order statistics) which also needs to be supplied externally. The underlying idea of this approach is to connect the LES with an alternative and cheaper approach for the wall region. For instance, the mean velocity at the boundary $\langle v_i(y_1) \rangle$ and the turbulence intensities $v_i'(y_1)$ could be derived from a RANS. In the tests presented here, we have used the LES value from the other side of the channel when the other wall was treated classically. This is thus an asymmetric simulation. When both walls have been treated with the artificial boundary conditions described before (symmetric simulation), the first order statistics $\langle v_i(y_1) \rangle$ and the second order statistics $v_i'(y_1)$ have been taken from the LES of Kravchenko.

It must be noted that, in their present form, the artificial boundary conditions do not impose the stress $\langle \delta u(y_1) \delta v(y_1) \rangle$. Since this stress is perhaps the most important quantity in the wall region of a turbulent flow, it must be verified *a posteriori* that the predicted value is indeed correct.

The simulations that are presented in this report correspond to $n_x = 48$, $n_y = 65$, and $n_z = 48$. When the artificial boundary conditions are placed at $y^+ = 100$, 25% of the grid points are removed from the simulation in the asymmetric simulation and 50% in the symmetric one.

3. Numerical results

The first results we obtained were very disappointing. Trying to impose the linear law for the typical time scale of the velocity fluctuations ($\gamma_u = \gamma_v = \gamma_w = 2$

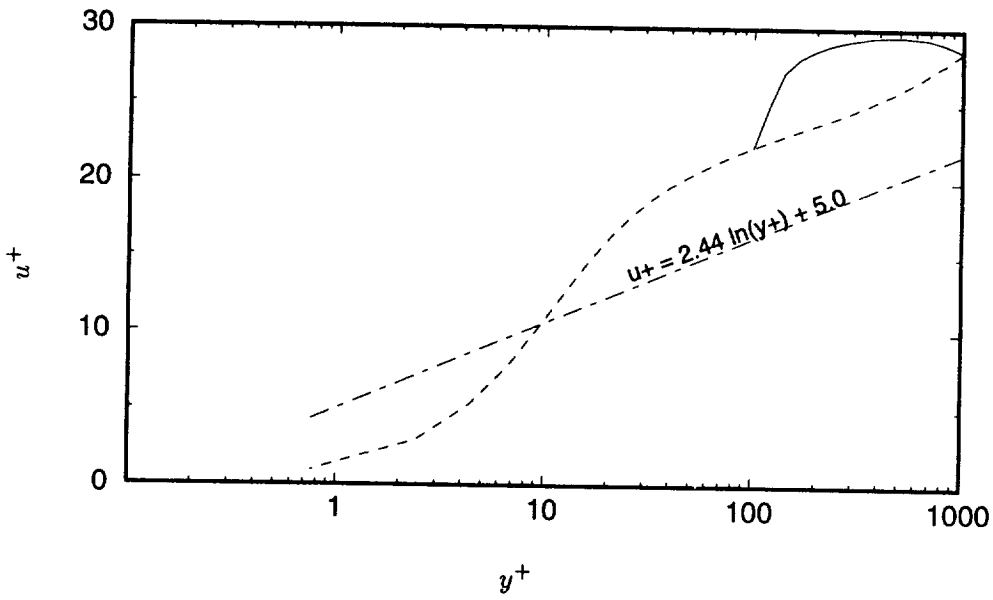

FIGURE 2. Mean velocity profile for the asymmetric computation. $\gamma_u = \gamma_v = \gamma_w = 2$. ——— : lower half, artificial boundary conditions; ---- : upper half, classical boundary conditions. Non-dimensionalization is based on the mean friction velocity.

leads to very poor results for all the relevant quantities. For instance, the mean velocity profile (Fig. 2) for the asymmetric computation was totally different in the upper half and the lower half of the channel. This shows that the artificial boundary conditions (2.3) with $\gamma_u = \gamma_v = \gamma_w = 2$ are not able to correctly mimic the dynamics of the flow between $0 < y^+ < y_1^+$.

This has strongly motivated the use of the dynamic evaluation of the parameters γ_i. As can be seen in Fig. 3a, when measured on the wall with classical boundary conditions, the dynamic values for these parameters are very close to 1.

This result is somewhat puzzling because it shows that the scaling argument used for motivating the artificial boundary conditions is not valid. In particular, the time scales (and the length scales) do not grow linearly in the log-layer of our LES. A possible reason for that is the lack of resolution in our coarse LES at $Re_\tau = 1000$, not only in y, but also in x and z; even on the "resolved" wall, the mean velocity profile does not fall on the curve $u^+ = 2.44 \ln(y^+) + 5.0$, see Figs. 2 and 3. Recall that LES's of the channel flow using structured grids (i.e., uniform Δx and Δz) are often quite coarse in x and z in the log region close to the wall; structures are not completely resolved there. Thus, the grid used here is not sufficient to capture the wide range of scales necessary for the expected scaling $\gamma_i = 2$ to hold. Another possibility is that the proposed scaling $\gamma_i = 2$ should not hold anyway because the dominant integral scale (in the streamwise direction) does not scale with the distance to the wall. This point should certainly be addressed further in a follow up of this work, using both DNS data and resolved LES data such as Kravchenko,

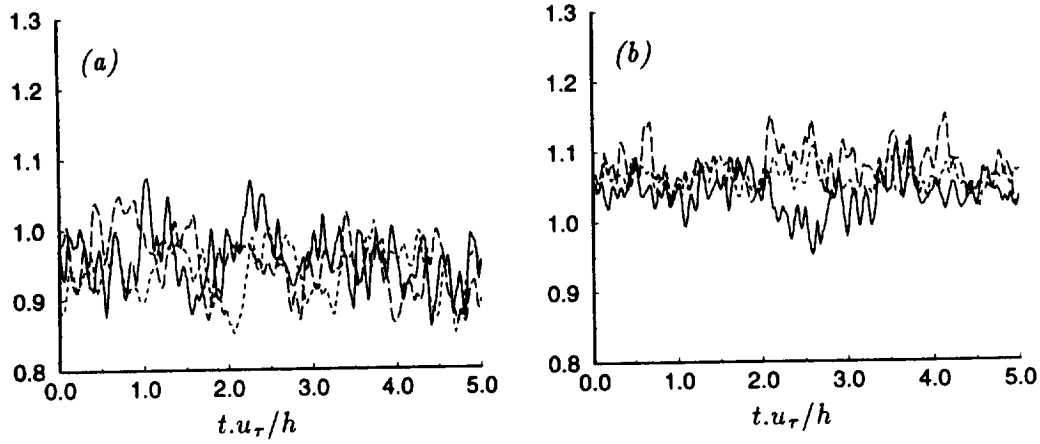

FIGURE 3. Time evolutions for the γ parameters. (a) upper half, classical boundary conditions; (b) lower half, artificial boundary conditions. ——— : γ_u; ---- : γ_v; — — — : γ_w.

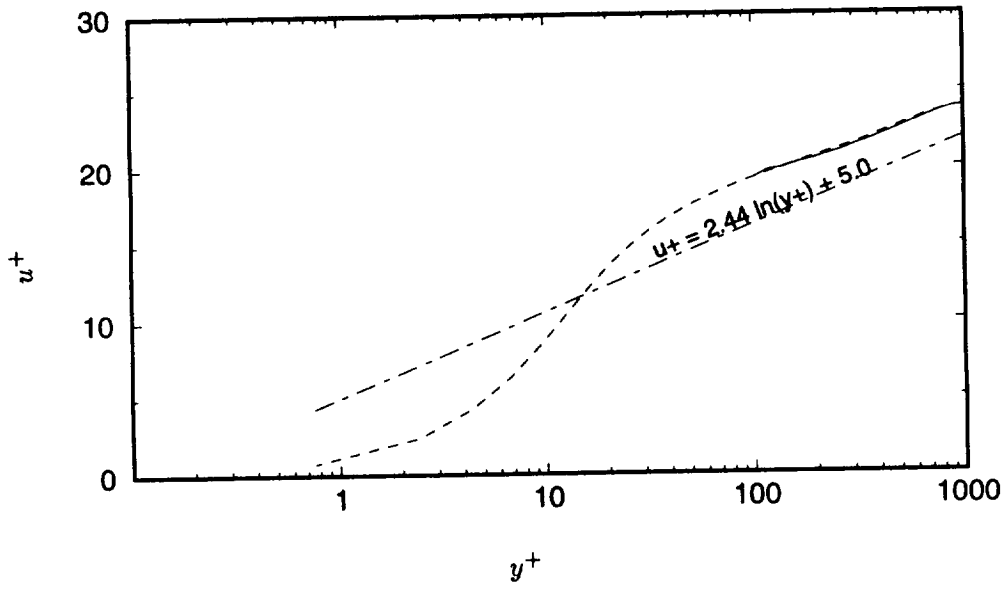

FIGURE 4. Mean velocity profile for the asymmetric computation. γ's computed dynamically. ——— : lower half, artificial boundary conditions; ---- : upper half, classical boundary conditions.

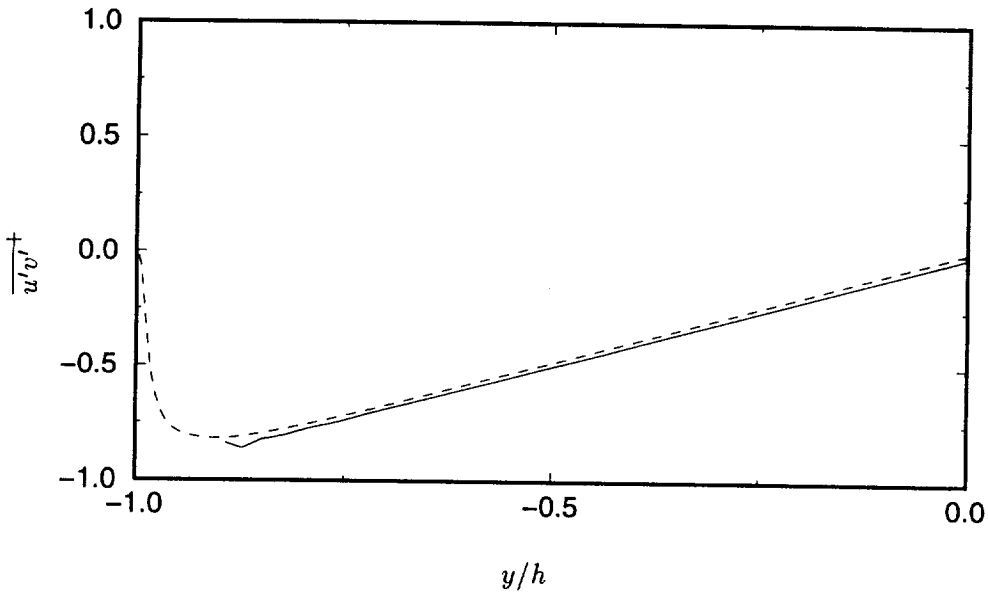

FIGURE 5. Resolved shear stress for the asymmetric computation. γ's computed dynamically. ——— : lower half, artificial boundary conditions; ---- : classical boundary conditions, upper half.

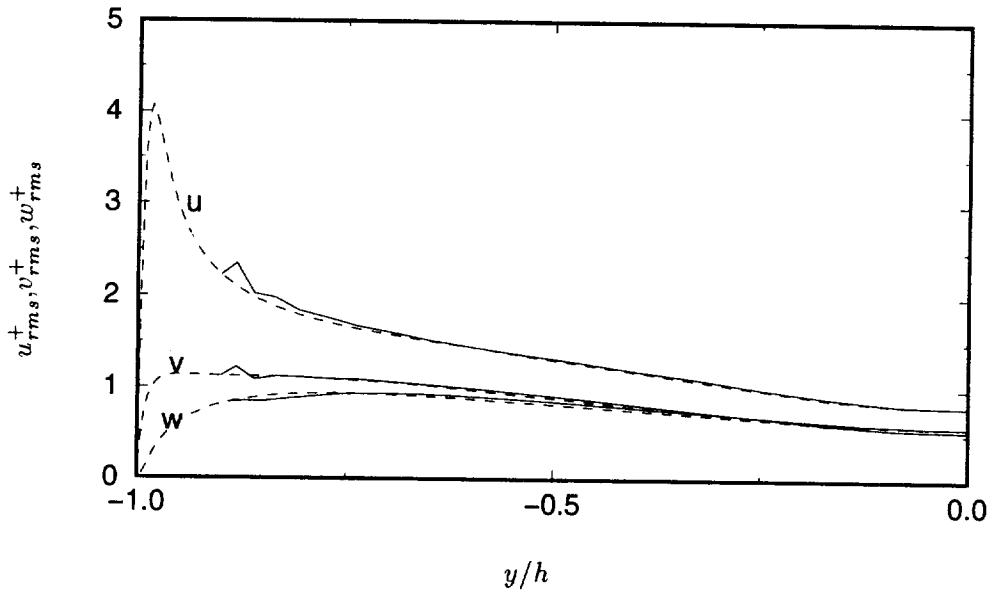

FIGURE 6. Turbulence intensities for the asymmetric computation. γ's computed dynamically. ——— : lower half, artificial boundary conditions; ---- : upper half, classical boundary conditions.

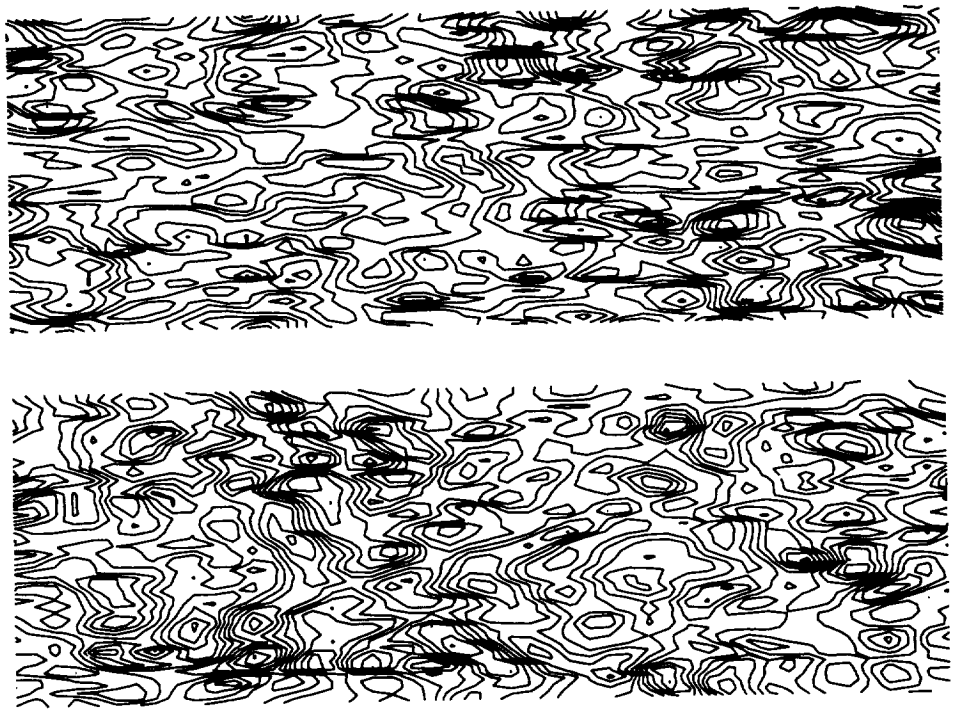

FIGURE 7. Iso-lines of v-velocity in the plane $y = 0.8h$ (top) and $y = -0.8h$ (bottom). γ's computed dynamically. Flow is from left to right.

Moin & Moser (1996).

Proceeding nevertheless, using the dynamic values of the γ_i into the artificial boundary conditions, leads to very interesting results. As shown in Fig. 3b, the computed values for γ_i near the wall with artificial boundary conditions remain close to unity although slightly greater than near the top 'resolved' wall. We present hereafter the results for the first and second order statistics through the channel.

Remarkably, all these quantities are almost symmetric although the boundaries on the two sides of the channel are treated very differently. This shows that the artificial boundary conditions with the dynamic computation of the parameters γ_i give a good representation of the velocity field at y_1. Note that the stress $\langle \delta u \delta v \rangle$ has the correct behavior although it is not prescribed explicitly by the boundary conditions.

The turbulence intensities and the stress show some fluctuations with respect to the expected values very close to the artificial boundary. This is due, in part, to the fact that the velocity fluctuations imposed by the artificial boundary conditions require rather severe fluctuations in the pressure field in order to enforce the

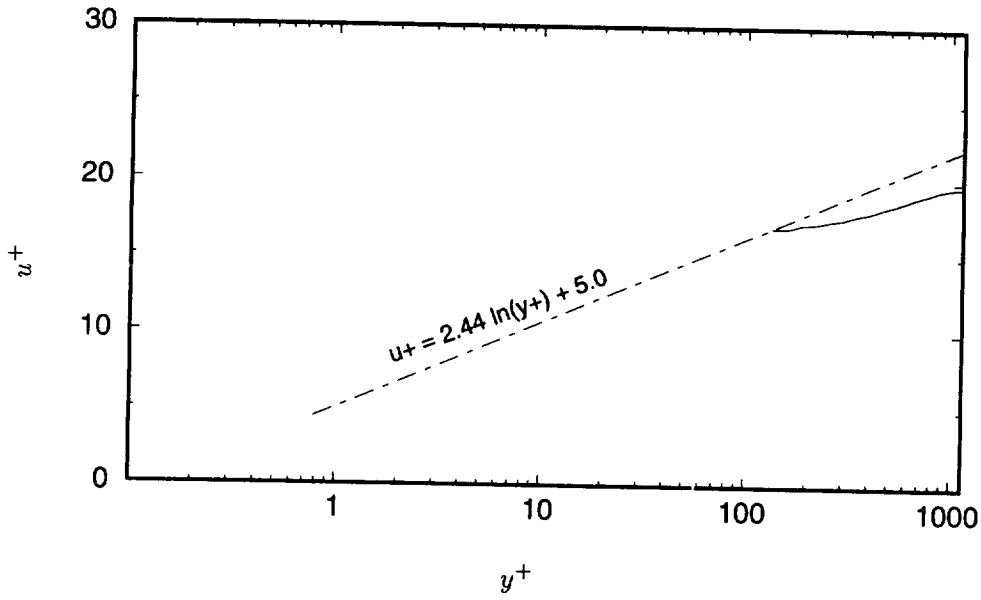

FIGURE 8. Mean velocity profile in wall units for the symmetric computation. γ's computed dynamically. Artificial boundary conditions on both sides.

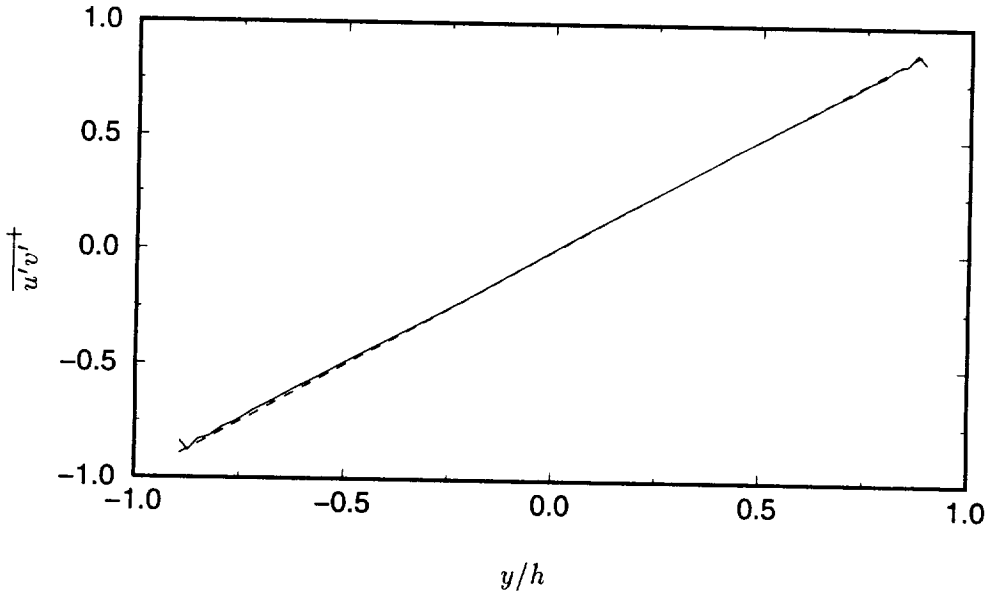

FIGURE 9. Resolved shear stress for the symmetric channel computation. γ's computed dynamically. ——— : artificial boundary conditions on both sides; - - - - : theoretical value.

incompressibility conditions. These pressure fluctuations might then propagate in the near boundary region and affect the velocity field (see Jiménez & Vasco, this volume).

The two-point correlations of the velocity field are not directly imposed by the conditions (2.3), but, of course, the velocity components produced by these boundary conditions are not random and do include some structures (see Fig. 7). However, the two-point statistics show that the turbulence structure is affected by the artificial boundary conditions (too large spanwise correlation near the artificial boundary).

These results remain, however, very encouraging. The fact that the flow remains almost perfectly symmetric even when the walls are treated differently shows at least that this approach should be investigated further. Unfortunately, the next step in the evaluation of the peculiar boundary conditions (2.3) is less conclusive. Indeed, we have tried to use the same conditions on both sides of the channel; the results for the mean profile are, of course, symmetric, but they differ strongly from the reference LES of Kravchenko. In general, it is found that the second order statistics are much better predicted than the mean velocity profile. A possible explanation could be that the energy flux through the boundary is not at all controlled by the conditions (2.3). A badly predicted energy flux could indeed affect the mean profile more than the second order statistics.

4. Conclusion

It is very difficult to draw any definitive conclusion from the the preliminary study presented here. However, we have shown that simple artificial boundary conditions can be built with many desirable properties. In particular, we have developed and partially tested a simple procedure to easily impose the correct amplitude for the first and second order statistics of the velocity field at the artificial boundary, while some information regarding the structure of the turbulent flow is fed to the boundary from the computed neighboring core flow.

This procedure has been very successful when used only on one side of the channel flow. This result is encouraging. Unfortunately, when used on both sides, the obtained mean velocity profile is substantially different from the reference profile (here, the one obtained when running the coarse LES with the classical no-slip boundary condition on both walls). Most probably, in the asymmetric computations, the upper channel with the classical no-slip boundary conditions imposes enough constraint to keep the velocity profile close enough to the reference.

The coarse LES used in this preliminary study is quite poor; the resolution is too coarse for this high $Re_\tau = 1000$ channel. A follow up of this work would certainly require repeating some of the investigations with a better resolution: either rerun the high Re_τ investigations, with and without the approximate boundary conditions, but with finer resolution (possibly requiring embedded grids close to the wall), or run lower Re_τ investigations.

Thus, it remains to be shown that good quality results can indeed be obtained with the type of artificial boundary conditions presented here when the reference numerics are better. In particular, further development could require adaptations

that enforce additional constraints on the various fluxes at the artificial boundary (e.g., stress and/or energy fluxes).

REFERENCES

BAGGETT, J.S. 1997 Some modeling requirements for wall model in large eddy simulation. *CTR Annual Research Briefs 1997,* Center for Turbulence Research, NASA Ames/Stanford Univ.), 123-134.

JIMÉNEZ J. & VASCO C. 1998 Approximate lateral boundary conditions for turbulent simulations, in the present volume.

KRAVCHENKO A. G., MOIN, P. & MOSER, R. 1996 Zonal embedded grids for numerical simulations of wall-bounded turbulent flows. *J. Comp. Phys.* **127,** 412-423.